CiPEG | Centre for Integrated Petroleum Engineering and Geoscience

UNIVERSITY OF LEEDS

Improved Reservoir Characterisation and Appraisal of Tight Gas Sandstones

Nichola Jane Eardley

Submitted in accordance with the requirements for the degree of Doctor of Philosophy

The University of Leeds

School of Earth and Environment

2017

Declaration of authorship

The candidate confirms that the work submitted is her own and that appropriate credit has been given where reference has been made to the work of others.

This copy has been supplied on the understanding that it is copyright material and that no quotation from the Thesis may be published without proper acknowledgement.

Acknowledgment

I wish to thank Prof. Quentin Fisher, my lead supervisor, for his support during my PhD. His guidance and expert advice has helped me during my research and writing my Thesis.

I would also like to thank Prof. Paul Glover, my co-supervisor, for his suggestions and feedback on my research work.

I wish to express my gratitude to my colleagues Dr Carlos Grattoni, Dr Samuel Allshorn, Phil Guise, Dr John Martin, Kirk Handley, Dr Javed Haneef, Dr Konstantin Rybalcenko, Dr Faraydoon Najm, Dr Devan Hussein and Dr Ida Shafagh for their helpful technical insights and suggestions as well as their personal support.

I want to acknowledge the contribution of my research sponsors: BP, BG, EBN, GDF, SHELL, and Wintershall for providing financial support as well as core material for my research.

I wish to thank The University of Leeds and School of Earth and Environment for accepting me as a student and providing me this opportunity.

Finally, I wish to thank my family and friends for their personal support and encouragement during my PhD.

Abstract

Tight gas sandstone (TGS) formations contain a large volume of natural gas but they are often only marginally economic to develop. Therefore, there is a need to understand the petrophysical properties in particular what controls porosity and permeability. Reliable methods need to be identified by cross comparing methods and data needs to be collected that is representative of reservoir conditions. Most importantly, there is a need to reduce reservoir characterisation timeframes by gaining data especially permeability without core analysis.

It has often been suggested that the delicate nature of clays within TGS means that they need to be cleaned using critical point drying. A comparative study found that this does not seem to be the case and cleaning samples with solvents such as DCM/methanol within a Soxhlet extractor is adequate. Rock types based on the type and distribution of clays have different trends on porosity-permeability plots. This means that it is possible to estimate permeability by combining downhole measures of porosity with microstructural analysis of either side-wall cores or cuttings. Permeability can also be estimated from mercury injection analysis, however, NMR, BET or QXRD do not appear to be reliable methods to estimate permeability unless improvements are made to the models or methods.

Key petrophysical properties (permeability, formation resistivity factor) are very stress sensitive due to the presence of small grain-boundary microfractures formed as the core is uplifted to the surface. However, flow properties are not likely to be as stress sensitive in the reservoir as they are in the laboratory. This means it is not beneficial to develop the reservoirs more slowly under high pore pressures (known as restricted rate practise) in the hope of maximising recovery and profitability.

This thesis overall contributes to the knowledge of the properties of TGS and obtains different conclusions by studying different rock types. New methodologies were created to study the effects of core plug cleaning and the stress dependency of TGS. Alternative faster methods to obtain permeability were also found. The work could be used to increase data accuracy, identify poor vs good reservoirs, find faster experimental methods for core labs and potentially use the data to understand waste disposal and trap systems based on fluid flow and pore connectivity.

Table of Contents

List of Figures

List of Tables

Chapter 1 - Introduction

Natural gas is currently one of the main sources of energy used in the world. Energy Information Administration (EIA) (2017) stated that the amount of electricity generated in the USA from natural gas has been steadily increasing since the 1990s. It has surpassed all other sources in 2016 and is predicted to continue to increase up to 2040 despite increases in alternative energy sources (Figure 1.1). Furthermore, around the world, the demand for natural gas by region and sector (in transport, power and industry) has been increasing since 1965. British Petroleum (BP) (2015) predicts the increase will continue at a similar rate until at least 2035 (Figure 1.2).

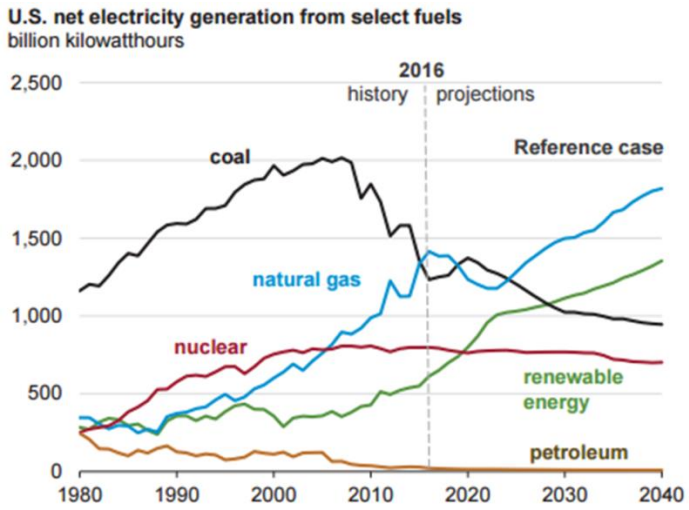

Figure 1.1 U.S electricity generation from selected fuels up to 2016 with predictions to 2040 showing that natural gas is predicted to surpass all other sources after 2025 (EIA, 2017).

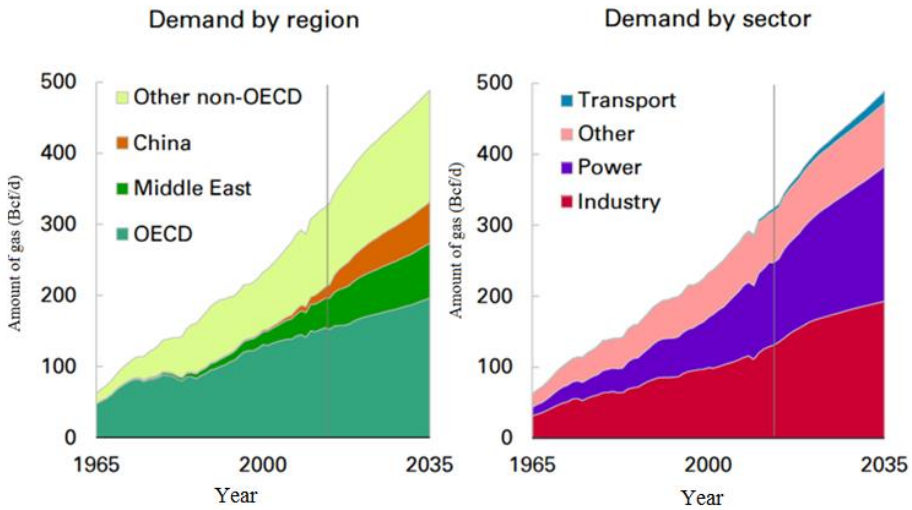

Figure 1.2 Increase in demand for natural gas by region and sector from 1965 to 2035 (BP Energy Outlook for 2035, 2015).

Traditionally, natural gas has been produced from conventional reservoirs in which the gas resides having migrated there from a source rock as a result of buoyancy. The gas is contained in the pore space and retained underground by a very low impermeable caprock (Figure 1.3). Conventional reservoirs contain only a small proportion of the gas that is known to exist in the subsurface, however, they are the easiest to exploit due to their permeability of 10 to 1000 mD (millidarcy) (Holditch, 2006) (Figure 1.4). Such reservoirs can be exploited by drilling wells into the structure and the gas is produced as a result of natural expansion.

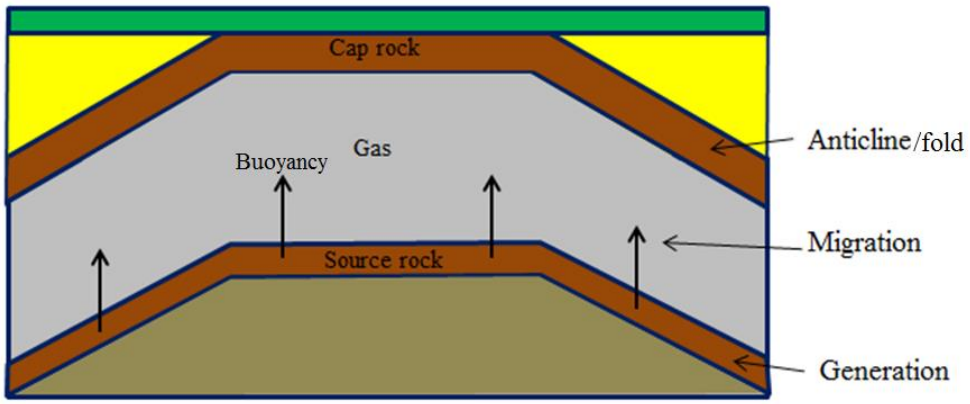

Figure 1.3 Gas migration from the source rock to the anticline structure by buoyancy, where the cap rock prevents the gas from escaping.

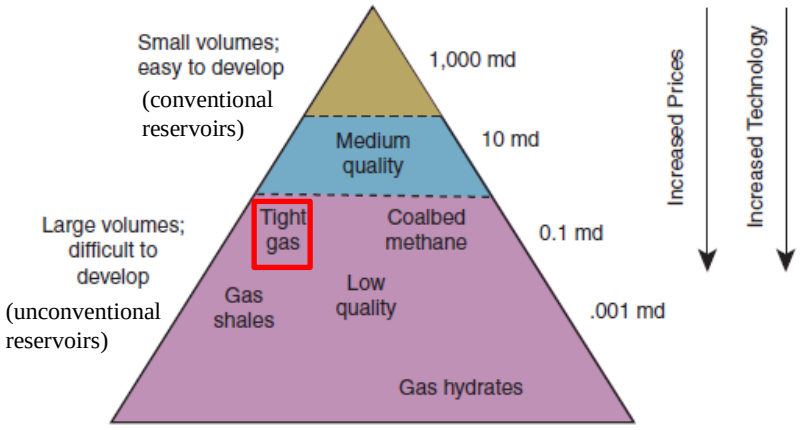

Figure 1.4 Resource triangle for natural gas with conventional reservoirs at the top and unconventional reservoirs at the bottom. The unconventional reservoirs have higher permeabilities and are easier to exploit but the reservoirs are smaller (Holditch 2006).

Many conventional gas reservoirs are nearing their completion so the petroleum industry has started to exploit gas from what are termed ‘unconventional reservoirs’. These include low permeability sandstones often referred to as ‘tight gas

sandstones', TGS, shales, coalbed methane and gas hydrates (Figure 1.4), this Thesis will focus on TGS. TGS are large reservoir deposits but they are difficult to develop, expensive and they require extensive production strategies such as horizontal wells and hydraulic fracturing.

TGS reservoirs are often only marginally economic to develop and they are time consuming, expensive and difficult to characterise in the laboratory. This is mainly due to the their low permeability, the fact that many properties (permeability and electrical resistivity) vary considerably as a function of the pore pressure and confining pressure and that large quantities of expensive core plugs need to be obtained for reservoir characterisation studies. The high cost and difficulty of reservoir characterisation adds to the unfavourable economics and increases the risk, therefore, companies could lose money. The expense of drilling wells and obtaining core plugs means that in many cases only a small section of the reservoir is cored. The results from core analysis can, however, be used to help interpret wire-line log measurements, these are generally taken throughout the drilled reservoir section. The length of time taken to measure properties in the laboratory is also a significant issue, it means that companies may need to wait a considerable amount of time after a well is drilled before making key decisions such as whether to abandon the prospect or hydraulically fracture the well.

A key challenge is therefore to increase the speed and accuracy of the characterisation of TGS reservoirs. The main aim of the current research is to achieve this by developing methods that rapidly characterize TGS reservoirs without the need for such extensive core analysis programs potentially from microstructure from SEM. The remainder of this introductory chapter provides an overview to tight gas sandstones – definition and characteristics (Section 1.1) and describes the objects, contributions and outline of this Thesis (Sections 1.2 and 1.3).

1.1 Tight Gas Sandstones: An Overview

1.1.1 Tight Gas Sandstone Definition

Reservoirs with a porosity of <10% and a permeability of <0.1 mD have been widely used as a definition of TGS (Kuuskraa, 1988; Holditch, 2006; Aguilera, 2008; Smith, 2009; Forsyth, 2011; Castillo, 2012). However, the flow rate of a TGS reservoir does

not depend solely on its permeability but also on the net pay thickness, the reservoir pressure, the fluid properties, the drainage area and the wellbore radius (Lee, 1982). In addition, profitable rates for tight gas sandstone resources in the USA are only achieved by using horizontal wells and/or extensive hydraulic fracturing. Therefore such production characteristics are often used as an alternative definition of tight gas sandstones rather than a specific porosity and permeability cut-off. In this sense, reservoirs with higher porosities and permeabilities might still be considered tight if they are located in places where horizontal wells and/or hydraulic fracturing are essential to produce them at economic rates. For example in offshore reservoirs, it is expensive to have many offshore platforms with several wells, therefore, one well is drilled and the reservoir is connected via horizontal wells.

1.1.2 Tight Gas Sandstone Petrophysical Characteristics

Tight gas sandstones (TGS) are composed of mostly quartz and feldspar (microcline and albite), together with a range of clays such as illite, kaolin as well as carbonates (Figure 1.5). The low permeability of these sandstones often results from the action of diagenetic processes, which are rock-fluid reactions that occur after the sand has been deposited (Ali, 2010; Fletcher, 2016). Clays often form as a product of the dissolution of unstable aluminosilicates such as feldspars (Figure 1.5) and can significantly reduce porosity and permeability. Kaolin tends to form at shallow depths whereas illite forms from kaolin at deeper depths under higher temperatures or pressures. Illite is a fibrous clay and tends to coat grains creating bridges across pore throats, whereas kaolin forms ‘stacked books’ which tend to infill pores (Figure 1.6). This morphology and structural position of clays within pore throats means that illite generally reduces permeability to a greater extent than kaolin.

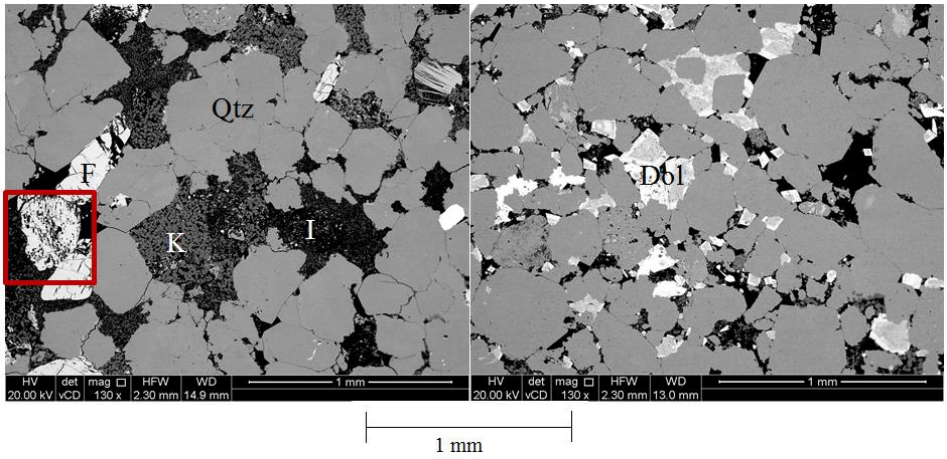

Figure 1.5 BSE image of the general microstructure of TGS showing the largest proportion of the rocks contain quartz (Qtz) with some feldspar (F), kaolin (K), illite, (I) and dolomite (dol) along with feldspar dissolution (red box).

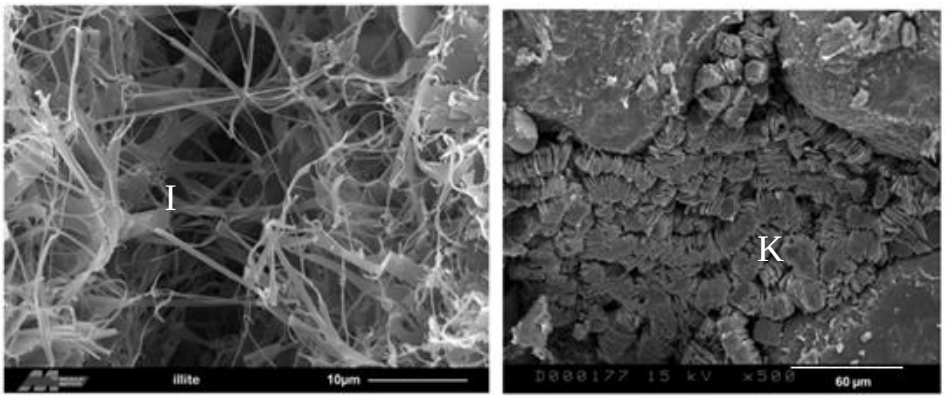

Figure 1.6 Illite (I) coating the grain surfaces and bridging pores (left) (Minersoc, 2016), and kaolin (K) infilling the pore space (right. As the illite coats grains and forms a fibrous network into the pore space the permeability is greatly reduced compared to when kaolin is present (Wilson, 2012).

Authigenic (precipitated in-situ) quartz can also dramatically reduce porosity and permeability; it generally forms during deep burial and may occur either as syntaxial (a mineral grows around another mineral of the same composition) overgrowths or outgrowths. Quartz overgrowths create sharp edges on the otherwise rounded sand grains, which makes them easier to identify (Figure 1.7). When there is extensive grain coating clay, quartz forms as outgrowths rather than overgrowths. The carbonate content of TGS can often dramatically reduce porosity and permeability as they infill large areas of the pore system. A wide range of carbonate minerals are found in TGS e.g. calcite ($CaCO_3$), dolomite (Mg replaces Ca in calcite), ankerite (the Mg in dolomite is replaced by Fe and Mn) and siderite (Fe carbonate). These may form throughout the burial history of TGS and their distribution is very difficult to predict.

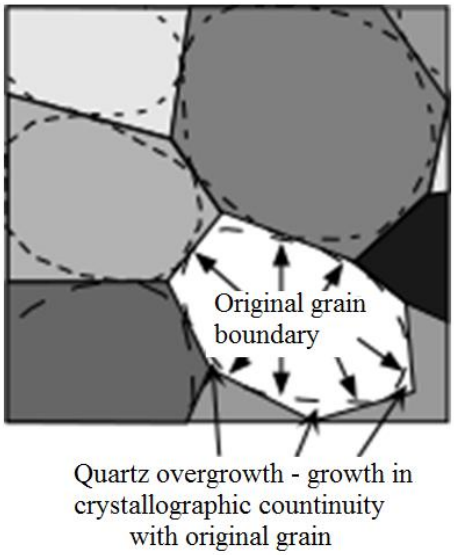

Figure 1.7 Quartz overgrowths around the original quartz grains. The overgrowth cement grows outward until it reaches the adjacent grain, this forms a interlocking texture and can reduce permeability significantly. The original grain can be identified if fine grained clay was originally present on the quartz grains (Tulane, 2016).

TGS have varied textures with a grain size of very fine to coarse grained, round to sub-angular grains, which can be very well sorted to poorly sorted. This texture depends upon the depositional environment (Tiab and Donaldson, 2004), i.e., alluvial fans (mass of sediment flows off a mountain or into the deep ocean), streams and lakes, dunes, deltas (river flows into the sea or a lake), beaches, turbidites and offshore sandbars (Jones, 2011) (Figure 1.8). TGS can also have small pore throats ranging from 30 nm to <2 μm (Nelson, 2009). They often have grain boundary microfractures (at the μm scale) (Figure 1.9) which represent a small portion of the total porosity but have disproportionate control on the permeability (Castillo, 2012). Primary and secondary porosity can be present. Primary porosity is formed during the deposition of the sediment between grains (intergranular) or between cleavage planes on minerals (intercrystalline). Secondary porosity is formed from the dissolution of grains or by fracturing, where the latter usually cuts through the existing grains or microporosity within the clay minerals (Figure 1.10).

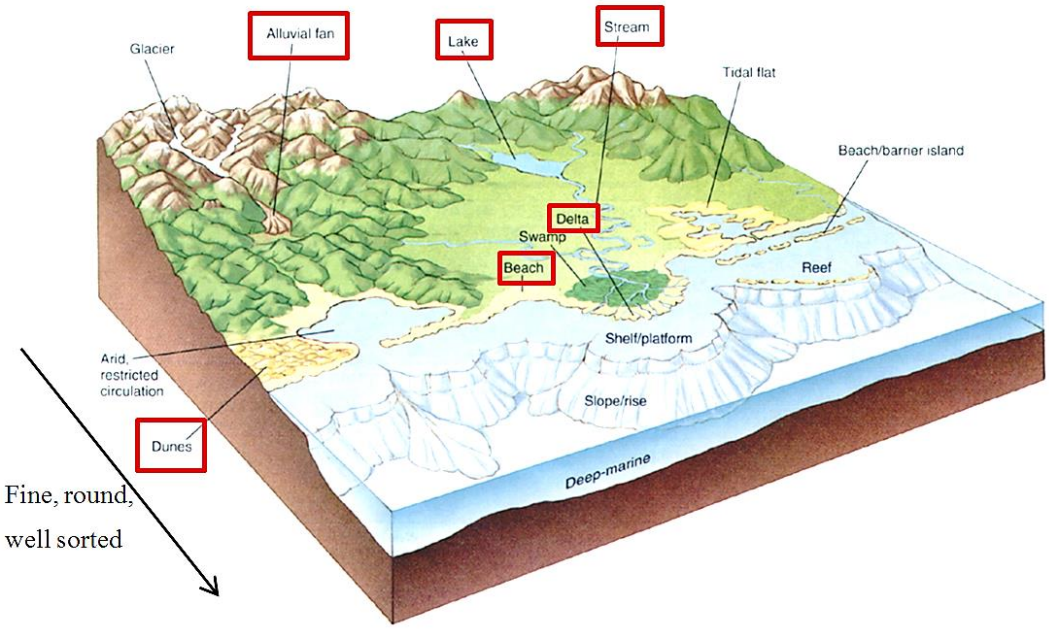

Figure 1.8 Sedimentary depositional environments where sandstones are usefully deposited – dunes, alluvial fans, lakes, streams, beaches, deltas, turbidites. Those deposits further from the source will be finer, rounder and more well sorted (Jones 2001).

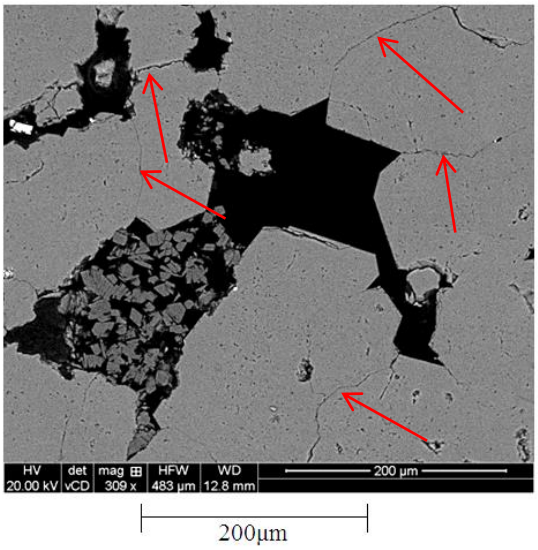

Figure 1.9 BSE image showing the microfractures that surround the grains (red arrows). They form a small volume of the overall porosity but their closure can have a large control on permeability.

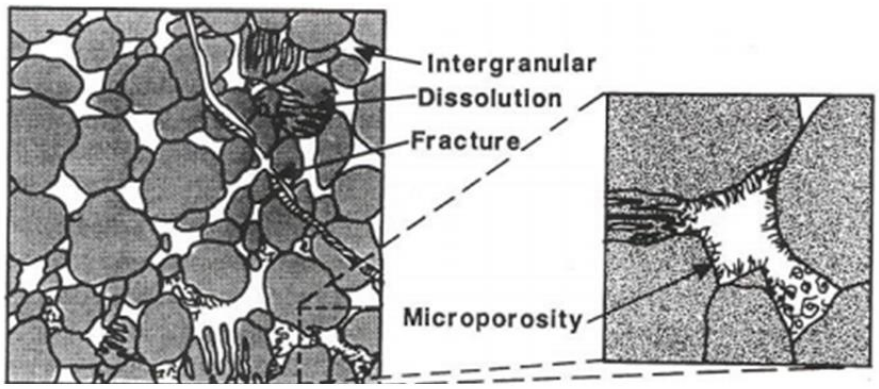

Figure 1.10 Primary porosity –intergranular between grains and secondary porosity - dissolution of feldspar, fractures and microporosity between clay grains (Tiab and Donaldson, 2004).

1.1.3 Issues of Extracting Gas from TGS Reservoirs

Many uncertainties still exist in the exploration, appraisal and production of tight gas sandstones (TGS) reservoirs and there will always be pressures to reduce costs throughout the value chain. The first three issues described below are addressed within this Thesis, while the last two are important to consider when producing gas from TGS reservoirs.

- Depending on the gas price it is very costly to extracting gas from TGS and they are usually only marginally economic to develop. To determine whether it is worth drilling low quality rocks like TGS, information about the petrophysical properties of the rock and what controls porosity and permeability are required.
- Undertaking a representative study of TGS in the laboratory requires a lot of core material as there are a lot of experiments that are needed to understand the properties, however, it is time consuming and costly to extract core from the subsurface. This is because each tripping round of the coring operation has to be carefully planned and the well has to be designed accordingly to take a particular amount of core from a pre-defined depth. In addition, many downhole tools are of limited use as they cannot directly measure key properties such as permeability and generally need calibrating with core analysis data.
- A large number of TGS properties are extremely sensitive to the confining and gas pressure under which measurements are made (Fatt, 1952; Vairogs et al., 1971; Farquhar et al., 1993 and Al-Hinai, 2008). It is therefore important to understand whether the flow properties of rocks are stress sensitive in the

subsurface and if so: (i) acknowledge that experiments within the laboratory should be performed at *in-situ* conditions, and (ii) companies may wish to develop the reservoirs more slowly under high pore pressures (known as restricted rate practise) in the hope of maximizing recovery and profitability.

- It is important to identify the highest permeability areas that create the most promising pay zones. This is however difficult as they often occur in complex deep geological structures which have been affected by regional tectonics (Holditch, 2006). This can have implications on the strength of the rock, bore hold stability, hydraulic fracturing propagation, geophysical surveys and wireline logs, and may significantly increase costs potentially making a discovery unprofitable.
- There is a need for effective production strategies. For example, much of the reservoir volume needs to be connected to reduce the number of wells needed to drain the reservoirs. This requires up-to-date vertical and horizontal wells with single and multiple hydraulic fractures.

1.2 Objectives

The main issues of extracting gas from tight gas sandstones (TGS) were outlined in Section 1.1.3. Improvements in characterisation of TGS and methods for core analysis are the two main aims. The specific objectives of this research are:

- An improved understanding of the petrophysical properties of TGS using a range of instruments and techniques.
- Understand what controls porosity-permeability relationships by dividing TGS according to attributes such as their mineralogy, microstructure and depositional environment.
- An investigation into the most appropriate and cost effective methods to clean core plugs by comparing different cleaning methods and finding the methodology which does not affect the petrophysical properties especially the microstructure.
- Reduction in timescales for reservoir characterisation by gaining petrophysical data especially permeability without the need for core analysis. Measurements which do not require core plugs such as scanning electron microscope (SEM), nuclear magnetic resonance (NMR), mercury injection capillary pressure

(MICP), quantitative X-ray diffraction (QXRD) and surface area analysis; the Brunauer-Emmett-Teller (BET) methods were utilised and analysed.

- To determine the effects of stress on porosity, permeability and the electrical properties, to review MICP permeability estimations under stress and to determine the cause of the stress dependency and whether properties of TGS are stress sensitive in the subsurface.

This research work is important as TGS are only marginally economic so rock properties have to be understood further. Also, methods have to be compared, alternatives found and improvements made to make experiments more accurate. Therefore, this work will contribute to the knowledge already available on the pertrophysical properties of TGS by presenting results from a range of experiments made on a variety of rock types, present new methods that have been designed to support or disprove other research work and identify faster methods that can be utilised instead of core plugs. The research work can be used to identify reliable methods, locate good vs poor reservoir for reservoir engineers, reduce experimental time frames for core labs and potentially use the data to understand waste disposal and trap systems.

1.3 Outline of the Thesis

The remainder of this Thesis is divided into the following 8 chapters.

- **Chapter 2** provides a review of the main topics addressed within this Thesis including - key petrophysical properties (porosity, saturation, permeability, wettability, surface and interfacial tension, capillary pressure, diagenesis), the stress sensitivity of petrophysical properties, electrical properties and the main methodologies used as well as rock typing.
- **Chapter 3** describes the samples analysed, sample preparation techniques as well as the experimental methods and instrumentation used during the study.
- **Chapter 4** provides a comparison of the petrophysical properties (porosity, permeability, electrical properties, pore size, composition, pore throat size and microstructure) of TGS after cleaning samples using four different methods (i) Soxhlet extractor with dichloromethane (DCM)/methanol, (ii) Soxhlet extractor

with toluene, (iii) critical point drying with CO_2 and acetone and (iv) critical point drying with CO_2 and methanol.

- **Chapter 5** presents a routine core analysis (RCA) program (porosity, permeability, microstructure and QXRD) on core plugs and off-cuts from 25 TGS. It looks in particular into what controls porosity and permeability, the effects of pore pressure equilibrium time on permeability, brine permeability vs gas permeability, estimating permeability and flow rates using microstructure and QXRD data and the accuracy of RCA methodologies.
- **Chapter 6** presents a special core analysis (SCAL) program (electrical, NMR, MICP and BET) on whole core plugs and off-cuts from 25 TGS. It looks in particular at the relationships between porosity and the electrical properties, estimating permeability using NMR, BET and MICP data and the accuracy of SCAL methodologies.
- **Chapter 7** presents the effects of stress on porosity, permeability, electrical properties and MICP data.
- **Chapter 8** studies the closure of microfractures under stress, their possible effect on the stress dependency found within TGS in the laboratory and how this stress dependency is extrapolated to the subsurface.
- **Chapter 9** provides a conclusion with a summary, recommendations for future work and how the research work contributes and can be applied to core labs and reservoir engineering's.

Chapter 2 - The Petrophysics of Tight Gas Sandstones – A Review

This chapter provides a review of key petrophysical properties important to the characterisation of TGS reservoirs and the background theory of the methodologies used to study TGS. The chapter starts by reviewing porosity, saturation, permeability, wettability, surface and interfacial tension, capillary pressure, diagenesis, stress sensitivity of the properties of TGS and also the electrical properties (Section 2.1 to 2.9). This is followed by the background theory of the main methodologies used where a detailed methodology is presented in Chapter 3 (Section 2.10) and an investigation into rock typing (Section 2.11).

2.1 Porosity

Porosity (ϕ) is the proportion of pore space within rocks and can be expressed as either a fraction or percentage (Asquith, 1982; Nimmo, 2004; Tiab and Donaldson, 2004). Porosity may be classified as either effective or total where the effective porosity is a measure of the connected voids, and the total porosity is a measure of the total void space both connected and isolated (Tiab and Donaldson, 2004). Knowledge of the porosity of a reservoir rock is crucial because it provides a measure of the potential of the rock to store petroleum.

The porosity of freshly deposited sands is independent of grain-size and is controlled by grain-sorting and grain-packing (Beard and Weyl, 1973). Porosity decreases as grain sorting becomes poorer (Beard and Weyl, 1973; Cade et al., 1994) as the finer grains infill the coarser grains. It should, however, be noted that many diagenetic reactions which are rock-fluid reactions that occur after the sand has been deposited (Ali, 2010; Fletcher, 2016) are controlled by surface area so although grain-size might not impact the initial porosity of a sandstone it may have a significant impact on its final porosity. For example, quartz cementation is one of the main diagenetic processes responsible for the reduction of porosity in sandstones during deep burial and its rate is controlled by the reactive surface areas of quartz available for precipitation (Walderhaug, 1996).

Grain packing also has a significant impact on the porosity of sands prior to diagenetic alteration. It can be defined as reduction in porosity as a consequence of

the reduction in bulk rock volume (Cade et al., 1994). For example, a group of spheres with equal grain-sizes will have a porosity of 48% if the packing is cubic, and a porosity of 26% if the packing is rhombic (Figure 2.1). However, such arrangements are idealistic representations and in reality sediments may have different sized grains and packing. These arrangements vary throughout the rock leading to differences in porosities within one sample. For example, a sample which has both cubic and rhombic packing may potentially have an average porosity between 48% and 26% i.e. 37%. In addition to the two types of packing arrangements, if the grain size also varies where there is both fine and coarse grains, the porosity will reduce below 37% as the finer grains will infill the coarser grains.

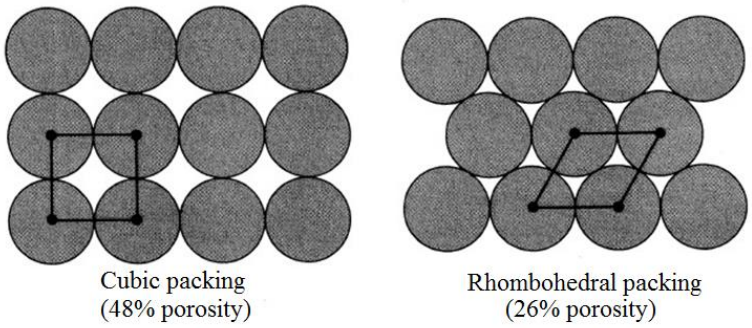

Figure 2.1 Porosity of a pack of spheres with cubic packing (left) and rhombic packing (right). The cubic packing has a porosity of 48% and the rhombic packing has a porosity of 26%.

The detrital clay content of sandstones, which is the deposits that have been transported from elsewhere, also has a significant impact on grain-sorting and hence porosity. For example, Revil et al. (2002) provided a theoretical model showing the impact of sand:clay ratios and sorting on porosity (Figure 2.2). The clean sand has a porosity that equals ϕ_{sd} (40%) but as clay is added to the mixture the porosity begins to decrease because the pore space gets filled with clay and the sorting is reduced. Eventually, a critical clay content is reached where all the macro-pores are filled with clay and microporosity (ϕ_m). If the clay content is increased beyond this point, the clay will replace the sand grains, which causes the porosity to increase as less pore space is filled by the sand grains and the sorting increases. The pure shale member has the highest porosity of 60% at ϕ_{sh} because the shale matrix which has porosity replaces sand grains with zero porosity.

Laminated sediment (layers of different types of sediments e.g sand and clay or different porosities) has a higher porosity than would be assumed based simply on the grain-size distribution as it could be composed of layers of well sorted grains. For example, two laminated sediments one containing 60% layers of pure sand, and one 40% layers with pure shale, would have an overall porosity of 40% or 60% respectively (Figure 2.2). In comparison a homogeneous sediment containing 60% sand and 40% clay would have a porosity of 24% (Figure 2.2) as the clay infills the sand grains and reduces the sorting.

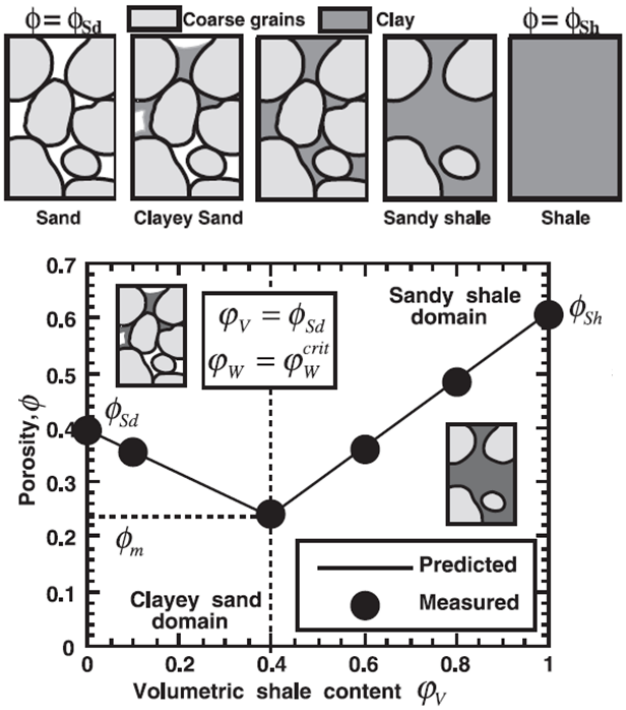

Figure 2.2 Porosity as a function of volumetric shale content. The sample with only sand grains have a porosity of ϕ_{sd}*. The porosity then decreases as the pore space is filled with shale and the sorting decreases. The minimum porosity of 24% is the critical point whereby all the pore space is filled with clay (*ϕ_m*). The porosity then increases to 60% as the sand grains are replaced by shale whereby the sand has zero porosity (*ϕ_{sh}*) (Revil et al., 2002).*

2.2 Saturation

In rocks containing two or more immiscible phases (i.e. brine, gas and/or oil), the proportion of pore space filled with a specific phase is referred to as the fluid saturation (Tiab and Donaldson, 2004; Amiri, 2015). Saturation is expressed as a fraction, or percent, of the total pore volume occupied by the water (S_w), oil (S_o) and/or gas (S_g). For example, the gas saturation in a rock is calculated using:

$$S_g = \frac{V_g}{V_p} \qquad \text{Equation 2.1}$$

where S_g is the gas saturation (%), V_g is the volume of gas in the rock (m^3) and V_p is the total pore volume of the rock (m^3). Saturation needs to be determined accurately when attempting to characterize petroleum reservoirs because it is needed to calculate the initial volume of petroleum present, which then allows calculations on the potential profit that may be gained by exploiting the reservoir (Amiri, 2015).

2.3 Permeability

The Hagen-Poiseuille flow equation for flow through a straight pipe was derived by Leonard Poiseuille and Gotthilf Hagen (1938-1939):

$$Q = -\frac{\Delta P \pi r^4}{8\mu L} \qquad \text{Equation 2.2}$$

where Q is flow rate (cm^3/s), ΔP is the change in hydrodynamic potential (*atm*), r is pipe radius (cm), μ is viscosity (cP) and L is pipe length (cm). In 1856, Darcy investigated the flow of water through sand filters for water purification. He noticed that the rate of flow of a single phase incompressible fluid flowing horizontal through the porous medium was directly proportional to the hydrodynamic potential applied, the area open to flow and is inversely proportional to the viscosity of the fluid and the length of the porous media, this is referred to as Darcy's Law:

$$Q = -\frac{K\,A}{\mu}\frac{\Delta P}{L} \qquad \text{Equation 2.3}$$

where K is permeability (mD) and A is area (cm^2). Permeability is important as it provides the flow capabilities of the reservoir and therefore how much gas will be produced.

The relationship presented in Equation 2.2 suggests that flow is dependent upon the radius of the pores (i.e. r^4). This equation is consistent with more sophisticated numerical modeling and laboratory data, which shows that permeability reduces as grain-size gets smaller and the sorting gets worse (Figure 2.3 and Table 2.1). The smaller the grains, the smaller the pores and the lower the permeability. If the

smaller grains infill the larger grains the permeability reduces. Grain size is particularly controlled by sedimentary environment. Therefore, it would be expected that sedimentary facies would have a primary control on the permeability of the samples.

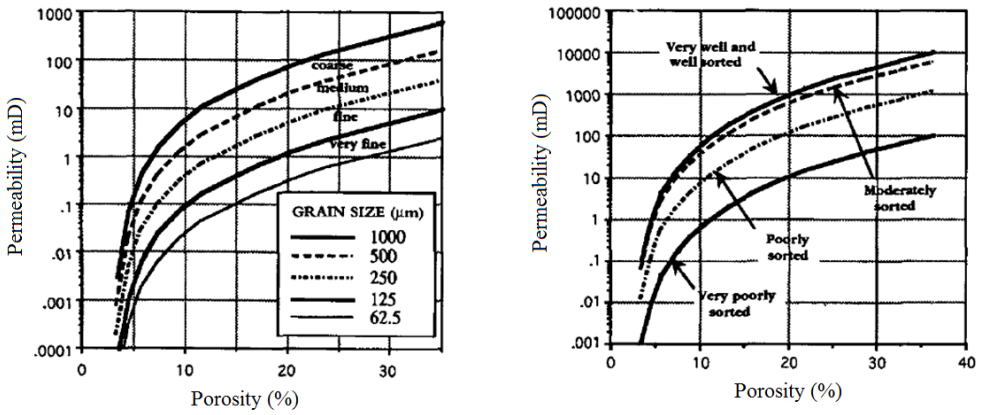

Figure 2.3 The impact of grain-size (left) and sorting (right) on permeability where those samples with coarse well sorted gains have higher permeabilities (Cade et al., 1994).

Table 2.1 Impact of grain-size and sorting on permeability showing the upper and lower permeability values. The permeability (K) increases with sorting and grain size (Beard and Weyl, 1973).

Size	Coarse		Medium		Fine		Very fine	
Sorting	Upper K (md)	Lower K (md)	Upper K (md)	Lower K (md)	Upper K (md)	Lower K (md)	Upper K (md)	Lower K (md)
Extremely well	475	238	119	59	30	15	7.4	3.7
Very well	458	239	115	57	29	14	7.2	3.6
Well	302	151	76	38	19	9.4	4.7	2.4
Moderately	110	55	28	14	7	7	2.1	1.1
Poorly	45	23	12	6	3.7	3.7	0.93	0.45
Very poor	14	7	3.5	1.7	0.83	0.42	0.21	0.1

Gases are compressible, so when they are flowing through a core they will travel slower at the high pressure input end (as it is compressed into a smaller volume) than at the output end where it expands. Therefore, the compressibility term is added (Dake, 1978):

$$Q = -\frac{K\,A}{\mu B}\frac{\Delta P}{L} \qquad \text{Equation 2.4}$$

where B is the gas formation volume factor, expressed as:

$$B = \frac{V_R}{V_{SC}} = \frac{znRT}{p} = \frac{p_{sc}Tz}{pT_{sc}} \qquad \text{Equation 2.5}$$

where V_R is volume of gas at reservoir conditions (m^3), V_{SC} is volume of gas at standard conditions (m^3), z is compressibility factor (unitless), n is number of moles (mol), R is ideal gas-law constant (J mol^{-1} K^{-1}), T is absolute temperature (K), p is absolute pressure (Pa), P_{sc} is pressure at standard conditions (Pa) and T_{sc} is temperature at standard conditions (K).

An additional consequence of using gas for permeability measurement is that the gas molecules slip on the solid surface, which creates a deviation from Poiseuille flow. Gas slippage is associated with non-laminar gas flow and occurs when the size of the average pore throat is less than the mean free path of the gas molecules. This results in higher flow rates than would be predicted from Darcy's Law on a molecular level. Therefore, a correction needs to be applied to permeabilities calculated using Darcy's Law to take into account gas slippage; this is known as the Klinkenberg correction:

$$K_{kg} = K_{ab}\left(1 + \frac{b}{P_m}\right) \qquad \text{Equation 2.6}$$

where: K_{kg} Klinkenberg permeability (mD), K_{ab} is the absolute or liquid permeability (mD), b is the Klinkenberg slippage constant or b-factor (psi^{-1}) and P_m is the mean flow pressure (psi).

The Klinkenberg correction uses measurements at a range of gas pressures, which are extrapolated to an infinite gas pressure of $1/P_m = 0$. The correction can be applied by measuring the effect of mean pressure on gas permeability (Klinkenberg, 1941). The apparent permeability, K_g, is then plotted against the inverse of the mean flow pressure, ($1/P_m$), and the intercept of the resulting straight line with $1/P_m = 0$ is equal to the absolute permeability (Figure 2.4).

The limitation of this method is due to extrapolation of the trend line as there is no data between $1/P_m = 0$ and the first data point. The trend line could actually be represented by the blue trend line on Figure 2.4 leading to a lower absolute permeability value. To ensure accurate values are obtained more data points should be collected to reduce the extrapolation.

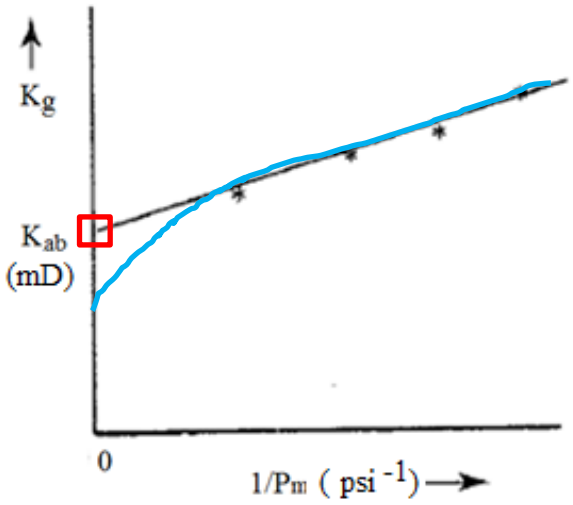

Figure 2.4 K_g *vs the inverse of the mean flow pressure. A range of pressures are extrapolated to an infinite gas pressure to obtain the absolute permeability (red square) which is inputted into Equation 2.6 to obtain the Klinkenberg permeability.*

2.4 Wettability

Wettability describes the preference of a solid to be in contact with one fluid rather than another (Abdallah, 2007). It plays an important part in most petroleum reservoir production problems, including restoration of samples (Cuiec, 1975; Cuiec, 1977), relative permeability or capillary pressure characteristics (Wang, 1988; Lefebvre, 1973; Batycky, 1981), water flooding (Morrow 1986, Anderson 1987), imbibition (Cuiec, 1986), and EOR. (Kremesec, 1978; Slattery, 1979).

Three types of wettabilties can arise – water wet, oil wet and neutral wettability (Figure 2.5). The angle of contact (θ) between the liquid interface and the solid is a function of the relative wetting characteristics of the two fluids with respect to the solid (Tiab and Donaldson, 2004). In a water wet system a drop of a preferentially wetting fluid will displace the non-wetting fluid; at the extreme it will spread over the entire surface (Abdallah, 2007). This is because the adhesive forces between the liquid and the solid is greater than the cohesive force between the gas and water. Conversely, in an oil-wet system when a wetting fluid is dropped onto a surface it will bead up, minimizing its contact with the solid (Abdallah, 2007). This is because the cohesive forces between the oil and water are greater than the adhesive forces between the water and solid. If the condition is neither strongly water wetting nor strongly oil-wetting, it is termed neutral-wetting (Abdallah, 2007). This model could also apply for a gas, water and solid system.

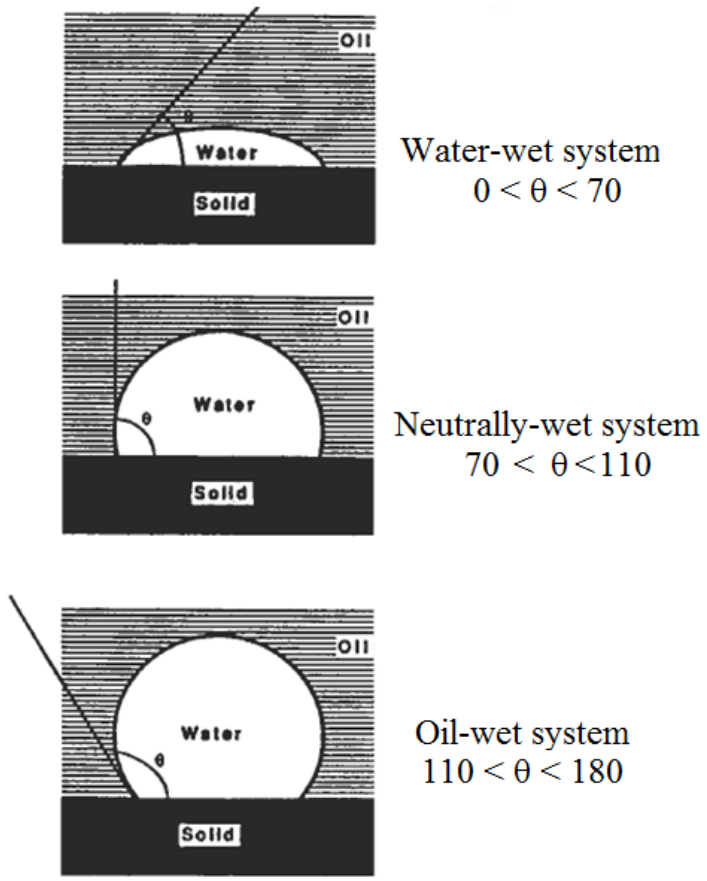

Figure 2.5 Schematic diagram showing water wet, neutral and oil wet systems. The water wet system occurs when the cohesion between the oil and water is less than the adhesion between the water and the solid. The oil wet occurs when the cohesion between the oil and water is greater than the adhesion between the solid and the water. The neutral system has conditions in-between (Tiab and Donaldson, 2004).

2.5 Surface and Interfacial Tension

Water molecules within a bulk liquid are surrounded by other molecules providing uniform molecular cohesion (Tiab and Donaldson, 2004). The water molecules at a surface to a gas cohere to the water molecules on and below the surface more than they adhere to the gas molecules above the surface (Tiab and Donaldson, 2004). This creates an inward force towards the bulk liquid, which generates a stretchy film like structure that contracts to the smallest area (sphere) to produce a surface tension (Tiab and Donaldson, 2004). The tension between two immiscible phases (e.g. water and gas) is termed interfacial tension. The boundary layers are curved due to the preferential wetting of the pore walls by one of the fluids (Tiab and Donaldson, 2004). Interfacial tension can be measured in the laboratory and is usually expressed as a force per unit length (Kristanto, 2003; and Ahmed, 2006).

2.6 Capillary Pressure

The capillary pressure is the pressure difference between two immiscible fluids:

$$P_c = P_{nw} - P_w \qquad \text{Equation 2.7}$$

where P_c is the capillary pressure (psi), P_{nw} is the non-wetting pressure (psi) and P_w is the wetting pressure (psi) (Figure 2.6). In a petroleum reservoir, the phases can either be water, oil, and/or gas. Capillary pressure is also used to describe the pressure difference required for a non-wetting fluid to pass through a pore throat by displacing a wetting fluid. This pressure difference depends on the size of the pore throats and their connectivity.

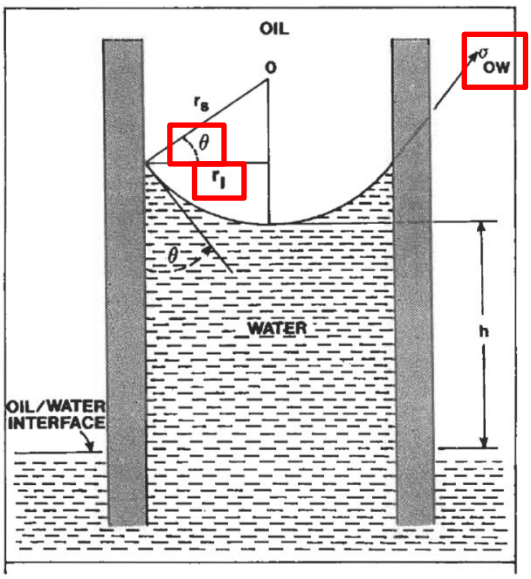

Figure 2.6 Capillary rise of water in contact with a immiscible fluid - oil in a capillary tube showing the interfacial tension (σ), contact angle (θ) and pore radius (r) used to derive the pressure difference Equation 2.16.

At a very low capillary pressure (i.e. just above 0 psi), the non-wetting phase can only enter the larger surface pores (Figure 2.7). An increase in capillary pressure beyond the entry pressure (P_{ct}) allows the non-wetting phase to enter the pore space and the wetting phase starts to be expelled (Figure 2.7), which increases the non-wetting phase saturation. As the radius of a pore throat decreases, a higher capillary pressure is needed for the non-wetting phase to force out the wetting phase (Figure 2.7). In other words, the wetting phase saturation decreases as capillary pressure is increased. Eventually, non-wetting phase saturation is increased to a level that forms

a continuous pathway through the porous media; the capillary pressure at which this occurs is known as the threshold pressure (Katz and Thompson, 1987).

The smallest pores remain saturated with the wetting fluid when the force driving the non-wetting fluid into the reservoir rock is insufficient to overcome the capillary forces associated with the smallest pores; this is often termed the irreducible water saturation (S_{wi}) (Figure 2.7). No more wetting fluid can be expelled from the pores at this particular capillary pressure or higher. The spatial distribution of irreducible water in water-wet rocks has been studied in detail by Zhou et al. (2000). Four different forms of irreducible water are identified: (1) hydration water attached to the clay surface (Hill et al., 1979); (2) pendular rings due to irregular pore geometry; (3) water trapped in dead ends of the pore network system; and (4) water by-passed in pores during two-phase flow. Some publications categorize (1) as clay-bound water and generally group (2), (3), and (4) as capillary-bound water (Peveraro and Thomas, 2010).

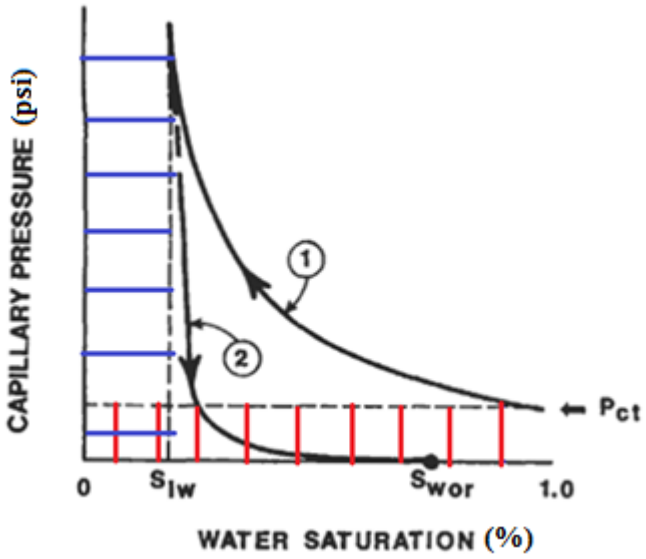

Figure 2.7 Capillary pressure vs water saturation showing the decrease in wetting fluid saturation as the non-wetting fluid is injected. None of the wetting fluid is forced out until the entry pressure is reached (P_{ct}) (red area). More of the wetting fluid is forced out as the pressure increases. A continues pathway through the rock is reached at the threshold pressure. At some pressure or above no more of the wetting fluid is forced out, this is known as the irreducible water saturation (blue area). This irreducible fluid is trapped inside small pores with narrow pore throats and the S_{wi} varies for different rocks dependent on the pore size (Tiab and Donaldson, 2004).

2.7 Impact of Diagenesis on Petrophysical Properties

Diagenesis is the term used to describe the changes that occur within a sediment after it has been deposited; it may result in changes in the mineralogy and pore structure, which in turn cause changes in petrophysical properties (Holland, 1982; Sampath and Keighin, 1982; Walls, 1982b; Dibble, et al., 1983; Pallatt, et al., 1984; Randolph, et al., 1984 and Luffel, et al., 1991). Diagenesis occurs as a result of both mechanical, chemical processes as well as reservoir temperature and pressure . The extent of diagenetic alteration is controlled by variables such as the depositional environment, mineralogy, temperature, stress, fluid pressure, fluid composition and time. Tight gas sandstones generally have experienced significant diagenetic alteration, understanding the diagenesis of TGS is therefore fundamental to understanding and predicting the petrophysical properties of TGS reservoirs.

2.7.1 Mechanical Compaction

Mechanical compaction can create a the loss of porosity with depth (Figure 2.8). It is caused by the increase in stress acting on the sediment as the thickness of the overburden increases due to continued sediment deposition. The increased stress causes grains to rearrange and pack more efficiently for example, water and sand in a beach environment.

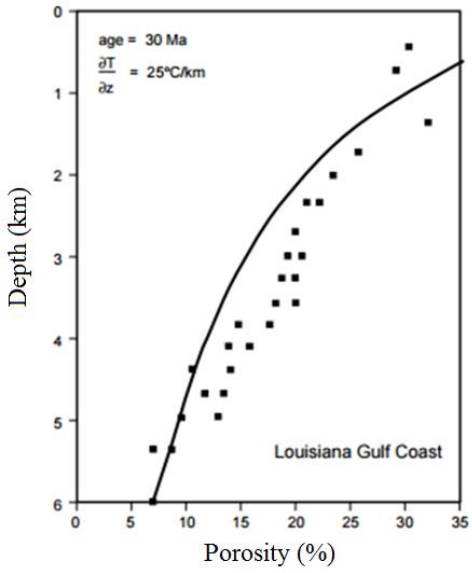

Figure 2.8 Porosity-depth trend for Louisiana Gulf Coast sand. The porosity decreases with depth due to applied pressure (Bjorkum, 1998).

2.7.2 Chemical Diagenesis

Chemical diagenesis involves the precipitation and dissolution of minerals. Since the 1970s, controversy into the controls of chemical diagenesis of sandstone has existed. The controversy is related to the extent to which elements are transported into and out of the system i.e. open and closed system diagenesis and their effect on the reservoir quality. For example, Nedkvitne and Bjorlykke (2006) stated that K-feldspar dissolution is extremely insoluble and so are unlikely to be transported large distances. Instead, K-feldspar dissolution usually results in the precipitation of clay minerals in nearby pores. If they are repositioned as cements in the same rock or one mineral changes to another, porosity may not change unless there is also a volume change (Rittenhouse, 1973).

Burley (1984) divided chemical diagenesis into three categories: eodiagenetic, telediagentic and mesodiagenetic. Eodiagenetic processes are those that are heavily influenced by the groundwater such as clay infiltration, evaporation, carbonate and clay precipitation, as well as the dissolution of unstable grains such as Fe-Mg silicates and Ca-rich plagioclase. Telediagentic processes are those that occur after the sediment has been uplifted, eroded and exposed to different pore fluids. Mesodiagenetic reactions occur during deep burial, often in a closed system, and include processes such as quartz cementation, illitization of clay and K-feldspar dissolution.

TGS reservoirs tend to have experienced significant diagenetic alteration through processes such as quartz cementation, clay mineral neoformation, carbonate precipitation, and mineral dissolution; the latter process may create what is referred to as secondary porosity. Quartz diagenesis is a particularly important process responsible for the reduction in porosity and permeability of sandstones. It is now widely accepted that the rate of quartz cementation is controlled by time and temperature and hence burial depth (Figure 2.9) and the reactive quartz surface area (e.g. Walderhaug, 1996). In terms of the latter, if quartz grains within sandstone do not contain grain-coatings, quartz cement generally forms as syntaxial (same composition) overgrowths (Figure 2.10). However, the presence of grain-coatings, such as clay and microcrystalline quartz, on detrital quartz suppress the formation of

quartz overgrowths and instead quartz cement tends to form as what are often referred to as outgrowths (Figure 2.10).

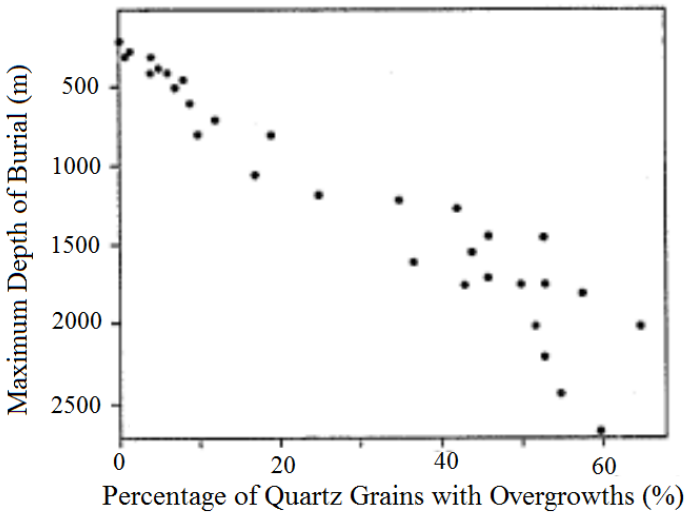

Figure 2.9 Depth as a function of the percentage of grains with overgrowths, showing an increase in the % of quartz overgrowths with depth. This occurs as the conditions of temperature and pressure become more ideal potentially allowing for pressure solution (Wilson, 1994).

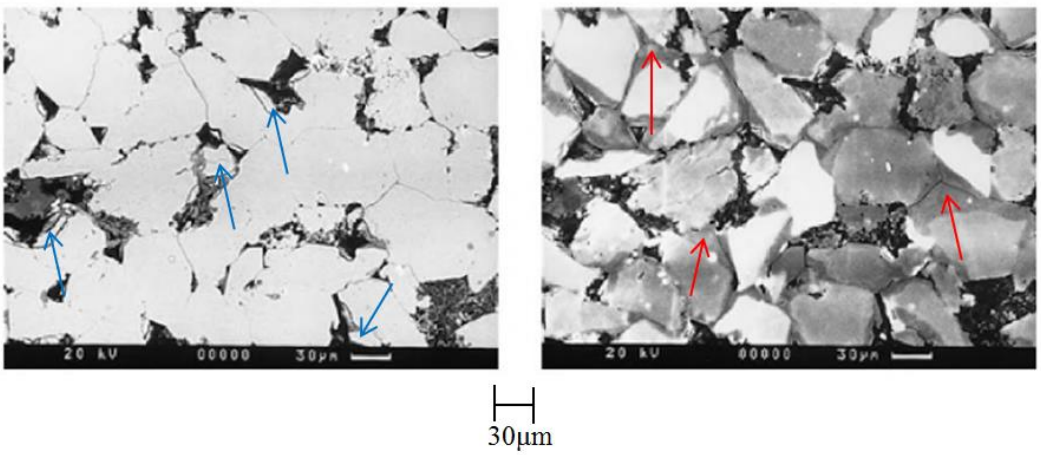

Figure 2.10 Quartz outgrowths (blue arrow) (left) and overgrowths (red arrow) (right) where the quartz overgrowths form when there is little grain coating clay (Fisher et al., 2000).

Clay mineral precipitation may have an important impact on the porosity and permeability of sandstones. A large range of clay minerals are encountered in sandstones including: (i) smectite, (ii) illite; (iii) kaolin and (iv) chlorite. These clays form by three main mechanisms: inheritance, neoformation and transformation (Eberl, 1984). *"Origin by inheritance means that a clay mineral found in a natural deposit originated from reactions that occurred in another area during a previous stage in the rock cycle*". "*Origin by neoformation means that the clay mineral has*

precipitated from a solution or has formed from the reaction of amorphous material". "Origins by transformation requires that the clay mineral that has kept some of its inherited structure intact while undergoing chemical reaction".

It has been argued that both the mineralogy and structural position of these clay minerals within sandstone control its poroperm properties. For example, Rossel (1982) stated that sandstones containing feldspar of up to 7% of the bulk volume have permeabilities four times that of samples with similar amounts of kaolin, and as much as twenty times higher than samples with comparable amounts of illite and/or chlorite. The 7% feldspar is significant as feldspar can react to kaolin and illlite further reducing permeability. In addition, Neasham (1977) divided clays into discrete particles, pore lining and pore bridging (Figure 2.11), where he explained that pore bridging its thought to have the highest impact on permeability. This is important for this research as the TGS sample contain both illite and kaolin and their quantities and positon could have a major control on the porosity and permeability

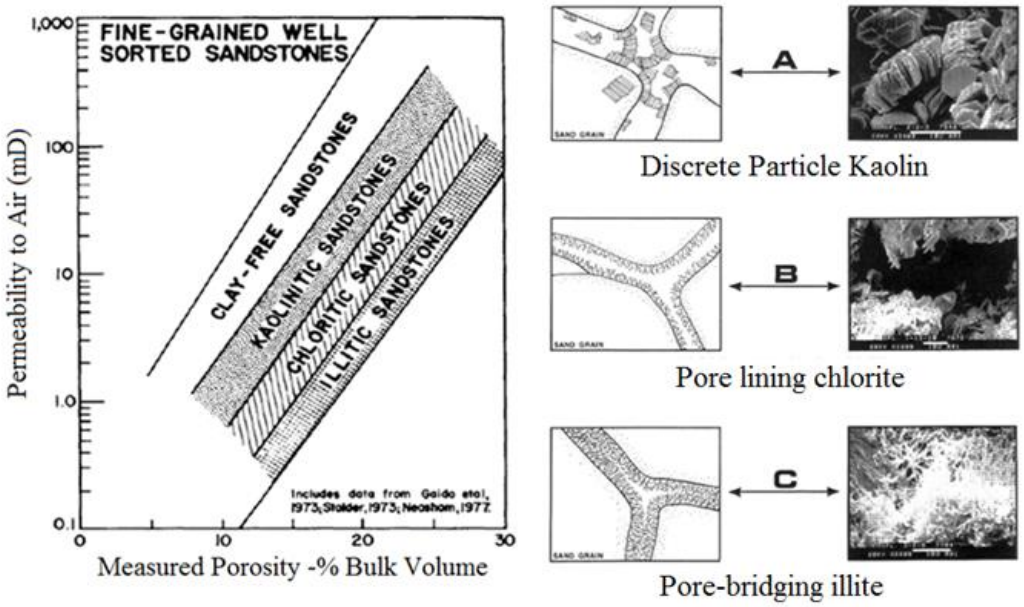

Figure 2.11 Impact of clay type on porosity-permeability, trends (left). The illite has the most effect on permeability where those samples which are clay free have the highest permeabilities (Wilson, 1982). The classification of the structural position of clay minerals in sandstone (right). The illite bridges pores and starts to infill pores which causes the decrease in permeability whereas even though kaolin is pore filling pore space is still intact between the grains (Neasham, 1977)

Dolomite is by far the most common carbonate cement observed in the TGS examined during this study. In general, the dolomite forms as 10-100 µm rhombs that partially fill pore space. Overall, it forms in a similar position to the discrete

clays shown in Figure 2.11, therefore it is expected to have a similar impact on porosity-permeability relationships.

Secondary porosity formation has often been suggested to be a diagenetic process that increases the porosity and permeability of sandstones (Schmidt and McDonald, 1979). It occurs because detrital material is not in physiochemical equilibrium with its environment when deposited (Keighin, 1979). Wilson (1994) stated that secondary pores can form from fractures; shrinking of framework grains, matrix or cement or the dissolution of framework grains, cements or replacement minerals. In terms of the latter, K-feldspar is probably the most common phase that is dissolved during diagenesis to create secondary porosity in the presence of clay.

2.8 Impact of Stress and Pore Pressure on Petrophysical Properties

Stress is measured in force per unit area and can be expressed as a tensile, compression or shear force. Total vertical stress is the stress applied by the overlying material whereas horizontal stress is controlled by tectonic stresses due to movements in the earth's crust. These tectonic stresses can affect the total vertical stress. The stresses in the subsurface and the confining pressure (C_p) imposed on samples in the laboratory are different; the former can be different in all directions whereas the latter is the same in all directions.

Rocks that experience increasing stress will deform. Deformation refers to the change in shape due to the forces acting on the rock. It depends on the elasticity and rigidity of the rock as well as the stress history, temperature and time. The strain is a measure of the resultant deformation, it is the ratio of the change in dimension of the material to the original dimension of the material. The material fails when the stress applied is greater than the strength of that material.

Fluid within the pore space can apply a force between grains, this is referred to as pore pressure (P_p) and this pressure can reduce the total stress acting on grain contacts. Confining pressure and pore pressure are related by the differential pressure (P_d), which is obtained by subtracting the pore pressure from the confining pressure. An effective stress parameter (α) is usually added to account for the difference in the stress sensitive nature of rock properties to confining and pore pressure (Biot and

Willis, 1957; Zoback, 1975; Berryman, 1992; Hornby, 1996; Al-Wardy and Zimmerman, 2004; Hofmann, 2005 and Shafer, 2008):

$$P_e = C_P - (\alpha P_P) \qquad \text{Equation 2.8}$$

where P_e is the effective stress (psi). The effective stress parameter is different for each petrophysical property (Berryman, 1992). The most commonly used is the Biot (1957) coefficient, which is the effective stress parameter for volume change; this is likely to be different to the effective stress parameter for permeability.

It has been reported that the effective stress parameter for permeability of quartz-rich sandstones can range from 0.6 to 0.75 (David and Dorot, 1989), crystalline rocks can range from 0.5 to 1 (Kranz et al., 1979) and clay-bearing sandstones can vary from 1 to 7.1 where the effective stress parameter increases with the clay content (Zoback, 1975; Kwon et al., 2001) (Figure 2.12).

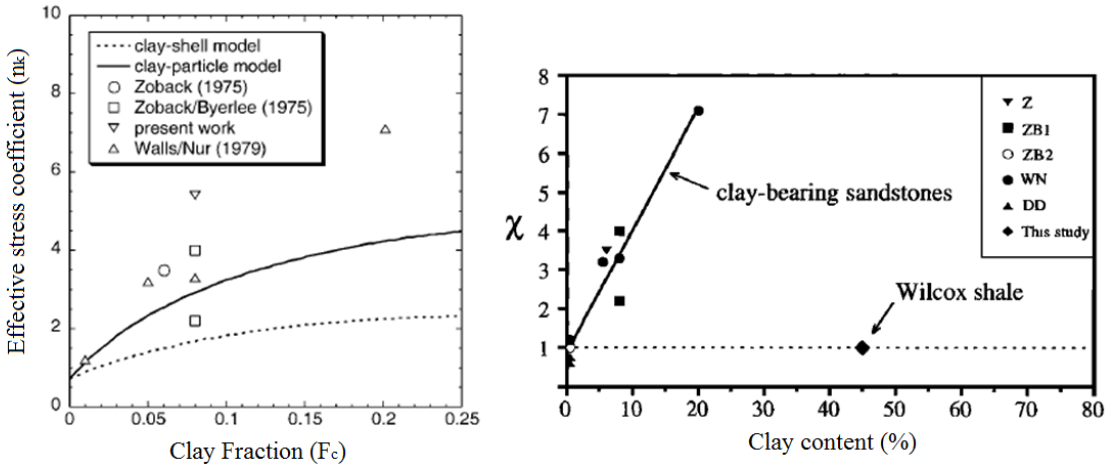

Figure 2.12 An increase in the effective stress parameter for permeability with clay fraction. Left – Al Wardy and Zimmerman (2004) and right – Kwon et al. (2001) where ZB2 is Zoback and Byerlee (1975, 1976), WN is Walls and Nur (1979) and DD is David and Dorot (1989).

2.8.1 Stress Dependency of Permeability

It has long since been recognized that laboratory measurements of the permeability of tight gas sandstones are very stress sensitive (Thomas and Ward, 1972; Kilmer et al., 1987; Sigal, 2002; and Zhu, et al., 2008) (Chapter 7). Fatt (1952) found that at 3,000 psi overburden pressure, the permeability of eight sandstone core samples ranged from 59 to 89% of the permeability without overburden pressure. Similarly,

Ostensen (1986) found that tight-gas-sand cores can lose 90% or more of their permeability when re-stressed to the net reservoir overburden stress. Likewise, Ali (1987) found that with an increase in pressure from 100 to 6000 psi, the permeability dropped between 10 - 14%.

In general, the stress sensitivity of petrophysical properties tends to increase with decreasing permeability (McNally, 1958; Glanville, 1959; Vairogs, 1971) (Figure 2.13). A possible explanation is that microfractures formed as a result of stress release have more of an impact on the permeability in tight rocks than in high permeable rocks. The permeability is more affected by stress than porosity (Section 2.8.2). For example, Petunin (2011) found that permeability decayed by 10 - 20% with increasing stress while the porosity decreased by about 3%. This is because the

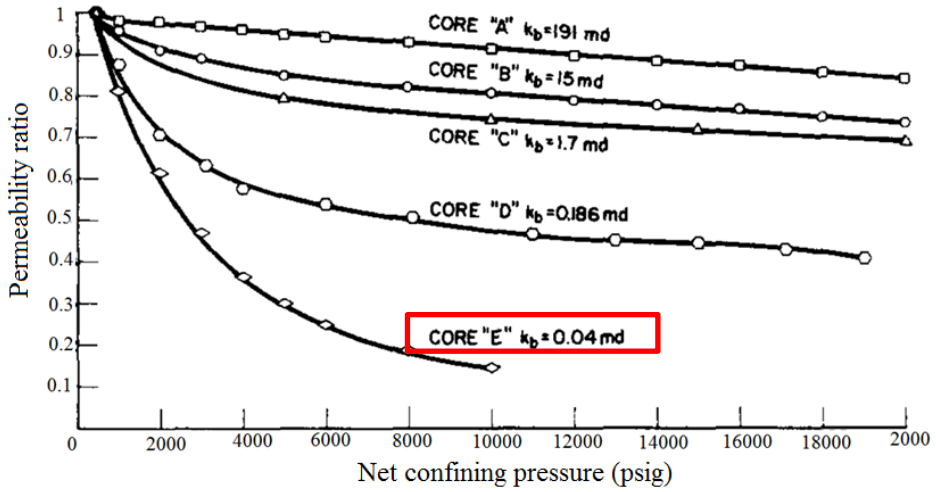

Figure 2.13 Permeability ratio as a function of confining pressure for five different permeability samples. The lower permeable sample (red box) is the most stress sensitive as seen by the steeper decrease in permeability with pressure (Vairogs, 1971).

2.8.2 Slit Porosity/Microfractures

Several authors have indicated that decrease in permeability with stress is related to the presence of slit-shaped pores that close as confining pressure is increased (Jones and Owen, 1980; Ostensen, 1983) (Chapter 8). These slit shaped pores are known as microfractures and there is a large amount of evidence for the presence of microfractures in TGS within the literature (Ostensen, 1983; Brower and Morrow, 1985; Hyman, 1991; Laubach, 1996; Roberts, 1996; Lopez, 2004; Apaydin, 2011; Chun, 2013).

In many siliciclastic petroleum reservoirs, microfractures with sizes of microns to millimetres are more common than large fractures and can be sampled effectively even in small volumes of rock (Laubach, 1989). They reflect tectonic, overpressure and diagenetic origins (Chun, 2013). However, they can form during drilling, from core expansion or contraction and during sample preparation (Chun, 2013), where fatigue failure in rocks is closely related to their petrological, physical and mechanical properties (Homand-Etienne, 1984; Burdine, 1963). The presence of slit porosity is important as it means that the permeability of sandstone may become decoupled from its porosity i.e the permeability is more affected by the closure of these microfractures than porosity as porosity is affected more by the closure of the larger pores which are not very stress sensitive. In addition, it implies that the properties of the samples could be very stress sensitive in the subsurface.

2.9 Electrical Properties

Ohms law is the fundamental physical law that relates the current flowing through a material to the potential gradient. It states that in an electrical circuit, the current passing through a conductor between two points, is directly proportional to the difference in electrical potential, and is inversely proportional to the resistance of the material (Equation 2.9). By rearranging Equation 2.9, the resistance can be determined (Equation 2.10).

$$I = \frac{V}{R} \qquad \text{Equation 2.9}$$

$$R = \frac{V}{I} \qquad \text{Equation 2.10}$$

where: I is the current (amps), V is the difference in electrical potential (volts), R is the resistance (Ω). This resistance along with the cross sectional area and length provide the resistivity (Equation 2.11).

$$\rho = R\,\frac{A}{L} \qquad \text{Equation 2.11}$$

where: ρ resistivity (Ω-m), L is length (meters) and A is area (square meters).

The resistivity demonstrates how strongly the rock opposes the flow of an electrical current when fully saturated with a fluid. The resistivity can be temperature corrected to the temperature found within the reservoir (Equation 2.12).

$$R_{2} = R_{1}\ \frac{T_1}{T_2} \qquad \text{Equation 2.12}$$

where: R_2 is the resistance at 25°C, R_1 is the original resistance, T_1 is the original temperature and T_2 is the temperature of the reservoir (25°C).

Archie (1942) considered a porous medium of porosity and named the unitless ratio of the resistivity of the fully saturated rock (R_o), to that of the ratio of pore fluid saturating the pores (R_w), the formation resistivity factor (*FRF*) (Glover, 2014):

$$FRF = \frac{R_o}{R_w} \qquad \text{Equation 2.13}$$

where *FRF* is formation resistivity factor (unitless), R_o is resistivity of the rock 100% saturated with brine (Ω-m) and R_w is resistivity of the brine (Ω-m). This *FRF* was chosen as it was approximately constant for any given formation. This first expression led Archie to conclude that the *FRF* depends on the porosity:

$$FRF = \phi^{-m} \qquad \text{Equation 2.14}$$

where ϕ is porosity (%) and *m* is cementation exponent (unitless).

A plot of the log of porosity vs the log of the *FRF* provides a straight line where the slope is equal to the *m* exponent:

$$m = -\frac{Log\ (FRF)}{Log\ (\emptyset)} \qquad \text{Equation 2.15}$$

The cementation exponent is a factor created by Archie, which was argued to relate to the degree of cementation and connectivity. A value of 1 is not observed in real rocks and represents a series of capillary tubes. A value of 1.5 represents a case when the rock is composed of perfect spheres (Sen et al., 1981; Mendelson and Cohen, 1982). Sandstones are around 2 and a value of 2.5 to 5 is seen in carbonates as they have well defined fracture networks (Glover, 2014).

2.10 Laboratory Techniques

2.10.1 Sample Cleaning

Soxhlet extractor is the most commonly used method to clean core plugs (Ward, 1980; Shafer, 2013); it involves heating and condensing a solvent, which passes through the rock. This method is performed to remove drilling fluids, salts and oil from core plugs. It has been argued that the Soxhlet extraction technique may damage clays (McPhee et al., 2015). Therefore, a comparison was made between the Soxhlet extractor method and critical point drying with CO_2 (Chapter 4). The main advantage of the latter method is the lack of surface tension, which is thought to preserve fine structures such as clay. The background theory is presented in Section 2.10.1.1.

A range of factors can influence the effectiveness of the cleaning process, these include: (i) the core size where a large diameter makes it harder for the solvent to reach the centre; (ii) the length of time that the sample is cleaned - longer cleaning times are more effective; and (iii) the sample permeability where lower values slow down the cleaning process (Tapping, 1982). The effectiveness of cleaning also depends on the way fluids are attracted to the rock pore structure, i.e. the bonds between the adsorbate and the adsorbent (Cuiec, 1975). If Van der Waals forces, are present, a limited number of solvents or even a single solvent may succeed in removing the adsorbed products (Cuiec, 1975). To ensure thorough cleaning and to restore the rock to a water-wet state, there needs to be an equilibrium between the adsorbate and the adsorbent (Cuiec, 1975).

The solvent type is important as some may be soluble with the solid component depending on the polarity values, or become miscible with another fluid depending on the fluid type (Cuiec, 1975). The solvent must be gentle enough to prevent damage to the mineral constituents of the rock (Anderson, 2013). Similarly, RP40 (1998) states that selected solvents should not attack, alter, or destroy the structure of the core and Keelan (1972) summarized that the solvents should not react with the rock. Likewise, care must be taken to ensure additional pore space is not created resulting from dehydration of clays and hydrous minerals, or from erosion caused by high flow rates as solvent passes through the core (Anderson, 2013). The correct

solvent is important as the cleaning process may have a large impact on the (i) core porosity; (ii) grain density; (iii) electrical data; (iv) water saturation; (v) pay thickness; (vi) hydrocarbons in-place; and (vii) recoverable hydrocarbon values (Tapping, 1982).

2.10.1.1 Critical Point Drying

Solid, liquid and vapour are the three states of matter. At one specific temperature and pressure all three co-exist in equilibrium with each other, this is known as the triple point (Figure 2.14). To form a gas from a liquid, the substance must pass the interface between the two states. The boundary between liquids and gases has a surface which can damage fine structures such as clay (Evangelista et al., 2004). However, if the temperature and pressure of the liquid solvent is increased to the critical point, the density of the liquid reduces and gas increases, therefore they converge. This causes the meniscus between them to flatten indicating a reduction in the surface tension (Evangelista et al., 2004). Therefore, the liquid surface becomes very unsteady and ultimately disappears. This is known as 'continuity of state', which suggests a drying technique for which the surface tension can be reduced to zero (Evangelista et al., 2004).

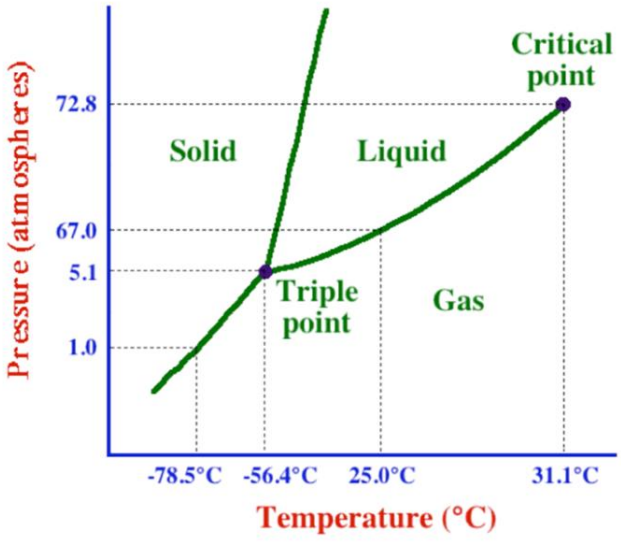

Figure 2.14 Boiling point curve for CO_2. As the temperature and pressure increase all three states – solid, liquid and gas become stable (triple point). As the temperature and pressure continue to increase the liquid and gas reach a critical point where both are stable. This occurs when the density of the liquid decreases as the liquid expands due to an increase in temperature and the density of the gas decreases as the gas compresses due to an increase in pressure. At this critical point the CO_2 is now a supercritical fluid, this occurs at 31.1°C and 72.8 atm (Rochelle and Moore, 2002).

The critical point is the temperature and pressure at which all physical properties of the liquid and gas phases of a substance are equal (Huggett, 1982). This single phase forming at the critical point is termed a supercritical fluid (McNally, 1992; Rochelle, 2002; and Knox, 2005). A range of supercritical fluids are available, they each have a distinct critical temperature and pressure (Table 2.2).

Table 2.2 Critical temperatures and pressures of a range of super critical solvents, CO_2 is shown in red (Knox, 2005).

Solvent	T_c/K	P_c/bar	ω
Carbon dioxide	304	73.7	0.225
Water	647	221	0.344
Ethane	305	48.7	0.099
Ethene	282	50.4	0.087
Propane	370	42.5	0.152
Ammonia	405	114	0.257
Nitrous oxide	310	72.5	0.141
Trifluoromethane	299	48.4	0.267

Note: ω is surface tension in N/m

Supercritical fluids are intermediates between two phases, liquids and gases (Bouchaour, 2003; Knox, 2005) (Table 2.3). The choice of supercritical fluid depends on the suitability to the process being studied, as well as its toxicity, hazard rate, cost and availability (Knox, 2005). In this research CO_2 is used as it has an easily accessible critical point (temperature of 31°C and a pressure of 74 bar - 1073 psi), is non-hazardous, inexpensive and non-flammable (Kiran, 1992; Brown, 2000; Bouchaour, 2003).

Table 2.3 Density and viscosity of supercritical fluids (red box) vs gases and liquids (McNally, 1992).

	Gas	SF	Liquid
Density(g/cm^3)	10^{-3}	0.1-1	1
Diff. Coeff.(cm^2/s)	10^{-1}	10^{-3}-10^{-4}	$< 10^{-5}$
Viscosity(g/cm·s)	10^{-4}	10^{-3}-10^{-4}	10^{-2}

Carbon dioxide is not very soluble in polar solvents such as water (Huggett, 1982; Bouchaour, 2003; Pandithange, 2012). This can be improved by varying temperature or pressure or adding a co-solvent (Bouchaour, 2003). The co-solvent used must have a greater affinity for the polar solvent than the carbon dioxide. In rocks containing saturated water, ethanol, acetone or methanol can be used (Huggett, 1982;

Pandithange, 2012). Critical point drying is a three stage process. Firstly, the sample is saturated with the co-solvent, which dissolves the water. Secondly, the co-solvent is replaced by the liquid CO_2 at the critical temperature and pressure (Figure 2.15 a-b, b-c). Lastly, the liquid CO_2 is converted to a gas by decreasing the pressure at a constant temperature (Figure 2.15 c-d).

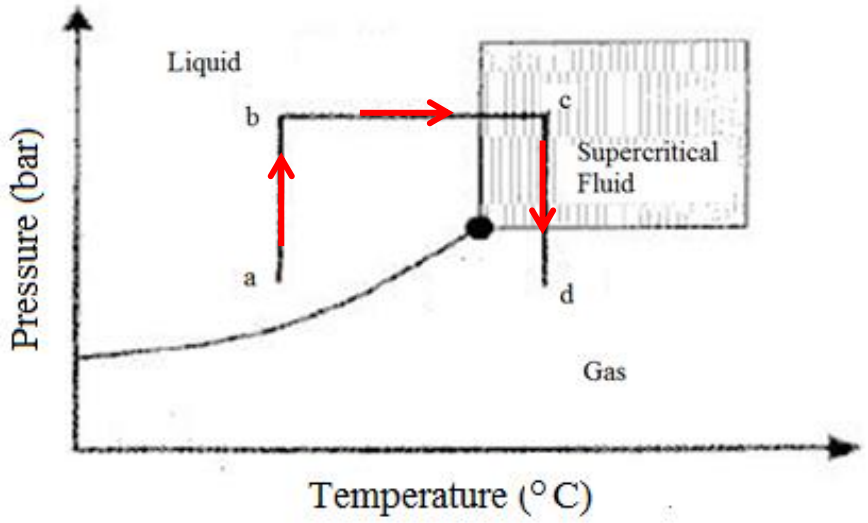

Figure 2.15 Phase diagram showing the pressure and temperature paths used in the critical point drying method. First the pressure is increased (a-b), than the temperature is increased (b-c) whereby a supercritical fluid is created and finally the pressure is decreased at a constant temperature (c-d) to form a gas without a change in state (Bouchaour, 2003).

2.10.2 Scanning Electron Microscope (SEM)

SEM's have variable magnification from X20 to X20,000 and approximately 1000 times the depth of focus (the larger the depth of focus the more focused the image) of the conventional light microscopes (Weinbrandt, 1969; Welton, 1984) where the latter property is the most important (Weinbrandt, 1969; Timur, 1971; Welton, 1984). This is because no electron trajectory is inclined more than 0.5° from the optic axis, in contrast with the more than 60° in optical microscopy (Figure 2.16). The great depth of resolution of the SEM has opened the way for extremely detailed studies of pore systems in rocks (Timur, 1971).

Figure 2.16 Electron trajectory of a light microscope >60° (left) and a SEM = 0.5°(right). The narrow electron beam leads to higher resolution images (Weinbrandt, 1969).

The SEM functions by focussing an electron beam onto the specimen (Weinbrandt, 1969). The interaction between the electron beam and the sample generates a range of signals including: secondary electrons (SE), backscatter electrons (BSE), light (CL) and X-rays (Figure 2.17). The SE signal provides topographic information as more electrons are detected from peaks in the sample than depressions. The amplitude of the BSE signal is directly proportional to the mean atomic number of the mineral; where phases of different mass have different grey values from 0 to 225. Pores appear black as they have a value of 0 and heavy minerals like siderite, dolomite and ankerite appear white as they have a value of 225. The BSE is good for detecting certain minerals but cannot be used to differentiate between minerals that have the same mean atomic number (quartz and albite). Therefore, other methods are needed to determine their distribution and abundance. The most reliable way to identify minerals through the SEM is to measure their elemental compositions determined by the energy-dispersive X-ray system (EDX) (Pittman, 1979; Welton, 1984).

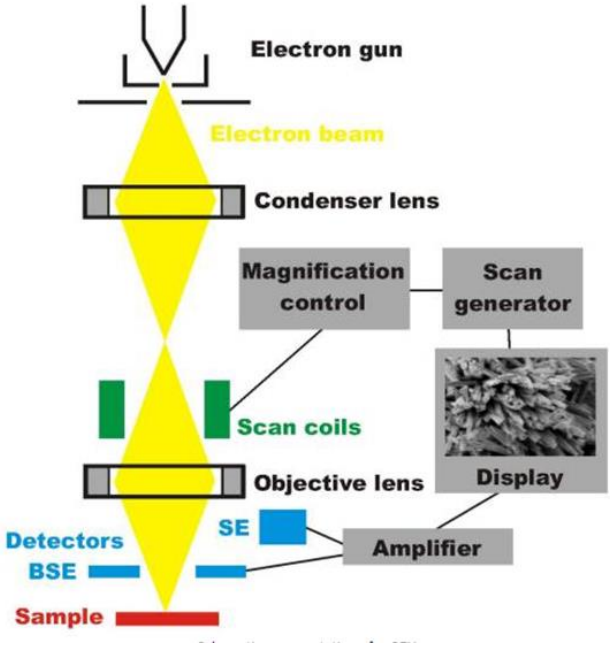

Figure 2.17 Schematic drawing of the SEM with the electron gun which produces the electrons, lenses to focus the beam, the backscattered electron for compositional analysis based on atomic number and secondary electron detector providing topographic information, it is useful for imaging broken surfaces on a sample (Krumeich, 2015).

The SEM is an ideal tool to study the composition of samples as well as the texture (Clelland, 1991; Schwartz, 1980; Welton, 1984), microporosity (Pittmann, 1979), macroporosity (Bonnie, 1992) and correlate the microstructure of rocks with their petrophysical properties (porosity) for permeability estimation (Bonnie 1992). Bonnie (1992) compared the image derived porosity and permeability with the core plug values. The results obtained indicate that the image-derived porosity agrees with the core-plug-derived value to within 2.5% and the permeability is reproduced within a factor of 2.5 (Figure 2.18). Similarly, Clelland (1991) compared plug and image analysis porosities and found a similar positive trend (Figure 2.19). Bonnie (1992) and Clelland (1991) concluded that the deviations are attributed partly to plug heterogeneities, which could have been improved by analysing more than one slice from each rock.

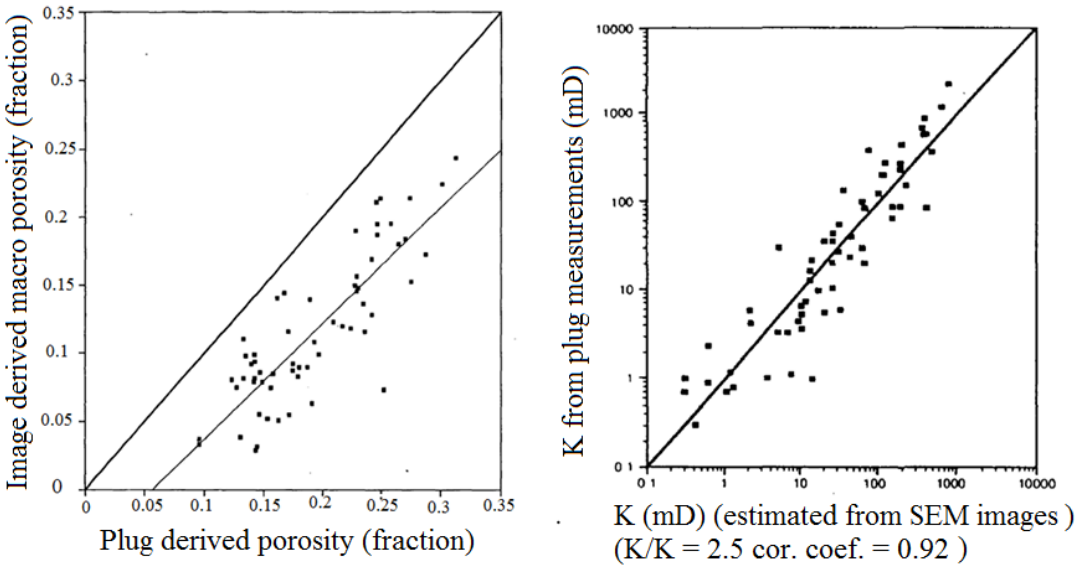

Figure 2.18 Image analysis porosity vs plug porosity showing a 2.5% difference (left) and plug permeability vs image analysis permeability showing results are reproduced within a factor or 2.5 (right). Scatter is due to heterogeneity (Bonnie, 1992).

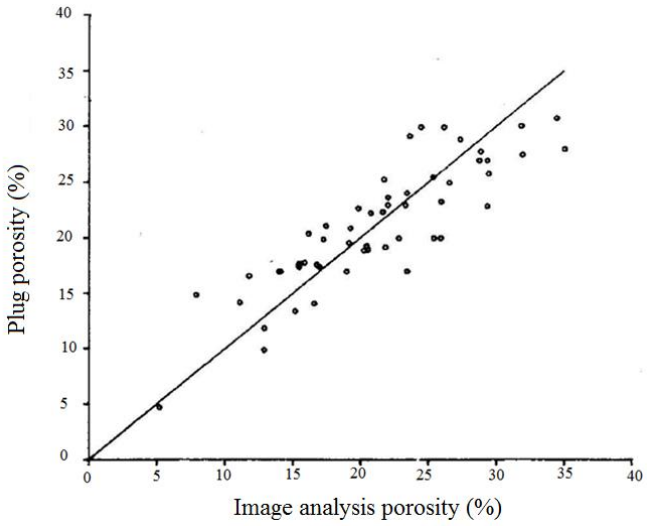

Figure 2.19 Plug porosity vs image analysis porosity showing a moderate trend with scatter due to heterogeneity (Clelland, 1991).

2.10.3 Nuclear Magnetic Resonance (NMR)

NMR is used to determine the pore size distribution and may be used to estimate permeability (Chapter 6). NMR works by re-orientating the hydrogen nuclei within the water molecules of a saturated sample by imposing a magnetic field. Once the magnetic field is removed, the nuclei spin as they return back to their original position. They do this by losing energy when they hit surfaces; a process known as

relaxation. There are two components T_1 and T_2, T_1 represents the time it takes till the nuclei return to their original position and the T_2 represents the time it takes till the nuclei, after spinning, are no longer in synchronisation with each other i.e. they are spinning in different directions/orientations. The relaxation rate depends on pore size. In particular, a fast decay occurs when the pore size is small, and a slow decay when the pore size is large (Figure 2.20).

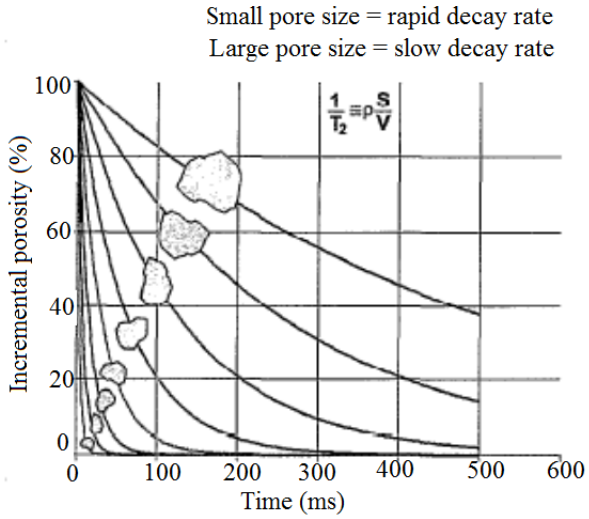

Figure 2.20 Incremental porosity as a function of time for a range of different sized pores. The decay rate is faster with a decrease in pore size, where the decay rate is dependent on the surface to volume ratio and wettability (Ostroff, 1999).

These decay rates are for individual pores only, therefore, the end curve will be a combination (average) of the different curves (Figure 2.21). This can be transposed into a pore size distribution. Finally, a range of T_2 cut-offs can be defined (Figure 2.21). A major cut-off is the division between the producible fluid often known as the free fluid index (FFI), which resides in large pores, and the bound fluid often known as the irreducible water volume (BVI), which resides in the small pores or attached to the clay surface.

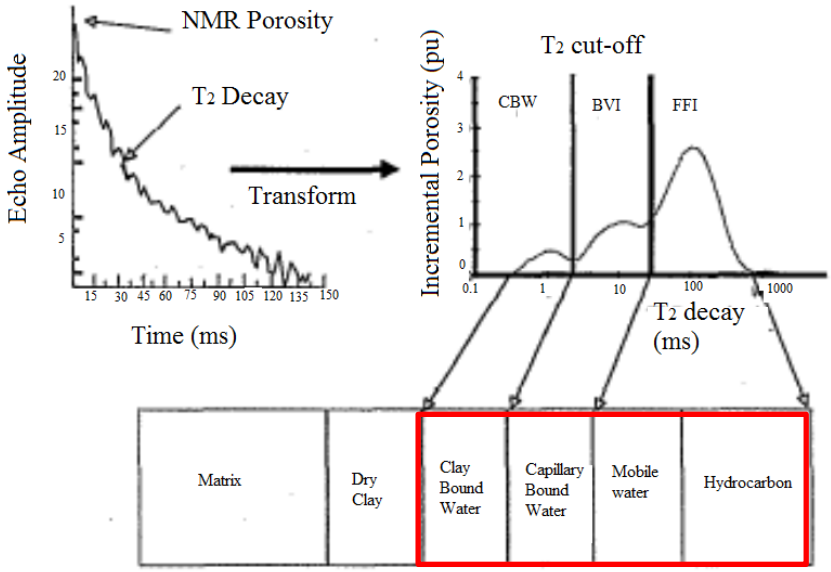

Figure 2.21: The average of the T_2 decay curves vs time (left) and how the T_2 cut-offs can be used to describe the pore structure (right) showing the three common cut-offs used – clay bound fluid, capillary bound fluid and free fluid (Ostroff, 1999).

2.10.4 Mercury Injection Capillary Pressure (MICP)

A mercury injection porosimeter is an instrument that forces mercury into a sample due to an increase in pressure. The non-wetting property of mercury combined with its low compressibility makes it ideal for determining the pore throat size distribution (Chapter 6). The pore throat size is determined using the Young-Laplace equation:

$$\Delta p = \frac{2\gamma \cos\theta}{r} \qquad \text{Equation 2.16}$$

where Δp *is* pressure difference (psi), γ is interfacial tension between air and mercury (N/m) (420), θ is the contact angle (~140°) and r is pore throat radius (m). In addition, the permeability can be empirically estimated using a variety of models – Swanson (1981), Purcell (1949), Katz and Thompson (1986, 1987) and Winland (1980); this is discussed further in Chapter 6 and 7.

2.10.5 Surface Area Analysis; the Brunauer-Emmett-Teller (BET) Method

The BET method is based on the physical adsorption of a vapour or gas onto the surface of a solid (Naderi, 2012). It provides the surface area, which may also be

used to estimate permeability using the Kozeny-Carmen (1927) equation (Chapter 6).

$$k = c\frac{\emptyset^3}{s_s^2} \qquad \text{Equation 2.17}$$

where k is the absolute permeability (mD), c is the Kozeny constant, S_s is specific surface (m^2/g), and $ø$ is porosity (fraction).

The gas/vapour is known as the adsorbate whereas the solid surface capable of absorbing is known as an adsorbent. The molecules migrate into pores and the adsorbate starts to build up during the experiment (Lowell and Shields, 1991). The number of molecules attached to a solid surface increases as the gas pressure increases and the temperature decreases; until a point is reached where it is reasonable to consider a monolayer has formed. This process is exothermic and is more reactive with fine particles than with a bulk core sample (Webb, 1998).

The amount of accumulated gas adsorbed is plotted agaisnt gas pressure at one temperature to generate an isotherm. The adsorption isotherm is a measure of the molar quantity of gas taken up or released at a constant temperature by an initial clean surface as a function of gas pressure (Webb, 1998). This is based on the pore size and surface area of the surface. The equation for the volume of gas adsorbed for a type I isotherm is (Langmuir, 1916):

$$\frac{P}{V_a} = \frac{1}{V_m B} + \frac{P}{V_m} \qquad \text{Equation 2.18}$$

where: V_a is the volume of gas adsorbed at pressure P (m^3), V_m is volume of gas required to form a monolayer (m^3), B is empirical constant and P is pressure of the adsorbate (psi). The equation for the volume of gas adsorbed for a type II isotherm is (Brunauer, Emmett and Teller, 1938):

$$\frac{n}{n_m} = \frac{Cx}{(1-x)(1-x+Cx)} \qquad \text{Equation 2.19}$$

where: n is quantity adsorbed (mol), n_m is monolayer capacity (mol), C adsorption coefficient (unitless) and x is relative pressure at equilibrium P/P_O (psi).

2.10.6 Quantitative X-ray Diffraction (QXRD)

The XRD method is used to determine the crystal structure of minerals. A crystalline lattice is a regular three dimensional distribution of atoms, they are arranged so that they form parallel lines separated from each other by a certain distance (*d*). The *d* spacing is different in each mineral and is a fundamental part of the QXRD analysis.

The QXRD works by focussing a beam of X-rays on to the mineral surface. The beam is diffracted via Bragg's Law (Equation 2.20). Diffraction will only occur when the distance travelled by the rays reflected off the mineral planes differ by a complete number of wavelengths ($n\,\lambda$). In addition, the Bragg's Law must always be satisfied so that if the *d* spacing is changed, the angle must also vary.

$$n\,\lambda = 2\,d\,sin\,\theta \qquad \text{Equation 2.20}$$

where: λ is the wavelength of the X-ray (Hz), *d* is the spacing of the crystal layers (μm), Θ is the incident angle (the angle between incident ray and the scatter plane) (degrees) and *n* is an integer (unitless). The end result is a diffractogram (diagram showing the intensity of the diffracted radiation in relation to the angle of diffraction from the mineral) where each phase is represented by a number of peaks, and therefore analysing the group of peaks enables the individual phases to be identified. A quantitative analysis can be made using an intensity ratio method (RIR) a detailed methodology can be found in Hillier (2000).

2.11 Rock Typing

Rock typing involves defining common flow and storage characteristics for different lithologies (Porras, 2001; and Lieber, 2013). Rock types are defined to help reservoir engineers assign petrophysical parameters to different zones with similar characteristics, so that flow unit effectiveness could be determined for a detailed description of a reservoir (Hamon, 2003; Porras, 2001). In this research, rock types were generated to define the controls on porosity, permeability and electrical properties with the help of SEM, XRD and depositional environment (Chapter 5 and 6).

The most widely quoted definition for rock typing is often attributed to Gunter et al. (1997a, b), however, it was first given by Archie (1950), which stated that rock types

are "*units of rock deposited under similar conditions, which experience similar diagenetic processes, resulting in a unique porosity-permeability relationship, capillary pressure profile and water saturation for a given height above free water in a reservoir*".

Porras et al. (1999) and Perez et al. (2005) split rock types into lithofacies, petrofacies and electrofacies. The lithofacies are stated as "*map-able stratigraphic units, laterally distinguishable from the adjacent intervals based upon lithological characteristics that are related with the appearance, texture, or composition of the rock*" (Perez et al., 2005). The petrofacies are intervals of a rock with a similar average pore throat radius, thus having similar fluid flow characteristic (Porras et al., 1999). The electrofacies are *"a similar set of log responses that characterise a specific rock type and allows it to be distinguished from others"* (Perez et al., 2005).

Newshame and Rushings (2001) split rock types into two groups: petrographic and hydraulic. Petrographic rock types are based on pore scale microscope imaging of the current pore structure as well as the rock texture, composition, clay mineralogy and diagenesis. However, hydraulic rock types are based on the pore scale that quantifies the physical flow and storage properties of the rock relative to the native fluids. Hamon (2003) stated that rock types are split up into routine and special core analysis types. The routine defined rock types use porosity, permeability, grain density and mercury injection capillary pressure curves as markers of the geometry of the rock pore network. The data is clustered into subsets having similar flow and storage capacity.

Chapter 3 – Methodologies in Studying TGS

3.1 Introduction

A total of 34 TGS core plugs were studied during this project, they ranged in age from Carboniferous - Jurassic and were deposited in a range of environments including fluvial channels, lower shoreface, deltas and aeolian dunes (Table 3.1). The aim of this chapter is to provide a detailed review of the methodologies used to study these 34 samples. A detailed procedure or references are provided enabling each experiment to be reproduced. This is supported by pictorial and schematic representations.

This chapter is broken up into three subsections:

- **Section 3.2** presents the sub-sectioning of the 34 TGS, core plug preparation and core plug characterisation (CT scanner, dimensions and weights).
- **Section 3.3** presents the methodologies used to study off-cuts from core plugs. The standards used to calibrate the systems are also provided throughout this section.
- **Section 3.4** presents the methodologies used to study core plugs. The standards used to calibrate the systems are also provided throughout this section.

Table 3.1 The 34 TGS studied throughout this research along with their age, depositional environment and depth. Namurian is part of the Carboniferous from 326 to 313 Ma, Rotliegend is late Carboniferous between 302.5 to 260 Ma, Carboniferous is from 359.2 to 299 Ma and Jurassic is from 201.3 to 145 Ma.

Company	Sample	Age	Deposition Environment	Depth (m)
BP	2_2	Namurian	Deltaic sandstone	2868.8
BP	2_3	Namurian	Deltaic sandstone	2873.6
BP	3_1	Namurian	Fluvial channel	3652.8
WIN	4_26	Rotliegend	High energy fluvial channel	4518.4
WIN	5_16b	Rotliegend	Aeolian dune base	4105.4
SHELL	1_83	Rotliegend	Aeolian wet sandflat	2447.1
SHELL	1_111	Rotliegend	Aeolian homogenised	2455.6
SHELL	1_216	Rotliegend	Aeolian wet sandflat	2489.5
SHELL	2_1b	Rotliegend	Aeolian homogenised	2453.8
SHELL	2_9b	Rotliegend	Aeolian homogenised	2493.5
BP	3_4	Namurian	Crevasse splay/levee	3654.2
BP	3_5	Namurian	Crevasse splay/levee	3654.2
BP	3_6	Namurian	Crevasse splay/levee	3659.0
SHELL	4_202	Rotliegend	Interdune	2595.2
SHELL	4_389	Rotliegend	Dune (core)	2662.5
EBN	4_10	Westphalian	Channel	3188.4
WIN	9_5	Carboniferous	Sheetflood	3835.8
BP	2_5	Namurian	Deltaic sandstone	2810.7
SHELL	4_409	Rotliegend	Damp sandflat	2669.5
GDF	1_6	Carboniferous	Low sinuosity fluvial channel	4020.4
EBN	3_40	Rotliegend	Wadi channel (fluvial braid)	3463.7
SHELL	4_370	Rotliegend	Dune (core)	2656.1
GDF	1_1	Rotliegend	Fluvial Sheetflood	3915.4
GDF	1_7	Carboniferous	Low sinuosity fluvial channel	4022.0
GDF	2_4	Rotliegend	Fluvial Sheetflood	4126.8
WCA	2	Rotliegend	Structured sheetflood	4193.4
WCB	1	Rotliegend	Structured sheetflood	4194.1
WCB	6	Rotliegend	Structured sheetflood	4194.1
WCB	5	Rotliegend	Structured sheetflood	4194.1
WCA	4	Rotliegend	Structured sheetflood	4193.4
WCA	3	Rotliegend	Structured sheetflood	4193.4
WCB	11	Rotliegend	Structured sheetflood	4194.1
WCB	2	Rotliegend	Structured sheetflood	4194.1
BP	4_5	Jurassic	Lower shoreface	3742.5

3.2 Petrophysical Properties of TGS

The first step involved selecting and sub-sectioning the samples to be studied (Section 3.2.1). Core plugs were either provided or rock material was cored to provide samples. Core plugs and offcuts were then cleaned using dichloromethane

(DCM)/methanol in a Soxhlet extractor (Section 3.2.2). The core plugs were then CT scanned, off-cuts were then taken from the base of the core plugs and then the remaining core was photographed, weighed and dimensions were determined (Section 3.2.3).

The offcuts were studied with a scanning electron microscope (SEM), mercury injection capillary pressure (MICP), Brunauer-Emmett-Teller (BET) surface area and quantitative X-ray diffraction (QXRD) (Section 3.3). The grain volume was determined using a helium porosimeter (Section 3.4.1) and permeability using either pulse decay or steady state permeametry (Section 3.4.2). The core plugs were then saturated with brine of the same composition as the reservoir (Section 3.4.3) before brine permeability, electrical properties and NMR T_2 distribution were determined (Section 3.4.4 to 3.4.6). A workflow is presented in Figure 3.1.

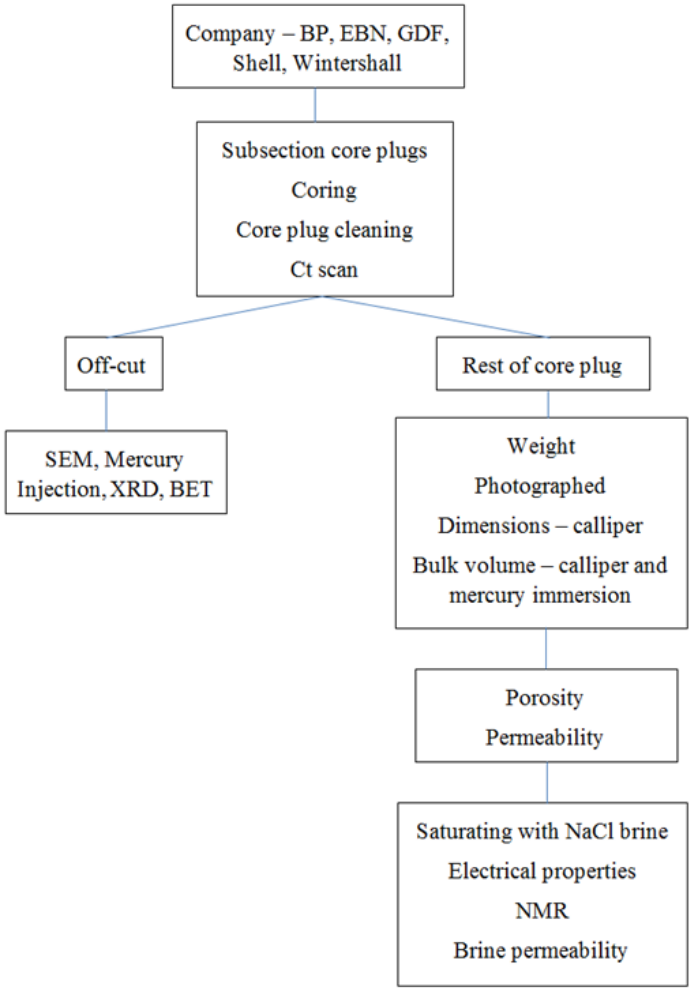

Figure 3.1 Workflow of the experimental methods each sample underwent to study the petrophysical characteristics of tight gas sandstones.

3.2.1 Sub-sectioning the TGS Samples

A total of 34 TGS samples were studied (Table 3.1). The first 25 samples were chosen based on their permeability and divided into core sets. Each core set consisted of 5 core plugs with a similar initial permeability which was provided by the companies, these divisions were chosen to ensure a range of TGS were studied with different properties (Table 3.2). Routine core analysis (Chapter 5) and special core analysis (Chapter 6) as well as the stress dependence of properties (Chapter 7) were measured. The WCA/WCB samples were used to assess optimal cleaning methods (Chapter 4) and BP4_5 sample was chosen for a metal injection experiment to assess the distribution of microfractures (Chapter 8).

Table 3.2 Sub-sectioning of the 34 TGS samples used in this research. The first 25 samples were used in Chapter 5, 6 and 7, the next 8 samples were in the cleaning comparison in Chapter 4 and the last sample was used in the metal injection experiment in Chapter 8.

Core set /Explanation	Company	Sample
1 – Medium Permeability 0.03 – 1.1 mD	BP	2_2
	BP	2_3
	BP	3_1
	WIN	4_26
	WIN	5_16b
2 – Low Permeability 0.001 – 0.3 mD	SHELL	1_83
	SHELL	1_111
	SHELL	1_216
	SHELL	2_1b
	SHELL	2_9b
3 - Medium Permeability 0.03 – 1.1 mD	BP	3_4
	BP	3_5
	BP	3_6
	SHELL	4-202
	SHELL	4_389
4 – Low Permeability 0.001 – 0.6 mD	EBN	4_10
	WIN	9_5
	BP	2_5
	SHELL	4_409
	GDF	1_6
5– High Permeability 1.1 – 4.1 mD	EBN	3_40
	SHELL	4_370
	GDF	1_1
	GDF	1_7
	GDF	2_4
Cleaning comparison	WCA	2
	WCB	1
	WCB	6
	WCB	5
	WCA	4
	WCA	3
	WCB	11
	WCB	2
Cause of stress dependency	BP	4_5

3.2.2 Core Plug Preparation

The 25 TGS samples were either provided as large cores preserved in wax that needed to be further cored or pre-cored material was provided. Core plugs were taken from the preserved cores using a 1.5 inch drill bit and cut to a length of ~5 cm. All cores regardless of initial status would have contained drilling fluids that were not present in the subsurface. It was therefore important to remove these without further damaging the pore structure of the samples. The cleaning process using the Soxhlet extractor with dichloromethane (DCM)/methanol (Figure 3.2) involved placing the core plug into the main sample chamber (A) and the solvent into the bottom chamber (B). The solvent was heated from below to 39.6ºC, the vapour travelled up the distillation arm (C) and condensed into the sample chamber due to a flux of cold water from above (D). The chamber containing the core slowly filled with the solvent and overtime, the DCM/methanol removed the unwanted fluids and salt. The chamber was automatically emptied by a siphon side arm along which it flowed back into the solvent chamber (E). The change in colour of the solvent within the sample chamber as well as the core were both monitored. The samples were deemed clean when the fresh DCM/methanol did not discolour during the Sohxlet extractor process.

The DCM/methanol within the pores and surface of the sample had to be removed to ensure the core was free from any substances prior to analysis with gas. This was achieved by drying the core plug in a humidity controlled oven at 60^{o}C for 2 days. It was deemed dry when a stable weight was reached.

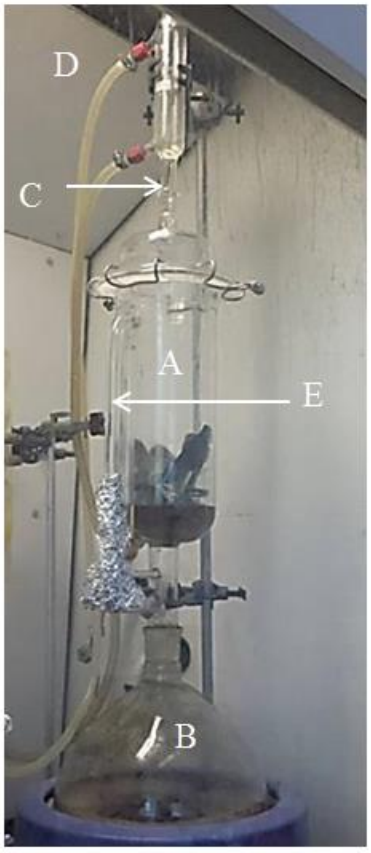

Figure 3.2 Soxhlet extractor used to clean core samples. The solvent is heated and the vapour travels up the distiller where it condenses into the sample chamber due to a flux of cold water. The solvent level increases in the sample chamber and the substances are removed by the warm solvent. The cycle is repeated as required. A = sample chamber, B = solvent chamber, C = distiller, D = condenser and E = siphon.

The advantage of this method is that it cleans a wide sample size; it is easy to carry out as it involves little setup and the system requires minimal observation. The disadvantages are that certain rock types might require different conditions (solvents, temperatures) which was not considered here. The oven drying of the sample could damage fine clays and cause the movement of grains from one location to another which can block pore throats and lead to reductions in permeability. Therefore, to understand the effect on the microstructure of clays, a comparison was made between the Soxhlet extractor method and a critical point drying method with acetone (used to extract water) and methanol (used to extract salts) in Chapter 4.

3.2.3 Core Plug Characterisation

A Picker PQ2000 dual energy CT-scanner (a fourth generation medical scanner) was used to scan and provide an image of the internal structure. This was done to

determine sample heterogeneity based on their density variations and identify any core damage. Once the core plugs had been CT scanned, off-cuts were taken (and used to make thin sections for optical microscopy and SEM (Section 3.3.1), cubes for MICP (Section 3.3.2) and were crushed for BET (Section 3.3.3) and QXRD (Section 3.3.4) analysis.

The remaining core material was weighed, photographed and the dimensions measured. The dry weight was measured using a top pan balance where 3 significant figures were noted. The dry weight was used to determine the grain and bulk density (Appendix B). Photographs were taken from the side, top and bottom of the core so that the general surface heterogeneity could be recorded. It also provided a visual record of the core. The length and diameter were measured three times using electronic callipers. All the dimensions were then averaged and the diameter was then used to quantify the cross sectional area of the core plug. The length and diameter were used to determine the bulk volume (Section 3.4.1).

3.3 Off-cut Analysis

3.3.1 Microstructural Analysis - Scanning Electron Microscope (SEM)

To create the thin section, the sample was cut with a diamond saw blade to a suitable size for polishing (48 x 26 mm). The sample was ground flat using a 75 μm diamond plate and vacuum impregnated with blue epoxy resin. The sample was then finely ground on a 10 μm diamond plate before mounting the sample with the ground face down on to a glass slide. The sample was left to rest for 90 minutes for the resin to cure. After this, the sample was ground to the desirable thickness of 30 μm using a Buehler Petrothin cutter/grinder. The sample was polished with diamond paste and suspensions starting with 3 μm then 1 μm, then ¼ μm using paper cloth polishing pads on a Buehler Automet 250 system. Finally the sample was hand lapped with aluminium oxide slurry to give a pre-polished finer surface. The process took about 8 to 10 hours over 2 days.

The thin section samples were carbon coated and attached to a sample holder using copper tape and placed into an FEI Quanta Field Emission Gun (FEG) 650 instrument for BSEM analysis. The samples were examined using an accelerating voltage of 20 KeV, a spot size of 5 and an objective aperture of 4. The main minerals

were then identified by energy dispersive X-ray analysis (EDX) using AZtec software. A detailed microstructural analysis was conducted using a back scattered electron (BSE) to identify the texture, presence of microfractures, diagenesis as well as the distribution of clay and microporosity. The BSE images were saved in an 8bit (256 grey levels) digital form and analyzed using the ImageJ image analysis software.

3.3.2 Mercury Injection Capillary Pressure (MICP)

Mercury injection analysis was performed using a Micrometritics Autopore V porosimeter. The dry sample was placed into an evacuated penetrometer which was attached to a glass capillary tube and filled with mercury. Atmospheric pressure was applied allowing the mercury to enter the larger pores. The pressure was increased from 2 psi to 55000 psi and left for 10 seconds to allow for pressure equilibrium to enable the mercury to enter the smaller pores. The pore diameter was estimated using the Young-Laplace equation (Equation 2.16). The bulk density (BD – g/cm^3) was determined from the mass of the sample and the sample bulk volume:

$$BD = \frac{\text{Sample mass}}{\text{Sample volume}} \qquad \text{Equation 3.1}$$

and the grain density (GD – g/cm^3) was determined from the mass of the sample, sample volume and the total intrusive volume:

$$GD = \frac{\text{sample mass}}{(\text{sample volume} - \text{intrusive volume})} \qquad \text{Equation 3.2}$$

The advantage of the MICP methodology is that it provides pore size distribution and bulk and grain density values, the latter can be compared to the values estimated using caliper, helium porosimeter and QXRD. The disadvantages are that the core plug must be cut to provide the off-cut and the sample size may not be fully representative of the reservoir. In addition, mercury is harmful and therefore care must be taken when carrying out the experiment.

3.3.3 BET Surface Area

A Quantachrome version 10.01 instrument was used to quantify the surface area. Prior to performing the experiment, the samples were weighed to ~5 g using a top pan balance of an accuracy of +- 0.05, ground using a pestle and mortar and sieved. A 250 – 500 μm sieve was used as this was the average grain size. Once the sample was prepared, it was placed into the sample chamber where it was degassed to remove adsorbed contaminants. The degassing was performed for 2 hours on each sample and involved a combination of heat (120°C) and a vacuum. The sample was then cooled to cryogenic temperature of -195.8°C (77 K) and ~28 g N_2 gas at a liquid density of 0.81 g/cm^3 was admitted to the sample in controlled increments. The pressure was allowed to reach equilibrium in 60 seconds and the quantity of gas adsorbed was calculated. The amount of gas adsorbed onto the surface of the grains defines the adsorption isotherm (see Section 2.10.5 Chapter 2).

The advantage of the BET surface area methodology is that it provides the surface area of the sample, which can be linked to permeability. The disadvantage is that the core plug must be cut to provide the off-cut, which must be subsequently ground, and the sample size may not be fully representative of the sample.

3.3.4 Quantitative X-ray diffraction (QXRD)

Quantitative X-ray diffraction analysis was conducted on ~5 g of partly crushed sample at the University of Leeds using a Philips PW1050 diffractometer and the Macaulay Scientific Consulting Ltd in Aberdeen using a Siemens D5000. The samples at both institutes were mixed with 20 wt.% corundum which acted as an internal standard. The weighted samples were transferred to a McCrone mill with ethanol, ground for ~ 12 minute and the slurry was spray dried (Hillier, 1999). The samples were top loaded into a 2.5 cm diameter circular cavity holder. After that, X-ray radiation was diffracted by the crystals and based on the angle between the diffracted and the transmitted beam, a diffraction pattern was recorded from 2-75°2θ using Cobalt Kα radiation. The sample was rotated throughout the procedure enabling the intensity of each diffraction to be measured at every spot. The main phases present in the sample mixture were obtained using reference patterns from the

International Centre for Diffraction Database (ICDD) and a reference intensity ratio method (RIR). A detailed methodology can be found in Hillier (2000).

The grain density was determined using the percentage of each mineral determined from the QXRD ($\%_M$) and the grain density of each mineral in nature (GD_M):

$$GD = \frac{100}{\left(\frac{\%_M}{GD_M} + \frac{\%_M}{GD_M} \ldots\right)} \quad \text{Equation 3.3}$$

The advantages of the QXRD methodology are that it provides quantitative information of the minerals present in the rock. The total amount and types of digenetic minerals such as clay and dolomite can give an indication of the productivity of the reservoir. The disadvantages are that it requires crushed material, the sample size may not be fully representative of the reservoir and for trace minerals there is an uncertainty as to whether the phases are present.

3.4 Core plug Analysis

3.4.1 Porosity

Porosity is measured from the bulk volume and grain volume:

$$\emptyset = \frac{BV - GV}{BV} X100 \quad \text{Equation 3.4}$$

where ϕ is porosity (%), BV is bulk volume (cm^3), and GV is grain volume (cm^3). The bulk volume was determined using electronic callipers and mercury immersion. For the former, the length and diameter was measured using electronic callipers (API, 1998) and a bulk volume (BV) was determined:

$$BV = \pi \ L \ r^2 \quad \text{Equation 3.5}$$

where π is Pi, L is the length (cm) and r is the radius (cm). In the latter, a mercury bath was placed on a single-pan electronic balance, and a core plug was immersed into the mercury using a pronged fork. From the weight of mercury displaced when the full core was submerged in the mercury (g), and a mercury density of 13.5377 g/cm^3, another bulk volume can be determined (API, 1998):

$$BV_{Hg} = \frac{weight\ Hg\ displaced}{13.5377} \qquad \text{Equation 3.6}$$

The grain volume was determined using a Quanta Chrome SPY-4 helium porosimeter using Boyle's law. Boyle's law states that for any fixed known temperature, the pressure and volume are inversely proportional; thus the sum of the pressure and the volume of a particular gas are related to the amount of gas occupying that volume. Therefore, when there is a change in the pressure or the volume of the gas, the grain volume in the core can be determined (API, 1998). The effects of temperature are incorporated to provide a more accurate GV value:

$$\frac{P_1 V_1}{T_1} = \frac{P_2 V_2}{T_2} \qquad \text{Equation 3.7}$$

$$GV = \frac{sample\ cell\ V + Expansion\ V}{(1 \frac{P_1}{P_2})} \qquad \text{Equation 3.8}$$

where P_1 is pressure before (Pa), P_2 is pressure after (Pa), V_1 is the volume before (cm^3), V_2 is the volume after (cm^3) and T_2 is temperature before (°C), T_2 is the volume after (°C).

To check the accuracy of the device the system needed to be regularly calibrated. This was done in two ways. Firstly, using a chrome plated calibration cylinder that was provided with the instrument. Secondly, with five porosity standards purchased from Core Test Ltd (Figure 3.3). The system needed to be calibrated prior to analysing a set of core plugs. This was achieved by calibrating the reference and core chamber volumes using first an empty volume and then with steel balls of different sizes depending on the size of the core plugs being used. For a 3.8 cm diameter core plug a steel ball of volume 56.56 cm^3 was used, and for a 2.5 cm diameter core plug two balls 2.095 cm^3 and 7.07 cm^3 were used. The calibration was repeated at least three times.

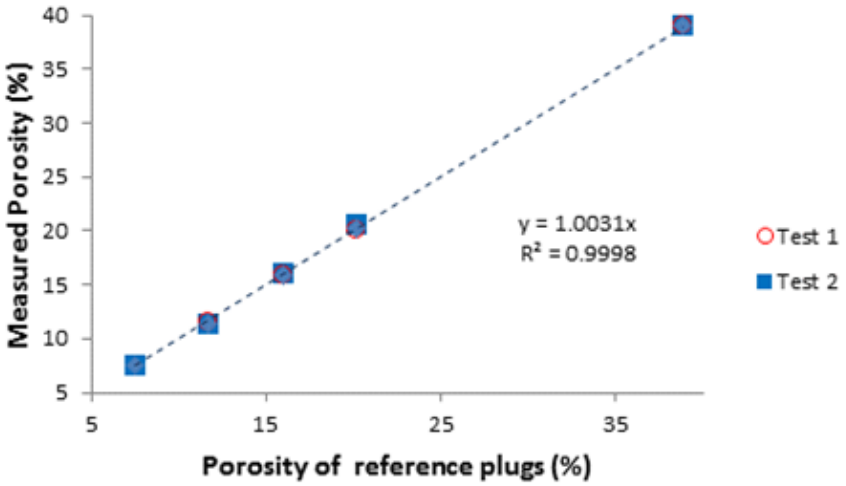

Figure 3.3 Measured porosity as a function of reference plug porosity showing results from the analysis of the 5 Core Test samples. The 1:1 regression and very high correlation coefficient highlights the accuracy of the technique.

After the calibration, a core plug was placed in the sample chamber of a Quanta Chrome SPY 4 porosimeter (Figure 3.4). Both 1 in and 1.5 in diameter samples could be used. Helium gas was admitted into the reference chamber until the pressure reached ~ 15 psi. The pressure in the reference chamber was left until it was stable, then P_1 (initial absolute pressure) was recorded. The gas was then expanded into the core chamber. The resulting lower pressure - P_2 (final absolute pressure), was measured after the system had reached stability. The grain volume was determined using Equation 3.7 and Equation 3.8 (API, 1998).

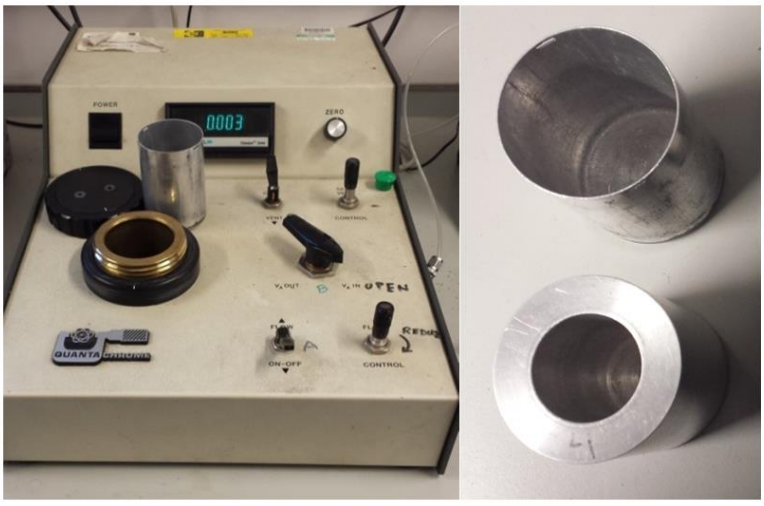

Figure 3.4 Helium porosimeter instrument used to determine the grain volume (left), sample chamber for 3.8 cm and 2.5 cm core samples (right).

The grain volume determined using the helium porosimeter was used to determine the grain density using Equation 3.9:

$$GD = \frac{W}{GV} \qquad \text{Equation 3.9}$$

where *GD* is grain density (g/cm^3), *W* is dry weight (g). This was compared to values estimated using mercury injection pycnometry and QXRD values (Section 3.3.2 and 3.3.4). In addition, the bulk density was determined using a calliper bulk volume:

$$BD = \frac{W}{BV} \qquad \text{Equation 3.10}$$

where *BD* is bulk density (g/cm^3). This was compared to the mercury injection bulk density values (Section 3.3.2). The comparisons were made to provide a range of methods to determine the same parameter.

The advantages are that the core plug is not damaged and the helium does not react with the core plug, therefore, it can be used for other measurements. The measurement is quick and simple to carry out and all 1 and 1.5 inch sample sizes can be tested. However, changes in the temperature can affect the measurements, therefore, the temperature must be recorded. In addition, the measurement is made on a sample that is unstressed.

3.4.2 Gas Permeability

The samples with a permeability of > 0.1 mD are measured using a steady-state method. In the steady-state test, steady-state flow is established through the specimen, and the permeability is calculated from the measured flow rate and pressure gradient. If the permeability is low (< 0.1 mD), long periods of time are required to establish steady-state flow, thus, these procedures are impractical therefore, transient tests such as pulse decay permeametery (PDP) are used.

The PDP method for measuring gas permeability has been described fully by Brace et al. (1968). The PDP consists of a cylindrical sample that is connected to two fluid reservoirs. At the start of the experiment, the fluid pressure in the upstream reservoir is increased. The pressure transient is logged as the fluid flows across the sample to

the downstream reservoir. The permeability of the sample is calculated from the pressure transient.

Jones (1997) explains that the most time consuming part of the conventional pulse decay technique is allowing the system to reach pressure equilibrium prior to the pressure pulse. Therefore, he designed a new set up which reduces this time by incorporating two additional larger reservoirs (100 cm^3) along with two smaller reservoirs (5 cm^3) (Figure 3.5). The larger reservoirs allowed the system to reach equilibrium faster, however, upon shutting valves 3 and 4; they would not contribute to the pressure decay leading to an overall faster experiment.

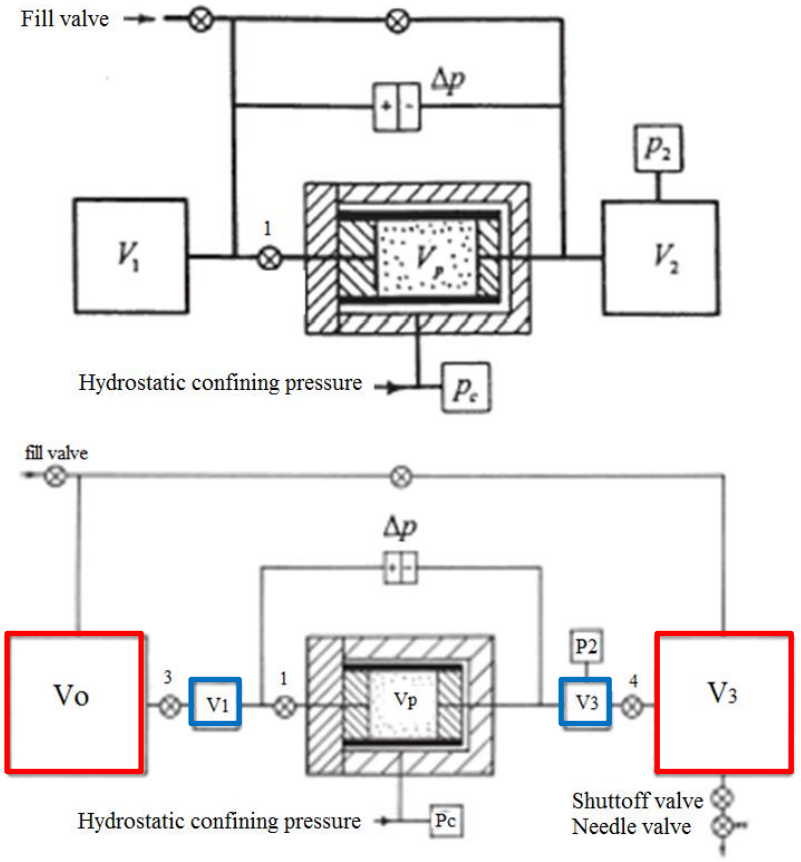

Figure 3.5 Apparatus for the conventional pulse decay measurement designed by Brace et al. (1968) showing the presence of only two small volumes (V_1 and V_2) (top). The modified setup designed by Jones (1997) showing the presence of the two smaller volumes as well as two larger volumes.(bottom). The larger volumes (red box) allow the system to reach equilibrium faster whereas the smaller volumes (blue box) are used in the pressure decay therefore allowing for a faster experiment.

To perform the pulse decay experiment, the dry core was placed into a jacketed core holder (A) and the end caps were shut tightly. The confining pressure was applied using the hand pump (B) (Figure 3.6) where a range of confining pressures were

used (Table 3.3). Oil was used to confine the cores and helium gas was used as the permeant.

The pore pressure entering the system was then increased using the gas cylinder (C) (Figure 3.6) where a range of pore pressures were used (Table 3.3). The system was left for 300 seconds to equilibrate; which is known as the soaking time. Once the test was started, the upstream, downstream, mean pressure and differential pressure were logged over time. Once the upstream and downstream pressures had equilibrated, the confining pressure, pore pressure and permeability were all recorded and the test was repeated at a higher confining pressure.

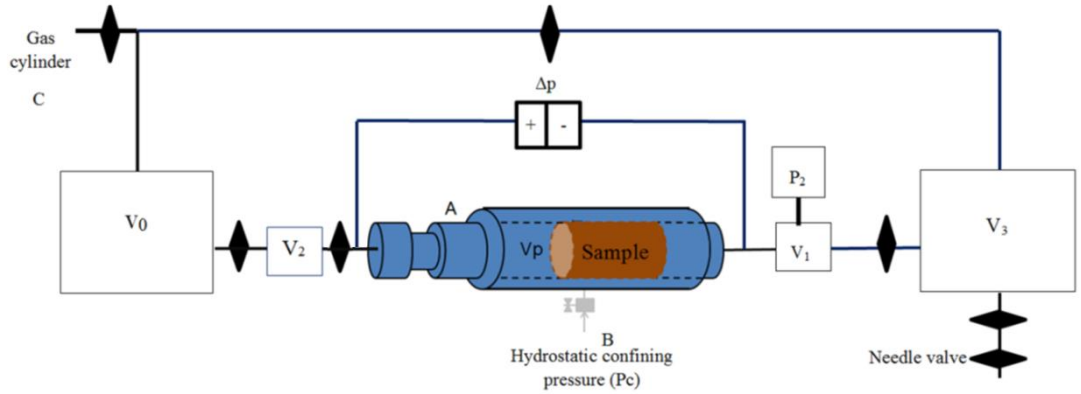

Figure 3.6 Schematic drawing of the permeameter used during this study: core holders (A), Enerpac hand pump used to supply the confining pressure (B), the gas cylinder used to supply the pore pressure (C) and the two smaller volumes - V_2 , V_1 and larger volumes - V_0, V_3.

Table 3.3 Confining and pore pressures used in the pulse decay, steady state and draw down experiments for all samples.

Pulse decay		**Steady state**	**Drawdown**	
Confining pressure (psi)	**Pore pressure (psi)**	**Confining pressure (psi)**	**Confining pressure (psi)**	**Pore pressure (psi)**
1500	1000	500	10,000	5000, 4000, 3000, 2000, 1000
2500	250, 500, 1000	1500		
3500	250, 500, 1000			

The steady state method used the same setup as the pulse decay experiment except a flow meter was used to measure the flow of gas through the core and different software was used to record the pressure changes during the experiment. The gas at a particular flow rate and pressure was introduced at the upstream end and over time, the differential pressure decayed as the gas flows from the upstream towards the downstream. Once the setup had reached equilibrium, the flow rate, differential

pressure and pore pressures were noted. By measuring the pressure drop across the core, a gas permeability was determined using Darcy equation.

The pulse decay and steady state equipment was calibrated on a regular basis using plastic plugs of known permeability. Each plug has a fine capillary of known diameter embedded within it. Plots of measured vs calculated permeability show that in all cases the measurements were in agreement of the theoretical values (Figure 3.7).

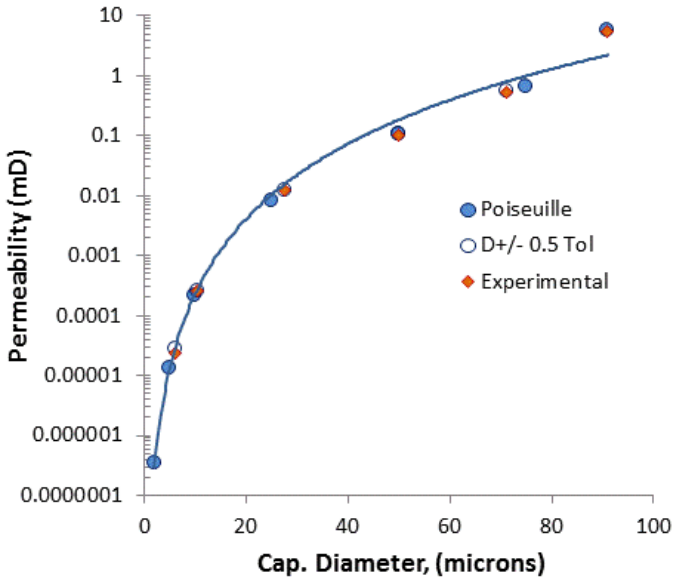

Figure 3.7 Plot of measured and calculated permeability vs capillary diameter from a series of standards, as well as the uncertainties in the calculated permeability resulting from the 0.5% uncertainties in the capillary diameter. The data shows that is all cases the measurement is in agreement with the theoretical values.

To enable the permeability data to be more representative of reservoir conditions during production, drawdown tests (fixed C_P and decreasing P_P) were carried out using the setup depicted in Figure 3.8. The sample was placed into the core holder and the end platens tightly shut (D). The confining pressure was then increased using the foot pump (E) and the cores were subjected to a confining pressure that was close to the stress in the subsurface (Table 3.3). The experimental setup was similar to the PDP set up based on Jones (1997), except a positive displacement pump was used to regulate the pore pressure (F) and higher confining and pore pressures were used.

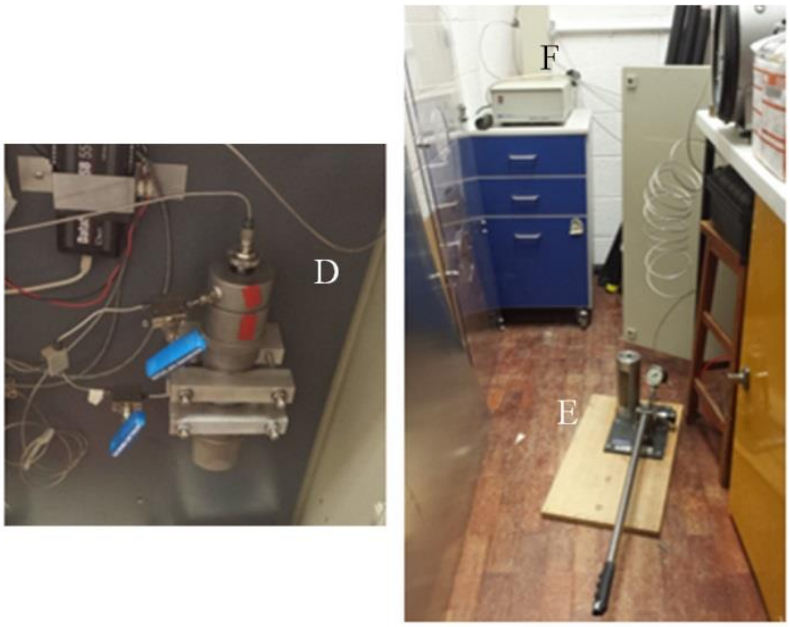

Figure 3.8 Drawdown setup showing the core holder (left) (D), foot pump used to apply the confining pressure (E), and the water pump used to regulate the pore pressure (F) (right).The set-up works the same way as the traditional pulse decay sown in Figure 3.6.

The advantage of these methodologies is that the core plug is not damaged and the gas does not react with the rock; therefore, the core plug can be used for other measurements. The measurement is simple to carry out and both 1 and 1.5 in core plugs can be tested. However, the core must not be too short as this can create gas pockets or have any sharp edges as this can damage the core holder. The core plug must be free of any large vugs on the surface as these can act as flow paths leading to an over prediction of the permeability.

3.4.3 Saturating Cores with Brine

Each core sample was saturated in brine that closely matched the reservoir brine (Table 3.4). This formed the basis for the electrical, NMR and brine permeability measurements. The NaCl was weighed out (200 or 300 g) using a top pan balance. The solid was dissolved in de-ionised water in a beaker and transferred to a 1 litre volumetric flask. The beaker was rinsed and the remaining contents were added to the flask. This was done to ensure all the salt was transferred. More de-ionised water was added to create exactly 1 litre of solution and the flask was then sealed and shaken. Subsequently, the cores were saturated with the brine under vacuum for 48 hours, and then atmospheric pressure was applied so that the brine displaced the air. It was assumed that no more air was present within the core when no more air

bubbles were produced. To ensure the core was fully saturated, each core was placed under 1500 psi for 2 days to expel the remaining gas within the smaller pores. Finally, the samples were left in the brine in plastic containers and sealed with a lid to ensure the brine did not evaporate.

Table 3.4 Brine compositions for each well used in this research where all wells except SHELL1 and 2 required 20% NaCl solution.

Company/Well	
BP2, BP3, GDF1, GDF2, EBN3, EBN4, SHELL4, WIN1 WIN7, WIN9,	SHELL1, SHELL2
200g of NaCl in 100ml of de-ionised water: 20% NaCl	300g of NaCl in 100ml of de-ionised water: 30% NaCl

3.4.4 Brine Permeability

Brine permeability measurements were conducted using a pulse decay permeametery described by Amaefule (1986). To carry out the experiment, a fully saturated sample was placed into a core holder (A) which was housed in a temperature controlled environment and 1500 psi confining pressure was applied using the hand pump (B) and left to stabilise for 2 days (Figure 3.9). The 196 ml brine pump was filled with brine and a back pressure of 120 psi was applied to keep the pressure constant over the sample.

The pressure on the pump was increased to 850 KPa (123 psi) and the brine was left to flow through the core for a few minutes. The upstream valve was then closed and the pressure in the pump was increased to 1350 Kpa (196 psi). The upstream valve was opened to allow brine to move through the sample and the pressure decayed from the upstream to the downstream reservoir back to the starting value. The upstream pressure, temperature and differential pressure as a function of time are monitored and automatically recorded. The permeability of the sample is determined using:

$$K = \left(\frac{\mu\ \beta\ V_1\ \ L}{A}\right) m\ 1000 \qquad \text{Equation 3.11}$$

where is μ is the viscosity (cP), β is the water compressibility, V_1 is the volume used (cm^3), L is length (cm), A is area (cm^2), m is slope of graph of change in pressure vs time using the method described in Amaefule (1986).

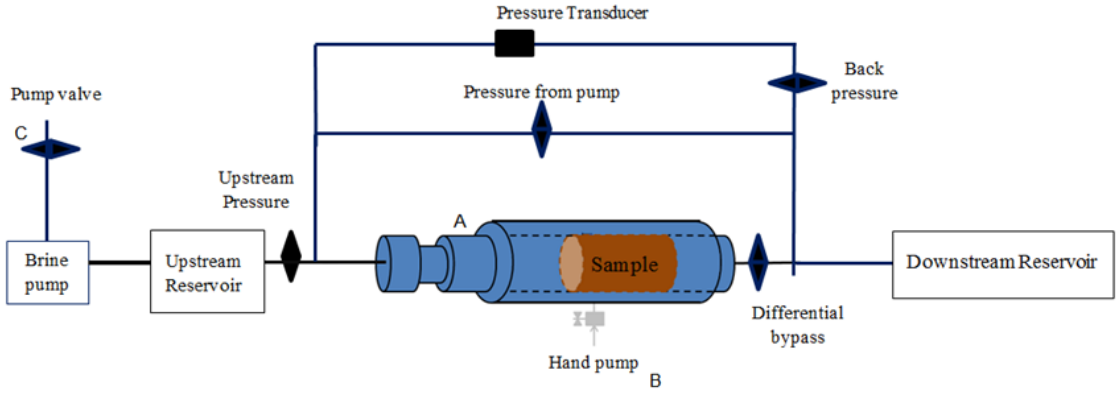

Figure 3.9 Schematic drawing of the set up used to measure the brine permeability. Core holder (A), hand pump supplying the C_P (B), the upstream and downstream volumes, valve C to fill or empty the pump and the 4 valves used to perform the experiment.

Comparisons of brine permeability measured in steady state conditions vs. pulse decay conditions are provided (Figure 3.10). Each point represents a different core plug and both techniques were applied to the same plug under similar stress conditions. It can be seen that all measurements are within a factor of 3 of each other.

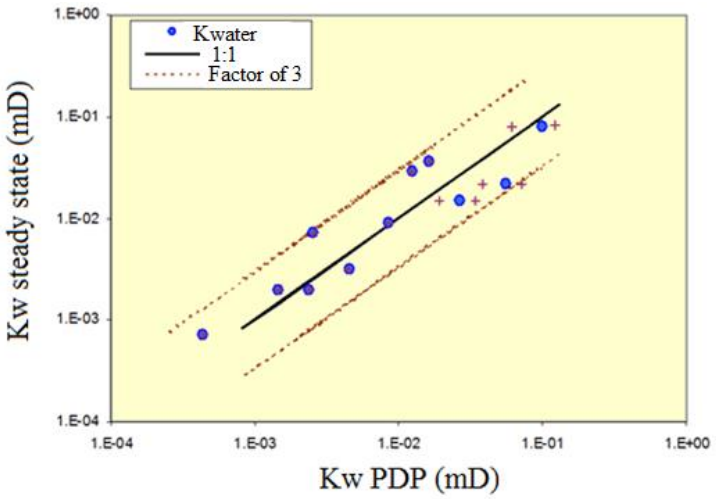

Figure 3.10 Steady state vs pulse decay brine permeability data showing the reliability of the brine permeability set up where all the measurements are in a factor of 3 of each other.

An advantage of the experiment is that the core plug is not damaged. The disadvantages include the need to saturate the samples; therefore, experiments with gas cannot be performed afterwards. It is time consuming to set-up and run the experiment especially with tight rocks. The core must not be too short as this can create gas pockets or have any sharp edges as this can damage the core holder. The core plug must be free of any large vugs on the surface as these can act as flow paths

leading to an over prediction of the permeability. In addition, the brine could react with the minerals in particular the clays.

3.4.5 Electrical Properties

Electrical resistivity measurements of the brine-saturated core plugs were taken at a frequency of 2 kHz using a Quadtech 7600 RLC meter (Figure 3.11). To perform the experiment a fully saturated sample was placed into a core holder and 1500 psi confining pressure was applied using the hand pump. In case a spacer is required, a metal one must be used to allow conductivity between the end platen and the sample. The resistivity meter was calibrated using a resistor of known resistance. If the correct reading was not displayed, an internal calibration was completed by first having the two electrodes apart (open) and secondly when they are connected to each other (closed). The resistor of was then reapplied to see if the correct value was displayed.

The core plug was placed into the core holder and 1500 psi confining pressure was applied. A two-electrode set-up was used where electrically isolated silver-coated electrodes were placed at both ends of the core. The sample was allowed to reach equilibrium over 3 days while the resistance and temperature were monitored over time. The resistance at the laboratory temperature was corrected to reservoir temperature using Equation 2.12 in Section 2.9. Formation resistivity factor (*FRF*) and cementation exponent (m) were then determined after the sample had reached equilibrium using Equation 2.13 to 2.15 in Section 2.9.

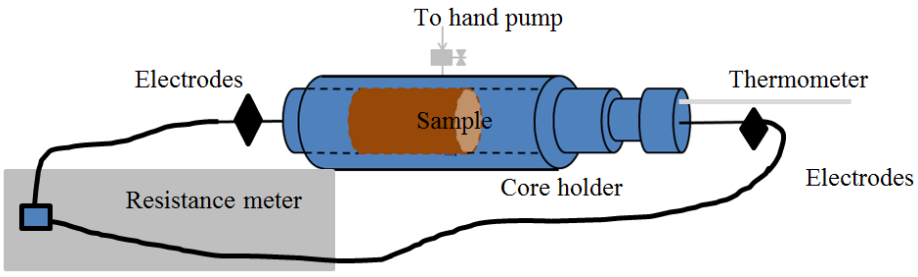

Figure 3.11 Schematic drawing of the set up used to measure the electrical properties. The core holder used to house the core plug, resistance meter used to measure the electrical properties hand pump used to supply the confining pressure and the thermometer used to log the temperatures inside the core plug to correct the data to reservoir temperatures.

The advantages are that the core plug is not damaged during the experiment and it is easy to carry out as it involves little setup and the system requires minimal

observation. However, samples have to be saturated; consequently, experiments with gas cannot be performed afterwards. The experiment is very temperature sensitive and calibrations have to be performed which are time consuming especially with tight rocks.

3.4.6 Nuclear Magnetic Resonance (NMR)

Brine saturated core plugs were analysed using a Maran Ultra NMR spectrometer. A brine saturated core plug was removed from the storage containers and excess brine was removed by rolling the core plug on a wet paper towel to ensure that the fluid did not get drawn out of the surface pores. The core plug was weighed to provide the saturated weight and wrapped in cling film to prevent the core from drying out. The core plug was placed in a sample holder and checked to ensure that the core plug sat within the centre of the magnetic field and then the core plug was placed into the NMR spectrometer. The system was started and left until the analysis was complete. The normalised signal vs the T_2 was plotted to provide the pore size distribution (example: Figure 3.12).

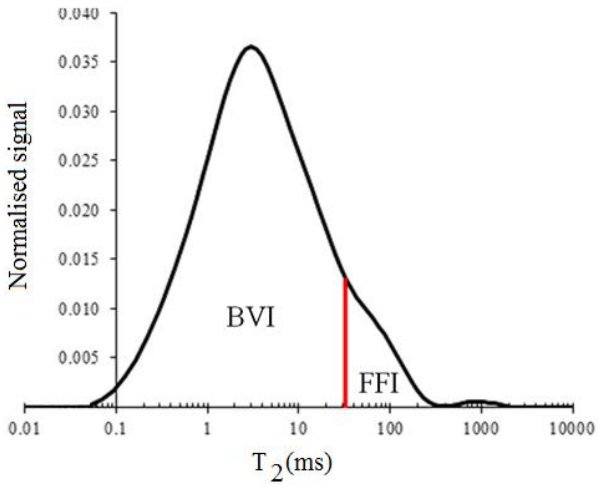

Figure 3.12 Normalised signal vs T_2 for one core sample. The 33ms cut-off for sandstones is shown in red dividing the bound and moveable fluid.

The NMR instrument was calibrated on a regular basis. This was done using a series of porous samples where each had a known pore size distribution and water content. In addition, the system was calibrated prior to each sample analysis using pure oil.

Porosity, free fluid index: bulk irreducible water volume ratio (FFI/BVI) and T_2 cut-off was used to estimate the permeability. The two most widely used methods for

calculating permeability from NMR data and the ones used in this research are based on the Timur-Coates (Equation 3.12) and the Schlumberger Doll Research (SDR) (Equation 3.13):

$$K = \left[\left(\frac{\emptyset}{C}\right)^{a}\left(\frac{FFI}{BVI}\right)\right]^{b} \qquad \text{Equation 3.12}$$

where ϕ is the helium porosity (%), *C* is the formation dependent variable, *FFI*/*BVI* is the ratio or bound to moveable water, *a* and *b* are the exponents which are usually a value of 2 and *K* is permeability (mD).

$$K_{SDR} = C\emptyset^{a}\,T_{2lm}^{b} \qquad \text{Equation 3.13}$$

where K_{SDR} is permeability *(*mD*)*, T_{2lm} is the geometric mean of the T_2 distribution (s) and *a* and *b* are usually a value of 4 and 2 respectively. The advantages of this technique are that it can be used on a range of sample types from rocks to liquids. It requires little sample preparation, is rapid; does not destroy the sample and is automated. The disadvantages are that the instrument is expensive and experiments with gas cannot be performed after the samples are saturated.

Chapter 4 – Comparison of Core Plug Cleaning Methods

4.1 Introduction

Traditional methods to clean core plugs such as the Soxhlet extractor using dichloromethane (DCM)/ methanol could damage the microstructure of samples containing delicate clays due to the temperatures, harsh chemicals and exposure to air (McPhee et al., 2015). The exposure to air can cause interfacial tension between the gas and the liquid within the core plug (Evangelista et al., 2004). Therefore, it is recommended that such samples should be cleaned using critical point drying where temperature and pressure of the liquid solvent is increased to the critical point and it is possible to pass from a liquid to a gas without a change in state, this removes the interfacial tension (Evangelista et al., 2004).

A comparison was made between four different cleaning methods - Soxhlet extractor with (i) DCM/methanol and (ii) toluene and critical point drying with CO_2 and (i) methanol and (ii) acetone. The aim was to determine what effect different cleaning methods have on the petrophysical properties of TGS and especially the clay structure. The DCM/methanol and toluene are common cleaning solvents used in oil saturated rocks; acetone is useful for removal of water and methanol for salts.

The methodology of the two cleaning processes is presented in Section 4.2 as well as the petrophysical properties performed after cleaning in Section 4.2.3. This is followed by the results in Section 4.3. A discussion is presented into whether the critical point drying method provides a more delicate cleaning procedure for the current TGS compared to the Soxhlet extractor and the main issues with the two methodologies in section 4.4. The work presented in this chapter is summarised in Section 4.5 together with recommendations for future work.

4.2 Methodology

4.2.1 Soxhlet Extractor with DCM/Methanol and Toluene

Two Wintershall cores (WCA/WCB) were cored to produce four 2.5 cm diameter core plugs (Table 3.2). As DCM/methanol were used in Section 3.2.1, a comparison was therefore made between (i) DCM /methanol and (ii) toluene where two of the cores were cleaned with DCM/methanol and the other two with toluene. The reason for this was that although DCM/methanol and toluene both extract oil, they may affect the microstructure of the core in different ways due to their different boiling temperatures and chemical reactivities.

The methodology used for Soxhlet extraction was presented in Section 3.2.2 and is based on the one presented in RP40 (API, 1998), however, some changes were made that are specific to this comparison. Firstly, DCM/methanol and toluene were used which have different boiling points of 40ºC and 110ºC respectively. Secondly, the samples used were left soaking in the solvent overnight before the solvent was circulated for a day, followed by a further day of soaking to ensure the sample was thoroughly cleaned. Thirdly, the core plugs were left to air dry instead of oven drying. This was because oven drying was thought to compress the clays and possibly cause fine clay to be dislodged, which can have a large effect on the permeability.

4.2.2 Critical Point Drying with CO_2 and Acetone and Methanol

Two cores (WCA/WCB) were cored to produce four 2.5 cm diameter core plugs (Table 3.2). The first step was to saturate the core plug with a polar solvent where two of the cores were saturated with acetone and the other two with methanol. The core plugs were left saturating for 24 hours under vacuum and then atmospheric pressure was applied so that the polar solvent displaced the air. The saturated sample was placed into the CO_2 chamber (Figure 4.1) and the back pressure regulator was attached to the sample chamber (Figure 4.2). The length and diameter was confined to 2.5 cm due to the sample chamber size.

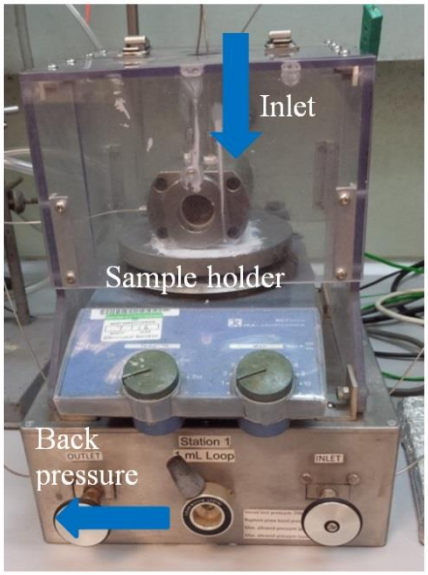

Figure 4.1 Sample cell chamber used to house the 1 inch core plug for the critical point drying method. The lower connector is to the back pressure and the inlet is from the CO_2 pump.

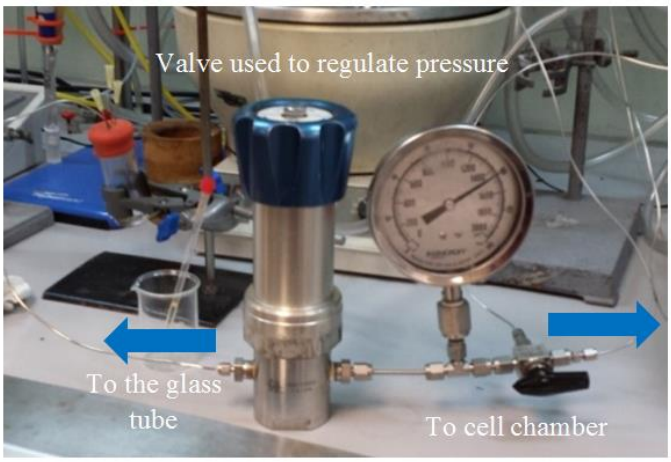

Figure 4.2 Back pressure regulator set to 100 bars (1450 psi). The left connector went to the glass tube containing the DMSO-d6 and the right connector to the chamber containing the sample.

The back pressure regulator was connected to a glass tube containing 5 ml of DMSO-d6 added using a pipette needle (Figure 4.3). DMSO-d6 is a tracer solvent as acetone, methanol and DMSO-d6 can be distinguished due to their different NMR peaks (Table 4.1). Therefore, DMSO-d6 was used to track the quantity of acetone/methanol removed over time. The glass tube was closed off with a rubber bung, this stopped the DMSO-d6 evaporating, however, small needles were attached to allow the CO_2 gas to escape (Figure 4.3).

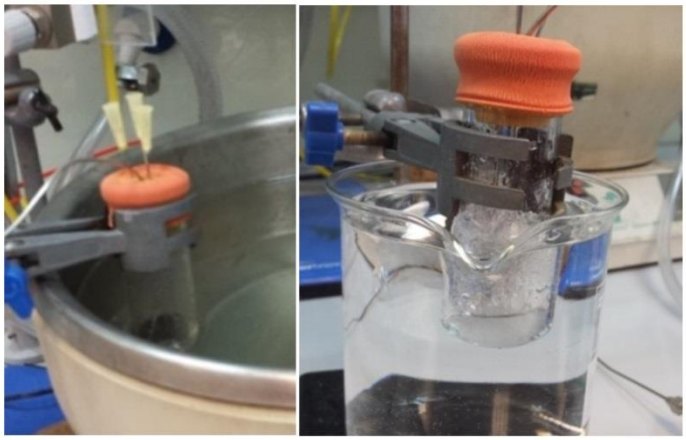

Figure 4.3 Glass tube containing 5ml of DMSO-d6 closed with a rubber bong and topped with needles to allow the CO_2 gas to escape (left). DMSO-d6 frozen in the glass tube where it freezes at room temperature (right). This was resolved by placing the glass tube into a water bath.

Table 4.1 NMR signals of acetone and methanol in DMSO-d6. As they have different signals they can be easily distinguished from each other (Gottlieb, 1997).

Solvent	**NMR signal in DMSO-d6**
Solvent residual signal	2.5
Acetone	2.1
Methanol	3.2

Liquid CO_2 was allowed to flush through the sample for 1 hour. Then the cell and back pressure were increased to 100 bar (1450 psi) and left for 20 minutes. The temperature was then increased to 40°C to reach critical point. Then the pressure of the supercritical CO_2 was decreased at a constant temperature of 40°C and allowed to flow through the sample to the glass tube at rate of 2 ml/minute. The CO_2 was then bubbled into the glass tube containing the DMS0-d6.

Throughout the experiment, 0.6 ml samples were taken out of the glass tube using a clean pipette, transferred to a NMR sample chamber and studied in a liquid NMR instrument. NMR samples were taken until no acetone/methanol was shown to be present in the glass tube. The NMR spectra were observed using MestReNova - a software that allows solvent peaks to be normalised and compared. The only issue with this experiment was that DMSO-d6 freezes at room temperature (Figure 4.3); this was prevented by placing the glass tube into a water bath.

4.2.3 Petrophysical Analysis used to Test Cleaning Techniques

Once the core plugs were cleaned, the samples went through a series of measurements (Figure 4.4); the methodologies for these measurements have been outlined in Chapter 3. Two cores were used for each solvent, porosity, gas permeability, brine permeability at 1500 psi, resistivity at 1500 psi and pore size was determined on the first core plug. Microstructural analysis, pore throat size and composition was determined on the second core plug. The mineralogy of two uncleaned core plugs were also analysed using QXRD to form a reference value. Though the analysis was performed on a selected number of TGS they contained the most delicate minerals e.g. illite. Therefore, if the critical point drying method is not important for these samples it will not be important for other tight gas sandstone samples that have similar quantities of delicate illite as well as those samples that contain less or no illite.

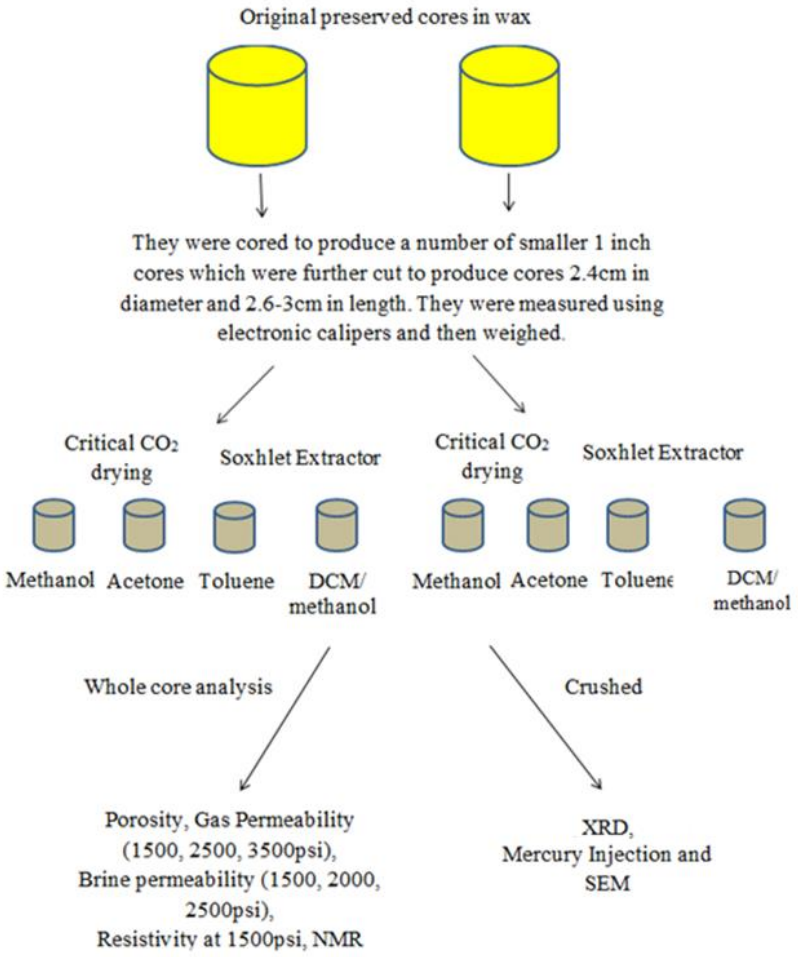

Figure 4.4 Workflow for the cleaning comparison and the petrophysical properties studied after cleaning for each sample.

4.3 Results

This section presents the NMR spectra for samples taken during the critical point CO_2 drying (Section 4.3.1). A comparison between the petrophysical data conducted on the two cleaning methods is then presented. This includes - porosity, permeability, resistivity, pore size, composition, pore throat size and microstructure (Section 4.3.2 to 4.3.8). The dimensions and weights of the core plugs before and after cleaning and the NMR spectra observed using MestReNova are presented in Appendix A.

4.3.1 NMR Spectra Data

Liquid NMR samples were studied to determine when the acetone and methanol had been removed from the core plugs during the critical point CO_2 drying method. A table of the peak ratios between acetone, methanol and DMSO-D6 as well as the NMR spectra are presented in Appendix A, and an example of the decrease in the amount of acetone over time for WCA_4 is presented in Figure 4.5. The main observation is a decrease in each solvent over time relative to a normalised DMSO-d6 value of 1.

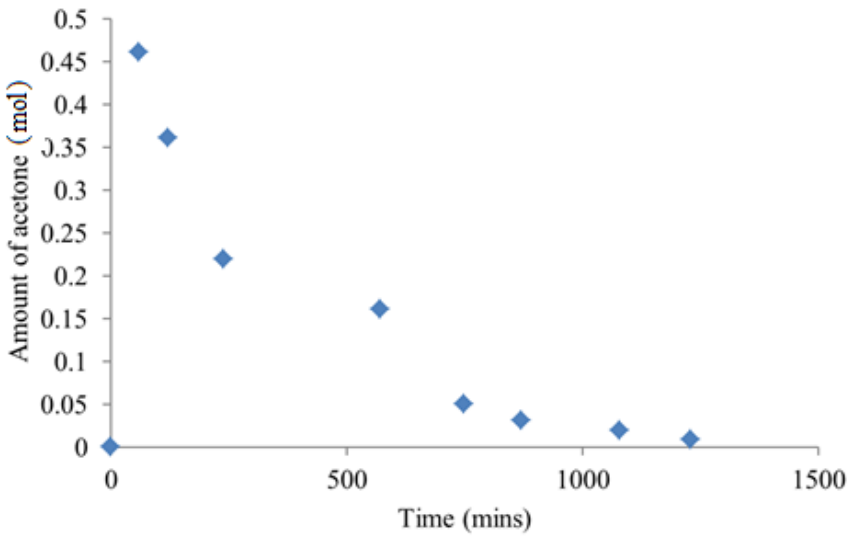

Figure 4.5 Graph of acetone amount in moles vs time in minutes for sample WCA_4. There is a decrease in acetone amount with time where it took approximately 20.8 hours for the acetone to be removed from the core plug. However, it is unclear what is happening between theses points as no data was collected.

4.3.2 Porosity

The grain volume, bulk volume and porosity for each sample is presented in Table 4.2 along with their averages in Table 4.3. The percentage difference for grain volume for the two cleaning methods was 4.3%. The percentage difference for bulk volume from callipers for the two cleaning methods was 2%. This created an average porosity percentage difference of 24% (Figure 4.6). The percentage difference for bulk volume from mercury immersion was 2%. This created an average porosity percentage difference of 14%. The bulk volume and therefore porosity is higher for the callipers. In addition, the porosities (averaged from porosity 1 and 2) are 19% higher after cleaning with the critical point drying with CO_2 (Figure 4.6).

Table 4.2 Grain volume, bulk volume from calliper and mercury immersion, and porosity for each of the core plugs.

Solvent	Sample	Grain volume (cm^3)	Bulk volume (Callipers) (cm^3)	Bulk volume (Hg immersion) (cm^3)	Porosity 1 (%)	Porosity 2 (%)
CO_2 + Acetone	WCB_1	11.4	12.9	12.7	12	10
CO_2 + Methanol	WCA_2	12.8	14.9	14.7	14	12
DCM/methanol	WCB_6	12.9	14.4	14.3	9.9	9.7
Toluene	WCB_5	12.4	13.9	13.7	10	9.3

Note: method 1: bulk volume from calliper, method 2: bulk volume from mercury immersion.

Table 4.3 Average grain volume, bulk volume and porosity for the core plugs cleaned with the Soxhlet extractor and critical point drying methods

Cleaning method	Soxhlet extractor		Critical point drying	
Solvent	DCM/methanol	Toluene	Methanol	Acetone
Average grain volume (cm^3)	12.7		12.1	
Average bulk volume (Callipers) (cm^3)	14.2		13.9	
Average porosity (%)	10		13	
Average bulk volume (Hg immersion) (cm^3)	14		13.7	
Average porosity (%)	9.5		11	

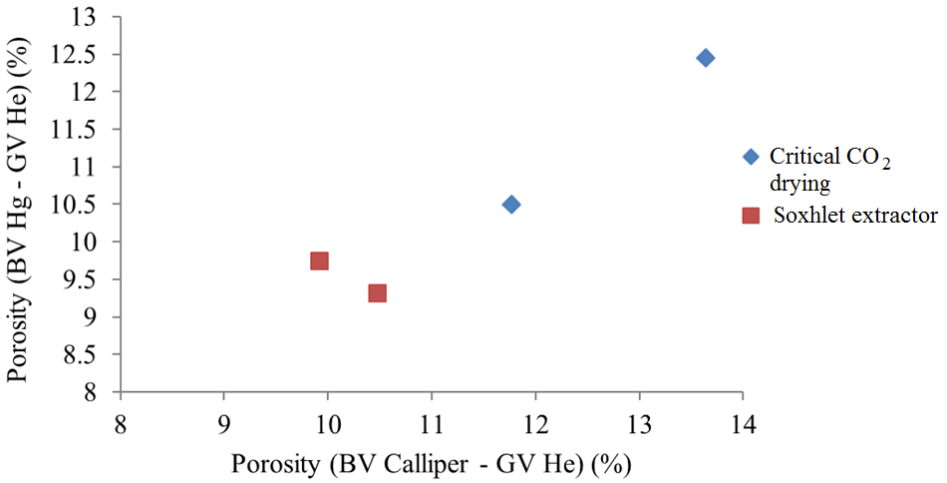

Figure 4.6 Porosity using BV from Hg immersion vs porosity using BV from callipers. The samples cleaned using critical point drying with CO_2 have higher porosities (blue) then those cleaned using the Soxhlet extractor (red).

4.3.3 Permeability

The permeability was determined from 1500 to 3500 psi confining pressure for each core (Table 4.4). The apparent permeability and the Klinkenberg-corrected permeability decrease as the confining pressure increases (Figure 4.7). In addition, the permeability was lower by 49% for the cores cleaned with the Soxhlet extractor.

Table 4.4 Apparent and Klinkenberg-corrected permeability for each of the core plugs.

Sample	**Cleaning method**	**K_{ap} (md) 1500 psi**	**K_{ap} (mD) 2500 psi**	**K_{ap} (mD) 3500 psi**	**K_{kl} (md) 1500 psi**	**K_{kl} (mD) 2500 psi**	**K_{kl} (mD) 3500 psi**
WCB_1	CO_2 + Acetone	0.029	0.019	0.013	0.026	0.019	0.013
WCA_2	CO_2 + Methanol	0.02	0.017	0.013	0.018	0.017	0.013
WCB_6	DCM /methanol	0.012	0.0068	0.0067	0.011	0.0066	0.0068
WCB_5	Toluene	0.014	0.01	0.007	0.0122	0.0097	0.007

Note: K_{ap} = apparent permeability and K_{kl} = Klinkenberg permeability.

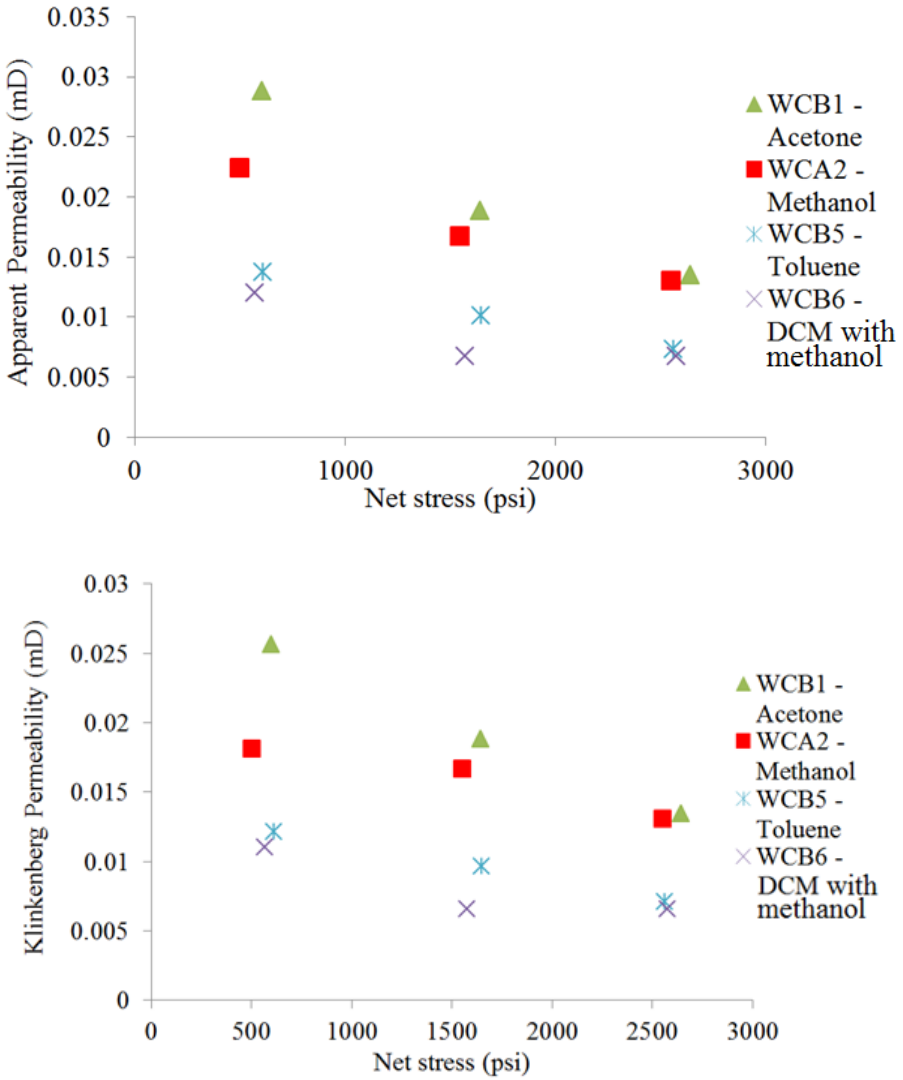

Figure 4.7 Apparent and Klinkenberg-corrected permeability vs net stress for each sample showing the permeability is higher for those cleaned using the critical point drying with CO_2 method.

The brine permeability ranges from 0.00029 to 0.0017 mD (Table 4.5 and Figure 4.8). The brine permeability values are lower than the gas permeability values. The permeabilities are similar for WCA_2, WCB_5 and WCB_1 where WCA_2 has the highest permeability. WCB_6 has the lowest permeability, which is lower by 1 order of magnitude.

Table 4.5 Brine permeability for each sample at 1500 psi confining pressure, the K_w represents brine permeability.

Cleaning method	Sample	Kw at 1500 psi (mD)
CO_2 + Acetone	WCB_1	0.0012
CO_2 + Methanol	WCA_2	0.0017
DCM/methanol	WCB_6	0.00029
Toluene	WCB_5	0.0013

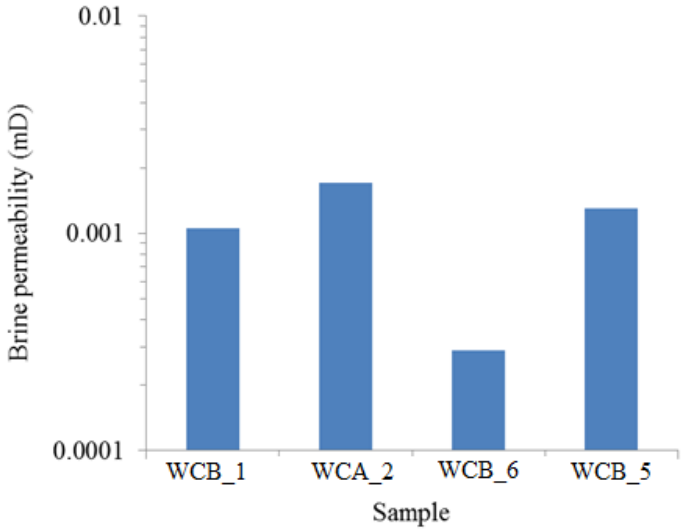

Figure 4.8 Brine permeability for each sample where WCB_6 has a lower permeability compared to the other samples.

4.3.4 Electrical Properties

The resistivity and *m* both have a small difference of 2.2 and 0.3 respectively whereas, *FRF* has a larger range of 44 (Table 4.6). There is no pattern seen with the electrical data as WCB_1 and WCB_5 seem to have similar values despite their different cleaning methods. In addition, WCA_2 and WCB_6 have the lowest values which are different to WCB_1 and WCB_5.

Table 4.6 Resistivity, formation resistivity factor (FRF) and cementation exponent (m) for all four core plugs. The samples in red have similar values despite their different cleaning methods and those samples in blue have lower different values

Sample	Solvent	Resistivity (ohm-m)	*FRF* (unitless)	*m* (unitless)
WCB_1	CO_2 + Acetone	5.1	104	2.2
WCA_2	CO_2 + Methanol	2.9	60	2.1
WCB_6	DCM/methanol	3.7	76	1.9
WCB_5	Toluene	5.0	102	2.1

4.3.5 Nuclear Magnetic Resonance (NMR)

A graph of the normalised signal vs the T_2 relaxation is presented in Figure 4.9. The cores cleaned with the critical point drying with CO_2 show the same overall pore size distribution as those cleaned using the Soxhlet extractor process. The only difference observed is a greater number of larger pores from the DCM/methanol cleaned core plug.

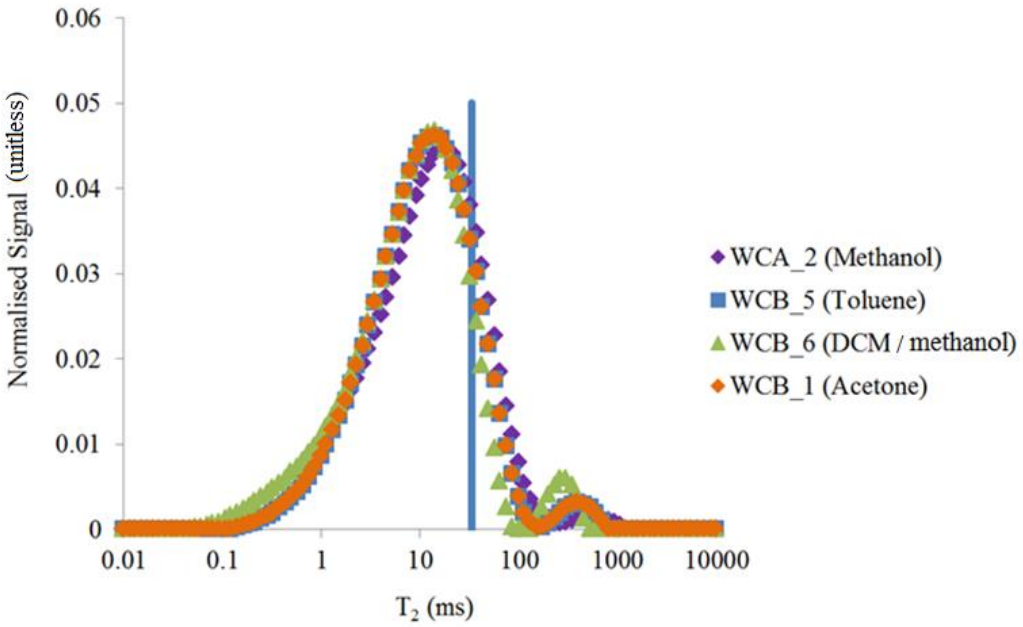

Figure 4.9 Normalised signal vs NMR T_2 for all four cores along with the 33 ms T_2 cut-off for sandstones in blue. The WCB_6 sample has some of the largest pores, however, there is no overall significant difference in the T_2 distribution.

4.3.6 Quantitative X-ray Diffraction (QXRD)

All the samples contain similar quantities of quartz and albite as the main two constituents and this did not seem to change with the cleaning procedure (Table 4.7). The amount of illite appeared to increase after cleaning in all cases, however, when the amount of illite and mica is combined, similar amounts are observed between the samples. There was no calcite identified in the unclean cores and the critical dried cores have less dolomite than the Soxhlet extractor cores.

Table 4.7 QXRD data presenting the weight percentage of each mineral for all four core plug plus the composition of two unclean core plugs. The quartz and feldspar do not change much, calcite is only present after cleaning, the dolomite and mica decreases after cleaning and the illite increases after cleaning.

Solvent	Sample	Quartz	Albite	Calcite	Dolomite	Mica	Illite-smectite	Mica+illite
Unclean	WCA	68.5	7.8	0.0	7.3	12	6	18
Unclean	WCB	68.2	6.8	0.0	14	12	1.3	13
Acetone	WCA_4	68.3	8.6	1.6	5.8	8.3	6.4	15
Methanol	WCA_3	67.1	7.7	3.6	3.2	9.9	7.9	18
DCM/methanol	WCB_11	68.6	7.4	0.7	9	10	4.6	15
Toluene	WCB_2	70.0	7	0	10	11	4.1	15

4.3.7 Mercury Injection Capillary Pressure (MICP)

Mercury injection data was used to study the pore throat size distribution. The distributions for all the samples from the two cleaning methods do not seem to vary much where the pore throat ranges from 0.005 µm to 0.75 µm (Figure 4.10). In addition, the cumulative mercury saturations are all similar (Figure 4.11).

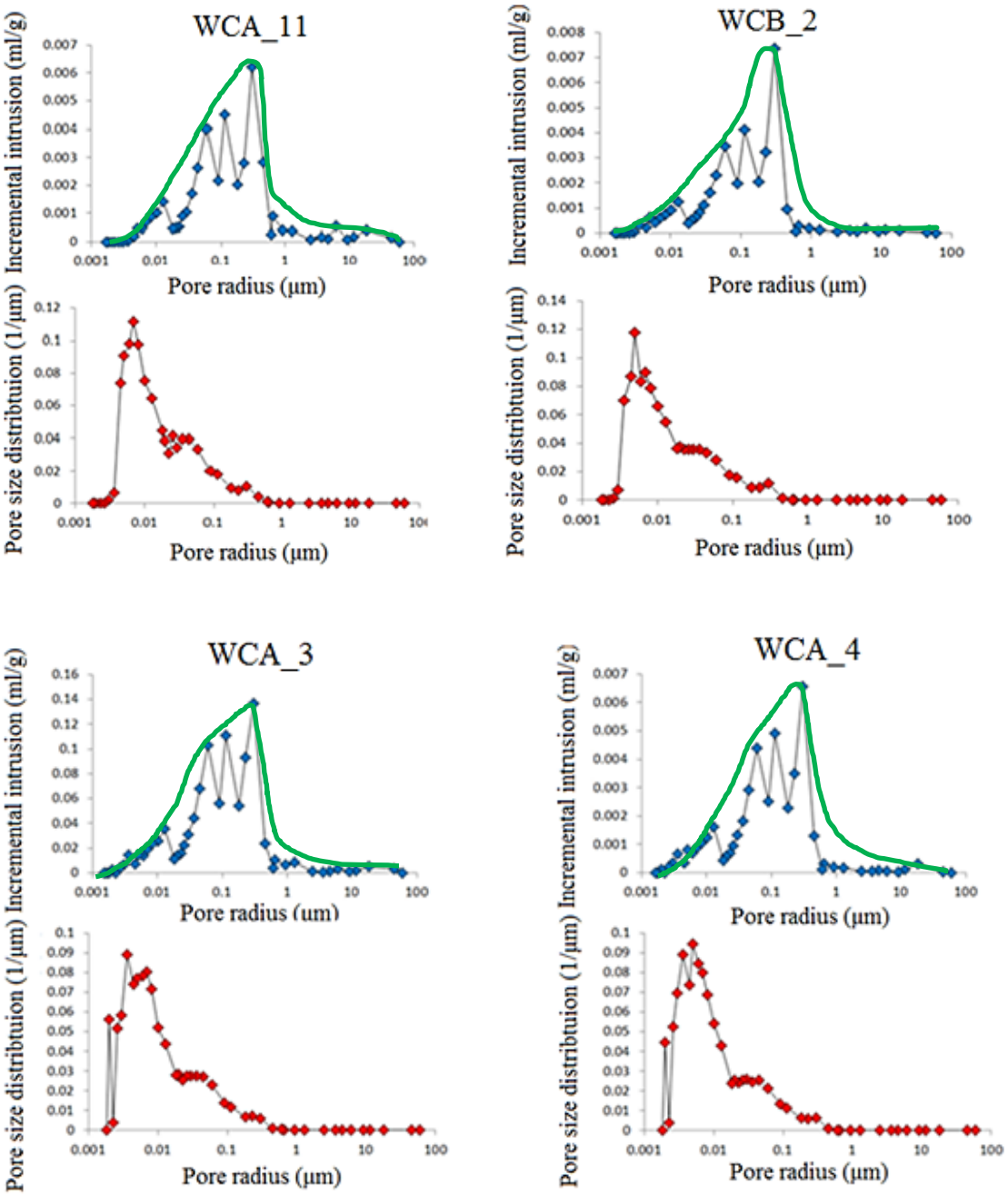

Figure 4.10 Incremental intrusion vs pore radius (top) pore size distribution vs pore radius (bottom). The pore throat size distribution does not change significnatly.WCB_11 – DCM /methanol, WCB_2 – toluene, WCA_3 – methanol and WCA_4 – acetone.

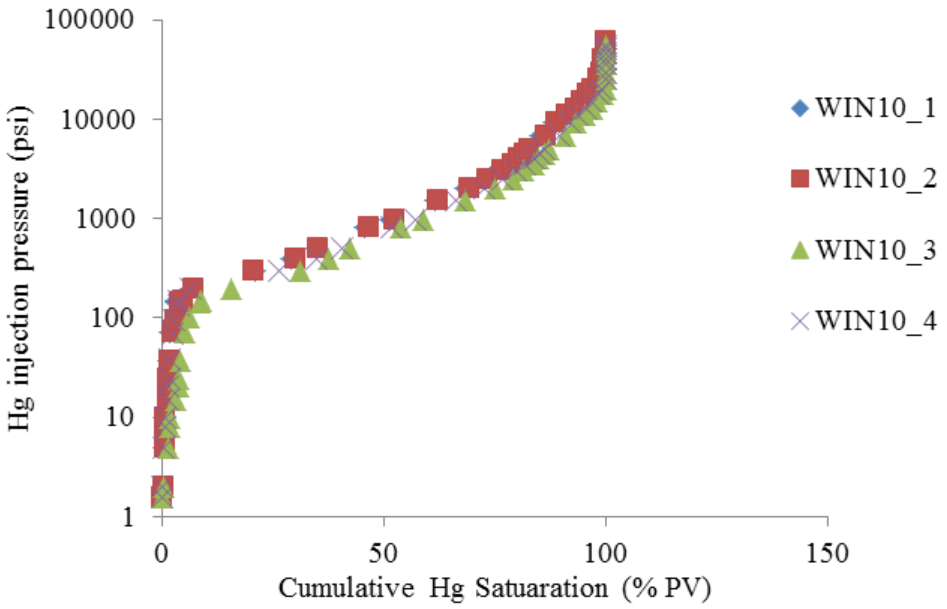

Figure 4.11 Mercury pressure vs cumulative mercury saturation for the four core plugs. There is no significant difference seen between the pressure and mercury saturation implying the pore throat size are similar.

4.3.8 Scanning Electron Microscope (SEM)

The SEM was used to compare the microstructure and especially the clay structure between the two cleaning methods. There is no difference in the microstructure between the four cores. The four samples have fine, sub-rounded to rounded grains and are poorly sorted. They all contain microfractures between grain contacts and the pores are connected by narrow pore throats. Fibrous illite is the only clay present (Figure 4.12). To further determine if the microstructure is consistent between the four core plugs broken surfaces were analysed (Figure 4.13). There appears to be no difference in the clay structure as the illite is well structured and there is no evidence of clay compression.

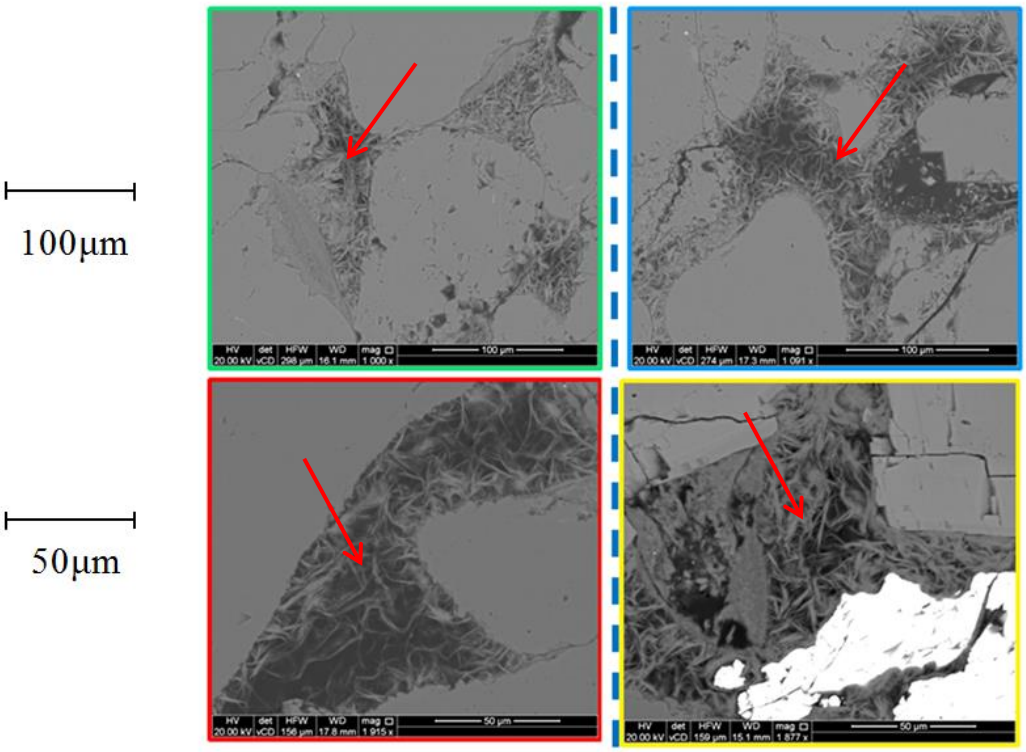

Figure 4.12 BSE images showing the pores filled with illite - methanol (green), acetone (red), toluene (blue), DCM/methanol (orange). The illite is well structured regardless of the cleaning method.

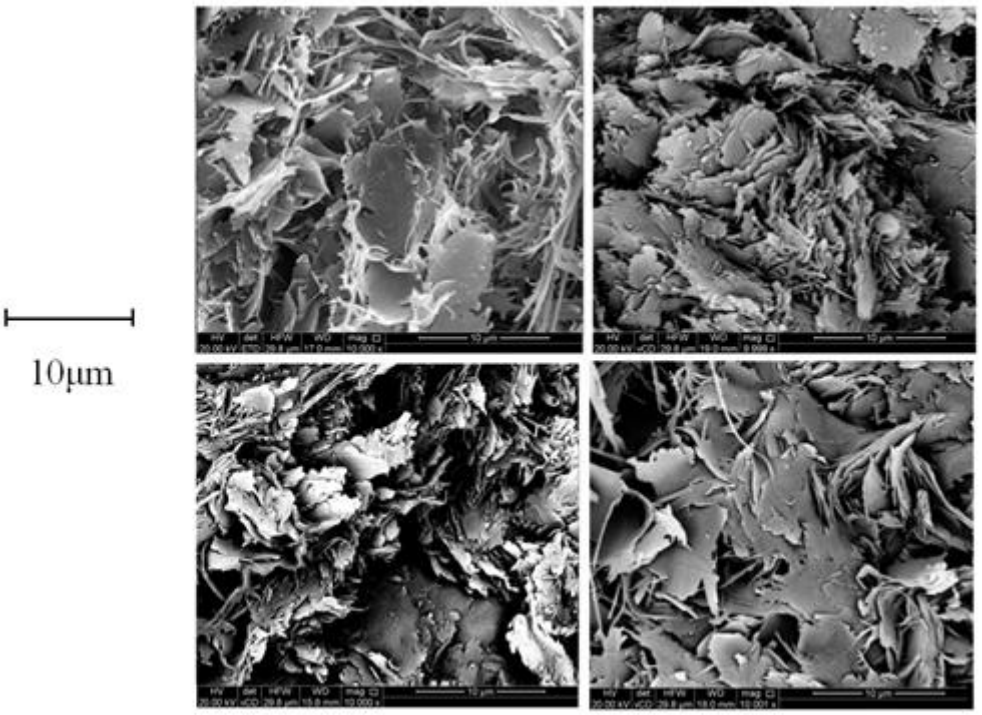

Figure 4.13 Secondary image of fibrous illite present in a core cleaned using critical point drying and acetone (top left), methanol (top right), Soxhlet extractor and toluene (bottom left) and DCM/methanol (bottom right). The illite forms thick blades that are not compressed regardless of the cleaning method.

4.4 Discussion

This section discusses the data presented in Section 4.3. It seeks to compare the data from the two cleaning methods to investigate if the petrophysical properties are affected by the cleaning methodology (Section 4.4.1). This is followed by a discussion of the issues encountered (Section 4.4.2).

4.4.1 Comparison of Cleaning Methods

A comparison is made between the expected petrophysical properties to what was actually observed after cleaning with the Soxhlet extractor and critical point drying with CO_2 (Table 4.8). In the critical point drying samples the clay structure was predicted to be better preserved and therefore the clay would infill more of the pores and pore throats. This would have caused an increase in the *FRF* and *m* values and a decrease in the porosity, permeability, pore throat size and NMR T_2 values. There should have been no difference seen in the QXRD data as the cleaning procedure should not have affected the composition.

Table 4.8 Comparison of the expected and observed petrophysical data from the two cleaning methods.

Method	Expected behaviour	Observed behaviour
Porosity	CPD method would have a lower porosity than SE method	CPD method had a higher porosity than SE method
Permeability	CPD method would have a lower permeability than SE method	CPD method had a higher permeability than SE method. However, at higher pressures they start to converge to similar values
Brine Permeability	CPD method would have a lower permeability than SE method	No distinct differences found
Electrical properties	CPD method would have a higher *FRF* and *m* values than SE method	No distinct differences found
NMR	CPD method would have a short T_2 value than the SE method	No distinct differences found
QXRD - clay	CPD method would have a similar amount of clay as the SE method	CPD method had a similar amount of clay as the SE method
QXRD - dolomite	CPD method would have a similar amount of dolomite as the SE method	CPD method had less dolomite than the SE method

MICP	CPD method would have smaller pore throats than the SE method	No distinct differences found
SEM	The clay should be more persevered in the CPD than the SE method	No distinct differences found

Note: CPD – critical point drying and SE – Soxhlet extractor.

No systematic differences in the petrophysical properties of samples cleaned in different ways could be observed. There is no evidence of flattening of clay in the Soxhlet extractor cleaned core plugs (Figure 4.12 and 4.13). The porosity was higher by 19% (2.3 porosity units) (Table 4.2) and the permeability was higher by 49% (0.009 mD) (Table 4.4) for core plugs cleaned by the critical point drying method. This is possible because the core plugs are from different depths so small variations in the porosity and permeability are expected.

The brine permeability for WCB_6 cleaned with DCM and methanol is 80% lower than the other three samples (WCB_1, WCA_2 and WCB_5) (Table 4.5). This is due to an experimental error potentially related to how the experiment was performed as there is no evidence in the BSE images, clay amount, pore size or pore throat size to explain why the permeabilities should be different. There may also have been some air trapped in the system or the sample was not fully saturated. However, in relation to air trapped, the brine was flown through the system prior to the experiment and air was removed using a back pressure. In relation to the saturation of the core plug, precautions were made to ensure the sample was fully saturated (vacuum pump followed by 1500psi confining pressure and a back pressure) and the lack of saturation would have been identified in the electrical data yet WCB_6 has some of the lowest FRF and *m* values..

There was no clear relationship between the electrical properties and the cleaning methods (Table 4.6). The difference of 44 for the *FRF* could be related to the original dimensions, however, the length varied by 0.44 cm and the diameter by 0.02 cm, therefore though the change in length can affect the final resistivity, the variation between the samples are not significant. Though the microstructure does not vary significantly between the four core plugs as observed by the NMR and MICP data, the T_2 distribution for WCA_2 (methanol) and WCB_6 (DCM and methanol) is shifted more to the right and WCB_6 had more larger pores, this could account for

their lower FRF values. In addition, though the samples are homogenous there may be variations due to sample depth.

The amount of mica plus illite as well as the amount of quartz and albite did not vary significantly between the cleaning methods (Table 4.7). This is expected as the samples are homogenous and from the same well though they are from different depths. Also the quantity of each mineral should not have changed as the solvents should not react with the minerals, it was predicted that only the structure of the minerals especially the clay would be affected. However, the calcite was not observed before cleaning but was observed after cleaning and the amount of illite appeared to increase after cleaning. These are experimental errors made during the analysis of the QXRD data. The change in illite content could reflect the difficulties distinguishing between illite and mica in QXRD, which poses questions on the reliability of the QXRD.

The dolomite content was much lower for the cores cleaned using critical CO_2, this could indicate that the CO_2 dissolved the dolomite. However, no signs of dissolution were observed in the SEM images. The final conclusion was that WCB had more initial dolomite than WCA (Table 4.9). Neverthless, the core plugs appeared to lose some dolomite after cleaning (Table 4.7 and Table 4.9). This is not expected and poses questions on the reliability of the QXRD data.

Table 4.9 Amount of dolomite before cleaning, after cleaning and the percentage difference between the three core plugs. The WCA samples have less dolomite at the start and the overall lose in dolomite is similar. The loss of dolomite with cleaning is unclear as there was no evidence of dolomite dissolution, it is therefore unclear how reliable the QXRD data is.

Sample	No cleaning (g)	Cleaned (g)	Difference (%)
WCB_11	14	9.0	5.1
WCB_2	14	10	4.0
WCA_3	7.3	3.2	4.1

This comparison implies that the current method of cleaning, Soxhlet extractor with DCM/methanol, is reliable. However, several publications have suggested that critical point drying results in less sample damage than other methods (Pallatt et al., 1984; Martill, 1990; Knox, 2005; Hawkins, 2007; Christie, 2011). Hawkins (2007) stated that critical point drying is used to dry samples that are typically very fragile or wet, without deforming or collapsing the structure. It also avoids sample

degradation, which occurs with air or vacuum drying. However, when observing the illite structure in one of the first studies made using critical point drying by Pallatt et al. (1984), the illite observed appears weaker and not as well developed compared to the strong blade like illite present in the samples in this research (Figure 4.14). Therefore, the critical point drying method may be useful for samples with very fibrous and almost 'cotton candy' appearance but not for the samples studied within this research.

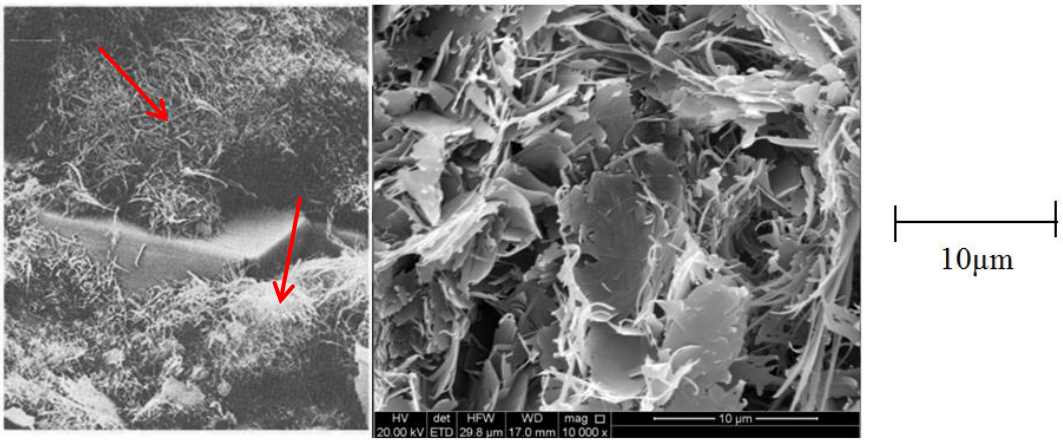

Figure 4.14 BSE images of illite cleaned using critical point drying showing the delicate 'cotton candy' appearance from Pallatt et al. (1984) which requires critical point drying (left). The thick blade like structure in the samples in this research (right) which can be cleaned using Soxhlet extractor.

4.4.2 Issues with the Critical Point Drying with CO_2 Method

A number of issues were identified during the critical point drying experiment. Some were solved within the time-frame but others should be considered in the future.

- If the acetone or methanol left the glass tube containing the DMSO-d6 solvent faster than the acetone or methanol in the sample, the sample might be mistakenly assumed to be clean when it is not. This is a significant issue and could lead to large errors. Therefore once the volume of acetone/methanol has reach 0 ml the CO_2 should be left flowing to ensure all the solvent is removed from the core plug.
- The amount of acetone/methanol was logged over time, however, NMR samples were only taken roughly every hour, and therefore it was unclear what was happening between those periods of time. In the future, NMR samples should be taken at more frequent intervals.

- In the critical point drying method it was unclear if the sample was fully saturated right to the centre of the core, or if some of the solvent was still present in the core after cleaning especially in the centre. This could only be determined by quickly cutting the core in half and observing the colour changes, however, this could not be done as further analysis was conducted on the core samples after cleaning.
- Overtime the level of the DMSO-d6 in the glass tube decreased, therefore the same amount of CO_2 was being bubbled into less solvent. This was solved by making sure the glass tube contained enough DMSO-d6 at the start.
- There could have been an uneven flow of CO_2 around the sample if the space either side of the core was uneven. To solve make sure the core plug is flat and that it sits well in the core chamber.
- Care was taken to ensure that the needles, glass tube, rubber bung and the NMR tubes were all cleaned by flushing with acetone followed by drying in an oven set at 100°C. However, some solution could remain in the needles leading to inaccuracies in the acetone levels in the NMR data, or adding to impurities in the sample saturated with methanol. The former was fixed by mixing the solvents in the glass tube prior to removing some of the solution with a pipette to ensure an even mix of solution was extracted. The latter was checked and no acetone peak was seen in the methanol rock data.
- The exact amount of substances removed from the core could not be quantified except by the weight change. This was not a large issue as the main aim was to just remove the solvents from the core plugs.

4.5 Conclusion

Before the cleaning comparison experiment was performed it was unclear if the Soxhlet extractor with DCM was a reliable cleaning method for TGS in terms of the effects on the clay structure. Therefore, in a comparison between the Soxhlet extractor with DCM/methanol and toluene and the critical point drying with CO_2 method with acetone and methanol was conducted. The latter method is thought to better preserve the microstructure because the temperature and pressure of the liquid solvent is increased to the critical point, which causes the meniscus to become flatter, indicating a reduction in the interfacial tension.

The illite clay within the samples irrespective of the cleaning method was well structured and fibrous and there was no significant difference between the petrophysical data. This was thought to be because the illite in these samples was well developed and stronger than in the studies that said critical point drying is important. The work in this chapter has shown that in the future the Soxhlet extractor can be used to clean the samples as it does not seem to affect the clay structure.

Nevertheless, only a few samples were studied so the data is not statistically strong and as these samples have a limited mineralogy, other samples with more complex mineralogy might be more affected. Further work is needed to apply these cleaning methods to a range of TGS rock types to demonstrate this. In addition, future work is needed to improve the QXRD methodology to ensure accurate data is being gathered.

Chapter 5 - Petrophysical Properties of TGS: Routine Core Analysis (RCA)

5.1 Introduction

Two of the most important aims in petrophysics is to obtain estimates of the porosity and permeability of reservoirs as they control the volume of hydrocarbons present and the rate at which they can be extracted. Estimation of likely production rates are particularly important for tight gas sandstone (TGS) reservoirs as they are often only marginally economic to develop so small differences in flow rate can mean the difference between making a profit and a loss. The marginal economics also means that it is important to cut time frames and costs in all stages of the value chain. One possibility is to reduce the amount of core taken as well as the extent of any core analysis program. It would therefore be desirable to be able to estimate porosity-permeability relationships without taking core. For example, estimating properties based on microstructural analysis of cuttings which could provide a faster alternative to core plugs.

A routine core analysis (RCA) program was carried out on 25 TGS samples (Table 3.2 in Chapter 3) to determine their porosity, permeability, microstructure and composition and therefore to help determine what controls porosity and permeability and provide an estimate of permeability without core plugs. Samples were grouped based on mineralogical (type and amount of diagenetic deposit), depositional (grain size, shape, sorting and depositional environment) and microstructural (clay type and position) characteristics to provide better porosity-permeability relationships and therefore a better prediction of permeability. The accuracy of porosity determination, pore pressure equilibrium times during permeability measurements and a comparison of brine and gas permeability are also presented and discussed to compliment the data.

A range of instruments such as electronic callipers, helium porosimeter, X-ray powder diffraction (QXRD) and scanning electron microscope (SEM) were used as well as techniques such as mercury immersion, pulse-decay and steady-state permeametry. A detailed methodology for each can be found in Chapter 3; however, a brief overview is presented in this chapter in Section 5.2. This is followed by the results where the accuracy of different methods is addressed (Section 5.3) and the

discussion of the main results (Section 5.4). The discussion seeks to bring together these results to understand them and compare how they agree or disagree with other published work. The work presented in this chapter is summarised in Section 5.5 together with recommendations for future work.

5.2 Methodology

The following section presents a brief overview of the methodologies used for the RCA program. The core plugs were cleaned in the Soxhlet extractor with dicholomethane (DCM)/methanol at 39.6°C and dried in an oven for 24 hours at 60°C. The core plugs were trimmed to produce off-cuts for polished thin sections. The thin sections were then coated in a thin layer of carbon prior to SEM analysis. The samples were then analysed using a FEI Quanta 650 SEM.

A detailed analysis was then conducted to identify the texture (mineral distribution, grain size, shape, sorting and pore size), presence of microfractures, micro-porosity, authigenic and detrial phases present and the diagenetic history of the sample. Once an area of interest had been identified, the images were saved in an 8bit (256 grey levels) digital form. The remaining off-cuts were ground for QXRD analysis. The composition was determined using a Philips PW1050 at the University of Leeds.

The remaining core plug material was used to determine the porosity and permeability. The porosity was determined from the bulk volume and grain volume. The bulk volume was measured using electronic callipers or mercury immersion. The grain volume was measured using a Quanta Chrome SPY-4 helium porosimeter. The dry weight and bulk volume were used to determine the bulk density and the dry weight and grain volume were used to calculate the grain density. The permeability was determined using both pulse-decay and steady-state methodologies. The confining pressure used in the pulse-decay experiment was 1500 psi and the pore pressure was 1000 psi. The confining pressure used in the steady state experiment was 500 psi.

Subsequent to the gas flow measurements the core plugs were saturated with 20 and 30% NaCl brine and brine permeability measured using steady-state or pulse decay permeametery. All brine permeability measurements were conducted at a confining pressure of 1500 psi.

5.2.1 Controls on Porosity and Permeability

The 25 TGS samples (Table 3.2 in Section 3.2.1) were divided based on - illite content and kaolin content, sorting, grain shape and grain size, depositional environment and clay type and position. The data for each of these properties was created from SEM and QXRD data. These properties were chosen as they may have a direct correlation with porosity and permeability. The properties were plotted as a third parameter on plots of permeability vs porosity. Some properties may affect porosity and permeability differently because porosity is related to the total amount of pore space whereas permeability is related to the size and connectivity of those pores.

5.3 Results

This section presents the porosity and permeability of TGS (Section 5.3.1 to 5.3.3), microstructure and diagenetic history (Section 5.3.4) and QXRD composition (Section 5.3.5). Most of the data is presented within this section though the dimensions, dry weights, bulk volume, bulk and grain density data of each sample is presented in Appendix B. The table of data for the controls on porosity and permeability are presented in Appendix C.

5.3.1 Porosity

There is a positive correlation close to the 1:1 line between the bulk volume measured using callipers and that obtained using mercury immersion (Figure 5.1). The arithmetic average is 55.6 cm^3 and 54.8 cm^3 for callipers and mercury immersion respectively. The bulk volume from callipers was 1.4% higher than the bulk volume using mercury immersion (Table 5.1).

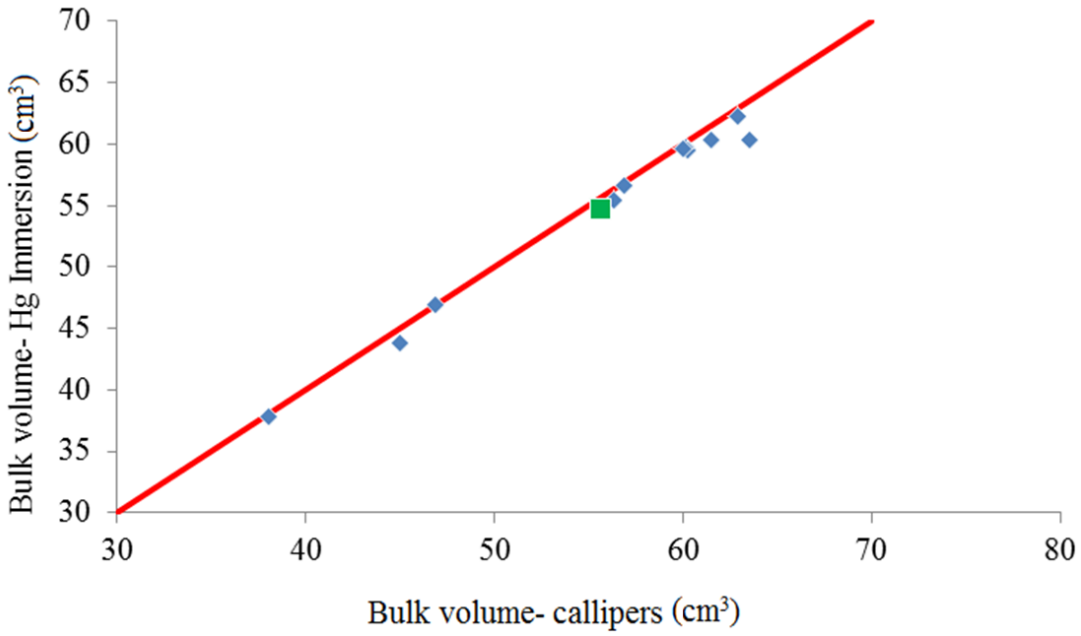

Figure 5.1 Bulk volume from mercury immersion as a function of bulk volume from callipers with the arithmetic average in green. The two methods of bulk volume determination are consistent; however a systematic scatter is seen with a lower bulk volume from mercury then the callipers.

Table 5.1 Range, arithmetic average, percentage difference and the standard deviation between the bulk volume methods. The bulk volume from callipers is on average 0.8 cm^3 larger.

	Callipers (cm^3)	**Mercury immersion (cm^3)**
Range	45 – 63	44 – 62
Arithmetic Averages	55.6	54.8
Difference (%)	1.4	
Standard deviation	8.4	8.1

The porosity measured using the calliper bulk volume is on average 6.2% larger than the porosity using a bulk volume from mercury immersion. The largest difference between the porosity using a bulk volume from calliper vs. mercury immersion was 40% (Table 5.2). The differences are systematic as all the samples are affected in the same way (Figure 5.2). Nevertheless, the R^2 value is 0.98 implying the two methods agree well.

Table 5.2 Porosity 1 - a bulk volume from calliper and porosity 2 – a bulk volume from mercury immersion along with the percentage difference for each sample. The porosity from method 1 is always lager than porosity 2.

Sample	Porosity 1 (%)	Porosity 2 (%)	Difference (%)
BP2_5	5	3	40
BP3_1	13	13	0
BP3_4	17	15	11.8
BP3_5	16	15	6.25
BP3_6	15	14	6.7
EBN4_10	8	7	12.5
SHELL4_370	15	13	13.3
GDF1_1	10	9	10
GDF1_6	5	5	0
GDF1_7	10	9	10
GDF2_4	11	10	9.1
WIN9_5	6	5	16.7

Notes: as the mercury penetrometer was only available later in the research some samples were not studied.

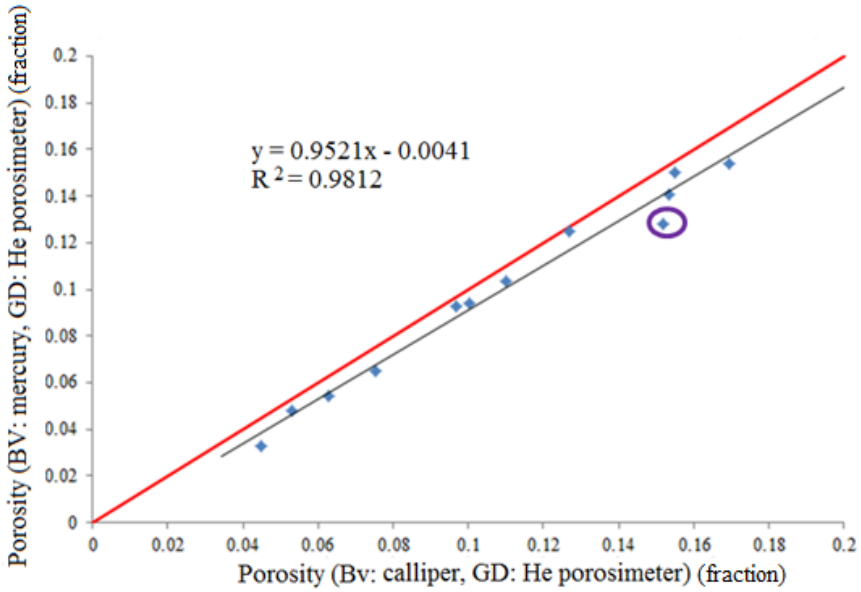

Figure 5.2 Porosity using BV from mercury immersion as a function of the porosity using BV from callipers (GV: grain volume and BV: bulk volume). The higher calliper bulk volume produces a higher porosity, however, the two methods agree well with a R^2 value of 0.98. The sample highlighted in purple has a higher helium porosity due to errors in the original bulk volume.

5.3.2 Permeability

The permeability of the cores ranges from 0.0012 to 4.1 mD at 500 psi net stress (Table 5.3). The arithmetic average is 0.77 mD with a standard deviation of 1.05. The brine permeability ranges from 0.0001 mD to 0.18 mD at 1500 psi confining pressure (Table 5.4). The arithmetic average is 0.03 mD with a standard deviation of

0.046. The brine permeability was compared to the gas permeability where on average the brine permeability was 90% lower than the gas permeability (Figure 5.3). The trend is good with a R^2 value of 0.77, however, there is scatter around the trend.

Table 5.3 Gas permeability measured at 500 psi net effective stress for all 25 core plugs ranging from 0.0098 to 4.1 mD.

Sample	Kg 500 psi (mD)	Sample	Kg 500 psi (mD)
BP2_2	0.13	SHELL2_1B	0.5
BP2_3	1	SHELL4_202	0.3
BP2_5	9.80E-03	SHELL4_370	1
BP3_1	0.7	SHELL4_389	0.9
BP3_4	1.1	SHELL4_409	0.0012
BP3-5	0.95	GDF1_1	1.3
BP3_6	1.3	GDF1_6	9.60E-03
EBN3_40	1.4	GDF1_7	4.1
EBN4_10	0.04	GDF2_4	3.6
SHELL1_83E	0.003	WIN4_26	0.1
SHELL1_111	0.02	WIN5_16B	0.03
SHELL1_216B	0.03	WIN9_5	9.20E-03
SHELL2_9B	0.6		

Notes: The samples in red were measured using the pulse-decay method and those in blue by the steady-state method.

Table 5.4 Brine permeability measured at 1500 psi confining pressure for all 25 core plugs. ranging from 0.0001 to 0.18 mD.

Sample	Kw at 1500psi (mD)	Sample	Kw at 1500psi (mD)
BP2_2	0.043	SHELL2_1B	0.051
BP2_3	0.018	SHELL4_202	0.006
BP2_5	0.001	SHELL4_370	0.047
BP3_1	0.017	SHELL4_389	0.004
BP3_4	0.04	SHELL4_409	0.001
BP3-5	0.04	GDF1_1	0.03
BP3_6	0.03	GDF1_6	0.003
EBN3_40	0.16	GDF1_7	0.056
EBN4_10	0.005	GDF2_4	0.18
SHELL1_83E	0.0001	WIN4_26	0.001
SHELL1_111	0.0003	WIN5_16B	0.001
SHELL1_216B	0.001	WIN9_5	0.001
SHELL2_9B	0.047		

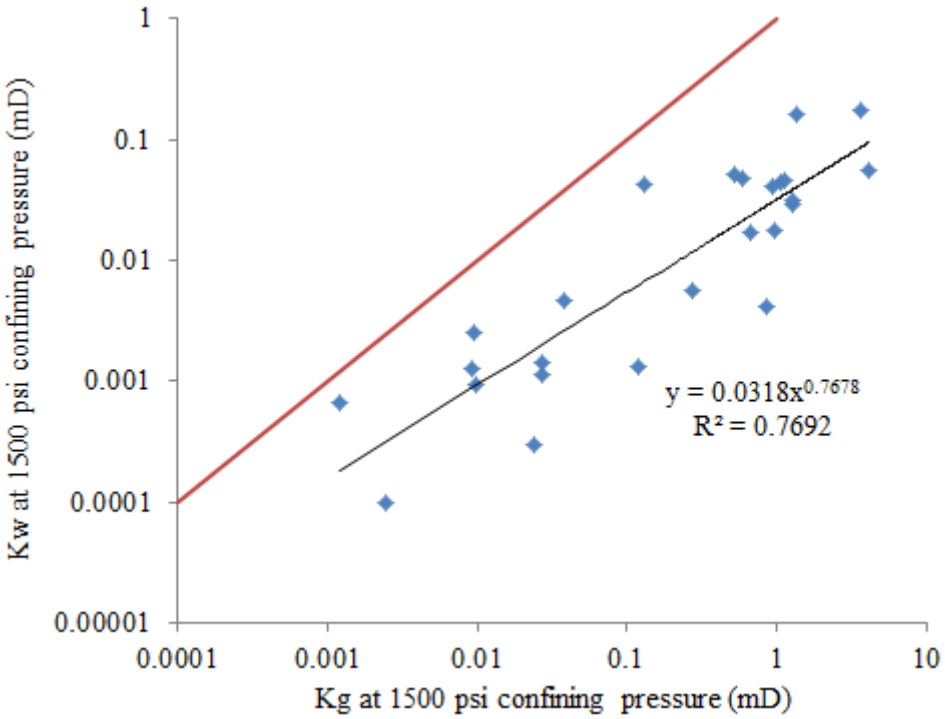

Figure 5.3 Absolute brine permeability as a function of the absolute helium permeability for all 25 samples. The brine permeability is 91% lower than the gas permeability the data provides a moderate tend line with a R^2 value of 0.77.

5.3.3 The Effect of Pore Pressure Equilibrium Time on Permeability

It was unclear how much time is needed for a sample to reach stress and pore pressure equilibrium after the confining pressure has been applied and before the gas has been allowed to flow from the upstream and downstream volumes. Therefore, a comparison was made between the permeability with 24 hours of pore pressure equilibrium and without pore pressure equilibrium with decreasing (unloading) and increasing (loading) pore pressure whilst keeping the confining pressure stable at 3500 psi (Figure 5.4 and Table 5.5). The largest percentage difference between the permeability values was found to be 25%. The largest difference occurred at a pore pressure of ~1000 psi in both the unloading and loading experiments.

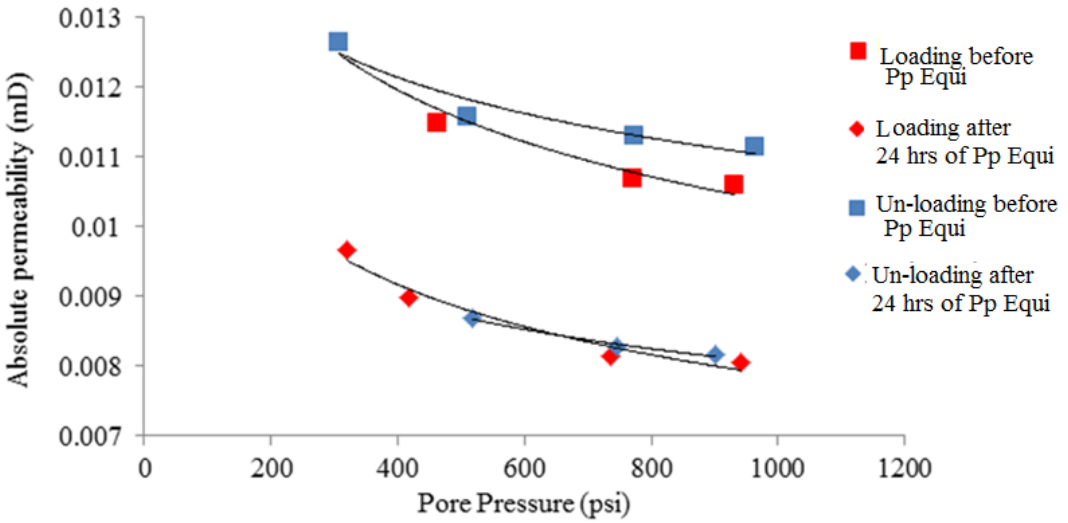

Figure 5.4 Plot of absolute permeability as a function of pore pressure. An increase in pore pressure in red and a decrease in pore pressure in blue both with and without pore pressure equilibrium with a constant confining pressure of 3500 psi. The largest difference was 25%.

Table 5.5 Percentage differences between the permeability when the core has experienced pore pressure equilibrium and one that has not during a loading and unloading experiment.

Net stress (psi)	**~300 (psi)**	**~400 (psi)**	**~700 (psi)**	**~1000 (psi)**
No pore pressure equilibrium (mD)	0.01	0.01	0.012	0.013
Pore pressure equilibrium (mD)	0.008	0.008	0.009	
Difference (%)	20	20	25	
Net stress (psi)	**~1000 (psi)**	**~700 (psi)**	**~400 (psi)**	**~300 (psi)**
No pore pressure equilibrium um (mD)	0.01	0.01	0.01	
Pore pressure equilibrium (mD)	0.008	0.008	0.009	0.01
Difference (%)	20	20	10	

5.3.4 Microstructural Analysis Results

This section presents the results of the analysis of off-cuts using SEM. The microstructure of samples from each well are described individually. Descriptions are supplemented with BSEM images that have the following abbreviations for each mineral: Qtz – quartz, F – feldspar, K – kaolin, I – illite, Dol – dolomite, Ferro-dol – dolomite overgrown with ferroan dolomite, Sid- siderite, M – mica, C – chlorite.

5.3.4.1 BP2

BP2_2, 2_3 and 2_5 have silt to coarse, sub-rounded to sub-angular and well sorted to moderately sorted grains. The main minerals are quartz, feldspar, kaolin, illite and dolomite (Figure 5.5). The samples experienced the precipitation of dolomite rhombs during shallow burial, which were overgrown by ferroan dolomite during deeper burial. The samples contain moderate quantities of kaolin, which infills the macropores (Figure 5.6). The kaolin precipitated after the dolomite but before the end of ferroan dolomite precipitation. The samples then experienced moderate amounts of quartz precipitation; the quartz cement occurs as outgrowths (Figure 5.7) and discontinuous overgrowths. The samples have experienced some K-feldspar dissolution and contain some large secondary pores that were probably created either by the dissolution of K-feldspar or some other aluminosilicate (Figure 5.8). In addition, microfractures that are around 1 μm wide are present between grain contacts (Figure 5.8). The main process responsible for a reduction in porosity and permeability of this well is quartz and kaolin cementation.

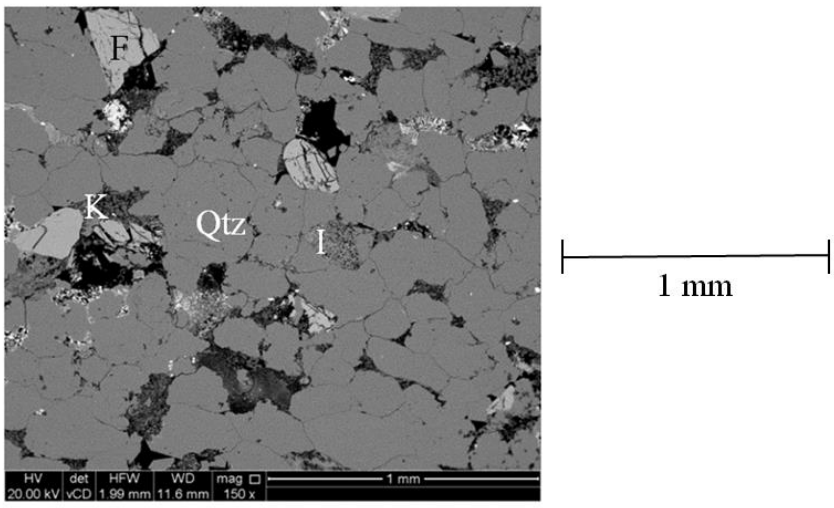

Figure 5.5 BSE image showing the general mineralogy of a sample from well BP2.

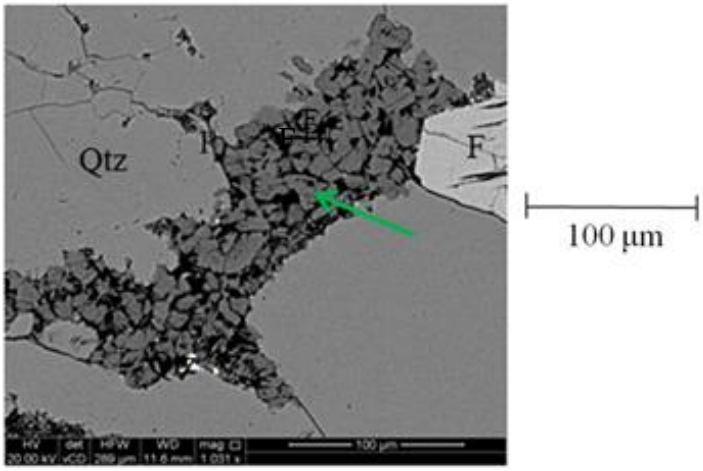

Figure 5.6 BSE image of BP2_2 showing the kaolin infilling the pores (green arrow).

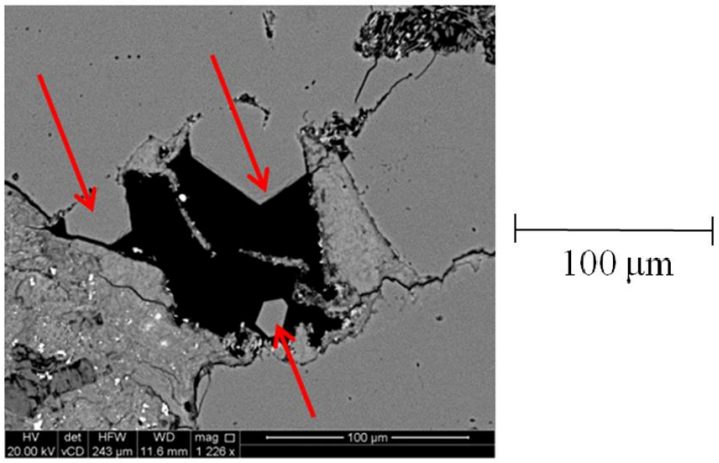

Figure 5.7 BSE image of BP2_3 showing quartz outgrowths (red arrow).

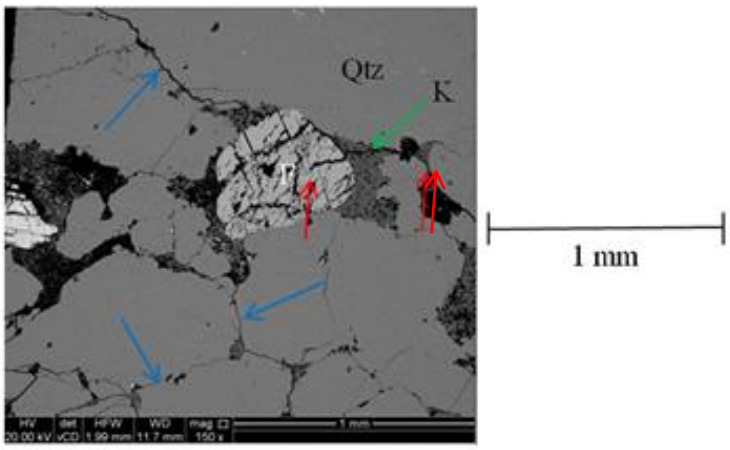

Figure 5.8 BSE image of BP2_3 showing the presence of feldspar dissolution (red arrow) and the microfractures present between grain contacts (blue arrows).

5.3.4.2 BP3

BP3_1, 3_4, 3_5, 3_6 have fine to medium, sub-rounded to sub-angular and well sorted grains. They all contain mostly quartz, feldspar and kaolin clay (Figure 5.9). The kaolin, which occurs as 10 µm stacks that occupy around 50% of the volume of most macro-pores present, precipitated before the quartz cement (Figure 5.10). The sample also contains small amounts of grain coating chlorite (Figure 5.11), which precipitated before the quartz. The samples have experienced some K-feldspar dissolution and they contain some large secondary pores that were probably created either by the dissolution of K-feldspar or some other aluminosilicate (Figure 5.11). The authigenic quartz occurs in moderate quantities (5-8%) as outgrowths and discontinuous overgrowths (Figure 5.12). The main diagenetic processes that have affected this well are kaolin and quartz cementation.

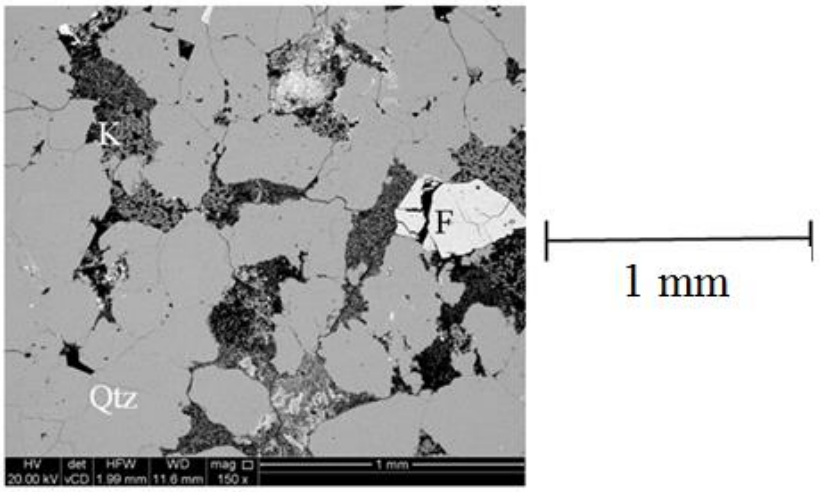

Figure 5.9 BSE image showing the general mineralogy of a sample from well BP3.

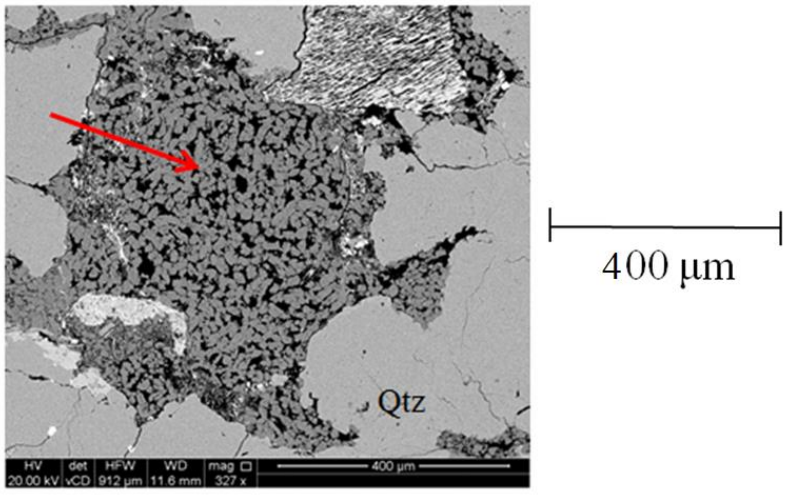

Figure 5.10 BSE image of kaolin infilling the pores in BP3_6 (red arrow).

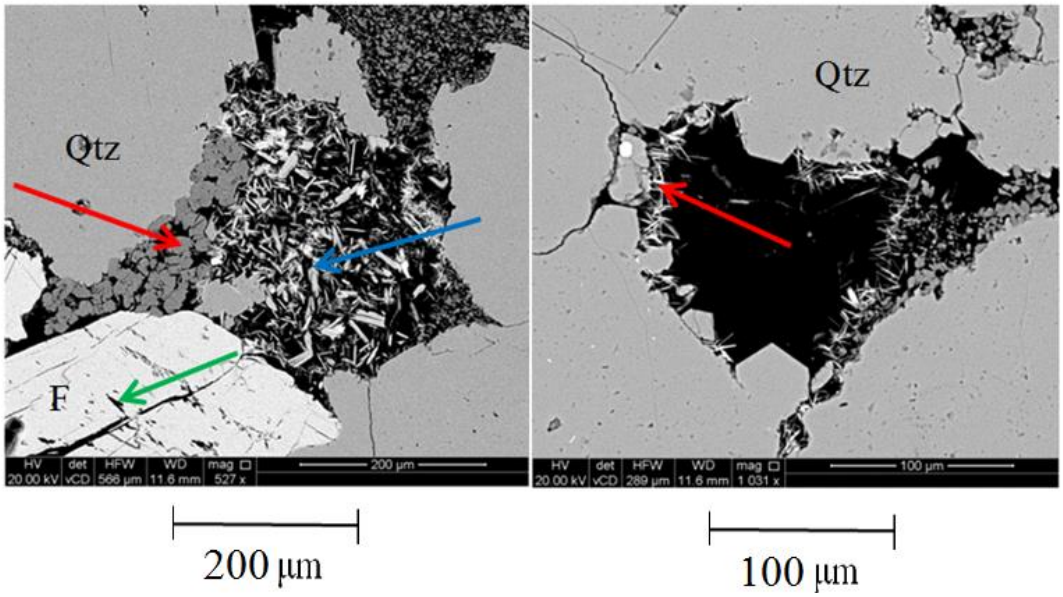

Figure 5.11 BSE image of pore filling kaolin (red arrow), chlorite (blue arrow) and feldspar dissolution (green arrow) in BP3_4 (left) and pore lining chlorite (red arrow) (right) in BP3_6.

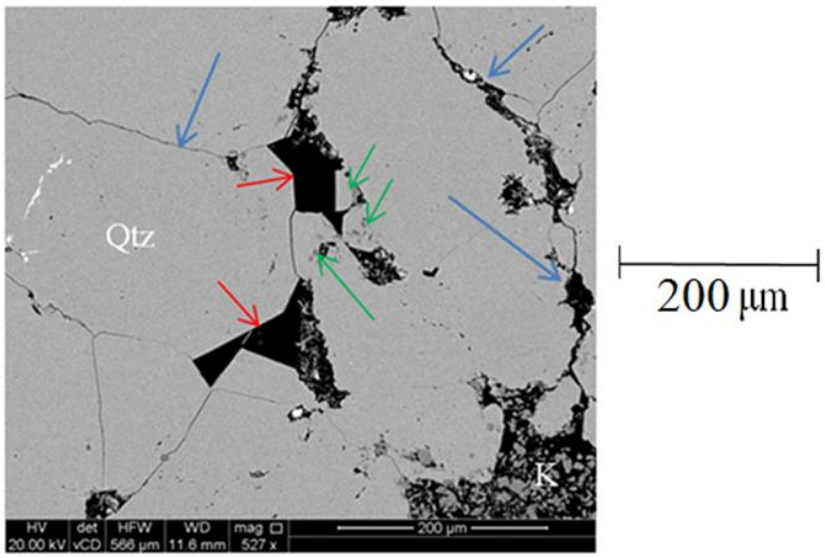

Figure 5.12 BSE image of BP3_4 showing quartz overgrowths (red arrow), outgrowths (green arrows) and microfractures that are around 1 µm between grain contacts (blue arrows).

5.3.4.3 EBN3

The EBN3_40 sample has medium, round and well sorted grains (Figure 5.13) and contains mostly quartz, feldspar and illite. The quartz occurs mainly as outgrowths; it occupies <3% of the rock volume (Figure 5.14 and Figure 5.15). The illite occurs as grain coating phase and infiltrating clays (Figure 5.15). It probably formed by the alteration of detrital or early authigenic clays such as kaolin during deep burial.

Some samples also contain small amounts of siderite and anhydrite cements, which appear to have formed after the authigenic quartz. The main diagenetic process to affect this well is illite precipitation; which had a large impact on reservoir quality.

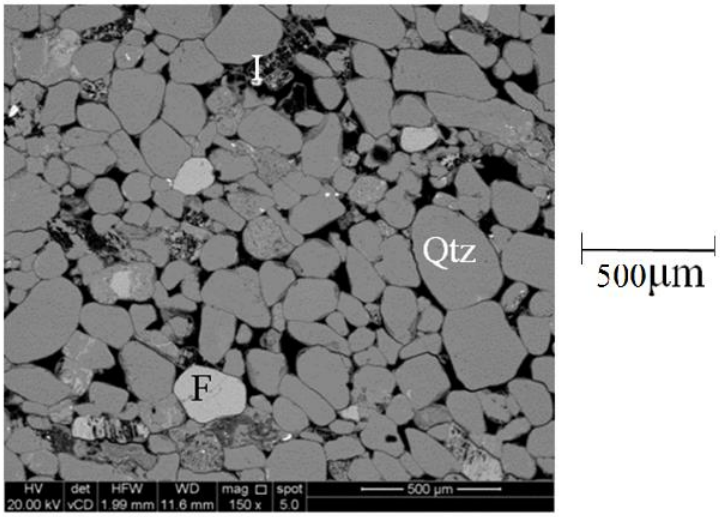

Figure 5.13 BSE image showing the general mineralogy of a sample from well EBN3.

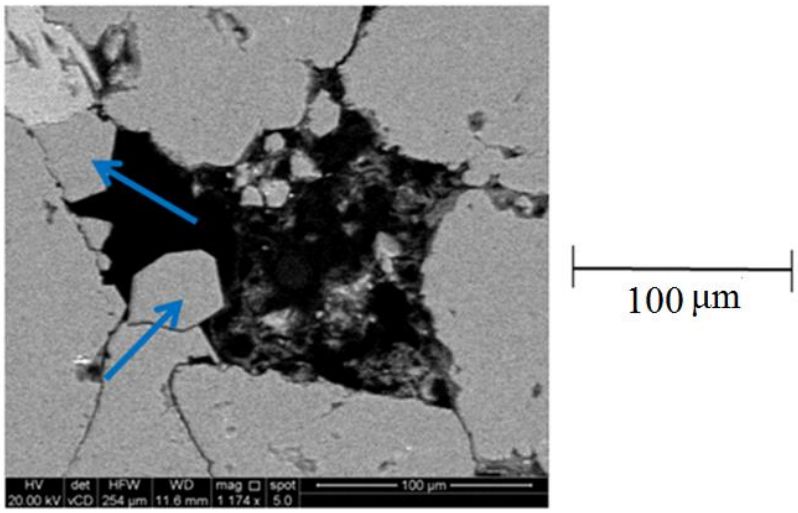

Figure 5.14 BSE image of quartz outgrowths (blue arrow).

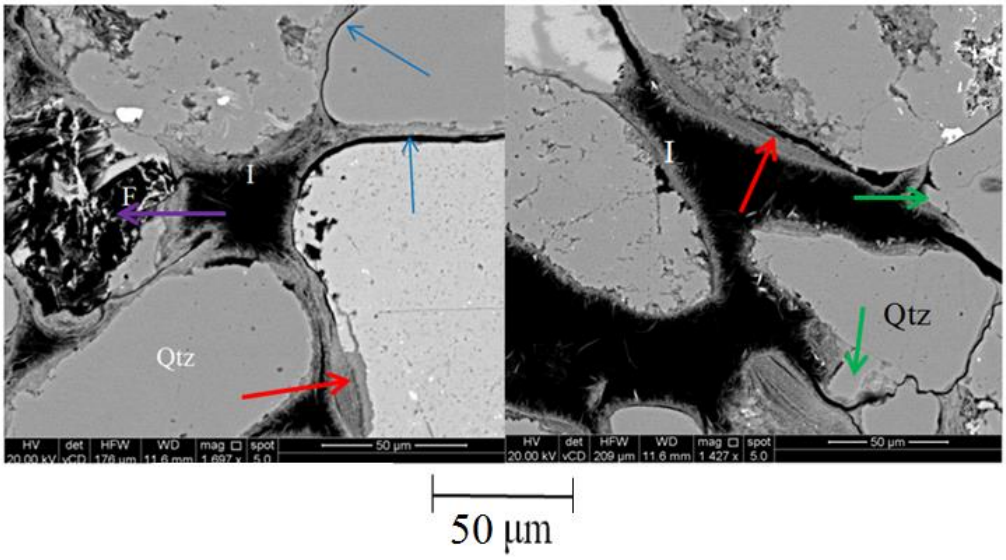

Figure 5.15 BSE image of EBN3_40 showing illite clay surrounding the grains, microfractures that are around 1 µm between grain contacts (blue arrow), feldspar dissolution (purple arrow), infiltrated clay (red arrow) and quartz outgrowths (green arrow).

5.3.4.4 EBN4

EBN4_10 has fine, sub-angular and moderate to well sorted grains and contain mostly quartz, feldspar, kaolin and siderite (Figure 5.16). The siderite occurs as ~100-200µm zoned rhombs that appear to have precipitated at relatively shallow depths (Figure 5.16). Most pores are filled by kaolin, which is both detrital and authigenic in nature (Figure 5.17). In addition to these cements all samples contain small to moderate amounts (~1-5% of the rocks volume) of authigenic quartz, which occurs as both outgrowths and overgrowths (Figure 5.18). Microfractures are also present between grain contacts. The main diagenetic process to affect this well is mechanical compaction as well as the precipitation of siderite and kaolin.

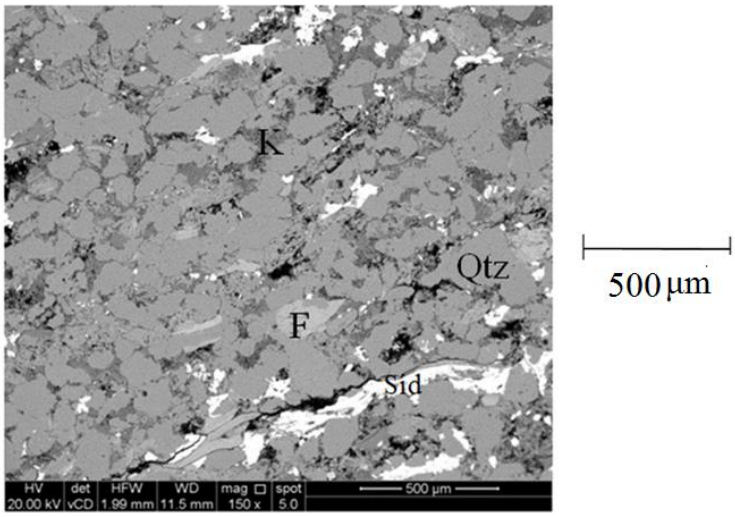

Figure 5.16 BSE image showing the general mineralogy of a sample from well EBN4.

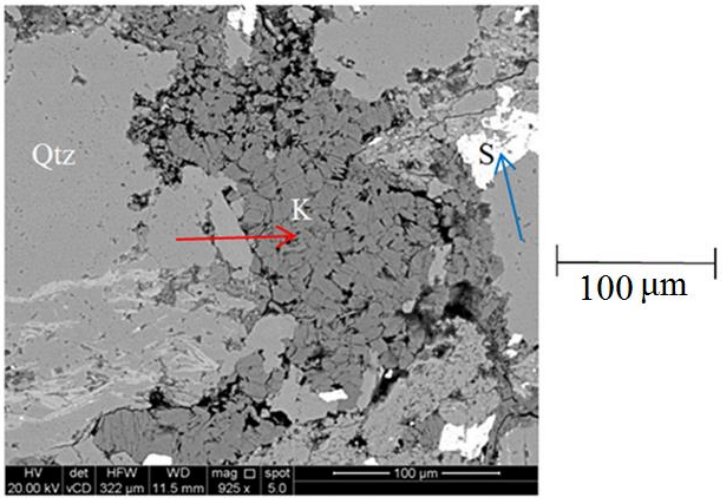

Figure 5.17 BSE image of EBN4_10 showing kaolin (red arrow) and siderite (blue arrow) infilling the pores.

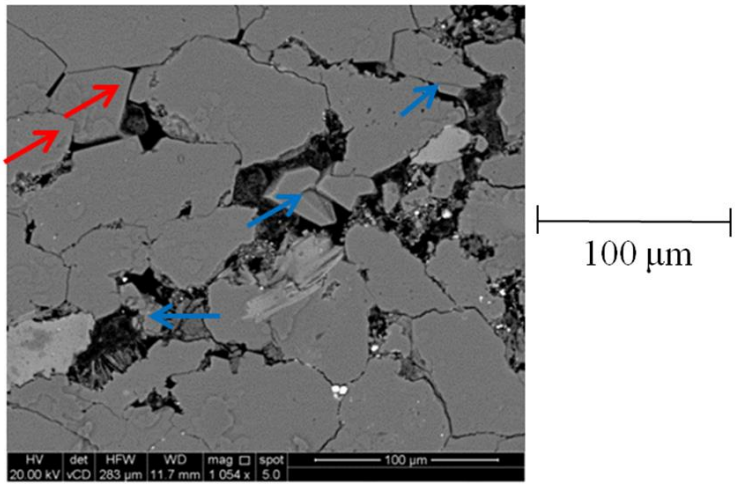

Figure 5.18 BSE image of EBN4_10 showing quartz overgrowths (red arrows) and outgrowths (blue arrows).

5.3.4.5 GDF1

GDF1_1, 1_6, 1_7 have very fine to medium, sub-angular and very well to moderately sorted grains and they all contain mostly quartz, feldspar, kaolin and dolomite (Figure 5.19). The first diagenetic process to affect the samples was dolomite cementation. The dolomite occurs as 50-100 µm rhombs that are overgrown by ferroan dolomite (Figure 5.20). The kaolin precipitated after the dolomite but is partially overgrown by ferroan dolomite suggesting that the two phases overlapped (Figure 5.20). The ferroan dolomite/ankerite appears to have precipitated over an extended period of the samples burial history with some evidence suggesting that it continued after the start of quartz cementation. Quartz cement is present in all samples and occurs as syntaxial overgrowths on detrital quartz grains (Figure 5.21). The main diagenetic process to affect this well is dolomite and kaolin cementation.

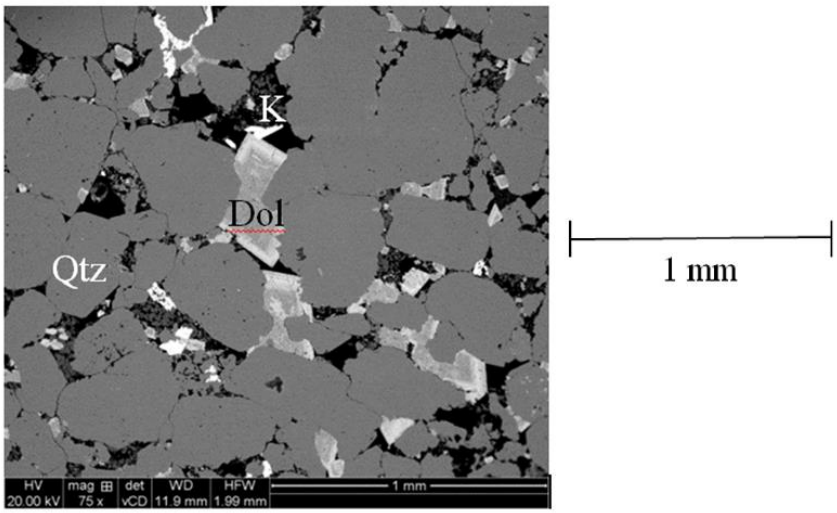

Figure 5.19 BSE image showing the general mineralogy of a sample from well GDF1.

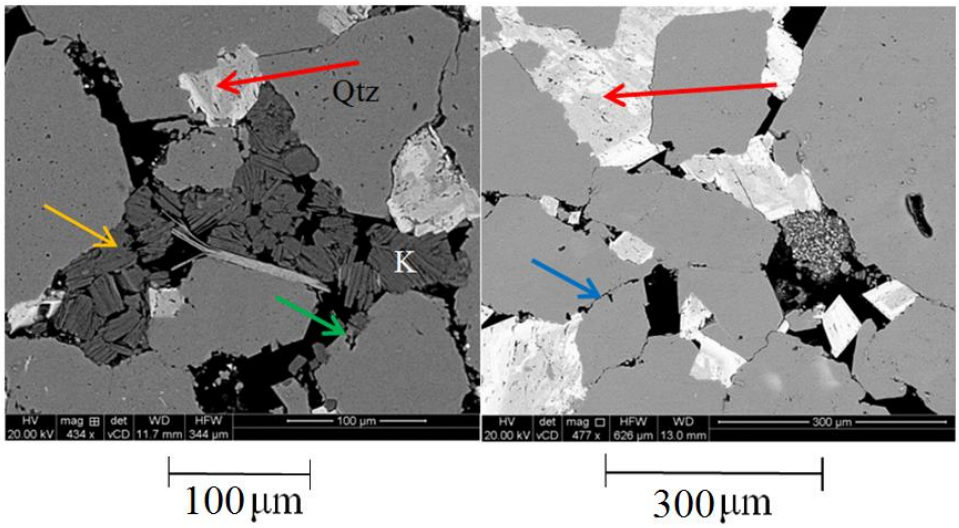

Figure 5.20 BSE image of GDF1_6 showing the presence of kaolin (yellow arrow), dolomite overgrown with ferroan-dolomite (red arrow), quartz overgrowing the kaolin (green arrows) and microfractures that are present between grain contacts (blue arrow).

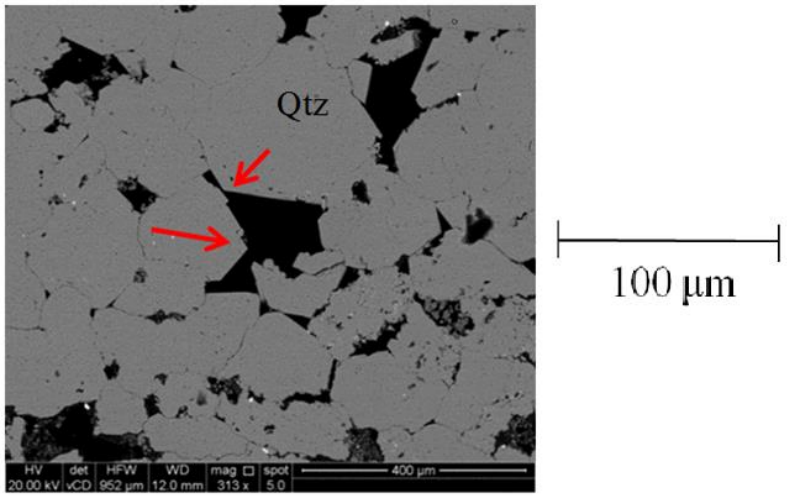

Figure 5.21 BSE image of GDF1_7 showing the presence of quartz overgrowths (red arrow).

5.3.4.6 GDF2

GDF2_4 has fine to medium, sub-angular and moderate sorted grains (Figure 5.22) and contains mostly quartz, feldspar, kaolin, dolomite siderite and barite. The first diagenetic process to affect the samples was dolomite cementation. The dolomite occurs as ~10-20 µm rhombs that are overgrown by large amounts of ferroan dolomite (Figure 5.23). The kaolin precipitated after the dolomite but is partially overgrown by ferroan dolomite suggesting that the two phases overlapped (Figure 5.23). The ferroan dolomite appears to have precipitated over an extended period of the samples burial history with some evidence suggesting that it continued after the

start of quartz cementation. Quartz cement is present in all samples and occurs as both overgrowths and outgrowths (Figure 5.24). The quartz can be observed to have been overgrown by both siderite and barite although these cements are not volumetrically important (Figure 5.25). The main diagenetic process to affect this well is dolomite and kaolin cementation.

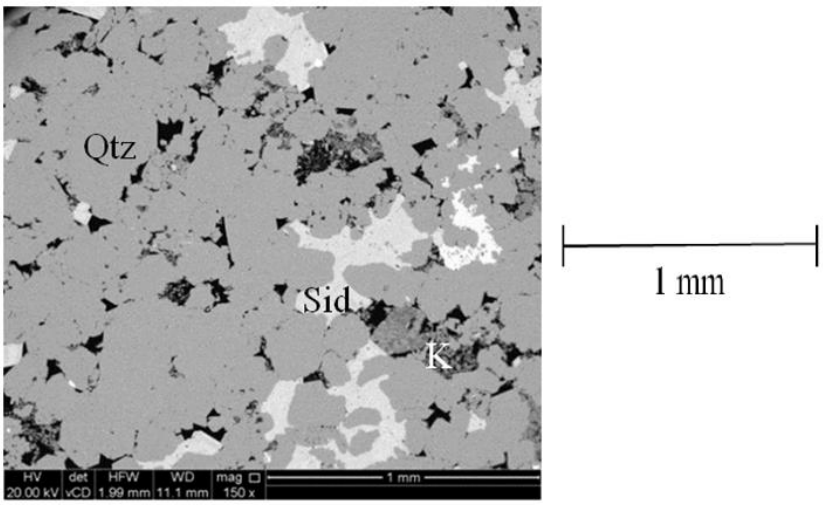

Figure 5.22 BSE image showing the general mineralogy of a sample from well GDF2.

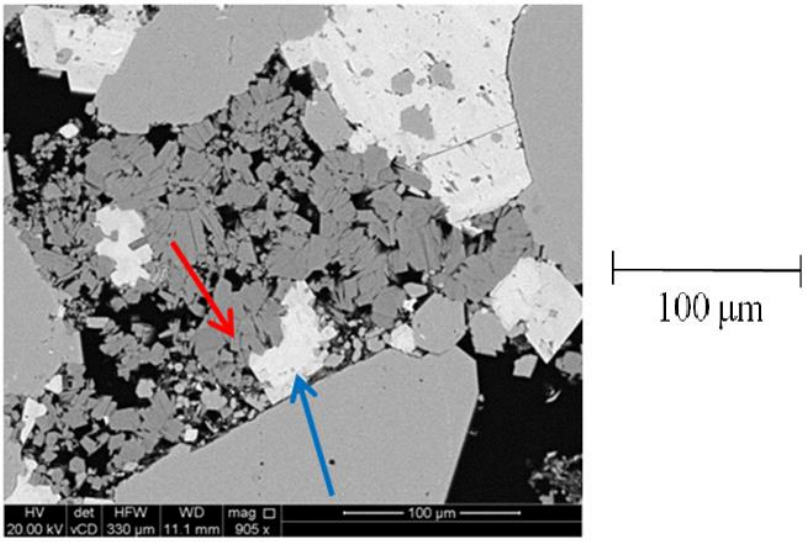

Figure 5.23 Pore filling kaolin (red arrow) partially overgrown by ferroan-dolomite (blue arrow).

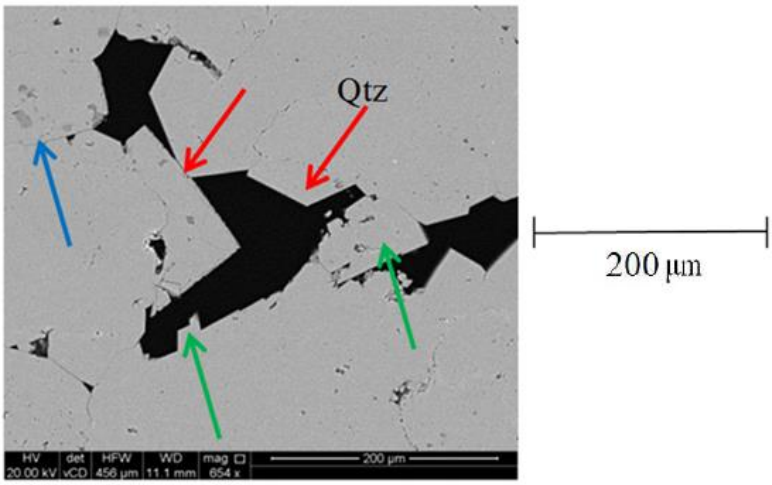

Figure 5.24 BSE image of quartz overgrowths (red arrows), outgrowths (green arrows) and microfractures between grain contacts (blue arrows).

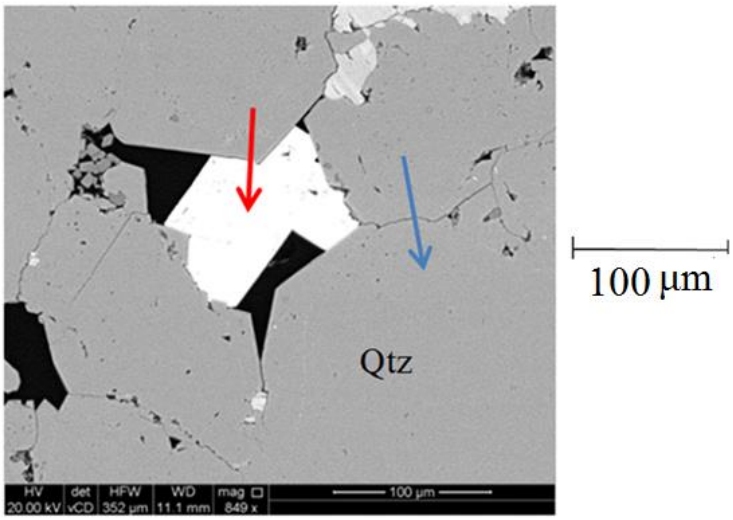

Figure 5.25 BSE image of barite (red arrow) overgrowing quartz (blue arrow).

5.3.4.7 SHELL1

SHELL1_83, 111 and 216 have very fine to medium, sub-rounded to sub-angular and moderate to well sorted grains (Figure 5.26). The samples experienced the precipitation of dolomite (Figure 5.27) and a Fe-Mg-rich clay (chlorite) during shallow burial. The samples experienced extensive minor quartz, illite, and dolomite/ankerite during deeper burial. The illite and chlorite occur as grain coats and pore filling cements (Figure 5.28). Diagenetic quartz occurs in small quantities (<2%) and generally occurs as outgrowths; its precipitation has been inhibited due to the large quantities of clay present. The main diagenetic processes to have affected the samples are the precipitation of authigenic dolomite, chlorite and illite.

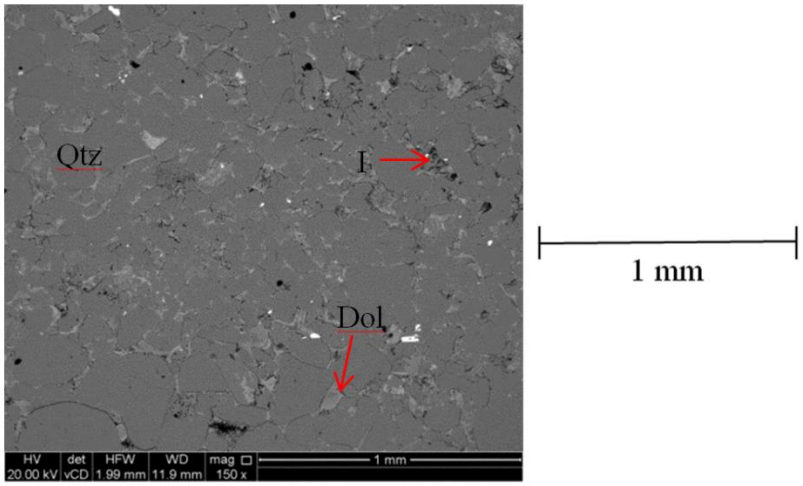

Figure 5.26 BSE image showing the general mineralogy of a sample from well SHELL1.

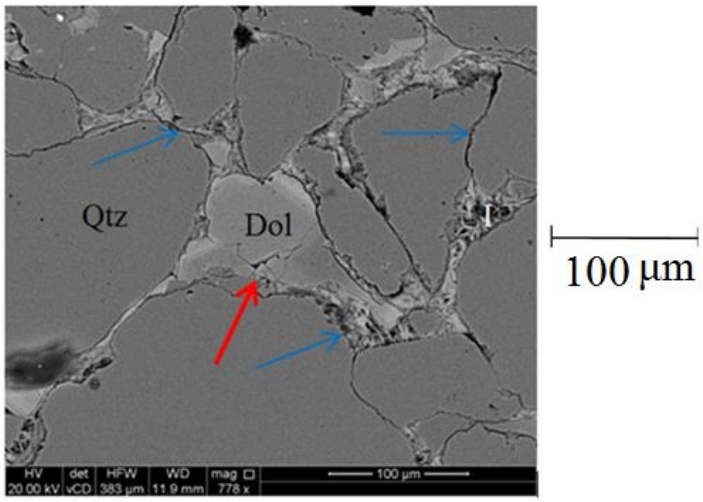

Figure 5.27 BSE image of SHELL1_83 showing the presence of dolomite overgrown with ferroan-dolomite (red arrow) and microfractures present between grain contacts (blue arrow).

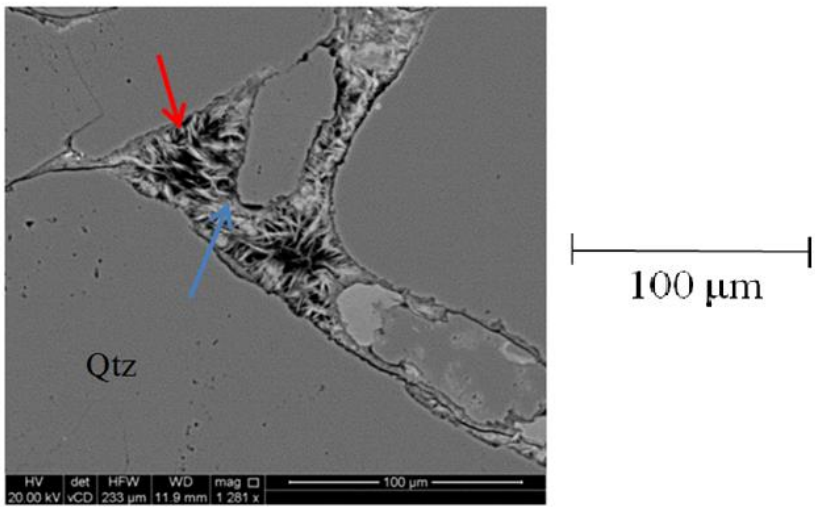

Figure 5.28 BSE image of SHELL1_111 showing the presence of pore lining illite (red arrow) and pore filling chlorite (blue arrow).

5.3.4.8 SHELL2

SHELL2_1, 9 have fine to medium, sub-rounded and moderate to well sorted grains (Figure 5.29) and contain mostly quartz, feldspar, illite and dolomite. The samples experienced infiltration of clays (Figure 5.30), precipitation of dolomite (Figure 5.31) and K-feldspar overgrowths (Figure 5.32) during shallow burial. The samples also experienced extensive diagenesis producing significant quantities of quartz, and small but variable amounts of ferroan dolomite, chlorite and illite during deeper burial. The main diagenetic process to have affected the samples is the precipitation of authigenic quartz, which accounts for between 2 and 11% of the pore volume. The authigenic quartz occurs as both outgrowths and a pore filling cement (Figure 5.30 and Figure 5.33).

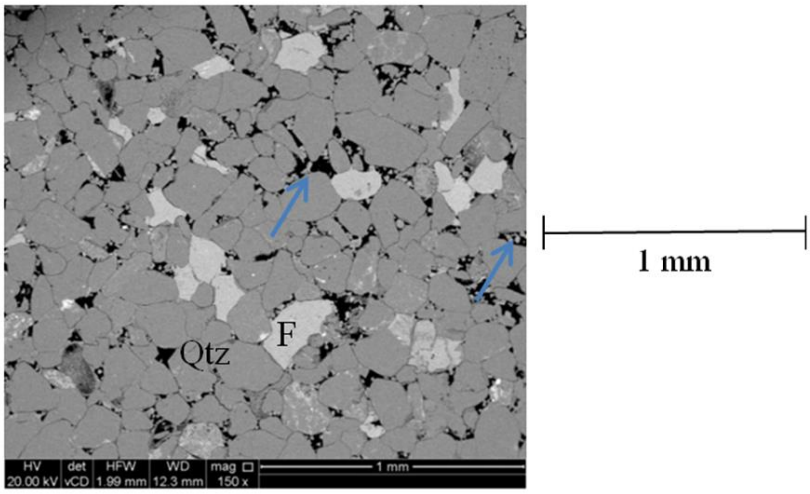

Figure 5.29 BSE image showing the general mineralogy of a sample from well SHELL2, the blue arrow shows the dolomite.

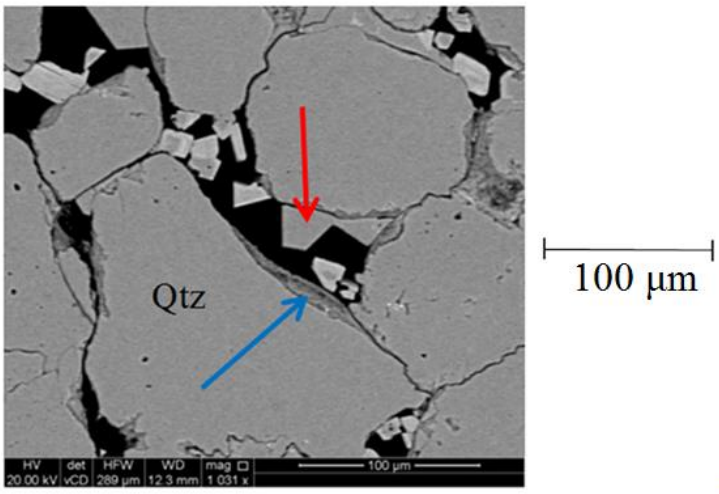

Figure 5.30 BSE image of SHELL2_1B showing quartz outgrowths (red arrow) and clay infiltration (blue arrow).

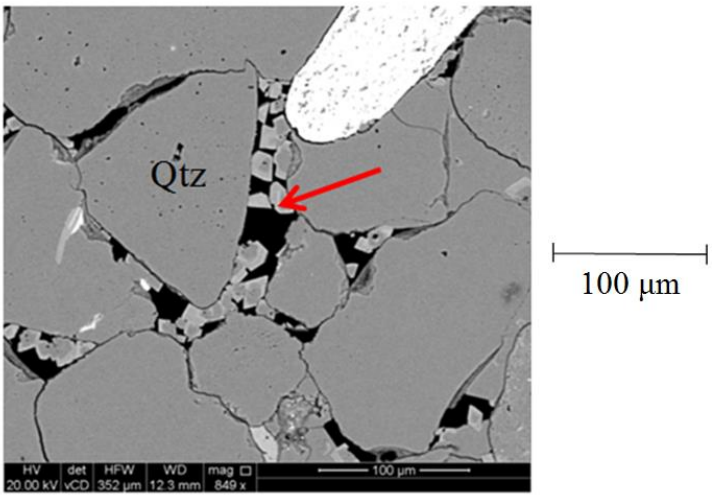

Figure 5.31 BSE image showing the presence of dolomite outgrown by ferroan-dolomite in SHELL2_1B (red arrow).

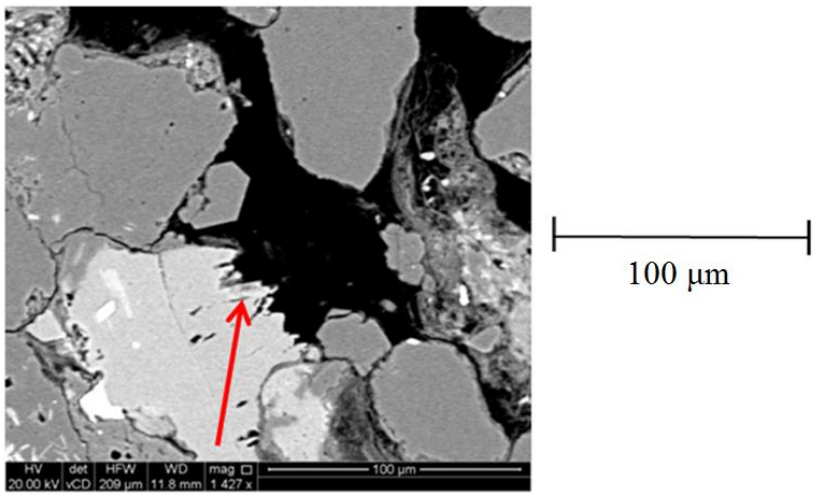

Figure 5.32 BSE image of SHELL2_9B showing K-feldspar overgrowths (red arrow).

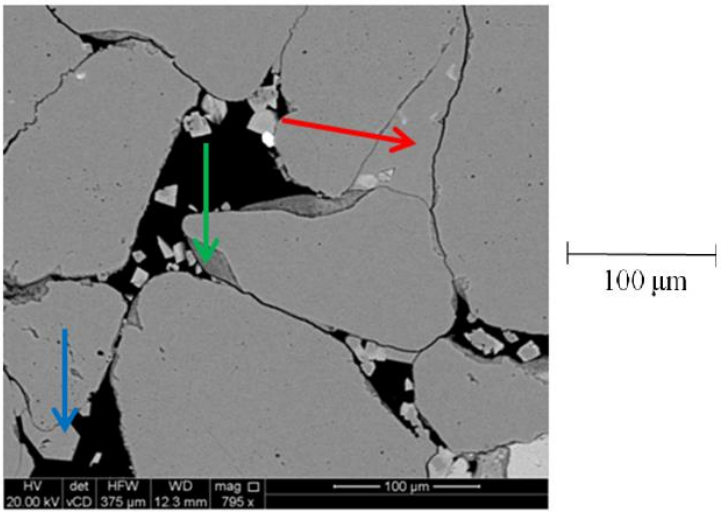

Figure 5.33 BSE image showing pore-filling quartz cement (red arrow), quartz outgrowth (blue arrow) and clay infiltration (green arrow) in SHELL2_1B.

5.3.4.9 SHELL4

SHELL4_202, 370, 389 and 409 have fine to coarse, sub-rounded to sub-angular and moderate to well sorted grains (Figure 5.34) and contains mostly quartz, feldspar and illite. The main diagenetic processes to affect the samples were the precipitation of magnesite during shallow burial (Figure 5.35) and hairy grain-coating illite during deep burial (Figure 5.36). The samples contain quartz outgrowths but these are generally not well developed due to the large amount of illite present (Figure 5.37). However, in some samples, lamina are present that contain larger concentrations of pore filling quartz cement. The magnesite occurs as a pore filling cement that it often far larger than the pore-size suggesting that it grew in a displacive manner during shallow burial. Small amounts of chlorite were also observed, which is intergrown with the illite. It is possible that the chlorite replaced an early authigenic clay such as Fe-Mg chlorite

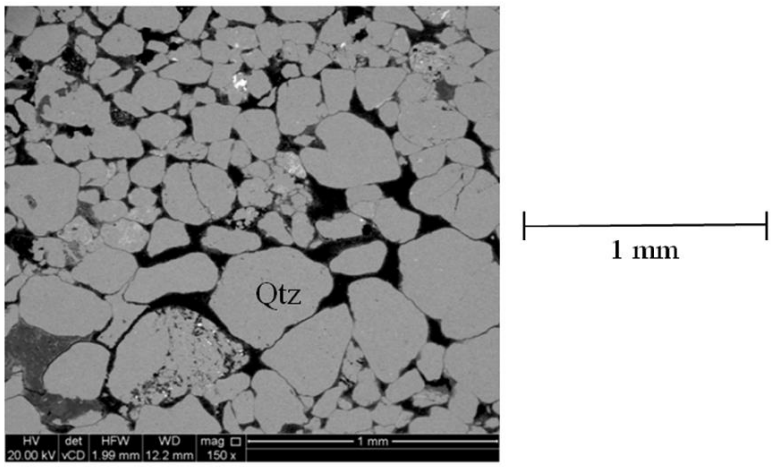

Figure 5.34 BSE image showing the general mineralogy of a sample from well SHELL4.

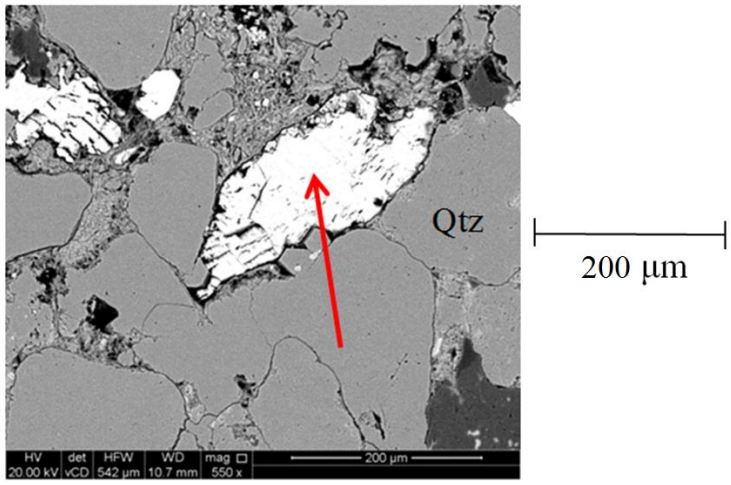

Figure 5.35 BSE image of magnesite (red arrow).

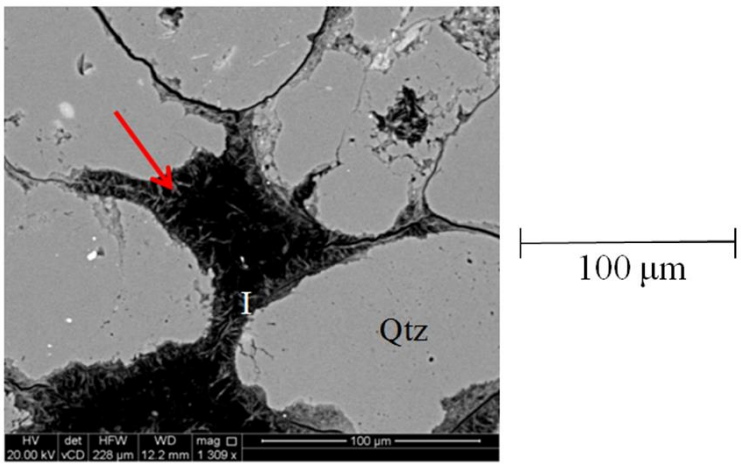

Figure 5.36 BSE image of grain coating illite (red arrow).

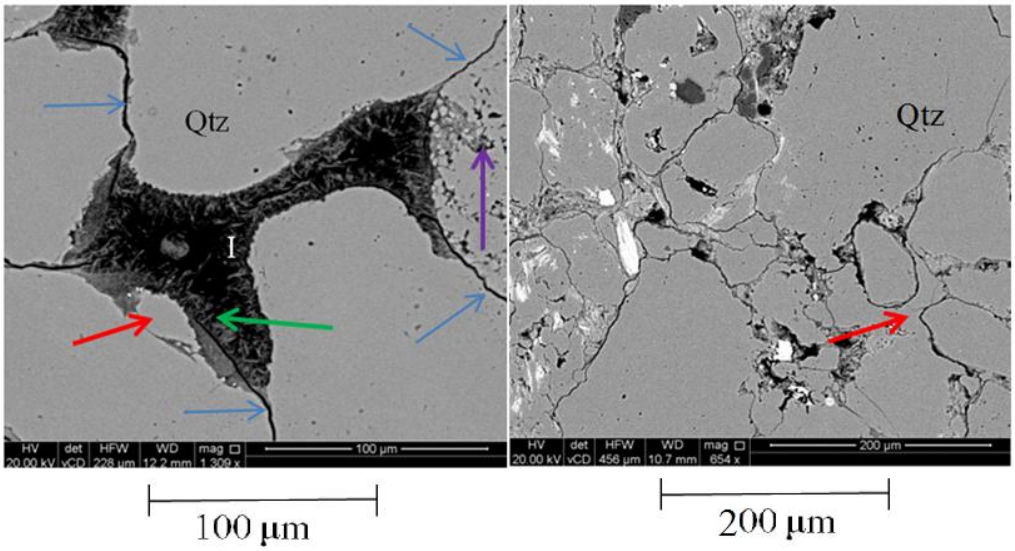

Figure 5.37 BSE image of SHELL4_202 showing quartz outgrowth and cement (red arrow), microfractures between grain contacts (blue arrow), grain coating illite (green arrow) and feldspar dissolution creating secondary pores (purple arrow).

5.3.4.10 WIN4

WIN4_26 has medium, sub-rounded and well sorted grains (Figure 5.38) and contains mostly quartz, feldspar, illite and dolomite. The first diagenetic processes to affect this samples was the precipitation of small to moderate quantities of dolomite during shallow burial; it occurs as around 100 µm rhombs, which were overgrown by Fe-rich dolomite (Figure 5.39). The samples then experienced the precipitation of moderately large quantities (5-10%) of quartz where the quartz cement occurs as overgrowths and as a pore filling cement (Figure 5.40). The final phase to precipitate was siderite (Figure 5.39). The low porosity and permeability of the samples is mainly a result of dolomite and quartz cementation.

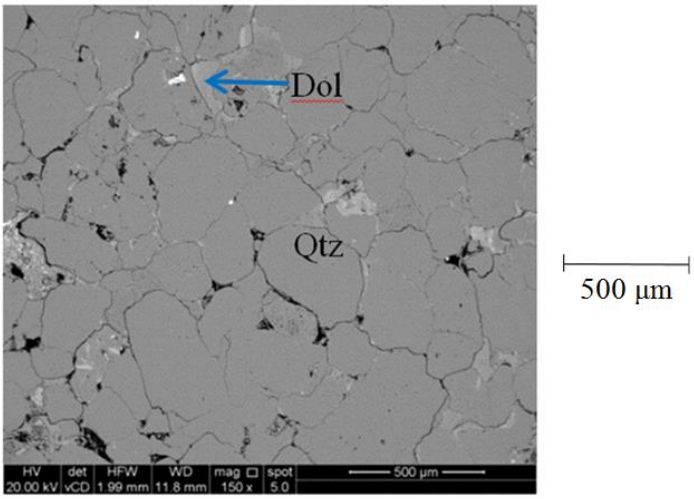

Figure 5.38 BSE image showing the general mineralogy of a sample from well WIN4.

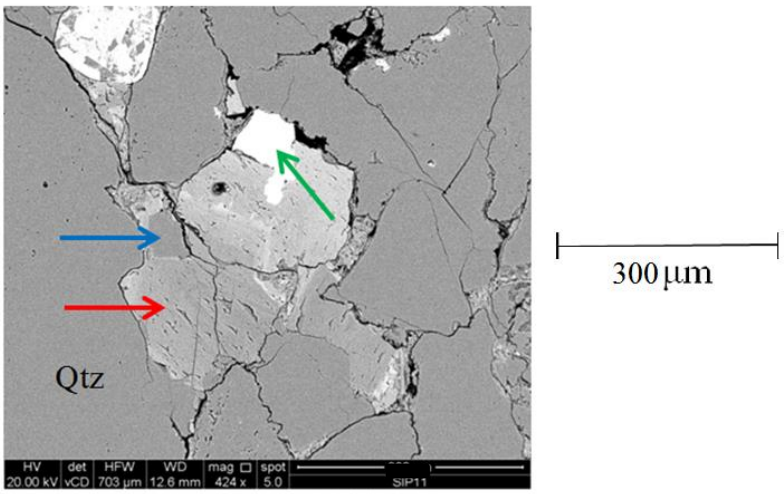

Figure 5.39 BSE image showing the infilling of the pores with dolomite (red arrow) overgrown with ferroan-dolomite (blue arrow) and overgrown by siderite (green arrow).

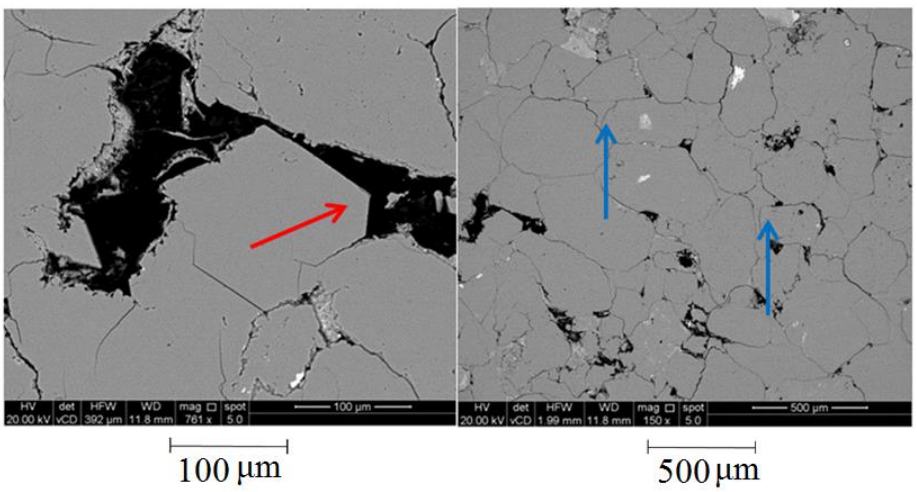

Figure 5.40 BSE of quartz overgrowth (red arrow) and quartz cement (blue arrow).

5.3.4.11 WIN5

WIN5_16B has very fine to medium, sub-rounded and well sorted grains and contains mostly quartz, feldspar and illite (Figure 5.41). The first diagenetic processes to affect this sample was the precipitation of small to moderate quantities of dolomite during shallow burial; it occurs as ~30 µm rhombs, which were overgrown by Fe-rich dolomite (Figure 5.41). The samples then experienced the precipitation of small amounts of quartz cement, which mainly occurs as outgrowths due to the presence of grain-coating clays (Figure 5.42). The final diagenetic process to affect these samples was the precipitation of large quantities (>5%) of illite during deeper burial (Figure 5.42). The low permeability of the samples is mainly due to illite cementation.

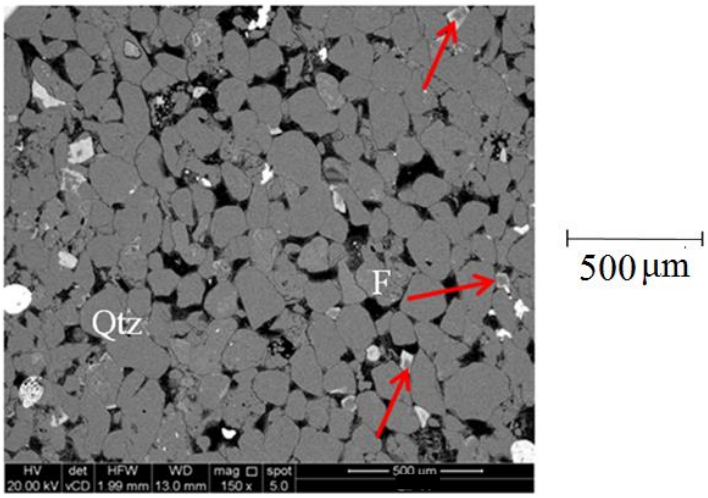

Figure 5.41 BSE image showing the general mineralogy of a sample from well WIN5; note the presence of dolomite overgrown with ferroan-dolomite (red arrow).

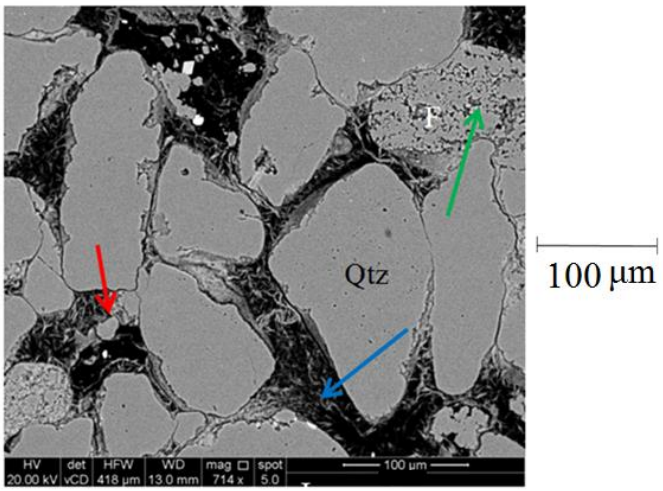

Figure 5.42 BSE image of WIN5_16B showing the presence of quartz outgrowths (red arrows), grain coating illite (blue arrows) and feldspar dissolution with secondary pores (green arrows).

5.3.4.12 WIN9

WIN9_5 has medium, sub-angular and well to moderately sorted grains (Figure 5.43) and contains mostly quartz, feldspar, illite and siderite. The main diagenetic processes to impact the sample was mechanical and chemical compaction, quartz, kaolin, chlorite and illite precipitation. The sample experienced kaolin precipitation during shallow burial (Figure 5.44). The kaolin typically occurs as ~10 µm stacks that partially fill macro-pores and secondary porosity. The sample was cemented by quartz and illite during deep burial. The quartz occurs as both outgrowths and overgrowths (Figure 5.44). The illite has a hairy nature, which is particularly effective at blocking pore throats (Figure 5.44). Most samples contain significant secondary porosity and it is possible that the illite formed as a result of the dissolution of K-feldspar and kaolin. K-feldspar is no longer present in the samples suggesting that the reaction could have been limited by the amount of potassium available. The amount of soft lithoclasts is an important control on the diagenetic processes that have affected the sample (Figure 5.45). WIN9_5 contains large volumes of soft lithoclasts therefore it has experienced extensive mechanical compaction but does not contain large volumes of other cements.

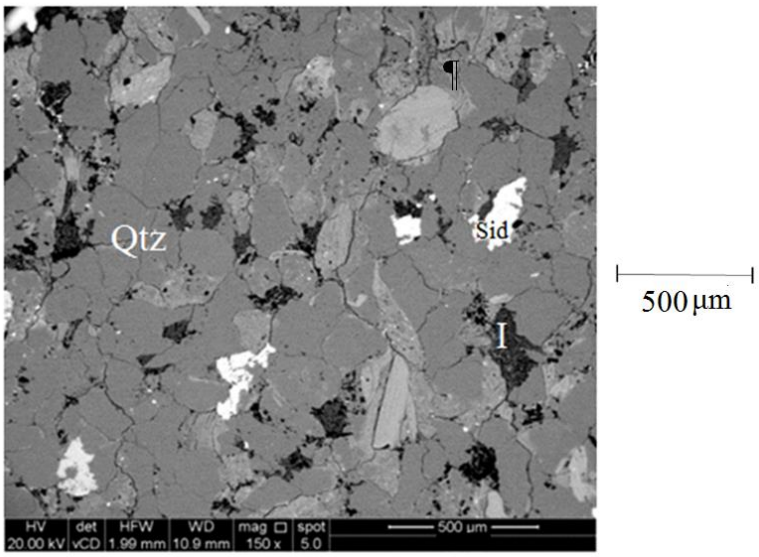

Figure 5.43 BSE image showing the general mineralogy of a sample from well WIN9.

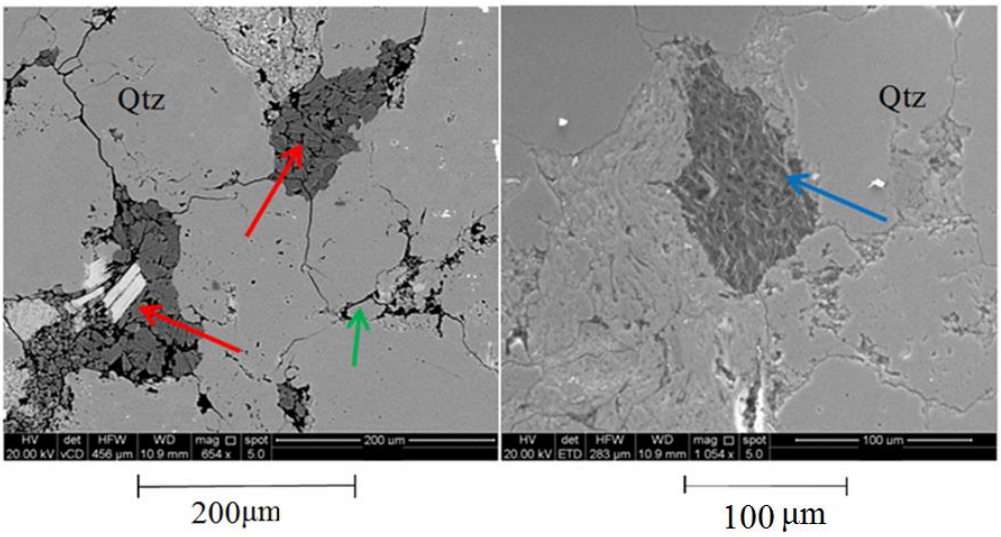

Figure 5.44 BSE image of kaolin (red arrow), illite (blue arrow) both pore filling and quartz outgrowths (green arrow).

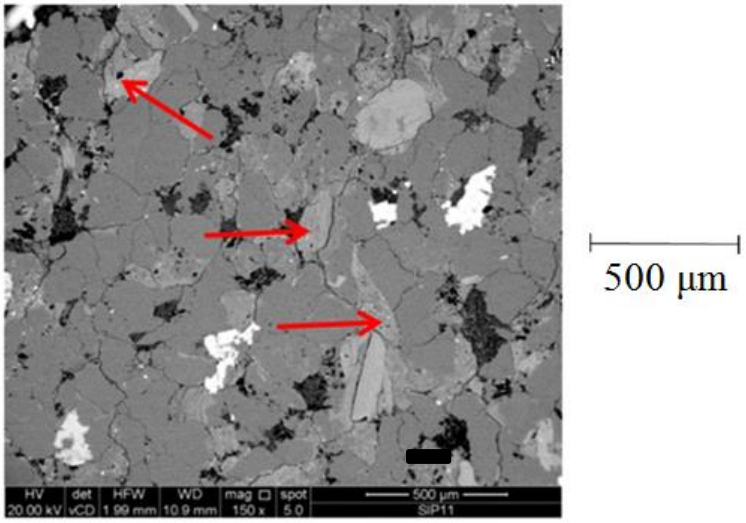

Figure 5.45 BSE image showing soft lithofacies which have experienced enhanced mechanical compaction (red arrows).

5.3.5 Quantitative X-ray Diffraction (QXRD)

The samples contained quartz ranging from 51 – 87%. There was also, albite (0 - 7.3%); dolomite (0 – 13.9%), siderite (0 - 7.9%), mica (0 - 14%), microcline (0 – 7.6%), pyrite (0.2 – 0.7%), magnesite (0 – 4.7%) and anhydrite (0 – 0.9%) in some samples. All the samples also contained clays, whose mineralogy varied between the wells but included illite (0 - 13%), kaolin (0 - 12%) and chlorite (0 – 8%). A bar chart showing the minerals and their concentrations for each sample is presented in Figure 5.46.

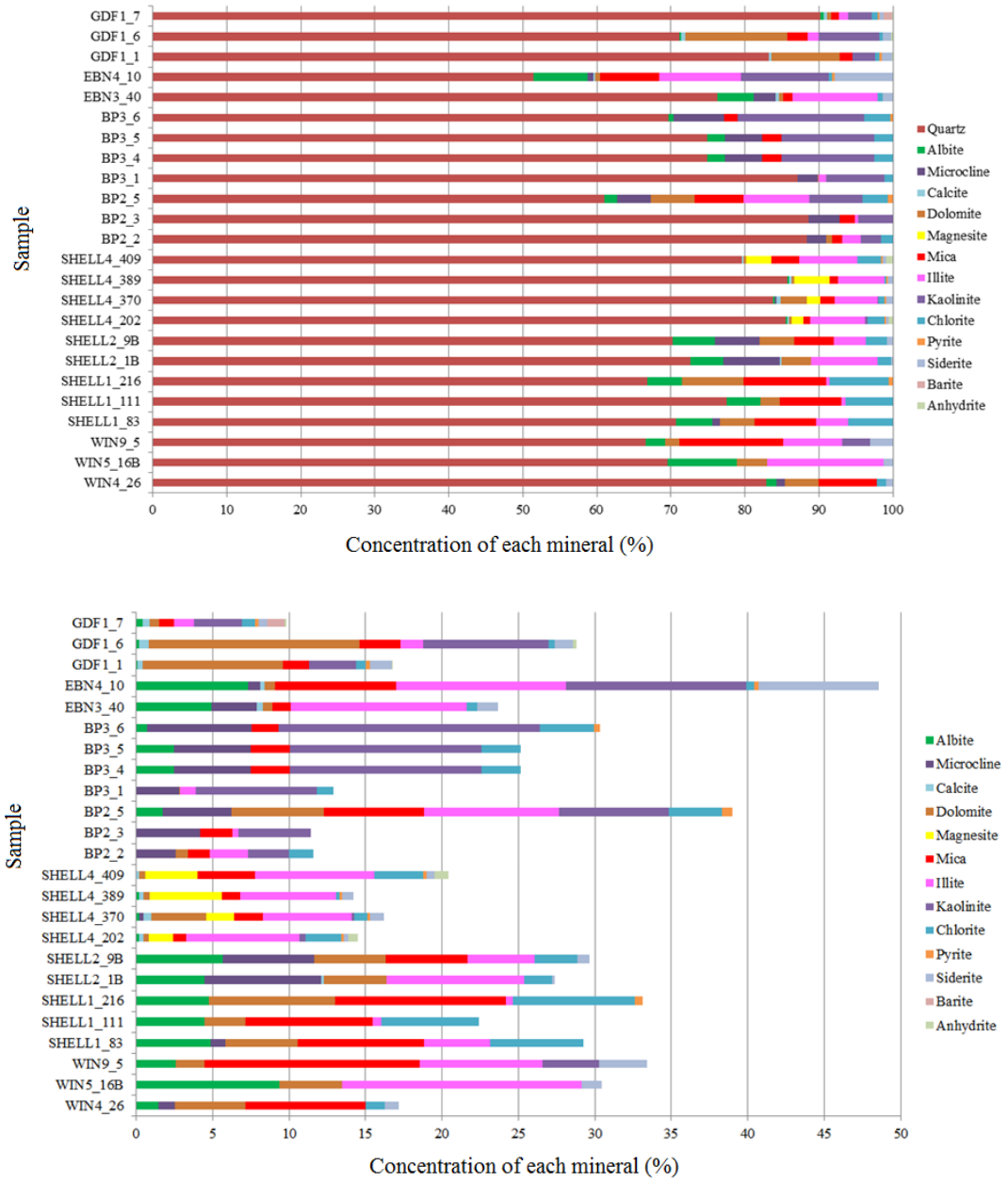

Figure 5.46 Bar chart of the minerals and the concentrations for each sample showing the most common mineral in TGS is quartz (top) and quartz-free basis (bottom).

5.4 Discussion

In this section, a comparison is made between calliper and mercury immersion bulk volume for porosity determination (Section 5.4.1). This is followed by an analysis of the pore pressure equilibrium for gas permeability (Section 5.4.2). Brine permeability is then compared to gas permeability and the differences between them are discussed (Section 5.4.3). The controls on porosity and permeability, permeability estimations using SEM and QXRD and a comparison between microstructure and reservoir flow rates are then studied (Section 5.4.4). Lastly, a survey of inaccuracies in RCA measurements is presented (Section 5.4.5).

5.4.1 Accuracy of Porosity Determination

The bulk volume from callipers is larger than the bulk volume from mercury immersion (Figure 5.1), therefore, the former produces higher porosities (Figure 5.2). There are limitations in both methodologies which can give rise to these differences in the bulk volume. It has been argued that the samples with vugs, fractures or unconsolidated material would have lower bulk volumes when measured using mercury immersion because mercury can enter the pores (API, 1998; McPhee et al., 2015; Taylor and Wardlaw, 1975). However, mercury does not enter cracks spontaneously under ambient stress conditions because it is a non-wetting fluid; therefore, these effects are only minor unless the fractures are large. The core plugs observed in this research did not contain any large fractures or vugs on the surface. Air can be trapped around the sample when the core plug is immersed in the mercury (API, 1998), this would increase the overall volume of the sample. However, in this research, the bulk volume from mercury immersion is lower than that of the calliper.

API (1998) argues that callipers cannot be used on unevenly shaped cores as not all the irregularities in the core shape are taken into account leading to high bulk volume values. Improvements can be made by making several measurements and taking averages. Similarly, Lin (2015) argued that the convex surfaces within the gabbro, granite, sandstone, tuffs and metal samples produced higher calliper bulk volumes (Figure 5.47). Likewise, Manger (1966) showed that core samples that are not precisely shaped can be expected to have overestimated bulk volumes.

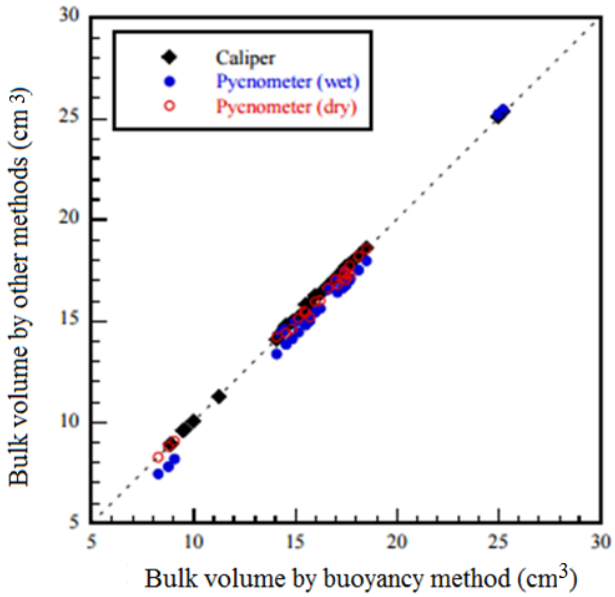

Figure 5.47 A comparison between three bulk volume methods showing a good 1:1 correlation, however, the callipers show a higher BV value compared to the two other methods (Lin, 2015).

Visual observation of the core plugs used within this research show that some of the surfaces are irregular and some of the core plugs are bulged. Variations in results are still present even when the diameter and length are measured several times and averaged. In contrast, the limitations from the mercury immersion method do not seem to apply to the TGS studied within this research. The mercury would not be able to identify the irregular nature of the core plugs made by small undulations or lose of grains unless large vugs are created. Mercury immersion appears to be the best method to use for bulk volume determination which is supported by a number of authors (Jenkins, 1960; API, 1998; Kennedy, 2015; Ghanizadeh, 2015; McPhee et al., 2015). Consequently, the lack of imperfect cylindrical shape seems to be the most likely reason for the higher calliper bulk volumes in these TGS and that the calliper is the source of error. Nevertheless, an investigation is needed whereby the bulk volume and porosity are measured on core plugs with known bulk volumes and porosities to confirm this conclusion.

5.4.2 Pore Pressure Equilibrium Time using Eclipse Model

Eclipse is a finite element simulator able to model laboratory scale fluid flow through various media. In this research it was used to enable a comparison to be made between the permeability and the time required for pore pressure equilibrium to be achieved through a sample prior to a pulse decay permeability measurement. For this purpose models of core samples where constructed using a Cartesian grid. This means that radial core samples had to be represented by rectangular parallelepiped, therefore, the flow areas had to be the same.

The errors obtained by Cartesian representation are minimal because once the flow areas are equalised there are no geometrical factors impacting the fluid flow. However, there may be errors regarding the heterogeneity of the core sample as it may contain different lithologies which in turn have different porosities and permeabilities. The model is not able to represent such detailed variation in rock properties, therefore, completely homogenous matrix was assumed.

For the Eclipse simulation a 5 cm long sample was modelled having permeabilities from 0.01 mD to 1 nD and a porosity of 10%. The upstream and downstream volumes were 30 cm^3 and the initial pressure was 1000 psi. The Eclipse simulation file can be found in Appendix B.

As a result of the simulation, a power law relationship between the permeability and the pore pressure equilibrium time was derived (Figure 5.48). According to the samples studied in this research with permeabilities ranging from 0.00005 mD to 4.1 mD, a maximum of ~11.4 hours is required for confining pressure equilibrium in the low permeability samples, but only ~0.5 seconds for the high permeability samples. This shows that (i) equilibrium time is important, (ii) equilibrium time increases with a decrease in permeability and (iii) one standard time should not be used for all samples.

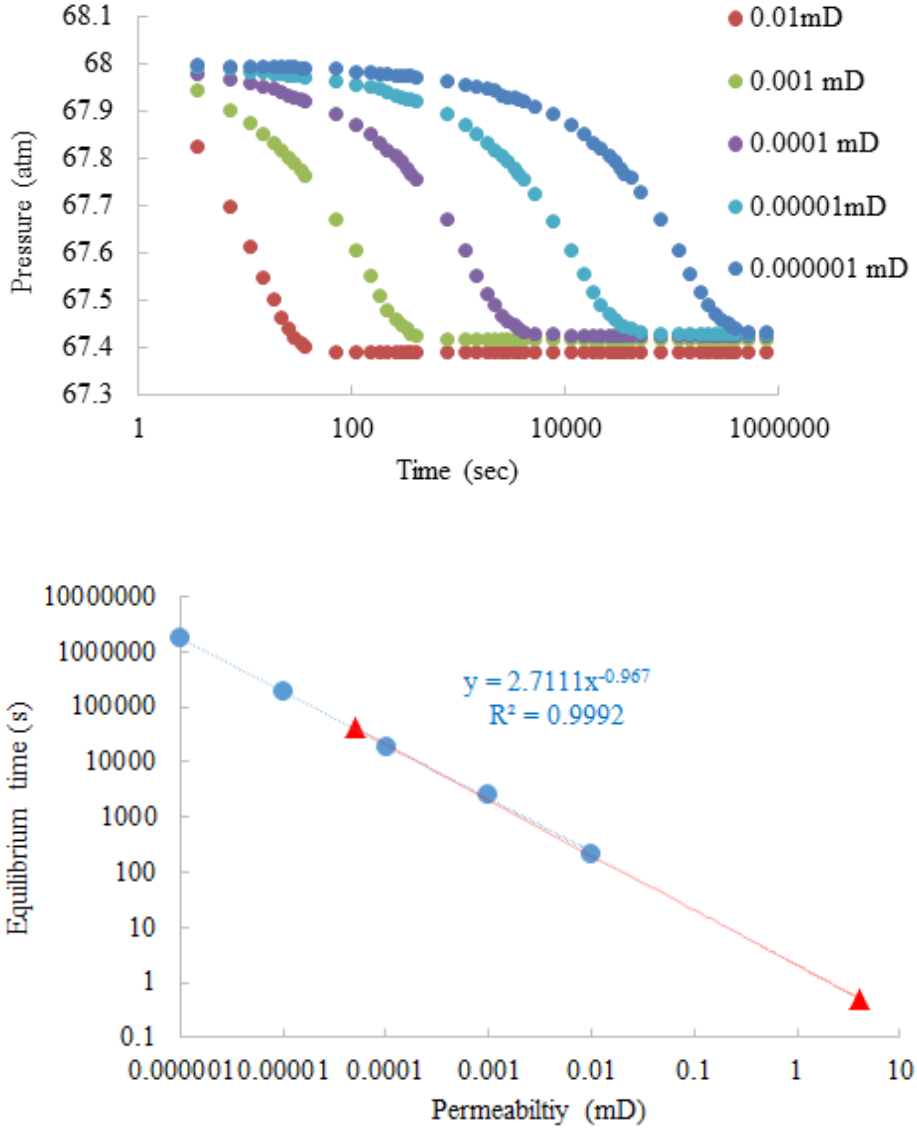

Figure 5.48 Pressure as a function of time (top) and permeability as a function of time (bottom). The 5 modelled permeabilities are in blue and the largest and smallest permeability values from this research are in red. There is an increase in equilibrium time with a decrease in permeability.

5.4.3 Brine Permeability vs Gas Permeability

The brine permeability was lower than the gas permeability by around an order of magnitude (Figure 5.3). There are many publications in the literature also reporting on samples having a lower permeability to brine than gas (Heid et al., 1950; Jones and Owens, 1980; Sampath and Keighin, 1982; Wei, 1986; Chowdiah, 1990; and Aben and Kurnitski, 2002). For example, Juhasz (1986) found that the brine permeability was three times lower than the gas permeability for the igneous rocks he was studying. Furthermore, Lokmane (2001) found that the liquid permeability

was 4.5 times lower than the intrinsic gas permeability for the fractured sandstones rocks he was studying. In addition, Heid (1950) showed that the lower the permeability, the greater the percentage difference between the permeability to liquid and the permeability to air at atmospheric pressure. Studies show that there is considerable scatter on plots of brine vs gas permeability (Lovelock, 1972; Sampath and Keighin, 1982; Pugh, 1991; Bloomfield and Williams, 1995) (Figure 5.49).

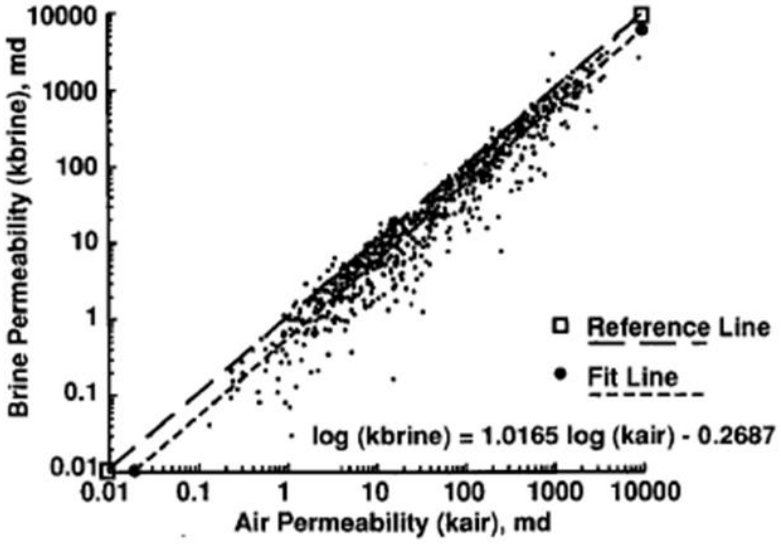

Figure 5.49 Brine permeability as a function of gas permeability for 895 sandstone and carbonate samples. The brine permeability is lower than the gas permeability and there is a bit of scatter. This plot consists of sandstones, dolomites and limestones, the scatter is improved when the data is divided into each rock types (Pugh, 1991).

A number of causes for the differences between gas and brine permeability have been proposed. An under-saturation of the core with brine may occur (Lovelock, 1972; Bloomfield, 1995; Pugh et al., 1991; Lokmane, 2001). Therefore, some of the pores, especially the smaller ones could be filled with gas reducing the pore connectivity for the brine. This is however unlikely as all the samples within this research were saturated using a vacuum pump followed by 1500 psi confining pressure. In addition, a 200 psi brine back pressure would be sufficient to compress any remaining gas.

Wei (1986), Pugh et al. (1991), Rahman (1994) and Bloomfield and Williams (1995) all associate this difference with the swelling of clays such as smectite or mixed layer illlite-smectite. This can cause a reduction in the pore throat size blocking the passage of brine. Nevertheless, within this research none of the TGS samples

contained any swelling clays where the main clays are illite and kaolin which do not expand as much as smectite (Table 5.6).

Table 5.6 Clay mineral expansion for smectite, illite and kaolin where the smectite have a much larger swelling percentage then the illite and kaolin present in the samples in this research (Shamburger et al., 1975)

Clay	Average free-swell (%)	Range (%)
Na-smectite	1500	1400–1600
Ca-smectite	102	65–145
Illite	89	60–120
Kaolinite	28	5–60

Cleaning and drying of samples may cause delicate clays to break down and be entrained within the brine flow (Lovelock, 1972; Bloomfield and Williams, 1995). When these particles of clay start to aggregate, they block pores and reduced permeability, this is called flocculation (Waal et al., 1988 and Luffel et al., 1993). The critical salt concentration (CSC) is the salt concentration below which there is a release of particles (Khilar and Fogler, 1984; Blume et al., 2004). The CSC differs from sediment to sediment (Table 5.7) but it is also dependent on the size of the salt cations (Blume et al., 2004). If the salinity of the fluid falls below the CSC, the permeability is significantly reduced due to the release of particles (Khilar, and Fogler, 1984; Ochi and Vernoux, 1998). In addition, the release of particles is related to the electrostatic repulsion between the fluid and the solid surface i.e. the zeta potential (Gornicka et al., 2016). If the zeta potential is low, then flocculation can occur (Gornicka et al., 2016).

Table 5.7 Na^+ critical salt concentrations found in the literature from different types of matric (Blume et al., 2004)

Authors	Matrix used	CSC (Na^+, M)
Khilar and Fogler (1984)	Berea sandstone	0.07
Kia et al. (1987)	Berea sandstone	0.03–0.04
Grolimund et al. (1998)	Silty loam soil	0.2
Quirk and Schofield (1955)	Silty loam soil	0.25
Mohan and Fogler (1997)	Stevens sandstone	0.25

Khilar and Fogler (1984) and Lever and Dawe (1984) carried out experiments to demonstrate what effect changing the salinity of the fluid entering the rock had on the permeability (Figure 5.50 and Figure 5.51). They all found that when the fresh

water was passed through a core the permeability dropped by a factor of 100 (Khilar and Fogler, 1984). Once the flow of the freshwater reverses, the permeability re-adjusts for a short period of time. This is because the clay particles are pushed back to the other side of the pores; therefore, the pores are no longer obstructed by clay. Finally, a rise in permeability is seen when the flow is changed back to a salt solution, this is because the CSC value is reapplied.

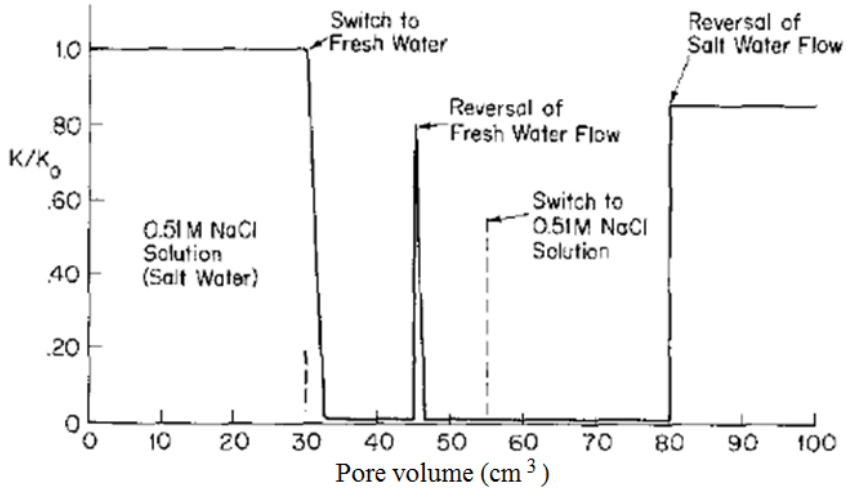

Figure 5.50 Change in permeability due to flocculation of clay with a change in salinity of brine. The permeability decreases as the salt water is replaced by fresh water as the salinity drops below the CSC. There is a sudden increase in permeability as the flow of fresh water is reversed causing the clay particles to be pushed to the other side. Once the fresh water is replaced with the salt water the permeability does not increase until all the fresh water has been flushed out (Khilar and Fogler, 1984).

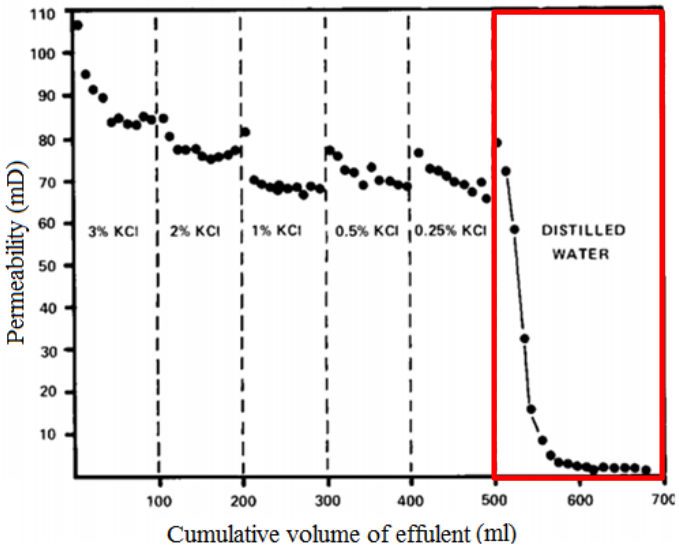

Figure 5.51 Water sensitivity of the Hopeman Sandstone, from Clashach Quarry, Scotland. Permeability drops to less than 1 mD (red box) when distilled water is passed through the core plug due to clay flocculation as the salinity of the fluid drops below the CSC (Lever and Dawe, 1984).

A number of authors have stated that the release of particles is related to the electrical double layer. Changes in electrical double-layer thickness cause the loss of permeability (Aveyard and Hayden, 1973; Oiphen, 1977). Lever and Dawe (1986) wrote "*that due to isomorphous substitution in the lattice, clay minerals generally have a net negative charge which is balanced by cations held weakly at the surface by Van der Waals forces*". As the cations are readily exchangeable, an electrical double-layer will form, the double-layer will be relatively compressed in a solution of high ionic strength and expanded in those of low ionic strength (Lever and Dawe, 1986). Therefore, a reduction in salinity will cause a large expansion of the electrical double layer, adjacent particles will repel each other, and fines will be entrained in the fluid flow (Lever and Dawe, 1986).

The salinity of the brine used within this research is high: 200 and 300 g of NaCl in 100 ml of water (34.2-51.3 mol/L). These salinities greatly exceed the salinities stated by Khilar and Fogler (1984) and Lever and Dawe (1986) where flocculation is not occurring. This implies flocculation is not occurring in this research. However, when comparing the brine permeabilities for samples saturated at 20 and 30% NaCl there is no clear trend as those saturated with 30% and 20% NaCl have some of the smallest and largest permeabilities (Table 5.8).

Table 5.8 Brine permeability ordered from lowest to highest permeability and coloured occurring to the salinity. There is no clear pattern as those samples with the highest salinity of 30% have some of the largest and smallest permeabilities.

Sample	Kw at 1500 psi (mD)	Sample	Kw at 1500 psi (mD)
SHELL1_83E	0.0001	BP2_3	0.018
SHELL1_111	0.0003	BP3_6	0.03
BP2_5	0.001	GDF1_1	0.03
SHELL1_216B	0.001	BP3_4	0.04
SHELL4_409	0.001	BP3-5	0.04
WIN4_26	0.001	BP2_2	0.043
WIN5_16B	0.001	SHELL2_9B	0.047
WIN9_5	0.001	SHELL4_370	0.047
GDF1_6	0.003	SHELL2_1B	0.051
SHELL4_389	0.004	GDF1_7	0.056
EBN4_10	0.005	EBN3_40	0.16
SHELL4_202	0.006	GDF2_4	0.18
BP3_1	0.017		

Note: those highlighted in yellow are 30% NaCl and those highlighted in green are 20% NaCl.

The differences between gas and brine permeability do not appear to be due to a lack of saturation of the core plug or swelling of clay and there is no clear evidence to support or disprove clay flocculation. Other possibilities could be due to an overestimation rather than an underestimation by the gas permeability due to adsorption of gas onto the sample. The pulse decay machine cannot distinguish between pore permeability and adsorption, therefore, it assumes the decrease in gas is completely dependent on the pore permeability and hence the overall gas permeability is overestimated. However, this will not occur with helium as helium does not react with the mineral surface and adsorption would only happen with methane (Cui et al., 2009; and Fisher et al., 2016).

The lower the permeability value of a sample, the higher the chance the permeability values could be inaccurate. However, the brine permeability was found to be underestimated at higher permeabilities in various publications but the effects were greater for the lower permeable samples. Therefore the difference may be artefacts of studying low permeability samples. The differences could also be due to experimental errors made during the data collection, however, this seems unlikely as the differences are systematic and these differences between gas and brine permeability are present in a number of publications.

This research work is inconclusive as to the cause of the differences between gas and brine permeabilities. Flocculation appears not to be possible under the salinities used, nevertheless, future work is required to design an experiment to determine if flocculation is possible under the salinities used in this research.

5.4.4 Controls on Porosity and Permeability Trends

This section presents the rock types generated using mineralogical, depositional and microstructural data. The mineralogical rock types include illite, kaolin and other diagenetic deposits like quartz, albite and dolomite (Section 5.4.4.1). The depositional rock types include grain sorting, grain shape and grain size as well as a variety of depositional environments (Section 5.4.4.2). The microstructural rock types include low clay content, pore filling clay and grain coating/bridging clay (Section 5.4.4.3). Permeability is estimated using SEM and microstructural data and flow rates are correlated with microstructure.

5.4.4.1 Mineralogical Controls

Rossel (1982) implied that the surface area is highest in illlitic sandstone due to their thin thread like nature which causes the porosity to be lower than samples that contain kaolin and/or feldspar. The illite in the samples in this research form large fibrous blades and intertwine to form a large interconnected mass (Section 5.3.4), therefore, it is likely the illite will have a large surface area. However, when observing the illite content with porosity there is a slight increase in porosity with illite content and there is a lot of scatter and the trend is poor with a R^2 value of 0.14 (Figure 5.52).

A number of authors state that illite surrounds grains and bridges pores therefore blocking pore throats and reducing the size and increasing the sinuosity of pathways (Stalder, 1973; Morris and Shepperd, 1982; Tiab and Donaldson, 1994; Wilson, 2012; Nolen-Hoeksema, 2014). The illite in this research did surround and bridge pores as seen in the BSE images in Section 5.3.4 (for example Figure 5.15 and Figure 5.28). When observing the illite content with permeability there is no trend as there is a lot of scatter and the trend is very poor with a R^2 value of 0.0003 (Figure 5.52).

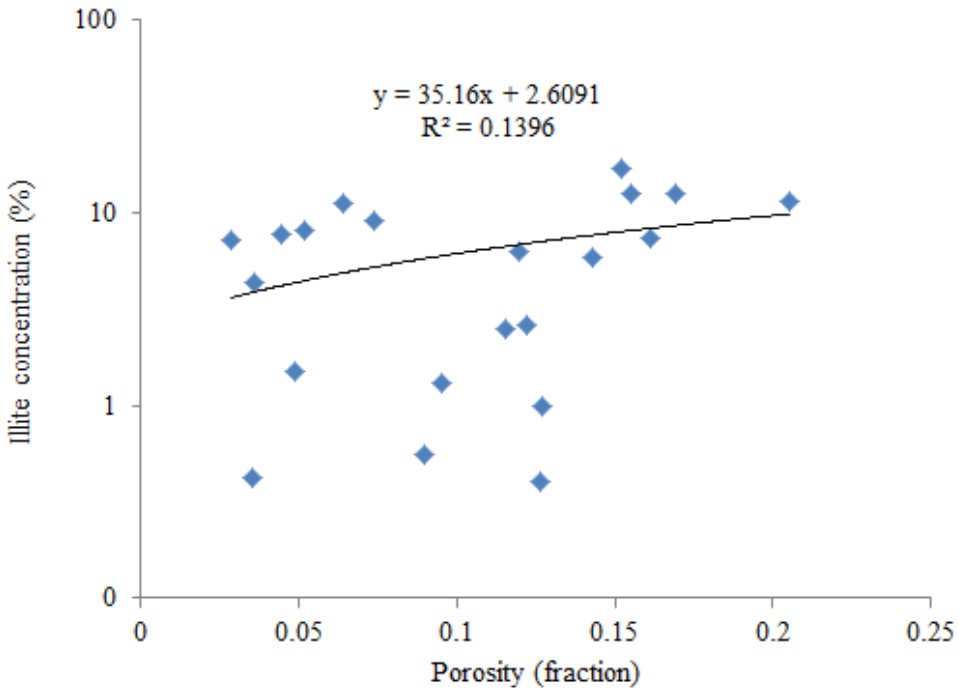

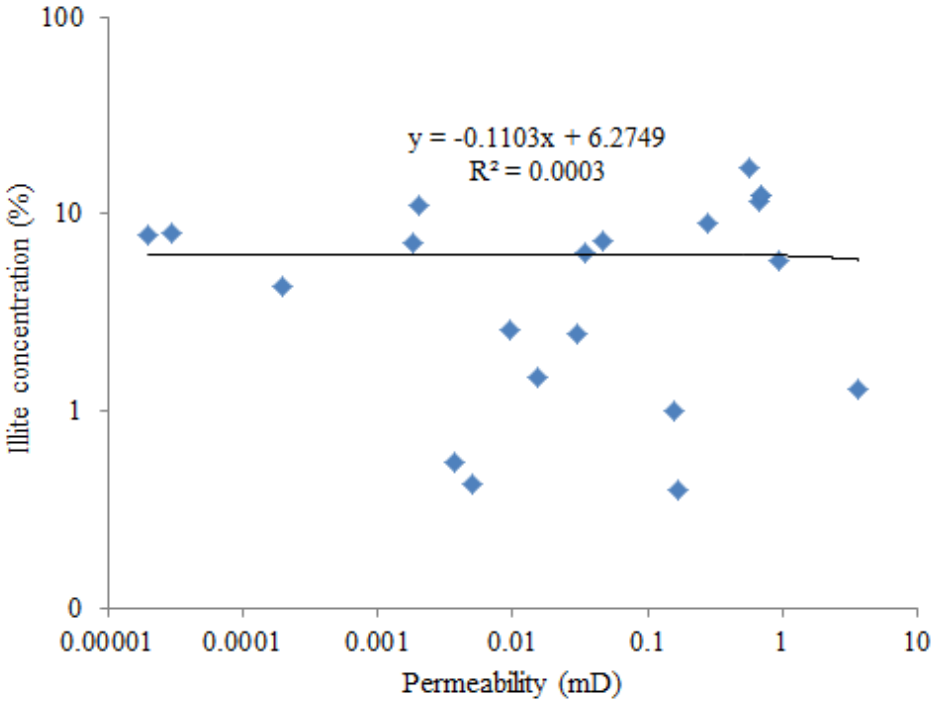

Figure 5.52 Illite as a function of porosity showing an increase in porosity with illite content (top) and permeability (bottom) showing poor trends with R^2 values of 0.14 and 0.0003 respectively.

A number of authors state that the porosity and permeability decrease as the kaolin content increases (Stalder, 1973; Morris and Shepperd, 1982; Tiab and Donaldson, 1994). This is because the kaolin forms dense 'booklets' and blocks pores, this is observed in this research as shown in Figure 5.6 and Figure 5.10 (Section 5.3.4). When observing the kaolin content with porosity and permeability there is a slight decrease in porosity and permeability with an increase in kaolin content but there is a lot of scatter and the trend is poor with a R^2 value of 0.17 and 0.14 respectively (Figure 5.53).

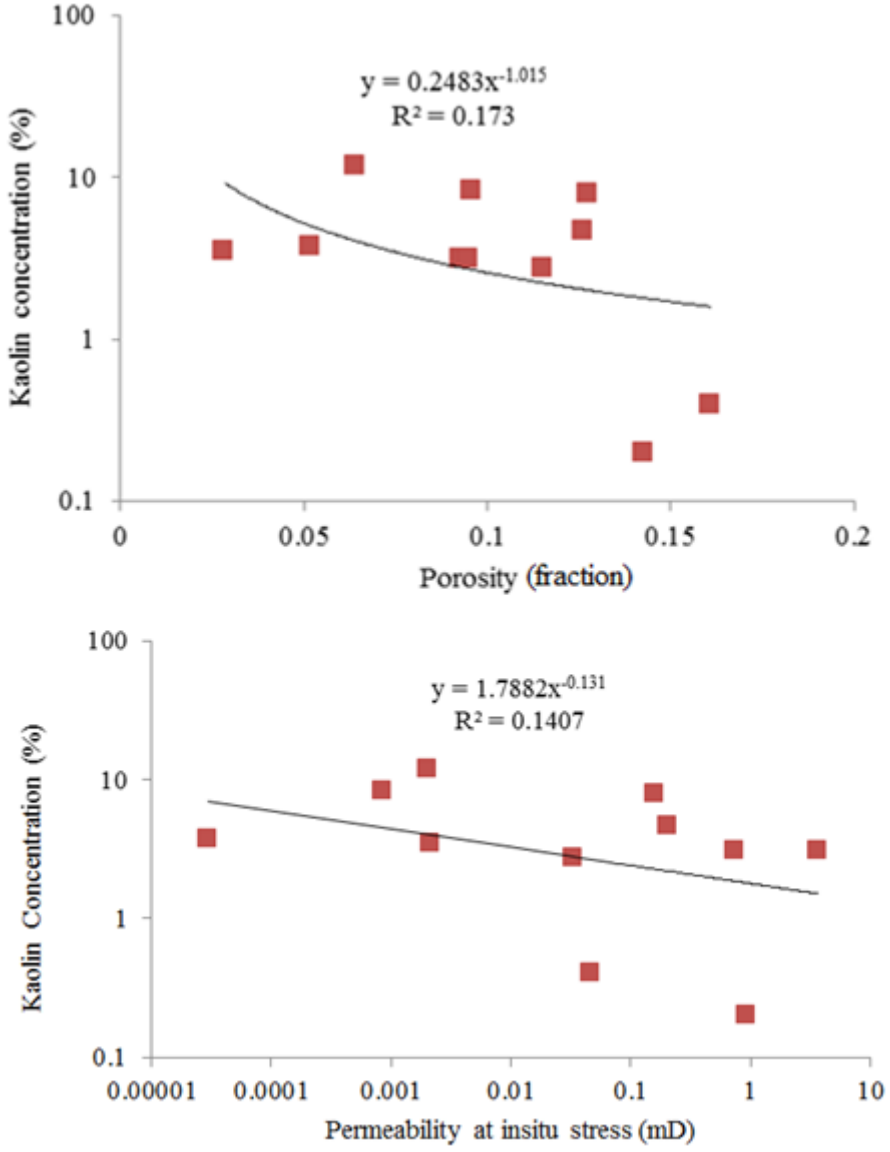

Figure 5.53 Kaolin as a function of porosity (top) and permeability (bottom) showing a decrease in permeability and porosity with an increase in kaolin content, however, the trend is poor with R^2 values of 0.17 and 0.14 respectively.

The lack of relationship between illite and kaolin content with porosity and permeability in Figure 5.52 and Figure 5.53 is possibly because it is difficult to determine the amount of clay using QXRD (Pevear and Mumpton, 1989). Hillier (2000) stated that the composition in the sample may not be the same as that in the whole rock. QXRD also struggles to distinguish detrital from authigenic phyllosilicates and QXRD provides no indication of the pore-scale distribution of clay minerals which is a key control on permeability. Nevertheless, the latter can be obtained using SEM. This may imply the methodology used needs to be adjusted. In

addition, it could be due to experimental errors when carrying out the QXRD experiment which supports the inaccuracies seen in Chapter 4.

An attempt was made to correlate other mineral amounts from QXRD with the porosity and permeability. Samples were scaled according to the quantity of quartz and dolomite (Figure 5.54). There is more quartz with higher permeabilities but there is some scatter, overall, no strong correlations were identified. Samples were then divided into a range of classes according to the minerals present (Figure 5.55). The different groups do occupy different regions in the porosity-permeability cross-plots for example, illite tends to have a low permeability for a given porosity, quartz samples have high permeabilities for a given porosity (supports Figure 5.54) and samples with dolomite and illite have low permeabilities for a given porosity. However, there is a lot of overlap and scatter making it difficult to estimate accurate permeability values. Therefore, this section implies that the type and amount of diagenetic deposit is not the main control on porosity-permeability trend. Nevertheless, the trends may improve if more samples were studied as currently some groups e.g. kaolin, only have one sample.

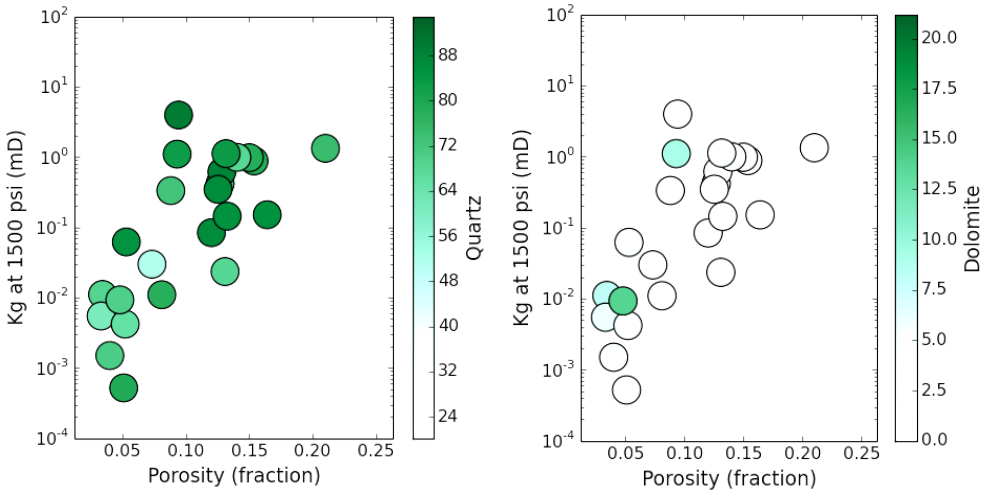

Figure 5.54 Permeability as a function of porosity with points scaled according to the quantity of quartz and dolomite from QXRD. There is no obvious trend observed.

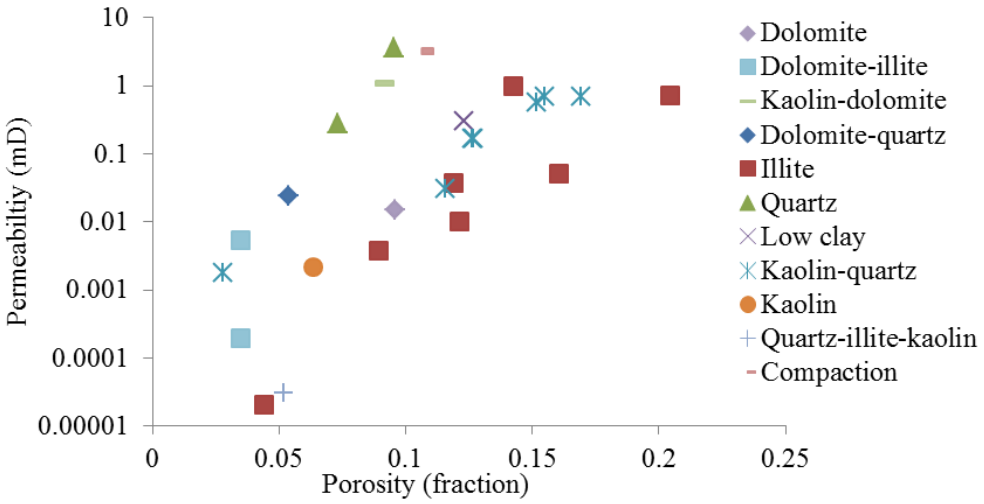

Figure 5.55 Permeability as a function of porosity scaled according to diagenesis from QXRD data whereby there is no obvious trend.

5.4.4.2 Depositional Controls

Theoretically, it is expected that a decrease in sorting should reduce permeability and porosity (Rogers and Head, 2006; Beard and Weyl, 1973; Cade et al., 1994; Njoku, 2011) (Figure 5.56) because the smaller grains can infill the space between larger grains thus blocking pores and pore throats. Similarly, an increase in grain size should cause the permeability to increase as larger grains create larger pores (Nelson, 1994; Njoku, 2011; Raza, 2015).

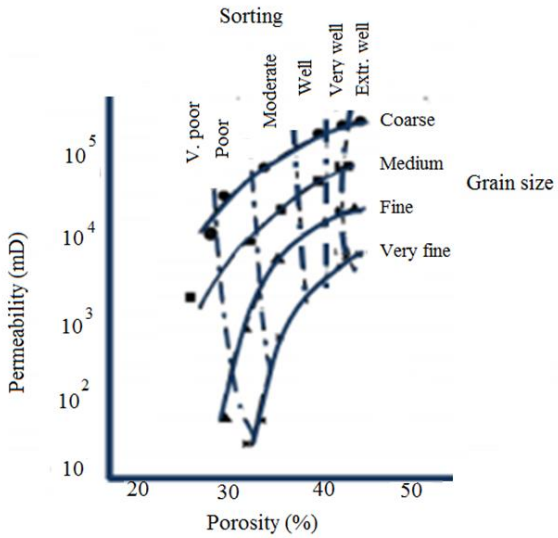

Figure 5.56 Permeability as a function of porosity with grain size and sorting. The permeability for a constant porosity increases with sorting and grain size (Njoku, 2011).

The data in this research contradicts published studies (Beard and Weyl, 1973; Cade et al., 1994; Neslon, 1994; Rogers and Head, 2006; Njoku, 2011; Weibel, 2012; Raza, 2015), which claim that porosity and permeability depend on grain sorting and grain size. In particular, there is no obvious permeability vs porosity relationship with grain sorting (Figure 5.57), grain size (Figure 5.58) and grain shape (Figure 5.59). The lack of relationship with grain sorting, shape and size is caused by extensive and diverse diagenetic alteration such as the formation of clay (Section 5.3.4). This phenomena is mentioned in several other studies (e.g. Hans, 1967; Rittenhouse, 1973; Hower, 1974; Keighin, 1979; Wilson, 1994). The results of this diagenetic alteration has considerably changed the original pore size of the sediment within the sample. In comparison, the studies that developed the relationships between porosity, permeability and sedimentary fabric were conducted on unconsolidated material that had not experienced diagenetic alteration.

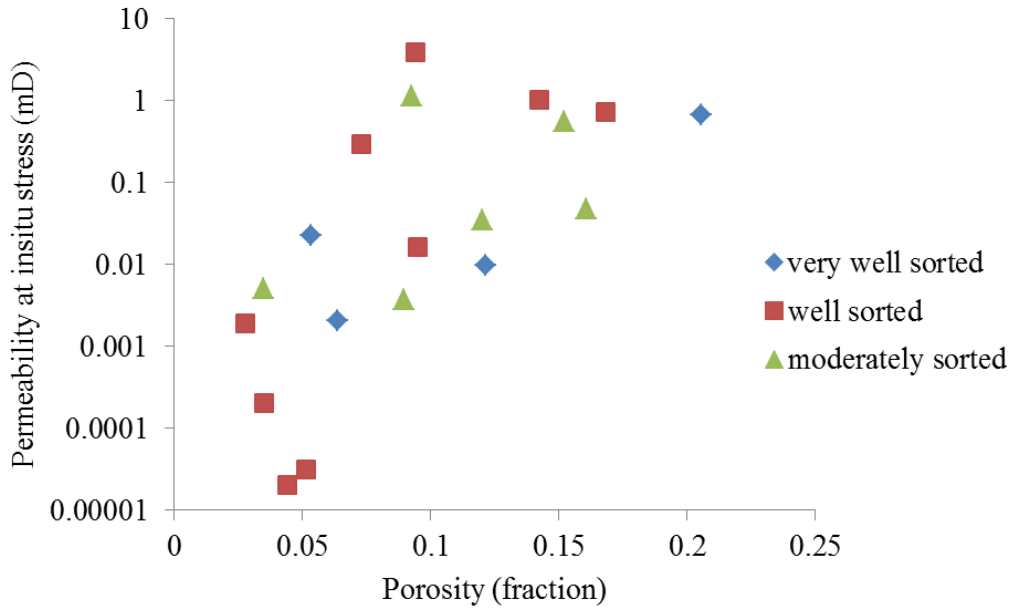

Figure 5.57 Permeability as a function of porosity with the sorting mapped onto the distribution showing no clear trend.

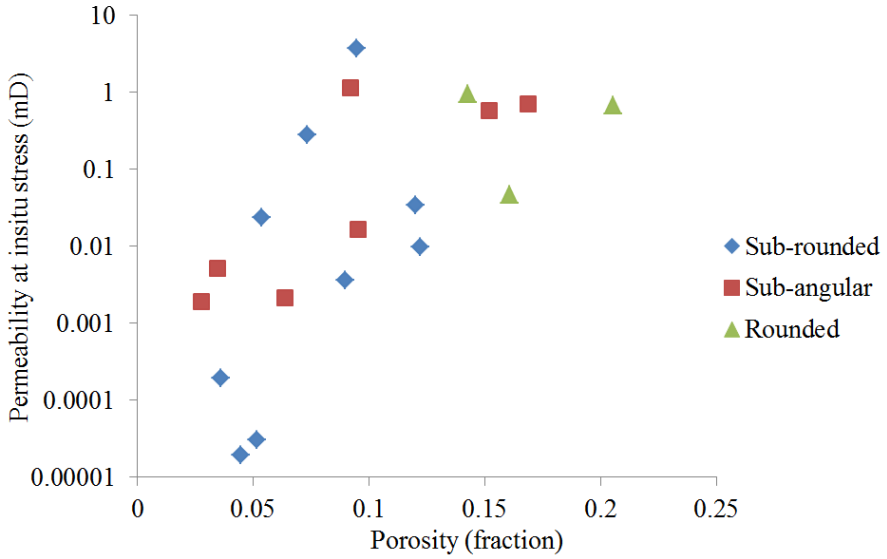

Figure 5.58 Permeability as a function of porosity with the grain shape mapped onto the distribution showing no clear trend.

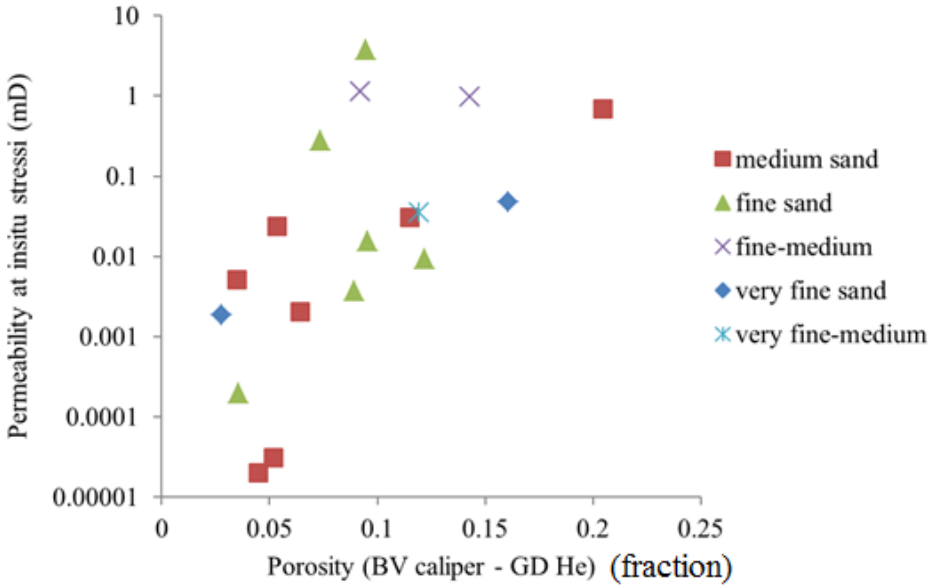

Figure 5.59 Permeability as a function of porosity with the grain size mapped onto the distribution showing no clear trend.

Some authors imply that as the texture does not play a major control on the porosity-permeability relationships neither does the depositional environment (Boles and Franks, 1979; McGowen, 1994; Merleti, 2014). The lack of trend was also observed within this research (Figure 5.60). Nevertheless, the environment in which the sediments were deposited did originally control the porosity and permeability (Ali et al., 2010). Depositional environment may sometimes control the composition of the framework grains (Rezaee and Lemon, 1996), which in turn may impact later

diagenetic alteration (Rezaee and Lemon, 1996; Ali et al., 2010). In other words, theoretical reasons exist on why depositional environment could influence diagenetic processes (Rezaee and Lemon, 1996).

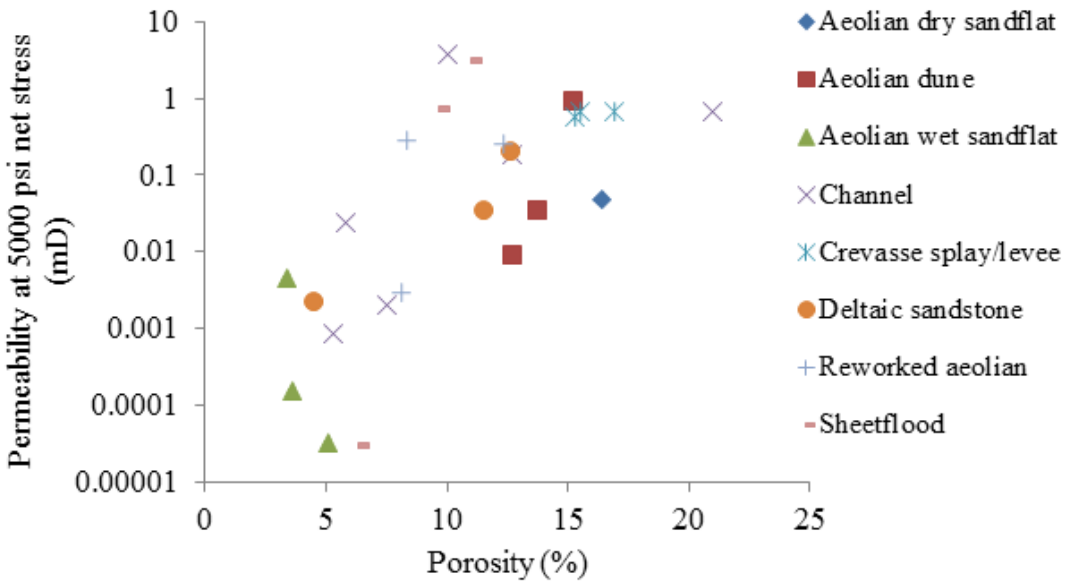

Figure 5.60 Permeability as a function of porosity with each depositional environment showing no clear trend.

5.4.4.3 Microstructural Controls

Samples with pore bridging or pore lining illite have the lowest permeability as they can provide partial to complete barriers to fluid flow (Neasham, 1977; Lokmane et al., 2009). In contrast, the samples with discrete clay like kaolin had higher permeabilities (Stalder, 1973; Wilson, 1982, 1994) and those with little or no clay have the highest permeabilities (Wilson, 1982). Nevertheless, Cade et al. (1994) stated that although permeability tends to be higher in samples with kaolin compared to illite, this does not mean the kaolin would not decrease the permeability.

To determine if the samples in this research conform to these correlations, the samples were divided according to whether they contain pore bridging / grain coating clays, pore filling clays or if they have low amounts of clay. Those samples with low amounts of clay generally have the highest permeabilities for a given porosity; those samples with pore bridging clay have the lowest permeabilities for a given porosity and finally those samples with discrete pore filling clay have permeabilities in-between (Figure 5.61). This supports the trends found in the literature.

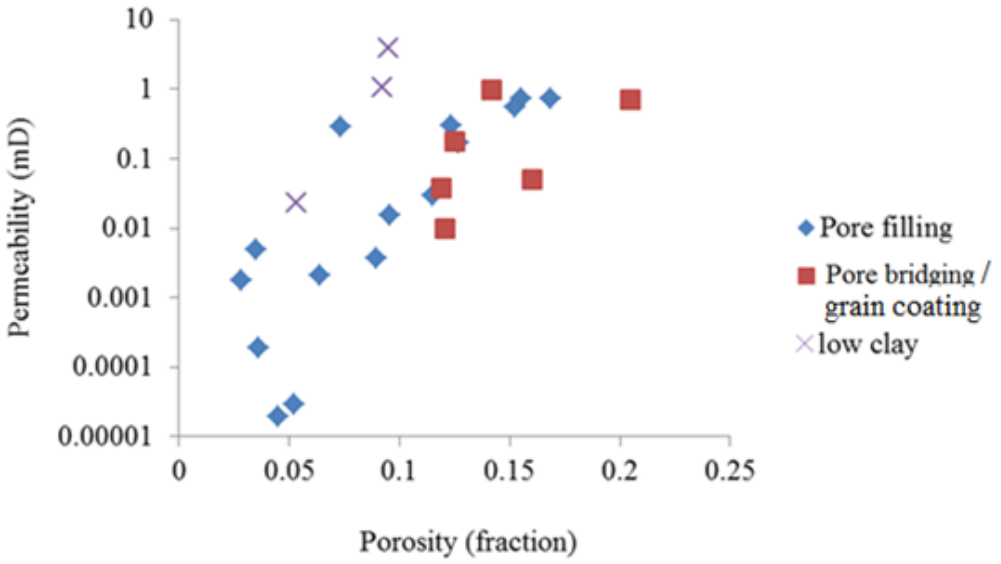

Figure 5.61 Permeability at 1500 psi as a function of the porosity with the three rock types – pore filling, pore bridging and low clay mapped on top. Those with low clay have the highest permeabilities and those with grain coating clay have the lowest permeabilities.

Lower permeability samples within the grain coating rock type have illite that starts to infill the pores as it builds from the grain walls. Those samples with higher permeabilities within the grain coating rock type have illite that just surrounds the grains leaving the pore virtually intact (Figure 5.62). Therefore, the position of clay within the pores plays a significant role on the final permeability.

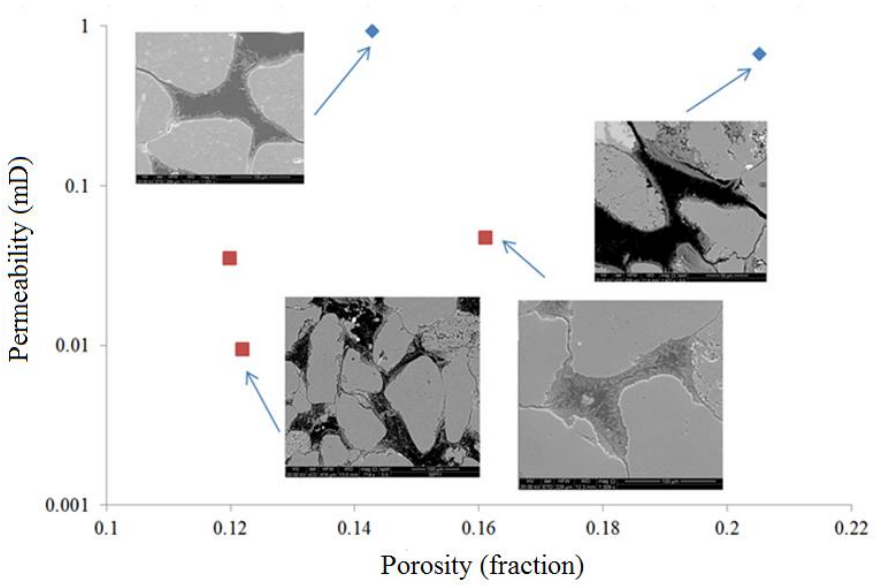

Figure 5.62 Permeability as a function of porosity for the pore bridging clay samples shown in red in Figure 5.61. Those samples with grain coating clay have higher permeabilities then those with bridging clay as the pore is almost intact in the former.

The helium porosimeter is used as a proxy for porosity values that would be obtained from wire-line log data. The overall aim is to use microstructural data from core or cuttings to establish porosity-permeability relationships and then using porosity from wireline log analysis to estimate permeability throughout the logged reservoir interval. The permeability was estimated for the 25 TGS by first rock typing each sample based on their microstructure; the rock types were chosen on whether they had pore filling, grain coating/ grain bridging clays or a low clay content (Figure 5.63). This rock typing method was used because good correlations were identified in Figure 5.61. The key relationships between permeability and porosity at *in-situ* stress for low clay, pore filling clay and grain coating clay is:

$$Kg = 0.00005e^{112.31\emptyset} \quad \text{Equation 5.1}$$

$$Kg = 0.00004e^{61.647\emptyset} \quad \text{Equation 5.2}$$

$$Kg = 0.0011e^{31.232\emptyset} \quad \text{Equation 5.3}$$

where Kg is permeability (mD) and $\emptyset$ is porosity (fraction). Using Equation 5.1 to Equation 5.3 and the helium porosity a permeability value was estimated and compared to the gas permeability from Section 5.3.2 (Table 5.9, Figure 5.64). This methodology of estimating the permeability was moderate as the R^2 value was 0.73 but there is some scatter at both the lower and upper permeability end. The reason for this scatter could be because the permeability vs porosity in Figure 5.61 is itself scattered. Nevertheless, this method of permeability estimation has the potential to estimate permeability using wireline log porosity and the microstructure from SEM. In addition, it is sufficient to imply that the clay type and position are the prominent cause of the porosity-permeability trends instead of considering all mineral types or diagenetic deposits as thought in Section 5.4.4.1.

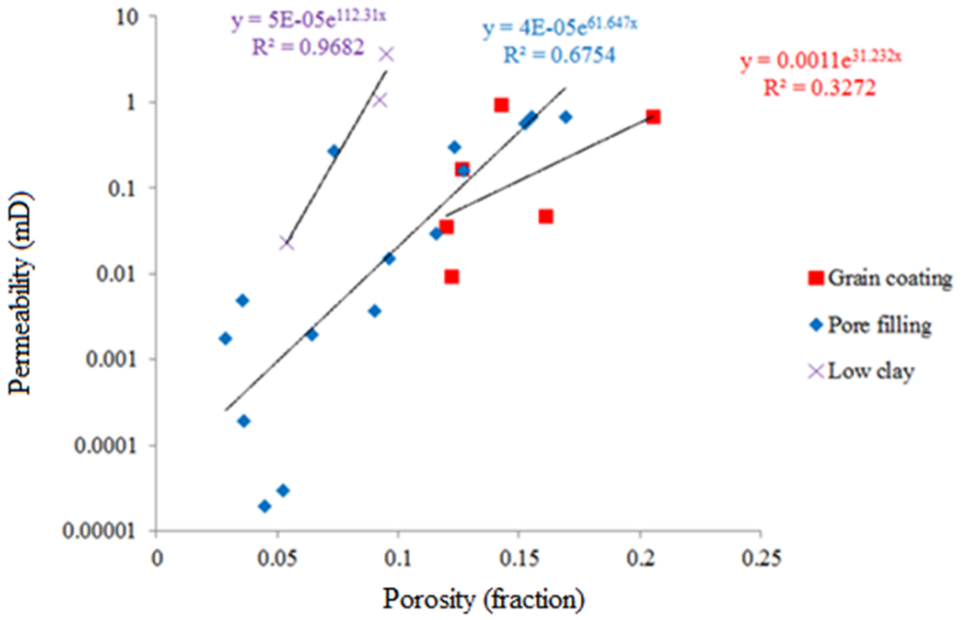

Figure 5.63 Permeability as a function of porosity along with the samples divided according to their microstructure as well as their overall trends. The trend lines were used to determine permeability using porosity where there is a potential to use wireline log porosity and microstructure from SEM without whole core plugs.

Table 5.9 Measured permeability and porosity, microstructure and estimated permeability using trend lines in Figure 5.63 for all 25 TGS.

Well	Sample	Kg at in situ stress (mD)	Porosity (fraction)	Microstructure	Estimated permeability (mD)
WIN5	16B	0.009	0.122	Grain coating	0.050
BP2	3	0.168	0.126		0.057
SHELL4	370	0.93	0.143		0.095
SHELL4	389	0.035	0.120		0.046
SHELL4	202	0.047	0.161		0.168
EBN3	40	0.67	0.205		0.668
BP3	5	0.69	0.155	Pore filling	0.573
BP2	2	0.030	0.115		0.049
BP3	6	0.56	0.15222		0.476
BP3	4	0.69	0.169		1.363
GDF1	6	0.0154	0.096		0.015
EBN4	10	0.002	0.064		0.002
WIN 9	5	0.00003	0.052		0.001
BP3	1	0.160	0.127		0.101
SHELL1	83	0.000193	0.036		0.000
SHELL2	1	0.2754	0.074		0.004
SHELL2	9	0.3	0.123		0.079
SHELL4	409	0.00002	0.045		0.001
SHELL1	111	0.0037	0.090		0.010
BP2	5	0.0018	0.028		0.000
SHELL1	216	0.00498	0.035		0.000
WIN4	26	0.023	0.054	Low clay	0.021
GDF1	1	1.09	0.093		1.643

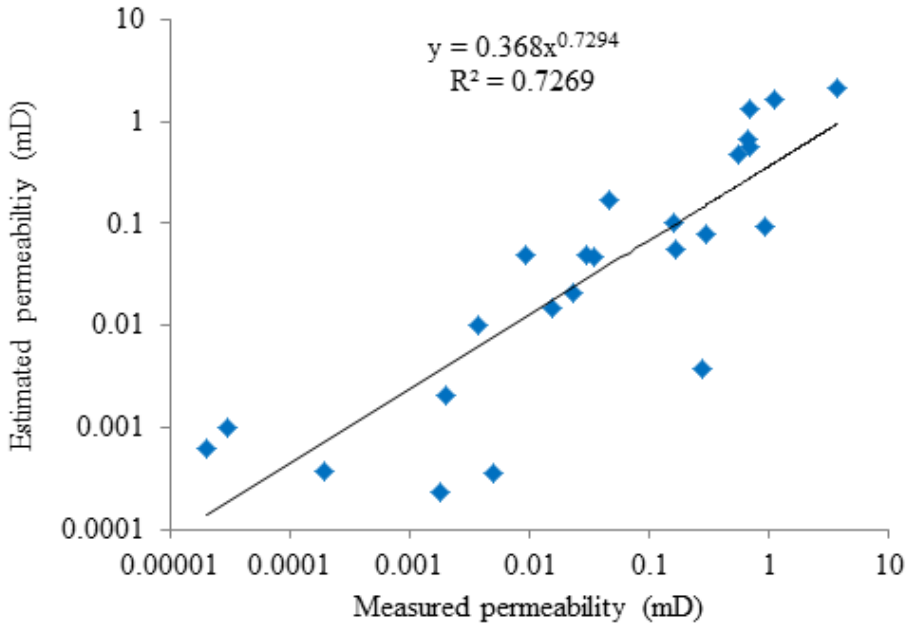

Figure 5.64 Estimated permeability from trend lines in Equation 5.1 to 5.3 as a function of measured permeability showing a moderate trend with a R^2 value of 0.73. There is some scatter potentially because there is scatter seen in the original plot in Figure 5.63.

A comparison was made between the flow rate of the reservoir and the clay type and position. The microstructure determined from studying the SEM images was compared to the measured flow rates for three wells (Table 5.10). It was observed that the wells that contained grain coating illite had low flow rates of 2.5 mmscf/day (Table 5.10). The flow rate is higher when pore filling kaolin is present (31 mmscf/day) compared to if illite was present (Table 5.10 – blue vs yellow) though the flow rate is much higher if the overall clay content is low (51 mmscf/day). This agrees with the data presented in Figure 5.61 and in the literature. However, it has been mentioned that in the case of high clay content, effects such as non-detrital grains, mechanical compaction, quartz overgrowth and cementation can be supressed (Wilson, 1994; Walderhaun, 1996). This is observed in well SHELL4 in Figure 5.37 (Section 5.3.4).

This comparison has shown that grain coating/bridging clays do reduce the permeabilities and therefore flow rate more than kaolin and the microstructure relates well to the flow rates of the reservoir. To predict reservoir quality and identify sweet spots ahead of the drilling, determination of specific distribution of different diagenetic processes is needed. However, the extent to which these processes impact reservoir quality can vary significantly both laterally and vertically

over short distances throughout the reservoir making the prediction of reservoir quality a difficult task. Understanding how reservoir quality is likely to change over short distances would significantly improve decisions made during the appraisal of TGS reservoirs. Nevertheless, this work has shown that the microstructure could potentially be used to assess whether drilling more wells in a prospect is likely to lead to economic production.

Table 5.10 Measured flow rate, microstructure and diagenesis present for SHELL1, BP and SHELL 2 wells. Those wells with grain coating illite have the lowest flow rates and those wells with little or no clay have the highest flow rates.

Well	Sample	Measured flow rate (mmscf/day)	Description
SHELL1	83	2.5	Grain coating illite + dolomite
	11	2.5	Grain coating illite
	216	2.5	Grain coating illite +dolomite
BP3	3_1	31	Pore filling kaolin +quartz
	3_4	31	Pore filling kaolin + quartz
	3_6	31	Pore filling kaolin + quartz
SHELL2	1b	51	Low clay + quartz
	9b	51	Low clay - grain coating

A comparison was made between the clay type/position and the cementation exponent (*m*) and BET surface area as the clay type and position linked well to the porosity and permeability (Figure 5.65). However, the clay type and position does not correlate with other petrophysical properties as seen by the scatter; therefore, this microstructure-based rock typing cannot be used to determine other properties. Future work is required to find a way to correlate the microstructure with other petrophysical properties of TGS.

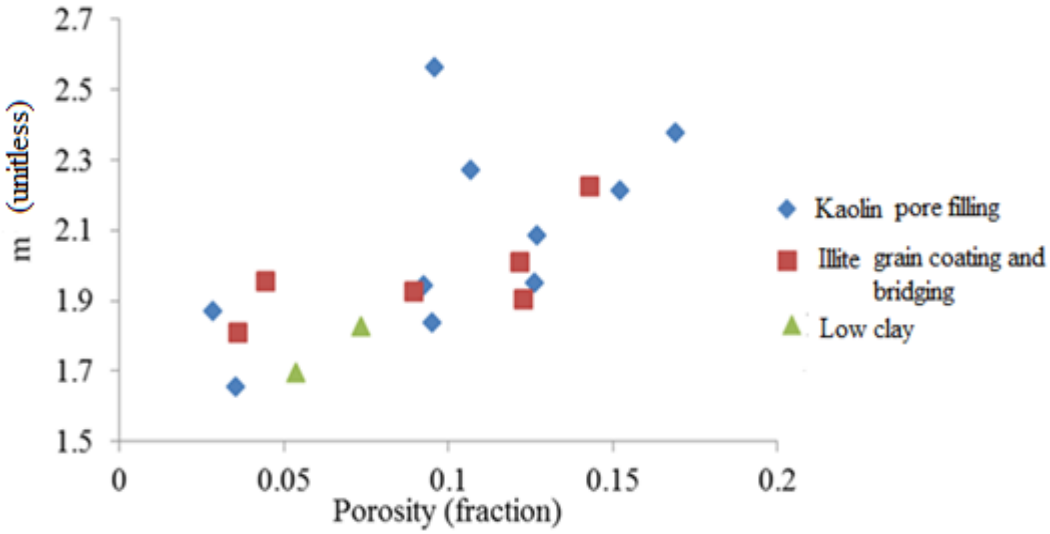

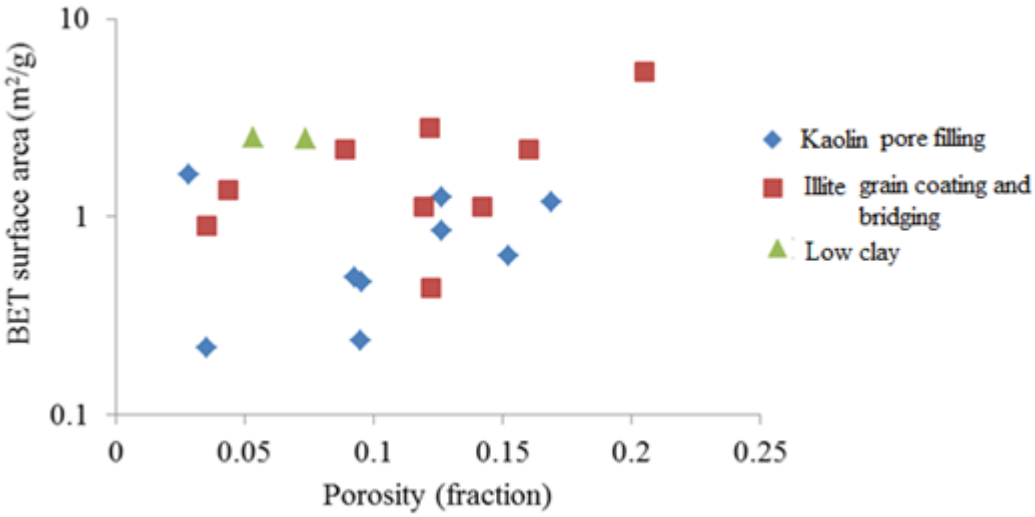

Figure 5.65 Cementation exponent and surface area as a function of porosity showing no clear trends implying the clay position cannot be used to determine other properties.

5.4.5 Survey of Inconsistencies from RCA measurements

It is important to understand the accuracy of the data when conducting a large-scale petrophysical examination on a range of rocks. Inaccuracies in the measurements can arise from the set-up, the methodology and the sample. They are briefly discussed below.

In all the experiments the effects of temperature are important. Some experimental set-ups were placed in temperature-controlled rooms e.g. the brine permeametery, however, other experiments were not and the temperature was noted and data corrected to the subsurface temperature. In addition, the temperature in the laboratory is also logged to enable any large changes in temperature to be observed. In the future place all the samples into temperature controlled rooms.

The cleaning of the cores in a Soxhlet extractor removed the original fluids from the core to prepare it for future tests. However, certain rock types or tests may require particular cleaning methods. This was not the case as seen in Chapter 4, however, other rock types may behave differently. In addition, when the samples were cleaned or dried in the oven the force of extraction could have led to fines movement. This in turn could lead to the blockage of pores and reduced absolute gas and brine permeability. This was not studied in this research but if fines movement is found to occur, precautions should be made to prevent it.

The CT scanner was easy to use and the images were produced in a short period of time. However, it lacked resolution so only very dense minerals or large fractures could be identified.

QXRD required a small amount of material and as the samples in the database have been affected by extensive diagenesis, the samples may show some heterogeneity. It was therefore unclear if the off-cuts represent the reservoir or not. In addition, QXRD cannot distinguish between clay types and it does not relate the clay type to the positon in the pore network.

The helium porosimeter is fast and samples can be reused as helium gas does not react with the rock. In addition, irregular samples can be studied. However, no realistic reservoir overburden pressure was applied in this method therefore the measured values may not be representative of the reservoir. This is addressed more in Chapter 7. In addition, if water is not removed from the pores during the drying process, the grain volume would be too low as the gas may not reach every part of the core plug.

In the permeability test if the sample is short, spacers can be used to increase the length. Consequently there could have been a poor contact with the spacer and the sample leading to a disproportional flow of gas. Also if the sample is not a perfect cylinder, air gaps could occur between the sample and the rubber sleeve leading to a poor contact between the sample and the end platens. In order to reduce these errors, any samples with sharp edges were sanded down and the sample was compressed tightly to ensure a good connection.

The brine permeability experiment is non-destructive. However, it also posed some issues about confining pressure equilibrium. Consequently, the data was recorded until the differential pressure and mean pressure were stable. In addition, the low confining pressure of 1500 psi is not representative of the reservoir. This is addressed more in Chapter 7.

5.5 Conclusion

The mercury immersion method should be used to determine the bulk volume as measuring the dimensions of the samples using a calliper tends to overestimate the bulk volume and hence porosity by around 1 porosity unit. It was found that ~11.4 hours is required for pore pressure equilibrium prior to the pressure transient flow for permeability measurements for the lower permeable samples whereas only 0.5 seconds is required for the higher permeability samples.

The brine permeability was always less than the gas permeability by around an order of magnitude. The current data implies that a lack of saturation and swelling of clays is not the cause. Flocculation does not seem possible due to the high salinities of brine used in this research, however, further analysis is needed to study this.

The 25 TGS samples from the 12 wells have experienced extensive diagenesis which was observed using SEM. The type and structural position of clays appears to have been the main control on porosity-permeability relationships. The microstructure also provided a moderate estimation of permeability and the microstructure linked well to the flow rate of the reservoir. Future work is however needed to predict other properties from microstructure. The microstructure obtained from the SEM can be used to predict flow rates and permeabilities from cuttings soon after a well has been drilled, this has the potential to reduce the amount of core plugs that need to be studied and reduce the time frames and cost of petrophysical analysis. Nevertheless, there are potential limitations relating to how representative the samples are of the reservoir rocks, future work would be to study more rock types particularly from the same well.

Chapter 6 – Petrophysical Properties of TGS: Special Core Analysis (SCAL)

6.1 Introduction

A special core analysis (SCAL) program was undertaken to complement the RCA data and to further understand the petrophysical properties of TGS. SCAL programs often involve measurements such as electrical properties, capillary pressure, nuclear magnetic resonance (NMR) and BET measurements. Capillary pressures and NMR measurements are controlled by the pore dimensions and BET surface area is related to grain size, therefore, they can be sued to predict permeability.

SCAL programs are usually performed on core plugs; however, as TGS are only marginally economic, there is a need to determine the petrophysical properties without core samples. For instance, cuttings can be analyzed using BET for surface area analysis. Samples that are too small to take core plugs could be used for mercury injection capillary pressure (MICP) and/or BET surface area. In addition, MICP, NMR, BET can be conducted on sidewall cores. A key aim of the chapter is to assess the feasibility of using this information to estimate other petrophysical properties such as permeability. Electrical properties as a function of porosity and surface area relationships with permeability are also presented and discussed to compliment the data.

A SCAL program was carried out on 25 TGS samples (Table 3.2 in Chapter 3) to determine the electrical properties, NMR pore size, BET surface area and MICP pore throat size of 25 TGS samples (Section 6.3.1 - 6.3.4). A detailed methodology of each method can be found in Chapter 3; however, a brief overview is presented in this chapter in Section 6.2. The results are then discussed in Section 6.4. The discussion seeks to bring together these results to understand them in more depth and compare how they agree or disagree with other published work. The work presented in this chapter is summarised in Section 6.5 together with recommendations for future work.

6.2 Methodology

Following the gas flow measurements presented in Chapter 5 the core plugs for the experiments were saturated with 20 and 30% NaCl brine. The resistance of each sample was measured at a frequency of 2 kHz using a Quadtech 7600 RLC meter. The resistivity, formation resistivity factor (*FRF)* and cementation exponent (*m*) were then calculated (Equation 2.13 and Equation 2.15). The T_2 distribution was determined using a Maran Ultra NMR spectrometer. The BVI/FFI ratio was calculated using the obtained T_2 distribution and a T_2 cut-off of 33 ms.

Around 1 - 2 cm^3 of the off-cuts was used for the MICP measurements using a Micrometritics Autopore V pycnometer. In addition, 5g off-cut material was pulverised for BET surface area analysis and the surface area was determined using a Quantachrome version 10.01 BET Instrument.

6.3 Results

This section first presents the electrical properties – *FRF* and *m* vs porosity and permeability (Section 6.3.1), NMR pore size distribution (Section 6.3.2), BET surface area (Section 6.3.3) and MICP pore throat size (Section 6.3.4). The BET, NMR and MICP, data was used to estimate permeability as presented in Section 6.4.2 and 6.4.3. Most of the data is presented within this section though the bulk and grain density MICP data is presented in Appendix B, the table of data for NMR, BET and MICP is provided in Appendix D and the table of data for BET and MICP permeability estimations in Appendix E.

6.3.1 Electrical Properties

The *FRF* ranged from 30 – 370 with an arithmetic average of 160. The *m* ranged from 1.6 - 2.6 with an arithmetic average of 2.1 (Table 6.1 and Figure 6.1). The FRF decreased with an increase in porosity and permeability (Figure 6.2) whereas the *m* increased with an increase in porosity and permeability (Figure 6.3).

Table 6.1 Formation resistivity factor and cementation exponent for each sample ordered by increasing porosity. The FRF ranges from 30 to 370 and the m ranges from 1.6 to 2.6.

Sample	*FRF* (unitless)	*m* (unitless)	Porosity (fraction)
BP2_5	300	1.6	0.03
SHELL1_83	310	1.8	0.04
SHELL1_216	280	1.8	0.04
SHELL4_409	310	1.9	0.05
WIN9_5	340	2.0	0.05
WIN4_26	220	1.8	0.05
EBN4_10	100	1.7	0.06
SHELL2_1B	120	1.8	0.07
SHELL1_111B	170	2.1	0.09
GDF1_1	110	2.0	0.09
GDF1_6	370	2.5	0.1
GDF1_7	85	1.9	0.1
GDF2_4	200	2.4	0.11
SHELL4_389	100	2.2	0.12
BP2_2	110	2.2	0.12
WIN5_16B	74	2.0	0.12
BP3_1	90	2.2	0.13
BP2_3	150	2.4	0.13
SHELL4_370	60	2.1	0.14
BP3_6	58	2.2	0.15
BP3_5	59	2.2	0.16
SHELL4_202	120	2.6	0.16
BP3_4	62	2.3	0.17
EBN3_40	30	2.2	0.2

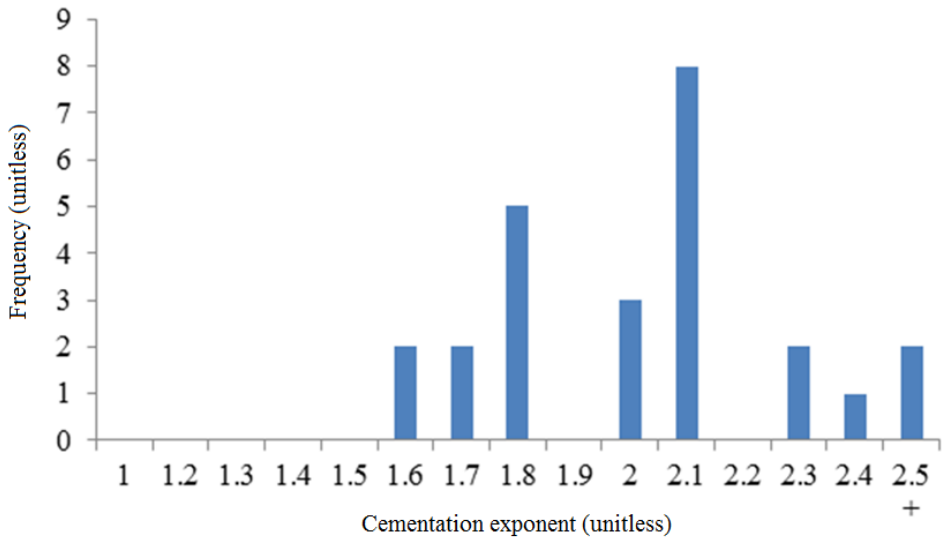

Figure 6.1 Frequency of each cementation exponent occurring as a function of the cementation exponent value where the m exponent ranged from 1.6 to +2.5.

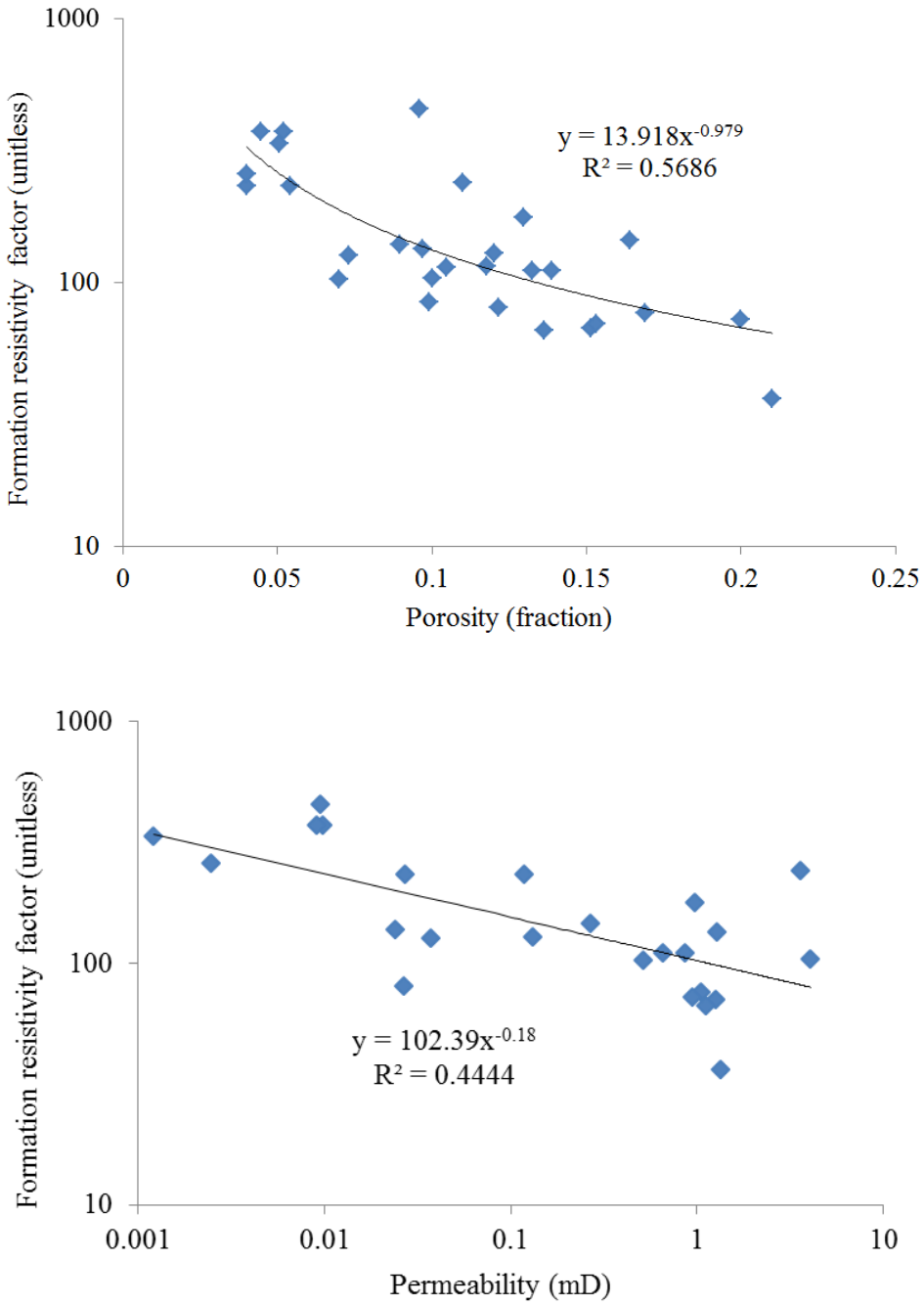

Figure 6.2 Formation resistivity factor as a function of porosity (top) and permeability (bottom). There is a decrease in FRF with an increase in porosity and permeability though the trends are very scattered leading to low R^2 values.

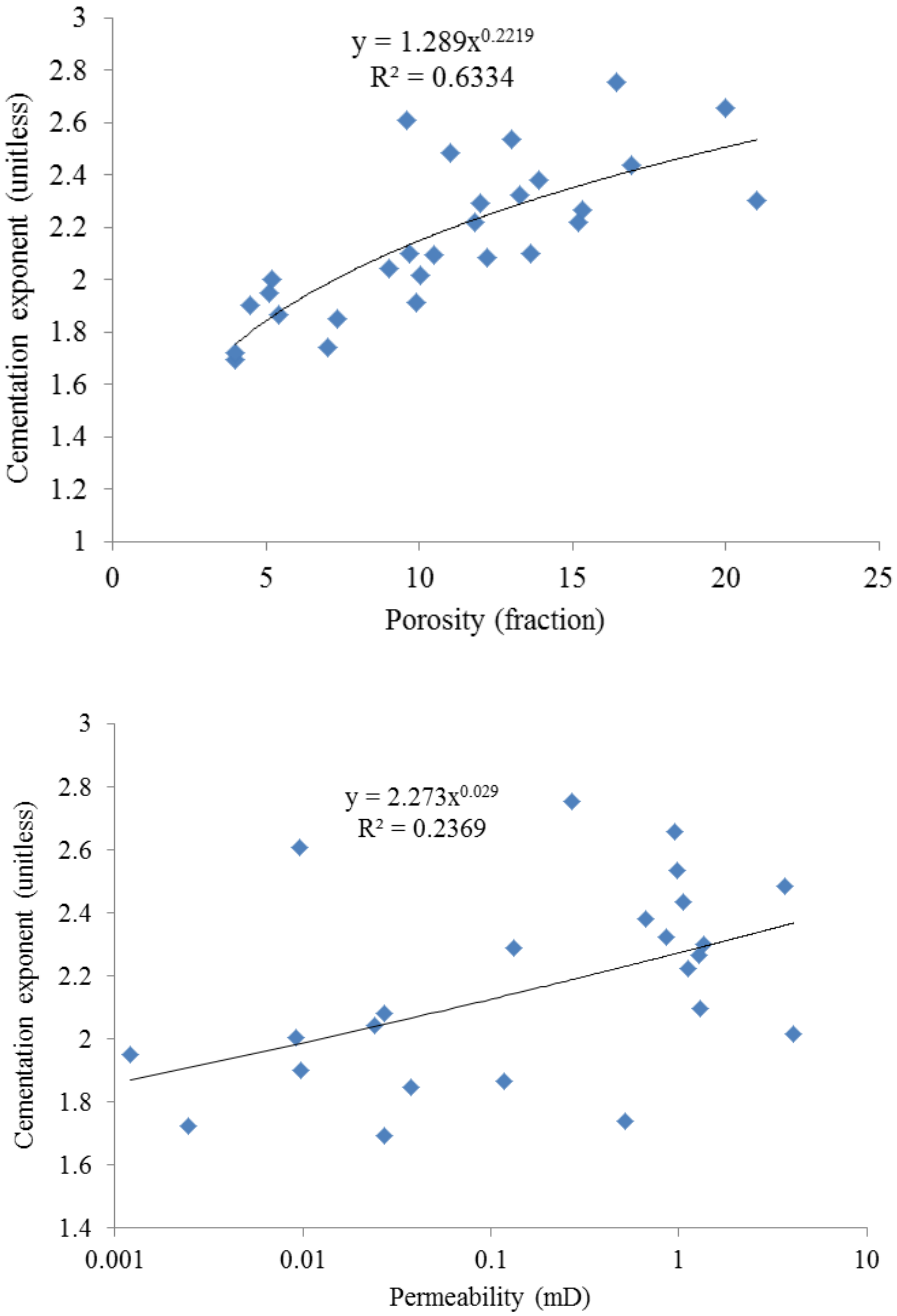

Figure 6.3 Cementation exponent as a function of porosity (top) and permeability (bottom). There is an increase in m with porosity and permeability though the trends with permeability is very scattered leading to the low R^2 value..

6.3.2 Nuclear Magnetic Resonance (NMR)

Most of the core plugs have a unimodal pore size distribution. However, SHELL4_370, SHELL4_409, BP2_3, BP3_1, and SHELL 2_1B are all bimodal whereas SHELL2_9b, BP2_3 and BP3_1 are trimodal (Figure 6.4). Out of the 25 TGS studied within this research, 15 of the samples have more bound fluid (arithmetic average 0.7) than free fluid (arithmetic average 0.3) when a T_2 cut-off of 33 ms is used (Table 6.2).

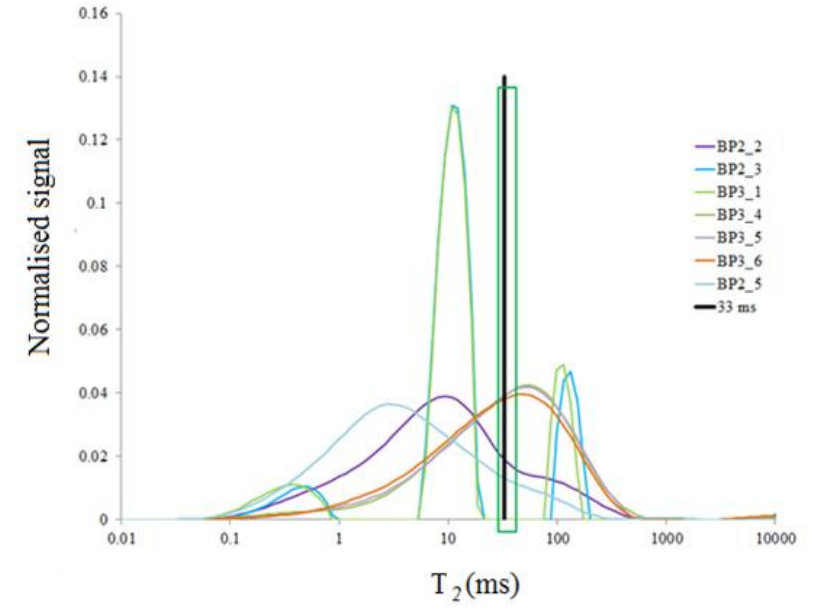

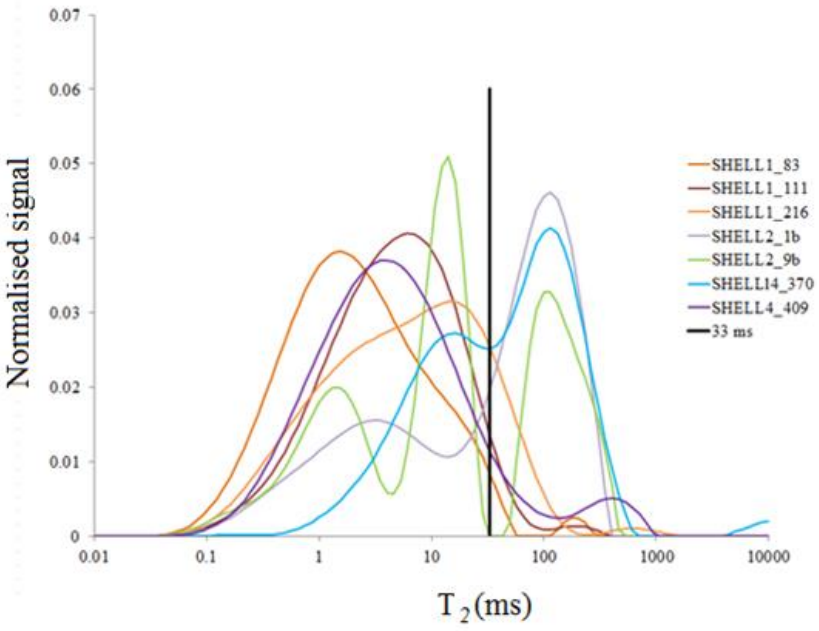

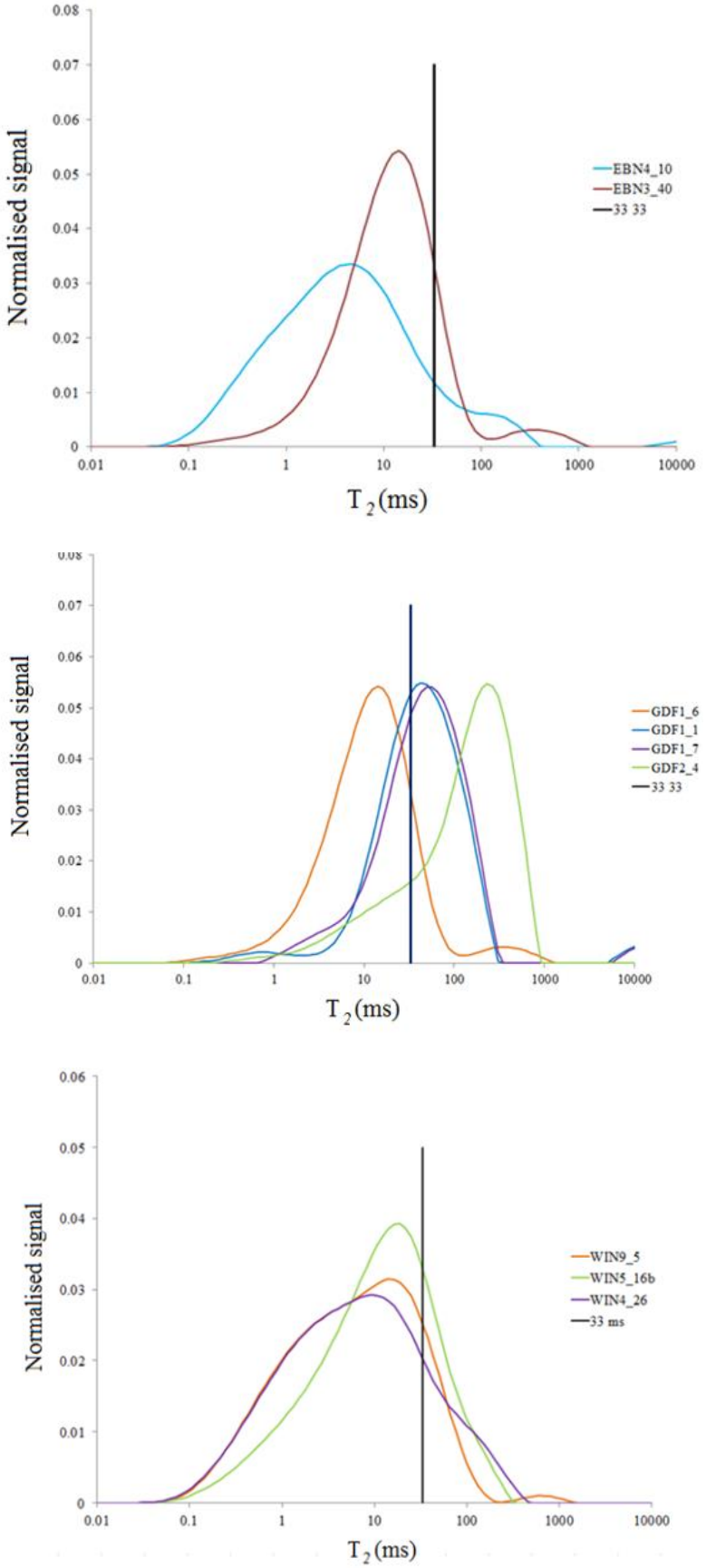

Figure 6.4 T_2 distribution of pore sizes for all samples split by well along with the 33 ms T_2 cut-off in black. Unimodal, bimodal and trimodel pore systems are present.

Table 6.2 Table of mean NMR T_2 and the bound to free fluid ratio using 33 ms T_2 cut-off for all 25 core samples. 60% of the samples had more bound fluid than free fluid.

Well	Sample	NMR T_2 (unitless)	BVI (unitless)	FFI (unitless)	BVI/FFI (unitless)
WIN4	26	6	1	0	5
WIN5	16B	10	0.8	0.2	4
SHELL1	83	2	1	0.03	32
SHELL1	111	4	1	0.05	19
SHELL1	216	7	0.9	0.2	6
SHELL2	1	23	0.4	0.6	1
SHELL2	9	14	0.7	0.4	2
BP2	2	8	0.8	0.2	4
BP2	3	12	0.8	0.2	4
BP3	1	11	0.8	0.2	4
BP2	5	4	0.9	0.1	9
BP3	4	28	0.5	0.5	1
BP3	5	28	0.5	0.5	1
BP3	6	25	0.5	0.5	1
EBN3	40	3	0.8	0.2	5
EBN4	10	4	0.9	0.1	9
SHELL4	202				
SHELL4	370	39	0.5	0.6	1
SHELL4	389				
SHELL4	409	5	1	0.06	16
WIN 9	5	6	0.9	0.1	7
GDF1	1	39	0.4	0.6	1
GDF1	6	11	0.9	0.1	7
GDF1	7	41	0.4	0.6	1
GDF2	4	100	0.2	0.8	0

Note: those samples in grey were not studied before they were placed inside the core holder studied in Chapter 7.

6.3.3 BET Surface Area

The BET surface area results are presented in Table 6.3. The values range from 0.2 m^2/g to 5.3 m^2/g, with an arithmetic average of 1.4 m^2/g. EBN3_40 exhibits the highest surface area of 5.3 m^2/g whereas GDF1_7 and SHELL1_216 exhibit the smallest surface area of 0.2 m^2/g.

Table 6.3 BET surface area results for all 25 samples where the surface area ranged from 0.2 to 2.8 m^2/g. Those samples in red could not be performed due to a lack of material.

Sample	BET (m^2/g)		Sample	BET (m^2/g)
WIN4_26	0.9		SHELL4_409	1.3
SHELL1_83	0.9		BP3_4	1.2
BP3_1	0.9		BP2_3	1.2
BP3_6	0.6		BP3_5	1.2
WIN5_16B	2.7		WIN 9_5	
SHELL1_111	2.2		GDF1_1	0.5
BP2_2	1.8		GDF1_6	0.5
BP2_5	1.6		GDF1_7	0.2
EBN3_40	5.3		SHELL1_216	0.2
EBN4_10	2.8		SHELL2_1	0.5
SHELL4_202	2.2		SHELL2_9	0.4
SHELL4_370	1.1		GDF2_4	
SHELL4_389	1.1			

6.3.4 Mercury Injection Capillary Pressure (MICP)

The data provided by mercury porosimeter can be used to generate two distributions. The first, incremental intrusion vs pore throat radius shows the total distribution of pore throat radius in which the mercury injection apparatus has the capacity to measure i.e. between the intrusion pressure and the maximum pressure at which the instrument is capable (55,000 psi in this case) (Figure 6.5). The second, pore radius distribution vs pore throat radius, states the true pore throat radius distribution as it shows the number of pore throat radii that are at a particular size (Figure 6.6). Both distributions are important as usage of only the first distribution would imply the sample has a large range of pore throat radii sizes, however, it would not indicate the number of radii for each of those sizes. The second distribution would show that some of the pore radii form a fraction of the total pore radius whereas others may be more dominant.

For example, it appears the samples have a pore throat radius between 0.002 and 45 μm (Figure 6.5). However, Figure 6.6 shows that the sample have a range from 0.002 to 5 μm. This shows that those larger radii above 5 μm form a very small proportion of the actual radii as shown by the near horizontal lines above 5 μm on Figure 6.6.

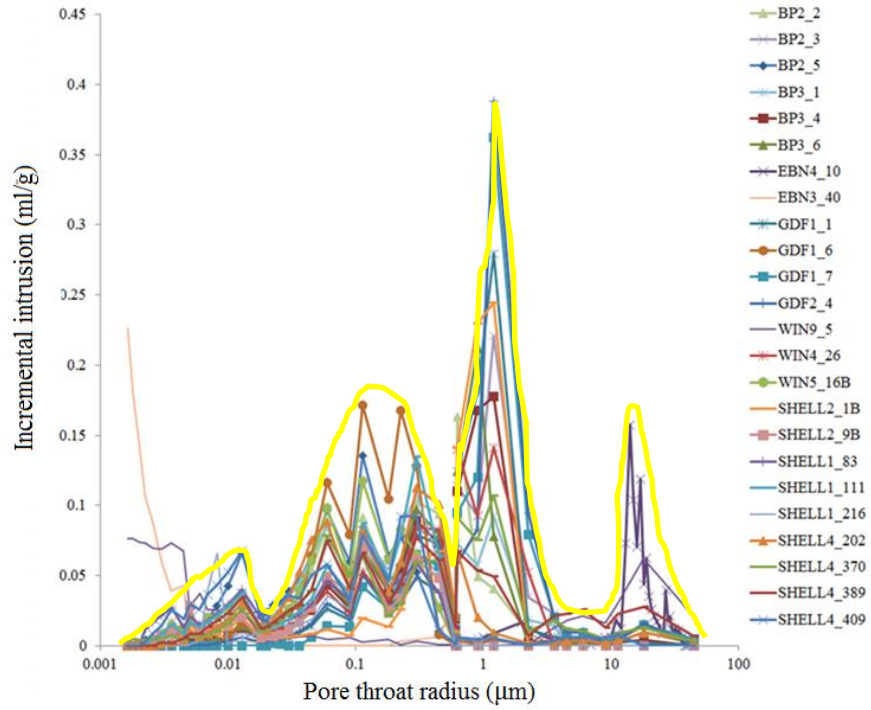

Figure 6.5 Incremental intrusion as a function of the pore throat radius. Pore throat size - 0.002 to 45 µm with average distribution shown in yellow. The distribution for divided according to well is presented in Appendix E.

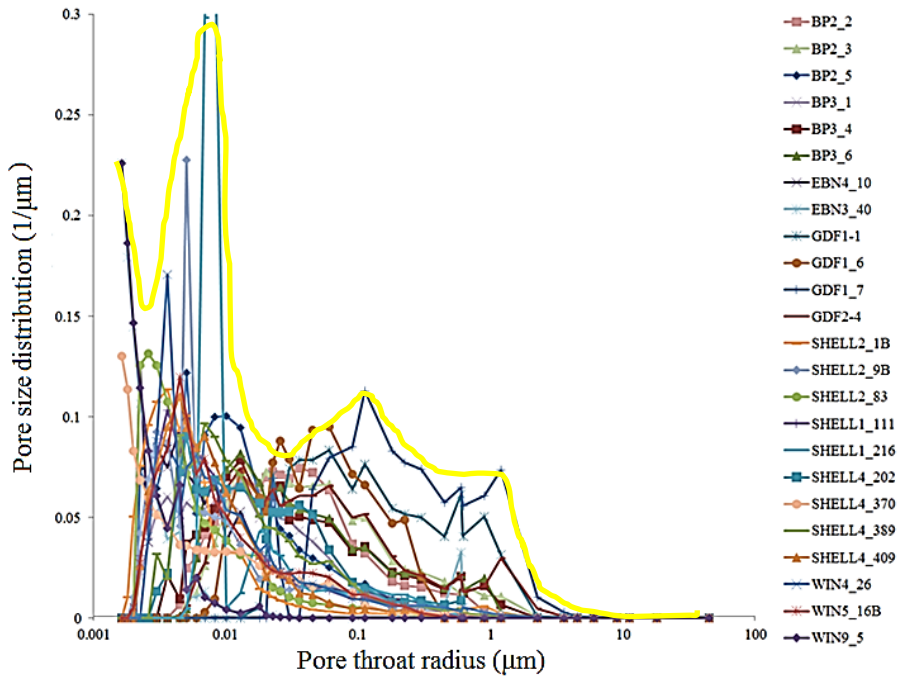

Figure 6.6 Pore throat radius distribution as a function of the pore throat radius. Pore throat size - 0.002 to 5 µm with average distribution shown in yellow. The distribution for divided according to well is presented in Appendix E.

6.4 Discussion

This section discusses the *FRF* and *m* vs porosity and permeability (Section 6.4.1) as well as the control of surface area on porosity and permeability (Section 6.4.2). This is followed by the estimations of permeability from NMR and MICP (Section 6.4.3). Lastly, inaccuracies in studying these SCAL properties in the laboratory are investigated (Section 6.4.4).

6.4.1 Electrical Properties as a function of Porosity and Permeability

The *FRF* increases with decreasing porosity and permeability (Seth, 1979; Biella, 1983; Rosales, 1982; Herrick, 1993; Sawyer, 2001; Glover, 2014; Byrnes and Cluff, 2009) (Figure 6.7). Archie describes that the *FRF* depends on the porosity and the efficiency or inefficiency of the pores to conduct a current through a rock i.e. FRF depends on the connectivity and tortuosity (Archie, 1942; Waxman, 1968; Sethi, 1979; Boral, 1987; Glover, 2009, Ling, 2012) (Equation 2.14). Fluid will not be able to flow easily through the pores if the pores are not well connected and the flow paths have a high tortuosity. Therefore, electrical current will not be able to pass through the pores and pore throats easily, that in turn will increase the *FRF* of the rock. These trends were also confirmed in this research as seen in Figure 6.2 and Figure 6.7.

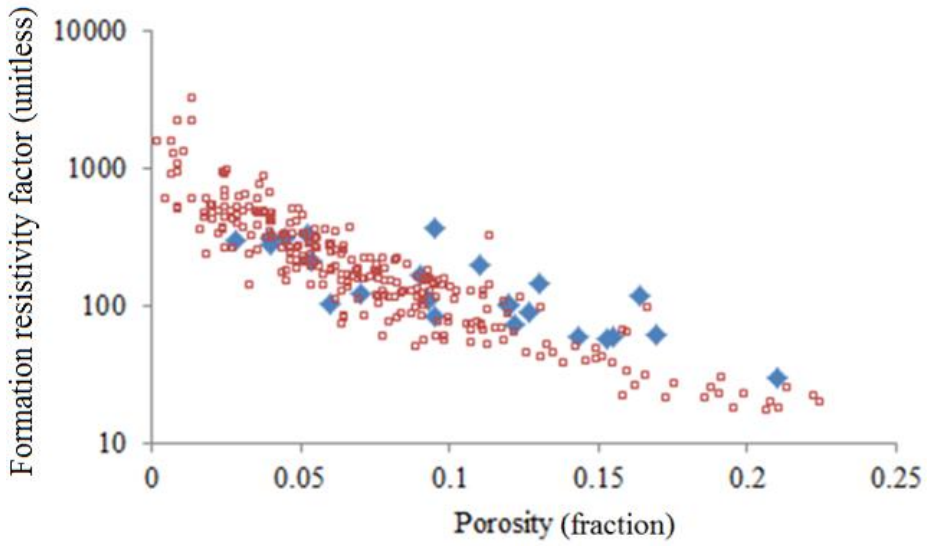

Figure 6.7 Formation resistivity factor as a function of porosity whereby the FRF increases with decreasing porosity. There is a good comparison between the laboratory data (blue) with a arithmetic average m value of ~2.1 and the Discovery Group Mesaverde dataset (red) with a arithmetic average m value of 1.9.

The cementation exponent increases with an increase in porosity and permeability (Figure 6.3). This contradicts a number of publications (Neustaedte, 1968; Boral, 1987; Guuyod, 1944; Towel, 1962; and Glover, 2014). Guyod (1944) and Towel (1962) both stated that *m* is related to the tortuosity and connectivity of the pores and Glover (2014) stated that *m* increases as the connectedness decreases, therefore, it is expected that *m* should increase with a decrease in porosity and permeability. Nevertheless, the same relationship, increase in *m* with an increase in porosity, was observed in the Discovery Group Mesaverde dataset (Figure 6.8).

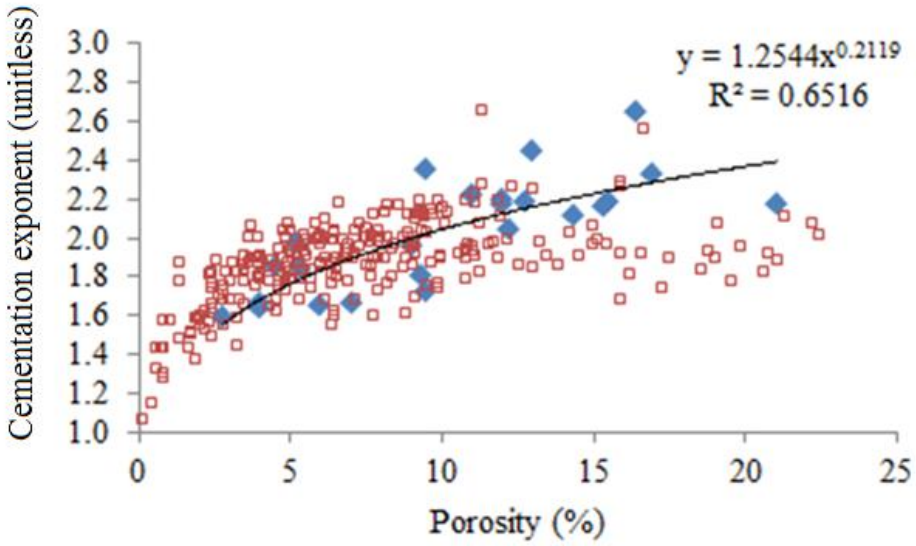

Figure 6.8 Cementation exponent as a function of porosity (blue) showing the m value increases with porosity. There is a good comparison between the laboratory data (blue) with a arithmetic average m value of ~2 and the Discovery Group Mesaverde dataset (red).

Wang and Lucia (1993) stated that *m* could be lower than 1.8 if fractures or vug pore types are present. This supports the idea that the presence of microfractures in the TGS, as identified in Section 5.3.4, could increase the connectivity therefore reduce the *m* value even in low porosity and permeability samples. Watfa and Nurmi (1987) also found that the presence of fractures provides a possible explanation for low values of *m*. Similarly, Cluff and Byrnes (2008) suggested that the lower *m* values are due to slot porosity, which lowers the tortuosity.

Apaydin et al. (2011) wrote that microfractures lack the connectivity to contribute to the fluid flow in high permeability matrix. This could contribute to the higher *m* values at higher permeabilities. SEM analysis suggests that the microfractures range from 1 to 5 μm in the TGS within this research (Chapter 5, Section 5.3.4), therefore, they form a small fraction of the total porosity. Consequently, though the

microfractures will provide a connectivity through the rock, they will not contribute as much to the permeability for higher permeable samples compared to lower permeable samples.

Higher values of *m* with an increase in porosity could be due to the presence of isolated secondary pores, the presence of poikilitic cements/clasts and/or laminations. A data set obtained from samples from a North American reservoir – Mesaverde, shows the presence of higher *m* values at higher porosity (Figure 6.8). The reservoir contains significant evidence for the presence of isolated secondary pores (Figure 6.9). These pores increase the bulk porosity, however, as the electrical properties are governed by the matrix porosity, despite the increase in bulk porosity, the connectivity is low, therefore, the current flow is restricted and the *m* value increases. Secondary pores are also located within dissolved out feldspar for example Figure 5.15 in Section 5.3.4.

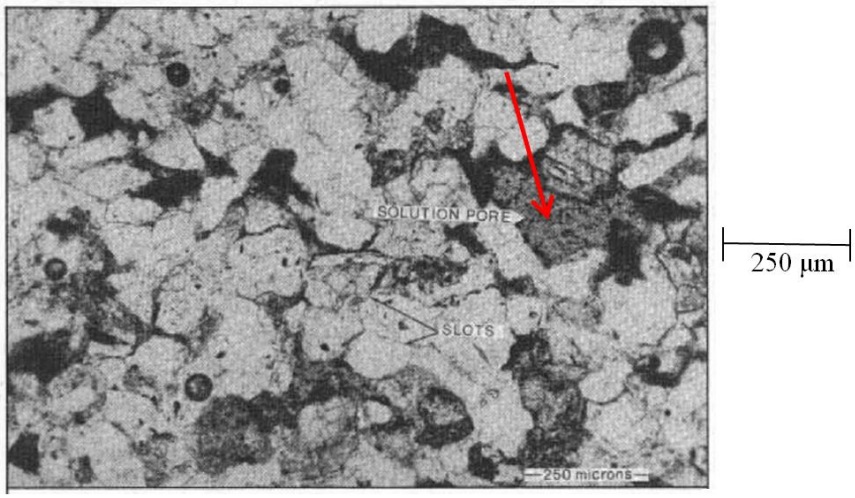

Figure 6.9 BSEM image of the TGS samples from North America showing the presence of large secondary pores (red arrow) where these pores increase porosity but do not contribute to the connectivity so the m value increases (Soeder and Randolph, 1987).

Herrick and Kennedy (1996) developed a triple porosity model for carbonates consisting of matrix porosity (ϕ_m), fractures (ϕ_f) and isolated secondary pores (ϕ_s). The isolated pores are formed for example from dissolved feldspar. This model was applied to TGS were the total porosity is equivalent to:

$$\emptyset_T = \emptyset_m + \emptyset_f + \emptyset_s \qquad \text{Equation 6.1}$$

The total electrical resistivity, R_T of the water saturated rock is then defined as:

$$R_T = \frac{R_m + R_f + R_s}{R_m * R_f * R_s} \qquad \text{Equation 6.2}$$

where R_m, R_f and R_s are the resistivities of the matrix, fracture and secondary pores respectively. For simplicity, it is assumed that the secondary pores are totally isolated and do not contribute to the flow of electrical current. So using Archies Law:

$$\frac{R_T}{R_w} = \frac{1}{\emptyset_T{}^{m_T}} = \frac{\frac{1}{\emptyset_m{}^{m_m}} + \frac{1}{\emptyset_f{}^{m_f}}}{\frac{1}{\emptyset_m{}^{m_m}} * \frac{1}{\emptyset_f{}^{m_f}}} \qquad \text{Equation 6.3}$$

where, m_T, m_m and m_f are the cementation exponents of the rock, matrix and fractures respectively. Assuming that $m_m = 2$ and $m_f = 1$:

$$\emptyset_T{}^{m_T} = (\emptyset_T - \emptyset_f - \emptyset_s)^2 + \emptyset_f \qquad \text{Equation 6.4}$$

Incorporating different proportions of fracture and secondary porosity into this equation helps identify the factors which affect *m*. Fractures were found to increase the connectivity and therefore lower the *m* value (Figure 6.10). The isolated pores were found to increase the bulk porosity, however, as the current flow is controlled by the connected pores or fractures, even with an increase in porosity, the connectivity is low and the *m* value is high (Figure 6.10).

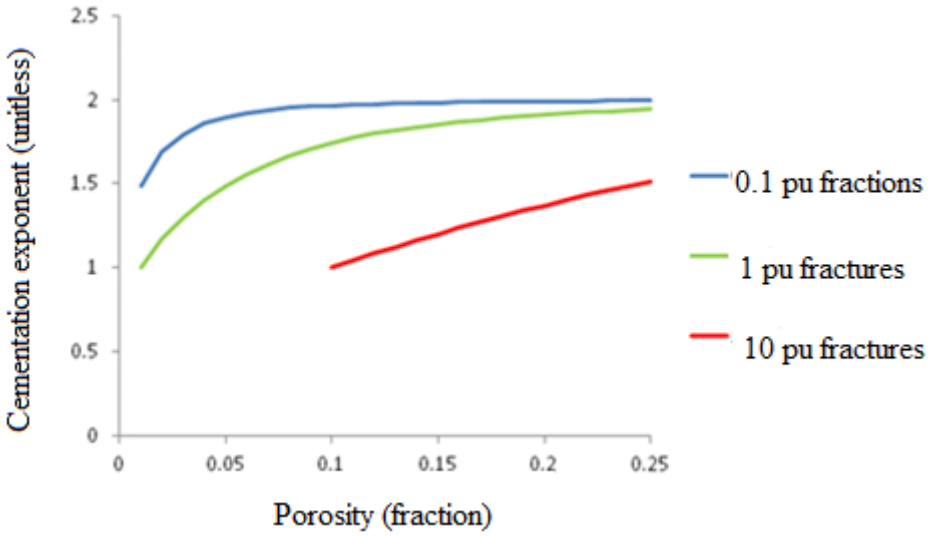

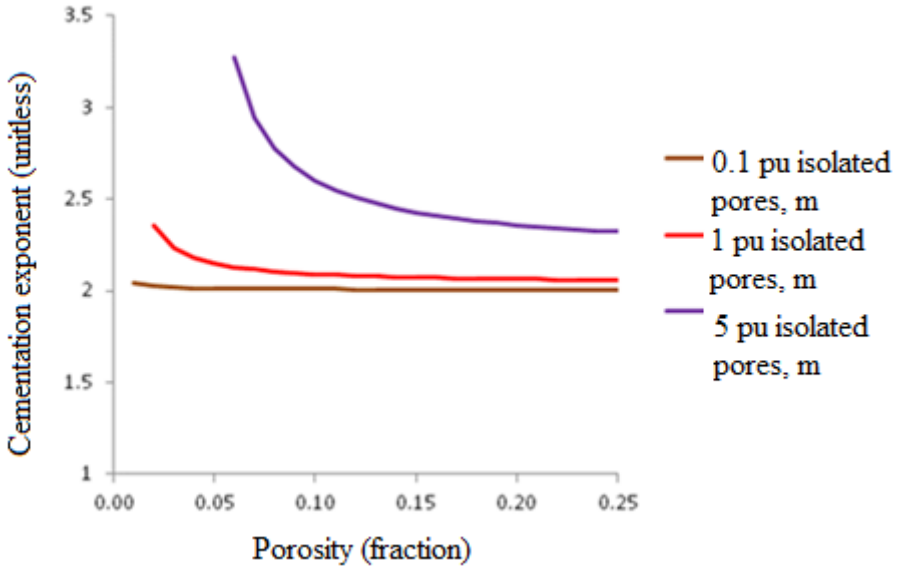

Figure 6.10 Two models showing the impact of fractures and secondary pores on the m value. Impact of fractures (top) where the fractures increase the m and therefore the connectivity. Secondary porosity (bottom) where the isolated pores do not contribute to the connectivity and therefore the m value increases. Note: pu is porosity units.

Isolated pores can form either side of poikilitic cements or clasts in the form of anhydrite or calcite cements (Herrick and Kennedy, 1996). The electrical current is forced to flow around the clasts, which can create stagnant zones. These stagnant zones do not contribute to the electrical conduction and therefore the *m* value increases (Figure 6.11). However, poikilitic cements were not identified in the CT images of the 25 TGS (Figure 6.12).

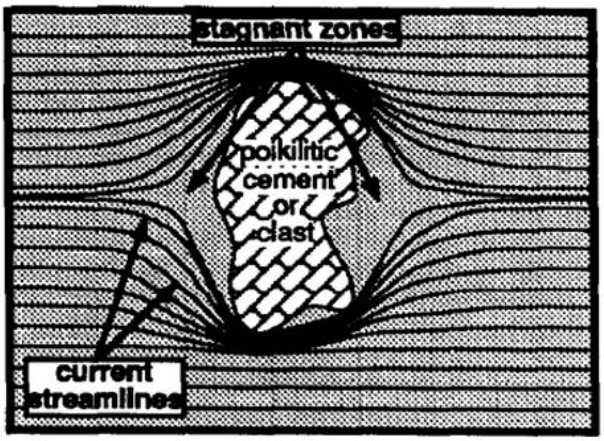

Figure 6.11 Diagram from Herrick and Kennedy (1996) showing how Poikilitic cements can create stagnant zones and increase the m value, however, these were not found in the samples in this research.

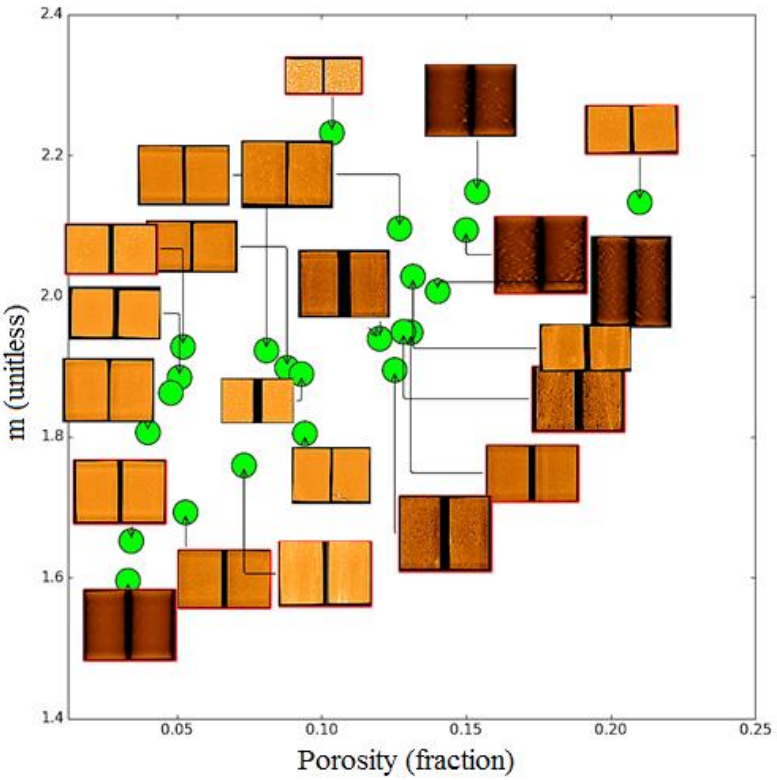

Figure 6.12 Cementation exponent as a function of porosity showing the lack of poikilitic cements in the CT images for the 25 TGS samples.

The *m* value is predicted to vary for a rock containing different proportions of high and low porosity layers. A model was presented by Herrick and Kennedy (1996, 2004) where they defined layer 1 as having a cementation exponent of m_1 and layer 2 having a cementation exponent of m_2. Therefore electrical properties parallel to the layering:

$$\frac{1}{\overline{FRF}} = \overline{\emptyset^m} = \beta\emptyset_1^{m_1} + (1-\beta)\emptyset_2^{m_2} \qquad \text{Equation 6.5}$$

and electrical properties perpendicular to layering:

$$\frac{1}{\overline{\overline{FRF}}} = \overline{\overline{\emptyset^m}} = \frac{1}{\frac{\beta}{\emptyset_1^{m_1}} + \frac{1-\beta}{\emptyset_2^{m_2}}} \qquad \text{Equation 6.6}$$

where *FRF* is the formation resistivity factor (unitless), ϕ is porosity (%), *m* is the cementation exponent (unitless) and β is the volume of the fine-grained sand component (m^3).

A model was created showing how *m* varies for a rock containing different proportions of high porosity (40%) and low porosity (10%) layers (Figure 6.13). It is assumed that both have an *m* value of 2 but due to the presence of parallel layers, the *m* value is between 1.75 and 2 whereas with perpendicular layers, the *m* value is increased to 3. However, when this model is applied to the current research, there seems to be a small difference between the *m* values of layered rocks, this is because these samples show less porosity variation (Figure 6.13).

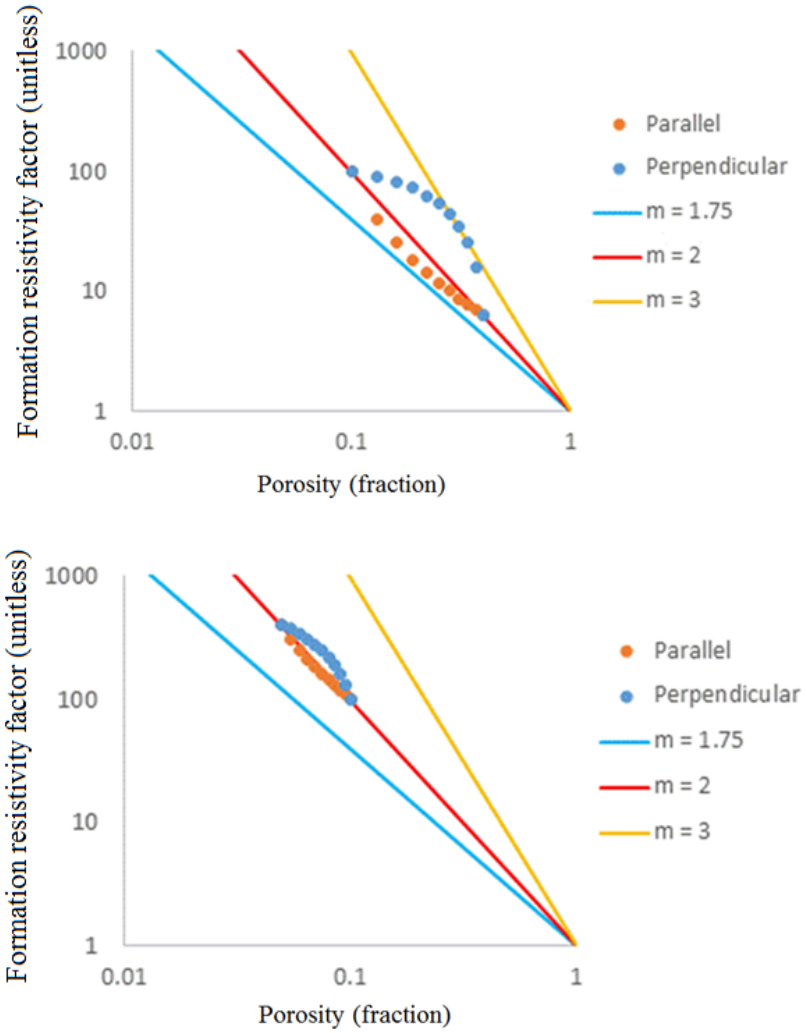

Figure 6.13 Variation of the cementation exponent as a function of the orientation of the measurement. The presence of parallel layers causes the m value to vary from 1.75 to 2 as despite the variation in porosity between the layers the current will pick the easiest pathway with the highest porosity. The presence of perpendicular layers causes the m value to increases to 3 as the lowest porosity layer dominates, as the overall porosity increase the higher porosity layer dominates and the m value reduces to 2 (top). In this research, the porosity values show less variation therefore the parallel and perpendicular layers make little difference to the m value (bottom).

Poikilitic cements are not present within any of the 25 TGS samples. Laminations do not appear to have a major impact on the samples because the porosity does not vary significantly between the individual lamina. Therefore, based on the current research data the most likely reason for the higher *m* values at higher porosities and permeabilities is due to the presence of isolated secondary pores.

6.4.2 Controls on Porosity and Permeability - Surface Area

The well-established Kozeny-Carmen (1927) equation indicates that permeability is inversely related to surface area (Equation 2.17). Based on the Kozeny-Carmen (1927) equation, samples with a low permeability for a given porosity have higher surface areas. This is because samples with smaller pores have lower permeabilities but higher surface areas than samples with larger pores for a fixed porosity. In addition, the highest surface area is found with illite sandstone, which produces the lowest permeability compared with sandstones containing kaolin, which has a lower surface area (Rossel, 1982). This supports data in Chapter 5.

To determine if the current study agrees with the Konzey-Karmen (1927) equation whereby permeability is inversely related to surface area, the BET surface area was correlated with porosity and permeability (Figure 6.14). There is a slight correlation between BET and the position on the porosity-permeability trend whereby the permeability decreases as the surface area increase.

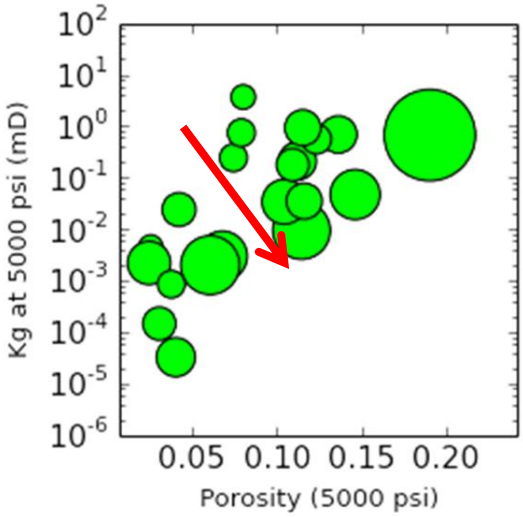

Figure 6.14 Permeability as a function of porosity scaled according to BET (larger BET value – larger circle size). There is an increase in surface area with a decrease in permeability as shown by the red arrow.

The permeability was estimated using Equation 2.17 and was compared to the gas permeability. Some samples show a large difference between the measured gas permeability and the permeability estimated from the Kozeny-Carmen (1927) equation where both permeabilities over and underestimate the permeability leading to the scatter around the 1:1 line (Figure 6.15). The largest difference was an underestimation of the gas permeability by two orders of magnitude. Nevertheless, the R^2 value is moderate at 0.61.

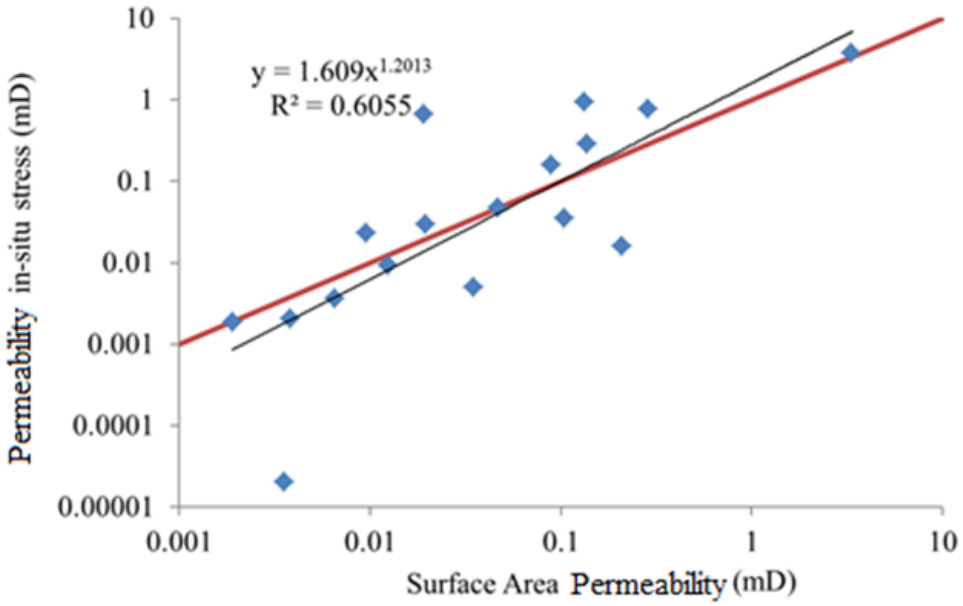

Figure 6.15 Gas permeability as a function of the estimated permeability using the Kozeny-Carmen equation. There is a lot of scatter both above and below the 1:1 line but the R^2 value is moderate at 0.61.

The scatter seen in Figure 6.15 possess questions on the reliability of the BET data. Therefore, the surface areas from two different laboratories were compared MCA services, Royston and University of Leeds. There was a poor correlation between the BET made in the two laboratories (Figure 6.16). Surface area was also correlated with the electrical properties, MICP pore throat size, NMR T_2 cut-off and illite and kaolin content (Figure 6.17 to Figure 6.21). The R^2 values are low implying there are no significant trends.

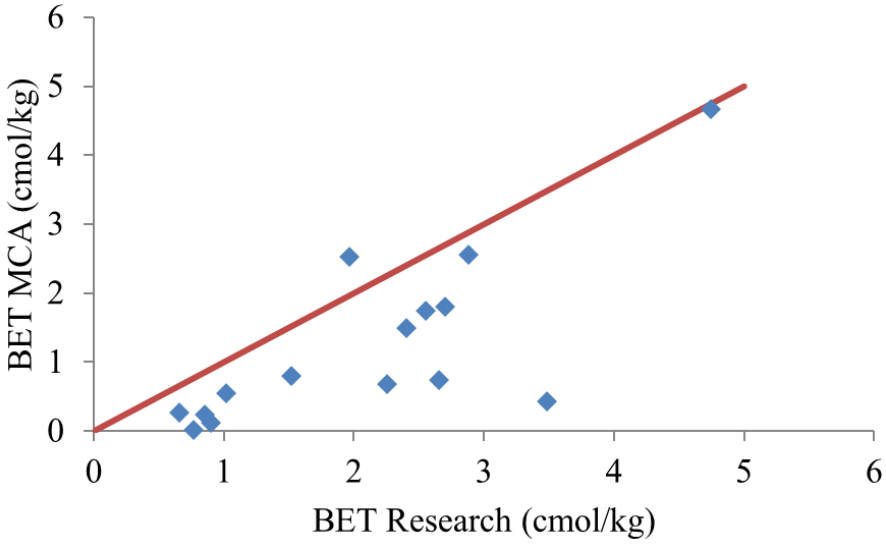

Figure 6.16 BET results from MCA services, Royston as a function of the BET results from Leeds showing a poor correlation with a lot of scatter.

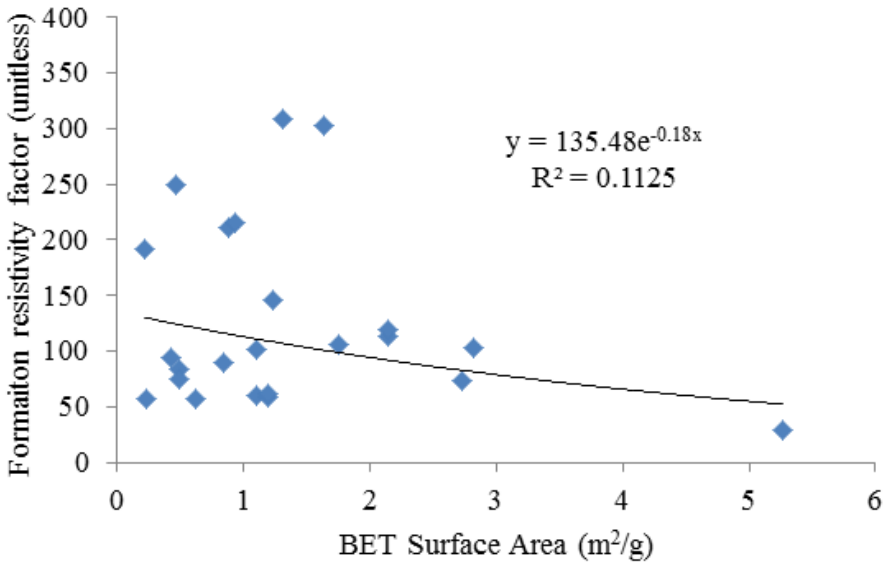

Figure 6.17 Formation resistivity factor as a function of BET surface area. A decrease in FRF *with surface area, however, the trend line is poor.*

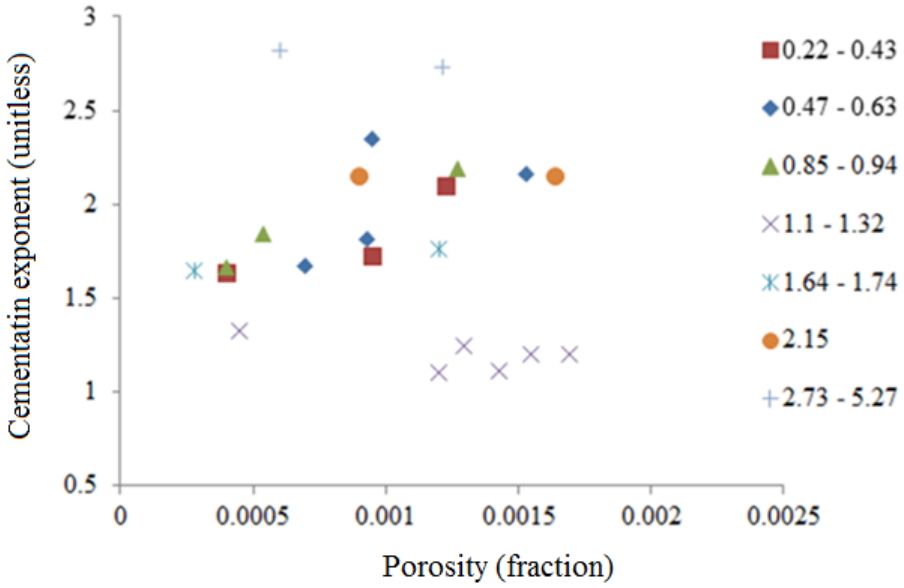

Figure 6.18 Cementation exponent as a function of porosity divided by BET surface area showing no clear trend.

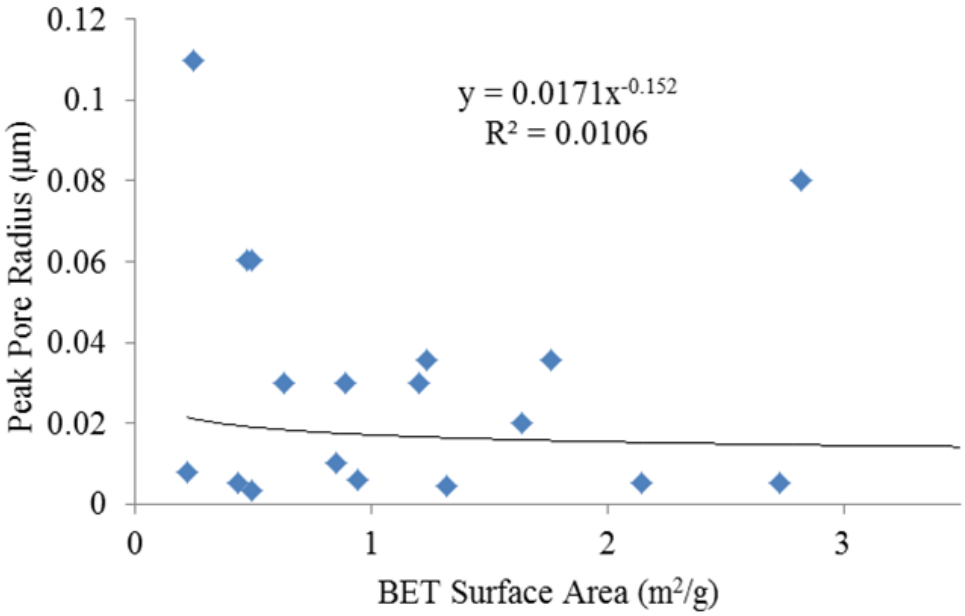

Figure 6.19 Peak pore radius from mercury injection as a function of BET surface area showing a poor trend.

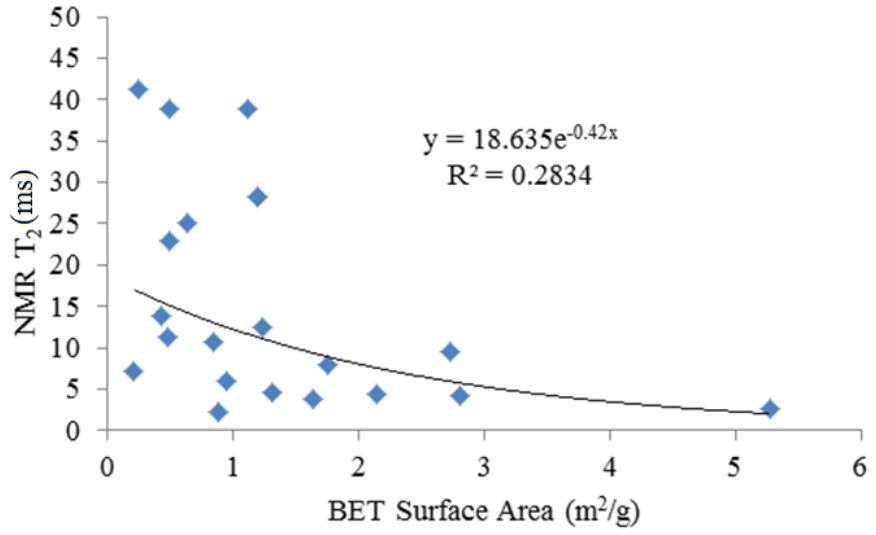

Figure 6.20 NMR T_2 cut-off as a function of BET surface area showing a poor trend.

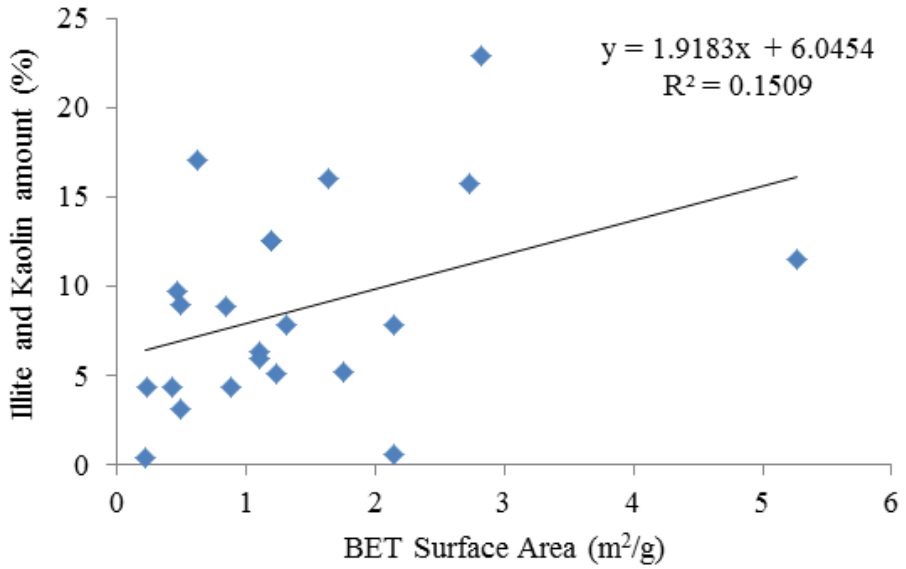

Figure 6.21 Illite and kaolin content as a function of BET surface are showing a poor trend.

There are a number of reasons for the lack of correlation and scatter described within this section. Rosenbrand et al. (2015) stated that the Kozeny-Carmen (1927) equation is derived for porous medium with a homogeneous pore size, whereas there are variations in the pore size within the samples in this research (Figure 6.4). Berthier et al. (2016) implied that the diffusion of N_2 is slow in the small micro-pores which could be an issue in the current TGS samples. In addition, there could also be experimental errors for example, the degassing stage before admitting the nitrogen may not have been carried out accurately, or it was not carried out for long

enough, or the time for equilibrium prior to obtaining that amount of gas adsorbed may have been too short.

The surface area can be accurately improved by using krypton because of its low vapor pressure at the same temperature as nitrogen (Rouquerol et al. 2013). Therefore, the lack of correlation may simply reflect the lack of precision of the measurement technique. Consequently, there is a need to develop a more accurate methodology that is specific for TGS whereby the degassing and equilibrium stages need to be adjusted and a range of adsorbent gases studied.

6.4.3 Permeability Estimations

This section presents the estimation of permeability using two methods – NMR and MICP. The NMR method uses the Coates et al. (1991) and Schlumberger-Doll-Research (SDR) models. The MICP method uses the Swanson (1981), Purcell (1949), Katz and Thompson (1986, 1987) and Winland (1980) models.

6.4.3.1 Nuclear Magnetic Resonance (NMR)

Several authors have attempted to calculate permeability from NMR data; these models include the Coates et al. (1991) model (Eqation 3.12) and the SDR model (Kenyon et al., 1988) (Equation 3.13). A comparison was made between the predicted NMR and the measured gas permeability from this research (Table 6.4). The data from the Coates et al. (1991) and SDR models compared to the gas permeability is scattered above and below the 1:1 line. This behaviour is more pronounced in the SDR model. The model from Coates et al. (1991) underestimates the measured permeability by around one order of magnitude, however, some of the samples are still overestimated (Figure 6.22). The SDR model underestimates the measured permeabilities by around three orders of magnitude however; some of the samples are also overestimated (Figure 6.23).

Table 6.4 Table of permeability form the Coates et al. (1991) and SDR models as a function of the measured gas permeability.

Well	Sample	Permeability at 1500psi C_p (mD)	Coates et al. (1991) (mD)	Ratio difference	SDR (mD)	Ratio difference
WIN4	26	0.12	0.01	10.3	0.001	1.0
WIN5	16B	0.03	0.09	347.1	0.08	308.5
Shell1	83	0.0030	0.0001	4.1	0.00003	1.0
Shell1	111	0.02	0.002	9.3	0.005	20.9
Shell1	216	0.03	0.004	14.1	0.0003	1.1
Shell2	1	0.52	0.95	184.6	0.06	12.0
Shell2	9	0.59	0.44	74.1	0.17	29.1
BP2	2	0.13	0.08	63.1	0.05	34.2
BP2	3	0.98	0.1	10.2	0.16	15.9
BP3	1	0.67	0.1	15.2	0.12	17.9
BP2	5	0.03	0.001	3.6	0.00004	0.1
BP3	4	1.06	3.36	317.3	2.60	245.3
BP3	5	0.95	2.61	274.8	1.86	195.8
BP3	6	1.27	1.82	143.5	1.35	106.5
EBN3	40	1.35				
EBN4	10	0.04	0.005	13.5	0.001	2.9
Shell4	202	0.27				0.0
Shell4	370	1.12	3.05	272.2	2.5	223.7
Shell4	389	0.86				
Shell4	409	0.001	0.0008	67.0	0.0003	28.7
WIN 9	5	0.01	0.006	65.8	0.0009	9.8
GDF1	1	1.29	1.51	116.8	0.44	34.3
GDF1	6	0.01	0.005	55.1	0.0028	29.5
GDF1	7	4.08	1.87	45.8	0.55	13.6
GDF2	4	3.64	19.43	533.8	6.05	166.2

Notes: the ratio difference is the difference between the estimated Coates and SDR model permeabilities to the laboratory gas permeabilities. The cells shaded grey do not have any NMR data. C_p is confining pressure. Those samples were the model values overestimate the measured values are in green those where the model underestimated the measured values are in red.

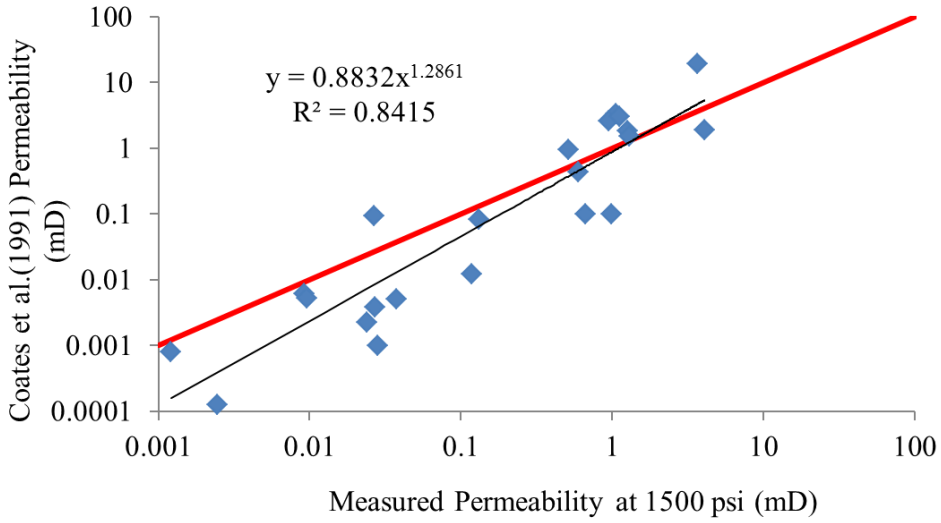

Figure 6.22 Permeability from the Coates et al. (1991) model as a function of the measured permeability showing a good trend with a R^2 value of 0.84. The red line is the 1:1 line.

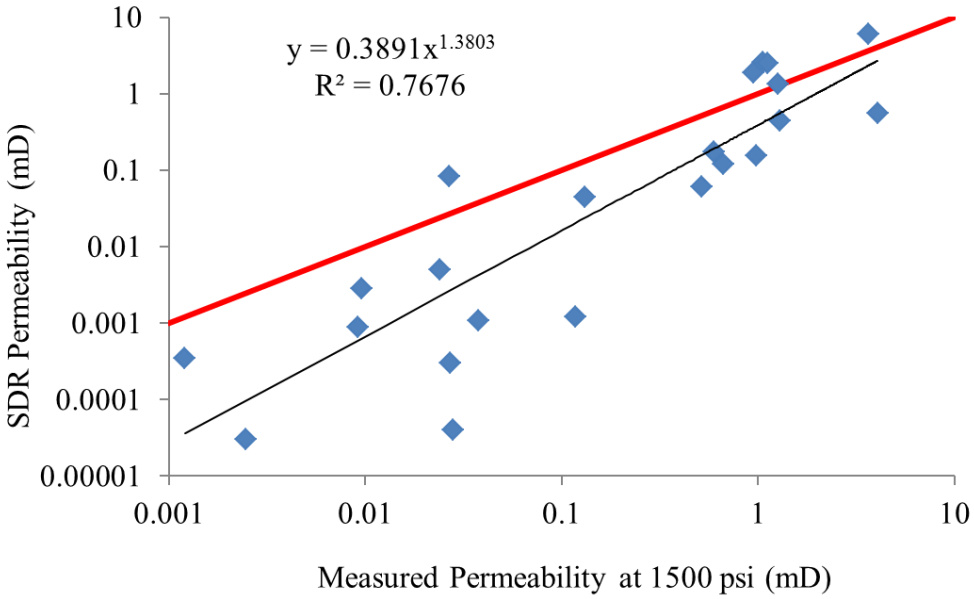

Figure 6.23 Permeability from the SDR model as a function of the measured permeability showing a good trend with a R^2 value of 0.77. The red line is the 1:1 line.

The variation in the permeability data in Figure 6.22 and Figure 6.23 could be related to the coefficients used in the models where there are variations in the values used within the literature. In terms of the Coates at al. (1991) model, Allen et al. (2000), Tiab and Donaldson (2004) and Chen (2008) all argued that the *C* coefficient is 10 and the exponents are 4 and 2 for *a* and *b* respectively. Whereas, Ayala (2007) reported that *C* is 20 for TGS. In terms of the SDR model, Allen et al. (2000), stated that *a* and *b* are 4 and 2 respectively. Tiab and Donaldson (2004) stated that *C*, *a* and

b are 4, 4 and 2 respectively. Xiao et al. (2013) stated that if not enough core sample is available 10, 4 and 2 should be used for *C*, *a* and *b*. It is therefore unclear, which values should be used and whether using one value for all sandstones is realistic.

The coefficients appear to vary depending on the particular properties of the rock. For example, Tiab and Donaldson (2004) argued that the *C* coefficient is 10 and the exponents are 4 and 2 for *m* and *n* respectively only if (i) the irreducible water saturation is well defined, (ii) the porosity is intergranular, and (iii) the rock contains little clay in the pore throats. In addition, Rezaee (2015) reported that the *C* value is usually 10 for sandstones but decreases with clay content. Coates et al. (1999) stated that the *C* in both models are dependent on the process that created the formation and can be different for different formations.

Machado et al. (2008) found the trends were improved when the original models were modified. They adjusted the coefficient and exponents in the Coates et al. (1991) and SDR models to match the absolute permeability of 13 low permeability gas sands. They determined that the *C*, *a* and *b* are 3.9, 1.7 and 110 respectively for the Coates et al. (1991) model and 7.3 $x10^{-11}$, 4.6 and 2.7 respectively for the SDR model. This therefore shows that using constant values for the coefficients is not reliable.

The value of the empirical coefficient C and *a* and *b* exponents in the Coates et al. (1991) model was determined for 25 TGS using a Microsoft Excel based derivation method. The average empirical coefficient *C* was 18.3; however the *a* and *b* exponents do not allow the equation to converge to the unique value. Despite that, by changing both *a* and *b* at the same time, the value can be achieved where the average value for *a* was 1.6 and the average *b* value was 1.4. Therefore a value of 10 for the empirical coefficient *C is* not ideal for every sample.

The value of the empirical coefficient, *m* and *n* exponents in the SDR model was also determined for 25 TGS using the Excel method. The average empirical coefficient *C* was 191.2, the average *a* exponent was 3.5 and the average *b* exponent was 3.1. It is therefore clear that a value of 4 for the empirical coefficient *C* is not feasible for every sample. This may imply the coefficients *C* is the main source of error especially in the SDR model as the average *a* and *b* values in both models are close to the values used in this research.

Another reason for the scatter could be related to the FFI and BVI values obtained from the T_2 cut-off, however, this would only affect the Coates et al. (1991) model. The T_2 cut-off for sandstone has been quoted as 33 ms in a number of publications (Howard et al., 1990, 1992; Kenyon, 1992 and Straley et al., 1991, 1997). Recent studies have found a T_2 cut-off of 33 ms to be too large for sandstones. For example, Liang et al. (2015) found that the T_2 cut-off for the TGS samples they were studying ranged from 4.7 to 26 ms with an average value of 17 ms. Dastidar (2004) found that the T_2 cut-off for 15 turbidites ranged from 5 to 15 ms. This gave a 30 – 50% more free fluid than the recommended T_2 cut-off of 33 ms. Similarly, Haldia (2013) indicated that the use of 33 ms as the T_2 cut-off produced a low FFI of 5 – 6% despite the high porosity and permeability of the sandstone under study.

Some authors found a longer T_2 cut-off range for example, Ayala (2007) stated that the T_2 cut-off ranged from 20 to 50 ms with an average of 30 ms for the TGS field he was studying. In addition, Lonnes (2003) found a cut-off range of 23 to 300 ms for a range of sandstones. It is clear from the literature that a single value for the T_2 is not realistic for all sandstones.

The value of the T_2 can vary due to different grain sizes, surface to volume ratio of the pore sizes and the presence of clay. Xu et al. (2013) compared two pore network systems, one with large grains and one with smaller grains. The larger the grains the larger the pores and the larger the transverse relaxation time (T_2). Therefore, samples with larger grains should have a larger T_2 cut-off then samples with smaller grains (Figure 6.24).

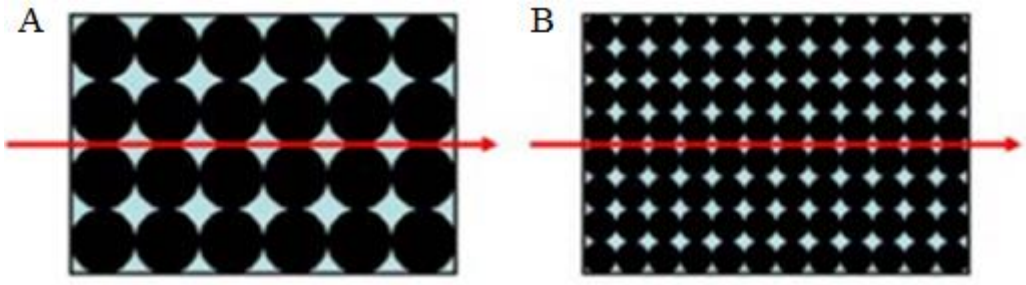

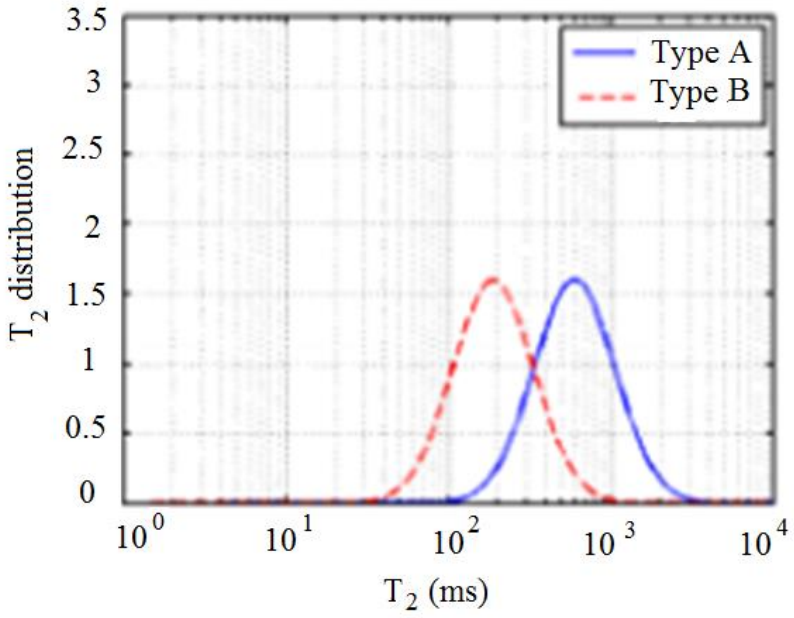

Figure 6.24 T_2 distribution for a large grain size (A) and smaller grain size (B). The larger grain size has a longer T_2 time as the pore size is larger.

Haldia (2013) stated that it could be related to the surface to volume ratio of the pore space. If the surface: volume ratio is increased, the relaxation time decreases and the T_2 cut-off decreases:

$$\frac{1}{T_2} = \rho \frac{S}{V} \qquad \text{Equation 6.7}$$

where T_2 is the relation time (ms), p is density (g/cm^3) , S is surface area (m^2/g) , V is volume (cm^3). Therefore the T_2 cut-off should be lower for a sample with a larger surface to volume ratio. Haldia (2013) also stated that if there is grain coating or bridging clays micro pores can be created. If the micro pores and macro pores have a good connectivity in the pore system, the protons in the macro pores will have access to the micro pores and they will relax faster than if the micro pores were not present. Therefore those samples with grain coating or bridging clay should have lower T_2 cut-offs.

Different sandstone rock types may have different grain sizes, pore sizes and microstructures, however, these properties are assumed to be the same by using a single value of 33 ms as the T_2 cut-off. This could be the reason for the scatter in Figure 6.22 and Figure 6.23. Future work is needed to understand more about what

controls the T_2 cut-off and determine what cut-off should be used to enable a better estimation of permeability that is specific for TGS.

The T_2 cut-off can be determined by comparing the T_2 distribution of a fully saturated sample to a sample at irreducible saturation (Figure 6.25) (Coates et al., 1999). The latter is obtained using a centrifuge or the porous plate technique. This could be employed during future analysis and could provide more accurate T_2 cut-off values for permeability estimations.

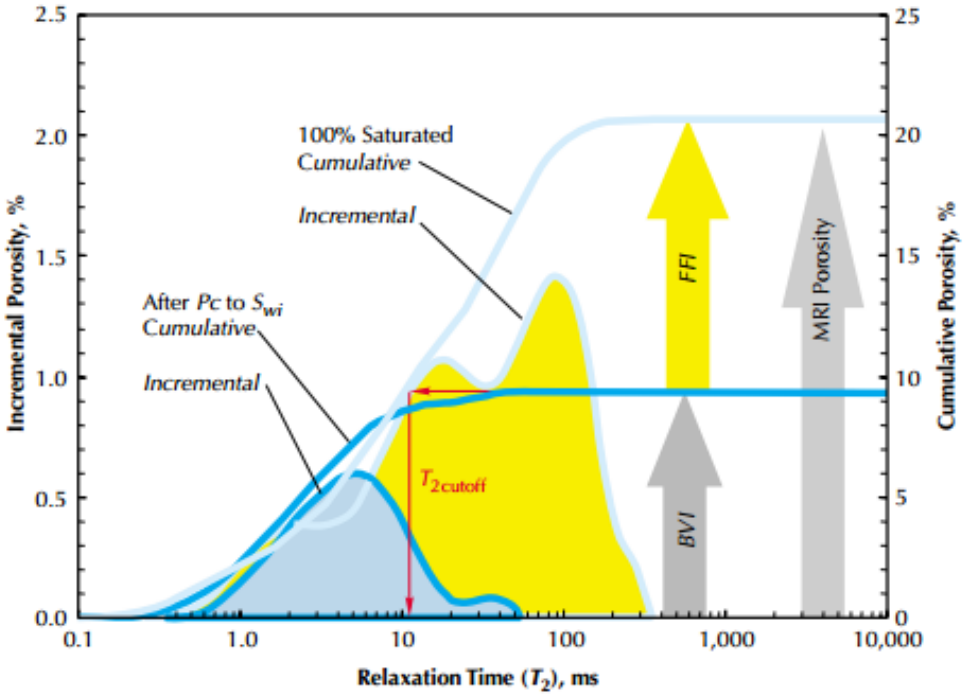

Figure 6.25 Incremental porosity and cumulative porosity as a function of relaxation time. The T_2 cut-off can be obtained by comparing the NMR measurements on a fully saturated sample vs a sample at irreducible saturation thereby providing a more accurate BVI/FFI ratio (Coates et al., 1999).

Although the plots of permeability estimated from NMR vs measured permeability for all 25 TGS show a lot of scatter, correlations for individual wells are much better even when using the commonly quoted coefficients (Figure 6.26 to Figure 6.29). The R^2 values are all above 0.9 for wells GDF1, BP3, BP2 and SHELL4. This suggests that the technique could offer accurate predictions of permeability if calibrated for individual wells. Nevertheless, the plots were only made for a few samples and further work would be needed to apply this to more TGS wells and identify the fundamental control.

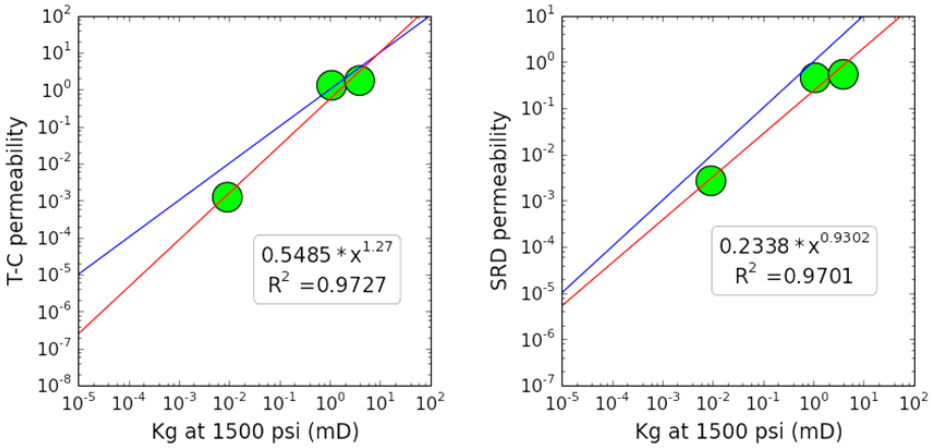

Figure 6.26 Coates et al. (1991) model and SDR permeability as a function of gas permeability at 1500 psi for well GDF1 showing a good trend. The red line is the trend line and the blue line is the 1:1 line.

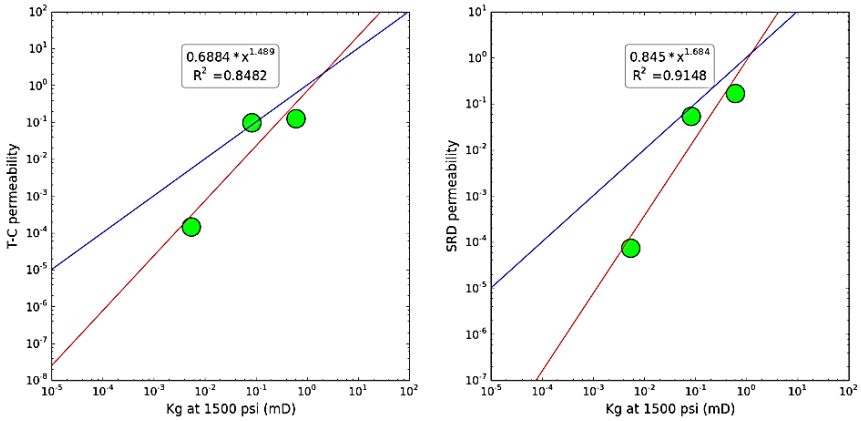

Figure 6.27 Coates et al. (1991) model and SDR permeability as a function of gas permeability at 1500 psi for well BP2 showing a good trend. The red line is the trend line and the blue line is the 1:1 line.

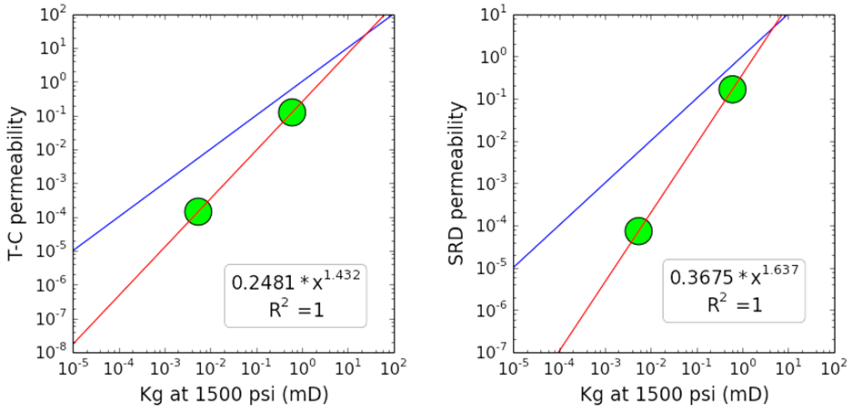

Figure 6.28 Coates et al. (1991) model and SDR permeability as a function of gas permeability at 1500 psi for well BP3 showing a good trend. The red line is the trend line and the blue line is the 1:1 line.

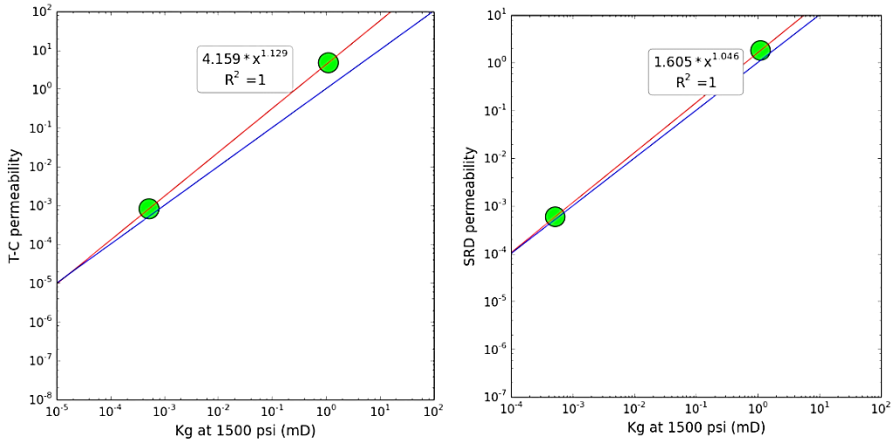

Figure 6.29 Coates et al. (1991) model and SDR permeability as a function of gas permeability at 1500 psi for well SHELL4. The red line is the trend line and the blue line is the 1:1 line.

To enable an understanding of what controls the accuracy of the NMR permeability estimations, the residual (difference between observed and the predicted data) of Figure 6.23 (the SDR estimated permeability vs the measured permeability) was determined. The residual was plotted against a range of different properties to obtain the best trend. The results show that the strongest correlation is with the cementation exponent (Figure 6.30).

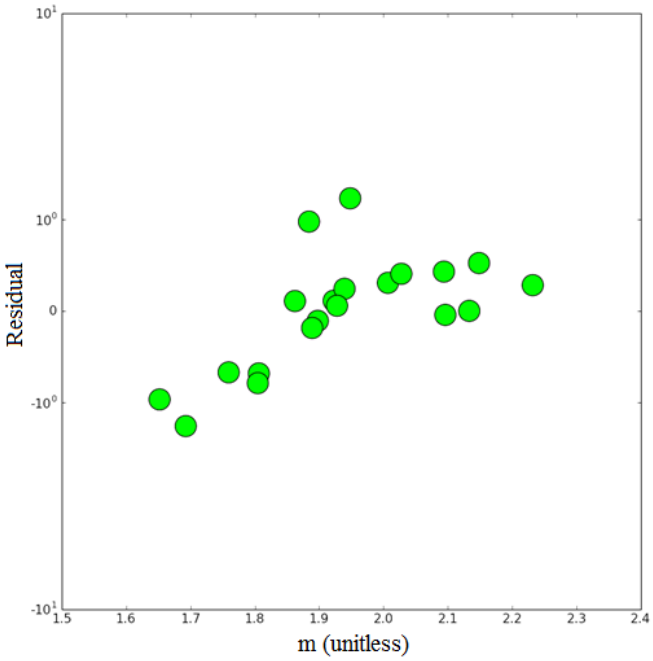

Figure 6.30 The residual of Figure 6.23 (SDR estimated permeability vs the measured permeability) as a function of the cementation exponent.

An attempt was made to further understand the correlation between the residual and *m*. The presence of secondary pores will not significantly increase the overall pore throat size; however, NMR will detect these large pores and will predict a larger permeability compared to the measured values because the estimated permeability is also based on an ineffective pore size. This will create a positive residual between estimated NMR permeability and measured permeability (K_{nmr}-$K_{measured}$) denoted as +ve K_{nmr}-$K_{measured}$. The secondary pores will not contribute to the electrical flow so the *m* value would be high (Section 6.4.1) (Figure 6.31).

Pore-lining and bridging clays will tend to increase the pore size/pore throat size ratio. The bridging clay block pore throats meaning lower measured permeability, however, the model does not take into account these bridging clays which results in a overestimation of permeability and hence a positive value for the K_{nmr}-$K_{measured}$ residual (Figure 6.31). The clays block pore throats meaning the connectivity is low and the *m* value is high

Fractures may have a very small pore volume yet dominate flow of both fluid and electrical current. NMR results that indicate a low volume would be interpreted as low permeability by the theoretical models, which in turn will underestimate the permeability values. This will create a negative value for the K_{nmr}-$K_{measured}$ residual (Figure 6.31). The *m* values are low because the microfractures increase the connectivity even at low porosities (Section 6.4.1).

The presence of secondary pores, pore lining and bridging clays and fractures could help understand the trends found within Figure 6.22 and Figure 6.23. It could also be a combination of these controls i.e. the unknown value of the *C* coefficient in the models as well as the use of a single T_2 cut-off value. Future work is needed to study these controls in more detail to identify the underlying course for the development of improved NMR-based permeability.

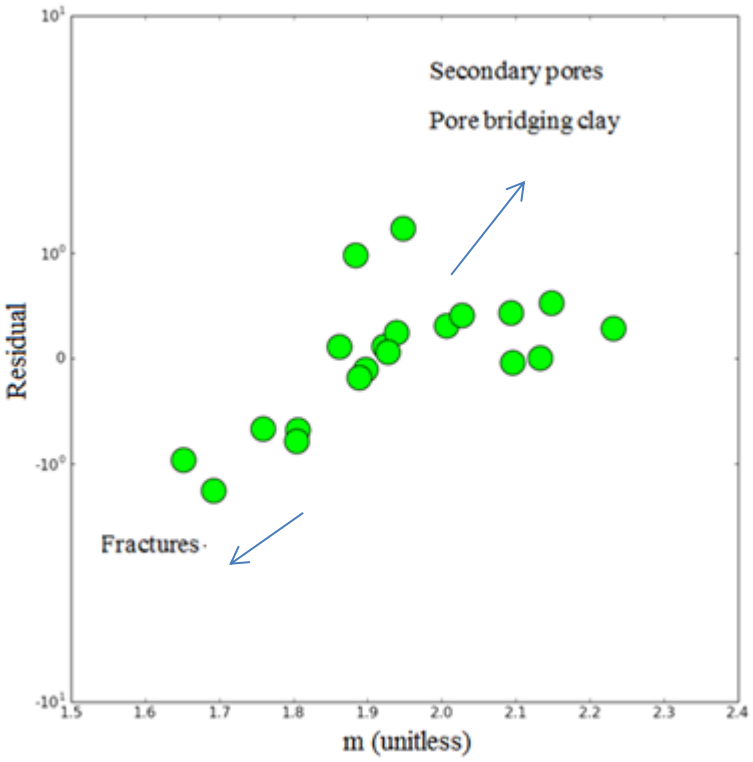

Figure 6.31The residual of Figure 6.23 as a function of cementation exponent showing the possible controls for the scatter seen in Figure 6.23. The secondary pores and bridging clay increase m whereas fractures reduce m.

6.4.3.2 Mercury Injection Capillary Pressure (MICP)

MICP data is very easy and fast to obtain. Based on the equation by Leonard Poiseuille and Gotthilf Hagen (1938-1939) (Equation 2.2), it should be possible to estimate permeability from MICP data as permeability is controlled by the pore size distribution. Many empirical and theoretical relationships are available to make such estimates. The most commonly used relationships were tested within this thesis project: Swanson (1981), Purcell (1949), Katz and Thompson (1986, 1987) and Winland (1980).

The most popular relationship used to calculate permeability from MICP data is the Swanson method (1981):

$$K_{air} = 399\left(\frac{S_{Hg}}{P_c}\right)^{1.691}_{apex} \qquad \text{Equation 6.8}$$

where K_{air} is the air permeability (mD), S_{Hg} is the bulk volume mercury saturation (%) and P_c is the capillary pressure (psi) corresponding to the apex of a hyperbolic

log-log Hg injection plot. The apex is obtained by plotting Hg saturation/capillary pressure against Hg saturation as suggested by Pittman (1992) (Figure 6.32). This apex point represents all the major connected pore space which have been intruded with mercury and control permeability (Comisky et al., 2007). For an air system, the fitting parameters are 399 and 1.691 as noted by Katz and Thompson (1986 and 1987).

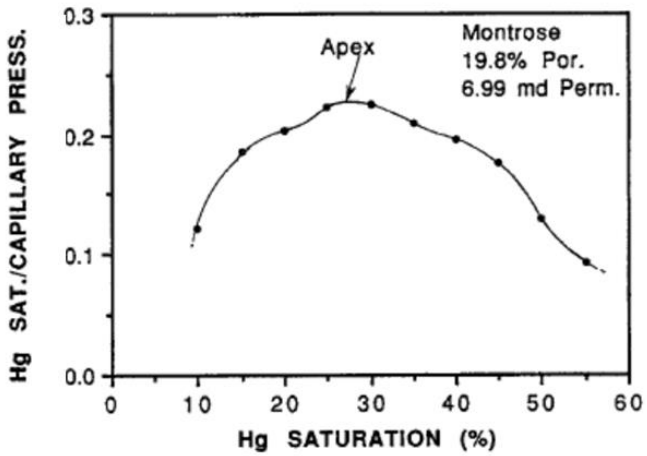

Figure 6.32 Plot of Hg saturation vs Hg saturation/capillary pressure to obtain the apex for Equation 6.10 (Pittman, 1992).

Using a Excel based derivative method moree accurate fitting parameters were obtained - 101 and 1.58. This created a modified model where the same terms are described in Equation 6.10:

$$K_{air} = 101\left(\frac{S_{Hg}}{P_c}\right)^{1.58}_{apex} \qquad \text{Equation 6.9}$$

The estimated permeability was plotted against the *in-situ* permeability (Figure 6.33). The points lie close to the 1:1 line providing a R^2 value of 0.81, however, there is some scatter around the 1:1 line at both the lower and higher permeability ends.

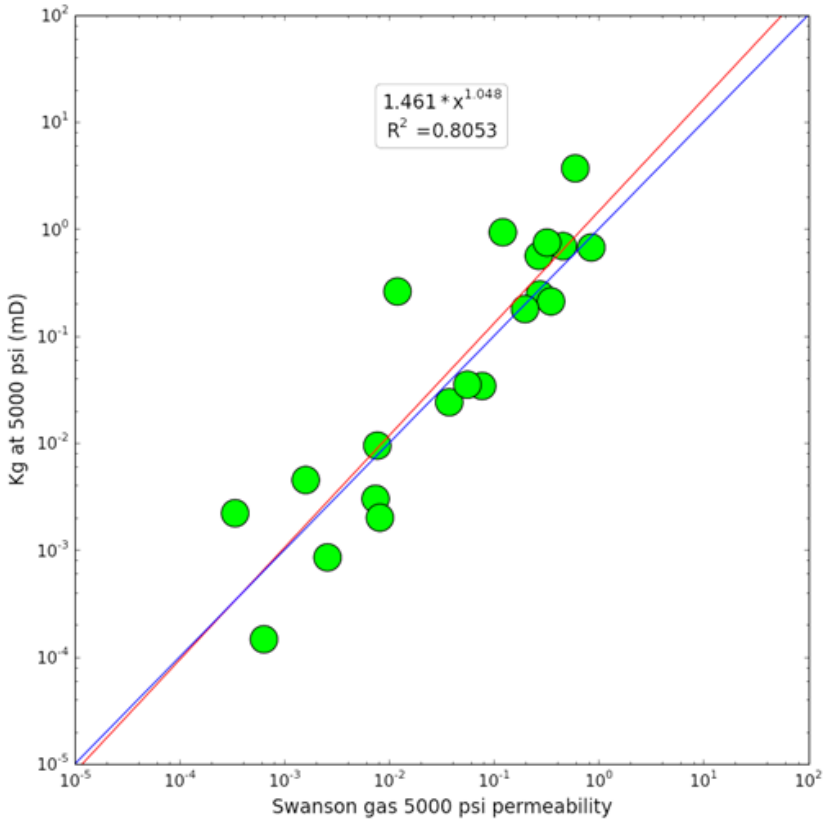

Figure 6.33 Permeability at in-situ stress as a function of the estimated Swanson (1981) permeability showing a good trend. The red line is the trend line and the blue line is the 1:1 line.

Purcell (1949) suggested treating rocks as bundles of capillaries in which flow along the capillaries could be modelled using a flow law dependent upon the diameter of the capillaries. The equation proposed is:

$$k = Cf\emptyset \sum_{S_{Hg}=100}^{S_{Hg}=0} \frac{S_{Hg}^{i}}{(P_{Hg}^{i})^{2}} \qquad \text{Equation 6.10}$$

where P^{i}_{Hg} is the average Hg pressure of the increment (inHg), S^{i}_{Hg} is the fractional saturation of that increment (fraction), C is a units conversion constant (unitless) (~14000 for fractional porosity, Hg pressure in psi, and saturation in %), f is an empirical lithology factor (unitless), and ø is the fractional porosity (fraction). Purcell (1949) used f = 0.216 but Comisky et al. (2007) suggested that f = 0.15 which provided a better fit of the Klinkenberg corrected permeability of low permeable rocks.

An Excel based derivative method was used to determine more accurate fitting parameters. This created a modified model where the same terms are described in Equation 6.12:

$$k = 35000\emptyset \sum_{S_{Hg}=100}^{S_{Hg}=0} \frac{S_{Hg}^{i}}{(P_{Hg}^{i})^{2}} \qquad \text{Equation 6.11}$$

The estimated permeability was plotted against the *in-situ* permeability (Figure 6.34). Although a good trend was obtained with a R^2 value of 0.85, there is an underestimation of the measured permeability at the lower permeability end.

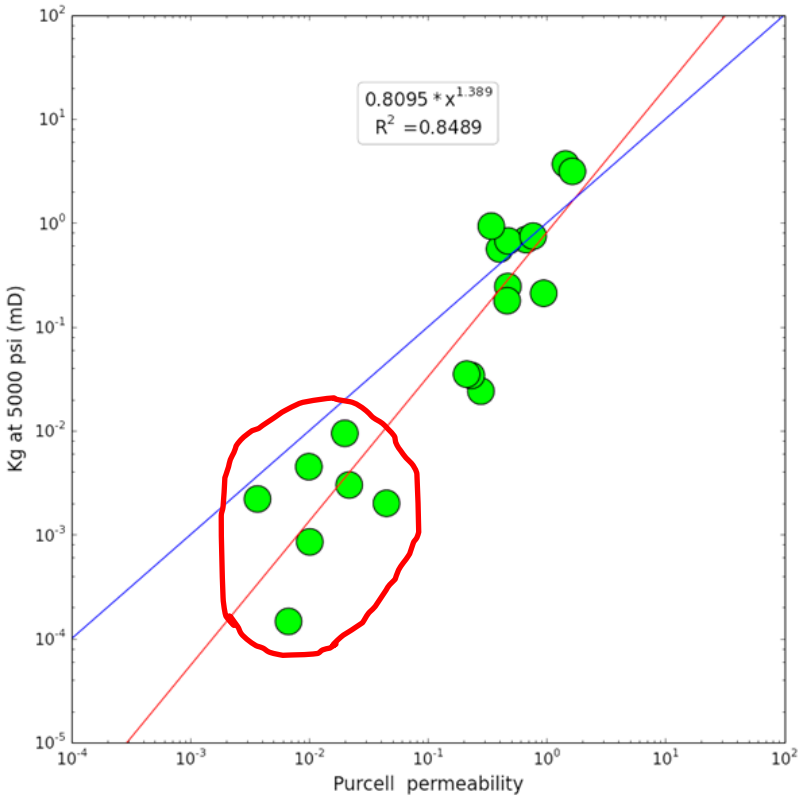

Figure 6.34 Permeability at in-situ stress as a function of the estimated Purcell (1949) permeability. There is a underestimation of the measured permeability at the lower permeability end. The red line is the trend line and the blue line is the 1:1 line.

Katz and Thompson (1986, 1987) derived a characteristic length scale for porous media - L_c. This is the pore diameter at which a continuous filament of Hg exists throughout the sample (i.e. it is the pore diameter at the threshold pressure). The equation for the Katz and Thompson model is:

$$k_{Lc} = \left[\frac{1013}{226}\right] L_c^2 \left[\frac{\sigma_o}{\sigma_w}\right] \qquad \text{Equation 6.12}$$

where the electrical conductivity ratio (σ_o/σ_w) is the formation resistivity factor (*FRF*) (unitless). The estimated permeability was plotted against the *in-situ* permeability. There is a good trend with a R^2 value of 0.72 but there is an underestimation of the measured permeability at the lower permeability end (Figure 6.35).

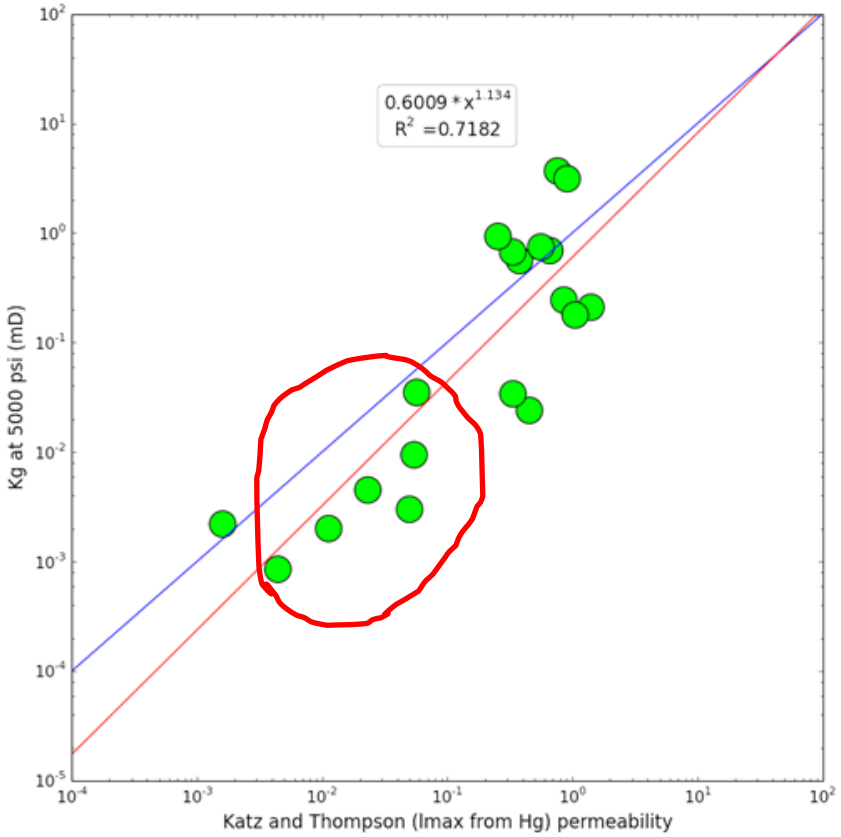

Figure 6.35 Permeability at in-situ stress as a function of the estimated Katz and Thompson (1986, 1987). There is a underestimation of the measured permeability at the lower permeability end. The red line is the trend line and the blue line is the 1:1.

Another relationship established by Winland (1980) exists, where pore radius, porosity and absolute permeability are accounted for:

$$Log(r_{35}) = 0.732 + 0.588 Log_{10}(K_{air}) - 0.864 Log(\emptyset) \qquad \text{Equation 6.13}$$

where r_{35} is the pore aperture radius corresponding to a S_{hg} of 35% (μm), K_{air} is the absolute permeability (mD) and ϕ is porosity (%). An Excel based derivative method

was used to determine more accurate fitting parameters, this created a modified model:

$$Log(r_{35}) = 0.955 + 0.56(K_{air}) - 0.44Log(\emptyset) \qquad \text{Equation 6.14}$$

The estimated permeability was plotted against the *in-situ* stress (Figure 6.36). There is a good trend with a R^2 value of 0.88, however, there is an underestimation of the measured permeability at the lower permeability end.

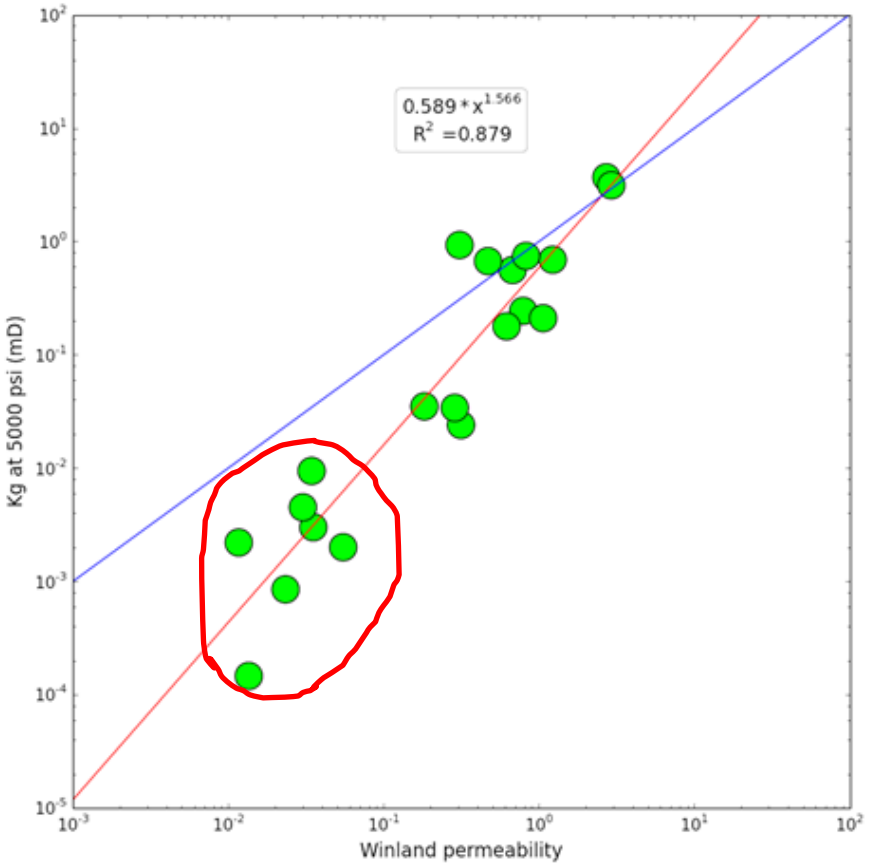

Figure 6.36 Permeability at in-situ stress as a function of the estimated Winland (1980) permeability. There is a underestimation of the measured permeability at the lower permeability end. The red line is the trend line and the blue line is the 1:1.

Kamath (1992), Ma and Morrow (1996), Comisky et al. (2007) and Brown (2015) all show that the MICP method does not provide a reliable estimation of permeability at the lower permeability end. Brown (2015) stated that the estimated MICP permeability only accounts for matrix permeability and not the fracture permeability. Therefore, the MICP permeability should be underestimated relative to the measured gas permeability. As microfractures are present at grain contacts in every sample (Section 5.3.4) the MICP models may not be accurate for the samples in this

research. Nevertheless, as there was actually an underestimation by the measured permeability not an overestimation (Figure 6.33 to Figure 6.36), the theory presented by Brown (2015) is unlikely to be.

Comisky et al. (2007) stated that most MICP models were not developed for tight rocks where the methods are based on datasets with permeabilities more than 1 mD. Similarly, Wells and Amaefule (1985) stated that the Swanson model works best for samples with permeabilities greater than 10 mD. Brown (2015) also stated that the precision and accuracy is low in tight rocks. This could account for the underestimation seen at the lower permeability end (Figure 6.33 to Figure 6.36) as 72% TGS studies in this research have permeabilities less than 1 mD.

Brown (2015) stated that another explanation for the differences in the permeability data could be due to the stress sensitivity of permeability. The measured permeability in this research was obtained at a single stress of 5000 psi whereas the models provide permeability at a particular threshold pressure which is specific for the samples and lower than 5000 psi. This could give inaccuracies if the samples are stress dependent. The effects of stress on the MICP permeability is presented in Section 7.4.5, this may help understand the underlying course of the underestimation of the permeability.

6.4.4 Survey of Inconsistencies from SCAL measurements

It is important to understand the accuracy of the data when conducting a large-scale petrophysical examination on a range of rocks. Inaccuracies in the measurements can arise from the set-up, the methodology and the sample. They are briefly discussed below.

A vacuum pump was used to saturate the core plugs, it is easy to perform, requires little maintenance and is used to saturate the core plugs for the NMR and resistivity, as well as measurements of the effects of stress on TGS (Chapter 7). However, it was unclear if all the pores were saturated. In terms of NMR, the predicted pore sizes would not be a true distribution as those pores that remained dry would not be accounted for. As the pores that remained dry may be the smaller pores, this shifts the mean pore sizes to a higher value. In terms of the resistivity, higher resistivity values would be measured. Nevertheless, in this research the

samples were saturated using a vacuum pump followed by 1500 psi confining pressure therefore it is likely the samples are saturated.

The electrical measurements are non-destructive, easy to setup and required little maintenance. However, poor contacts between the electrodes and sample can lead to higher than average resistance. This was the case in some samples as the resistivity data collected increased excrementally compared to the other samples under study. Consequently the confining pressure had to be released, the sample removed and the set-up adjusted. In addition, it was unclear how long the sample had to be kept under observation for the resistance experiment, therefore, each sample was placed at 1500 psi confining pressure and the resistance monitored until there was no change, this typically took 3 days. The system was fragile so calibrations were required regularly. No other pressures were studied in this Chapter, however, the effects of stress on the electrical properties is further studied in Chapter 7.

NMR is non-destructive and can be done automatically. However, it was assumed that there is no surface water between the sample and the cling film in which it was wrapped. If this assumption is not true, this would have an effect on the pore size distribution. To ensure this did not occur, surface water was removed using a partially saturated paper towel prior to sealing and the cling film was applied tightly.

6.5 Conclusion

FRF increased with decreasing porosity and permeability as *FRF* is related to connectivity and therefore fluid flow for current transfer. The cementation exponent increases with an increase in porosity and permeability. The lower *m* values are related to the microfractures because though the microfractures are small, they increase the connectivity even at low porosities or permeabilities. The higher *m* values are most likely related to the presence of isolated secondary pores which increase the porosity but as they do not contribute to the overall fluid flow, the *m* value is high.

Scatter was observed when estimating the permeability using BET, NMR and MICP. The lack of trend in the BET surface area could be related to the lack of pressure equilibrium as well as the use of N_2 gas rather than krypton as the absorbate. This is,

however, an assumption and future work is needed to adjust the current methodology until a reliable method specific for TGS is designed.

The Coates et al. (1991) model underestimates the laboratory permeability by around one order of magnitude and the SDR model underestimates the laboratory permeabilities by around three orders of magnitude. This is possibly due to the incorrect value of the *C* constant used within the models and/or the inaccuracies in using the standard 33 ms as the T_2 cut-off as the T_2 cut-off varies due to changes in grain size, pore size or due to the presence of clay. Improvements in the trends do however occur when individual wells are considered. Future work is needed to make the models more specific for TGS.

Microstructural analysis has identified other causes for this scatter, which include (i) secondary pores - when present the estimated NMR permeability tends to overestimate permeability, (ii) bridging clay – when present the estimated NMR permeability tends to overestimate permeability and (iii) fractures - when present the estimated NMR permeability tends to underestimate permeability. More samples should be studied and more work is needed to understand the fundamental controls on the relationship between NMR signals and the permeability in order to improve the NMR permeability estimation.

The measured permeability underestimated the estimated MICP permeability at the lower permeability end. This is possibly because the models may not be suitable for low permeability samples. In addition, the stress conditions used for the measured permeability data are higher, 5000 psi net stress, compared to the estimated permeability data which use threshold pressure in their models. This could give inaccuracies if the samples are stress dependent as the stress conditions in the comparisons are not the same. The study into the effects of stress in Chapter 7 may provide more insight into the trends. Despite the trends observed in this chapter, the work has shown that there is the potential to estimate permeability from cuttings (BET, MICP) and or side wall cores (NMR), this may cut down on the amount of core plugs that need to be studied.

Chapter 7 - The Impact of Stress on the Petrophysical Properties of TGS

7.1 Introduction

In this research, some experiments (e.g. porosity, Chapter 5) were not performed under any confining pressure or were measured under low confining pressure of 1500 psi (e.g. permeability, Chapter 5 and resistivity, Chapter 6). It is important to study TGS under *in-situ* stresses as it has been repeatedly shown experimentally that many properties of TGS are stress dependent (Fatt, 1952; Vairogs et al., 1971; Thomas and Ward, 1972; Walls, 1982; Farquhar et al., 1993; Davies and Davies, 1999 and Al-Hinai, 2008). Fatt (1952) stated that at 3000psi overburden pressure the permeability is 59 to 89% of the permeability without overburden pressure.

This chapter examines the impact of stress on porosity, permeability and the electrical properties of 25 TGS samples (Table 3.2) between 1500 and 10,000 psi confining pressure to further understand the *in-situ* behaviour of the properties of TGS. The methodologies are presented in Section 7.2. Results are presented in Section 7.3 and then discussed in Section 7.4. The discussion seeks to bring together these results to understand them and compare how they agree or disagree with other published work. The work in this chapter is then summarised in Section 7.5.

7.2 Methods

The following section presents the methodologies used to study the impact of stress on 25 samples from core set 1 to 5 (Table 3.2). Each core set consisted of 5 core plugs with a similar initial permeability. The petrophysical properties measured include porosity, permeability and electrical properties. For the porosity and electrical properties, the brine saturated cores plus a small amount of brine was placed into a core holder and sealed (Figure 7.1). The extra brine ensured good electrical contact between the end of the sample and the end-platens of the core holder.

Confining pressure was applied using a hydraulic pump and increased to 1500 psi. The top end of the core holder was connected to a pressure transducer and temperature data logger to log the pressures and temperatures respectively. The amount of brine expelled was measured using a burette and the resistance was monitored with a resistance meter (Section 3.4.5).

The resistance at laboratory temperature was then temperature corrected to the reservoir temperature (Equation 2.12 in Section 2.9). This was used to calculate the *FRF* and cementation exponent (Equation 2.13 and Equation 2.15 in Section 2.9). Furthermore, the pore volume reduction vs stress was used to determine porosity vs stress using this relationship:

$$\emptyset = \left(\frac{1}{1 + \frac{GV}{(PV_A - (VB_{1-4500psi} - VB_{0psi}))}} \right) * 100 \qquad \text{Equation 7.1}$$

where ϕ is porosity (%), *GV* is the grain volume (cm^3), PV_A is pore volume at ambient conditions (cm^3) and *VB* is the volume of brine (cm^3).

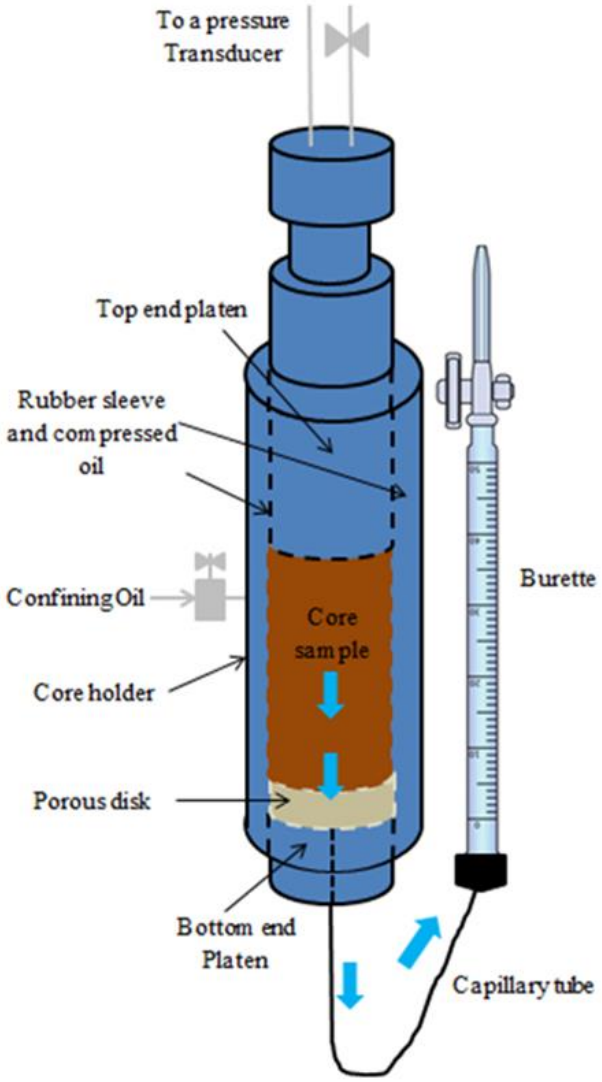

Figure 7.1 Schematic drawing of the set up to measure the effects of stress on TGS – 25 of these were set up to hold the 25 samples from core set 1 to 5 (Table 3.2).

Once the amount of brine expelled and the resistance were stable, the confining pressure was increased in 1000 psi increments and the pore volume reduction and resistance was monitored. The experiment was stopped once the confining pressure had reached 4500 psi and there was no change in the resistance or the amount of brine expelled. The entire experiment took up to 11 months.

The porosity value obtained using Equation 7.1 was compared to a porosity value at increasing confining pressures from 500 to 5000 psi using the relationship presented by the Discovery Group Mesaverde dataset (Byrnes, 2009):

$$\emptyset = \left((A * logCp) + B\right) * \emptyset_{0Pc} \qquad \text{Equation 7.2}$$

where $\emptyset$ is porosity, C_p is confining pressure and $\emptyset_{oPc}$ is porosity at 0 psi capillary pressure. The porosity-stress exponents – A and B can be determined using Equation 7.3 and Equation 7.4. These equations were obtained from the slope and intercept of the trends in Figure 7.2 (Figure 7.3 and Figure 7.4).

$$A = 0.00549 - \left(\frac{0.155}{(\emptyset_{0Pc})^{0.5}}\right) \qquad \text{Equation 7.3}$$

$$B = \frac{1.045 + 0.128}{(\emptyset_{0Pc})} \qquad \text{Equation 7.4}$$

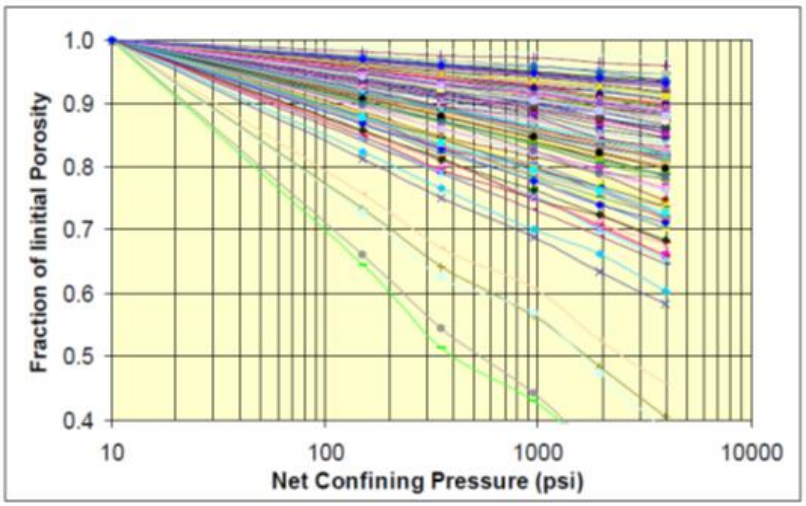

Figure 7.2 Plot of initial pore volume vs net confining stress for 113 Mesaverde samples (Byrnes, 2009).

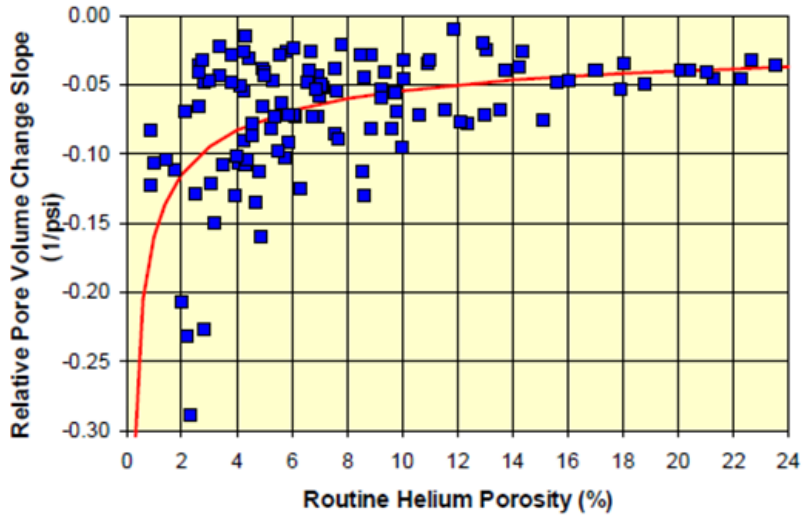

Figure 7.3 Slope of log-linear curves in Figure 7.2 with porosity. The relationship between the slope and porosity is expressed in Equation 7.3 (Byrnes, 2009).

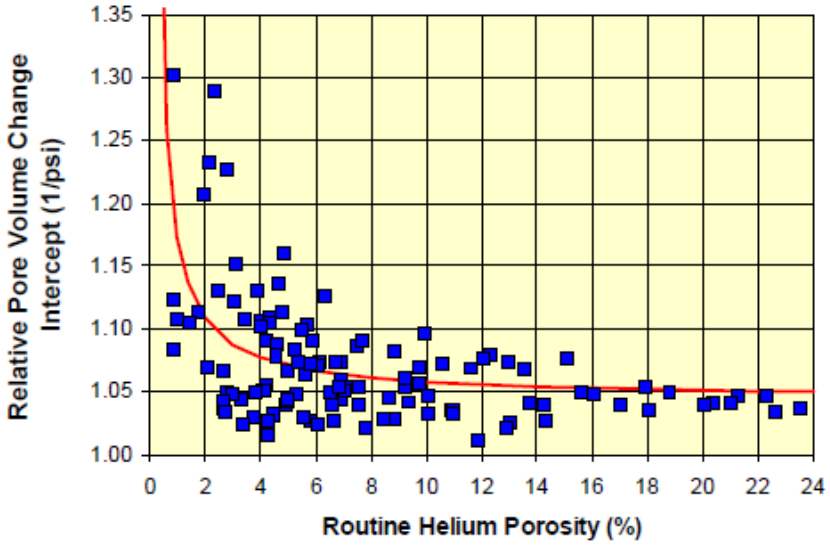

Figure 7.4 Intercept of log-linear curves in Figure 7.2 with porosity. The relationship between the intercept and porosity is expressed in Equation 7.4 (Byrnes, 2009).

The permeability at reservoir conditions was determined using a drawdown test (fixed C_P and decreasing P_P). The drawdown test used a pulse-decay permeametry instrument based on the design by Jones (1972) (Section 3.4.2). The confining pressure used was 10,000 psi and the pore pressure 1500-5000 psi. This was compared to the lower stress data at 500, 1500 and 5000 psi net stress.

The permeability was estimated from MICP data presented in Chapter 6 using the Swanson (1981), Purcell (1949), Katz and Thompson (1986, 1987) and Winland (1980) models. In Chapter 6 the measured permeability at 5000 psi net stress was compared to the estimated permeability. In this chapter the measured permeability at

a net confining pressure equivalent to mercury threshold pressure is compared to the estimated permeability.

The permeability at the threshold pressure was estimated by fitting the following logarithmic relationship to the permeability vs net stress data:

$$k_\sigma = A + Blog(\sigma) \qquad \text{Equation 7.5}$$

where k_σ is the gas permeability at a net threshold pressure of σ (psi) (mD) and *A* and *B* are empirical constants where A is slope and B is y intercept. The permeability-stress exponents – A and B were obtained for each sample by fitting a logarithmic relationship to the intercept and slope (obtained from the permeability vs net stress data) vs permeability data. The A and B values for each sample was obtained by inserting the permeability of each sample into the logarithmic equation for A and B. The A and B values were then used to obtain the permeability at a chosen threshold pressure using Equation 7.5. A good correlation exists between the permeability at the threshold pressure of the sample and the constants A and B (Figure 7.5); this allows the gas permeability at other stresses to be calculated.

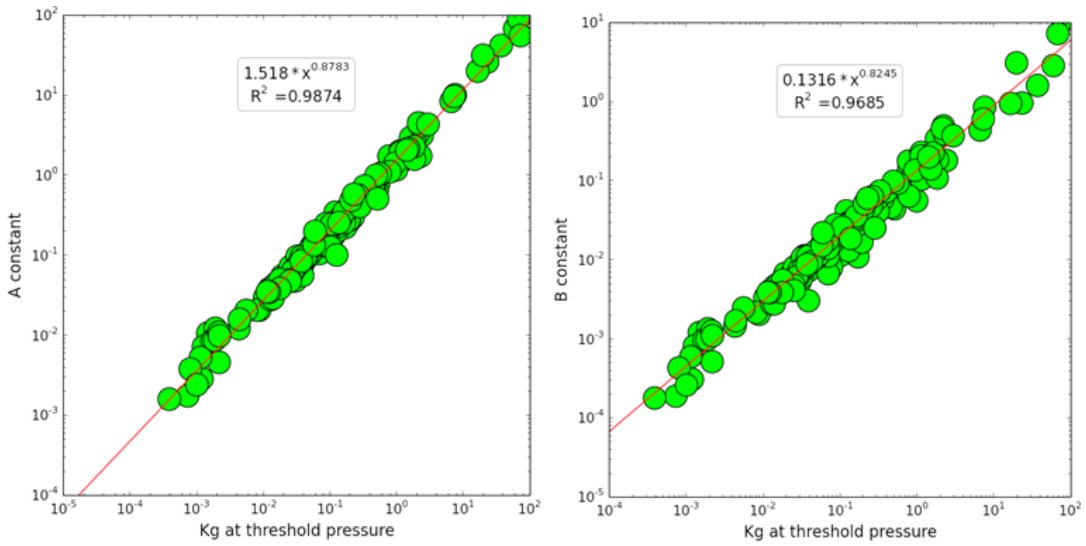

Figure 7.5 Plot of the constant A (left) and constant B (right) on the logarithmic stress relationship for tight gas sandstone permeability showing a good trend. The 25 TGS used in this research were plotted with other TGS data from Fisher (2016).

7.3 Results

This section provides the results of experiments that aim to investigate the impact of confining pressure and stress on the petrophysical properties of TGS. Porosity (Section 7.3.1), permeability (Section 7.3.2), electrical properties (Section 7.3.3) for 25 TGS are presented. Most of the data is presented within this section, however, tables presenting the effects of stress on the petrophysical properties of the 25 TGS are provided in Appendix F.

7.3.1 Porosity vs Stress

The porosity reduction experiments were conducted on core sets 1 to 4 (Table 3.2 in Section 3.2.1). Most of the porosity data showed minor pressure dependency as seen by the almost horizontal data points (Figure 7.6 to Figure 7.9). However, SHELL4_202 had the largest percentage decrease of 7.6% (1.4 pu) with an increase in confining pressure.

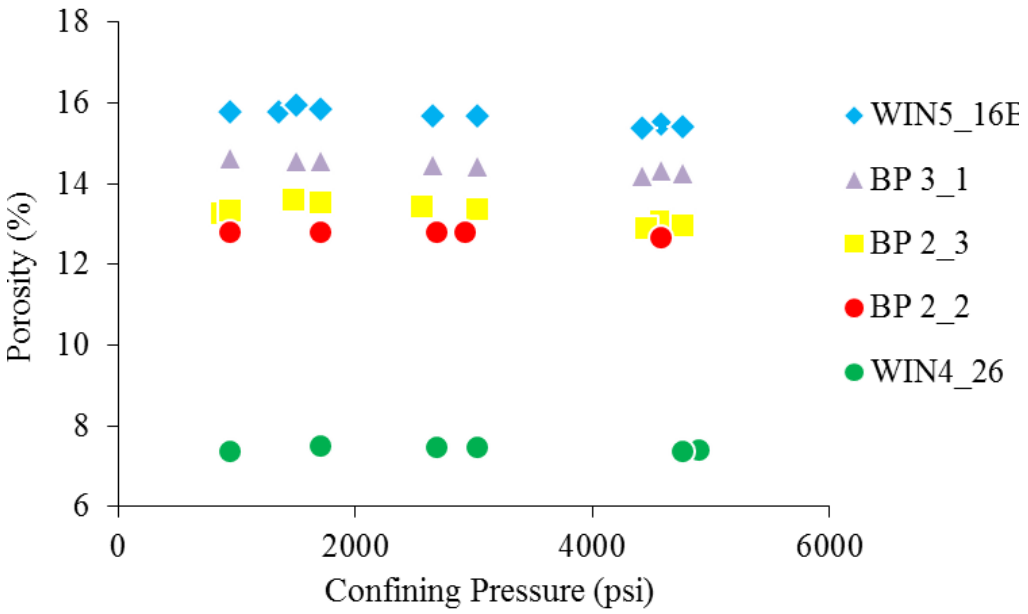

Figure 7.6 Linear plot of porosity as a function of confining pressure for core set 1 showing little variation with pressure.

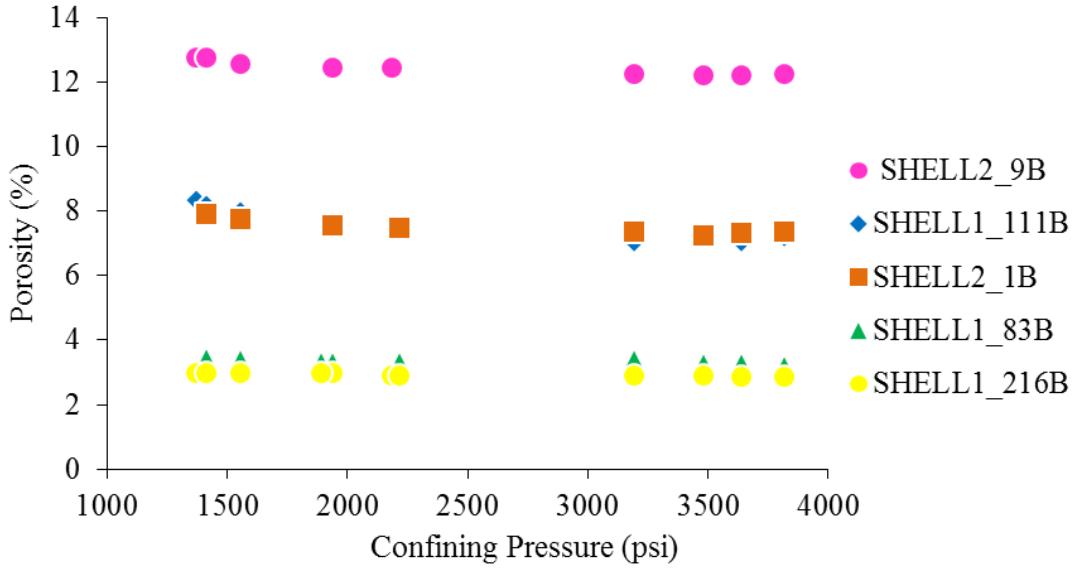

Figure 7.7 Linear plot of porosity as a function of confining pressure for core set 2 showing little variation with pressure.

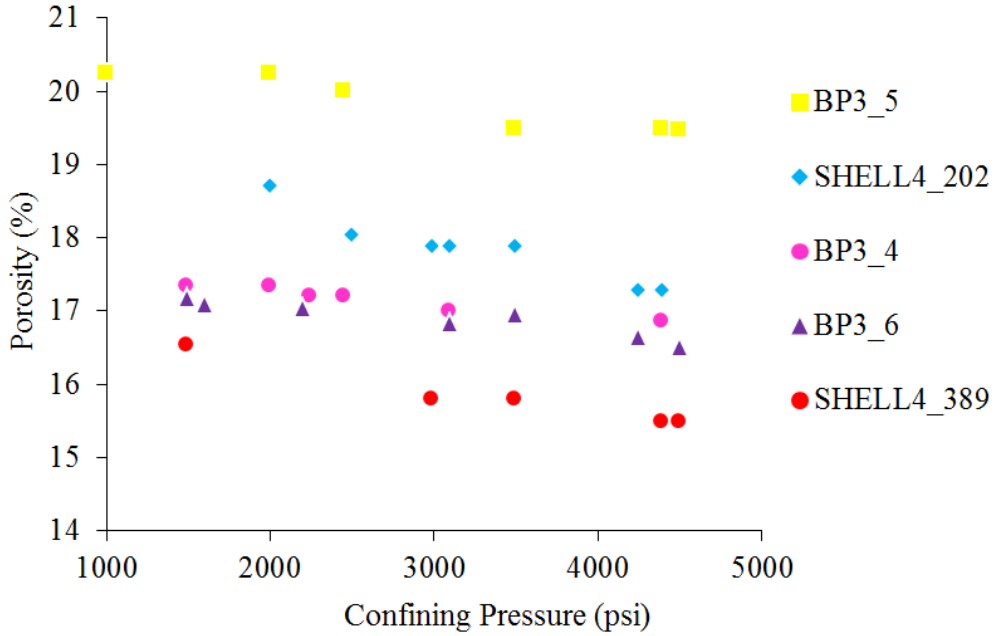

Figure 7.8 Linear plot of porosity as a function of confining pressure for core set 3 showing a slight decrease in porosity with pressure.

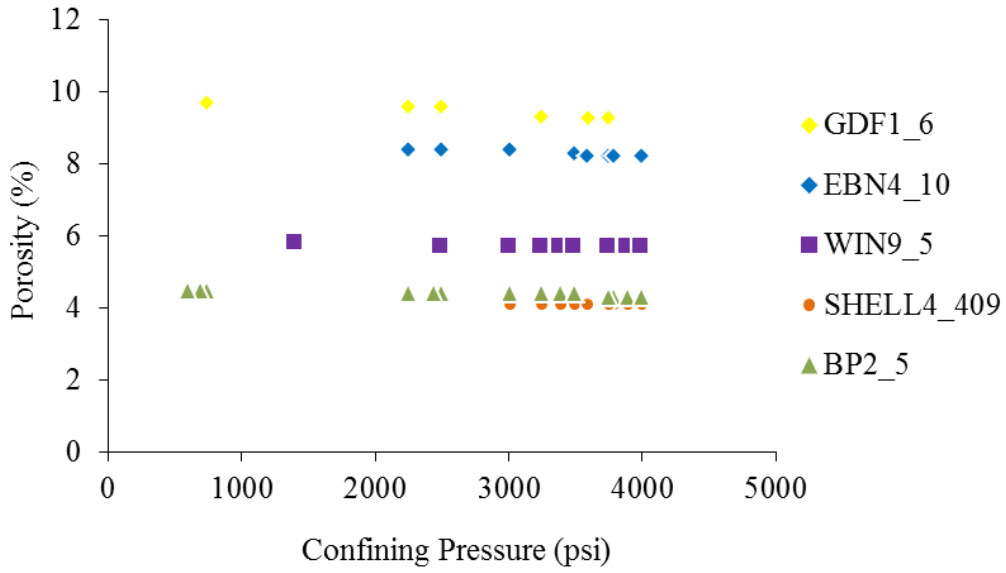

Figure 7.9 Linear plot of porosity as a function of confining pressure for core set 4 showing little variation with pressure. (The lower pressure data for SHELL4_409 was not included due to experimental problems).

7.3.2 Permeability vs Stress

Permeability decreases with an increase in confining pressure (Table 7.1 and Figure 7.10). The permeability of the cores ranges from 6.5 x 10^{-6} to 3.9 mD at 9000 psi, 3 x 10^{-5} to 3.7 mD at 5000 psi, 5.2 x 10^{-4} to 4 mD at 1500 psi and 1.2 x 10^{-3} to 4.1 mD at 500 psi net stress from Chapter 5 (Table 7.1). In addition, the higher permeable samples are not very stress sensitive (Figure 7.10 and Figure 7.11). The lower net effective stress data is on average three times larger than the higher net effective stress data as the data points are far from the 1:1 line at the lower permeability end, whereas, the data converges to the 1:1 line at the higher permeability end (Figure 7.11).

Table 7.1 Gas permeability measured from 1500 to 9000 psi net effective stress for all 25 core plugs showing a decrease in permeabiltiy with stress.

Sample	Kg 500 psi (mD)	Kg1500 psi (mD)	Kg at 5000 psi (mD)	Kg at 9000 psi (mD)
BP2_2	0.13	0.08	0.03	
BP2_3	1	0.6	0.2	
BP2_5	$9.80E^{-03}$	$5.50E^{-03}$	$2.20E^{-03}$	$1.80E^{-04}$
BP3_1	0.7	0.4	0.2	
BP3_4	1.1	0.9	0.7	
BP3-5	0.95	1	0.7	
BP3_6	1.3	1	0.6	
EBN3_40	1.4	1.3	0.7	0.3
EBN4_10	0.04	0.03	0.002	$3.70E^{-04}$
SHELL1_83E	0.003	0.0015	$1.50E^{-04}$	
SHELL1_111	0.02	0.011	0.003	
SHELL1_216B	0.03	0.011	0.005	
SHELL2_9B	0.6	0.4	0.3	
SHELL2_1B	0.5	0.3	0.3	
SHELL4_202	0.3	0.2	0.05	0.05
SHELL4_370	1	1	0.9	0.9
SHELL4_389	0.9	0.1	0.04	0.03
SHELL4_409	$1.2E^{-03}$	$5.2E^{-4}$	3.25E-05	6.50E-06
GDF1_1	1.3	1.1	0.8	0.8
GDF1_6	$9.60E^{-03}$	$9.30E^{-03}$	$8.50E^{-04}$	$2.30E^{-04}$
GDF1_7	4.1	4	3.7	3.4
GDF2_4	3.6	3.1	3.1	3.9
WIN4_26	0.1	0.06	0.02	
WIN5_16B	0.03	0.02	0.01	
WIN9_5	$9.20E^{-03}$	$4.20E^{-03}$	$3.00E^{-05}$	$7.00E^{-06}$

Notes: those samples at 9000 psi that are shaded in grey were not performed as the higher pressure instrument was not available until later on in the research. The samples in red are pulse-decay and those in blue are steady-state.

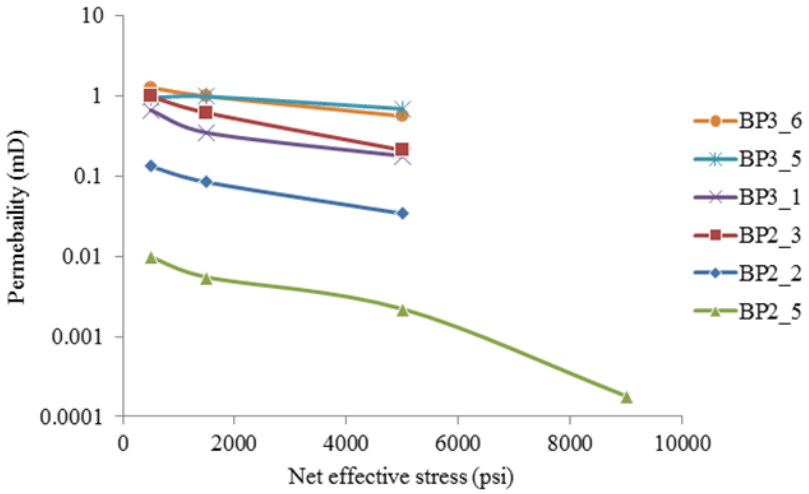

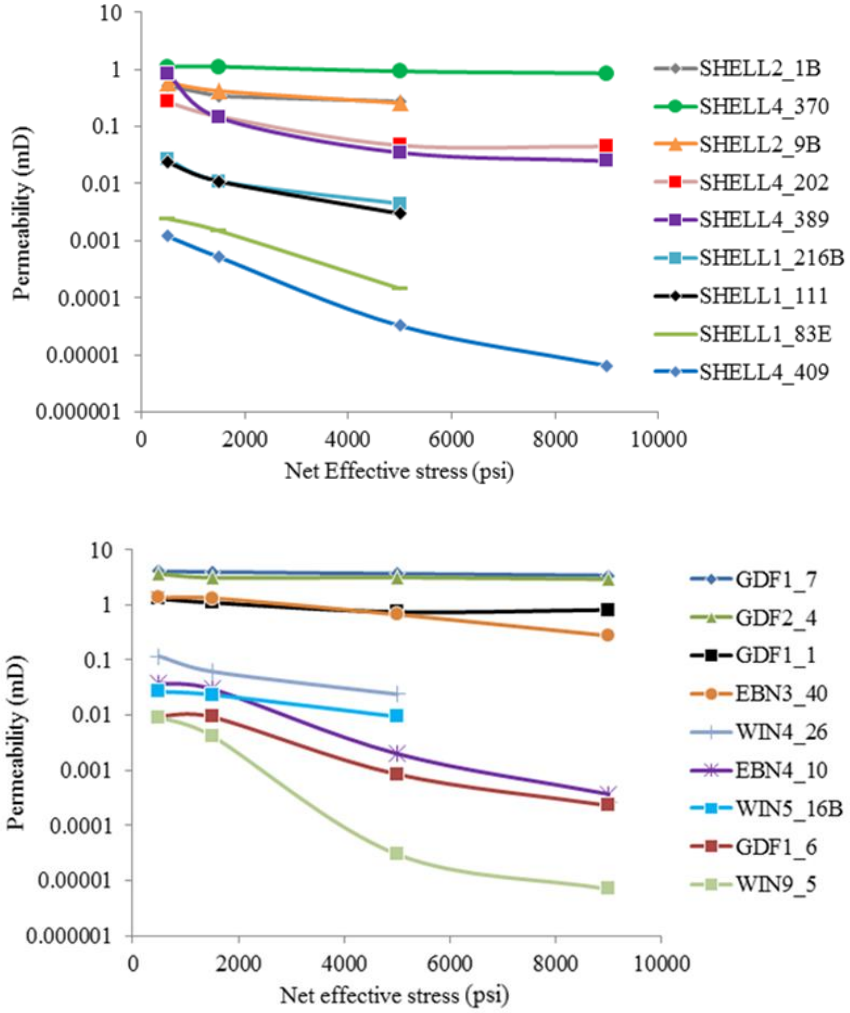

Figure 7.10 Permeability as a function of net effectives stress for all samples. There is a decrease in permeability for the lower permeable samples whereas the higher permeable samples are less stress sensitive.

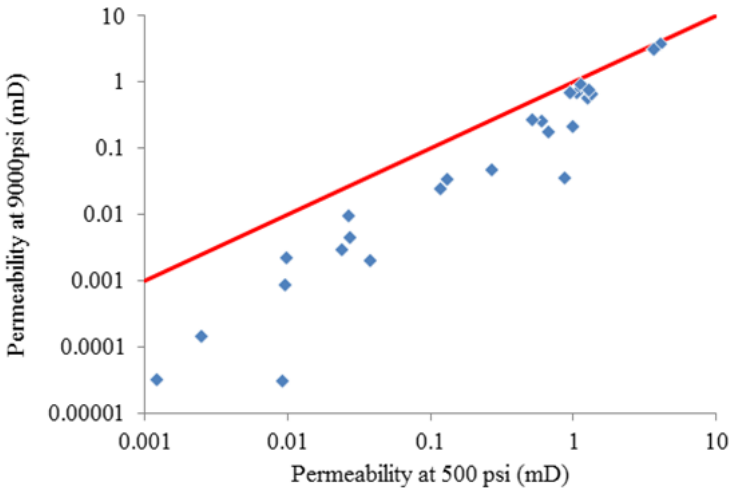

Figure 7.11 Plot of permeability at 9000 psi net effective stress as a function of permeability at 500 psi net effective stress. There is a larger permeability difference for the lower permeability samples.

7.3.3 Formation Resistivity Factor and Cementation Exponent vs Stress and Porosity

The effect of confining pressure on the *FRF* of fully saturated samples was measured on all the core sets (Table 3.2 in Section 3.2.1). The *FRF* increases with confining pressure where the average *FRF* at 1000 psi confining pressure and 4500 psi confining pressure is ~183 and ~ 624 respectively leading to a 57% increase in *FRF* (Figure 7.12 to Figure 7.16). The largest increase was ~ 1100 for WIN9_5.

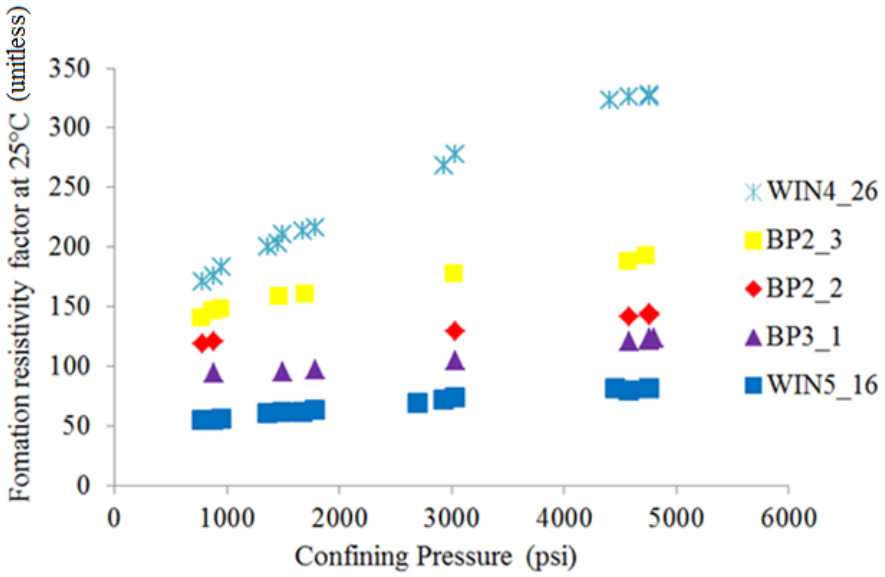

Figure 7.12 Linear plot of formation resistivity factor as a function of confining pressure for core set 1 showing an increase in FRF with pressure.

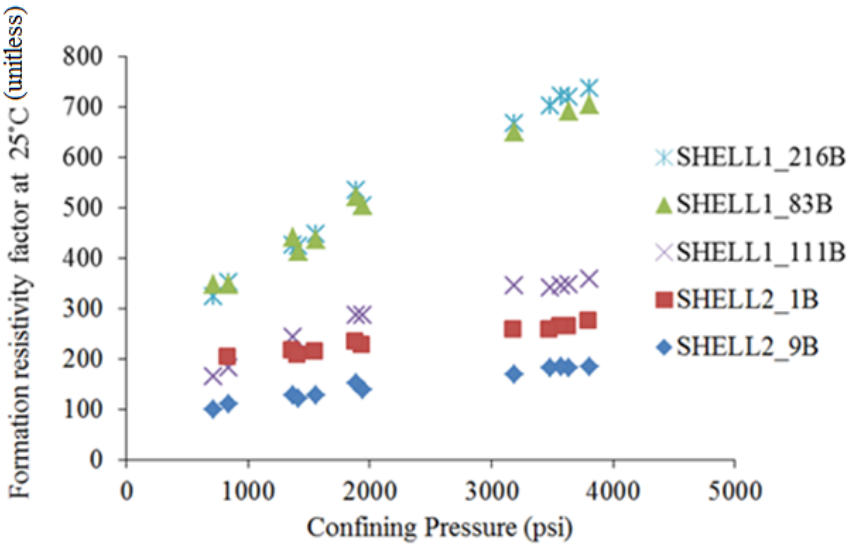

Figure 7.13 Linear plot of formation resistivity factor as a function of confining pressure for call set 2 showing an increase in FRF with pressure.

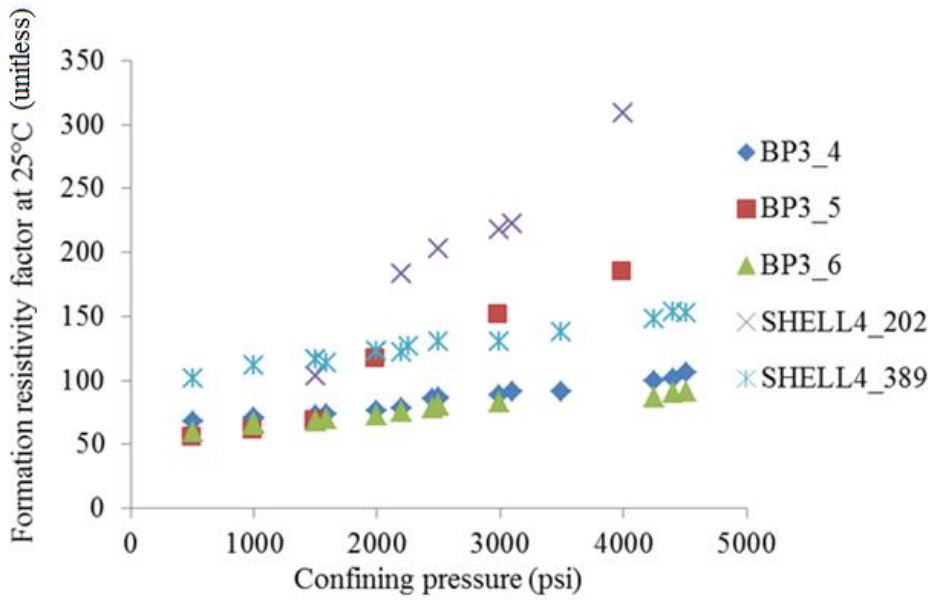

Figure 7.14 Linear plot of formation resistivity factor as a function of confining pressure for core set 3 showing an increase in FRF with pressure.

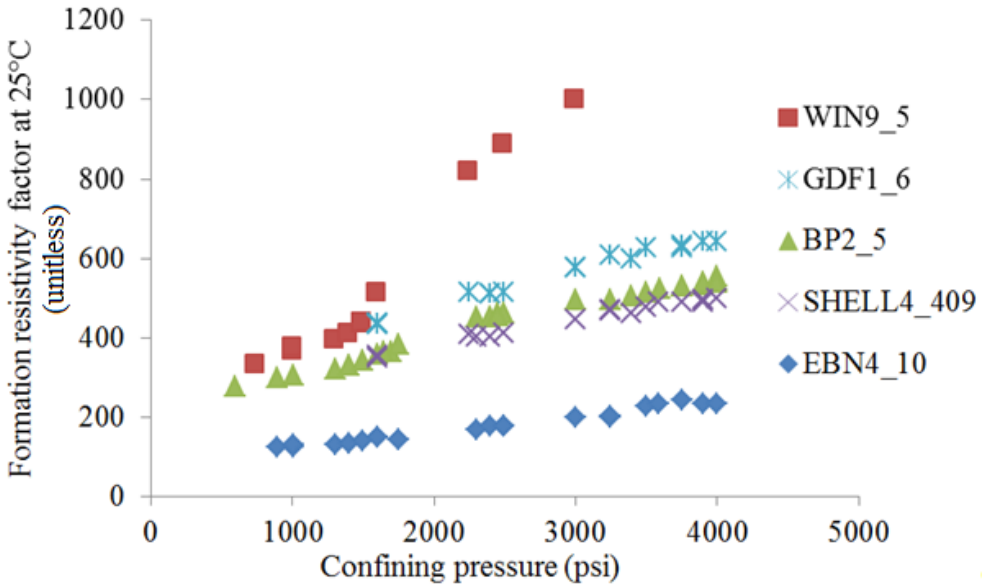

Figure 7.15 Linear plot of formation resistivity factor as a function of confining pressure for core set 4 showing an increase in FRF with pressure.

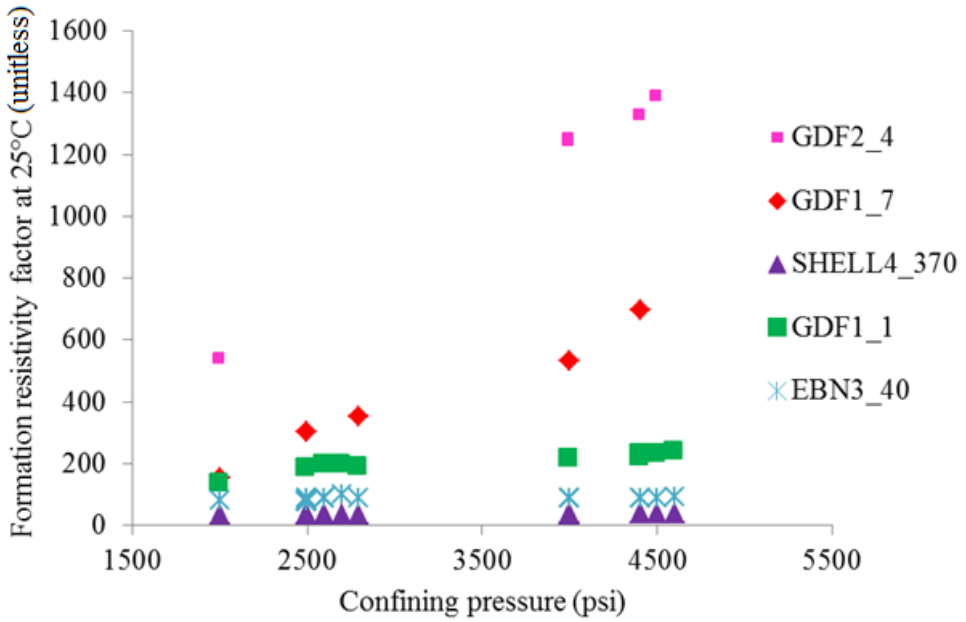

Figure 7.16 Linear plot of formation resistivity factor as a function of confining pressure for core set 5 showing an increase in FRF with pressure.

The effect of confining pressure on the cementation exponent of fully saturated samples was measured on all the core sets (Table 3.2 in Section 3.2.1). The results indicate that *m* increases with confining pressure where the average *m* at 1000 psi and 4500 psi is ~ 2 and ~2.2 respectively leading to a 8% increase in *m* (Figure 7.17 to Figure 7.21). In addition, *m* increased with porosity (Figure 7.22), this supports the data presented in Section 6.4.1 Figure 6.8.

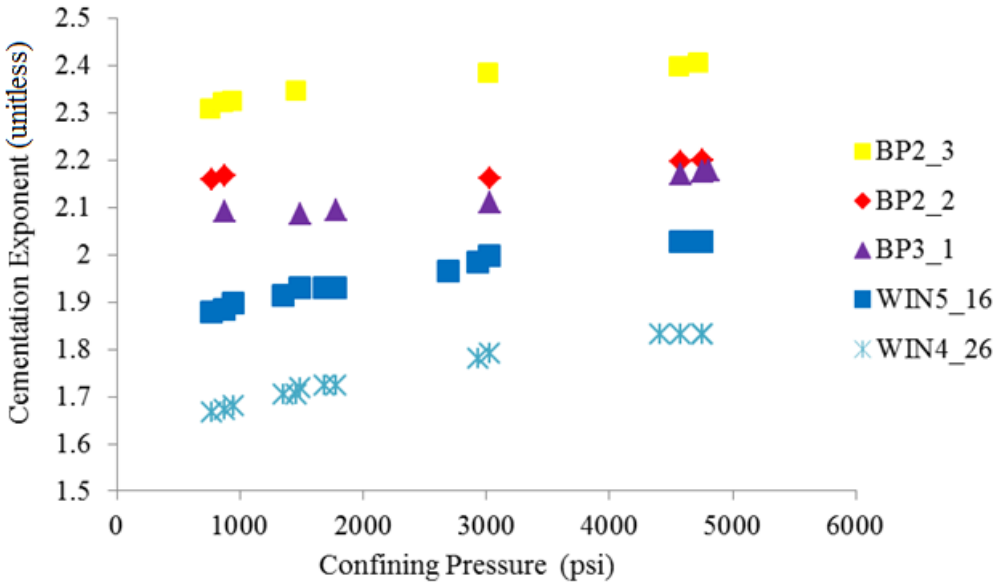

Figure 7.17 Linear plot of cementation exponent vs confining pressure for core set 1 showing an increase in m with pressure.

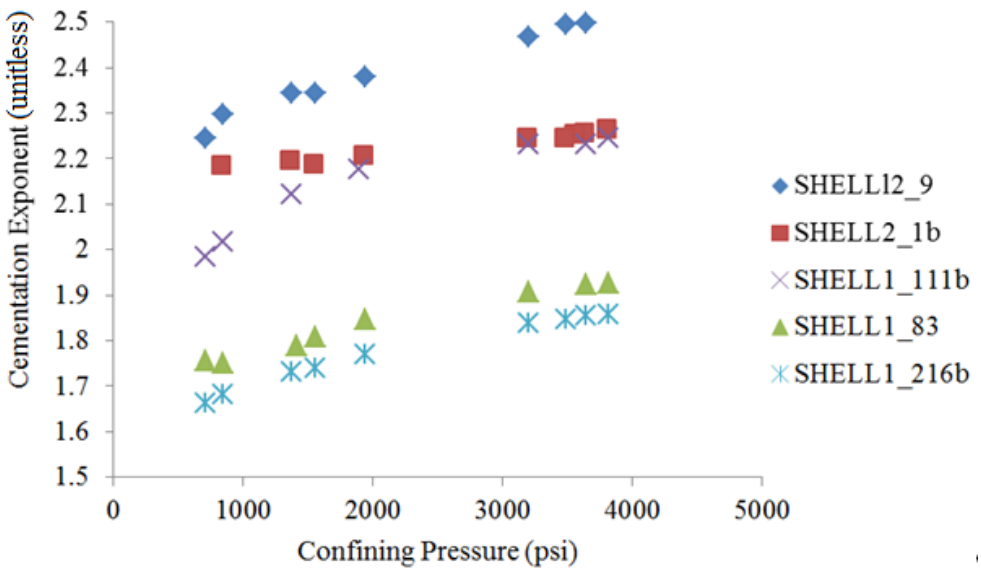

Figure 7.18 Linear plot of cementation exponent vs confining pressure for core set 2 showing an increase in m with pressure.

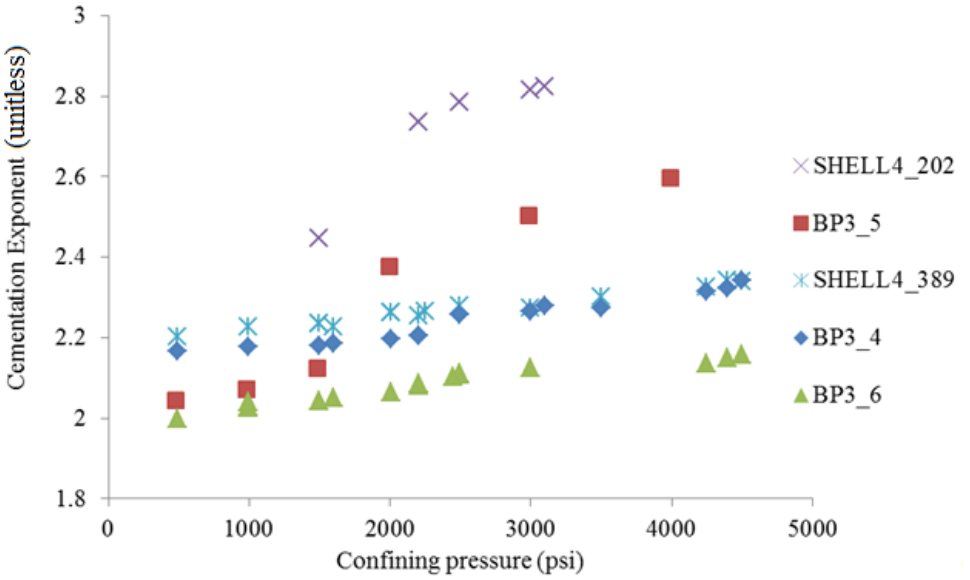

Figure 7.19 Linear plot of cementation exponent vs confining pressure for core set 3 showing an increase in m with pressure.

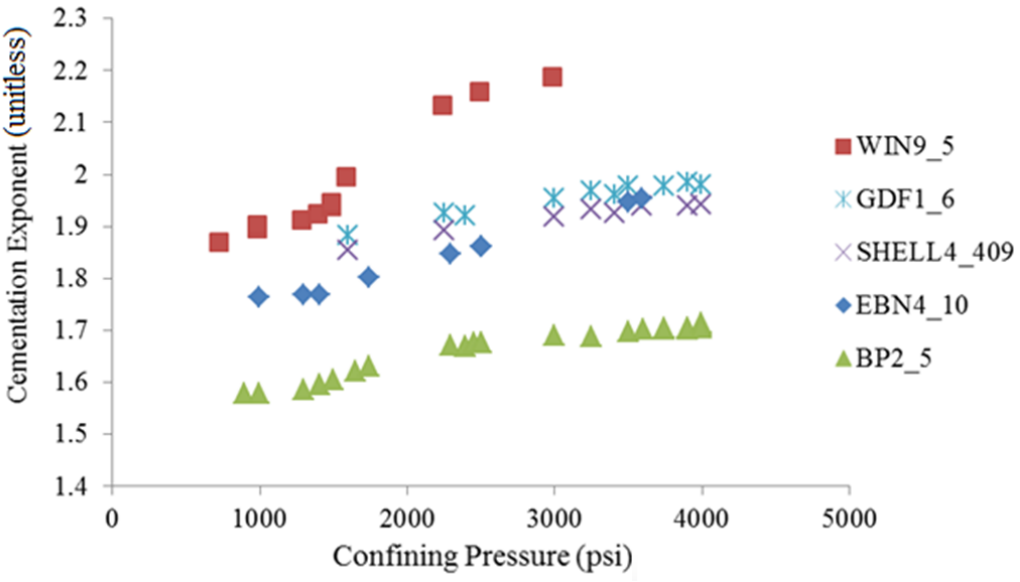

Figure 7.20 Linear plot of cementation exponent vs confining pressure for core set 4 showing an increase in m with pressure.

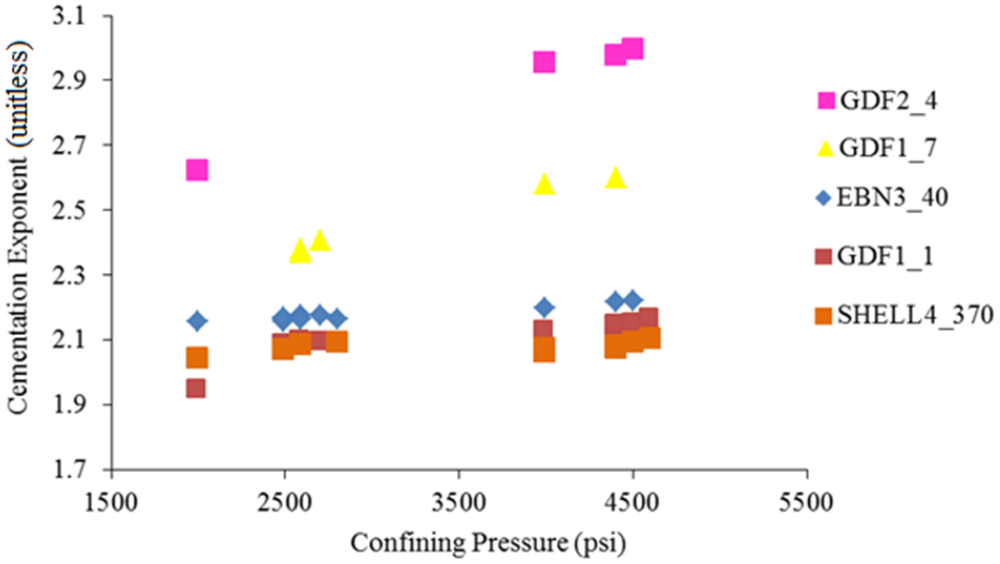

Figure 7.21 Linear plot of cementation exponent vs confining pressure for core set 5 showing an increase in m with pressure.

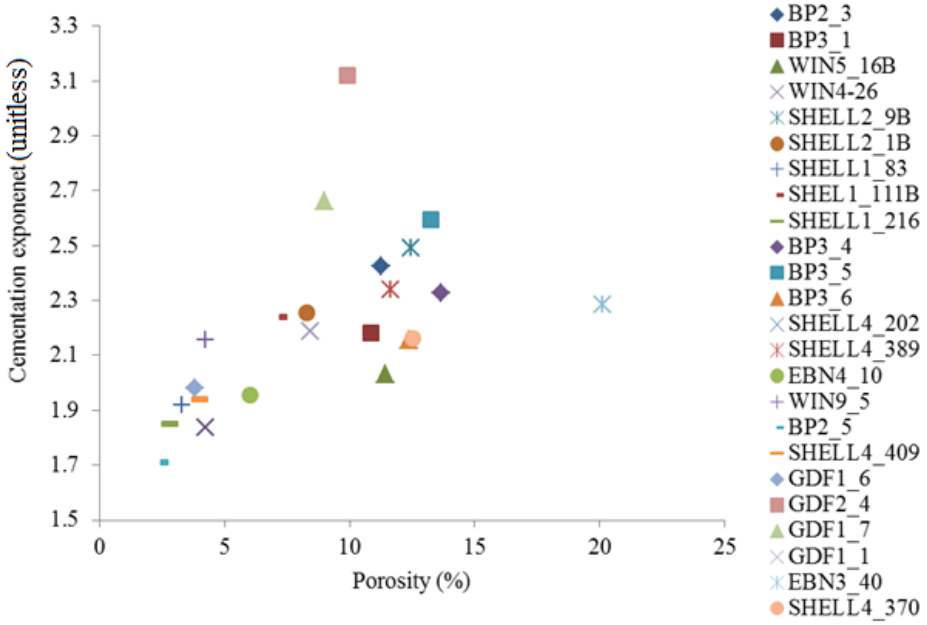

Figure 7.22 Linear plot of cementation exponent as a function of porosity for all five core sets at a confining pressure of ~4500 psi showing an increase in m with porosity.

7.4 Discussion

This section discusses the effects of confining pressure on porosity (Section 7.4.1), impact of stress on gas permeability (Section 7.4.2), impact of confining pressure on brine permeability (Section 7.4.3) and the impact of confining pressure on *FRF* and cementation exponent (Section 7.4.4). This is followed by the impact of threshold pressure on MICP permeability (Section 7.4.5).

7.4.1 Impact of Confining Pressure on Porosity

A comparison was made between i) porosity from 1500 psi to 4500 psi confining pressure, ii) the porosity at 500-4500 psi net stress vs stress data presented by the Discovery Group Mesaverde dataset (Byrnes and Cluff, 2009), and iii) the average porosity at 4500 psi net stress using the relationships developed for the Discovery Group Mesaverde dataset (Byrnes and Cluff, 2009) vs ambient porosity presented in Chapter 5. The aim was to understand how porosity values obtained from laboratory measurements relate to subsurface values.

Porosity does not decrease dramatically with increasing confining pressure from 1500 to 4500 psi where the largest percentage difference was just 7.6% (Figure 7.6 to Figure 7.9). The Discovery Group Mesaverde dataset and the porosity measured

between 500 and 4500 psi are both consistent and they do not change significantly with an increase in confining pressure as seen by the horizontal lines (Appendix F). The difference between the ambient porosity data from Chapter 5 compared to the average porosity at 4500 psi confining pressure using the relationships developed for the Discovery Group Mesaverde dataset (Byrnes and Cluff, 2009) was an average of 3.5 porosity units (Table 7.2). Nevertheless, these small changes in porosity could still lead to considerable changes in other derived properties such as gas in place (GIP). Therefore, a sensitivity analysis needs to be conducted depending on the desired properties of the reservoir (for example the volume), to determine the potential impact of this possible variation.

Table 7.2 Ambient porosity and the Discovery Group Mesaverde dataset porosity at 4500 psi using the porosity stress exponents in Equation 7.3 as well as the difference in porosity units (pu).

Core set	**Sample**	**Ambient porosity (%)**	**Porosity-stress exponents**		**Porosity 4500 psi (%)**	**Difference (pu)**
			A	B	3.7	
1	BP2_2	12	-0.05	1.06	10.5	1.5
	BP2_3	13	-0.05	1.06	7.1	5.9
	BP3_1	13	-0.05	1.06	9.2	3.8
	WIN4_26	6	-0.07	1.07	2.6	3.4
	WIN5_16B	13	-0.05	1.06	12.1	0.9
2	SHELL1_83E	4	-0.08	1.08	0.3	3.7
	SHELL1_111	8	-0.06	1.06	8.3	0.3
	SHELL2_9B	12	-0.05	1.06	7.6	4.4
	SHELL2_1B	8	-0.06	1.06	4.8	3.2
	Shell1_216	3	-0.10	1.09	1.9	1.1
3	BP3_4	17	-0.04	1.05	16.5	0.5
	BP3-5	16	-0.04	1.05	5.2	10.8
	BP3_6	15	-0.05	1.05	12.3	2.7
	SHELL4_202	16	-0.04	1.05	8.2	7.8
	SHELL4_389	14	-0.05	1.05	9.4	4.6
4	EBN4_10	8	-0.06	1.06	4.0	4.1
	WIN9_5	6	-0.07	1.07	4.8	1.2
	BP2_5	5	-0.07	1.07	3.6	1.4
	SHELL4_409	5	-0.07	1.07	4.0	1.0
	GDF1_6	5	-0.07	1.07	3.9	1.2
5	GDF1_7	10	-0.05	1.06	8.5	1.5
	GDF2_4	11	-0.05	1.06	6.8	4.3
	EBN3_40	21	-0.04	1.05	16.5	4.5
	SHELL4_370	15	-0.05	1.05	4.5	10.5
	GDF1_1	10	-0.05	1.06	8.1	1.90

The Discovery Group Mesaverde dataset porosity values are sometimes lower than those made at 500-4500 psi net stress during the current study (Appendix F). This

could be because the methodology of porosity determination with confining pressure is different. The Discovery dataset uses porosity stress exponents obtained from the slope and intercept of a graph of porosity as a function of net confining pressure, an ambient porosity of the sample and the log of the confining pressure. Porosity reduction was calculated during the current study using the grain volume, original pore volume and the amount of brine expelled at 0 psi and 500 to 4500 psi confining pressure. However, the Discovery Group Mesaverde dataset porosity values could have just been lower than the porosity values of the samples used in this research.

Many other studies have indicated that porosity is not as stress dependent as other properties (e.g. Fatt and Davis, 1952; Fatt, 1953, 1958; Dobryni, 1962; Vairogs et al. 1971; Thomas and Ward, 1972; Luffel, 1991 - Figure 7.23 and Byrnes, 1996 - Figure 7.23). For example, Byrnes (1996) found that the helium porosity values measured at ambient stress tend to be within 95% of those in the reservoir. Jones and Owens (1980); Luffel (1991) found that the porosity decreased by 0.5 to 1.0 porosity units from ambient to net overburden stress. Chen (2002) found a large decrease in porosity in two samples (sample 20 and 39 in Figure 7.24), which was in contrast to the third sample (sample 52 in Figure 7.24). The samples that had experienced a large porosity reduction had large axial directional fractures whereas the sample whose porosity was not so stress dependent did not contain these fractures.

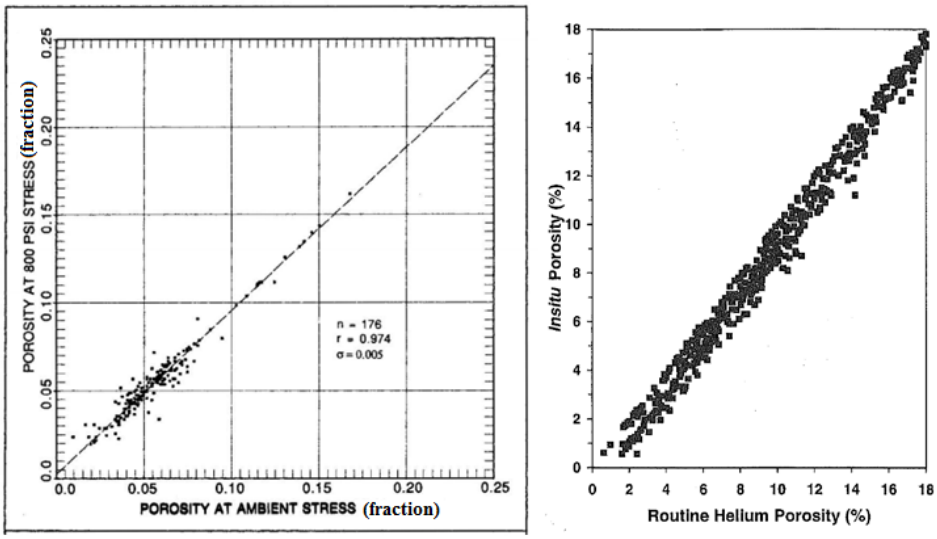

Figure 7.23 Porosity at 800 psi as a function of ambient porosity showing the data points sit close to and on the 1:1 line (from Luffel 1991) (left). In-situ porosity as a function of routine helium porosity showing the data points sit close too and on the 1:1 line (Byrnes, 1996) (right).

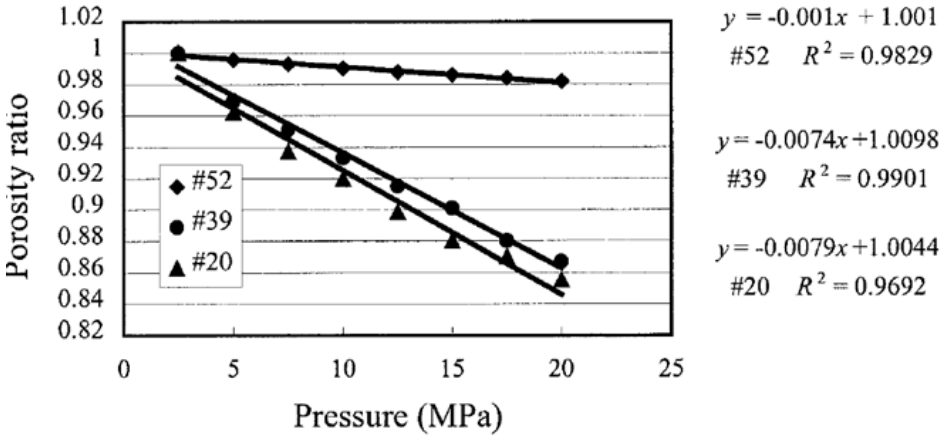

Figure 7.24 Porosity as a function of pressure showing small change in porosity for sample 52 and large changes for the fractured samples - 20 and 39 (Chen, 2000).

Byrnes (1996) stated that in low permeability sandstones the pore space is enclosed by a ridged framework which resists the effects of stress. BSE analysis (Chapter 5) indicates that some samples contain illite that coats the grains which could potentially resist compression. However, this is not likely as although the illite is well structured and forms thick blades, the illite is the most delicate mineral in the TGS in this research.

Bernabe et al. (2003) stated that the conductive porosity (i.e. pore throats) that control the permeability are more stress sensitive then the non-conductive porosity (i.e. the pore bodies). During the BSE examination microfractures of 1-5 μm width were found between grain contacts. Therefore, if the larger pores which occupy the largest amount of pore space are not as deformed compared to the grain boundary microfractures which occupy the smallest pore space, the porosity will not decrease dramatically. This is potentially the reason for the lack of stress dependency for porosity. The evidence for the closure of microfractures rather than the closure of large pore bodies with stress will be discussed in Chapter 8.

7.4.2 Impact of Stress on Gas Permeability

The gas permeability decreases by 69% from 500 psi to 9000 psi net stress (Table 7.1, Section 7.3.2). Several studies have shown that permeability of tight gas sandstones decreases with stress. For example, Gray et al. (1963) showed that permeability of several Berea and Bandera sandstone decreases upon application of simulated overburden pressure. Ostensen (1983) argued that flow rates in tight gas

reservoirs are frequently much lower than predictions based on routine core analysis data and that a factor of ten is not uncommon. Similarly, Byrnes (1996) stated that *in-situ* effective gas permeability ranges from 10 to 1000 times less than routine air permeability. Sigal (2002) argued that applied net confining pressure can sometimes lead to an order of magnitude decrease in permeability. Jones (1997) found the gas permeability decreased by 90% in the tight gas reservoirs when the cores were compressed.

Many studies have also shown that the stress dependency of permeability increases with decreasing permeability (Fatt, 1952 and 1953; McNally et al., 1958; Wyble, 1958; Gray, 1963; Vairogs, 1971 (Figure 7.25); Thomas and Ward, 1972; Brighenti, 1989; Byrnes, 1996 (Figure 7.26) and Jones, 2001). The same conclusion can be found in this research as seen in Figure 7.11. Latchie et al. (1958) found that the irreversible reduction of permeability was 4% in the high permeability cores and reached up to 60% in the low permeability cores. Junchang et al. (2013) concluded that from the mercury injection data the lower the initial gas permeability the stronger the stress sensitivity as they have fewer larger pore throats.

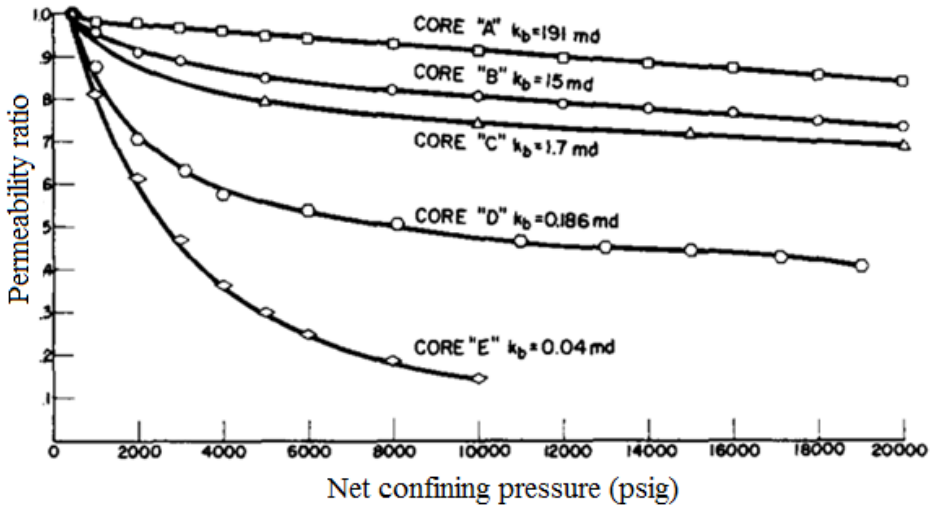

Figure 7.25 Permeability ratio as a function of net confining pressure showing those samples with low permeabilities are more stress dependent then the higher permeable samples (Vairogs, 1971)

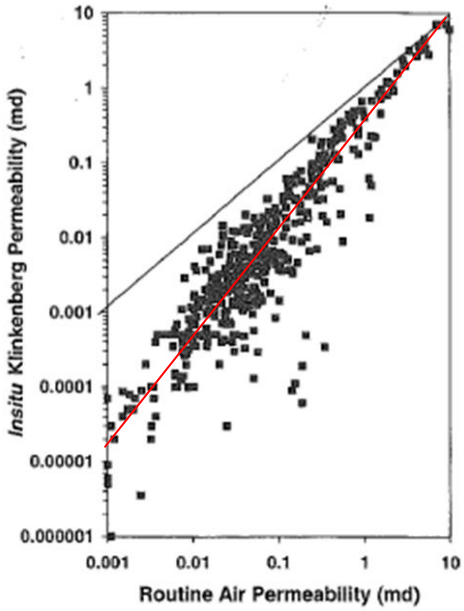

Figure 7.26 Log: log plot of in-situ permeability as a function of routine air permeability showing those samples with low permeabilities are more stress dependent then the higher permeable samples (Byrnes, 1996).

One of the possible reason for the decrease in permeability is related to the decrease in the cross-sectional area of the fluid flow paths as net confining pressure is increased (Sigal, 2002). More specifically, Takahashi et al. (1995) stated that the reduction in permeability is due to the closure of low aspect ratio pores; this is supported by Jones and Owen (1980) and Ostensen (1983). Microfractures were present around grain contacts in all the TGS samples and their closure could have a drastic effect on the connectivity of the pores (Section 5.3.4 and Figure 7.27). This is further studied in Chapter 8.

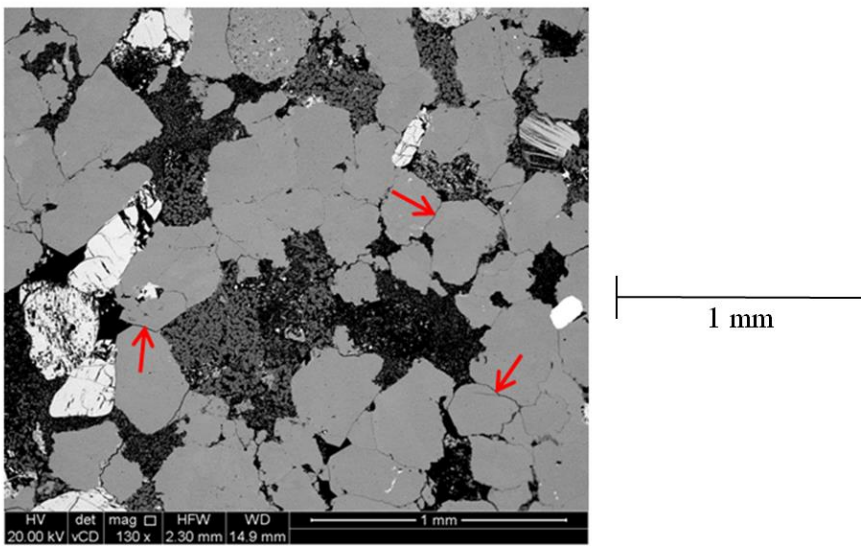

Figure 7.27 BSEM image of BP3_4 showing the presence of microfractures surrounding all the grains (red arrow). These microfractures close under stress and reduce permeability.

Another reason for the decrease in permeability with an increase in pore pressure could be due to the narrow pore sizes present in TGS therefore a phenomena called slippage could occur. Slippage effect as described by Klinkenberg (1941) occurs when the mean path of the gas molecule is longer than the distance between the pore wall and the molecule. This results in non-laminar flow of gas along the flow direction as molecules do not collide with each other anymore and instead flow along the pore throat. This flow is inversely proportional to the pressure, whereby a reduction in pore pressure causes an increase in the mean free path of the molecule. This is observed in this research where the permeability is found to increase with a fixed confining pressure but decrease in the pore pressure (Figure 7.28).

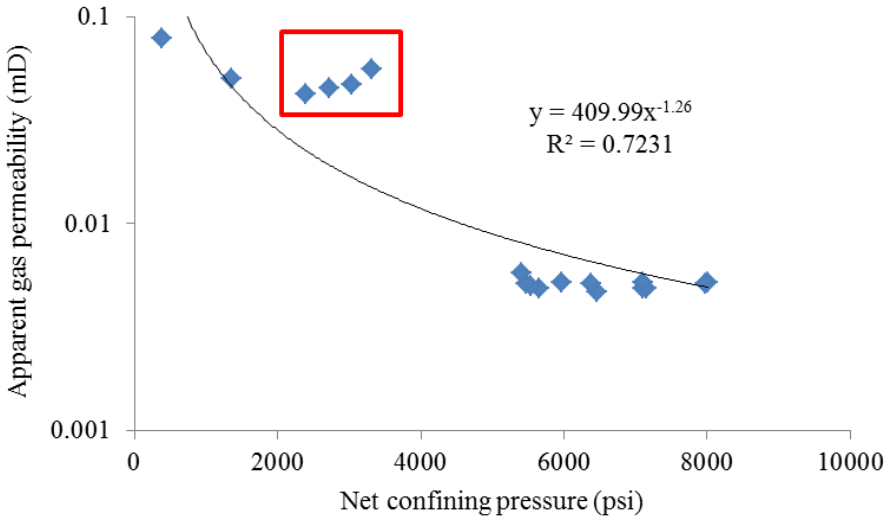

Figure 7.28 Apparent gas permeability vs net confining pressure for EBN3_10. The permeability data in the red box is due to a fixed confining pressure and reduced gas pressure leading to an increase in permeability with net stress. Similar trends are found with the other 24 samples (Table 3.1) .

Slippage is strongest at the pore throats which are equal or lower than the free molecular flow path, this pore throat size is presented as 10-100 nm by Javadpour (2009) and Freeman (2011). In TGS there might be pores of this size but most of the pores are likely to be larger i.e. 30-2000 nm from Nelson (2009). Therefore though there is evidence for both slippage and microfractures it is most likely that the effects of microfracture are stronger than the effects of slippage. These microfractures could act as flow pathways at low stress but could close at higher confining pressures causing the permeability to decrease. The evidence for the closure of the microfractures as the cause of the stress dependency found in TGS will be addressed in Chapter 8.

7.4.3 Impact of Confining Pressure on Brine Permeability

Initial experiments indicated that brine permeability was not as stress sensitive as gas permeability. For example, the gas permeability decreased by 99% for WIN9_5 and by 61% for BP2_5. In comparison, the brine permeability decreased by 38% for WIN9_5 and 51% for BP2_5 (Figure 7.29). It was suspected that the brine permeability appeared not to be as stress sensitive because the presence of brine had prevented the samples reaching pressure equilibrium. Therefore, an experiment was conducted in which a sample was saturated at the maximum confining pressure and permeability measurements were made as the confining pressure was (i) decreased in 2 hour increments, (ii) followed by an increase in confining pressure after 24 hours, (iii) followed by a decrease in confining pressure after 4 days (Figure 7.30).

The data shows that brine permeability decreases by 80% after 4 days of pressure equilibration compared to 40% after 2 hours of pressure equilibration. Therefore, the lack of stress dependency is indeed due to the time allowed for the sample to reach pressure equilibrium at each pressure step. The pores and pore throats that should have been closed at a particular pressure were still open after 2 hours of pressure equilibrium; however, after 4 days of pressure equilibrium, the sample had time to adjust to the applied pressure. The data shows that longer time periods are required for the sample to reach equilibrium after confining pressure is increased than the 2 hours that was initially used. Future work is needed to model this equilibrium time.

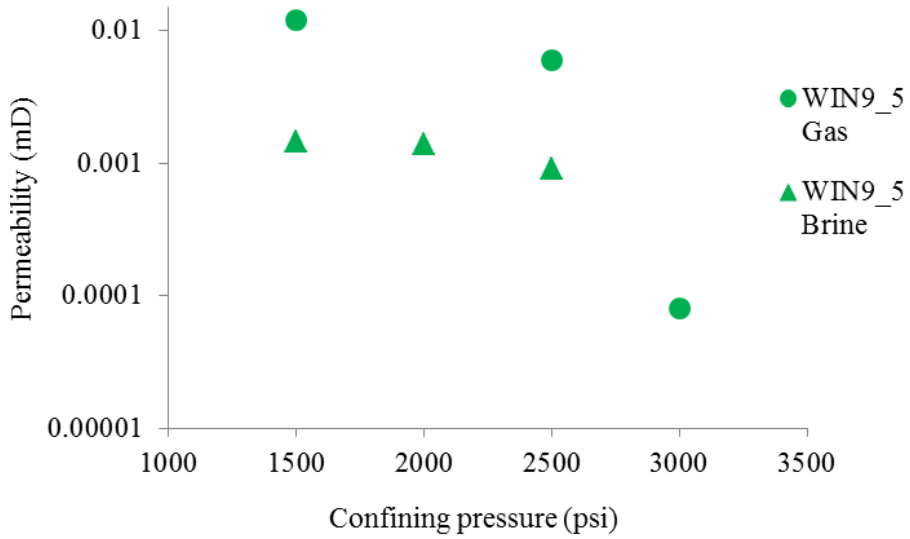

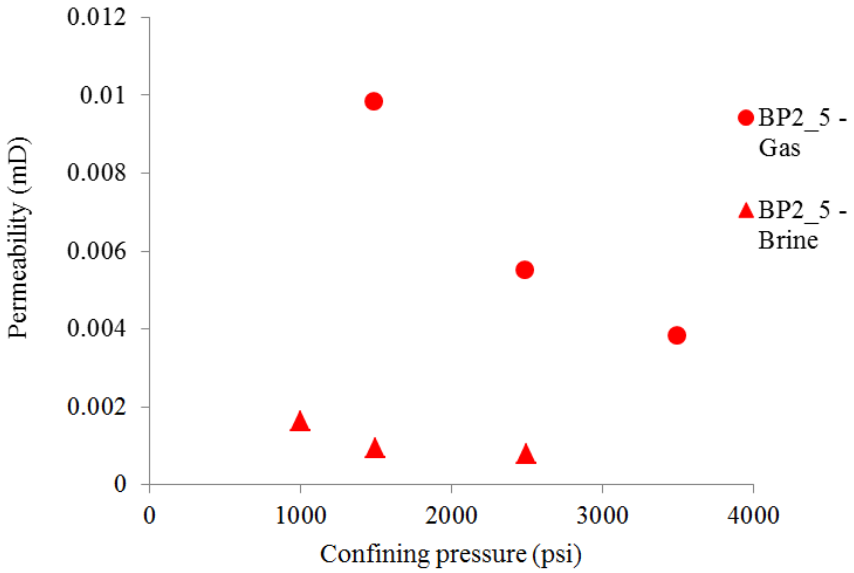

Figure 7.29 Permeability as a function of confining pressure for WIN9_5 and BP2_5 showing the gas permeability is more stress sensitive than the brine permeability.

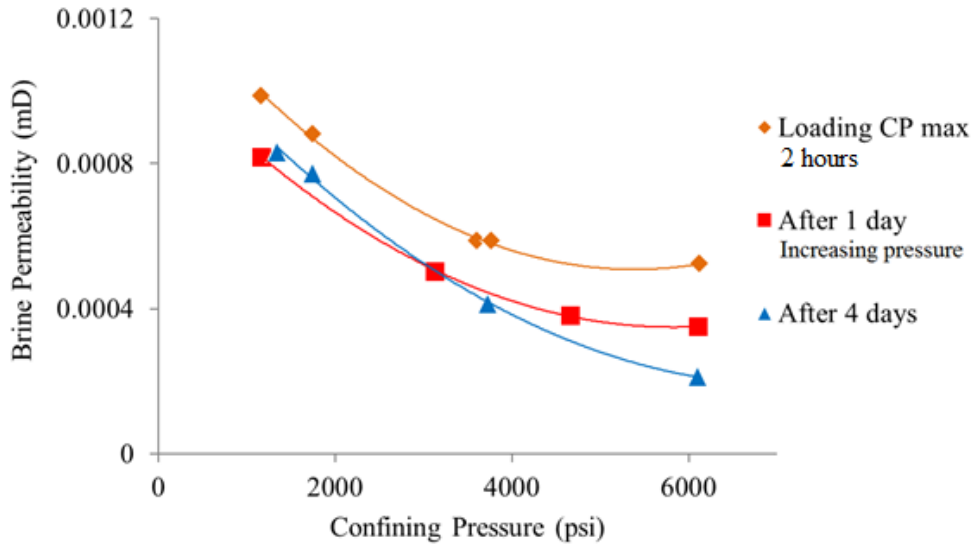

Figure 7.30 Brine permeability as a function of confining pressure for different equilibration times (orange: instant loading to maximum pressure then decrease in 2 hour increments, red: increasing pressures in 1 day increments and blue: decreasing pressure in 4 day increments). There is a 40% difference in the reduction in permeability between the sample at 4 days of pressure equilibrium vs 2 hours.

7.4.4 Impact of Stress on Electrical Properties

The *FRF* (Figure 7.12 to Figure 7.16 in Section 7.3.3) and *m* (Figure 7.17 to Figure 7.21 Section 7.3.3) increased with net confining pressure. This has been previously reported by several authors (Glanville, 1959; Fatt, 1957; Mahmood, 1991; Hausenblas, 1995 (Figure 7.31) and Mohammed, 2015). The effects are greatest for

lower porosity samples (Glanville, 1959 and Mahmood, 1991), which supports the current research data, for example, WIN4_26 has the lowest porosity of around 4.5% (Figure 7.6) and therefore the highest *FRF* (170-387) (Figure 7.12) in core set 1. Similar patterns can be seen in core sets 2 and 3.

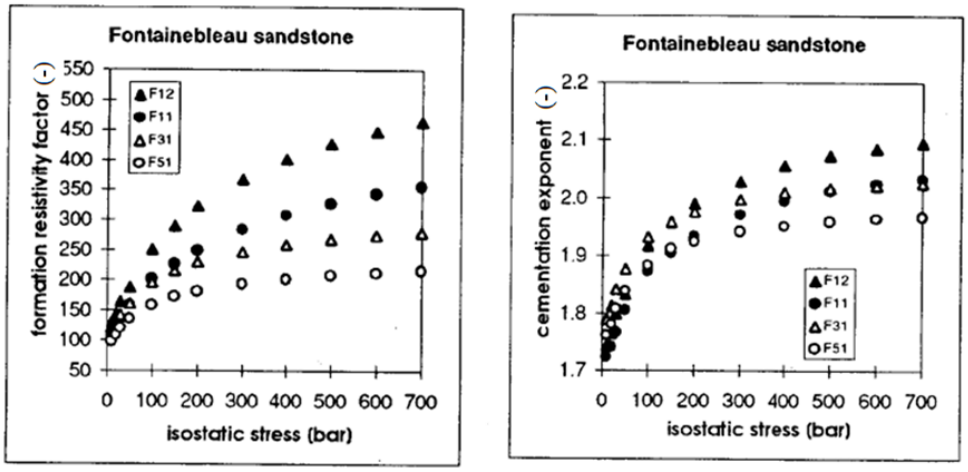

Figure 7.31 Formation resistivity factor and cementation exponent vs stress showing an increase in FRF and m with stress (from Hausenblas, 1995).

The stress sensitivity present in the electrical properties is related to changes in the pore structure (Mahmood, 1991) and especially the closure of microfractures (Brace et al,. 1965; Wyble, 1958; Mohammed, 2015 and Zisser and Nover, 2009). Dobrynin (1962) pointed out that the resistivity curves for the cores at 100% saturation and irreducible water saturation do not change in shape (Figure 7.32). This shows that the primary pores have very little influence on the resistivity changes, and that the changes in resistivity must be primarily cause by the reduction in the microfractures. Hausenblas (1995) stated that the closure of pore throats reduces the size of the conductive pathways, which in turn have a greater impact on the resistivity for low porosity samples compared to high porosity samples. Zisser and Nover (2009) stated that it is the increased tortuosity of the transport path and the closure of thin aspect ratio pores and cracks which can create dead end pores.

Microfractures were found between grain contacts which increase the connectivity of the pores and improve fluid and therefore current flow (Section 5.3.4). Therefore, at lower stresses the lower FRF and *m* values are attributed to the presence of microfractures. In contrast at higher stresses these microfractures may close and the FRF and *m* increase as the connectivity decreases. The evidence for the closure of

the microfractures as the cause of the stress dependency found in TGS will be addressed in Chapter 8.

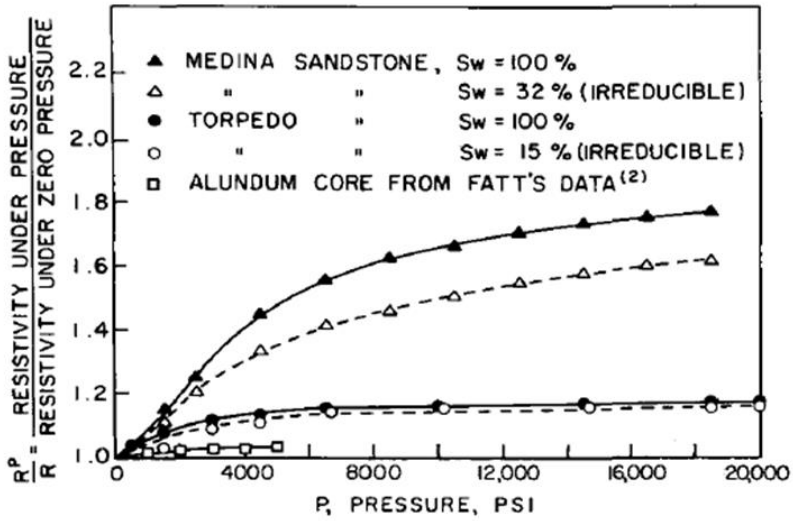

Figure 7.32 Relative resistivity as a function of net overburden pressure. This work used samples without any microfractures, this produced trend lines that do not change when a 100% water saturated core plug is compared with a core plug at irreducible saturation (from Dobrynin, 1962).

Some samples have a large increase in *FRF* with confining pressure (BP2_5, BP3_5, GDF1_6, 7, GDF2_4, SHELL1_83, 111, 216, SHELL2_1B, 9B, SHELL4_202, 409, WIN4_26 and WIN9_5). The large *FRF* are not related to the size of the pores or their connectivity as they have porosities that range from 3.4 to 16% and permeabilities that range from 0.002 to 4 mD. It was thought the large *FRF* could be related to the different brine concentrations used as experiments on samples SHELL1, 2, GDF1 and 2 were conducted with a lower concentration of NaCl brine composition compared to the other TGS samples. However, based on Equation 2.13, Chapter 2 *FRF* is related to the resistivity of a rock fully saturated vs the resistivity of fluid which it is saturated with. Therefore, changing the resistivity of the fluid will have little effect on FRF. Another possibility was that the higher *FRF* values could be related to a low water saturation (Glanville, 1959), which is more evident for low porosity samples (Brace and Orange, 1965). However, these samples were first saturated under vacuum for 2 days followed by 2 days under 1500 psi, therefore, this is possibly not the case here.

The large *FRF* is likely due to a lack of contact between the sample and the end platens in the core holder. Samples were removed when the electrical properties

appeared to be unrealistic, the system readjusted and the sample re-loaded. However, as the set-up was fragile and was composed of many components it was difficult to resolve. Future work is needed to design a simpler set-up with less connections to improve the accuracy of the data.

7.4.5 Permeability Estimations from Mercury Injection Data

Many studies have compared permeability estimated from MICP data to measured permeability values. It is often argued that traditional Hg-injection method is a hydrostatic measurement because no confining pressure is applied to the sample during the analysis. In the current study, it was argued that mercury compresses the sample until it enters the pore space therefore the threshold pressure which is the pressure at which a continues pathway is created through the sample (Tiab and Donaldson, 2016) is equivalent to the confining pressure. Therefore, it is more sensible to compare the permeability estimated from the MICP data to the permeability measured at a net confining pressure that is equal to the threshold pressure of the sample.

In Chapter 6 (Section 6.4.3.2), the MICP permeability was compared to the gas permeability at a higher single confining pressure of 5000 psi net stress which created an underestimation of the measured permeability at the lower permeability end. However, once the MICP permeability is compared to gas permeability at threshold pressure the trends are improved (Figure 7.33 to Figure 7.36). This implies that similar pressure conditions are needed to make a reliable comparison. The inaccuracies in estimating the permeability of tight rocks with the MICP models as presented in Chapter 6 could still contribute to the trends in Figure 6.33 to Figure 6.36, nevertheless, the pressure effects appear to be more pronounced in these TGS. This indications that the effects of stress are important in permeability experiments.

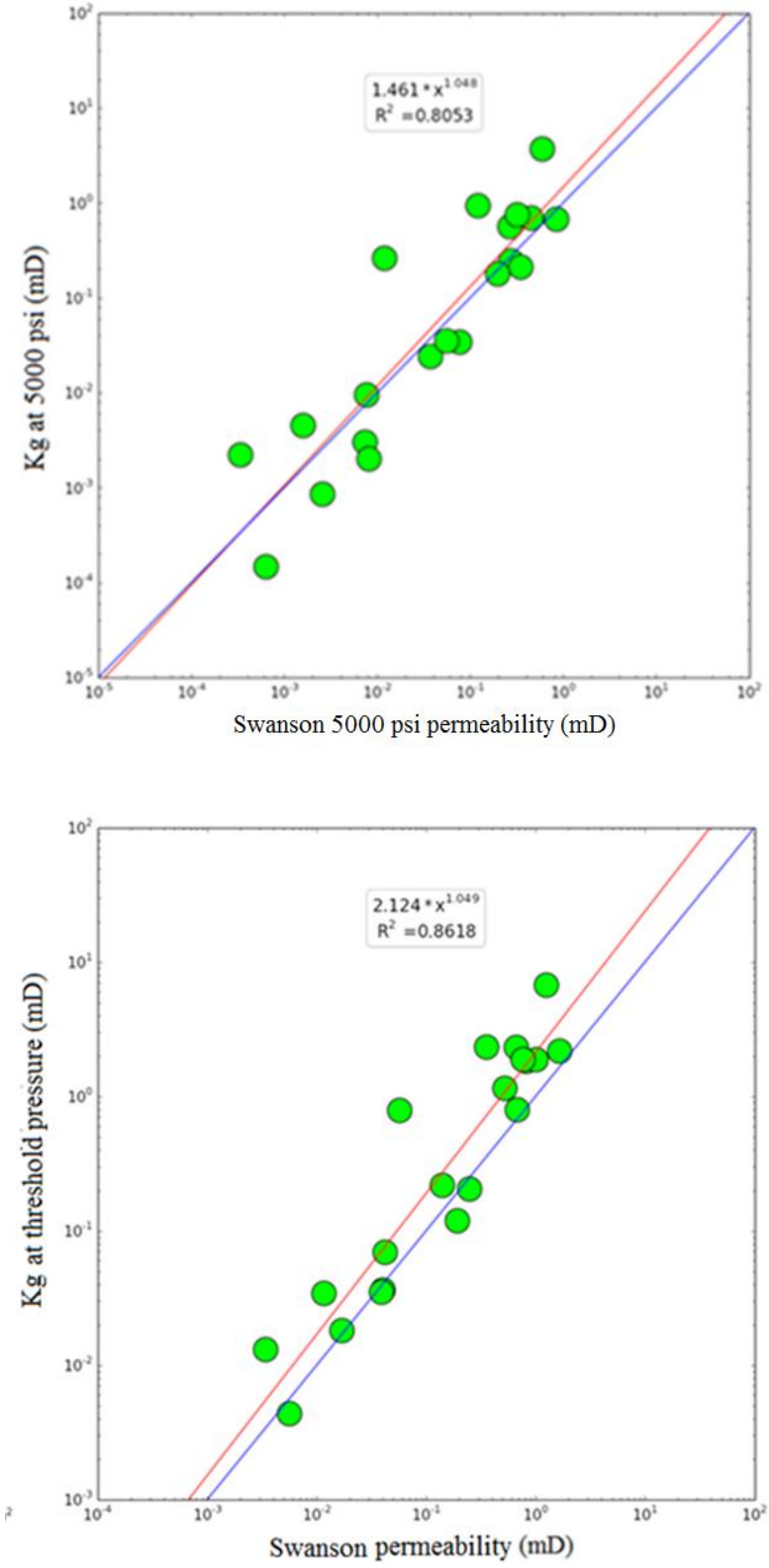

Figure 7.33 Permeability at in-situ stress (top) and threshold pressure (bottom) as a function of the estimated Swanson permeability. The trend is improved by plotting against the threshold pressure. The red line is the trend line and the blue line is the 1:1.

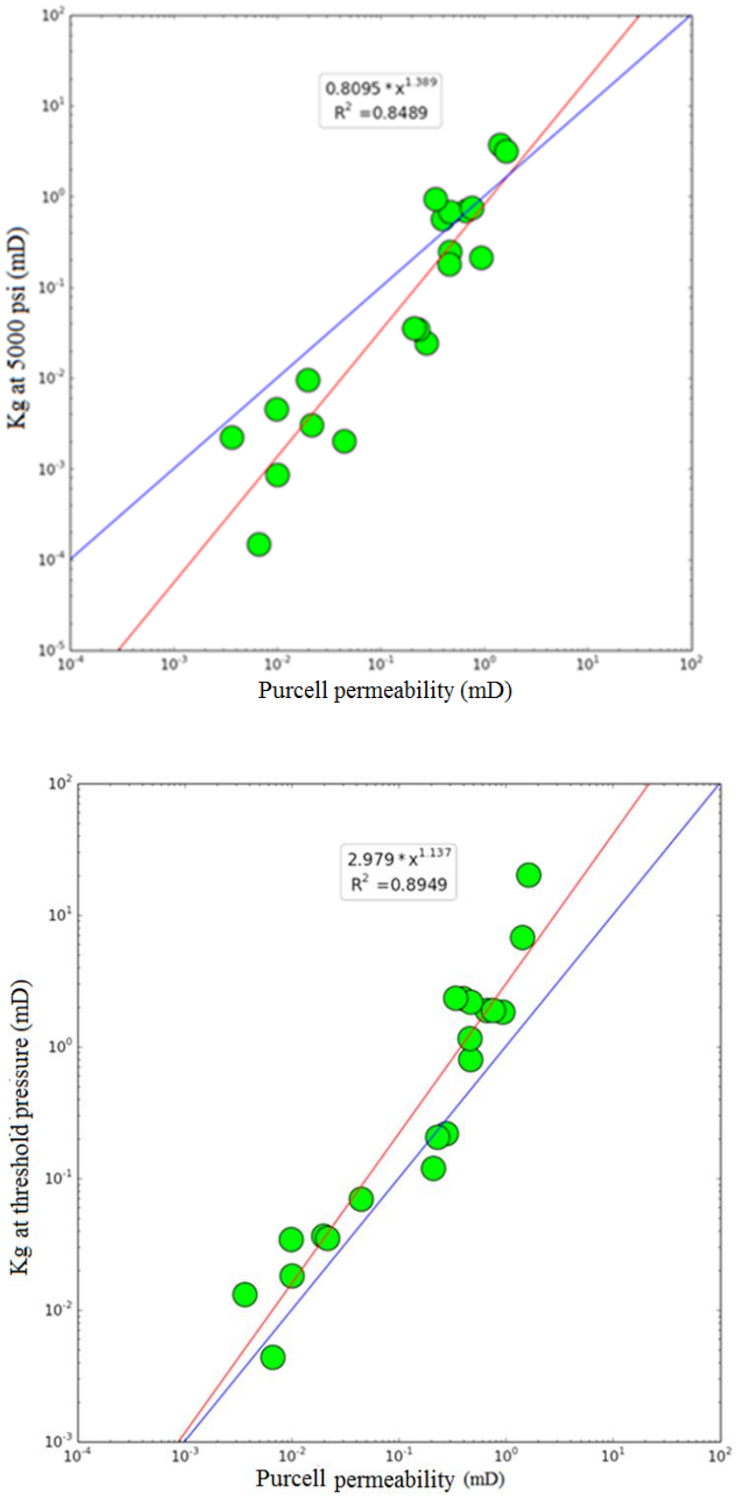

Figure 7.34 Permeability at in-situ stress (top) and threshold pressure (bottom) as a function of the estimated Purcell permeability. The trend is improved by plotting against the threshold pressure. The red line is the trend line and the blue line is the 1:1.

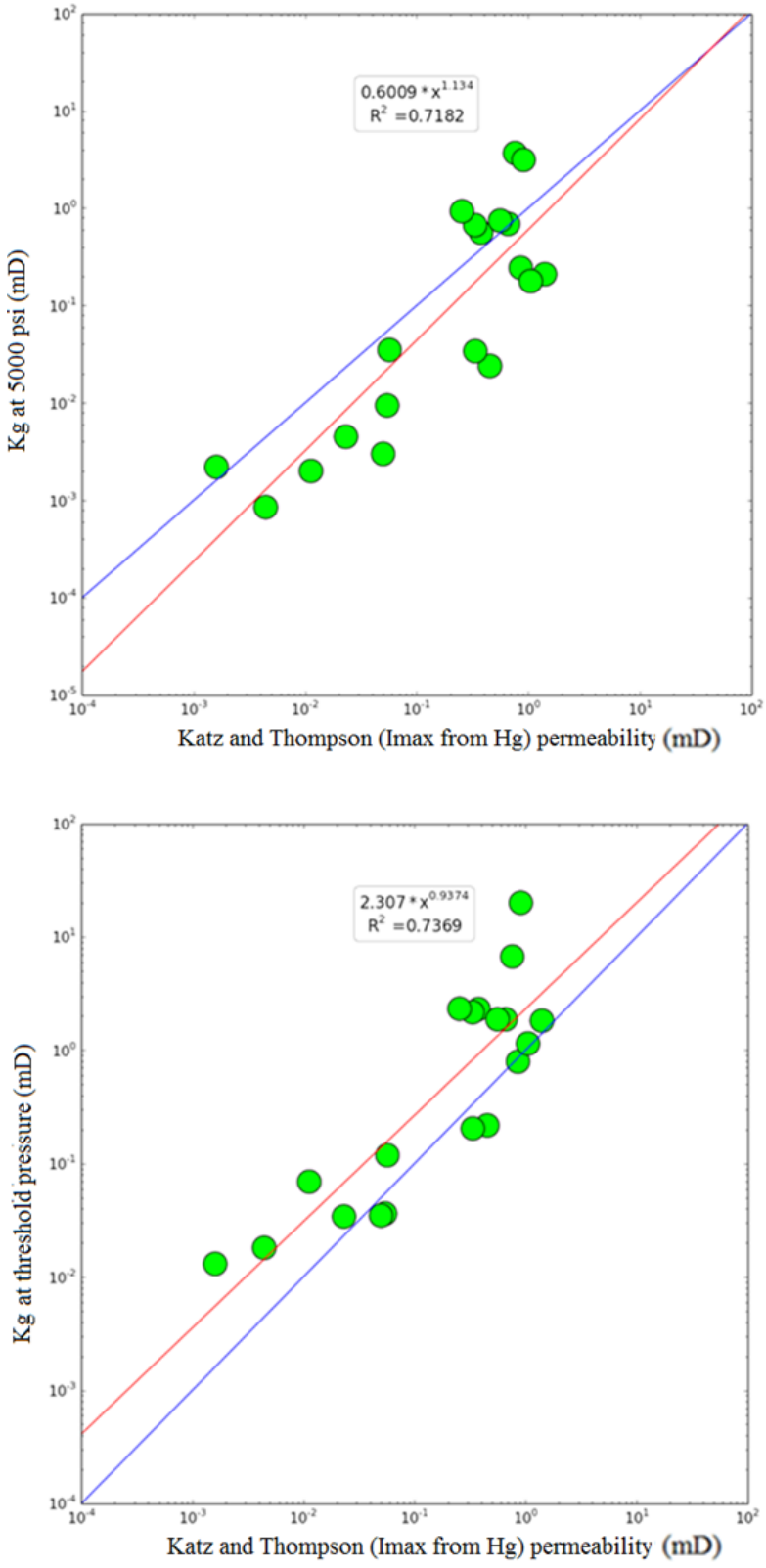

Figure 7.35 Permeability at in-situ stress (top) and threshold pressure (bottom) as a function of the estimated Katz and Thompson. The trend is improved by plotting against the threshold pressure. The red line is the trend line and the blue line is the 1:1.

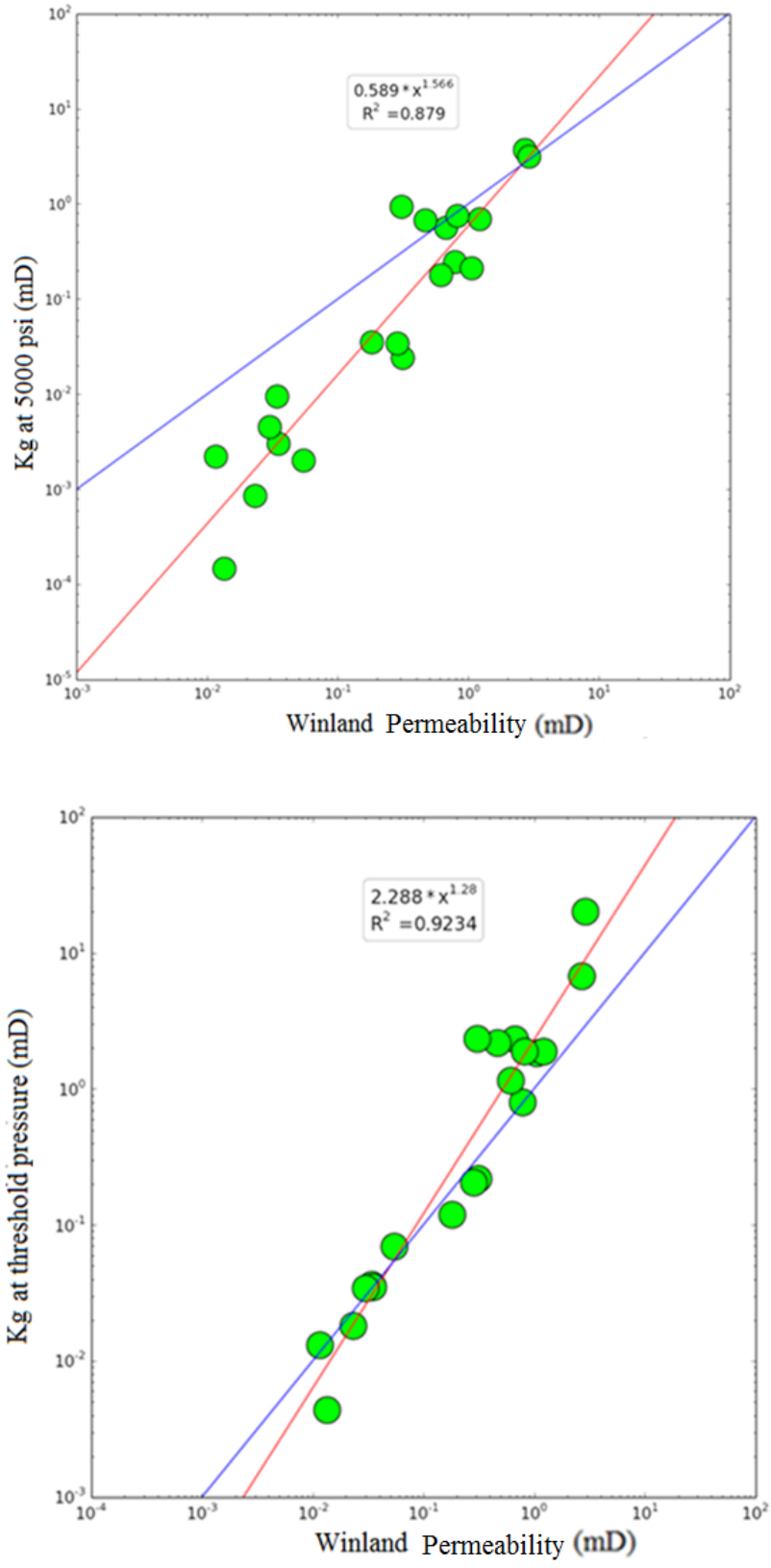

Figure 7.36 Permeability at in-situ stress (top) and threshold pressure (bottom) as a function of the estimated Winland permeability. The trend is improved by plotting against the threshold pressure. The red line is the trend line and the blue line is the 1:1.

The estimation of permeability using MICP data can also be improved by rock typing the samples according to the amount and position of clays. In particular, samples with low clay contents tend to have extremely good correlations between predicted and measured permeability; the data are relatively tightly scattered around the best-fit line (Figure 7.37). Samples with pore-filling clays have a similar trend to those with a low clay content but show more scatter around the best fit line (Figure 7.37). Samples with grain coating clays have the worst correlation between estimated and measured permeability and show large amounts of scatter (Figure 7.37). This compares well to the conclusions found in Chapter 5 that the position of clays is an important control on permeability.

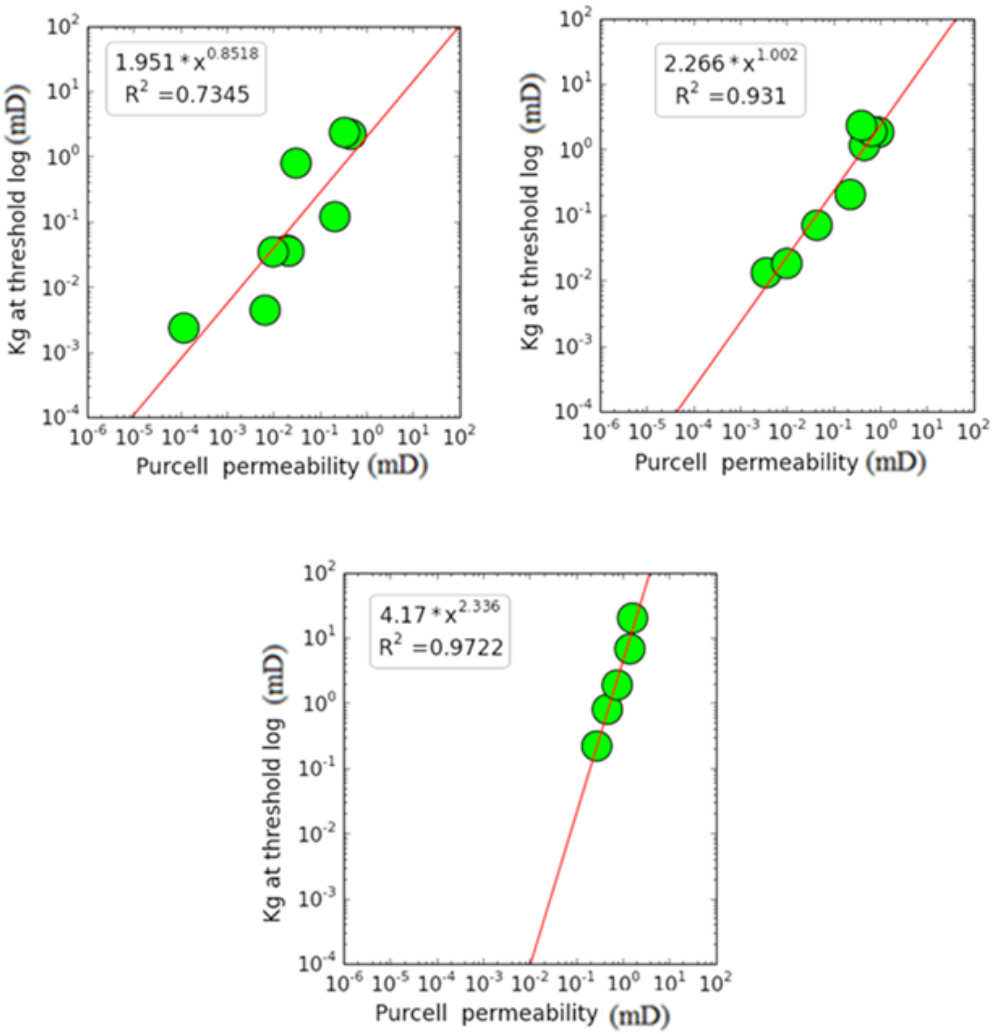

Figure 7.37 Permeability of samples with grain coating clay (top, left), pore filling clay (top, right) and low clay content (bottom) measured at the Hg-air threshold pressure as a function of the permeability estimated using the Purcell method. The clay free samples have the best trend.

7.5 Conclusion

The petrophysical properties of TGS are stress sensitive when measured in the laboratory. The extent of this stress sensitivity is different for each property and varies from sample to sample. Porosity is the least sensitive to stress with values in the subsurface being around 95% of that measured at ambient conditions. Permeability is the most stress sensitive with values in excess of an order of magnitude lower *in-situ* compared to ambient conditions. Electrical properties have a stress sensitivity that is midway between that of porosity and permeability. The brine permeability was found to be stress sensitive but more time is required for mechanical equilibrium to ensure the permeability is not overestimated.

The main reason for the stress sensitive nature of permeability and electrical properties is possibly related to the closure of microfractures. These microfractures form a small proportion of the overall porosity so their closure may not have a large effect on the porosity. The evidence for the closure of microfractures is presented in Chapter 8.

Mercury compresses the sample until it enters the pore space hence it was found that the permeability estimated from the MICP data should be compared to the permeability measured at a net confining pressure that is equal to the threshold pressure of the sample. In doing so, the trend between the estimated permeability from the MICP data and the measured permeability at threshold pressure is improved. This implies that similar conditions are needed for a reliable comparison and that permeability is effected by stress. The results are further improved if different correlations are applied to different rock types. Results from clay-free sandstones are particularly good whereas results from samples containing grain-coating clays are the least accurate. Samples with pore-filling clays fall somewhere between these end-members. This further demonstrates that clay position is a key control on permeability.

Chapter 8 - Microfracture Closure on the effects on TGS Stress Dependency

8.1 Introduction

The results presented in Chapter 7 show that many properties of TGS are stress dependent. This stress dependency is thought to be related to the presence of microfractures (Joel, 1982; Chun, 2013). However, it is unclear whether microfractures that cause the stress dependency are present in the subsurface. If not, it is likely that petrophysical properties will not be as stress dependent in the subsurface as they are in the laboratory. This is important because it would have a significant impact on development planning. For example, if permeability is stress dependent in the subsurface there may be benefits to implement restricted rate practice where gas is produced at higher pore pressures to maintain higher permeabilities.

The microfractures can be studied in more detail by injecting low melting point eutectic alloys such as Wood's metal (50% bismuth, 26.7% lead, 13.3% tin and 10% cadmium) or Field's metal (51% indium, 32.5% bismuth and 16.5% tin) (Lipchitz, 2013) into the sample. Metal injection is a useful technique to study the pore structure as it offers the possibility of freezing the invaded networks at any stage of its injection (Darot and Reuschle, 1999). This enables the pore structure under stress to be observed by optical or scanning electron microscopy.

In this study, Field's metal was injected into a sample under different confining pressures and the metal distribution was determined using SEM to assess whether: (i) the microfractures are the main cause of the stress dependency seen in Chapter 7 and (ii) TGS are stress dependent in the subsurface. Field's metal was chosen as it is nonreactive with water, non-toxic and has an ideal viscosity of 27 mPa-s at 80°C (Lipchitz, 2013). The methodology is presented in Section 8.2, the results of the experiment are presented in Section 8.3; followed by a discussion of the results in Section 8.4. The work in this chapter is then summarised in Section 8.5.

8.2 Methodology

8.2.1 Sample Preparation

Sample BP4_5 was first cleaned with DCM using the Soxhlet extractor process as described in Section 3.2.1. Gas porosity and permeability were then measured using the method described in Section 3.4.1 and 3.4.2. They were both conducted to allow a comparison with image analysis values and the latter was also conducted to determine the stress dependency of permeability for this specific sample.

The solid Field's metal was located inside a 4 ml stainless steel chamber, which was plugged at the base (Figure 8.1 and Figure 8.2 - A). A stainless steel platen was placed on top, which has a central hole to allow the metal to enter the core (Figure 8.1 and Figure 8.2 - B). The sample sat above the stainless steel platen (C) and was topped with a stainless steel cap to stop the metal entering the set-up (Figure 8.2- D). Fine-grained sand was placed above and below the sample to ensure there was a good contact as the sample was not perfectly flat (Figure 8.2). In addition, heat shrink was added around the stainless steel chamber and sample to ensure the metal did not escape.

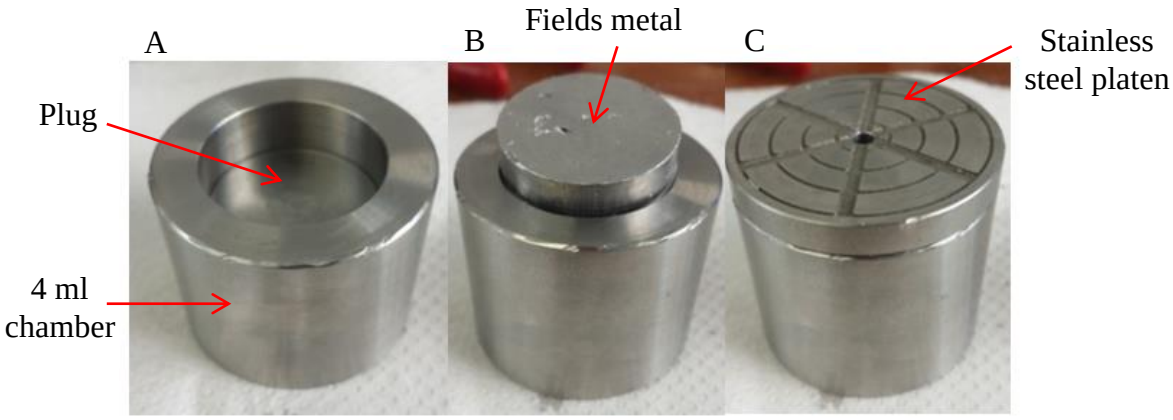

Figure 8.1 Stainless steel 4ml chamber which housed the Field's metal along which was plugged at the base to stop the metal leaking out (A), fields metal (B) and the stainless steel platen with central hole to allow the metal to enter the core plug (C).

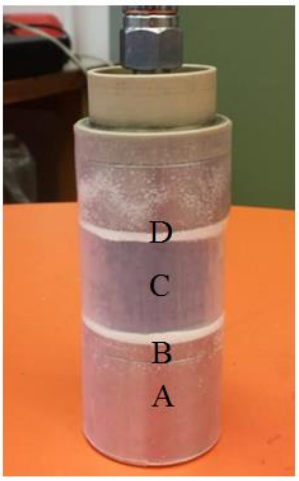

Figure 8.2 4ml stainless steel chamber containing Field's metal (A), stainless steel platern (B), core plug (C), fine grained sand at the top and base and stainless steel cap (D).

8.2.2 Experiment

The first objective was to inject as much Field's metal into the core plug as possible. The core plug as seen in Figure 8.2 was placed into a core holder, and the core holder was placed vertically into an oven. The temperature was increased to 80°C and left to stabilise for a few hours (Figure 8.3). The core holder was placed vertically to ensure the molten metal did not start to flow into the core before the confining pressure and pore pressure was applied.

The core holder was connected to two 103 ml Teledyne ISCO model 260D positive displacement pumps. One was linked to a piston which drove the confining pressure and the other pump drove the pore pressure. The latter had two connections, one to the core holder within the oven and one to a beaker containing water where the water was used to drive the pump. A vacuum pump was attached to the top of the core holder to draw up the metal and draw out the air.

Once a stable temperature of 80°C was achieved and the metal assumed to be fully molten, the confining pressure was increased to 1500 psi and the pore pressure to 250 psi. The setup was left to stabilise and was monitored for 48 hours by observing the change in water level within the pumps. The conductivity across the core was also monitored which enabled the exact time at which the metal had reached the top of the core plug to be known. It was assumed that no more metal was entering the sample when the conductivity and water level in the pump was stable.

The oven was turned off and the pore pressure lowered to allow the metal to solidify for 24 hours. The core holder was left under confining pressure as it was assumed that the metal may shrink away from the pore walls when it cools. The sample within the core holder was CT-scanned to determine the distribution of Field's metal. The confining pressure was removed and the sample photographed and weighed. The former was for reference and the latter to determine the amount of metal injected.

The core plug was trimmed at the lower and upper end and prepared for SEM analysis (see Section 3.3.1). The sample was replaced into the core holder and the same experiment was performed at the same confining pressure of 1500 psi but higher pore pressures of 500 then 1000 psi. Following this, the net stress was increased to 2500, 3500 and 4500 psi. The second objective at higher net stress ranges was to re-distribute the metal; therefore, no pore pressure was needed to push in any further metal.

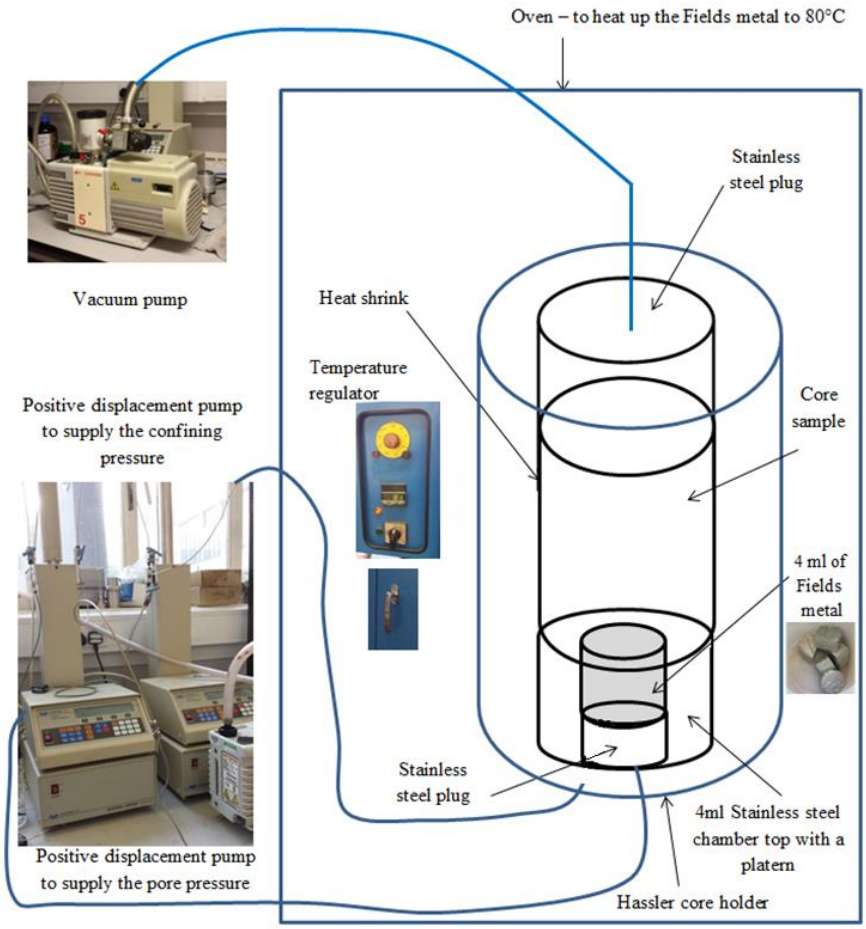

Figure 8.3 Schematic drawing of the Field's metal injection experimental to determine the cause of the stress dependency of TGS. The area drawn in black represents Figure 8.2.

8.3 Results

This section will provide the results to allow an investigate as to whether microfractures are the main cause of the stress dependency found within TGS. Details of the BP4_5 core plug used are presented in Section 8.3.1. This is followed by the CT images after metal injection Section 8.3.2. SEM images showing the location of Field's metal between 500 and 4500 psi net stress are presented in Section 8.3.3. The dry weight and core plug images of the sample before and after each pressure step is presented in Section 8.3.4. This is followed by an estimation of porosity using image analysis in Section 8.3.5.

8.3.1 Core and Microstructural Information

The BP4_5 sample has a permeability of 0.07 mD below 3500 psi confining pressure and 0.02 mD above 4100 psi confining pressure (Table 8.1 and Figure 8.4); it also has a porosity at ambient stress of 11% (Table 8.2). It is highly laminated as can be seen from the core and CT image (Figure 8.5 and Figure 8.6). The BSE images show the presence 1-5 μm microfractures surrounding all the grains (Figure 8.7).

Table 8.1 Permeability from 1500 to 10,000 psi confining pressure and ~1000 psi pore pressure for BP4_4.

Confining pressure (psi)	Pore pressure (psi)	Net stress (psi)	Permeability (mD)
1500	964	536	0.073
2500	911	1589	0.071
3500	947	2553	0.067
4122	1083	3039	0.02
4998	1083	3915	0.018
7000	1027	5973	0.01
10000	984	9016	0.010

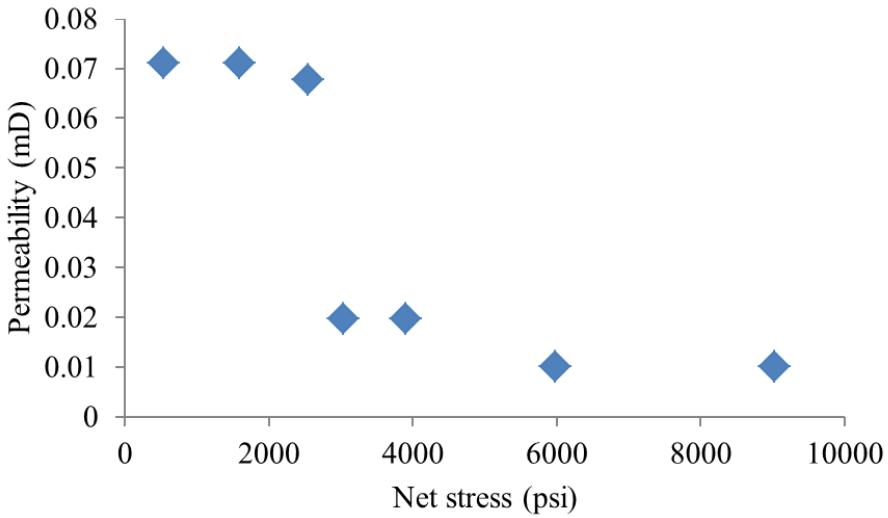

Figure 8.4 Permeability as a function of net stress for BP4_5 showing a slow rate of permeability decrease below 2500 psi and above 3000 psi and a faster rate of decrease between 2500 psi and 3000 psi.

Table 8.2 Dimensions, dry weight, bulk volume, porosity, permeability and in-situ pressure of the reservoir for BP4_5.

BP4_5	**Data**
Length (cm)`	4
Diameter (cm)	3
Dry weight (g)	90
Bulk volume (cm^3)	38
Permeability (mD) – 1500 and 5000 psi	0.073 and 0.018
Porosity (%)	11
Net stress of the reservoir (psi) C_p, P_p (psi)	8140 12300, 4130

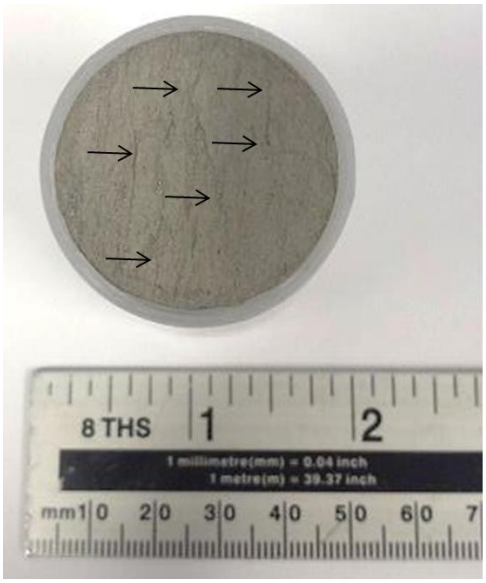

Figure 8.5 Core photo of BP4_5 with black arrows showing the location of the laminations.

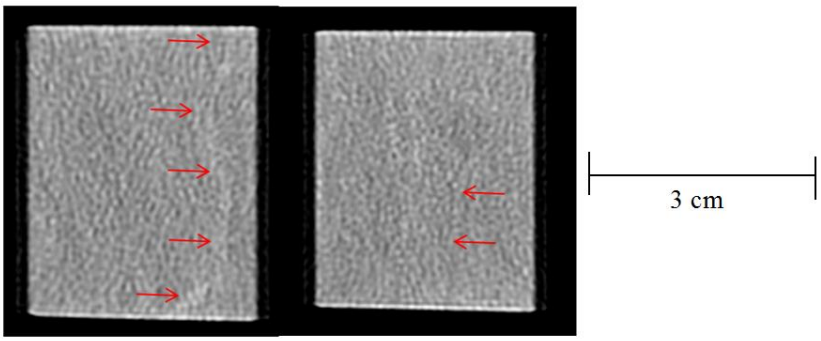

Figure 8.6 CT images of the BP4_5 core plug showing the presence of fractures cutting through the core (left) or part of the core plug (right). These are not the microfractures.

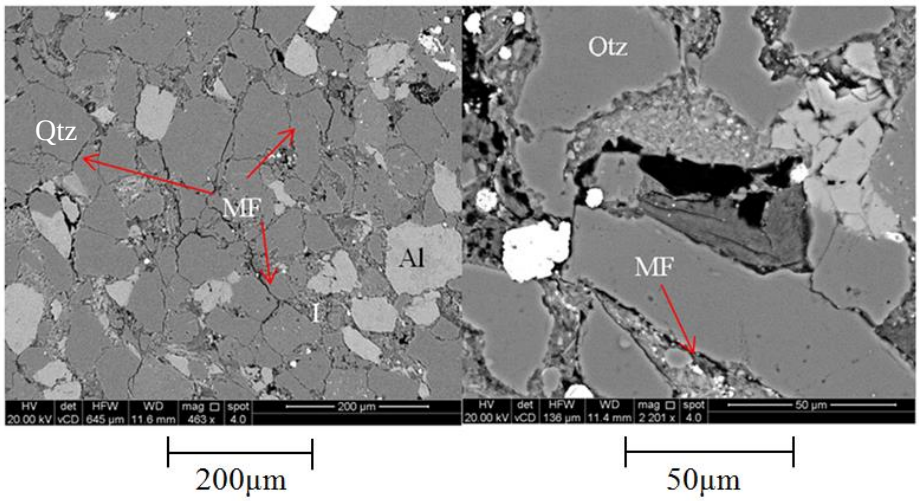

Figure 8.7 BSE images prior to metal injection showing the main components – Quartz - Qtz, Albite – Al, Illite – I, MF – microfractures.

8.3.2 CT Images Showing Field's Metal Injection

The Field's metal started to move up through the laminations at 1250 psi net stress (1500 psi C_P, 250 psi P_P) to reach the top of the core plug (Figure 8.8). These laminations are much larger than the microfractures under study (Figure 8.5 and Figure 8.6) and they provide a pathway to fully saturate the sample with metal. It is predicted that with an increase in pore pressure from 250 to 1000 psi, the maximum pore pressure used, the metal will start to saturate the smaller pores and microfractures and move along the lowest capillary pressure pathways. This was not tested as the metal had completely saturated the core plug and the CT scanner could not create an internal image after 250 psi P_p, however, the smaller pores and microfractures were filled with metal as can be seen in the BSE images in Section 8.3.3.

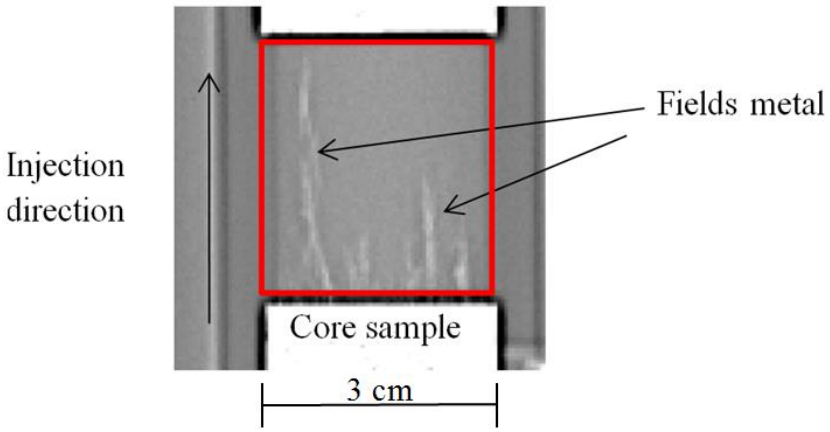

Figure 8.8 CT image of the core holder and core plug after Field's metal Injection (1500 psi C_p and 250 psi P_p) showing the presence of the metal within the larger vertical laminations in the core plug.

8.3.3 Microstructure after Field's Metal Injection using SEM

The SEM images after metal injection show a decrease in the amount of metal in the core plug as the net stress increases from 500 to 4500 psi (Figure 8.9 to Figure 8.12). At 500 psi net stress, the metal occurs along the grain scale microfractures, is continuous throughout the sample (Figure 8.9a, b) and has reached pore sizes as small as 1 μm (Figure 8.9c). This is also the case at 2500 psi net stress, however, there is less metal than at 500 psi net stress (Figure 8.10). At 3500 and 4500 psi net stress there is a lack of metal within the microfractures and the metal is more isolated within the larger pores (Figure 8.11 and Figure 8.12a). In addition, some pores show evidence of pinching of the metal (Figure 8.12b) and metal snap-off (Figure 8.12c).

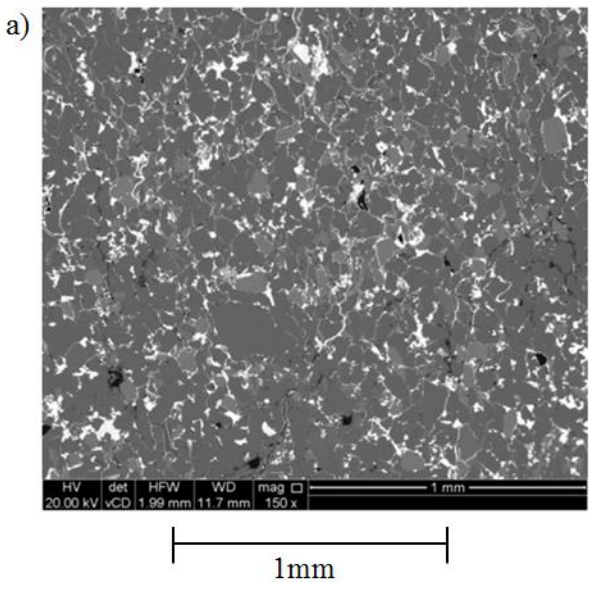

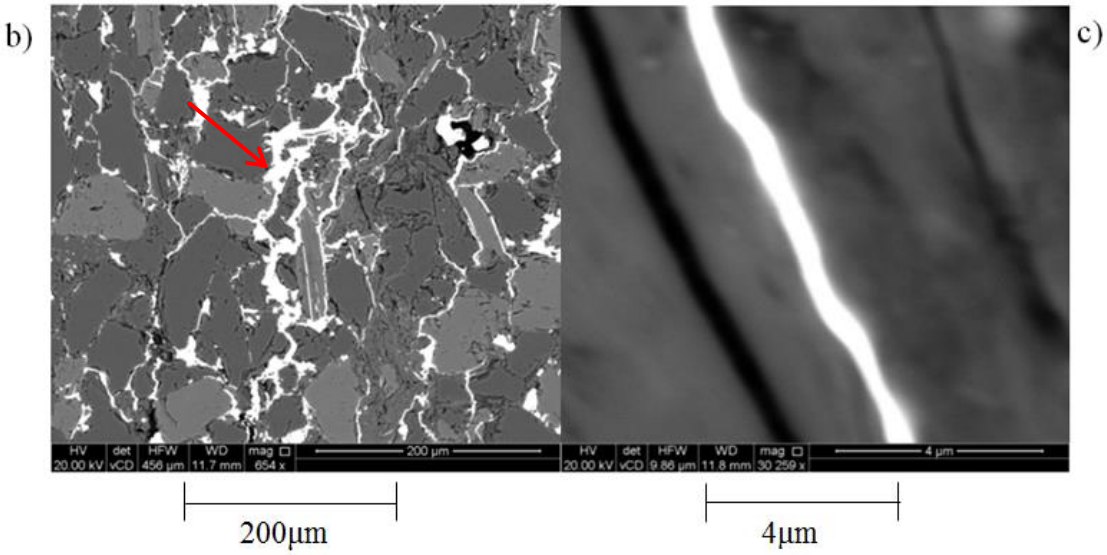

Figure 8.9 BSE image showing the metal distributed in all pore sizes (a), the continuous nature of the metal through the microfractures (b), and the presence of metal within microfractures as small as 1 µm at 500 psi net stress (c).

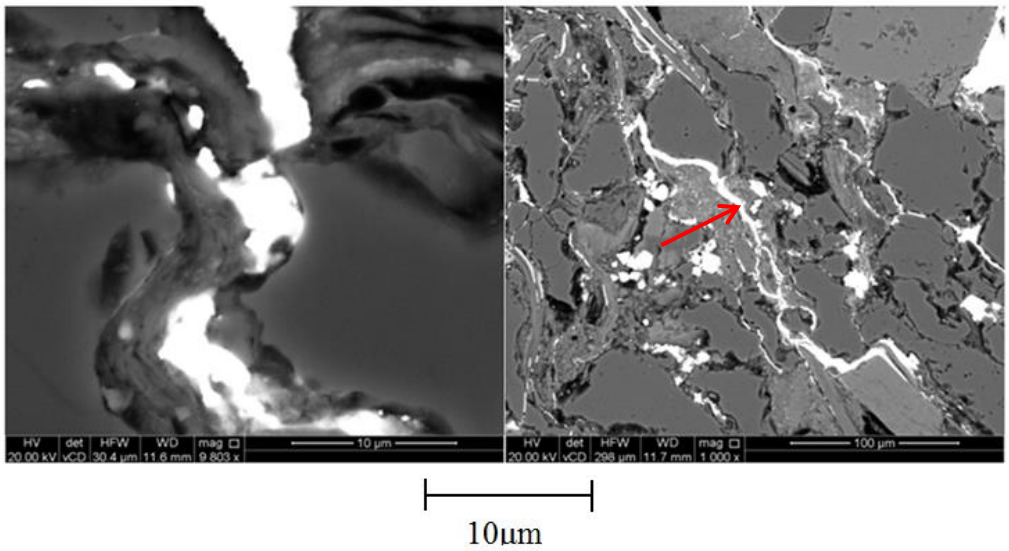

Figure 8.10 BSE SEM image showing the metal distributed in the microfractures at 2500 psi net stress although there is less metal then at 500 psi.

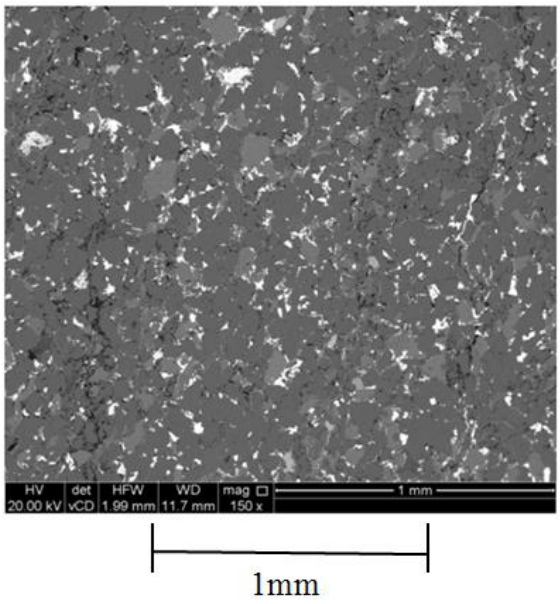

Figure 8.11 BSE SEM image showing the metal distributed in the larger pores at 3500 psi net stress.

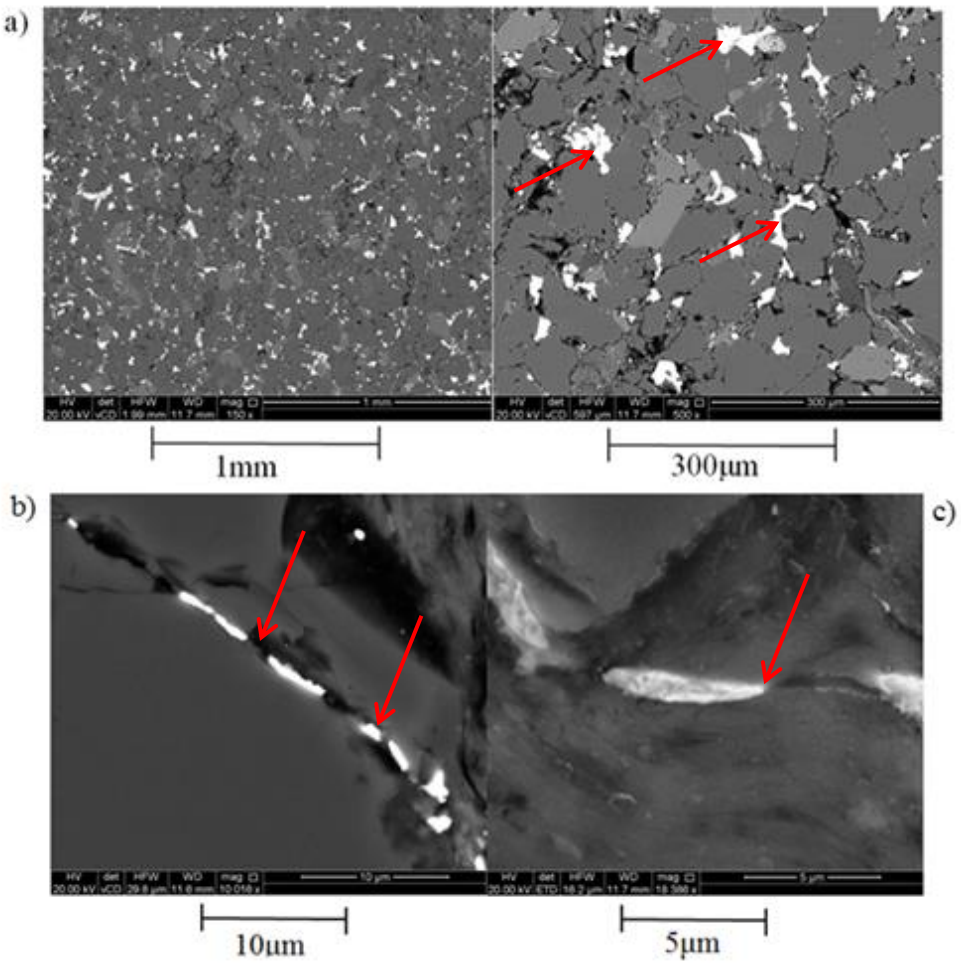

Figure 8.12 BSE SEM images showing the metal distributed in the large isolated pores at 4500 psi net stress (a), the metal "snap off" (b) and the pinching of pore throats (c).

8.3.4 Dry Weight and Core Plug Images

The dry weight before and after metal injection at each net stress was determined (Table 8.3). It appeared that more metal had entered the sample (12.6%) above the original porosity of the sample (11%) at 500 psi net stress, nevertheless, when observing the sample some metal had solidified on the outside of the core plug (Figure 8.13). Therefore, the 12.6% is not the true amount of metal injected at 500 psi net stress. More metal was pushed out at 3500 psi net stress compared to 2500 psi and 4500 psi net stress. There is more metal in the sample at 500 psi as it appears shiny as opposed to the dullness of the sample at higher net stress values (Figure 8.14).

Table 8.3 The change in weight of the BP4_5 sample after metal injection at 500 psi net stress and after an applied net stress of 2500 to 4500 psi.

Dry weight (start) - g	90.3
Weight after injection (500 psi) -g	103.3
Amount injected - g	13
Amount injected - %	12.6
Weight before 2nd pressure step of 2500 - g	86.5
Weight after 2nd pressure step of 2500 psi- g	84
Amount of metal pushed out at 2500 psi - g	2.5
Amount of metal pushed out at 2500 psi - %	3
Weight before 3rd pressure step of 3500 psi - g	64.5
Weight after 3rd pressure step of 3500 psi - g	58.6
Amount of metal pushed out at 3500 psi - g	6.9
Amount of metal pushed out at 3500 psi - %	11.8
Weight before 4th pressure step of 4500 psi - g	51.7
Weight after 4th pressure step of 4500 psi - g	49
Amount of metal pushed out at 4500 psi - g	2.7
Amount of metal pushed out at 4500 psi - %	5.5

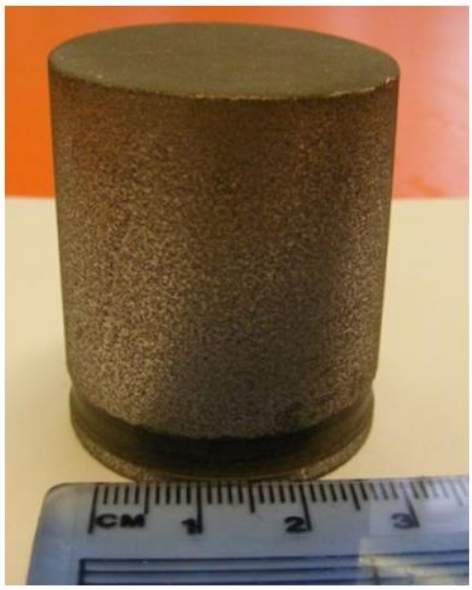

Figure 8.13 BP 4_5 sample after metal injection at 500 psi net stress showing the metal has solidified on the outer surface of the core plug leading to a high metal injection percentage above the porosity of the sample at 500 psi.

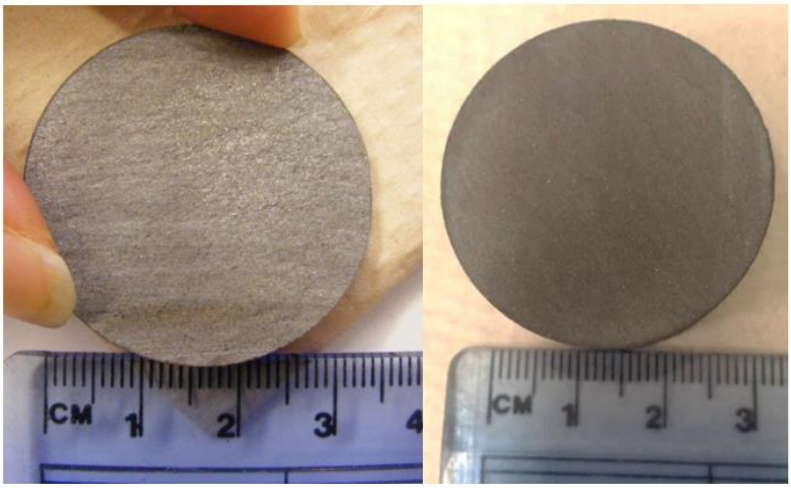

Figure 8.14 Slice of BP4_5 after injection at 500 psi net stress (left) and 4500 psi net stress (right) showing more metal at the lower net stress as it appears more shiny.

8.3.5 Estimation of Porosity using Image Analysis

A thin section slide was made of the sample after each net stress and the thin section was studied using a scanning electron microscope. BSE images were taken and the percentage amount of pore space was calculated using image analysis software - Image J. The area covered by the metal appears white which is referred to as true porosity and the area covered by pores appears red which is referred to as closed porosity (Figure 8.15 and Figure 8.16). The true porosity was determined by taking the closed porosity away from the original porosity from Table 8.2. The percentage

area of pores closed is 0.8% and 2.8% at 500 and 4500 psi net stress respectively. Therefore, the true porosity at 500 psi net stress is 10.2% (true porosity = 11% (original porosity from Table 8.2) - 0.8%) and at 4500 psi net stress it is 8.2% (true porosity = 11% (original porosity from Table 8.2) – 2.8) (Figure 8.15 and Figure 8.16). Both porosities are lower than the helium porosity.

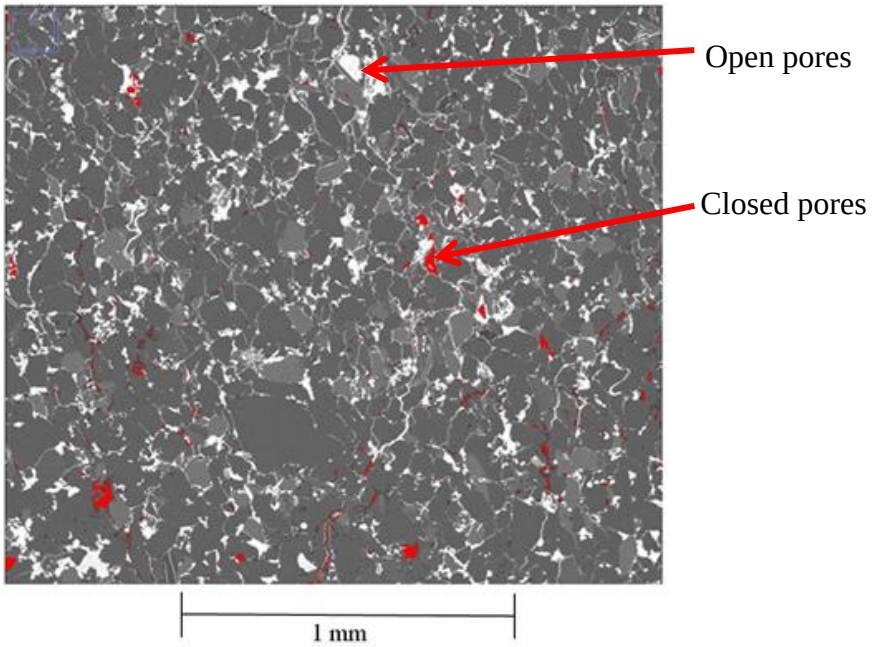

Figure 8.15 Porosity from image analysis on a BSE SEM image of the closed pores at 500 psi net stress (0.8% red) leading to a porosity of 10.2%

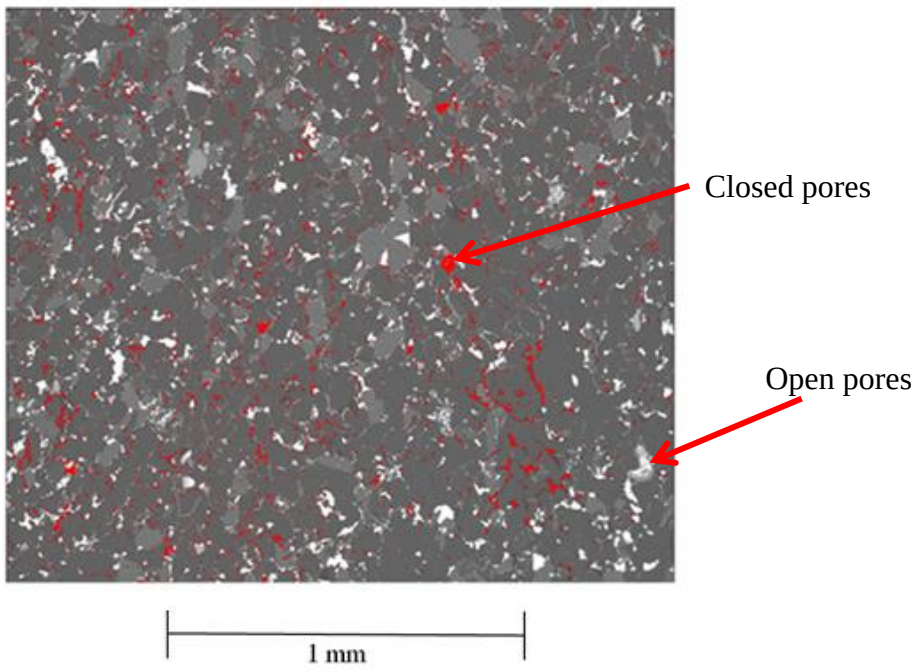

Figure 8.16 Porosity from image analysis on a BSE SEM image of the closed pores at 4500 psi net stress (2.8% red) leading to a porosity of 8.2%.

8.4 Discussion

8.4.1 Causes of the Stress Dependency found in TGS

There is evidence in the literature for the closure of microfractures with applied stress. Thomas and Ward (1972), Nelson et al. (1976), Walsh (1966) argued that the impact of stress on permeability is higher in rocks containing microfractures than those containing only natural porosity. Zhang et al. (2013) stated that microfractures are easy to deform under the action of external force (Figure 8.17). Joel (1982) claimed that flat cracks are closed easily by increasing overburden pressure, and their effect on permeability can be seen in Figure 8.18. At higher effective stress, their contributions to flow have been almost eliminated. Lorenz (1999) stated that the effective stress normal to a fracture increases during drawdown of reservoir pressure, and is capable of narrowing fracture apertures in the system. Hyman (1991) found that relatively few induced microfractures, 0 to 7% of the total microfractures encountered, are observed in the stressed thin sections. This compares to 20% to 50% induced microfractures detected in the unstressed thin sections.

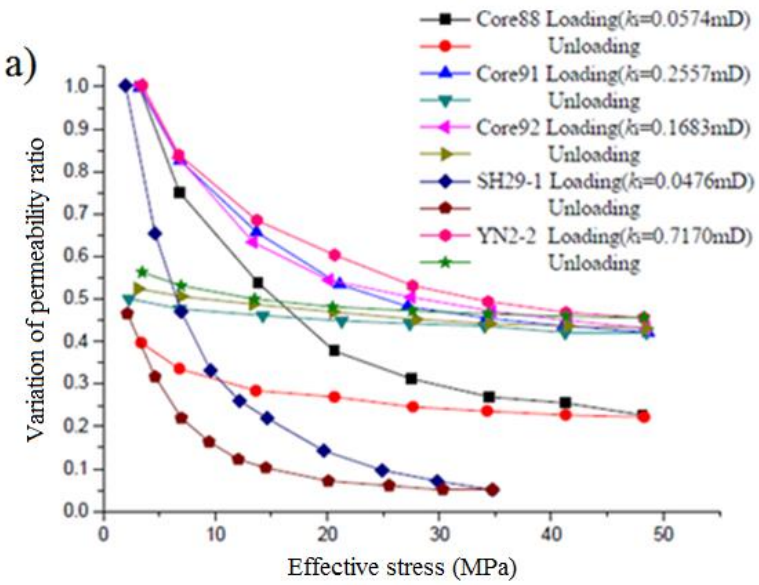

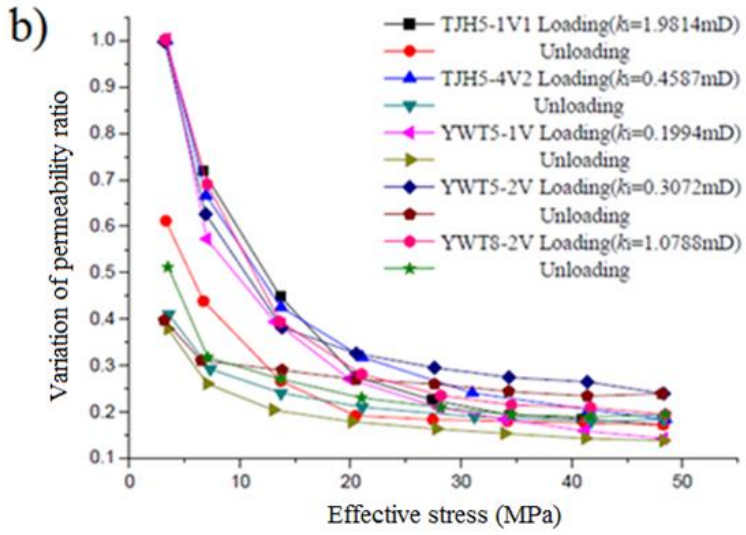

Figure 8.17 Permeability ratio as a function of the effective stress for a matrix core (a) and a microfracture core (b) showing a greater stress sensitivity with samples with microfractures (Zhang et al., 2013)

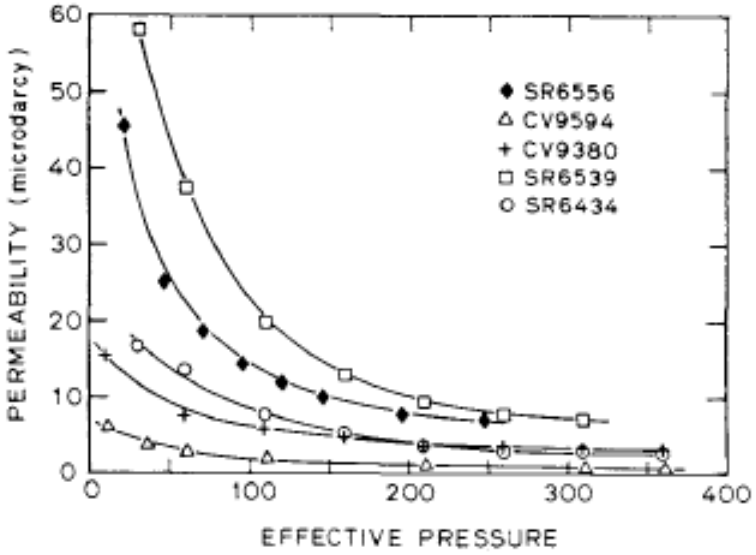

Figure 8.18 Permeability as a function of effective pressure for some tight sandstones showing a decrease in permeability with effective pressure (Joel, 1982).

The data in this chapter supports the conclusions from other publications that microfractures close under stress. The metal at 500 to 2500 psi net stress saturated all the pores, was present along grain scale microfractures and was more continuous through the sample. At 3500 to 4500 psi net stress the metal is present mostly in the larger pores and less metal was present in the microfractures. Observations of the weight change of the sample, which is related to the amount of metal leaving the sample, suggests that most of the metal was forced out at 3500 psi net stress compared to 2500 psi and > 3500 psi net stress.

Less metal is being forced out of the sample (thus smaller weight change) at the lower net stresses (<2500 psi), therefore it can be assumed that pores and microfractures are not being compressed that much. On the other hand, at 4500 psi net stress it might be expected that more metal would be forced out as the stress is higher. However, as most of microfractures have already closed, the only metal leaving at this stress would be from the pores. Overall, TGS with high permeabilities are not very stress dependent (Figure 7.11, Chapter 7), therefore the amount of metal forced out at higher stresses would be expected to be lower compared to the amount forced out at microfracture closure stresses.

More metal came out of the sample between 2500-3500 psi because the microfractures are closing in this region. This in turn forces out the Field's metal from these microfractures, causing the weight change. This is consistent with the gas permeability data as the permeability decreases gradually between 2500 psi and 3500 psi net stress (Figure 8.4).

Some isolated pods of metal were found within the microfractures between 3500 and 4500 psi net stress despite the original theory that the microfracture are shut at this stress (Figure 8.12b). This occurs in a similar way with mercury during drainage and imbibition experiments (Pickell, et al., 1966; Roff, 1970; Li and Waedlaw, 1986; Ioannidis and Chatis, 1993a; Tsakiroglou, 1997; Smith et al., 2002; Al-Gharbi and Blunt, 2003). Many publications state that this is because the mercury will enter the pore at a pressure determined by the entrance size and not the overall pore size (Giesche, 2005). Therefore, if the mercury enters a pore with a narrow pore throat, at higher stresses the mercury will break at the pore throat trapping the mercury, this is known as the ink bottle theory. This has been observed in pores using Wood's metal (Kaufmann, 2010), therefore, it is predicted it will occur in a similar way in the Field's metal. As the metal 'snapped off' with an increase in stress, the metal was able to keep segments of the microfractures open, whereas, the area that was not filled by the metal was closed; this is seen by the pinching of the metal in Figure 8.12c.

In this chapter, the porosity of BP4_5 sample did not vary much as the porosity at 4500 psi was only 2 porosity units lower than that at 500 psi (Section 8.3.5). There are several possibilities for the minor stress dependency of porosity. There is an issue in terms of how representative the sample is to the reservoir as the SEM samples are

very small (Santarelli, 1998; Egermann et al., 2004). Nevertheless, if this was the case this would affect all the samples regardless of the applied stress and a similar conclusion was observed in Chapter 7.

The metal may have contracted as it solidified, which is a common property for Wood's metal (Kaufmann, 2010) and therefore it may occur in Field's metal as they have similar properties. This may cause some pores to be partially open which should have been closed leading to higher porosities then expected at higher stresses. When observing the Field's metal inside the microfractures and pores there is no evidence of metal shrinkage.

The microfractures form a small proportion of the overall porosity, therefore, their closure has little impact on the overall porosity as the porosity is more controlled by the closure of larger pores which are not very stress dependent (Mavko et al., 2009). This is supported by the fact that the closure of microfractures impacted the permeability and electrical properties in Chapter 7 as these properties are more controlled by the closure of microfractures (Jones and Owen, 1980; Ostensen, 1983; Takahashi et al., 1995). The closure of microfractures is more likely to be the case for the lack of porosity change with stress as there is clear evidence for the presence of microfractures in Chapter 5 (Section 5.3.4) and the closure of microfractures with stress in this chapter.

8.4.2 Impact of Stress on Subsurface Properties

The data and discussions presented within Chapter 7 suggest that key petrophysical properties are very sensitive to net stress under laboratory conditions. There is significant evidence that microfractures are responsible for the stress dependence of petrophysical properties in TGS. Consequently, a central issue regarding the stress sensitivity is whether or not the microfractures are natural or result from damage during or after drilling and therefore whether the TGS are stress sensitive in the subsurface.

Hyman (1991); Gale et al. (2007); Chalmers et al. (2012) and Liu et al. (2013) all indicated that artificial microfractures can be identified due to their lack of cementation. The TGS in this research have undergone extensive diagenetic changes with the infilling of pores and throats with clay and the build-up of secondary

minerals like quartz, dolomite and siderite. These diagenetic deposits have greatly affected the petrophysical properties of TGS (Chapter 5 and 6). However, no mineral deposits were found within the microfractures (Chapter 5).

Hyman (1991) and Loucks (2016) both indicated that artificial microfractures surround the grains rather than fracturing them. The microfractures observed during the current project are present at grain contacts (Section 5.3.4). The microfractures in a number of studies were found to close under stresses lower than that within the reservoir (Thomas and Ward, 1972; Vairogs et al. 1971). The Field's metal experiment has also shown that microfractures present at ambient stress are closed between 2500 and 3500 psi net stress. In addition, the stress at which the microfractures are closing in the laboratory is lower than the *in-situ* net stress of 8149 psi at which the core was taken.

Microfractures have been found to form artificially as a result of drilling, core expansion or contraction during or shortly after coring, core handling, or sample preparation (Lui et al., 2013). Loucks (2016) argued that they can form during the preparation of thin sections for SEM analysis and also a consequence of breakage under low-confining pressure. Fjaer et al. (2008) argued that stress, thermal effects and chemical effects due to fluid exposure, are the main core alteration mechanisms. In addition, the cores may be further damaged by the action of the drill bit. Fjaer et al. (2008) presented a schematic illustration of a vertical well drilled in an initial stress field with a vertical and isotropic horizontal stress (Figure 8.19). The vertical stress decreases first as the well is drilled and the horizontal stress reduces as the core enters the core barrel. This creates a point where the horizontal stress is larger than the vertical stress. This can cause damage to the core and can create increased stress sensitivity (Holt et al., 2000).

This discussion in this section has shown that the microfractures in the 25 TGS (Table 3.1) would not be present in the subsurface therefore, they appear to have been created during or after drilling. This implies these microfractures would not be present within the subsurface. Therefore, the TGS are not as stress dependent in the subsurface as they are in the laboratory.

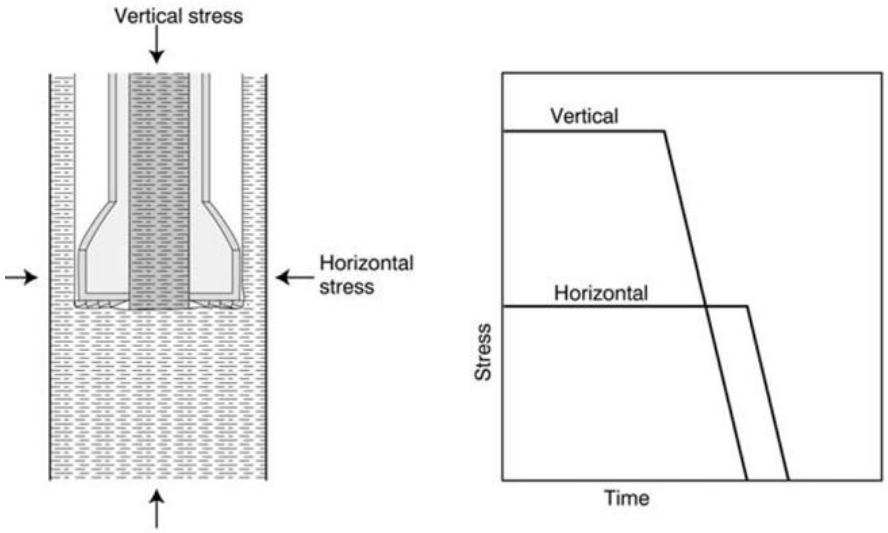

Figure 8.19 Schematic illustration of the effective stress alteration during coring in a normally stressed rock. As the well is drilled the vertical stress decreases, after some time the horizontal stress starts to decreases and there is a point where the horizontal is more than the vertical stress, at this point microfractures can be created (Holt et al., 2000).

8.5 Conclusion

The stress sensitivity shown in Chapter 7 appears to be mainly due to the presence of microfractures which close between 2500 and 3500 psi net stress. The first piece of evidence is the gas permeability decreased between 2500 and 3500 psi net stress. Secondly, the metal is present in all the pores, along grain scale microfractures and was more continuous through the sample at 500 to 2500 psi net stress. Thirdly, the metal was mostly present in the larger pores and less metal was present in the microfractures between 3500 and 4500 psi net stress. Fourthly, more metal was forced out at 3500 psi net stress compared to 2500 psi and > 3500 psi net stress. Below 2500 psi net stress the pressures are not high enough to compress all the pores and microfractures whereas above 3500 psi net stress the microfractures were closed and metal was only leaving the larger less stress sensitive pores.

The closure of these microfractures only has a small impact on porosity because they only represent a small proportion of pore volume. These microfractures do, however, have a significant impact on resistivity, the cementation exponent and permeability which shows why these properties are particularly stress sensitive. Nevertheless, these microfractures were found to be formed during or after coring rather than naturally as (i) there was no cement deposit present in the microfractures, (ii) the microfractures occur at grain contacts, and (iii) the microfractures closed under

lower stresses than those found in the subsurface. Therefore TGS samples are not likely to be as stress sensitive in the subsurface as they are in the laboratory.

The higher values of permeability and the low values of *FRF* and *m* at lower stresses are therefore not representative of subsurface conditions. Consequently, it is recommended that all permeability and electrical experiments on TGS in the future should be measured at subsurface stresses to remove the effects of these microfractures. In addition, implementing restricted rate practise, where gas is produced at higher pore pressures to maintain higher permeability, is not likely to be beneficial in terms of preserving subsurface permeability during production. Future work is needed to understand how the microfracture form.

Chapter 9 - Conclusions

An extensive petrophysical analysis was undertaken with the aim of improving the characterisation of tight gas sandstones reservoirs. The main objectives of the research work was to (i) improved the understanding of the petrophysical properties of tight gas sandstones (TGS), (ii) understand what controls porosity-permeability, (iii) identify the most appropriate and cost effective methods to clean TGS core plugs, (iv) reduction reservoir characterisation timescales, (v) determine the effects of stress on porosity, permeability, electrical properties and MICP permeability estimations and (vi) determine the cause of the stress dependency and whether properties of TGS are stress sensitive in the subsurface. These key aspects are summarized below.

9.1 Sample Cleaning

It has been suggested that the Soxhlet extractor using dichloromethane (DCM) with methanol could damage the microstructure of samples containing delicate clays. This is due to the creation of interfacial tension. Instead, some authors state that critical point drying removes the effects of interfacial tension, therefore, providing more delicate cleaning. A comparison was made between two cleaning methods with four solvents (Soxhlet with DCM/methanol and toluene and critical point drying with and acetone or methanol) at the start of the research work to study this further.

The porosity was 2.3 porosity units (19%) higher and permeability was 0.009 mD (49%) lower for the core plugs cleaned by critical point drying. However, with increased stress, the permeability for all the samples started to converge and those samples with higher permeabilities are from different depths. The brine permeability was 80% lower for the core plug cleaned with DCM/methanol, which is possibly an error as the other three samples have similar brine permeability values. There was no clear relationship in the electrical properties and no significant difference between the pore size and pore throat size. The illite clay was well structured in all the samples irrespective of their cleaning method. Nevertheless, the amount of illite, calcite and dolomite varied before and after cleaning possibly implying the QXRD method is inaccurate.

There was no significant difference between the petrophysical data and the clay structure, suggesting that the Soxhlet extraction method is a reliable cleaning method. However, other authors have found that the critical point drying method does preserve fine structures. Nevertheless, the samples within these studies had the most delicate clays whereas the illite in this research formed strong well-structured blades. Therefore, the critical point drying method is not required for the samples studied within this research, however, this may not be the case for other rock types with more delicate clays.

The main problem with the critical point drying method was that the DMSO-d6, the tracer solvent, solidified at room temperature. This was solved by placing the glass tube which contained the DMSO-d6 in a water bath. It was also unsure if the samples were fully saturated with the acetone/methanol. This was solved by first saturating the samples using a vacuum pump for 2 days followed by an applied confining pressure of 1500 psi for 2 days.

9.2 RCA and SCAL Properties of TGS

To improve on the current knowledge of the petrophysical properties of tight gas sandstones (TGS) an extensive petrophysical analysis was performed on 25 TGS. The gas permeability of samples ranged from 1.2×10^{-3} to 4.1 mD at 500 psi net stress. During the pulse decay experiment there were issues with oil leaking on the sample and equipment. This was due to the uneven nature of the sample and was solved by sanding down the sample.

An Eclipse simulation (finite element simulator able to model laboratory scale fluid flow through various media) using a Cartesian grid was used to model a 5 cm long sample having permeabilities from 0.01 mD to 1 nD, a porosity of 10%, upstream and downstream volumes of 30 cm^3 and an initial pressure of 1000 psi. The model was used to enable a comparison to be made between the permeability and the time required for pore pressure equilibrium to be achieved through a sample prior to a pulse decay permeability measurement. It was found that ~11.4 hours was required for the low permeability samples (0.00005 mD) and ~0.5 seconds for the high permeable samples (4.1 mD). This shows that equilibrium time is important especially for low permeable samples like TGS.

It was found that brine permeability was always lower than the gas permeability. A number of publications found this to be due to an undersaturation of the core samples with respect to the brine, or due to clay swelling or flocculation. The confining pressures and back pressures should have ensured the samples were fully saturated as well as the method used to saturate the core plugs and no swelling clays such as smectite were present. The cause is still unknown, however, flocculation is most likely not occurring, as the high salinities used in this research should prevent this, nevertheless an experiment needs to be designed to study this further.

The microstructure of the 12 wells from which the 25 TGS came from were analysed using SEM and QXRD. The samples have varied textures (fine to coarse, sub-rounded to angular, well sorted to moderate grains), compositions (quartz, feldspar, illite, kaolin, dolomite and siderite) and they have all been affected by extensive diagenetic processes (clay and dolomite cementation, quartz overgrowths and outgrowths, secondary porosity and mechanical compaction). Microfractures are also present between grain contacts, which act as the main cause of the stress dependency found in TGS.

The formation resistivity factor (*FRF)* increases as porosity and permeability decrease due to the reduction in the pore size and connectivity. It was expected that the cementation exponent would also increase with a decrease in porosity and permeability, however, the opposite was found. The samples with the lowest porosity and permeability have the lowest cementation exponents; this is possibly due to the presence of microfractures between grain contacts which increase the connectivity even at low porosities. The *m* is large at higher porosities and permeabilities as the microfractures do not contribute much to the pore connectivity. The larger *m* values are most likely related to the presence of isolated secondary pores. They increase the porosity but as they do not contribute to the overall fluid flow, the *m* value is high.

The effects of temperature were important during this study. Brine permeability and the electrical properties were found to fluctuate and it took long periods of time for them to reach equilibrium. This was solved by placing them in temperature controlled rooms.

The TGS have varied pore sizes with unimodal, biomodal and trimodal pores being present. The pore throat size ranged from 0.002 to 1 μm where some large pore throats were identified from 1 to 5 μm these are the microfractures. The surface area ranged from 0.2 to 5.3 m^2/g. BET was measured by two different laboratories and there were large discrepancies between the results. No strong correlations were identified between surface area and other properties such as permeability, *FRF*, peak pore radius, NMR T_2 cut-off, clay content and *m*. This possess questions on the reliability of the BET methodology and there is the need to adjust the methodology. Overall this Thesis has provided an extensive outlook on the petrophysical properties of a range of TGS rock types which can aid other research work.

9.3 Controls on Porosity and Permeability

Rock types based on mineralogy, microstructure, texture and the depositional environment were used to study the porosity-permeability trends. The trends between porosity and permeability with illite and kaolin content were poor where the R^2 values range from 0.13 to 017. In addition, no trends were found when comparing other diagenetic minerals with permeability and porosity. There is no obvious permeability vs porosity relationship with grain sorting, grain size, grain shape or depositional environment. The lack of relationship is caused by extensive and diverse diagenetic alteration such as the formation of clay.

The only good trend with permeability and porosity was found with the microstructure. Those samples with low clay content had the highest permeabilities for a given porosity whereas those samples with pore bridging clay had the lowest permeabilities for a given porosity. The pore filling clay had permeability values in between. It is therefore clear that the microstructure i.e. the clay type and position is the major control on the porosity-permeability relationships in TGS. This information could be used to determine permeability from wireline log porosity and microstructure from SEM without core plugs.

9.4 Reducing Time Scales for Reservoir Characterisation

A study into the reduction in timescales for reservoir characterisation by gaining petrophysical data without the need for core analysis was performed. The SEM was

found to be the most useful tool in providing the composition, distribution of phases, diagenetic history, texture, pore size and helped identify microfractures. It also enabled an understanding of what controls porosity and permeability and enabled permeability to be estimated using the structural position of clay.

QXRD did not provide a good estimation of permeability as the method is not specific enough for tight rocks, it struggles to distinguish detrital from authigenic phyllosilicates and does not provide any knowledge into the position of minerals. The Coates et al. (1991) model underestimated the laboratory permeability by around one order of magnitude and the SDR model underestimated the laboratory permeability by around three orders of magnitude. This could be due to the wrong *C* constant or because the key properties that affect the NMR T_2 relaxation time i.e. the grain size, pore size and clay type/position, are all assumed to be the same by using a single value of 33 ms as the T_2 cut-off. The permeability trend with NMR was however improved when each well was plotted separately as each well will have similar conditions and properties. This implies there is the potential to divide samples by well to gather more accurate permeability estimations.

Microstructural analysis has identified many of the causes of the scatter when comparing the measured gas permeability and estimated NMR permeabilities. In the presence of secondary pores and pore lining or bridging clay the predicted NMR permeability will be overestimated. In the presence of fractures the predicted NMR permeability will underestimate permeability.

MICP provided a good link between the estimated and measured permeabilities. However, there was an underestimation of the measured permeability at the lower permeability end. This is possibly because the measured permeability in this research was obtained at one single stress of 5000 psi whereas the models provide permeability at a particular threshold pressure. When the MICP permeability was compared to the measured permeability at threshold pressure the R^2 values increased implying the trends improved. This implies that similar conditions are needed for a reliable comparison and confirms that permeability is affected by stress.

The flow rate of the wells linked well to the microstructure. The samples with grain coating illite had flow rates of 2.5 mmscf/day whereas those with low amounts of clay had flow rates of 51 mmscf/day. Those samples with pore filling kaolin clay,

quartz cement/outgrowths, dolomite cement or those that have experienced compaction had flow rates of 31 mmscf/day. This confirms that the clay position is the major control on permeability and that there is a potential to identify good vs poor reservoir using a microscope.

This work has shown that a large amount of information can be gained without the need for core plug analysis. Specifically, side wall cores can be studied using NMR and cuttings can be studied using SEM and MICP data. The best methodologies for obtaining properties such as permeability without core plugs was the SEM and MICP. This means that key properties can be obtained quickly at a start of a research project where core analysis can be used once the area has shown to be profitable, ultimately cutting costs for core labs and oil and gas companies.

9.5 Impact of Stress on TGS

The effects of stress on porosity, permeability (gas and MICP) and electrical properties and the cause of the stress dependency were studied to understand whether properties are stress sensitive in the subsurface. Properties of TGS were found to be stress dependent within the laboratory. Porosity was found to be the least stress sensitive as seen by the almost horizontal data points where the largest increase was 7.6% (1.4 pu). Permeability was found to be the most stress sensitive where the lower stress data is about three times larger than the higher stress data. The electrical properties have a stress dependency between that of porosity and permeability where the *FRF* increased on average by 57% and the *m* by 8%. The brine permeability was originally thought not to be stress dependent, however, when sufficient amount of time was allowed for pressure equilibrium prior to the experiment, the brine permeability was found to be stress sensitive. There was a 40% decrease in permeability with an increase in the confining pressure equilibrium time period from 2 hrs to 4 days.

The main issue with the experimental setup used during the stress dependency studies was leakage of brine and breakage of the equipment. The setup contained many connections which led to the brine leaking, this was solved by ensuring everything was tight and old rusted connections were replaced. The equipment had many attachments such as the burette which easily broke, this was solved by ensure the burette was tightly fastened to the core holder.

The microfractures were found to be the main cause of these stress effects. This was studied by injecting a TGS sample with a eutectic alloy – Field's metal. The Field's metal was found to be present in the microfractures up to 2500 psi net stress but the Field's metal mainly resided within the larger isolated pores above 3500 psi net stress. This demonstrates that the microfractures are closing between 2500 and 3500 psi net stress. This was supported by the gas permeability data where the permeability decreases from 0.07 to 0.02 mD between 2500 and 3500 psi net stress. The closure of only these microfractures has a small impact on porosity because they only represent a small proportion of pore volume. These microfractures do, however, have a significant impact on the connectivity of the pores providing a reason why resistivity, cementation exponent and permeability are particularly stress sensitive.

Microfractures were present between grain contacts, they were not filled with any diagenetic deposits and they closed under stresses lower than that in the subsurface. Therefore, they are believed to be created during the coring or preparation of the core plugs. This implies they will not contribute to the *in-situ* permeability. In addition, restricted rate practice, where gas is produced at higher pore pressures to maintain higher permeabilities, is not beneficial. The significance of this work implies that petrophysical properties should be performed at or near the *in-situ* stress to remove the effects of the microfractures. This will ensure the permeabilities are not over estimated or the electrical data is underestimated.

9.6 Contributions and Applications

This Thesis overall contributes to the knowledge on tight gas sandstones (TGS) and their petrophysical properties by providing a RCA/SCAL program on 25 TGS. In particular it identifies what controls porosity-permeability i.e. the clay position. It obtains different conclusions as different rock types were studied. For example, clay position was found to be the major control on porosity and permeability trends rather than texture or clay amount as other research projects suggested. The reason clay structure was a major control was because the TGS in this research have been affected by extensive diagenesis. The Soxhlet extractor was found to be a moderate method to clean TGS samples rather than the critical point drying method as the clay was well structured compared to the studies that said critical point drying was

needed. Furthermore, the cementation exponent increased with porosity despite other research saying it increases with a decrease in porosity.

An experiment was designed to compare different cleaning methods. The Soxhlet extractor and critical point drying method with CO_2 was compared. It was found that the Soxhlet extractor with DCM/methanol is an adequate method to use for TGS with a similar clay structure.

Experimental data was compared to modelled data to estimate permeability (Kozeny-Carmen equation – BET surface area, SDR and Coates models – NMR and MICP models) and permeability was estimated using microstructure from SEM. The best methods for determining permeability were SEM and MICP. These provide alternative faster methods to estimations permeability without core plugs.

It was found that permeability and electrical properties vary with stress. Therefore, by obtaining these data under reservoir conditions more accurate data that is representative of reservoir conditions can be obtained. The main cause of the stress sensitivity was obtained and found to be due to the closure of microfractures at low stress. This was identified by designing a method where Fields metal was injected into a sample under different stresses and the location of the metal identified using the SEM. This work also enabled the microstructure of a sample to be studied under stress in a microscope, this is significant as it is important to understand how these rocks appear under stress.

This research work could be useful to the oil and gas industry in particular core labs as it increases data accuracy by identifying that some experiment need to be performed under higher stresses. It presents methods which work (porosity, permeability) and those that need improving (QXRD, BET, NMR). It has provided faster alternative methods to obtain key data such as permeability without the time consuming core analysis programs. The controls on porosity and permeability enable the recognition of good vs poor reservoir as those samples with a lot of pore bridging or grain clay will have lower permeabilties compared to those sample with little or no clay. In addition, as the flow of gas and brine and the microstructure and connectivity of pore systems in TGS has been studied, there is the potential to use the data to understand waste disposal and trap systems.

9.7 Future Work

The next step in this research would be to compare the effects of core plug cleaning using the Soxhlet extractor and critical point drying on more rock types to provide stronger statistical data. This may demonstrate that the Soxhlet extractor method of cleaning is suitable for those samples where the clay is not so delicate, whereas, those samples with delicate clays require delicate cleaning methods like critical point drying.

A modelling technique similar to that used for permeability needs to be employed prior to the brine permeability and electrical experiments to determine the pressure and electrical current stability times respectively. In addition, the difference between the brine and gas permeability needs to be further evaluated to ensure it is not an experimental error and a methodology needs to be developed to study the effects of flocculation by studying the change in brine permeability when the direction of the flow of brine and/or when the brine salinity is changed.

The inaccuracies in the QXRD and BET methods as well as the permeability estimations using QXRD and NMR also need to be studied in more detail. For the QXRD, improvements into the accuracy of the data collection and interpretation is required. For the BET and NMR, the methodology needs to be more suitable for TGS. In addition, for the NMR further analysis is required to understand why the data is improved when studying individual wells.

A more extensive study into the formation of the microfractures needs to be done. This could involve strength tests on artificial rocks to try to re-create the microfractures and determine the exact conditions at which they can be generated. In addition, microfractures should be accounted for in simulation models to distinguish between microfracture and matrix permeability.

In this work there were issues with temperature control especially with the stress dependency experiments where the temperature can affect the fluid movement. The laboratory was logged and data corrected for *in-situ* temperatures, however, in the future all instruments need to be placed in temperature controlled rooms. The set-up for the effects of stress on TGS was fragile and had many connections leading to breakages and there were issues with poor electrical contact. Future work would be to design a simpler set-up.

References

1. Aben, H., Kurnitski, V. (2002). Proceedings of Estonian Academy of Sciences, Geology March 2002. *Estonian Academy Publishers*. **5(1)**, 90.
2. Adebayo, T. A. (2015). Irreducible Water Saturation and Porosity Mathematical Models for Kwale Sands, Niger Delta. *Petroleum and Coal*. **57(5)**, 412 – 424.
3. Aguilera. R., Harding, T. G. (2008). State-of-the-Art Tight Gas Sands Characterisation and Production Technology. *Technology Brief*. **47(12)**, 37-42.
4. Al-Awadi, M., Clark, W. J., Moore, W. R., Herron, M., Zhang, T., Zhoa, W., Hurley, N., Kho, D., Montaron, B., Sadooni, F. (2009). Dolomite: Perspectives a on Preplxing Mineral. *Oilfield Review*. **21(3)**, 32-46.
5. Al-Hinai, S., Fisher, Q., Grattoni, C. (2008). Impact on Stress on Fluid Flow: A Detailed Study on Low Permeability Rocks. *Society of Core Analysis.* **25**, 12.
6. Ali, H. S., Al-Marhoun, M. A., Abu-Khamsin, S. A., Celik, M. S. (1987). The Effects of Overburden Pressure on Relative Permeability. *Society of Core Analysis.* **15730**, 335-340.
7. Ali, S. A., Clark, W. J., Dribus, J. R. (2010). Diagenesis and Reservoir Quality. *Oilfield Review*. **22(2)**, 14-28.
8. Allen, C., Bedford, J., Castelijns, K., Fairhurst, D., Gubelin, G., Heton, N., Minh, C. C., Pritchard, T., Ramamoorthy, R. (2000). Trends in NMR Logging. *Oilfield Review*. **12(3)**, 18.
9. Al-Wardy, W., Zimmerman, R. W. (2004). Effective Stress Law for the Permeability of Clay-Rich Sandstone. *Journal of Geophysical Research*. **109(B3)**, 10.
10. Amaefule, J. O., Walls, J. D., Ajufo, A. O., Peterson, E (1986). Laboratory Determination of Effective Liquid Permeability in Low-Quality Reservoir Rocks by the Pulse Decay Technique. *Society of Petroleum Engineers*. **15149**, 493-502.
11. Amiri, M., Ghiasi-Freez, J., Golkar, B., Hatampound, A. (2015). Improving Water Saturation Estimation in a Tight Shaly Sandstone Reservoir using

Artificial Neural Network Optimized by Imperialist Competitive Algorithm – A case study. *Journal of Petroleum Science and Engineering*. **127**, 347-358.

12. Anderson, M. A., Duncan, B., McLin, R. (2013). Core Truth in Formation Evaluation. *Oilfield Review*. **25(2)**, 16-26.
13. Apaydin, O. G., Ozkan, E., Raghavan, R. (2011). Effect of Discontinuous Micro-fractures on Ultra-tight Matrix Permeability of a Dual Porosity Medium. *Society of Petroleum Engineers.* **147391**, **15(4)**, 19.
14. API RP10. (1960). API Recommended Practice for Core-Analysis Procedure. *First Edition, API, New York City (Aug. 1960).* 236.
15. Archie, G. E. (1942). The Electrical Resistivity Log as an Aid in Determining some Reservoir Characteristic. *Transactions of the American Institute of Mining Engineers*. **146(1)**, 8.
16. Archie, G. E. (1950). Introduction to Petrophysics of Reservoir Rocks. *The American Association of Petroleum Geologists*. **34(5)**, 943-961.
17. Arnold, J., Clauser, C., Pechnig, R., Anferova, S., Anferov, V., Blumich, B. (2006). Porosity and Permeability from Mobile NMR Core-Scanning. *Petrophysics*. **47(4)**, 306-319.
18. Asquith, G., Gibson, C. (1982). Basic Well Log Analysis for Geologists. *The American Association of Petroleum Geologists*. **16**, 3-235.
19. Ayala, N. M., Munoz, R., Rico, R., Palacios, C., Torne, J. P., Leuro, J., Fam, M. (2007). New Integratlianged Applications using T1 and T2 Modes of Magnetic Resonance in Tight Gas Reservoir: A Case Study from Northern Mexico. *Society of Petroleum Engineers*. **107364**, 15.
20. Aveyard, R., Haydon, D. A. (1973). An Introduction to the Principles of Surface Chemistry. *Syndics of the Cambridge University Press*. 232.
21. Basan, P. B., Lowden, B. D., Strobel, J. (2003). Maximising the Value of NMR Core Date for Geologists and Petrophysics. *AAPG International Conference, Barcelona Spain, September 21-24, 2003*. 5.
22. Beard, D. C., and Weyl, P. K. (1973). Influence of Texture on Porosity and Permeability of Unconsolidated Sand. *American Association of Petroleum Geologists Bulletin*. **57(2)**, 349-369.
23. Berryman, J. G. (1992). Effective Stress for Transport Properties of Inhomogeneous Porous Rock. *Journal of Geophysical Research.* **97(17),** 409-24.

24. Bethier, P., Schweinar, K., Stanjek, H., Ghanizadeh, A., Clarkson, C. R., Busch, A., Kampman, N., Prinz, D., Amann-Hildenbrand, A., Krooss, B. M., Pipich, V. (2016). On the Use and Abuse of N2 Physisorption for the Characterisation of the Pore Structure of Shales. *The Clay Mineral Society Workshop, Lectures Series.* **12(12)**, 151-161.
25. Biot, M.A., and Willis, D.G. (1957). The Elastic Coefficients of the Theory of Consolidation. *Journal of Applied Mechanics*. **24**, 594-601.
26. Biella, G., Lozej, A., Tabacco, I. (1983). Experimental Study of some Hydrogeophysical Properties of Unconsolidated Porous Medium. *Ground Water*. **21(6)**, 741-752.
27. Bjorkum, P. A., Oelkers, E. H., Walderhaug, O., Murphy, W. M. (1998). Porosity Prediction in Quartzose Sandstone as a Function of Time, Temperature, Depth, Stylolite Frequency and Hydrocarbon Saturation. *American Association of Petroleum Geologists*. **82(4),** 637-648.
28. Block, S., McGowen, J. H. (1994) Chapter 4: Influence of Depositional Environment on Reservoir Quality Prediction. *Society for Sedimentary Geology*. **30**, 41-57.
29. Bloomfield, J. P., Williams, A. T. (1995). An Empirical Liquid Permeability-Gas Permeability Correlation for use in Aquifer Properties Studies. *Quarterly Journal of Engineering Geology*. **28**, 143-150.
30. Blume, T., Weisbrod, N., Selker, J. S. (2004). On the Critical Salt Concentrations for Particle Detachment in Homogeneous Sand and Heterogeneous Hanford Sediments. *Geoderma*. **124**, 121-132.
31. Boles, J. R., Franks, S. G. (1979). Clay Diagenesis in Wilcox Sandstone of Southwest Texas; Implications of Smectitie Diagenesis on Sandstone Cementation. *Journal of Sedimentary Research*. **49(1)**, 55-70.
32. Bonnie, J. H. M., Fens, T. W. (1992). Porosity and Permeability form SEM Based Image Analysis of Core Material. *Society of Petroleum Engineers*. **23619**, 45-59.
33. Boral, A. M. (1987). A New Correlation for the Cementation Exponent in Low-Porosity Carbonates. *Society of Petroleum Engineering, Formation Evaluation*. **2(4)**, 495-500.

34. Bouchaour, M., Diaf, N., Benosman, M., Merad, L., Sari, N-E. C. (2003). The Role of Supercritical CO_2 in the Drying of Porous Silicon. *Review of Renewable Energies: ICPWE*. 99-102.
35. Bp p.l.c. (2015). *Energy Outlook, 2035*. 98.
36. Brace, W. F., Orange, A. S., and Madden, T. R. (1965). The Effect of Pressure on the Electrical Resistivity of Water-Saturated Crystalline Rocks. *Journal of Geophysical Research.* **70(22)**, 5669-5678.
37. Brace, W. F., Walsh, J. B. and Frangos, W. T. (1968), Permeability of Granite Under High Pressure, *Journal of Geophysical Research.* **73**, 2225-2236.
38. Brighenti, G. (1989). Effect of Confining Pressure on Gas Permeability of Tight Sandstone. *International Society for Rock Mechanics. ISRM International Symposium, 30 August - 2 September, Pau, France*. 187-195.
39. Brown, Z. K. (2000). The Drying of Foods using Supercritical Carbon Dioxide. *Thesis at University of Birmingham, Department of Chemical Engineering.* **9(3)**, 249.
40. Brower, K. R., and Morrow, N. R. (1985). Fluid Flow in Cracks as Related to Low-Permeability Gas Sand. *Society of Petroleum Engineers*. **25(2)**, 191-201.
41. Brown, A.A. (2015) Interpreting Permeability from Mercury Injection Capillary Pressure Data. *AAPG Convention, Denver.* 3
42. Brunauer, S., Emmett, P.H., and Teller, E. (1938). Adsorption of Gases in Multi-molecular Layers. *Journal of the America Chemical Society*. **60(2)**, 309-319.
43. Bryant, S L., King, P. R., and Mellor, D. W. (1993a). Network Model Evaluation of Permeability and Spatial Correlation in a Real Random Sphere Packing. *Transport Porous Media*. **11(53)**, 53-70.
44. Byrnes, A. P. (1996). Reservoir Characteristics of Low-Permeability Sandstone in the Rocky Mountains. *The Mountain Geologist*. **34(1)**, 1-12.
45. Byrnes, A. P., Cluff, R. M., Webb, J. C. (2009). Analysis of Critical Permeability, Capillary Pressure and Electrical Properties for Mesaverde Tight Gas Sandstones From Western U.S. Basins. Final Scientific/Technical Report. *Oil and Natural Gas Technology*. **DOE: DE-FC26-05NT42660**, 355.
46. Burdine. N. T. (1963). Rock Failure under Dynamic Loading Conditions. *Journal of Society Petroleum Engineering*. **3(1)**, 8.

47. Burley, S. D. (1984). Patterns of Diagenesis in the Sherwood Sandstone Group (Triassic). *United Kingdom. Clay Minerals.* **19**, 403–404.
48. Cade, C. A., Evans, I. J., and Bryant, S. L. (1994). Analysis of Permeability Controls: A New Approach. *Clay Minerals.* **29(4)**, 491-501.
49. Caldwell, J., Engelmark, F., Neidell, N. S. (1997). Exploring for Stratigraphic Traps. *Oilfield Review*. 48-61.
50. Cannon, D. E., Minh, C. C., Kleiner, R. L. (1996). Quantitative NMR Interpretation. *Society of Petroleum Engineers***. 49010,** 227-287.
51. Castillo, P., Ou, L., Prasad, M. (2012). Petrophysical Description of Tight Gas Sands. *Society of Exploration Geophysics. SEG Las Vegas 2012 Annual Meeting.* **1513**, 5.
52. Chalmers, G. R. L., Ross. D. J. K., Bustin. R. M. (2012). Geological Controls on Matrix Permeability of Devonian Gas Shales in the Horn River and Liard basins, Northe Estern British Columbia. *Canada. International Journal of Coal Geology*. **103**, 120–31.
53. Chen, Q., Kinzelbach, W., Ye, C and Yue, Y. (2002). Variations of Permeability and Pore Size Distribution of Porous media with Pressure. *Journal of Environmental Quality*. **31**, 500-505.
54. Chen, S., Chen, J., Gillen, M., and Georgi, D. (2008). A New Approach Obtaining S_{wir} from NMR Log without Requiring $T_{2cutoff}$. *SPWLA 49th Annual Logging Symposium held in Edinburgh, Scotland, May 25-28, 2008*. 7.
55. Chowdiah, P., Soeder, D. J. (1990). Two-Phase Flow in Tight Gas Sands. *Institute of Gas Technology*. **30603**, 232.
56. Chun, L., Qingxin, G., Ronghu, Z., and Huiliang, Z. (2013). Characteristics and Origin of Micro-fracture in Lower Cretaceous Tight Sandstone from Kuqa Foreland Basin, NW China. *This paper was presented at the International Petroleum Technology Conference held in Beijing, China, 26-28 March 2013*. **16738**, 11.
57. Christie, F. (2011). A Comparison of Herbarium Dried, Critical Point Dried and Fresh Plant Material using High Vacuum and Variable Pressure SEM. *In* Focu. **21**, 5.

58. Clelland, W. D., Fens, T. W. (1991). Automated Rock Characterisation with SEM/Image-Analysis Techniques. *Society of Petroleum Engineering*. **6(4)**, 437-444.
59. Cluff, R. M., and Byrnes, A. P. (2008). Evidence for a Variable Archie Porosity Exponent "*m*" and Impact on Saturation Calculations for Mesaverde Tight Gas Sandstones; Piceance, Uinta, Green River, Wind River, and Powder River Basins. *American Association of Petroleum Geologists Rocky Mountain Section Meeting Abstracts, July, 2008, Denver, CO.* 32.
60. Coates, G. R., Miller, M., Gillen, M., and Henderson, G. (1991). An Investigation of a New Magnetic Resonance Imaging Log. *SPWLA 32" Annual Logging Symposium, June, paper.* 24
61. Coates, G. R., Xiao, L., Prammer, M. G. (1999). NMR Logging Principles and Applications. *Halliburton Energy Services Publication*. 251.
62. Comisky, J. T., Newsham, K. E., Rushing, J. A., and Blasingame, T. A. (2007). A comparative study of capillary-pressure-based empirical models for estimating absolute permeability in tight gas sands. *Society of Petroleum Engineering.* **110050**, 11-14.
63. Constantinides, G., and Payatakes, A. C. (1989). A Three-dimensional Network model for Consolidated Porous Media: Basic Studies. *Chemical Engineering. Communications*. **81**, 55-81.
64. Cosentino, L. (2001). Integrated Reservoir Studies. *BBS*. 305.
65. Cowgill, D. F., Pitman, J. K., Seevers, D. O. (1981). NMR Determination of Porosity and Permeability of Western Tight Gas Sands. *SPE/DOE*. **9875**, 437-448.
66. Cuiec, L. E. (1975). Restoration of the Natural State of Core Samples. *Presented at 50th Annual Fall meeting of Society of Petroleum Engineers of AIME, Dallas, Texas, September 28th-October*. **5634**, 23.
67. Cui, X., Bustin, A. M. M., Sebastian, E. (2009). Measurement of Gas Permeability and Diffusivity of Tight Reservoir Rock: Different approaches and their Applications. *Goefluids*. **9**, 208-223.
68. Cultron, G., Luque, A., Sebastian, E. (2012). Petrophysical and Durability tests on Sedimentary Stones to Evaluate their Quality as Building Materials. *Quarterly Journal of Engineering Geology and Hydrogeology*. **45**, 415-422.

69. Cray, S., Pellegrin, F., Simon, B. (1997). NMR Applications in the Gulf of Mexico. *SPWLA 38th Annual Logging Symposium, June 15-18, 1997*. 13.
70. Crotti, M. A. (2007). Water Saturation in Tight Gas Reservoirs. *Society of Petroleum Engineering*. **107145**. 5
71. Dake, L. P. (1978). Fundamentals of Reservoir Engineering. *Elsevier Science B.V*. 498.
72. Darot, M., Reuschle, T. (1999). Direct Assessment of Wood's Metal Wettability on Quartz. *Pure Applied Geophysics*. **155,** 119-129.
73. Dastidar, R., Rai, C., Sondergeld, C. (2004). Integrated NMR with other Petrophysical Information to Characterise a Turbidite Reservoir. *Society of Petroleum Engineers*. **89948**, 15.
74. Davies, J. P., Davies, D. K. (1999). Stress-Dependent Permeability: Characterisation and Modelling. *Society of Petroleum Engineers, SPE*. **56813**, 16.
75. David, C., Darot, M. (1989). Permeability and Conductivity of Sandstones. *International Society for Rock Mechanics International symposium, 30th August-2 September, Pau, France*. 203-209.
76. Dawe, R. A. (2000). Modern Petroleum Technology. *John Wiley and Sons Ltd.* **1(6)**.488.
77. Delbos, E. Mineralogical Society. [Online]. [06/06/16]. Available from: http://www.minersoc.org/photo.php?id=136.
78. Deschamos, R., Kohler, E., Gasparrini, M., Durand, O., Euzen, T., Nader, F. (2012). Impact of Mineralology and Diagenesis on Reservoir Quality of the Lower Cretaceous Upper Mannville Formation (Alberta, Canada). *Oil and Gas Science and Technology*. **67(1),** 31-58.
79. Dibble, W. E., Nue, A. (1983). Porosity Reduction in Sandstone. *Society of Petroleum Engineering of AIME*. **11970**, 5.
80. Dobrynin, V. (1962). Effect of Overburden Pressure on some Properties of Sandstones, *SPE Journal*. **2**, 360-366.
81. Drake, S. (2007). Unconventional Gas Plays. *Southwest Land Institute, AAPL.*
82. Eberl, D.D. (1984). Clay Mineral Formation and Transformation in Rocks and Soils. *Philosophical Transactions of the Royal Society A*. **374(2079)**, 241-257.

83. Edward, G. M. (1966). Method-Dependent Values of Bulk, Grain and Pore Volume as Related to Observed Porosity. *Geological Survey Bulletin.* **1203-D**, 26.
84. Egermann, P., Doerler, N., Fleury, M., Behot, J., Lenormand, R. (2004). Petrophysical Measurements from Drill Cutting on Added Value for the Reservoir Characterisation Process. *Society of Petroleum Engineers*. **88684**, 9.
85. EIA. (2017). Annual Energy Outlook 2017 with projections to 2050. U.*S Energy Information Administration*. 64.
86. Ellis, D. V. (1987). Well-logging for Earth Scientists. *Elsevier.* 532.
87. Evangelista, V., Barsanti, L., Passarelli, V., Gualtieri, P. (2004). From Cells to Proteins: Imaging Nature Across Dimensions. *Spinger*. 475.
88. Faga, A. T., Oyeneyin, B. M. (2000). Effects of Diagenesis on Neural-Network Grain Size Prediction. *Society of Petroleum Engineers.* **60305**, 5.
89. Farquhar. R. A., Smart., B. G. D., Todd, A. C. (1993). Stress Sensitivity of Low-Permeability Sandstone from the Rotliegendes Sandstone. *Society of Petroleum Engineering*. **26501**. 851-862.
90. Fatt, I., Davis D. H. (1952). Reduction in Permeability with Overburden Pressure. *Trans. AIME, Tech. Note, Technical note.* **147**, 329.
91. Fatt, I. (1953). The Effect of Overburden Pressure on Relative Permeability. *Petroleum Transactions, AIME*. **198**, 325-326.
92. Fatt, I. (1957). The Effect of Overburden Pressure on Relative Permeability. *Technical Note 194.* **198**, 325-326.
93. Fatt, I. (1958). Pore Volume Compressibilities of Sandstone Reservoir Rocks. *Journal of Petroleum Engineering.* **10(3)**, 64-67.
94. Fisher, Q., Grattoni, C., Martin, J. and Guise, P. (2012). Controls on the Porosity and Permeability of Tight Gas Sandstones. *CIPEG*. 125.
95. Fisher, Q. J., Grattoni, C, Rybalcenko, K., Lorinczi, P., and Leeftink, T. N. (2016). Laboratory Measurements of Porosity and Permeability of Shale. *Fifth EAGE Shale Workshop, Catania Sicily, EAGE*. 5.
96. Fisher, Q. J., Knipe, R. J., Worden, R. H. (2000). Microstructures of Deformed and Non-deformed Sandstones from the North Sea Implications for the Origins of Quartz Cement in Sandstones. *International Association of Sedimentologists*. **29**, 129-146.

97. Fjaer, E., Holt, R. M., Horsrud, P., Raaen, A. M., Risnes, R. (2008). Petroleum Related Rock Mechanics. 2nd Edition. *Elsevier*. 515.
98. Fletcher, C. J. N. (2016). Geology for Ground Engineering Projects. *Taylor and Francis Group*. 562.
99. Forsyth, D., Musharfi, N. M. Al., Marzooq, A. M. AL. (2011). Tight Gas Petrophysical Challenges in Saudi Aramco. *Society of Petroleum Engineers.* **149048**, 11.
100. Freeman, C. M. (2010). A Numerical Study of Microscale Flow behaviour in Tight Gas and Shale Gas Reservoir Systems. *SPE Annual Technical Conference and Exhibition, 19-22 September, Florence, Italy.* **141125-STU**. 9.
101. Gale, J. F.W., Reed, R. M., Holder, J. (2007). Natural Fractures in the Barnett Shale and their importance for Hydraulic Fracture Treatments. *AAPG Bulletin*. **91(4)**, 603-622.
102. Ghanizadeh, A., Bhowik, S., Haeri-Ardakani, O., Sanei, H., Clarkson, C. R. (2015). A Comparison of Shale Permeability Coefficients Derived using Multiple Non-steady-state Measurement Techniques: Examples from the Duvernay Formation, Alberta (Canada). *Fuel*. **140**, 371-387.
103. Glanville, C. R. (1959). Laboratory Study Indicates Significant Effect of Pressure on Resistivity of Reservoir Rock. *Journal of Petroleum Technology*. **11(4)**, 7.
104. Glover, P. W. J. (2009). What is the cementation exponent? A new interpretation: *The Leading Edge*. 82–85.
105. Glover, P. (2014). Treatise on Geophysics: Resources in the near Surface Earth – Geophysical Properties of near Surface Earth. *Electrical properties*. Second Edition, **11**, 58.
106. Gornicka, B., Gryzlo, K., Gorecki, L. (2016). Study of Electrokinetic Properties of Nanofluids used for the Preparation of Nanocomposites. *8th National Scientific Advances in Electrotechnology*. **113**, 6.
107. Gottlieb, H. E., Kotlyar, V. and Nundelman, A. (1997). NMR Chemical Shifts of Common Laboratory Solvents as Trace Impurities. The Journal of Organic Chemistry. **62(21)**, 7512-7515.
108. Gunter, G. W., Pinch, J. J., Finneran, J. M., Bryant, W. T. (1997a). Overview of An Integrated Process Model To Develop Petrophysical Description.

Presented at the SPE Annular Technical Conference and Exhibition, San Antonio, TX, October 5-8. **38748**, 475-479.

109. Gunter, G. W., Finneran, J. M., Hartmann D. J., Miller, J. D. (1997b). Early Determination of Reservoir Flow Units Using an Integrated Petrophysical Method. *Presented at the SPE Annular Technical Conference and Exhibition, San Antonio, TX, October 5-8*. **38679**, 8.
110. Guyod, H. (1952). Electrical well logging. *Fundamentals. Houston*. 103
111. Gray, D.H. (1963). The effect of Stress on Permeability of Sandstone Cores. *Society of Petroleum Engineers, SPE.* **3(2)**, 395-401.
112. Hagen, G. H. L. 1839. Uber die Bewegung des Wassers in engen cylindrischen R6hren. *Poggendorf's Annalen der Physik und Chemie*. **46**, 423-42.
113. Haldia, B. S., Singh, S., Bhanja, A. K., Samanta, A. (2013). A new Approach to Determine T_2 Cut-off Value with Integration of NMR, MDT Pressure Data in TS-V Sand of Charali Field. *10th Biennial International Conference & Exposition, Kochi, India.* 7.
114. Hamon, G. (2003). Two Phase Flow Rock Typing: Another Perspective. *Society of Petroleum Engineers.* **84035**, 12.
115. Hans, F. (1967). Influence of Different Types of Diagenesis on Sandstone Porosity. *World Petroleum Congress, 7th World Petroleum Congress, 2-9 April, Mexico.* **12130**, 353-369.
116. Hausenblas. M. (1995). Stress Dependence of the Cementation Exponent. *Society of Core Analysis, Conference Paper. **9518***, 10.
117. Heid, J. G., McMahon, J. J., Nielsen, R. F., Yuster, S. T. (1950). Study of the Permeability of Rocks to Homogeneous Fluids. *American Petroleum Institute, Drilling and Production Practice, 1 January, New York, New York*. **50**, 230-247.
118. Herrick, D. C., Kennedy, W. D. (1993). Electrical Efficiency: A Pore Geometric Model for the Electrical Properties of Rocks. *SPWLA 34th Annual Logging Symposium, June 13-16 June, Calgary, Alberta*. 20.
119. Herrick, D. C., and W. D. Kennedy. (1996). Electrical Properties of Rocks: Effects of Secondary Pores, Laminations, and Thin Beds. *Society of Professional Well-Log Analysts, SPWLA 34th Annual Logging Symposium.* **59(6)**.11.

120. Hillier, S. (1999). Use of an Air-Brush to Spray Dry Samples for X-ray Powder Diffraction. *Clay Minerals*. **34**, 127-135.

121. Hill, H. J., Shirley, O. J., and Klein, G. E., Edited by Waxman, M. H., and Thomas, E. C. (1979). Bound Water in Shaly Sands – its Relation to Qv and other Formation Parameters. *The Log Analyst*. **3**, 3 -19.

122. Hillier, S. (2000). Accurate Quantitative Analysis of Clay and Other Minerals in Sandstones by XRD: Comparison of a Rietveld and a reference Intensity Ratio (RIR) method and the Importance of Sample Preparation. *Clay Minerals*. **35**, 291-302.

123. Hofmann, R., Xiaoxia, X., Michael, B., Manika, P., Anne, K. F., Angela, P. (2005). Effective Pressure or what is the Effect of Pressure. *The leading edge*. **24(12)**, 1256-1261.

124. Holland, M. T. (1982). Reservoir Property Implications of Pore Geometry Modification Accompanying Sand Diagenesis, Anahuac Formation, Louisiana. *Presented at the 57th Annual Fall Technical Conference and Exhibition of the Society of Petroleum Engineers 9, New Orleans, LA, September 26-29.* **10991**, 1-12.

125. Holditch, S. A. (2006). Tight Gas Sands. *Journal of Petroleum Technology*. **58(6)**, 86-94.

126. Holt, R. M., Brignoli, M., Kenter, C. J. (2000). Core Duality: Quantification of Coring-Induced Rock Alteration. *International Journal of Rock Mechanics. Min. Sci*. **37(6)**, 889–907.

127. Homand-Etienne, F., Troalen, J. P. (1984). Behaviour of Granites and Limestones Subjected to Slow Homogeneous Temperature Change. *Engineering Geology*. **20(3)**, 219–233.

128. Hornby, B. E. (1966). An Experimental Investigation of Effective Stress Principles for Sedimentary Rocks. *Society of Exploration Geophysics Annual Meeting, 10-15 November, Denver, Colorado.* 1707-1711.

129. Howard, J. J., Kenyon, W. E., and Straley, C. (1990). Proton-magnetic-Resonance and Pore-size Variations in Reservoir Sandstones. *Society of Petroleum Engineers. Annual. Technical. Conference and Exhibition*. **20600**, 733-742.

130. Howard, J. J. Kenyon, W. E. (1992). Determination of Pore Size Distribution in Sedimentary Rocks by Proton Nuclear Magnetic Resonance: *Marine and Petroleum Geology*. **9(2)**, 139-145.

131. Hower, W. F. (1974). Influence of Clays on the Production of Hydrocarbons. *Society of Petroleum Engineers of AIME*. **4785**. 165-176.

132. Hawkins, D.M., Ellis, E.A., Stevenson , D. (2007). The Novel Critical Point Drying (CPD) Based Preparation and Transmission Electron Microscopy (TEM) Imaging of Protein Specific Molecularly Imprinted Polymers (HydroMIPs). *Journal of Materials Science*. **42(22),** 9465-9468.

133. Huggett, J. M. (1982). On the Nature of Fibrous Illite as Observed by Electron Microscope. *Clay Minerals*. **17(4)**, 433-441.

134. Hyman, L. A., Malek, D. J., and Walls, J. D. (1991). The Effects of Micro-fractures on Directional Permeability in Tight Gas Sands. *Society of Petroleum Engineers.* **21878**, 10.

135. Ioannidis, M. A., and Chatzis, I. (1993). Network Modelling of Pore Structure and Transport Properties of Porous Media. *Chemical Engineering Science*. **48(5),** 972.

136. Javadpour, F. (2009). Nanopores and Apparent permeability of Gas Flow in Mudrocks (Shales and Siltstone). *Journal of Canadian Petroleum Technology*. **48(08)**. 16-21.

137. Jenkins, R. J. (1960). Accuracy of Porosity Determination. *The Log Analysis*. **7(2)**, 29-34.

138. Joel, D. W. (1982). Tight Gas Sands – Permeability, Pore Structure, and Clay. *Journal of Petroleum Technology.* **34(11)**, 2708-2714.

139. Jones, S. C. (1972). A Rapid Accurate Unsteady-State Klinkenberg Permeameter, *Society of Petroleum. Engineers Journal.* **12(5),** 383–397.

140. Jones, F. O., and Owens, W. W. (1980). A Laboratory Study of Low-Permeability Gas Sands. *Journal of Petrophysical Technique,* **32(9)**, 1631-1640.

141. Jones, S.C. (1997) A Technique for Faster Pulse Decay Permeability Measurements in Tight Rocks. *Society of Petroleum Engineers, Formation Evaluation*. **12(1)**, 19-25.

142. Jones, C., Somerville, J. M.., Smart, B. G. D., Kirstetter, O, Hamilton, S.A., Edlmann, K. P. (2001). Permeability Prediction using Stress Sensitivity Petrophysical Properties. *Petroleum Geoscience*. **7(2)**, 211-219.

143. Jones, C., Jones, N. (2011). Laboratory Manual for Physical Geology. *McGraw-Hill*. 368.

144. Juhasz, I. (1986). Conversion of Routine Air Permeability Data into Stressed Brine Permeability Data. *10th European Formation Evaluation Symposium, Aberdeen, UK.* **34**, 39-51.

145. Junchang, S., Zhengming, Y., Qi, T. (2013). Comparative Study on Stress-Dependent Permeability of Ultra-low Permeability Sandstone Rock using Different Types of Fluid Media. *International Petroleum Technology Conference, Beijing China, 26-28 March 2013.* **16653**, 8.

146. Kamath, J. (1992). Evaluation of Accuracy of Estimating Air Permeability from Mercury Injection Data. *Society of Petroleum Engineering*. **7(4)**, 304-310.

147. Katz, A. J., Thompson A. H. (1986). Quantitative Prediction of Permeability in Porous Rock: Physical Review Letters. **34(11)**, 8179-8181.

148. Katz, A. J., Thompson, A. H. (1987). Prediction of rock Electrical Conductivity from Mercury Injection Measurements: *Journal of Geophysical Research*. **92(1),** 599-607.

149. Kaufmann, J. (2010). Pore Space analysis of Cement-based Materials by Combined Nitrogen Sorption – Wood's Metal Impregnation and Multi-Cycle Mercury Intrusion. *Cement and Concrete Composites*. **32**, 514-522.

150. Keelan, D. K. (1972). A Critical Review of Core Analysis Techniques. *The Journal of Canadian Petroleum.* **11(2)**, 42-57.

151. Keighin, C. W. (1979). Influence of Diagenetic Reactions on Reservoir Properties of the Nelsen, Farrer, And Tuscher Formations, Unita Basin, Utah. *SPE*. **7919**, 77-85.

152. Keller, W. D. (1962). Diagenesis in Clay Minerals – A Review. *Eleventh National Conference on clays and clay mineral.* 136-157.

153. Kennedy, M. (2015). Practical Petrophysics. *Elsevier Science Ltd*. 420.

154. Kennedy, W. D., and Herrick, D. C. (2004) Conductivity Anisotropy in a Shale-free Sandstone. *Petrophysics*. **45(1)**, 38-58.

155. Kenyon, W. E., Day, P. I., Straley, C., and Wlllemsen, J. F. (1988). A Three-Part Study of NMR Longitudinal Relaxation Properties of Water-Saturated Sandstone. *Society of Petroleum Engineering*. **3(3)**, 622-637.

156. Kenyon, W. E. (1992). Nuclear Magnetic Resonance as a Petrophysical Measurement. *Nuclear Geophysics.* **6(2)**, 153-171.

157. Khilar, K. C., Fogler, H. S. (1984). The Existence of a Critical Salt Concentration for Particle Release. *Journal of Colloid and Interface Science*. **101(1)**, 214-225.

158. Keighin, C.W. (1979). Influence of Diagenetic Reactions on Reservoir Properties of the Nelson, Farrer, and Tuscher formations, Uinta Basin, UTAH. *Society of Petroleum Engineering of AIME*. **7919**, 77-85.

159. Kilmer, N. H., Morrow, N. R., and Pitman, J. K. (1987). Pressure Sensitivity of Low Permeability Sandstones. *Journal of Petroleum Science and Engineering*. **1(1)**, 65-81.

160. Kiran, E., Brennecke, J. F. (1992). Current State of Supercritical Fluid Science and Technology. *American Chemical Society*. **514**, 8.

161. Kleinberg, R. L., Vinegar, H. J. (1996). NMR Properties of Reservoir Fluids. *The Log Analysis*. **37(6)**, 20-33.

162. Klinkenberg, L. J. (1941). The Permeability of Porous Media to Liquids and Gases, *Drilling and Production Practice, American Petroleum Inst*itute. **41**, 200–213.

163. Knox. D. E. (2005). Solubility's in Supercritical Fluids. *Pure Applied Chemistry*. **77(3)**, 513-530.

164. Kozeny, J. (1927). Ueber Kapillare Leitung des Wassers im Boden. *Sitzungsber Akad Wiss, Wien*. **136(2a)**, 271-306.

165. Kranz, R. L., Frankel, A. D., Engelder, T., and Scholz, C. H. (1979). The Permeability of Whole and Jointed Barre Granite. *International Journal of Rock Mechanics and Mining Sciences and Geomechanics Abstract*. **16(4)**, 225-234.

166. Krumeich, F. (2015). Scanning Electron Microscope (SEM). ETH Zurich Chemsitry Department. [Online]. [30/09/16]. Available from: http://www.microscopy.ethz.ch/sem.htm.

167. Kuuskraa, V. A., Haas, M. R. (1988). Natural Gas from Low Permeability Formations. *Presented at Gas Technology Symposium of the Society of Petroleum Engineers, Dallas, TX. June 13-15th*. **17746**, 18.

168. Kwon, O., Kronenberg, A.K., Gangi, A.F. and Johnson, B. (2001). Permeability of Wilcox Shale and it Effective Pressure Law. *Journal of Geophysical Research*. **106(19)**, 399-19353.

169. Langmuir, I. (1916). Part 1: The Research Laboratory of the General Electric Company. 2221.

170. Latchie, A. S. M., Hemstick, R. A., and Joung, L. W. (1958). The Effective Compressibility of Reservoir Rock and its Effect on Permeability. *Journal of Petroleum Technology*. **10(6)**,49-51.

171. Laubach, S. E. (1989). Paleostress Directions from the Preferred Orientation of Closed Micro-fractures (Fluid-Inclusion Plane) in Sandstone, East Texas basin, USA. *Journal of Structural Geology*. **11**, 603-611.

172. Laubach, S. E., Milliken, K. L. (1996). New Fracture Characterisation Methods for Siliciclastic Rocks. *Rock Mechanics*. **96**, 1209-1215.

173. Lee, W. J. (1982). Well Testing. *Society of Petroleum Engineers of AIME, Dallas, Texas.* **1**, 159.

174. Lever, A. and Dawe, R. A. (1984) Water-sensitivity and Migration of Fines in the Hopeman Sandstone. *Journal of Petroleum Geology*. **7**, 97-108.

175. Lever, A. and Dawe, R. A. (1987). Clay migration and entrapment in synthetic porous media. *Marine and Petroleum Geology*. **4(2)**, 112-118.

176. Liang, X., Zhi-qiang, M., Yan, J. (2015). Tight Gas Sandstone Reservoir Evaluation from Nuclear Magnetic Resonance (NMR) Logs: Case Studies. *Arabian Journal for Science and Engineering*. **40(4)**, 1223-1237.

177. Lieber, R., Dunn, J. (2013). A Proposed Petrophysical Rock Typing Workflow for an Unconventional Mudstone Reservoir – Example from The Niobrara Of The D J Basin. *SPWLA 54th Annual Logging Symposium, Jun 22-26*. 7.

178. Ling, K. (2012). Correlation between rock permeability and formation resistivity factor –a rigorous and theoretical derivation. *SPE*. **152724**, 10.

179. Liu. C., Zhang, R., Zhang, H., Yang, X., Wang, J. (2013). Characteristics and Origin of Microfractures in Lower Cretaceous Tight Sandstone from Kuqa

Foreland Basin, China. *International Petroeleum Technology Conference*. **16738**, 25.

180. Lipchitz, A., Lmbert, T., Harvel, G. D. (2013). Investigation of Fluid Dynamic Properties of Liquid Fields Metal. *Proceedings of the ASME 2013 Power Conference POWER2013 July 29-August 1, 2013, Boston, Massachusetts, USA.* **98224**, 9.
181. Lokmane, S. B. (2001). Hydraulic versus Pneumatic Measurements of Fractured Sandstone Permeability. *Petroleum Science and Engineering*. **36**, 183-192.
182. Lokmane, S. B., Main, L. G., Ngwenya, B. T., Elphick, S. C., Jones, C., Hamilton, S. A. (2009). Correlation between Microstructure and Flow Behavior in Porous Sandstone. *Petroleum Science and technology*. **27(511)**, 511-530.
183. Lonnes, S., Guzman-Garcia, A., Holland, R. (2003). NMR Petrophysical Predications on Cores. *SPWLA 44th Annual Logging Symposium, June 22-25, Galveston, Texas*. 14.
184. Lopez, R. V. W., Rodriguez, F. (2004). A Network Model for Two Phase Flow in Micro-fractured Porous Media. *Society of Petroleum Engineers*. **92056**, 8.
185. Loucks, R. G., and R. M. Ree. (2016). Natural Microfractures in Unconventional Shale-oil and Shale-gas Systems: Real, Hypothetical, or Wrongly Defined? *Gulf Coast Association of Geological Societies Journal*. **5**, 64–72.
186. Lovelock, P. E. R. (1972). Aquifer properties of the Permo-Traisassia Sandstones of the United Kingdom. P.h.D Thesis. 645.
187. Lowell, S., Shields, J. E. (1991). Powder Surface Area and Porosity. *Particle Technology Series, 3rd Edition. Chapman & Hall, New York.* **2**, 242.
188. Luffel, D. L., Herrington, K. L., Harrison, C. W. (1991). Fibrous Illite Controls Productivity in Frontier Gas Sands, Moxa Arch, Whyoming. *Presented at the SPE* 21876 *Rocky Mountain Regional Meeting and Low Permeability Reservoir Symposium, Denver, CO, April 15-17*. **7(4)**, 345-351.
189. Lyklema, J. J., De Keizer, A., Bijsterbosch, B. H., Fleer, G. J., and Cohen Stuart, M. A. (1995) Electric Double Layers. Chap 3 In Volume II: Solid-

Liquid interfaces. Fundamentals of Interface and Colloid Science. *Academic Press*. **3(2)**, 232.

190. Ma, S., Jian, M., Morrow, N. R. (1991). Evaluation of Capillary Flow. *Physical Review*. **17(3)**, 273-283.
191. Machado, V. D. F., Azeredo, R. B. D. V., Ramos, P. F., Coutinho, M. R., Carneiro, S. R. (2008). A NMR Permeability Model based on Partial Least Square (PLS) Regression Analysis for a Low Permeability Gas Sand in Santos Basin. *Society of Core Analysis*. **43**, 6.
192. Martill, D. M., Harper, L. (1990). An Application of Critical Point Drying to the Comparison of Modern and Fossilized Soft Tissue of Fishes. *Palaentology*, **33(2)**, 423-428.
193. Martinez, G. A., Davis, L. A. (2000). Petrophysical Measurements on Shales Using NMR. Society of Petroleum Engineers. **62851**, 10.
194. Mahmood, S. M., Maerefat, N. L., Chang, M-M. (1991). Laboratory Measurements of Electrical Resistivity at Reservoir Conditions. *Society of Petroleum Engineering, Formation Evaluation*. **6(3)**, 291-301.
195. Mavko, G., Mukerji, T., Dvorkin, J. (2009). The Rock Physics Handbook – Tools for Seismic Analysis of Porous Media. *Cambridge University Press*. **2**, 525.
196. Mendelson, K. S., Cohen, M. H. (1982). The Effect of Grain Anisotropy on the Electrical Properties of Sedimentary Rocks. *Geophysics*. **47(2)**. 257-263.
197. Merletti, G. D., Spain, D. R., Pour A., Zett, A. (2014). Understanding Depositional and Diangenetic Processes Improve Petrophysical Rock Typing Workflows in Tight Gas Reservoirs. *SPWLA 5th Annual Logging Symposium, 18-22 May, Abu Dhabi, United Arab Emirates.* 14.
198. Meyer, M T. (1991). Pore Combination Modelling: a Technique for Modelling the Permeability and Resistivity Properties of Complex Pore Systems. *Society of Petroleum Engineers, Annual Technical Conference and Exhibition, Dallas, Texas.* **22662**, 77-88.
199. McNally, M. E. P., Bright, F. V., Mclatchie, A. S., Hemstock, R. A., Young, J. W. (1958). The effective Compressibility of Reservoir Rock and its Effect on Permeability. *Presented at 32nd Annual Fall Meeting of Society of Petroleum Engineers in Dallas Texas, October 6-9.* **10(6)**, 49-51.

200. McNally, M. E. P., Bright, F. V. (1992). Fundamental Studies and Applications of Supercritical Fluids. *American Chemical Society*. **488**, 15.

201. McPhee, C., Reed, J., Zubizarreta, I. (2015). Core Analysis: A Practical Guide. *Elsevier*. **64**, 852.

202. Mohammed, T. E., Gonzales-Sirois, S., Giroux, B., Schmitt, D. R., Schmidt-Hattenberger, C. (2015). Effect of Pressure on Electrical Conductivity and Formation resistivity factor in Sandstone. *GeoConvensiton New Horizons, 4-8 May, Alberta Canada*. 5.

203. Morris, K. A., and Shepperd, C. M. (1982). The Role of Clay Minerals in Influencing Porosity and Permeability Characteristics in the Bridport Sands of Wytch Farm, Dorset. *Clay Minerals*. **17**, 41-54.

204. Naderi, M., Khoo, J., Acharya, M., Burnett, D. (2012). Isotherm Measurements for BET Surface Area Calculations using Inverse Gas Chromatography. *The Total Sorption Solution*. 4.

205. Neasham, J. W. (1977b). The Morphology of Dispersed Clay in Sandstone Reservoirs and its effect on Sandstone Shaliness, Pore Space and Fluid Flow Properties. *Society of Petroleum Engineers SPE Annual Fall Technical Conference and Exhibition, 9-12 October, Denver, Colorado.* **6858**, 8.

206. Nedkvitne, T., Bjorlykke, K. (2006). Secondary Porosity in the Brent Group (Middle Jurassic), Huldra Field, North Sea: Implication for Predicting Lateral Continuity of Sandstone. *Journal of Sedimentary Research*. **62(1),** 23.

207. Nelson, P. H. (2009). Pore-throat Sizes in Sandstones, Tight Sandstones and Shales. *American Association of Petroleum Geologists Bulletin*. **93(3)**, 329-340.

208. Nelson R. (1976). An Experimental Study of Fracture Permeability in Porous Rock. *The 17th US Symposium on Rock Mechanics (USRMS).* **76**, 277-236.

209. Nes, O. M., Skjetne, T. (1993). Shale Porosities as Determined by NMR. 4.

210. Neustaedter, R. H. (1968) Log Evaluation of Deep Ellenburger Gas Zones. *Paper SPE 2071, Deep Drilling and Development Symposium, March 28, Delaware basin, Monahans, Texas.* **2071**, 7.

211. Newshame, K. E., Rushings, J. A. (2001). An Integrated Work Flow Process to Characterise Unconventional Gas Resources. *Part Geological Assessment and Petrophysical Evaluation.. Presented at SPE Annual Technical*

Conference and Exhibition, New Orleans, LA, September 30– October 3. **71351**, 11.

212. Nimmo, J. R. (2004). Porosity and Pore size Distribution. *Encyclopaedia of Soils in the Environment.* **3**, 8.

213. Njoku, C., Pirmez, C. (2011). Sedimentary Controls on Porosity and Permeability in Deepwater Turbidites. *Society of Petroleum Engineering*. **150805**, 5.

214. Nolen-Hoeksema, R. (2014). Flow through Pores. *Oilfield Review*. **26(3)**, 63-64.

215. Ochi, J., Vernoux, J-K. (1998). Permeability Decreases in Sandstone Reservoirs by Fluid Injection: Hydrodynamic and Chemical Effects. *Journal of Hydrology*. **208(3-4),** 237-249.

216. Oiphen, H. V. (1977). An Introduction to Clay Colloid Chemistry. *2nd edition. John Wiley & Sons, New York*. **57**, 120.

217. Ostensen, R. W. (1983). Micro-crack Permeability in Tight Gas Sandstone. *Society of Petroleum Engineers*. **23(6)**, 919-927.

218. Ostensen, R.W. (1986). The Effect of Stress-Dependent Permeability on Gas Production and Well Testing. *Society of Petroleum Engineers Formation Evaluation*. **1(3)**, 227-236.

219. Ostroff, G. M., Shorey, D. S., Georgi, D. T. (1999). Integration of NMR and Conventional Log Data for Improved Petrophysical Evaluation of Shaly Sands. *SPWLA. 40th Annual Logging Symposium, May 30-June 3, Oslo, Norway*. 14.

220. Pallatt, N., Wilson, J., and McHardy, B. (1984). The Relationships between Permeability and Morphology of Diangentic Illite in Reservoir Rocks. *Journal of Petroleum Technology*. **36(12)**, 2225-2227.

221. Pandithage, R. (2012). Brief Introduction to Critical Point Drying. Science Lab. [Online]. [28/0/2015]. Avalible on: [http://www.leica-microsystems.com/science-lab/brief-introduction-to-critical-point-drying/].

222. Petunin, V. V., Yin, X., Tutuncu, A. N. (2011). Porosity and Permeability Changes in Sandstone and Carbonates under Stress and their Correlation to Rock Texture. *Presented at the Canadian Unconventional Resources Conference, Calgary, Alberta, Canada, 15-17 November 2011*. **147401**, 14.

223. Perez, H. H., Datta-Grpta, A., Mishra, S. (2005). The Role of Electrofacies, lithofcaies and Hydraulic Flow Units in Permeability Prediction form Well Logs. A Comparative Analysis Using Classification Trees. *Presented at SPE Annual Conference and Exhibition, Denver, CO, October 5-8.* SPE *Reservoir Evaluation and Engineering, 2005.* **84301**, 143-155.

224. Pevear D.R., Mumpton F.A. (editors) (1989). Quantitative Mineral Analysis of Clays. *Clay Minerals Society, Workshop Lectures, 1. Colorado, USA*. 171.

225. Peveraro, R., and Thomas, E. C. (2010). Effective Porosity: a Defensible Definition for Shaly Sands. *SPWLA 51st Annual Logging Symposium, Perth, Australia, 19-23 June*. **97677**, 14.

226. Pittmann, E. D., Thomas, J. B. (1979). Some Applications of Scanning Electron Microscope to the Study of Reservoir Rock. *Journal of Petroleum Technology*. **31(11)**, 1375-1380.

227. Pittman, E. D. (1992). Relationship of porosity and permeability to various parameters derived from mercury injection-capillary pressure curves for sandstone**.** *AAPG Bulletin*. **76**, 191-198.

228. Poiseuille, J. L. M. 1838. Ecoulement des Liquides: Societe Phi/omatique de Paris. *Extraits des Proces- Verbaux des Seances Pendant I'Annee 1838. Paris: Rene et Cie*. **1(3)**,77-81.

229. Porras, J. C., Campos, O. (2001). Rock Typing: A Key Approach for Petrophysical Characterisation and Definition of Units, Santa Barbara Field, Eastern Venezuela Basin. *Society of Petroleum Engineers.* **69458**, 6.

230. Powers, M. C. (1953). A new roundness scale for sedimentary particles: *Journal of Sedimentary Petrology*. **23**, 117-119.

231. Pugh, V. J., Thomas, D. C., Gupta, S. P. (1991). Correlations for Liquid and Air Permeability's for Use in Reservoir Engineering Studies. *The Log Analyst 4th SEA Annual Technical Conference, 14-16 August, Dallas, Texas*. Paper **9012**, 493-498.

232. Pirson, S. J. (1963). Handbook of Well Log Analysis. *Prentice-Hall*. 326.

233. Profice, S., Lasseux, D., Jannot, Y., Jebara, N., Hamon, G. (2012). Permeability, Porosity and Klinkenberg Coefficient Determination on Crushed Porous Media. *International Symposium of the Society of Core Analysis, Austin, Texas, SPE*. **5(6)**, 9.

234. Purcell, W. R. (1949). Capillary pressures--their measurement using mercury and the calculation of permeability therefrom. *SPE*. **949039**, 39-48.

235. Pyrak-Nolte, L.J., Myer, L. R.., Cook, N.G.W., Witherspoon, P.A. (1987). Hydraulic Mechanical Properties of Natural Fractures in Low Permeability Rock. *International Society for Rock Mechanics 6th ISRM Congress, 30 August-3 September, Montreal, Canada*. 225-232.

236. Rahman, S. S., Rahman, M. W., Khan, F. A. (1994). Response of Low-Permeability, Illitic Sandstone to Drilling and Completion Fluids. *Journal of Petroleum Science and Engineering*. **12**, 309-322.

237. Randolph, P. L., Soeder, D. J, Chowdiah, P. (1984). Porosity and Permeability of Tight Sands. *Society of Petroleum Engineers, Department of Energy, Gas Research Institute.* **12836,** 57-67.

238. Raza, A., Bing. A. H., Nagarajan, R., Hamid, M. A. (2015). Experimental Investigation on Sandstone Rock Permeability of Pakistan Gas Fields. *Materials Science and Engineering*. **78**, 10.

239. Rezaee, M. R., and Lemon N. M. (1996). Influence of Depositional Environment on Diagenesis and Reservoir Quality: Tirrawarrar Sandstone Reservoir, Southern Cooper Basin, Australia. *Journal of petroleum Geology*. **19(4)**, 369-391.

240. Revil, A., Grauls, D., Brevart, O. (2002). Mechanical Compaction of Sand/Clay Mixtures. *Journal of Geophysical Research, Solid Earth*. **107**, 1-15

241. Rezaee, M. R., Otiei, H. M., Kazemzadeh, E. (2015). A New Method to Acquire *m* Exponent and Tortuosity Factor for Microscopically Heterogeneous Carbonates. *Petroleum Science and Engineering*. **56**, 241-251.

242. Rittenhouse, G. (1973). Pore Space Reduction in Sandstone – Controlling Factors and Some Engineering Implications. *Offshore Technology Conference, 6200 North Central Expresway Dallas, Texas.* **75206**, 683-693.

243. Roberts, A. P., Bentz, D. P., Knackstedt, M. A. (1996). Correlating Microstructure to the Petrophysical properties of porous rocks. *Presented at the SPE Asia Pacific Oil and Gas Conference, Adelaide, Australia, October 28th-31st*. **37024**, 551-560.

244. Rochelle, C. A., Moore, Y. A. (2002). The Solubility of Supercritical CO_2 into Pure Water and Synthetic Utsira Pore water. *British Geological Survey, Commissioned Report. **3***. 36.

245. Rogers, J. J. W. and Head, W. B. (1973). Relationships between Porosity, Median Size and Sorting Coefficient of Synthetic Sands. Journal of Sedimentary Research. **31(3),** 467-470.

246. Rouquerol, J., Rouquerol, F., Llewellyn, P., Maurin, G., and Sing, K. S. (2013). Adsorption by powders and porous solids: principles, methodology and applications. *Academic Press*. 467.

247. Rosales, C. P. (1982). On the Relationship between Formation Resistivity Factor and Porosity. *Society of Petroleum Engineers*. **22(4)**. 531-537.

248. Rosenbrand, E., Fabricius, I. L., Fisher, Q., Grattoni, C. (2014). Permeability in Roltliegend Gas Sandstone to Gas and Brine as Predicted from NMR, Mercury Injection and Image Analysis. *Marine and Petroleum Geology*. **64**, 189-202.

249. Rossel, N. C. (1982). Clay Mineral Diagensis in Rotliegend Aeolian Sandstone of the Southern North Sea. *Clay Minerals*. **17**, 69-77.

250. Sampath, K., Keighin, C. W. (1982). Factors Affecting Gas Slippage in Tight Sandstones. *Presented at the SPE/DOE Symposium on Low Permeability Gas Reservoirs. Paper 9870. Denver*. **34(11)**, 27-29.

251. Sandstones and Conglomerates. [Online]. [06/06/16]. Available from: http://www.tulane.edu/~sanelson/eens212/sandst&cong.htm.

252. Santarelli, F. J., Marsala, A. F., Brignoli, M., Rossi, E., Bona, N. (1998). Formation Evaluation from Logging on Cuttings. *Society of Petroleum Engineers.* **36851**, 238-245.

253. Sawyer, W. K., Pierce, C. I., Lowe, R.B. (2001). Electrical and Hydraulic Flow Properties of Application Petroleum Reservoir Rocks. *Petrophysics*. **42(2),** 71-83.

254. Schlumberger. (2009). Log Interpretation Charts. 310.

255. Schmidt, V., McDonald, D. A. (1979). The Role of Secondary Porosity in the course of Sandstone Diagenesis. *Society Economic Palaeontologists Mineralogists Special Publication.* **26**, 175-208.

256. Schwartz, D.E. (1980). Scanning Electron Microsope-Cold Stage: Viewing Fluid Saturated Reservoir Rock. *Society of Petroleum Engineers of AIME*. **9248**, 1-10.

257. Sen, P. N., Scala, C., Cohen, M.H. (1981). A Self-similar Model for Sedimentary Rocks with Application to the Dielectric Constant of Fused Glass Beads. *Geophysics*. **46(5)**, 781-795.

258. Sethi, D. K. (1979). Some Consideration about the Formation Resistivity Factor – Porosity Relations. *SPWLA 20th Annual Logging Symposium, June 3-6*. 2-12.

259. Shafer, J. L., Boitnott, G. N., Ewy, R. T. (2008). Effective Stress Laws for Petrophysical Rock Properties. *SPWLA 49th Annual Logging Symposium, May 25-28, Austin, Texas*. 15.

260. Shafer, J. (2013). Recent Advances in Core Analysis. *Petrophysics*. **54(6)**. 554-579.

261. Shapiro, S. A., Niemann, R., Khizhniak, G. P., Llyushin, P. Yu., Plotnikov, V. V., Galkin, S. V. (2015). Stress-dependent permeability versus stiff and compliant porosity: theory and experiments. *SEG New Orleans Annual Meeting*. 2990-2994.

262. Sharma, M. M., Yortsos, Y. C., and Handy, L. L. (1985). Release and Deposition of Clays in Sandstone. *SPE*. **13562**, 125-130.

263. Sigal, R. F. (2002). The Pressure Dependence of Permeability. *Petrophysics.* **43(2)**, 92-102.

264. Smith, T. M., Sayers, C. M., Sondergeld, C.H. (2009). Rock Properties in Low-Porosity/ Low-Permeability Sandstones. *Society of Exploration Geophysics*. **28(1)**, 48-59.

265. Souza, A., Carneiro, G., Zielinski, l., Polinski, R., Schwartz, L., Hürlimann, M. D., Boyd, A., Rios, E. H., Santos, B. C. D. C., Trevizan, W. A., Machado, V. D. F., Azeredo, R. D. V. (2013). Permeability Predication Improvement Using 2D NMR Diffusion-T_2 Maps. *SPWLA 54th Annual Logging Symposium, June 22-26, New Orleans, Louisiana*. 16.

266. Sperber, G. O., Ericsson, A., Hemmingsson, A., Jung, B., and Thuomas, K. A. (1986). Improved Formulae for Signal Amplitudes in Repeated NMR Sequences: Applications in NMR Imaging. *Magnetic Resonance in Medicine* **3(5)**, 685-698.

267. Stalder, P. J. (1973). Influence of Crystallographic Habit and Aggregate Structure of Authigenic Clay Minerals on Sandstone Permeability. **52(4),** 217-220.

268. Straley, C., Morriss, C. E., Kenyon, W. E., and Howard, J. J. (1991). NMR in Partially Saturated Rocks: Laboratory Insights on Free Fluid Index and Comparison with Borehole Logs. *SPWLA, 32nd Annual Logging Symposium, 16-19 June, Midland, Texas.* ***2****, 25.*

269. Straley, C., Rossini, D., Vinegar, H., Tutunjian, P. (1997). Core Analysis by Low Field NMR. *The Log Analyst.* **38(2)**, 84-96.

270. Suri, Y. (2011). Predicting Petrophysical Properties using SEM Image. *Society of Petroleum Engineers.* **144434**, 12.

271. Swanson, B. F. (1981). A Simple Correlation between Permeability and Mercury Capillary Pressure. *Society of Petroleum Engineering*. **8234**, 2488-2504.

272. Takahashi, M., Koide, H. (1995). Three Principle Stress Effects on Permeability of Shirahama Sandstone. *International Society for Rock Mechanics, 8th ISRM Congress, 25-29th September, Toyko, Japan.* 729-732.

273. Tapping, H. J. M. (1982). Porosity and Permeability Relationships to Cleaning Effectiveness in Whole Core Analysis. *Log Analyse.* **23(3)**, 3-7.

274. Taylor, P. R., Waldlaw, N. C. (1975). Increased Precision of Porosity Measurements Using a Modified Ruska Universal Porometer. *Core Analysis*. **14(2)**, 33-39.

275. Thomas, R. D., Ward, D. C. (1972). Effect of Overburden Pressure and Water Saturation on Gas Permeability of Tight Sandstone Cores. *Journal of Petroleum Technology*. **24(2)**, 120-125.

276. Thommes, M. (G.Q. Lu and X.S. Zhao, editors). (2004) Physical adsorption characterisation of ordered and amorphous mesoporous materials. *Nanoporous Materials: Science and Engineering*. **DOI: 10.1142/9781860946561_0011**, 317–364.

277. Tiab, D., Donaldson, E. C. (2004). Petrophysics: Theory and Practice of Measuring Reservoir Rocks and Fluid Transport Properties. *Burlington: Gulf Professional Publishing*. 889.

278. Tian, X., L. Cheng., W. Zhao., Y. Yan., X. He and Q. Guo. Experimental Study on Permeability Stress Sensitivity in Tight Sandstone Oil Reservoirs. *Sains Malaysiana*. **44 (5)**, 719 – 725.

279. Timur, A., Hempkins, W. B., and Weinbrandt., R. M. (1971). Scanning Electron Microscope Study of Pore Systems in Rocks. *Journal of Geophysical. Research.* **76**, 4932-4947.889.

280. Towel, G. (1962). An Analysis of the Formation Resistivity Factor-Porosity Relationship of Some Assumed Pore Geometries. *SPWLA 3RD Annual Logging Symposium, 17-18 May, Houston, Texas.* 30.

281. U.S. Energy Information Administration. [Online]. [24/01/2017]. Available from: http://www.eia.gov/energyexplained/?page=natural_gas_environment

282. Vulin, D., Peric, L., Kurevija, T. (2012). The use of Petrophysical Data for the Permeability Assessment of an Underground Nuclear Waste Repository. Mining *Geological Petroleum Engendering Bulletin*. **24(1)**, 121-133.

283. Vairogs, J., Hearn, C. L., Dareing, D. W., Rhoades, J. W. (1971). Effect of Rock Stress on Gas Production from Low Permeability Rocks. *Journal of petroleum Technology*. **23(9)**, 1161-1167.

284. Waal, J. A. D., Bil, K. J., Kantorowicz, J. D., Dicker, A. I. M. (1988). Petrophysical Core Analysis of Sandstones Containing Delicate Illite. *The Log Analyst*. **29(5)**, 317-332.

285. Walderhaug, O. (1996). Kinetic Modeling of Quartz Cementation and Porosity Loss in Deeply Buried Sandstone Reservoirs. *AAPG*. **80**, 731-745.

286. Walls, J. D. (1982b). Tight gas sands- Permeability, Pore Structure and Clay. *Journal of Petroleum Technology.* **34(11)**, 708–2714.

287. Walsh, I. B. and Brace, W. F. (1966). Elasticity of Rock: A Review of Recent Theoretical Studies. *Rock Mechanical Engineering Geology.* **4**, 283.

288. Wang, F. P., Lucia, F. J. (1993). Comparison of empirical models for calculating the vuggy porosity and cementation exponent of carbonates from log responses. *The University of Texas, Bureau of Economic Geology, Geological Circular.* **93-4**, 27.

289. Ward, C.E., Barnwell, J.L. (1980). Industrial Survey of Core Handling, Storage, and Analysis Procedures for ROS Measurements. U.*S. Department of Commerce NTIS*. 55.

290. Washburn, E. W. (1921). The Dynamics of Capillary Flow. *Physical Review*. **17**, 273-283.

291. Waxman, M. H., Smiths, L. J. M. (1968). Electrical Conductivities in Oil-Bearing Shaly Sands. *Society of Petroleum Engineers*. **1863-A**, 107-113.

292. Webb, P., Orr. C. (1998). Analytical Methods in Fine Particle Technology. *Micromeritics Instrument Corporation*, 301.

293. Welton. J. E. (1984). SEM Petrology Atlas. *The American Association of Petroleum Geologists.* **4**, 127.

294. Weibel, R., l. Kristensen., M. Olivarius., M. L. Hjuler., A. Mathiesen., L.H. Nielsen. (2012). Investigating Deviations from Overall Porosity-Permeability Trends. *Thirty-sixth Workshop on Geothermal Reservoir Engineering, Standford University, Standford, California, January 30 – February 1, 2012*. 16.

295. Wei, K. K., Morrow, N. R., Brower, K. R. (1986). Effect of Fluid, confining Pressure, and Temperature on Absolute Permeability's of Low Permeability Sandstone. *Society of Petroleum Engineering Formation Evaluation*. **13093**, 413-424.

296. Weinbrandt, R. M., Fatt, I. (1969). A Scanning Electron Microscope Study of the Pore Structure of Sandstone. *Society of Petroleum Engineers.* **21(5)**, 543-549.

297. Weinbrandt, R.M., Fatt, I. (1968). Scanning Electron Microscope Study of the Pore Structure of Sandstones. **21(5)**, 629-645.

298. Welton, J. E. (1984). SEM Petrology Atlas, Methods in Exploration Series No. 4. *The American Association of Petroleum Geologists.* 127.

299. Wells, J. D., Amaefule, JO. (1985). Capillary Pressure and Permeability Relationships in Tight Gas Sands. *Society of Petroleum Engineers*. **13879**, 293-312.

300. Wilson, M. D. (1982) Origins of clays controlling permeability in tight gas sands. *Journal of Petroleum Technology*. **34(12)**, 2871-2876.

301. Wilson, M. D., Stanton, P. T. (1994). Chapter 5: Diagenetic Mechanisms of Porosity and Permeability Reduction and Enhancement. *The Society for Sedimentary Geology*. 59-119.

302. Wilson, M.J., Wilson, L., and Patey, I. (2012). The Influence of Individual Clay Minerals on Formation Damage of Reservoir Sandstones: A Critical Review with some New Insights. *Clay Minerals.* **49**, 147-164.

303. Worden, R., W. R. H. ed., Morad, S. ed. (2000). Quartz Cementation in Sandstone. Oxford, *Blackwell Science Ltd*. **77(9)**, 333.

304. Wyble, D. O. (1958). Effect of Applied Pressure on the Conductivity, Porosity and Permeability of Sandstone. **10(11)**, 57-60.

305. Xiao, L., Zou, C. C., Mao, Z. Q., Liu, X. P., Ju, X. X., Jin, Y. (2013). Tight Gas Sand Permeability Estimation from Nuclear Magnetic Resonance (NMR) Logs Based on the Hydraulic Flow Unit (HFU) approach. *Society of Petroleum Engineers*. **167255**, 306 – 315. 4.

306. Xu, C., Torres-Verdin, C., Gao, S. (2013). Electrical vs. Hydraulic Rock Types in Clastic Reservoirs: Pore-Scale Understanding Verified with Field Observations in the Gulf of Mexico, U.S. *Society of Exploration Geophysicists. 2013 SEG Annual Meeting, 22-27 September, Houston, Texas. 611-615.*

307. Zammerilli, A., Murray, R.C., Davis, T., Littlefield, J. (2014). Environmental impacts of Unconventional Natural Gas Developments and Production. *Energy Sector Planning and Analysis (ESPA) for the United States Department of Energy (DOE), National Energy Technology Laboratory (NETL).* 139.

308. Zhang, J. (2007). Diagenesis and its effect on Reservoir Quality of Silurian Sandstones, Tabei area, Tarim Basin, China. *Petroleum Science*. **4(3)**, 1-13.

309. Zhang, H., He, S., Luan, G., Mo, S., LV, Z., Lei, G. (2013). Experimental Study on Stress Sensitivity of Ultra-low Permeability Sandstones. *Applied Mechanics and Materials.* **318**, 279-283.

310. Zhou, M., Lu, D., Dunsmuir, J., and Thomann, H. (2000). Irreducible Water Distribution in Sandstone Rock: Two Phase Flow Simulations in CT-Based Pore Network. *Physics and Chemistry of the Earth, Part A: Solid Earth and Geodesy*. **25(2)**, 169-174.

311. Zhu, W., Montsi, L., Wong, T-F. (2008). Characterising the Permeability-Porosity Relationships during Compactive Cataclastic Flow. *The 42nd U.S. Rock Mechanics Symposium (USRMS), 29 June-2 July, San Francisco, California*. 5.

312. Zisser, N., Nover, G. (2009). Anisotropy of Permeability and Complex Resistivity of Tight Sandstones subjected to Hydrostatic Pressure. *Journal of Applied Geophysics*. **68**, 356-370.

313. Zoback, M. D., Byerlee, J. D. (1975). Permeability and Effective Stress. *American Associations of Petroleum Geology Bulletin*. **59**, 154-58.

Appendix A

Dimensions and weights before and after cleaning with the four solvents

Cleaning/Solvent	Core/crushed	Sample	Length (cm)	Diameter (cm)	Weight before (g)	Weight after (g)	Weight loss (g)
Critical - Acetone	Core	WCB 1	2.7	2.5	30.8	30.6	0.2
	Crushed	WCA 4	3.0	2.5	33.8	33.5	0.3
Critical - Methanol	Core	WCA 2	3.1	2.5	34.8	34.3	0.5
	Crushed	WCA 3	3.0	2.5	33.0		
Soxhlet – DCM/methanol	Core	WCB 6	3.3	2.5	37.9		
	Crushed	WCB 11	3.0	2.5	34.6	34.4	0.2
Soxhlet -Toluene	Core	WCB 5	2.9	2.5	33.1	32.9	0.2
	Crushed	WCB 2	3.0	2.4	34.6		

Peak ratios of DMSO-d6 to acetone and methanol

Core	Solvent	Time (mins)	Peak ratio of DMSO-d6:Acetone/Methanol
WCA_4	Acetone	0	0:0
		60	1:0.46
		120	1:0.36
		240	1:0.22
		570	1:0.16
		750	1:0.05
		870	1:0.03
		1080	1:0.02
		1230	1:0.01
WCA_1	Acetone	1680	0
WCA_2	Methanol	0	1:0
		210	1:6.61
		1290	1:2.92
		1590	1:1.41

		2910	1:0.55
		3720	1:0.16
		5880	1:0.57
WCA_3	Methanol	0	1:0
		60	1:6.61
		180	1:2.92
		360	1:1.41
		480	1:0.5
		600	1:0.16
		780	1:0.52
		900	1:0.11
		1200	1:0.06
		1500	1:0.05
		1740	1:0.05
		22801:	1:0.02
		3420	1:0.01
		3720	1:0.02

Note: Those peak ratios highlighted in red did not fit the general trend of decreasing acetone and methanol amounts with time.

Liquid NMR spectra for the critical point drying with CO_2 samples

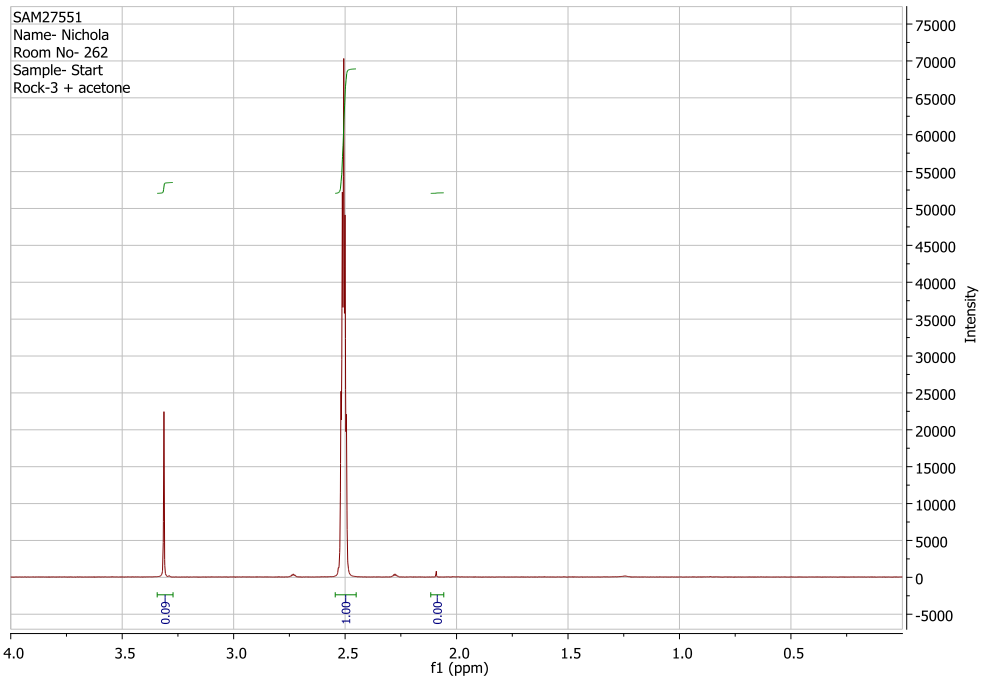

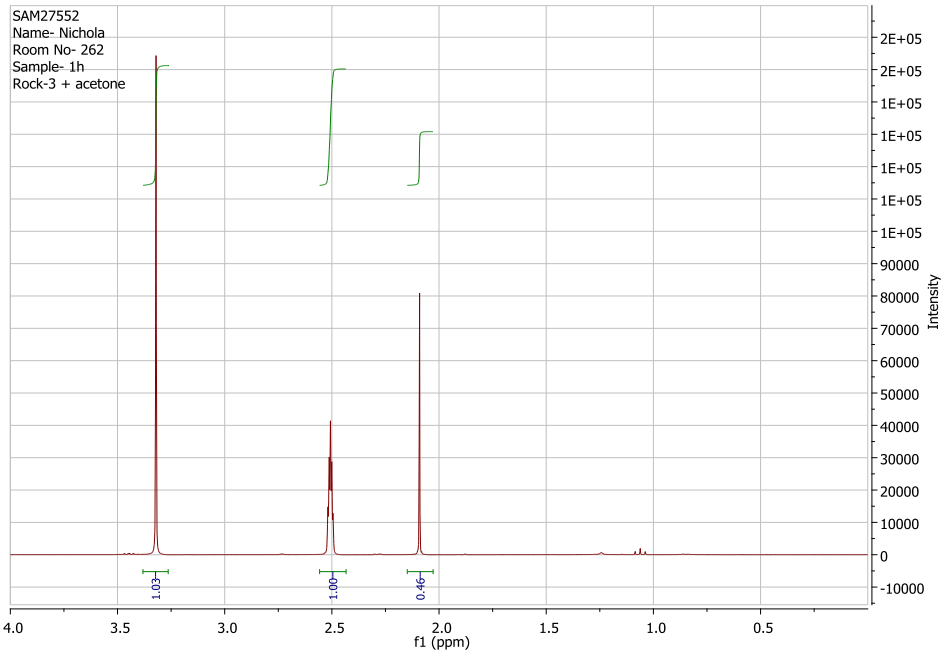

WCA_4 - first samples taken with no CO_2 flush through (top) and 60 minutes after flushing CO_2 (bottom).

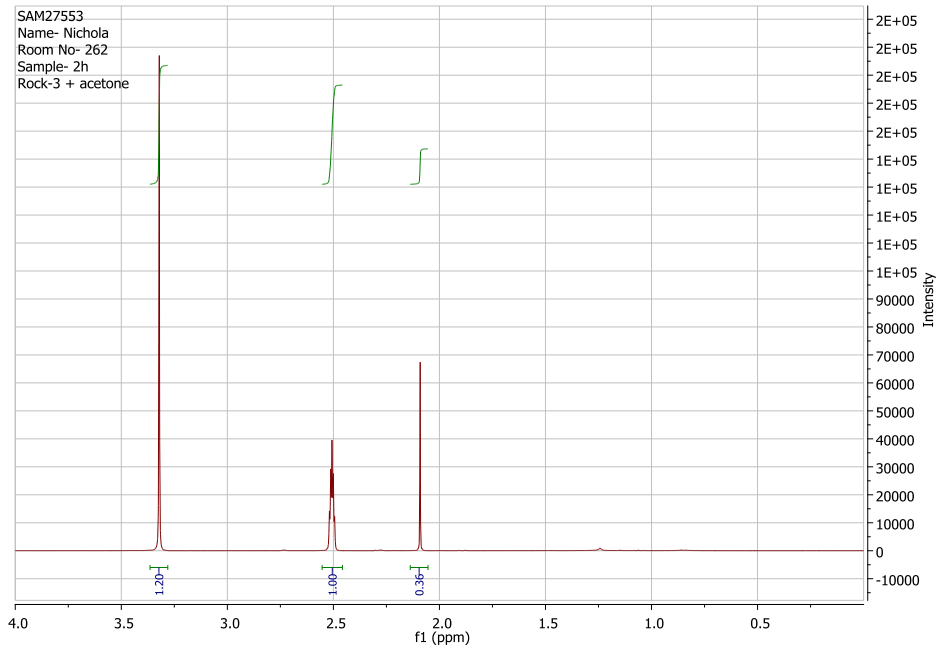

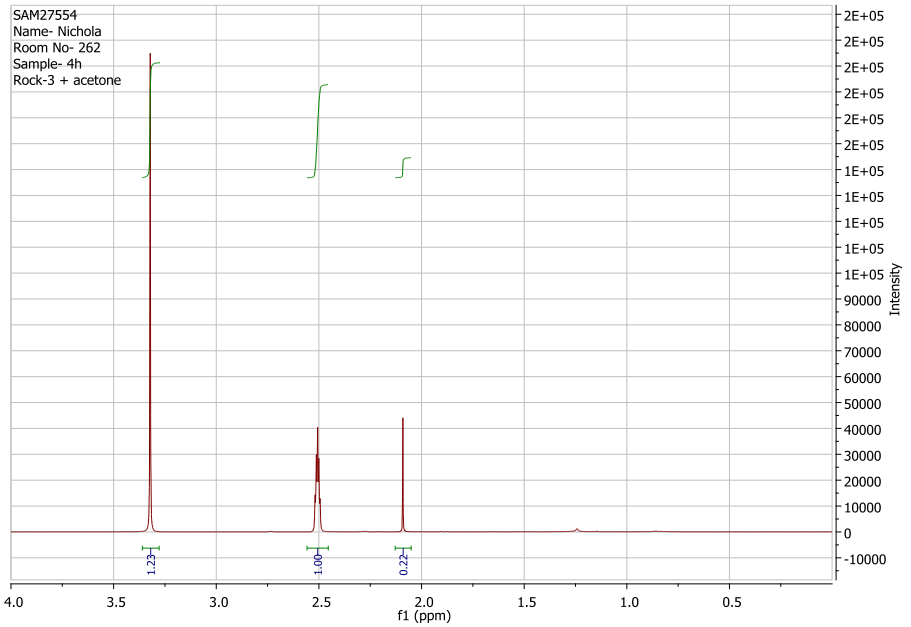

WCA_4 - 120 minutes after flushing CO_2 (top) and 240 minutes after flushing CO_2 (bottom).

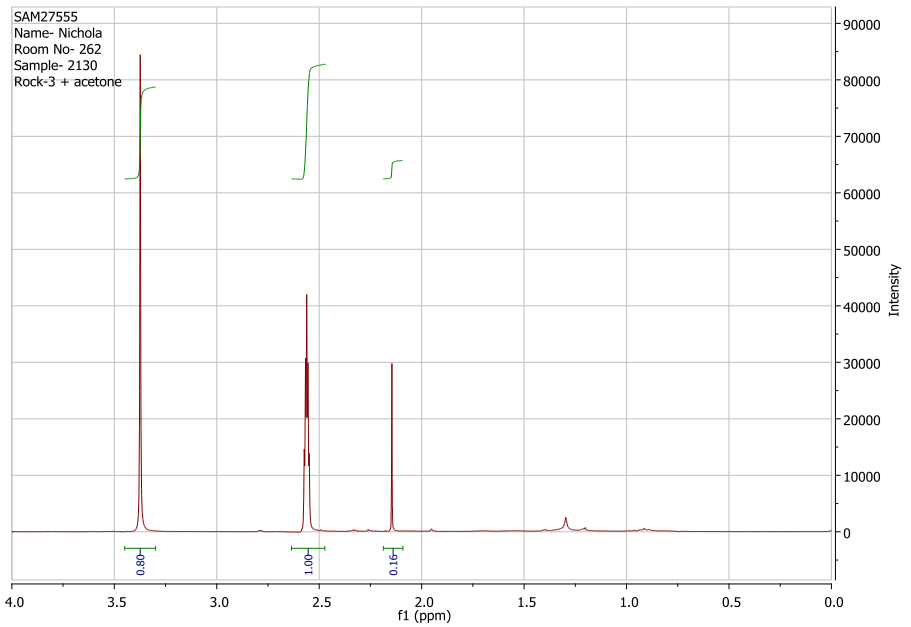

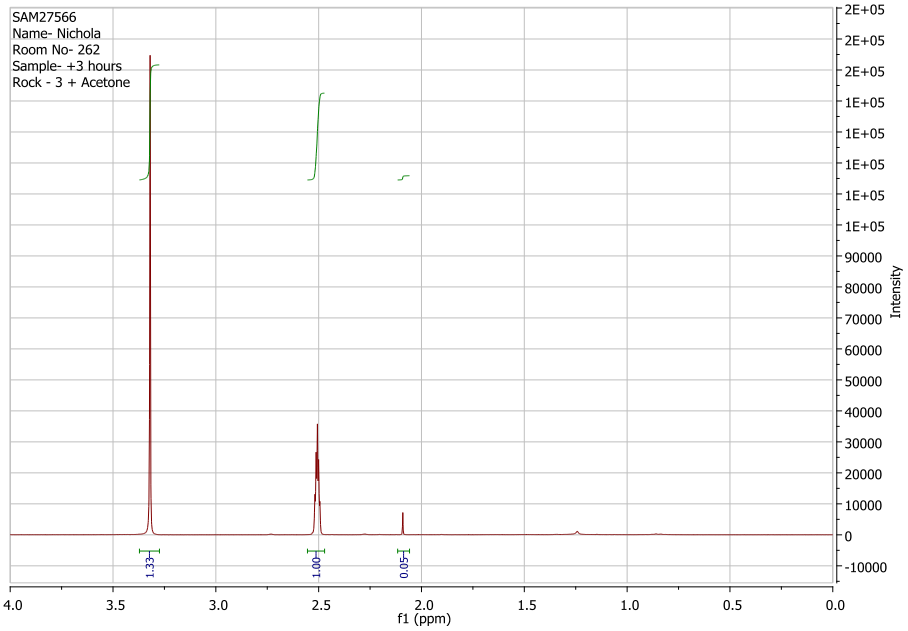

WCA_4 - 570 minutes after flushing CO_2 (top) and 750 minutes after flushing CO_2 (bottom).

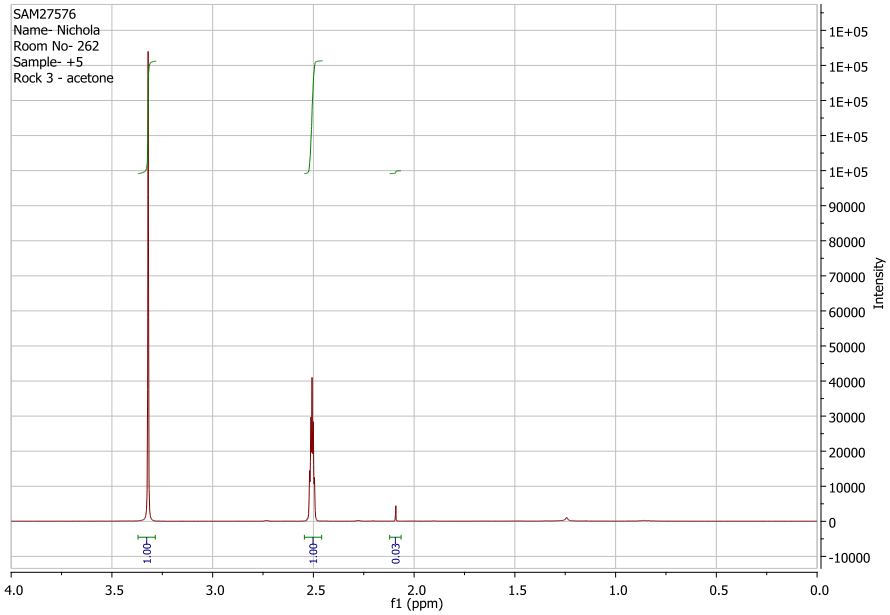

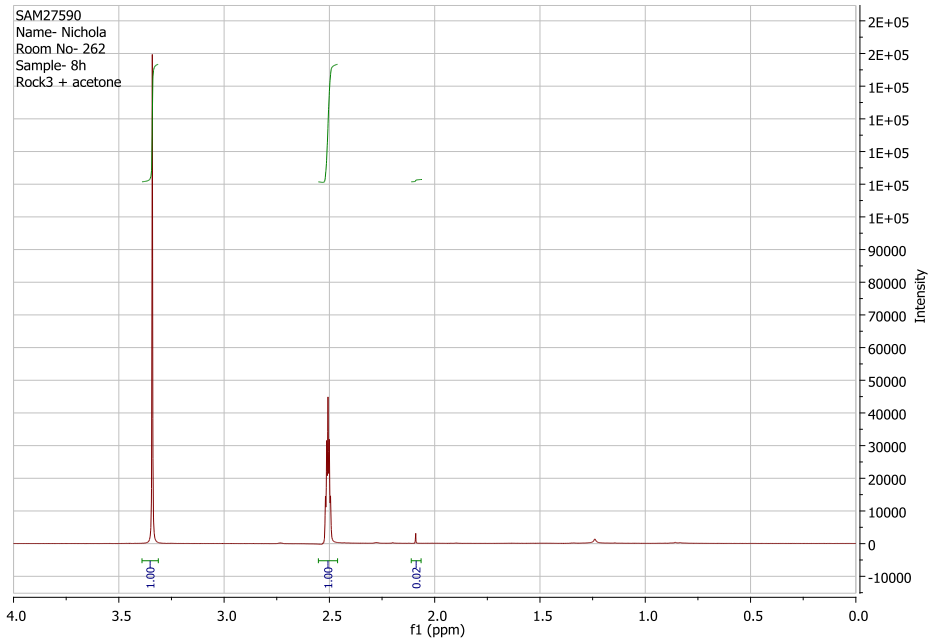

WCA_4 - 870 minutes after flushing CO_2 (top) and 1880 minutes after flushing CO_2 (bottom)

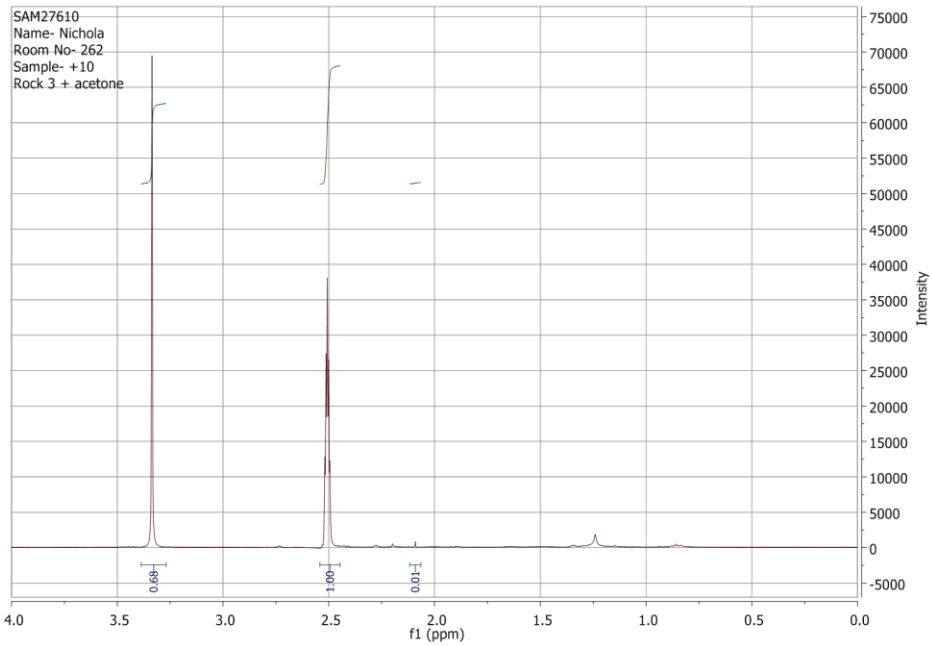

WCA_4 - 1230 minutes after flushing CO_2.

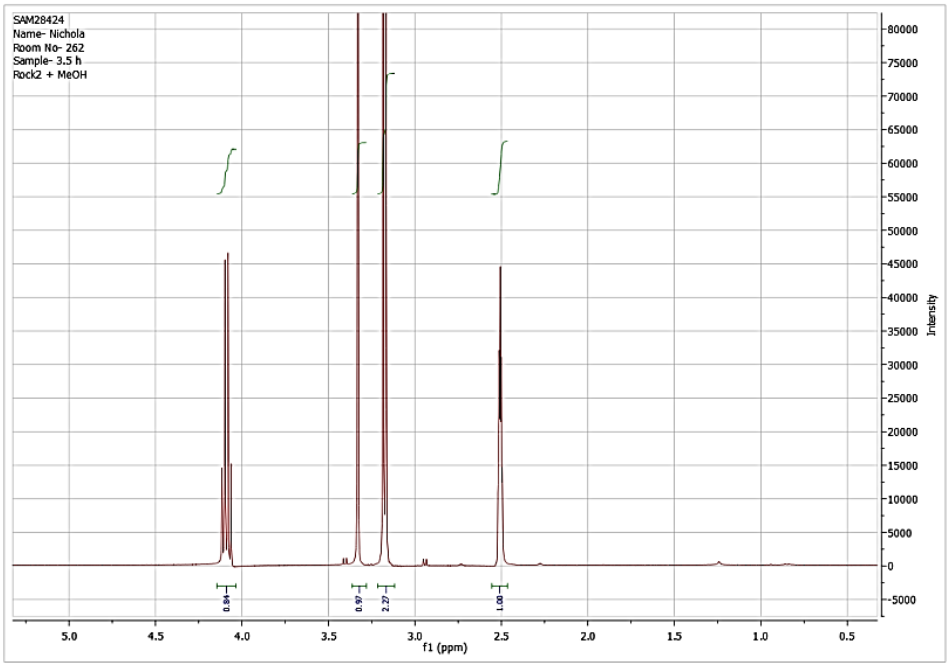

WCA_2 - 210 minutes after flushing CO_2.

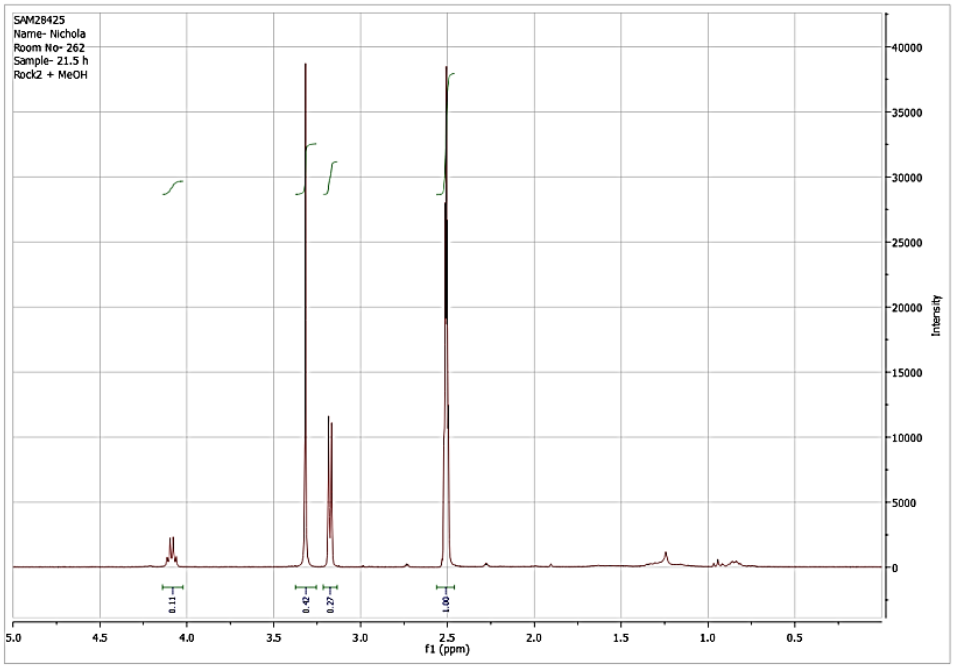

WCA_2 - 1290 minutes after flushing CO_2.

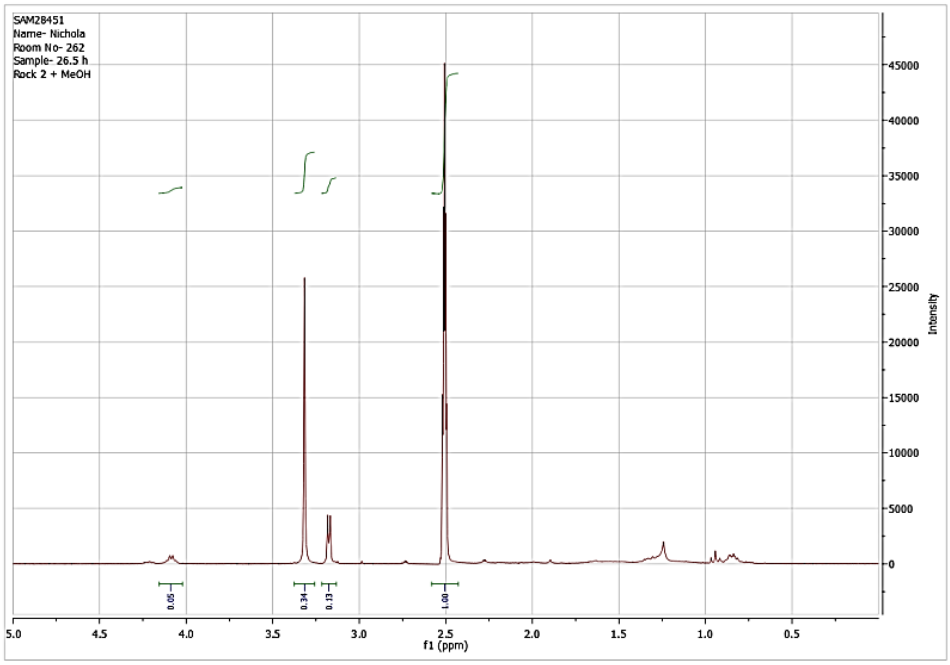

WCA_2 - 1590 minutes after flushing CO_2.

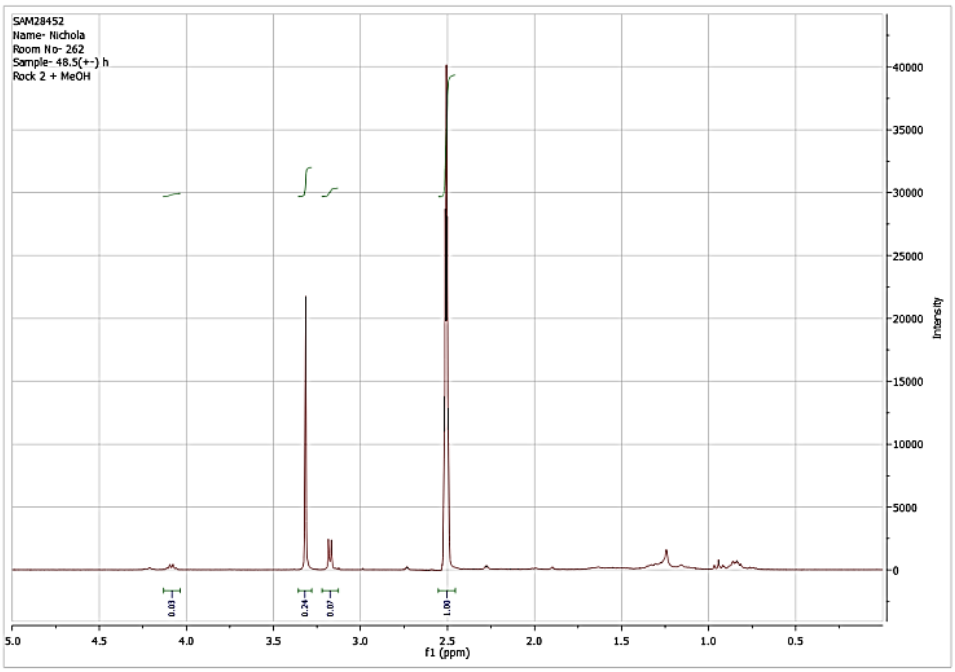

WCA_2 - 2910 minutes after flushing CO_2.

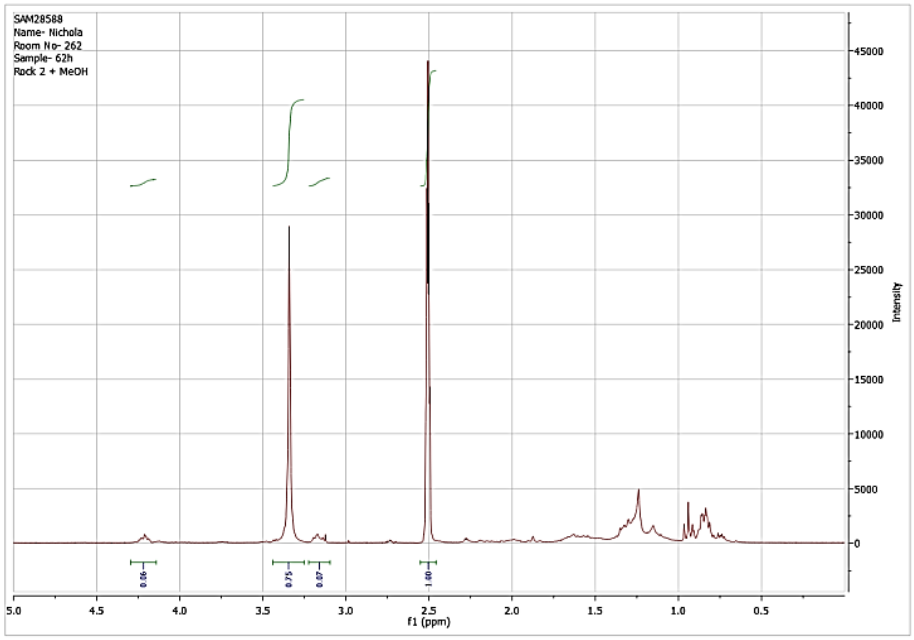

WCA_2 - 3720 minutes after flushing CO_2.

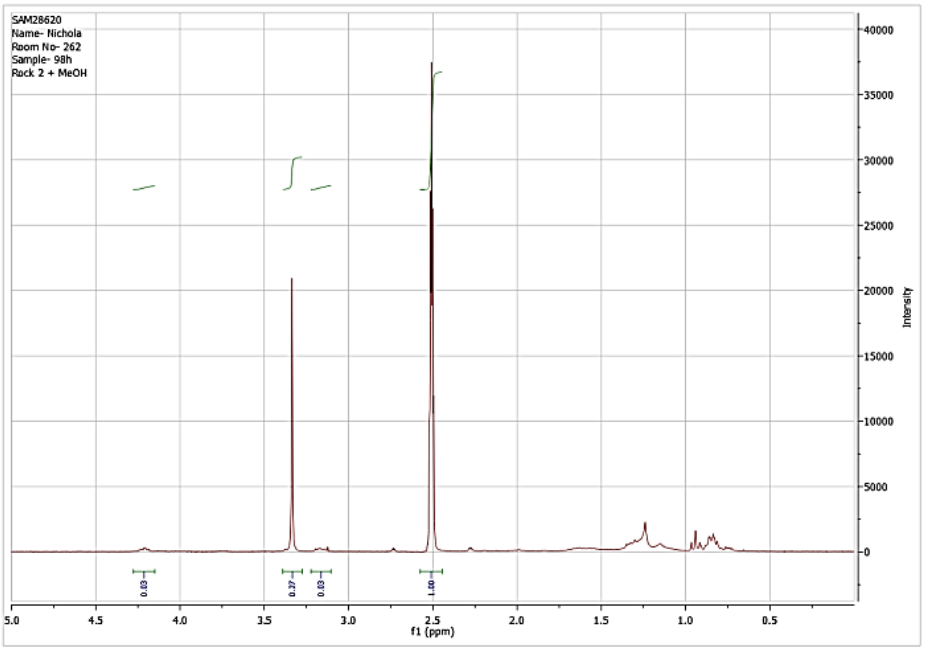

WCA_2 - 5880 minutes after flushing CO_2.

Appendix B

Dry weight and dimensions of the 25 TGS

Sample	Dry weight (g)	Length (cm)	Diameter (cm)	Sample	Dry weight (g)	Length (cm)	Diameter (cm)
BP2_2	166.3	6.6	3.7	SHELL4_370	101.5	4.1	3.8
BP2_3	151.6	6.1	3.7	SHELL4_389	100.8	3.9	3.8
BP2_5		5.6	3.8	SHELL4_409	122.9	4.3	3.8
BP3_1	168.1	6.8	3.7	GDF1_1		5.2	3.8
BP3_4	141.6	5.5	3.8	GDF1_6		5.8	3.8
BP3_5	141.1	5.7	3.8	GDF1_7	142.6	5.4	3.8
BP3_6		5.5	3.7	GDF2_4		3.5	3.8
EBN3_40	103.6	4.5	3.7	WIN4_26	142.6	5.0	3.8
EBN4_10	153.5	5.5	3.7	WIN5_16B	131.9	5.0	3.8
SHELL1_83E		4.6	3.8	WIN9_5	119.9	4.2	3.8
SHELL1_111	142.2	5.1	3.8	WIN10_1	30.8	2.7	2.5
SHELL1_216B	160.7	5.4	3.8	WIN10_2	34.8	3.1	2.5
SHELL2_9B		5.0	3.8	WIN10_3	34.6	3	2.5
SHELL2_1B	117.8	4.3	3.8	WIN10_4	33.1	2.9	2.5
SHELL4_202	106.6	4.4	3.7	BP4_5		5.1	

Bulk volume – calliper and mercury immersion for the 25 TGS samples

Sample	BV from caliper (cm^3)	BV from Hg (cm^3)	Sample	BV from caliper (cm^3)	BV from Hg (cm^3)
BP2_2	70.39	57.96	SHELL2_1B	48.51	
BP2_3	56.34	55.37	SHELL4_202	47.79	
BP2_5	62.94	62.18	SHELL4_370	44.97	43.75
BP3_1	72.71	59.24	SHELL4_389	43.53	
BP3_4	61.51	60.39	SHELL4_409	48.11	
BP3_5	60.20	59.83	GDF1_1	56.88	56.64
BP3_6	60.31	59.42	GDF1_6	63.51	60.31
EBN3_40	49.02		GDF1_7	60.07	59.68
EBN4_10	49.11	59.80	GDF2_4	38.10	37.83
SHELL1_83E			WIN4_26	56.45	
SHELL1_111	57.97		WIN5_16B	56.45	
SHELL1_216B	61.05		WIN9_5	46.91	46.89
SHELL2_9B					

Bulk density and grain density for the 25 TGS samples

Sample	Bulk density (Calliper) (gm/cm^3)	Bulk density (Hg immersion) (gm/cm^3)	Bulk density (Hg injection) (gm/cm^3)
BP2_2	2.36	2.34	2.30
BP2_3	2.32		2.27
BP2_5	2.63	2.62	2.57
BP3_1	2.32	2.32	2.14
BP3_4	2.23	2.27	2.27
BP3-5	2.26	2.28	
BP3_6	2.25	2.28	2.29
EBN3_40	2.11		
EBN4_10	2.57	2.57	2.49
SHELL1_83E	2.59		2.44
SHELL1_111	2.43		2.26
SHELL1_216B	2.61		2.57
SHELL2_9B	2.34		2.11
SHELL2_1B	2.46		
SHELL4_202	2.24		
SHELL4_370	2.28		
SHELL4_389	2.35		
SHELL4_409	2.57		
GDF1_1	2.44	2.44	2.43
GDF1_6	2.58	2.58	2.56
GDF1_7	2.39	2.39	2.38
GDF2_4			
WIN4_26	2.53		2.44
WIN5_16B	2.35	2.33	2.22
WIN9_5	2.57	2.58	2.55

Sample	Grain Density (He) (gm/cm^3)	Grain Density (Hg Injection) (gm/cm^3)	Grain density (QXRD)
BP2_2	2.66	2.61	2.69
BP2_3	2.65	2.57	2.65
BP2_5	2.71	2.67	2.70
BP3_1	2.65	2.54	2.64
BP3_4	2.68	2.64	2.57
BP3-5	2.68		
BP3_6	2.65	2.64	2.71
EBN3_40	2.68		
EBN4_10	2.75	2.68	2.71
SHELL1_83E	2.69	2.56	2.68
SHELL1_111	2.67	2.48	2.66
SHELL1_216B	2.71	2.66	2.63
SHELL2_9B	2.67	2.40	2.58
SHELL2_1B	2.66		2.66
SHELL4_202	2.67		2.69
SHELL4_370	2.66	2.64	2.69
SHELL4_389	2.67	2.62	2.69
SHELL4_409	2.69		2.72
GDF1_1	2.69	2.67	2.68
GDF1_6	2.71	2.70	2.72
GDF1_7	2.64	2.57	2.67
GDF2_4	2.72	2.66	
WIN4_26	2.67	2.62	2.61
WIN5_16B	2.68	2.57	2.70
WIN9_5	2.71	2.58	2.72

Bulk density - Hg immersion vs callipers for the 25 TGS samples

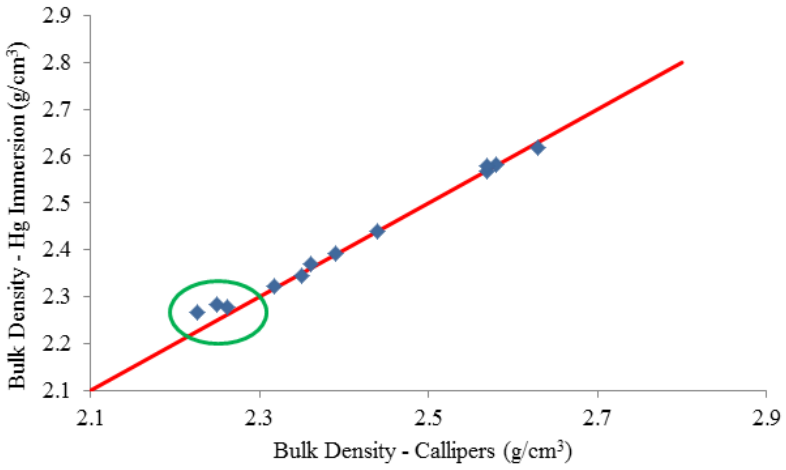

Bulk density – Hg injection vs callipers for the 25 TGS samples

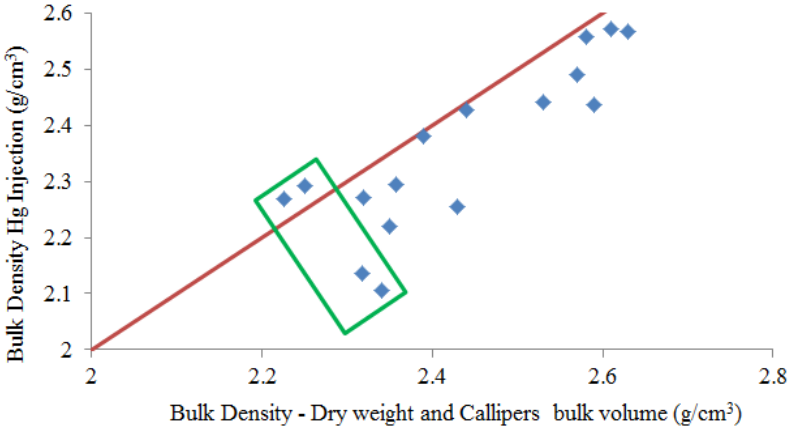

Bulk density – Hg immersion vs Hg injection for the 25 TGS samples

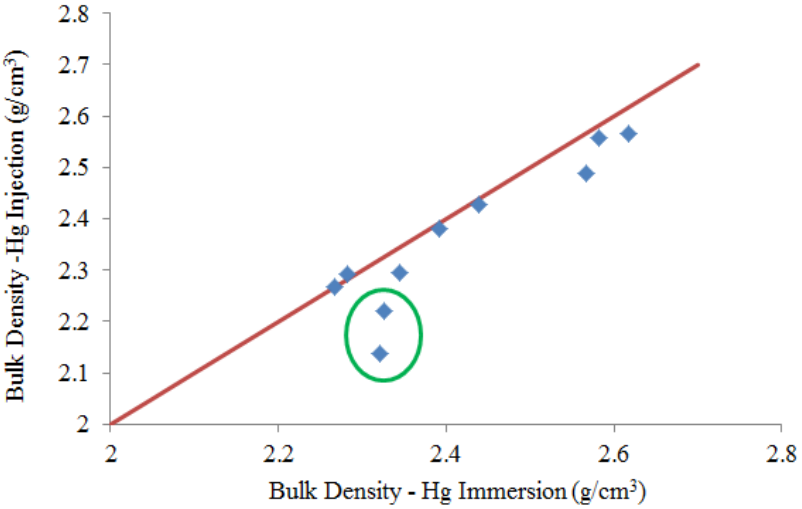

Grain density – Hg injection vs Helium porosimeter for the 25 TGS samples

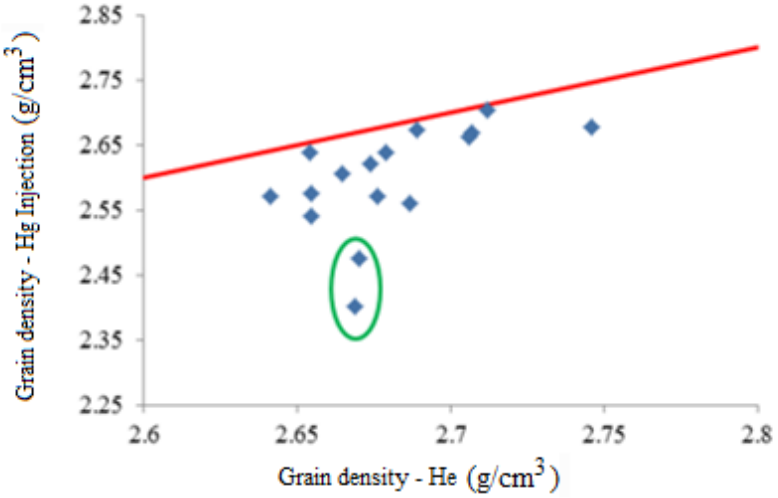

Grain density – QXRD vs helium porosimeter and Hg injection for the 25 TGS samples

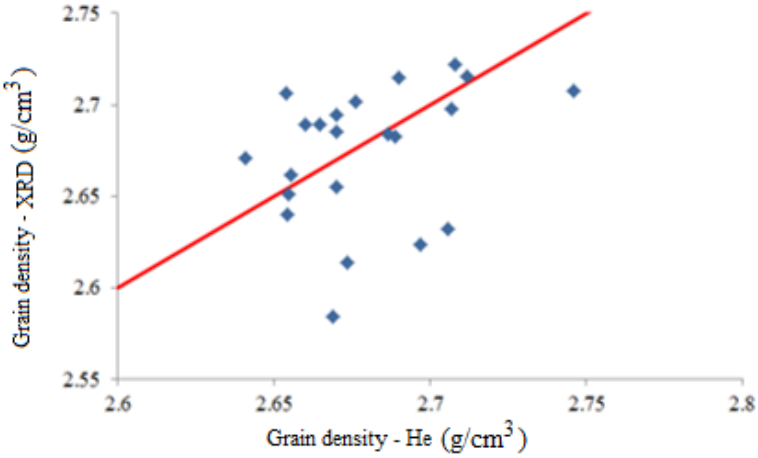

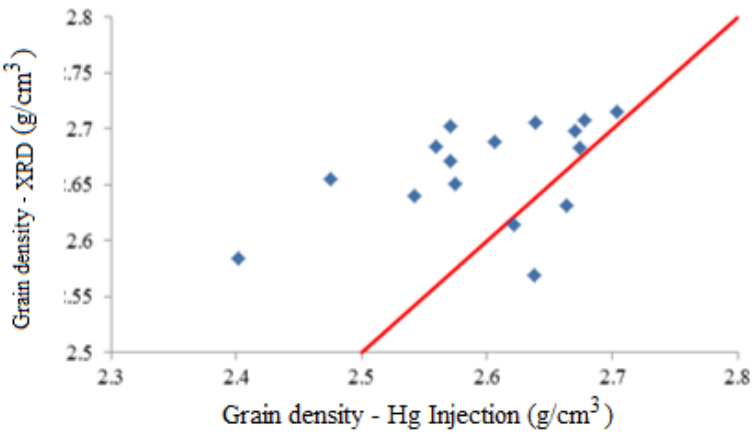

QXRD data for all 25 TGS samples

Sample / Amount (%)	Quartz	Albite	Microcline	Calcite	Dolomite	Magnesite	Mica	Illite-smectite
BP2_1	73.9	4.6	8	0.0	0.2	0.0	2.6	8.4
BP2_2	87	0.0	2.6	0.0	0.8	0.0	1.4	2.5
BP2_3	88.2	0.0	4.2	0.0	0.0	0.0	2.1	0.4
BP3_1	86.9	0.0	2.8	0.0	0.1	0.0	0.0	1
BP3_4	78.4	2.5	5.0	0.0	0.0	0.0	2.5	0.0
BP3_5	78.4	2.5	5.0	0.0	0.0	0.0	2.5	0.0
BP3_6	68.2	0.7	6.8	0.0	0.0	0.0	1.8	0.0
EBN3_40	74.7	4.9	3	0.4	0.6	0.0	1.2	11.5
EBN4_10	51.3	7.3	0.8	0.3	0.7	0.0	7.9	11.1
GDF1_1	83.2	0.1	0.0	0.3	9.2	0.0	1.7	0.0
GDF1_6	69.9	0.2	0.0	0.6	13.8	0.0	2.7	1.5
GDF1_7	90.1	0.4	0.0	0.5	0.6	0.0	1.0	1.3
GDF2_4								
SHELL4_202	85.6	0.2	0.0	0.3	0.3	1.6	0.9	7.4
SHELL4_370	83.5	0.2	0.3	0.5	3.6	1.8	1.9	5.8
SHELL4_389	85.3	0.2	0.0	0.3	0.4	4.7	1.2	6.3
SHELL4_409	79.4	0.0	0.0	0.2	0.4	3.4	3.8	7.8
SHELL1_83	70.5	4.9	1.0	0.0	4.8	0.0	8.2	4.3
SHELL1_111	78.1	4.5	0.0	0.0	2.7	0.0	8.4	0.6
SHELL1_216	69.1	4.7	0.0	0.0	8.3	0.0	11.2	0.4
SHELL2_1B	72.7	4.5	7.6	0.2	4.1	0.0	0.0	9
SHELL2_9B	73.7	5.7	6.0	0.0	4.7	0.0	5.3	4.4
WIN4_26	85.1	1.4	1.1	0.0	4.6	0.0	7.9	0.0
WIN5_16B	68.5	9.4	0.0	0.0	4.1	0.0	0.0	15.7
WIN9_5	65.4	2.6	0.0	0.0	1.9	0.0	14.1	8.0

Sample / Amount (%)	Kaolinite	Chlorite	Pyrite	Siderite	Barite	Anhydrite	Mica+illite	Clay
BP2_1	1.2	0.0	0.9	0.0	0.0	0.2	11.0	12.2
BP2_2	2.7	1.6	0.0	0.0	0.0	0.0	3.9	8.2
BP2_3	4.7	0.0	0.0	0.0	0.0	0.0	2.5	7.2
BP3_1	7.9	1.1	0.0	0.0	0.0	0.0	1.0	10.0
BP3_4	12.6	2.5	0.0	0.0	0.0	0.0	2.5	17.7
BP3_5	12.6	2.5	0.0	0.0	0.0	0.0	2.5	17.7
BP3_6	17.1	3.6	0.4	0.0	0.0	0.0	1.8	22.4
EBN3_40	0.0	0.7	0.0	1.4	0.0	0.0	12.7	13.4
EBN4_10	11.8	0.5	0.3	7.9	0.0	0.0	19.0	31.3
GDF1_1	3.1	0.6	0.3	1.4	0.0	0.1	1.7	5.4
GDF1_6	8.2	0.4	0.0	1.2	0.0	0.2	4.2	12.8
GDF1_7	3.1	0.9	0.2	0.6	1.1	0.1	2.3	6.3
GDF2_4								
SHELL4_202	0.4	2.3	0.2	0.3	0.0	0.6	8.3	11.0
SHELL4_370	0.2	0.8	0.2	0.9	0.0	0.0	7.7	8.7
SHELL4_389	0.0	0.2	0.2	0.7	0.0	0.0	7.5	7.7
SHELL4_409	0.0	3.2	0.2	0.5	0.0	0.9	11.6	14.8
SHELL1_83	0.0	6.1	0.0	0.0	0.0	0.0	12.6	18.7
SHELL1_111	0.0	6.4	0.0	0.0	0.0	0.0	8.9	15.3
SHELL1_216	0.0	8.0	0.5	0.0	0.0	0.0	11.6	19.6
SHELL2_1B	0.0	1.8	0.0	0.2	0.0	0.0	9.0	10.8
SHELL2_9B	0.0	2.8	0.0	0.8	0.0	0.0	9.7	12.5
WIN4_26	0.0	1.2	0.0	0.9	0.0	0.0	7.9	9.1
WIN5_16B	0.0	0.0	0.0	1.3	0.0	0.0	15.7	15.7
WIN9_5	3.7	0.0	0.0	3.1	0.0	0.0	22.1	25.8

Pore pressure equilibrium time eclipse file

```
--============================================================
RUNSPEC


TITLE
GAS-PULSE DECAY


--         Number of cells
--       NX      NY      NZ
--       --      --      --
DIMENS
        402       1       1   /


-- Phases
GAS


-- Units
LAB
--- METRIC LAB

-- Maximum well/connection/group values
--     #wells  #cons/w  #grps  #wells/grp2
--     ------  -------  -----  -----------
--WELLDIMS
--          2        3       2       1 /


-- Unified output files

UNIFOUT

-- Simulation start date
START

1 JAN 2000 /




--============================================================
GRID

-- Size of each cell in X, Y and Z directions
DX

1*30 400*0.0125 1*30 /

DY

402*3  /

DZ

402*3  /


--TVDSS of top layer only
--         X1  X2     Y1  Y2     Z1  Z2
--         --  --     --  --     --  --
BOX
          1   402       1   1      1   1  /

TOPS

402*0     /

ENDBOX


-- Permeability in X, Y and Z directions for each cell
PERMX

1*10000 400*0.000001 1*10000 /

PERMY

1*10000 400*0.000001 1*10000/

PERMZ

1*10000 400*0.000001 1*10000/

-- Porosity of each cell
PORO
1*1 400*0.1 1*1  /

-- Output file with geometry and rock properties (.INIT)

INIT
```

```
--=============================================================
PROPS

-- Densities in lb/ft3
--            Oil       Wat       Gas
--            ---       ---       ---
DENSITY
              49        63        0.074 /


-- PVT data for gas

PVDG
        1.02    14.4    0.0198
        3.40    4.3     0.0198
        5.10    2.9     0.0198
        6.80    2.2     0.0198
        8.50    1.7     0.0198
        10.2    1.4     0.0198
        11.9    1.2     0.0198
        13.6    1.1     0.0198
        15.3    0.96    0.0198
        17.0    0.86    0.0198
        18.7    0.78    0.0198
        20.4    0.72    0.0198
/

EXTRAPMS
1 /



-- Rock compressibility
--         P           Cr
--       ----        -----
ROCK
        1        1.12E-06 /
```

```
--=============================================================
SOLUTION


-- Output to Restart file for t=0 (.UNRST)
--     Restart file       Graphics
--     for init cond        only
--     -------------      --------
RPTRST
         BASIC=2           NORST=1 /

PRESSURE

1*68 400*1 1*68/

/


--=============================================================
SUMMARY


BPR
1 1 1 /
200 1 1/
401 1 1/
/
TCPU
EXCEL

--=============================================================
SCHEDULE


-- Output to Restart file for t>0 (.UNRST)
--     Restart file      Graphics
--      every step         only
--     ------------      --------
RPTRST
        BASIC=2           NORST=1 /


TSTEP
10*0.001
10*0.01
10*0.1
10*1
10*10
1*100 /

END
```

Appendix C

Sample divided according to grain sorting, grain shape and grain size

Well	Sample	Porosity (BV Calliper - GD He) (fraction)	Kg at in situ stress (mD)	Grain sorting
WIN4	26	0.054	0.023	Very well sorted
WIN5	16B	0.12	0.009	
EBN3	40	0.21	0.67	
EBN4	10	0.064	0.002	
SHELL1	83	0.036	0.00019	Well sorted
SHELL2	1	0.074	0.28	
BP2	5	0.028	0.0018	
BP3	4	0.17	0.69	
SHELL4	370	0.14	0.93	
SHELL4	409	0.045	0.00002	
WIN 9	5	0.052	0.00003	
GDF1	6	0.096	0.015	
GDF1	7	0.095	3.7	
SHELL1	111	0.090	0.0037	Moderately sorted
SHELL1	216	0.035	0.005	
BP3	6	0.15	0.56	
SHELL4	202	0.16	0.047	
SHELL4	389	0.12	0.035	
GDF1	1	0.093	1.09	

Well	Sample	Porosity (BV Calliper - GD He) (fraction)	Kg at in situ stress (mD)	Grain shape
WIN4	26	0.054	0.023	Sub-rounded
WIN5	16B	0.12	0.009	
SHELL1	83	0.036	0.00019	
SHELL1	111	0.09	0.0037	
SHELL2	1	0.074	0.28	
SHELL4	389	0.12	0.035	
SHELL4	409	0.045	0.00002	
WIN 9	5	0.052	0.00003	
GDF1	7	0.095	3.7	
SHELL1	216	0.035	0.005	Sub-angular
BP2	5	0.028	0.0018	
BP3	4	0.17	0.69	
BP3	6	0.15	0.56	
EBN4	10	0.064	0.002	
GDF1	1	0.093	1.09	
GDF1	6	0.096	0.015	
EBN3	40	0.21	0.67	Rounded
SHELL4	202	0.16	0.047	
SHELL4	370	0.14	0.93	

Well	Sample	Porosity (BV Calliper - GD He) (fraction)	Kg at in situ stress (mD	Grain size
BP3	4	0.17	0.69	Coarse
BP3	6	0.15	0.56	
BP2	3	0.13	0.17	
WIN4	26	0.054	0.023	Medium Sand
SHELL1	216	0.035	0.005	
BP2	2	0.12	0.03	
BP3	1	0.13	0.16	
EBN3	40	0.21	0.67	
EBN4	10	0.064	0.002	
SHELL4	409	0.045	0.00002	
WIN 9	5	0.052	0.00003	
SHELL4	370	0.14	0.93	Fine-medium
GDF1	1	0.093	1.09	
SHELL4	389	0.12	0.035	Very Fine - medium
WIN5	16B	0.12	0.009	Fine sand
SHELL1	83	0.036	0.00019	
SHELL1	111	0.09	0.0037	
GDF1	6	0.096	0.015	
GDF1	7	0.095	3.7	
SHELL2	1	0.074	0.28	
SHELL2	9	0.12	0.3	
BP2	5	0.028	0.0018	Very fine sand
SHELL4	202	0.16	0.047	
BP2	5	0.028	0.0018	

Sample divided according to illite and kaolin content

Well	**Sample**	**Porosity (BV Calliper - GD He) (fraction)**	**Kg *in-situ* stress (mD)**	**Illite (%)**
WIN5	16B	0.12	0.009	2.6
SHELL1	111	0.090	0.0037	0.6
GDF1	6	0.049	0.015	1.5
GDF1	7	0.095	3.7	1.3
BP2	2	0.12	0.03	2.5
BP2	3	0.13	0.17	0.4
BP3	1	0.13	0.16	1
SHELL1	216	0.035	0.005	0.4
SHELL4	370	0.14	0.93	5.8
SHELL1	83	0.036	0.00019	4.3
SHELL4	389	0.12	0.035	6.3
SHELL4	409	0.045	0.00002	7.8
SHELL4	202	0.16	0.047	7.4
WIN 9	5	0.052	0.00003	8.0
BP2	5	0.028	0.0018	7.2
SHELL2	1	0.074	0.28	9
EBN3	40	0.21	0.67	11.5
EBN4	10	0.064	0.002	11.1
BP3	4	0.17	0.69	12.6
BP3	5	0.16	0.69	12.6
BP3	6	0.15	0.56	17.1

Well	Sample	Porosity (BV caliper - GD He) (fraction)	Kg at in situ stress (mD)	kaolin (%)
SHELL4	202	0.16	0.047	0.4
SHELL4	370	0.14	0.93	0.2
BP2	2	0.12	0.034	2.7
WIN 9	5	0.052	0.00003	3.7
BP2	5	0.028	0.0022	3.5
GDF1	1	0.093	0.75	3.1
GDF1	7	0.095	3.7	3.1
BP2	3	0.13	0.21	4.7
GDF1	6	0.096	0.00085	8.2
BP3	1	0.13	0.16	7.9
EBN4	10	0.064	0.002	11.8

Sample divided according to microstructure

Well	Sample	Porosity (BV Calliper - GD He) (fraction)	Kg *in-situ* stress (mD)	Microstructure
BP3	5	0.16	0.69	Mixture
BP2	2	0.12	0.03	
EBN4	10	0.064	0.002	
WIN 9	5	0.052	0.00003	
GDF1	6	0.096	0.015	Kaolin
BP3	4	0.17	0.69	
BP3	6	0.15	0.56	
BP2	3	0.13	0.17	
BP2	5	0.028	0.0018	
SHELL1	216	0.035	0.005	
GDF1	7	0.095	3.7	
BP3	1	0.13	0.16	

Well	Sample	Porosity (BV Calliper - GD He) (fraction)	Kg *in-situ* stress (mD)	Microstructure
GDF1	1	0.093	0.75	Kaolin
GDF2	4	0.12	3.13	
SHELL4	409	0.045	0.00002	Iliite
SHELL2	9	0.12	0.26	
SHELL1	83	0.036	0.00019	
WIN5	16B	0.12	0.009	
SHELL4	370	0.14	0.93	
SHELL4	389	0.12	0.035	
SHELL4	202	0.16	0.047	
EBN3	40	0.21	0.67	
SHELL1	111	0.09	0.0037	
SHELL2	1	0.074	0.28	Low clay
WIN4	26	0.054	0.023	

Samples divided according to depositional environment

Well/Sample	Porosity (BV Calliper - GD He) (fraction)	Kg at in situ stress (mD)	Sedimentary facies
SHELL4_202	16.4	0.047	Aeolian dry sandflat
WIN5_16B	12.7	0.009	Aeolian dune
SHELL4_370	15.2	0.93	Aeolian dune
SHELL4_389	13.7	0.035	Aeolian dune
SHELL1_83E	3.6	1.50E-04	Aeolian wet sandflat
SHELL1_216B	3.4	0.0045	Aeolian wet sandflat
SHELL4_409	5.1	3.25E-05	Aeolian wet sandflat
BP3_1	12.7	0.18	Channel
EBN3_40	21	0.67	Channel
EBN4_10	7.5	0.002	Channel
GDF1_6	5.3	8.50E-04	Channel
GDF1_7	10	3.68	Channel
WIN4_26	5.8	0.024	Channel
BP3_4	16.9	0.69	Crevasse splay/levee
BP3-5	15.5	0.69	Crevasse splay/levee
BP3_6	15.3	0.56	Crevasse splay/levee
BP2_2	11.5	0.034	Deltaic sandstone
BP2_3	12.6	0.21	Deltaic sandstone
BP2_5	4.5	2.20E-03	Deltaic sandstone
SHELL1_111	8.1	0.003	Reworked aeolian
SHELL2_9B	12.3	0.26	Reworked aeolian
SHELL2_1B	8.3	0.28	Reworked aeolian
GDF1_1	9.7	0.75	Sheetflood
GDF2_4	11	3.13	Sheetflood
WIN9_5	6.3	3.00E-05	Sheetflood

Appendix D

Nuclear magnetic resonance (NMR) data for all 25 TGS samples

Sample	**EBN3_40**	**EBN4_10**	**GDF1_1**	**GDF1_6**	**GDF1_7**	**GDF2_4**
T_2 (ms)	**Normalised Signal**	**Normalised Signal**	**Normalised Signal**	**Normalised Signal**	**Normalised Signal**	**Normalised Signal**
0.01	4.37773E-12	2.20572E-11	9.66194E-14	4.37773E-12	0	0
0.0115	6.25682E-11	3.16072E-10	1.38092E-12	6.25682E-11	0	0
0.01322	6.32418E-10	3.20199E-09	1.3958E-11	6.32418E-10	0	0
0.0152	4.72931E-09	2.39922E-08	1.04386E-10	4.72931E-09	0	0
0.01748	2.72133E-08	1.38293E-07	6.00847E-10	2.72133E-08	0	0
0.02009	1.24676E-07	6.34534E-07	2.75639E-09	1.24676E-07	0	0
0.0231	4.68504E-07	2.38762E-06	1.04049E-08	4.68504E-07	0	0
0.02656	1.4819E-06	7.56159E-06	3.33389E-08	1.4819E-06	0	0
0.03054	4.03578E-06	2.06195E-05	9.36675E-08	4.03578E-06	0	0
0.03511	9.65249E-06	4.93906E-05	2.38854E-07	9.65249E-06	0	0
0.04037	2.06298E-05	0.000105775	5.71377E-07	2.06298E-05	0	0
0.04642	4.00025E-05	0.000205719	1.31317E-06	4.00025E-05	0	0
0.05337	7.13051E-05	0.000368377	2.92442E-06	7.13051E-05	0	0
0.06136	0.000118152	0.000614677	6.28108E-06	0.000118152	0	0
0.07055	0.000183675	0.000965633	1.28837E-05	0.000183675	0	0
0.08111	0.000269879	0.001440645	2.50388E-05	0.000269879	0	0
0.09326	0.00037702	0.002055843	4.59413E-05	0.00037702	0	0
0.10723	0.000503196	0.002822471	7.96017E-05	0.000503196	0	0
0.12328	0.000644417	0.003745317	0.000130591	0.000644417	0	0

0.14175	0.000795319	0.004821352	0.000203609	0.000795319	0	0
0.16298	0.000950479	0.00603888	0.000302883	0.000950479	0	0
0.18738	0.001106005	0.007377582	0.000431439	0.001106005	0	0
0.21544	0.001260927	0.008809753	0.000590296	0.001260927	0	8.05021E-05
0.24771	0.001418007	0.010302817	0.000777685	0.001418007	0	0.00018788
0.2848	0.0015838	0.011822754	0.000988467	0.0015838	0	0.000315238
0.32745	0.001768044	0.013337754	0.001213913	0.001768044	0	0.000456658
0.37649	0.001982628	0.014821358	0.001442013	0.001982628	0	0.000604935
0.43288	0.002240475	0.016254584	0.001658357	0.002240475	0	0.000752794
0.4977	0.002554776	0.017627049	0.001847534	0.002554776	0	0.000894285
0.57224	0.002938926	0.018937329	0.001994899	0.002938926	0	0.001026052
0.65793	0.00340732	0.020192653	0.002088548	0.00340732	8.81047E-05	0.00114813
0.75646	0.003976741	0.021407648	0.002121311	0.003976741	0.000436247	0.001264179
0.86975	0.004667796	0.0226017	0.002092492	0.004667796	0.000838477	0.001381178
1	0.005505763	0.023794724	0.00200892	0.005505763	0.001295769	0.001508788
1.14976	0.006520403	0.025001839	0.001884897	0.006520403	0.001805531	0.001658545
1.32194	0.00774451	0.026228038	0.001740828	0.00774451	0.002360865	0.001842901
1.51991	0.009211269	0.027464382	0.001600882	0.009211269	0.002950208	0.002074093
1.74753	0.01095081	0.028686823	0.001490528	0.01095081	0.003557647	0.002362811
2.00923	0.01298659	0.029858523	0.001435019	0.01298659	0.004164411	0.002716769
2.31013	0.015332332	0.030934833	0.001459644	0.015332332	0.00475202	0.003139444
2.65609	0.01799019	0.031870086	0.001591825	0.01799019	0.005307218	0.003629333
3.05386	0.02094997	0.03262341	0.001864475	0.02094997	0.005828149	0.004180013
3.51119	0.02418913	0.033162061	0.002319562	0.02418913	0.006330422	0.004781126
4.03702	0.027672557	0.033461357	0.003010631	0.027672557	0.006851157	0.005420117

4.64159	0.031351193	0.033501986	0.004003056	0.031351193	0.007449331	0.006084352
5.3367	0.035158738	0.033267354	0.005370901	0.035158738	0.00820166	0.006763104
6.13591	0.039006385	0.032742465	0.007189694	0.039006385	0.009194725	0.007448931
7.0548	0.042776584	0.031915697	0.009525316	0.042776584	0.010515195	0.008138191
8.11131	0.046318602	0.030782618	0.012420493	0.046318602	0.012240123	0.0088305
9.32603	0.049448822	0.029350735	0.015881485	0.049448822	0.014428679	0.009527217
10.7227	0.051958755	0.027643928	0.019867984	0.051958755	0.017115284	0.010229306
12.3285	0.053631547	0.025705114	0.024288792	0.053631547	0.020303461	0.010935278
14.1747	0.054266273	0.023596538	0.029004557	0.054266273	0.023959581	0.01164032
16.2975	0.053706814	0.021396594	0.033837341	0.053706814	0.028007086	0.012337442
18.7382	0.051870246	0.019193009	0.038584967	0.051870246	0.032322917	0.013021149
21.5443	0.048769203	0.017072783	0.043037837	0.048769203	0.036739103	0.013692944
24.7708	0.044522836	0.015109795	0.046995249	0.044522836	0.041052082	0.014367224
28.4804	0.039353498	0.013353378	0.050280196	0.039353498	0.045040346	0.015075825
32.7455	0.033568237	0.011821938	0.052752114	0.033568237	0.048488538	0.015870332
37.6494	0.027527809	0.010505712	0.05431733	0.027527809	0.051212689	0.016822023
43.2876	0.021607345	0.009379513	0.054936101	0.021607345	0.053080509	0.018019492
49.7702	0.016153597	0.008420174	0.05462363	0.016153597	0.054021385	0.019563336
57.2237	0.011444584	0.007619775	0.053442333	0.011444584	0.054023587	0.021556091
65.7933	0.007658166	0.00698656	0.05148404	0.007658166	0.053119716	0.024085609
75.6463	0.00485623	0.006532194	0.048845903	0.00485623	0.051364896	0.027202026
86.9749	0.002989749	0.006252199	0.045608377	0.002989749	0.048815205	0.030891981
100	0.001923744	0.006110725	0.041824367	0.001923744	0.045515112	0.035056695
114.976	0.001474884	0.006038621	0.037525705	0.001474884	0.041499857	0.039501799
132.194	0.001450599	0.005946061	0.032744805	0.001450599	0.036812377	0.04394486

151.991	0.001679185	0.005744551	0.027541482	0.001679185	0.031527506	0.048041648
174.753	0.002025671	0.005368721	0.022023138	0.002025671	0.025771312	0.051426613
200.923	0.002394667	0.004790585	0.016349278	0.002394667	0.019726598	0.053759398
231.013	0.002724735	0.004022486	0.010719175	0.002724735	0.013621146	0.054767024
265.609	0.002979534	0.003109946	0.005347073	0.002979534	0.007702227	0.054273923
305.386	0.00313951	0.002118755	0.000433936	0.00313951	0.002206071	0.052215585
351.119	0.003196231	0.001120483	0	0.003196231	0	0.048635556
403.702	0.003148764	0.000180554	0	0.003148764	0	0.04366931
464.159	0.003001667	0	0	0.003001667	0	0.037520104
533.67	0.002763786	0	0	0.002763786	0	0.030432126
613.591	0.002447155	0	0	0.002447155	0	0.022665043
705.48	0.002065959	0	0	0.002065959	0	0.014472974
811.131	0.001635563	0	0	0.001635563	0	0.006088897
932.603	0.00117109	0	0	0.00117109	0	0
1072.27	0.00068701	0	0	0.00068701	0	0
1232.85	0.00019619	0	0	0.00019619	0	0
1417.47	0	0	0	0	0	0
1629.75	0	0	0	0	0	0
1873.82	0	0	0	0	0	0
2154.43	0	0	0	0	0	0
2477.08	0	0	0	0	0	0
2848.04	0	0	0	0	0	0
3274.55	0	0	0	0	0	0
3764.94	0	0	0	0	0	0
4328.76	0	0	0	0	0	0

4977.02	0	0.000123099	0	0	0	0
5722.37	0	0.000328049	0.000789147	0	0.000189081	0
6579.33	0	0.000514537	0.001542036	0	0.00101076	0
7564.63	0	0.000683098	0.002217463	0	0.001748945	0
8697.49	0	0.000834724	0.002820786	0	0.002409214	0
10000	0	0.000970439	0.003357728	0	0.002997471	0

Sample	**SHELL4_370**	**SHELL4_409**	**SHELL1_83**	**SHELL1_111**	**SHELL1_216**	**SHELL2_1B**
T_2 (ms)	**Normalised Signal**	**Normalised Signal**	**Normalised Signal**	**Normalised Signal**	**Normalised Signal**	**Normalised Signal**
0.01	6.55764E-13	6.65016E-12	3.13451E-11	1.15358E-11	1.99228E-11	8.69291E-12
0.0115	9.37242E-12	9.50465E-11	4.47996E-10	1.64873E-10	2.85301E-10	1.24648E-10
0.01322	9.47332E-11	9.60699E-10	4.5282E-09	1.66648E-09	2.88863E-09	1.26347E-09
0.0152	7.08429E-10	7.18428E-09	3.38625E-08	1.24622E-08	2.16336E-08	9.47172E-09
0.01748	4.07641E-09	4.13405E-08	1.94851E-07	7.17097E-08	1.24643E-07	5.46191E-08
0.02009	1.86755E-08	1.89415E-07	8.92694E-07	3.28532E-07	5.71679E-07	2.50705E-07
0.0231	7.01733E-08	7.1198E-07	3.35448E-06	1.23451E-06	2.15025E-06	9.43665E-07
0.02656	2.2192E-07	2.25389E-06	1.061E-05	3.90455E-06	6.80647E-06	2.98952E-06
0.03054	6.04088E-07	6.15074E-06	2.88924E-05	1.06318E-05	1.85459E-05	8.15461E-06
0.03511	1.44334E-06	1.47756E-05	6.909E-05	2.54192E-05	4.43634E-05	1.95402E-05
0.04037	3.07856E-06	3.18452E-05	0.000147618	5.4293E-05	9.47827E-05	4.18676E-05
0.04642	5.94776E-06	6.2649E-05	0.00028614	0.000105179	0.000183611	8.14816E-05
0.05337	1.05363E-05	0.000114242	0.000509985	0.000187283	0.000326766	0.000146043
0.06136	1.7283E-05	0.000195665	0.000845674	0.000310116	0.000540381	0.000243996
0.07055	2.64446E-05	0.000318166	0.001318323	0.00048246	0.000838619	0.000383933

0.08111	3.79269E-05	0.00049531	0.001949667	0.000711573	0.001231702	0.000573966
0.09326	5.11183E-05	0.000742836	0.00275706	0.001002831	0.001724539	0.000821109
0.10723	6.48026E-05	0.001078228	0.003753342	0.001359857	0.002316233	0.001130688
0.12328	7.72583E-05	0.001520061	0.004947077	0.001785088	0.003000531	0.001505781
0.14175	8.66171E-05	0.002087189	0.006342694	0.002280702	0.003767056	0.001946705
0.16298	9.14606E-05	0.002797724	0.007940311	0.002849789	0.004602929	0.002450646
0.18738	9.15417E-05	0.003667715	0.009735369	0.003497648	0.005494296	0.003011538
0.21544	8.84954E-05	0.004709485	0.011718224	0.004232898	0.006427383	0.003620386
0.24771	8.64467E-05	0.005929769	0.01387371	0.005068028	0.007388975	0.004266158
0.2848	9.2446E-05	0.007328035	0.016180428	0.006019002	0.008366599	0.004937272
0.32745	0.000116613	0.00889549	0.018609629	0.007103777	0.009348767	0.005623454
0.37649	0.00017181	0.010615231	0.021123878	0.008339869	0.01032553	0.0063175
0.43288	0.000272704	0.012463675	0.023676103	0.009741404	0.011289315	0.007016333
0.4977	0.000434226	0.01441304	0.026209735	0.011316206	0.012235649	0.007720891
0.57224	0.00066966	0.016434209	0.028660274	0.013063411	0.013163291	0.008434707
0.65793	0.000988773	0.018499074	0.030958303	0.014972072	0.0140735	0.00916154
0.75646	0.001396527	0.020581809	0.033033701	0.01702095	0.014968564	0.009902775
0.86975	0.001892862	0.022658687	0.034820716	0.01917956	0.01585014	0.010655417
1	0.002473899	0.024706781	0.036263363	0.021410242	0.016718253	0.011411205
1.14976	0.003134438	0.026702114	0.037320209	0.023670772	0.017571578	0.012156926
1.32194	0.003871156	0.028618113	0.037967814	0.025916965	0.01840941	0.012875502
1.51991	0.004685506	0.030424437	0.038201321	0.028105194	0.019235138	0.013547376
1.74753	0.005585398	0.032086761	0.03803292	0.030194605	0.02006069	0.014151712
2.00923	0.006585036	0.033567494	0.037488505	0.032149209	0.020910949	0.01466737
2.31013	0.007702853	0.034827713	0.036604778	0.0339398	0.021826572	0.015073686

2.65609	0.008957961	0.035830491	0.035427408	0.035544741	0.02286353	0.015351455
3.05386	0.010365738	0.036544856	0.034010449	0.036949623	0.024087604	0.015484191
3.51119	0.011933225	0.036949121	0.032415532	0.038144897	0.025562757	0.015459869
4.03702	0.013654498	0.037032239	0.030709502	0.0391222	0.027333825	0.015272939
4.64159	0.015506626	0.036792541	0.028959876	0.039869995	0.029406109	0.014926277
5.3367	0.017446949	0.036234634	0.02722879	0.040369104	0.03172557	0.014432831
6.13591	0.019412897	0.035366677	0.025566968	0.040589635	0.034164689	0.013816993
7.0548	0.021325421	0.034199653	0.024009286	0.040489835	0.036519097	0.013115986
8.11131	0.023095871	0.032749207	0.022572864	0.040018234	0.038519176	0.012381207
9.32603	0.024635057	0.031038807	0.02125731	0.039119527	0.039860357	0.011678885
10.7227	0.025863045	0.029102233	0.020046179	0.037744491	0.040251232	0.011088781
12.3285	0.026718553	0.026983515	0.018908357	0.035862769	0.039473602	0.010699879
14.1747	0.02716839	0.024734407	0.017799076	0.033476365	0.037439935	0.010602856
16.2975	0.027217168	0.02241021	0.01666175	0.030630089	0.034229884	0.010880814
18.7382	0.026917109	0.020065921	0.015431892	0.027414705	0.030090636	0.0116006
21.5443	0.02637564	0.017753399	0.014044293	0.023959892	0.025396244	0.01280732
24.7708	0.025756555	0.015520073	0.01244368	0.020417493	0.020577291	0.014523009
28.4804	0.025269021	0.013408086	0.010598669	0.01693913	0.016041697	0.016748432
32.7455	0.025141235	0.011453384	0.008517492	0.01365565	0.01210972	0.019464565
37.6494	0.025579616	0.009684328	0.006262231	0.010664836	0.008978051	0.022630495
43.2876	0.026721059	0.008120003	0.003955677	0.008030588	0.006715318	0.026176097
49.7702	0.02858989	0.00676884	0.001774272	0.00579129	0.005281108	0.029990789
57.2237	0.031072145	0.005627647	0	0.00397035	0.004557014	0.033912384
65.7933	0.033916484	0.004682494	0	0.002580843	0.004380589	0.0377214
75.6463	0.036764672	0.003912981	0	0.001620761	0.004576753	0.041146238

86.9749	0.039207312	0.003299891	0	0.00106199	0.004984367	0.043882801
100	0.040853675	0.002834329	0	0.000842036	0.00547493	0.045628136
114.976	0.041399842	0.002522584	0	0.000866364	0.005961096	0.046122406
132.194	0.040679099	0.002382822	0.000804085	0.001022845	0.006394477	0.045189468
151.991	0.038683662	0.002433184	0.001806474	0.001203229	0.006755051	0.042765234
174.753	0.035554571	0.002676219	0.002396999	0.001322769	0.007038229	0.038906716
200.923	0.031545904	0.003086839	0.002423202	0.001331686	0.007243093	0.033780518
231.013	0.026974914	0.003609006	0.001846078	0.001216272	0.007366259	0.027634855
265.609	0.022170607	0.004162161	0.000731666	0.000991512	0.007400233	0.020763397
305.386	0.017431688	0.004654575	0	0.000690069	0.007335963	0.013468924
351.119	0.012998587	0.004998778	0	0.000350949	0.007165869	0.006033342
403.702	0.009040903	0.005124525	0	1.08512E-05	0.006887006	0
464.159	0.005657763	0.004986671	0	0	0.006502545	0
533.67	0.002886364	0.004567679	0	0	0.006021903	0
613.591	0.000715604	0.003875147	0	0	0.005459425	0
705.48	0	0.002936664	0	0	0.004832934	0
811.131	0	0.001793119	0	0	0.004161615	0
932.603	0	0.000492381	0	0	0.003464441	0
1072.27	0	0	0	0	0.002758927	0
1232.85	0	0	0	0	0.002060143	0
1417.47	0	0	0	0	0.001380543	0
1629.75	0	0	0	0	0.000729891	0
1873.82	0	0	0	0	0.000114934	0
2154.43	0	0	0	0	0	0
2477.08	0	0	0	0	0	0

2848.04	0	0	0	0	0	0
3274.55	0	0	0	0	0	0
3764.94	0	0	0	0	0	0
4328.76	0.000115387	0	0	0	0	0
4977.02	0.000506811	0	0	0	0	0
5722.37	0.000868599	0	0	0	0	0
6579.33	0.001199836	0	0	0	0	0
7564.63	0.001500699	0	0	0	0	0
8697.49	0.001772193	0	0	0	0	0
10000	0.00201593	0	0	0	0	0

Sample	**SHELL2_9b**	**SHELL1_216**	**WIN4_26**	**WIN5_16b**	**WIN9_5**	**BP3_4**
T_2 (ms)	**Normalised Signal**	**Normalised Signal**	**Normalised Signal**	**Normalised Signal**	**Normalised Signal**	**Normalised Signal**
0.01	2.07331E-11	1.54039E-11	1.91671E-11	1.00758E-11	1.54039E-11	6.07747E-12
0.0115	2.96904E-10	2.20158E-10	2.73944E-10	1.44477E-10	2.20158E-10	8.7088E-11
0.01322	3.00611E-09	2.22529E-09	2.76893E-09	1.46447E-09	2.22529E-09	8.82252E-10
0.0152	2.25134E-08	1.6641E-08	2.07065E-08	1.09785E-08	1.6641E-08	6.61062E-09
0.01748	1.29711E-07	9.57559E-08	1.19149E-07	6.33077E-08	9.57559E-08	3.81037E-08
0.02009	5.94907E-07	4.38707E-07	5.45866E-07	2.90577E-07	4.38707E-07	1.74826E-07
0.0231	2.2374E-06	1.64864E-06	2.05115E-06	1.09364E-06	1.64864E-06	6.5775E-07
0.02656	7.08028E-06	5.21555E-06	6.48719E-06	3.46361E-06	5.21555E-06	2.08233E-06
0.03054	1.92783E-05	1.42094E-05	1.76623E-05	9.44101E-06	1.42094E-05	5.67306E-06
0.03511	4.60443E-05	3.40136E-05	4.22195E-05	2.25877E-05	3.40136E-05	1.35623E-05
0.04037	9.80792E-05	7.28152E-05	9.01395E-05	4.82538E-05	7.28152E-05	2.89361E-05
0.04642	0.000188985	0.000141611	0.000174496	9.34312E-05	0.000141611	5.59127E-05
0.05337	0.000333373	0.000253676	0.000310337	0.000166119	0.000253676	9.90987E-05

0.06136	0.000543786	0.000423654	0.000512932	0.000274318	0.000423654	0.000162892
0.07055	0.000826946	0.000666476	0.000795845	0.000424915	0.000666476	0.0002507
0.08111	0.001180298	0.000996274	0.001169373	0.000622768	0.000996274	0.000364277
0.09326	0.001590143	0.001425344	0.001639683	0.00087025	0.001425344	0.000503329
0.10723	0.00203286	0.001963191	0.002208785	0.001167373	0.001963191	0.000665451
0.12328	0.002480062	0.002615712	0.002875167	0.001512467	0.002615712	0.000846372
0.14175	0.002907138	0.00338461	0.003634825	0.001903172	0.00338461	0.001040408
0.16298	0.003302736	0.004267096	0.004482306	0.002337421	0.004267096	0.001241018
0.18738	0.003675693	0.005255927	0.0054115	0.002814088	0.005255927	0.001441424
0.21544	0.004056499	0.006339791	0.006416012	0.003333097	0.006339791	0.001635262
0.24771	0.004492511	0.007504112	0.007489158	0.003895025	0.007504112	0.001817269
0.2848	0.005038817	0.008732226	0.008623704	0.00450042	0.008732226	0.001983931
0.32745	0.005748176	0.010006795	0.009811564	0.005149102	0.010006795	0.002133962
0.37649	0.006662916	0.011311147	0.011043568	0.005839755	0.011311147	0.002268479
0.43288	0.007809466	0.012630136	0.012309335	0.006569914	0.012630136	0.002390849
0.4977	0.009194034	0.013950317	0.013597201	0.007336339	0.013950317	0.002506382
0.57224	0.010797584	0.015259428	0.014894192	0.0081357	0.015259428	0.002622125
0.65793	0.012569998	0.016545657	0.016186075	0.008965453	0.016545657	0.002746965
0.75646	0.014425395	0.017797092	0.017457669	0.009824714	0.017797092	0.002891964
0.86975	0.016241598	0.019001815	0.01869334	0.010714878	0.019001815	0.003070713
1	0.017866148	0.02014841	0.019877726	0.011639805	0.02014841	0.003299365
1.14976	0.019129519	0.0212267	0.020996448	0.012605442	0.0212267	0.003596198
1.32194	0.01986452	0.022228293	0.022036849	0.013619087	0.022228293	0.003980751
1.51991	0.019929518	0.023146802	0.022988929	0.014688604	0.023146802	0.004472592
1.74753	0.01923299	0.023978037	0.023846522	0.015821756	0.023978037	0.005089874
2.00923	0.01775784	0.024720405	0.024608604	0.017025843	0.024720405	0.005847823
2.31013	0.015584719	0.025375892	0.025280348	0.018307294	0.025375892	0.006757456
2.65609	0.012912202	0.025951279	0.02587297	0.019671198	0.025951279	0.00782482
3.05386	0.010070202	0.026459017	0.026402314	0.02112038	0.026459017	0.009050819

3.51119	0.007519002	0.026917108	0.026885884	0.022654328	0.026917108	0.010431424
4.03702	0.005824664	0.027347621	0.027338967	0.024268005	0.027347621	0.01195777
4.64159	0.005599254	0.027773917	0.027770729	0.025951259	0.027773917	0.013615811
5.3367	0.007397658	0.028217114	0.028180925	0.02768879	0.028217114	0.01538578
6.13591	0.011572659	0.028692408	0.028558117	0.029460419	0.028692408	0.017242047
7.0548	0.018109747	0.029205502	0.028879776	0.031240721	0.029205502	0.019154129
8.11131	0.026484525	0.029749026	0.029114102	0.032996838	0.029749026	0.021089277
9.32603	0.035603514	0.030298989	0.029223252	0.034683926	0.030298989	0.023016683
10.7227	0.043889639	0.030812264	0.029166823	0.036239773	0.030812264	0.024912543
12.3285	0.049550068	0.031226355	0.028905512	0.037580985	0.031226355	0.02676448
14.1747	0.051007699	0.031463353	0.028405207	0.038604706	0.031463353	0.028573779
16.2975	0.047397551	0.031438407	0.027642054	0.039197854	0.031438407	0.030353511
18.7382	0.038955692	0.031072169	0.02660869	0.039253417	0.031072169	0.032122348
21.5443	0.027118785	0.030304379	0.025320419	0.038690605	0.030304379	0.033894255
24.7708	0.014236563	0.029105485	0.023819025	0.037473975	0.029105485	0.03566637
28.4804	0.002957594	0.027483103	0.022171351	0.035625966	0.027483103	0.037408236
32.7455	0	0.025480881	0.020461484	0.033229744	0.025480881	0.03905534
37.6494	0	0.023170398	0.018777471	0.03042086	0.023170398	0.040509441
43.2876	0	0.020638685	0.017196364	0.027369	0.020638685	0.041646288
49.7702	0.001986928	0.017976478	0.015771693	0.024253599	0.017976478	0.042329624
57.2237	0.010374412	0.01527098	0.014527056	0.021237975	0.01527098	0.042429665
65.7933	0.018855213	0.012604324	0.013456127	0.018446779	0.012604324	0.041843269
75.6463	0.025880739	0.010054829	0.012527991	0.015951699	0.010054829	0.040512553
86.9749	0.030561154	0.007697684	0.011694822	0.013768207	0.007697684	0.03843824
100	0.032713219	0.005601985	0.010900731	0.011863476	0.005601985	0.035684984
114.976	0.032711412	0.003824474	0.010091193	0.010173459	0.003824474	0.032376052
132.194	0.031226613	0.002402102	0.009221897	0.00862397	0.002402102	0.028679033
151.991	0.028957294	0.00134629	0.008266532	0.007150338	0.00134629	0.024784314
174.753	0.026428655	0.000640898	0.007220814	0.005710949	0.000640898	0.020881745

200.923	0.023899368	0.000245075	0.006102278	0.004292591	0.000245075	0.017139708
231.013	0.021367453	9.97879E-05	0.004945523	0.002907659	9.97879E-05	0.013690513
265.609	0.018644478	0.000136716	0.003794764	0.001586346	0.000136716	0.010623414
305.386	0.015457497	0.00028702	0.002695667	0.000366448	0.00028702	0.007984935
351.119	0.011540195	0.000488765	0.00168843	0	0.000488765	0.005784633
403.702	0.006700473	0.000691711	0.000803186	0	0.000691711	0.0040036
464.159	0.000850138	0.000859447	5.81202E-05	0	0.000859447	0.002603881
533.67	0	0.000969273	0	0	0.000969273	0.001536954
613.591	0	0.00101042	0	0	0.00101042	0.0007506
705.48	0	0.000981657	0	0	0.000981657	0.000193733
811.131	0	0.000888293	0	0	0.000888293	0
932.603	0	0.000739782	0	0	0.000739782	0
1072.27	0	0.000547525	0	0	0.000547525	0
1232.85	0	0.000323415	0	0	0.000323415	0
1417.47	0	7.85282E-05	0	0	7.85282E-05	0
1629.75	0	0	0	0	0	0
1873.82	0	0	0	0	0	0
2154.43	0	0	0	0	0	0
2477.08	0	0	0	0	0	0
2848.04	0	0	0	0	0	0
3274.55	0	0	0	0	0	0
3764.94	0	0	0	0	0	1.70196E-05
4328.76	0	0	0	0	0	0.00010436
4977.02	0	0	0	0	0	0.000185445
5722.37	0	0	0	0	0	0.000259867
6579.33	0	0	0	0	0	0.000327576
7564.63	0	0	0	0	0	0.000388748
8697.49	0	0	0	0	0	0.000443661
10000	0	0	0	0	0	0.000492744

Sample	BP3_1	BP2_2	BP2_3	BP3_5	BP3_6	BP2_5
T_2 (ms)	Normalised Signal	Normalised Signal	Normalised Signal	Normalised Signal	Normalised Signal	Normalised Signal
0.01	1.99132E-11	9.55676E-12	3.4111E-12	2.0323E-12	4.34844E-12	1.9263E-11
0.01149757	2.85535E-10	1.37034E-10	4.89117E-11	2.91221E-11	6.23116E-11	2.76032E-10
0.013219412	2.89428E-09	1.38902E-09	4.95787E-10	2.95025E-10	6.31253E-10	2.79637E-09
0.015199111	2.16973E-08	1.0413E-08	3.71676E-09	2.21059E-09	4.72991E-09	2.09529E-08
0.017475285	1.25119E-07	6.00469E-08	2.14342E-08	1.2742E-08	2.72632E-08	1.20774E-07
0.020092331	5.74328E-07	2.75621E-07	9.84108E-08	5.84655E-08	1.25086E-07	5.5414E-07
0.023101297	2.16209E-06	1.03748E-06	3.70765E-07	2.20004E-07	4.70586E-07	2.08499E-06
0.026560879	6.85218E-06	3.287E-06	1.1777E-06	6.96844E-07	1.48956E-06	6.6021E-06
0.030538555	1.87089E-05	8.96791E-06	3.23337E-06	1.90082E-06	4.05657E-06	1.79958E-05
0.035111916	4.49227E-05	2.14985E-05	7.85569E-06	4.55625E-06	9.68974E-06	4.30685E-05
0.040370174	9.66238E-05	4.61013E-05	1.72724E-05	9.7704E-06	2.06407E-05	9.20831E-05
0.04641589	0.000189253	8.98445E-05	3.50852E-05	1.90439E-05	3.97732E-05	0.000178584
0.053366993	0.000342434	0.000161362	6.69955E-05	3.42145E-05	7.01838E-05	0.000318382
0.061359074	0.000579302	0.000270324	0.000121777	5.73495E-05	0.000114622	0.00052794
0.070548019	0.000925015	0.000426733	0.000212237	9.06043E-05	0.000174863	0.00082259
0.081113083	0.001403957	0.000640097	0.000355707	0.000136061	0.000251233	0.001215054
0.093260338	0.002035457	0.000918472	0.000573655	0.000195565	0.000342462	0.001714509
0.10722672	0.002828587	0.001267505	0.000890302	0.000270596	0.000445923	0.002326268
0.12328468	0.003777333	0.001689665	0.001330387	0.000362237	0.000558235	0.003051939
0.14174742	0.004857511	0.002183916	0.001916329	0.000471255	0.000676077	0.00388989
0.16297508	0.006026275	0.002745979	0.002664835	0.000598289	0.000797064	0.004835921
0.18738174	0.007224248	0.003369154	0.003582651	0.000744026	0.000920554	0.005884094
0.21544347	0.008379649	0.004045494	0.004661029	0.000909285	0.001048296	0.007027732
0.24770764	0.009413541	0.004766973	0.005868751	0.001094894	0.001184829	0.008260574
0.28480359	0.010245161	0.005526339	0.007144487	0.001301406	0.001337533	0.009577941
0.32745493	0.010796032	0.006317443	0.008390333	0.001528773	0.001516243	0.010977715
0.37649359	0.010991581	0.007135186	0.009468807	0.001776174	0.001732399	0.012460836

0.43287613	0.010758998	0.00797542	0.01020496	0.002042175	0.001997777	0.014031086
0.49770236	0.010021379	0.008835225	0.010394059	0.002325278	0.002322926	0.01569403
0.57223676	0.008689634	0.009713752	0.009814493	0.002624727	0.002715515	0.017455006
0.65793323	0.006655576	0.010613524	0.008245362	0.002941328	0.003178898	0.019316294
0.75646332	0.003790198	0.011541711	0.005488596	0.003278036	0.003711286	0.021273538
0.86974902	0	0.01251085	0.001395094	0.003640253	0.004305957	0.023312019
1	0	0.013538614	0	0.004035845	0.004952747	0.025403433
1.149757	0	0.014646696	0	0.004475034	0.00564076	0.027504078
1.3219412	0	0.015858912	0	0.004970127	0.006361732	0.029555031
1.5199111	0	0.01719876	0	0.005535033	0.00711318	0.031484323
1.7475284	0	0.018686376	0	0.006184456	0.007900391	0.033211205
2.009233	0	0.020335091	0	0.0069328	0.008736449	0.034652298
2.3101296	0	0.022147746	0	0.007792884	0.009640234	0.035729775
2.6560879	0	0.024113412	0	0.0087746	0.010632822	0.036381028
3.0538555	0	0.026204993	0	0.009883682	0.011733363	0.036568695
3.5111917	0	0.028378074	0	0.011120753	0.012955316	0.036288766
4.0370173	0	0.030571296	0	0.012480966	0.01430392	0.035574099
4.6415889	0	0.032707924	0	0.013954508	0.015775029	0.034491495
5.3366992	0	0.034698415	0	0.015528013	0.017355563	0.033132162
6.1359072	0.016801664	0.036442896	0.021518375	0.017186611	0.019025334	0.031596982
7.0548022	0.051684339	0.037833778	0.054960177	0.018916018	0.020760045	0.029979493
8.1113081	0.08617973	0.038759406	0.087966275	0.02070416	0.022534879	0.02835061
9.3260332	0.114459431	0.039111251	0.115251063	0.022541822	0.024327543	0.026748913
10.722672	0.130260943	0.03879711	0.131022161	0.024422273	0.026119752	0.025179667
12.328468	0.128236403	0.037760675	0.1301286	0.026339841	0.027896554	0.023623956
14.174741	0.10546	0.03600377	0.109405496	0.028287496	0.029643517	0.022055406
16.297509	0.062646022	0.033603959	0.068842907	0.030253852	0.031343575	0.0204589
18.738174	0.004607424	0.030718477	0.012155381	0.032219638	0.032974502	0.018844125
21.544348	0	0.027569488	0	0.034154346	0.034508383	0.017248165

24.770764	0	0.02441074	0	0.03601377	0.035912741	0.015726035
28.480359	0	0.021484159	0	0.037739289	0.037152029	0.014333214
32.745492	0	0.018977975	0	0.039259603	0.038187747	0.013107777
37.649359	0	0.01699782	0	0.040494533	0.038976399	0.012059192
43.287613	0	0.015557542	0	0.041360971	0.039466275	0.011167161
49.770234	0	0.014589604	0	0.04177937	0.039595595	0.010389221
57.223676	0	0.013969593	0	0.041680566	0.03929486	0.00967231
65.79332	0	0.013546832	0	0.041012141	0.038494874	0.008963359
75.646336	0	0.01317325	0	0.039744512	0.037140174	0.008216562
86.974898	0.030651433	0.012726032	0	0.037876339	0.035204758	0.007398748
100	0.047554023	0.012121514	0.027340229	0.035438865	0.032705878	0.00649474
114.9757	0.048922901	0.011320526	0.04411724	0.032497886	0.029711111	0.005512308
132.19411	0.036771517	0.010325842	0.046778802	0.029152324	0.026335747	0.004484022
151.99111	0.01466218	0.009173849	0.037258319	0.025528126	0.022730272	0.003462937
174.75284	0	0.007922634	0.018666504	0.021767913	0.019061026	0.002511733
200.9233	0	0.006639001	0	0.018017982	0.015489095	0.00168872
231.01297	0	0.005386986	0	0.014414415	0.012152224	0.001035362
265.60878	0	0.004219775	0	0.011071866	0.009153047	0.000569185
305.38556	0	0.003175235	0	0.008075724	0.006554699	0.000283365
351.11919	0	0.002274978	0	0.005479281	0.004382866	0.000151725
403.70172	0	0.001526228	0	0.003304725	0.002631924	0.000136524
464.15888	0	0.000924737	0	0.001547728	0.001273267	0.000196437
533.66994	0	0.000458506	0	0.000183354	0.000263772	0.00029312
613.59075	0	0.000110977	0	0	0	0.000395216
705.48025	0	0	0	0	0	0.000480087
811.13081	0	0	0	0	0	0.000533866
932.60338	0	0	0	0	0	0.000549997
1072.2673	0	0	0	0	0	0.000527798
1232.8468	0	0	0	0	0	0.000470418

1417.4741	0	0	0	0	0	0.000383366
1629.7509	0	0	0	0	0	0.000273081
1873.8174	0	0	0	0	0	0.000146258
2154.4348	0	0	0	0	0	9.07791E-06
2477.0763	0	0	0	0	0	0
2848.0358	0	0	0	0	0	0
3274.5493	0	0	0	0	0.000120231	0
3764.9358	0	0	0	0	0.000300006	0
4328.7615	0	0	0	0	0.000466278	0
4977.0235	0	0	0	0.00012816	0.000618603	0
5722.3675	0	2.61376E-05	0	0.000327392	0.000756979	0
6579.332	0	6.38524E-05	0	0.000508498	0.000881819	0
7564.6335	0	9.79598E-05	0	0.000672041	0.000993889	0
8697.49	0	0.00012852	0	0.000818888	0.001093988	0
10000	0.001000876	0.00015587	0.001732508	0.000950193	0.00118308	0

BET surface area data for all 25 TGS samples

Well/Sample	BET (m^2/g)
WIN4_26	0.94
SHELL1_83	0.89
BP3_1	0.85
BP3_6	0.63
WIN5_16B	2.73
SHELL1_111	2.15
BP2_2	1.76
BP2_5	1.64
EBN3_40	5.27
EBN4_10	2.82
SHELL4_202	2.15
SHELL4_370	1.11
SHELL4_389	1.1
SHELL4_409	1.32
BP3_4	1.2
BP2_3	1.24
BP3_5	1.2
WIN 9_5	
GDF1_1	0.49
GDF1_6	0.47
GDF1_7	0.24
SHELL1_216	0.22
SHELL2_1	0.49
SHELL2_9	0.43
GDF2_4	

Mercury injection capillary pressure (MICP)– incremental data for all 25 TGS samples

	BP2_5	BP2_2	BP2_3	BP3_1	BP3_4	BP3_6	EBN4_10	GDF1_1
Pore throat radius (µm)	**incremental (frac)**	**incremental (frac)**	**incremental (frac)**	**incremental (frac)**	**incremental (frac)**	**incremental (frac)**	**incremental (frac)**	**incremental (frac)**
45.216	0.000	0.000	0.000	0.000	0.000	0.002	0.006	0.001
18.086	0.004	0.000	0.000	0.000	0.004	0.010	0.016	0.002
11.304	0.004	0.000	0.000	0.000	0.002	0.003	0.006	0.005
9.043	0.001	0.000	0.000	0.000	0.001	0.002	0.003	0.002
6.029	0.008	0.000	0.000	0.000	0.004	0.003	0.003	0.004
4.522	0.000	0.000	0.000	0.000	0.003	0.002	0.004	0.005
3.617	0.002	0.000	0.023	0.014	0.004	0.002	0.001	0.006
2.261	0.001	0.009	0.034	0.018	0.003	0.001	0.003	0.011
1.206	0.004	0.041	0.221	0.092	0.178	0.078	0.006	0.279
0.904	0.002	0.049	0.093	0.058	0.168	0.212	0.006	0.180
0.624	0.006	0.163	0.114	0.073	0.110	0.125	0.019	0.125
0.603	0.001	0.016	0.009	0.007	0.019	0.021	0.012	0.020
0.452	0.010	0.094	0.075	0.051	0.073	0.079	0.073	0.072
0.301	0.053	0.102	0.083	0.067	0.089	0.097	0.157	0.079
0.226	0.078	0.061	0.051	0.047	0.055	0.059	0.104	0.046
0.181	0.064	0.044	0.037	0.037	0.037	0.038	0.070	0.031
0.113	0.136	0.091	0.077	0.082	0.069	0.070	0.119	0.051
0.090	0.060	0.044	0.032	0.042	0.027	0.029	0.044	0.018
0.060	0.097	0.085	0.049	0.086	0.043	0.047	0.062	0.026
0.045	0.064	0.054	0.027	0.062	0.025	0.027	0.035	0.014

0.036	0.047	0.036	0.017	0.045	0.017	0.018	0.026	0.009
0.030	0.039	0.023	0.012	0.035	0.011	0.014	0.021	0.006
0.026	0.031	0.017	0.009	0.026	0.011	0.011	0.017	0.003
0.023	0.029	0.014	0.007	0.021	0.008	0.008	0.014	0.003
0.020	0.024	0.010	0.006	0.017	0.006	0.006	0.009	0.001
0.018	0.021	0.008	0.004	0.013	0.005	0.006	0.011	0.000
0.013	0.066	0.017	0.011	0.036	0.013	0.014	0.039	0.000
0.010	0.042	0.008	0.004	0.020	0.007	0.008	0.017	0.000
0.008	0.028	0.005	0.002	0.012	0.004	0.005	0.021	0.000
0.007	0.018	0.003	0.001	0.008	0.002	0.003	0.012	0.000
0.006	0.008	0.002	0.000	0.006	0.002	0.001	0.011	0.000
0.005	0.019	0.001	0.000	0.007	0.001	0.000	0.012	0.000
0.005	0.006	0.000	0.000	0.003	0.000	0.000	0.009	0.000
0.004	0.012	0.000	0.000	0.006	0.001	0.000	0.011	0.000
0.003	0.006	0.000	0.000	0.004	0.000	0.000	0.009	0.000
0.003	0.004	0.000	0.000	0.002	0.000	0.000	0.003	0.000
0.002	0.004	0.000	0.000	0.001	0.000	0.000	0.007	0.000
0.002	-0.002	0.000	0.000	0.000	0.000	0.000	0.000	0.000
0.002	-0.005	0.000	0.000	0.000	0.000	0.000	0.000	0.000
0.002	-0.003	0.000	0.000	0.000	0.000	0.000	0.000	0.000

	GDF1_6	GDF1_7	GDF2_4	SHELL4_202	SHELL4_370	SHELL4_389	SHELL4_409
Pore throat radius (μm)	**incremental (frac)**	**incremental (frac)**	**incremental (frac)**	**incremental (frac)**	**incremental (frac)**	**incremental (frac)**	**incremental (frac)**
45.216	0.005	0.005	0.001	0.003	0.003	0.006	0.000
18.086	0.014	0.015	0.016	0.009	0.013	0.028	0.000
11.304	0.005	0.007	0.004	0.003	0.009	0.023	0.008
9.043	0.001	0.003	0.002	0.002	0.005	0.013	0.005
6.029	0.000	0.009	0.010	0.004	0.010	0.026	0.006
4.522	0.001	0.010	0.009	0.003	0.012	0.023	0.006
3.617	0.001	0.020	0.018	0.003	0.018	0.022	0.004
2.261	0.001	0.079	0.095	0.002	0.011	0.007	0.001
1.206	0.004	0.362	0.388	0.009	0.107	0.049	0.005
0.904	0.001	0.120	0.083	0.020	0.076	0.054	0.005
0.624	0.004	0.094	0.059	0.068	0.091	0.067	0.006
0.603	0.001	0.011	0.010	0.023	0.019	0.013	0.001
0.452	0.008	0.057	0.038	0.101	0.061	0.061	0.011
0.301	0.128	0.065	0.049	0.112	0.059	0.077	0.093
0.226	0.168	0.038	0.031	0.060	0.030	0.044	0.092
0.181	0.104	0.026	0.026	0.038	0.021	0.031	0.046
0.113	0.171	0.042	0.051	0.082	0.064	0.066	0.079
0.090	0.079	0.013	0.021	0.042	0.050	0.041	0.033
0.060	0.116	0.014	0.030	0.089	0.078	0.075	0.058
0.045	0.064	0.006	0.016	0.075	0.039	0.040	0.050
0.036	0.029	0.000	0.010	0.052	0.030	0.029	0.034
0.030	0.024	0.000	0.007	0.034	0.023	0.025	0.036
0.026	0.020	0.001	0.005	0.025	0.018	0.021	0.031
0.023	0.013	0.002	0.004	0.019	0.015	0.017	0.027
0.020	0.007	0.000	0.003	0.011	0.011	0.013	0.017

0.018	0.007	0.000	0.002	0.013	0.010	0.012	0.021
0.013	0.016	0.000	0.006	0.031	0.027	0.035	0.068
0.010	0.006	0.000	0.003	0.018	0.016	0.023	0.052
0.008	0.001	0.000	0.002	0.013	0.011	0.018	0.043
0.007	0.000	0.000	0.001	0.009	0.008	0.014	0.036
0.006	0.000	0.000	0.000	0.007	0.006	0.008	0.026
0.005	0.000	0.000	0.000	0.010	0.007	0.008	0.030
0.005	0.000	0.000	0.000	0.004	0.004	0.005	0.019
0.004	0.000	0.000	0.000	0.002	0.007	0.002	0.026
0.003	0.000	0.000	0.000	0.001	0.006	0.002	0.014
0.003	0.000	0.000	0.000	0.000	0.005	0.000	0.009
0.002	0.000	0.000	0.000	0.000	0.004	0.000	0.003
0.002	0.000	0.000	0.000	0.000	0.004	0.000	0.000
0.002	0.000	0.000	0.000	0.000	0.005	0.000	0.000
0.002	0.000	0.000	0.000	0.000	0.004	0.000	0.000

	SHELL1_83	**SHELL1_111**	**SHELL1_216**	**SHELL2_1B**	**SHELL2_9B**	**WIN4_26**	**WIN5_16B**	**WIN9_5**
Pore throat radius (µm)	**incremental (frac)**	**incremental (frac)**	**incremental (frac)**	**incremental (frac)**	**incremental (frac)**	**incremental (frac)**	**incremental (frac)**	**incremental (frac)**
45.216	0.000	0.000	0.000	0.000	0.000	0.000	0.000	0.020
18.086	0.000	0.000	0.000	0.000	0.000	0.000	0.000	0.062
11.304	0.000	0.000	0.000	0.000	0.000	0.000	0.000	0.030
9.043	0.000	0.000	0.000	0.000	0.000	0.000	0.000	0.016
6.029	0.000	0.000	0.000	0.000	0.000	0.000	0.000	0.021
4.522	0.000	0.000	0.000	0.000	0.000	0.000	0.000	0.018
3.617	0.000	0.000	0.000	0.000	0.000	0.000	0.000	0.013
2.261	0.000	0.000	0.000	0.000	0.000	0.053	0.000	0.002

1.206	0.000	0.000	0.000	0.244	0.000	0.141	0.000	0.000
0.904	0.000	0.000	0.000	0.230	0.000	0.093	0.000	0.000
0.624	0.000	0.000	0.000	0.141	0.000	0.140	0.000	0.000
0.603	0.000	0.000	0.000	0.010	0.000	0.010	0.000	0.001
0.452	0.037	0.064	0.057	0.067	0.048	0.083	0.027	0.001
0.301	0.059	0.135	0.109	0.059	0.061	0.084	0.065	0.003
0.226	0.047	0.079	0.082	0.026	0.034	0.044	0.083	0.001
0.181	0.041	0.048	0.054	0.014	0.025	0.030	0.061	0.005
0.113	0.085	0.087	0.081	0.020	0.071	0.053	0.117	0.003
0.090	0.033	0.037	0.026	0.007	0.038	0.023	0.051	0.006
0.060	0.047	0.057	0.036	0.012	0.049	0.039	0.098	0.005
0.045	0.029	0.033	0.019	0.008	0.027	0.026	0.061	0.007
0.036	0.022	0.025	0.015	0.007	0.017	0.017	0.039	0.006
0.030	0.018	0.019	0.015	0.006	0.011	0.015	0.026	0.005
0.026	0.017	0.016	0.014	0.005	0.008	0.011	0.020	0.007
0.023	0.015	0.014	0.012	0.005	0.006	0.010	0.016	0.005
0.020	0.017	0.014	0.013	0.005	0.007	0.011	0.014	0.007
0.018	0.019	0.012	0.010	0.004	0.005	0.008	0.013	0.024
0.013	0.040	0.037	0.006	0.020	0.020	0.025	0.035	0.023
0.010	0.030	0.029	0.001	0.012	0.016	0.016	0.027	0.023
0.008	0.023	0.022	0.066	0.008	0.011	0.014	0.021	0.025
0.007	0.018	0.017	0.040	0.012	0.008	0.010	0.020	0.026
0.006	0.015	0.014	0.004	0.011	0.007	0.009	0.014	0.037
0.005	0.021	0.016	0.000	0.014	0.029	0.008	0.020	0.027
0.005	0.013	0.008	0.000	0.007	0.003	0.003	0.013	0.068
0.004	0.027	0.015	0.000	0.014	0.009	0.017	0.015	0.073
0.003	0.022	0.008	0.000	0.009	0.007	0.006	0.009	0.069
0.003	0.017	0.004	0.000	0.006	0.004	0.002	0.005	0.069
0.002	0.012	0.002	0.000	0.004	0.002	0.000	0.002	0.073
0.002	0.000	0.000	0.000	0.002	0.000	0.000	0.000	0.074

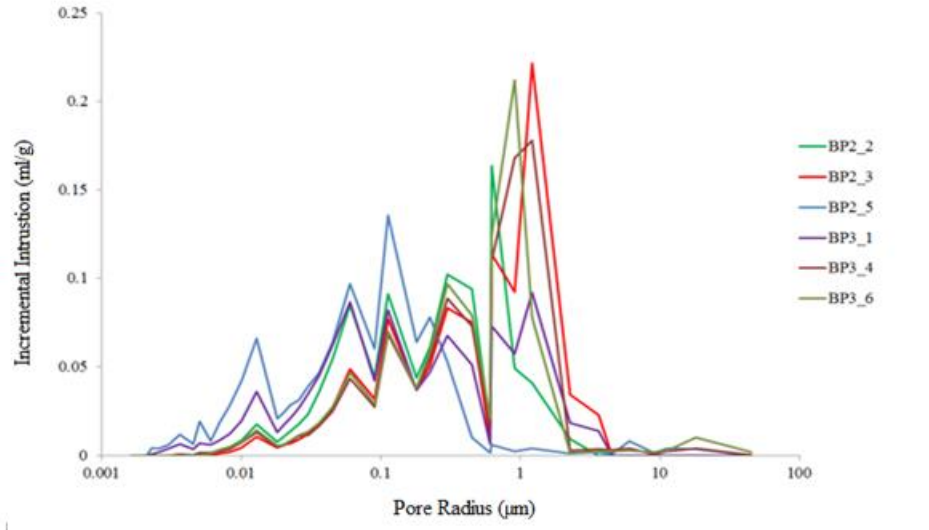
Incremental Intrusion (ml/g)
0.25
0.2
0.15
0.1
0.05
0
0.001
0.01
0.1
1
10
100
Pore Radius (µm)
BP2_2
BP2_3
BP2_5
BP3_1
BP3_4
BP3_6

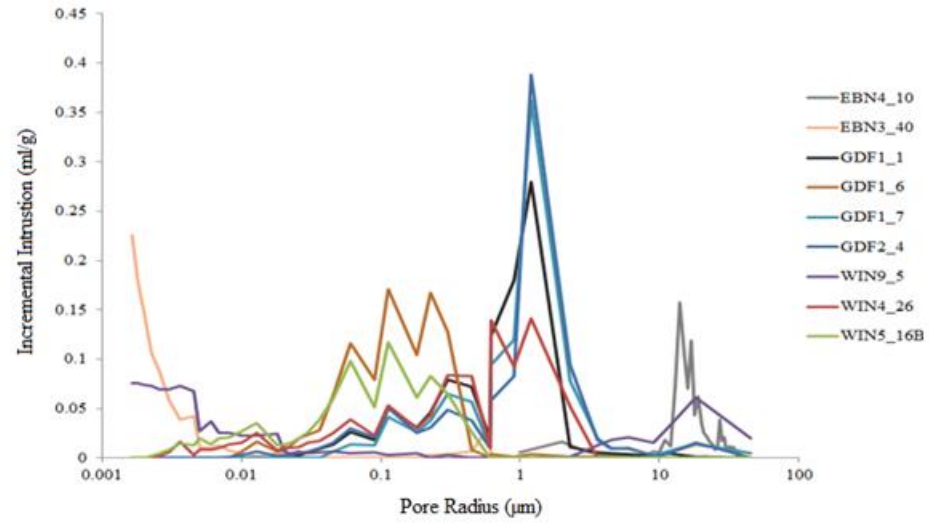
Incremental Intrusion (ml/g)
0.45
0.4
0.35
0.3
0.25
0.2
0.15
0.1
0.05
0
0.001
0.01
0.1
1
10
100
Pore Radius (µm)
EBN4_10
EBN3_40
GDF1_1
GDF1_6
GDF1_7
GDF2_4
WIN9_5
WIN4_26
WIN5_16B

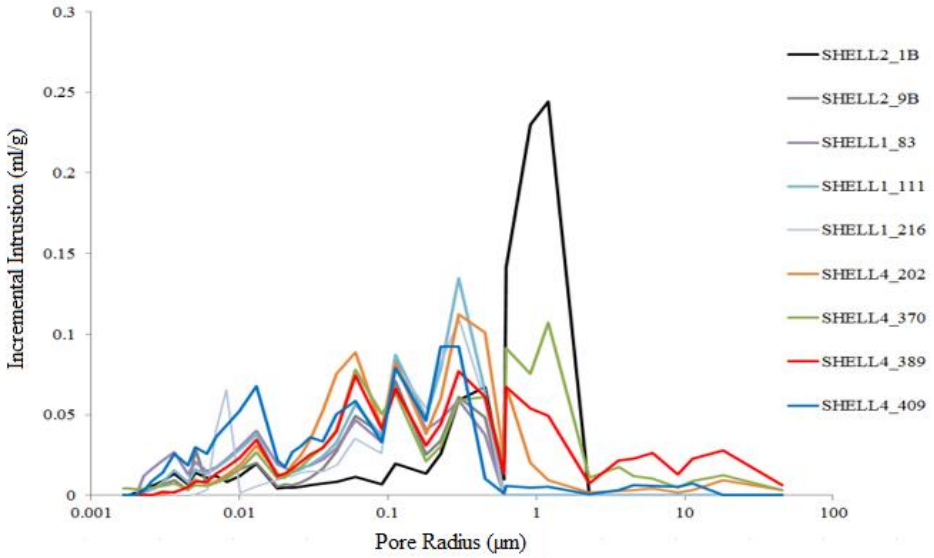
Incremental Intrusion (ml/g)
0.3
0.25
0.2
0.15
0.1
0.05
0
0.001
0.01
0.1
1
10
100
Pore Radius (µm)
SHELL2_1B
SHELL2_9B
SHELL1_83
SHELL1_111
SHELL1_216
SHELL4_202
SHELL4_370
SHELL4_389
SHELL4_409

Mercury injection capillary pressure (MICP) - normalised data for all 25 TGS samples

	BP2_2	BP2_3	BP2_5	BP3_1	BP3_4	BP3_6	EBN3_40	EBN4_10
Pore throat radius (μm)	**normalized psd**	**normalized psd**	**normalized psd**	**normalized psd**	**normalized psd**	**normalized psd**	**normalized psd**	**normalized psd**
45.216	0.000E+00	0.000E+00	0.000E+00	0.000E+00	1.957E-08	8.221E-07	0	6.595E-07
18.086	0.000E+00	0.000E+00	1.760E-06	0.000E+00	8.140E-06	1.963E-05	0	7.498E-06
11.304	0.000E+00	0.000E+00	4.775E-06	0.000E+00	1.255E-05	1.431E-05	0	7.529E-06
9.043	0.000E+00	0.000E+00	4.011E-06	0.000E+00	9.861E-06	2.434E-05	0	7.885E-06
6.029	0.000E+00	0.000E+00	2.096E-05	0.000E+00	4.466E-05	2.786E-05	0	8.226E-06
4.522	0.000E+00	0.000E+00	2.048E-06	0.000E+00	6.058E-05	4.112E-05	0	1.551E-05
3.617	0.000E+00	8.719E-04	1.464E-05	1.342E-04	1.100E-04	6.682E-05	0	4.754E-06
2.261	1.667E-04	1.112E-03	6.411E-06	1.510E-04	6.772E-05	3.456E-05	0	1.904E-05
1.206	1.099E-03	1.080E-02	3.820E-05	1.142E-03	6.982E-03	2.966E-03	3.19E-04	5.547E-05
0.904	3.283E-03	1.124E-02	5.484E-05	1.776E-03	1.641E-02	2.011E-02	7.03E-04	1.371E-04
0.624	1.273E-02	1.614E-02	1.631E-04	2.624E-03	1.254E-02	1.381E-02	3.22E-03	4.758E-04
0.603	1.183E-02	1.233E-02	3.703E-04	2.260E-03	2.097E-02	2.215E-02	3.27E-02	3.043E-03
0.452	1.251E-02	1.828E-02	4.814E-04	3.156E-03	1.428E-02	1.504E-02	6.56E-03	3.204E-03
0.301	1.537E-02	2.275E-02	2.784E-03	4.684E-03	1.952E-02	2.071E-02	4.41E-03	7.779E-03
0.226	1.634E-02	2.472E-02	7.318E-03	5.794E-03	2.140E-02	2.233E-02	3.31E-03	9.152E-03
0.181	1.835E-02	2.838E-02	9.372E-03	7.110E-03	2.279E-02	2.259E-02	2.48E-05	9.648E-03
0.113	3.248E-02	5.002E-02	1.697E-02	1.350E-02	3.572E-02	3.543E-02	7.29E-05	1.389E-02
0.090	3.693E-02	4.871E-02	1.765E-02	1.626E-02	3.338E-02	3.450E-02	2.11E-04	1.204E-02
0.060	6.387E-02	6.679E-02	2.552E-02	3.000E-02	4.758E-02	4.986E-02	1.56E-04	1.537E-02
0.045	7.254E-02	6.585E-02	3.001E-02	3.836E-02	4.881E-02	5.180E-02	3.30E-04	1.543E-02
0.036	7.472E-02	6.488E-02	3.412E-02	4.344E-02	5.074E-02	5.410E-02	5.98E-04	1.765E-02
0.030	6.938E-02	6.697E-02	4.095E-02	4.839E-02	4.896E-02	5.777E-02	8.40E-04	2.053E-02
0.026	7.108E-02	6.554E-02	4.457E-02	4.990E-02	6.578E-02	6.484E-02	1.29E-03	2.287E-02

0.023	7.292E-02	6.707E-02	5.380E-02	5.252E-02	6.050E-02	6.309E-02	2.00E-03	2.403E-02
0.020	6.993E-02	7.301E-02	5.695E-02	5.362E-02	5.674E-02	5.899E-02	3.02E-03	1.912E-02
0.018	6.482E-02	6.682E-02	6.044E-02	4.985E-02	5.886E-02	6.758E-02	4.63E-03	3.119E-02
0.013	7.072E-02	7.890E-02	9.493E-02	6.823E-02	7.864E-02	8.190E-02	2.26E-03	5.296E-02
0.010	5.712E-02	5.511E-02	1.004E-01	6.128E-02	7.027E-02	7.418E-02	4.63E-03	3.873E-02
0.008	4.827E-02	3.717E-02	1.003E-01	5.704E-02	5.431E-02	6.539E-02	7.38E-03	6.900E-02
0.007	4.151E-02	2.624E-02	9.109E-02	5.467E-02	4.503E-02	6.493E-02	1.34E-02	5.660E-02
0.006	3.056E-02	1.298E-02	5.229E-02	5.318E-02	4.157E-02	2.981E-02	1.05E-02	6.562E-02
0.005	2.479E-02	7.313E-03	1.222E-01	5.762E-02	3.708E-02	4.636E-03	1.08E-02	7.226E-02
0.005	6.673E-03	0.000E+00	7.374E-02	5.145E-02	9.596E-03	1.238E-03	4.31E-02	9.462E-02
0.004	0.000E+00	0.000E+00	8.620E-02	6.044E-02	2.121E-02	0.000E+00	3.94E-02	7.489E-02
0.003	0.000E+00	0.000E+00	6.470E-02	5.301E-02	0.000E+00	0.000E+00	5.96E-02	8.516E-02
0.003	0.000E+00	0.000E+00	5.878E-02	3.802E-02	0.000E+00	0.000E+00	8.76E-02	3.764E-02
0.002	0.000E+00	0.000E+00	7.455E-02	2.040E-02	0.000E+00	0.000E+00	1.07E-01	1.268E-01
0.002	0.000E+00	0.000E+00	-5.842E-02	0.000E+00	0.000E+00	0.000E+00	1.45E-01	0
0.002	0.000E+00	0.000E+00	-1.441E-01	0.000E+00	0.000E+00	0.000E+00	1.79E-01	0
0.002	0.000E+00	0.000E+00	-1.183E-01	0.000E+00	0.000E+00	0.000E+00	2.26E-01	0

	GDF1_1	**GDF1_6**	**GDF1_7**	**GDF2-4**	**SHELL2_83**	**SHELL1_111**	**SHELL1_216**	**SHELL2_1B**
Pore throat radius (µm)	**normalized psd**	**normalized psd**	**normalized psd**	**normalized psd**	**normalized psd**	**normalized psd**	**normalized psd**	**normalized psd**
45.216	1.010E-06	1.798E-06	1.265E-05	5.353E-07	0	0	0	0
18.086	9.227E-06	2.141E-05	1.559E-04	6.388E-05	0	0	0	0
11.304	7.148E-05	1.827E-05	1.762E-04	4.272E-05	0	0	0	0
9.043	7.667E-05	1.284E-05	1.702E-04	5.120E-05	0	0	0	6.319E-06
6.029	1.357E-04	3.836E-06	5.357E-04	2.195E-04	7.290E-05	0	2.474E-04	9.702E-06
4.522	2.575E-04	2.057E-05	1.011E-03	3.618E-04	9.015E-05	0	3.314E-04	1.308E-05

3.617	5.067E-04	2.142E-05	3.219E-03	1.110E-03	1.167E-04	0	3.983E-04	1.952E-05
2.261	8.574E-04	2.128E-05	1.065E-02	4.874E-03	4.363E-05	1.646E-04	2.113E-04	8.371E-06
1.206	3.151E-02	1.143E-04	7.373E-02	3.004E-02	3.500E-04	5.492E-04	1.146E-03	2.626E-03
0.904	5.065E-02	8.664E-05	6.078E-02	1.595E-02	4.090E-04	7.291E-04	1.300E-03	6.147E-03
0.624	4.087E-02	3.142E-04	5.578E-02	1.321E-02	6.677E-04	1.434E-03	2.218E-03	4.415E-03
0.603	6.174E-02	4.759E-04	6.522E-02	2.181E-02	6.082E-04	1.536E-03	1.613E-03	2.978E-03
0.452	4.047E-02	1.176E-03	5.740E-02	1.464E-02	9.581E-04	2.748E-03	4.022E-03	3.605E-03
0.301	5.001E-02	2.087E-02	7.399E-02	2.123E-02	1.699E-03	6.512E-03	8.676E-03	3.561E-03
0.226	5.200E-02	4.872E-02	7.757E-02	2.363E-02	2.427E-03	6.741E-03	1.158E-02	2.738E-03
0.181	5.460E-02	4.729E-02	8.318E-02	3.080E-02	3.248E-03	6.503E-03	1.191E-02	2.287E-03
0.113	7.656E-02	6.625E-02	1.131E-01	5.194E-02	5.812E-03	9.988E-03	1.531E-02	2.824E-03
0.090	6.421E-02	7.173E-02	8.512E-02	5.000E-02	5.271E-03	9.849E-03	1.157E-02	2.375E-03
0.060	8.348E-02	9.497E-02	7.968E-02	6.588E-02	6.720E-03	1.366E-02	1.416E-02	3.504E-03
0.045	7.862E-02	9.352E-02	6.405E-02	6.091E-02	7.567E-03	1.416E-02	1.328E-02	4.479E-03
0.036	7.876E-02	6.461E-02	0.000E+00	6.091E-02	8.817E-03	1.644E-02	1.658E-02	5.987E-03
0.030	7.445E-02	7.898E-02	0.000E+00	5.847E-02	1.063E-02	1.847E-02	2.395E-02	7.396E-03
0.026	5.094E-02	8.795E-02	2.511E-02	5.610E-02	1.359E-02	2.090E-02	3.127E-02	8.745E-03
0.023	7.128E-02	7.733E-02	6.937E-02	6.401E-02	1.555E-02	2.368E-02	3.311E-02	1.037E-02
0.020	3.194E-02	5.301E-02	0	5.932E-02	2.208E-02	2.967E-02	4.548E-02	1.289E-02
0.018	6.017E-03	6.024E-02	0	5.072E-02	3.104E-02	3.339E-02	4.292E-02	1.465E-02
0.013	0	7.237E-02	0	7.453E-02	3.161E-02	4.914E-02	1.252E-02	3.228E-02
0.010	0	4.737E-02	0	6.474E-02	3.873E-02	6.204E-02	5.152E-03	3.294E-02
0.008	0	9.515E-03	0	5.112E-02	4.409E-02	7.054E-02	3.515E-01	3.321E-02
0.007	0	2.977E-03	0	2.745E-02	4.743E-02	7.693E-02	2.981E-01	6.752E-02
0.006	0	0	0	1.956E-02	5.486E-02	8.262E-02	3.680E-02	8.433E-02
0.005	0	0	0	6.309E-03	7.200E-02	9.225E-02	4.567E-03	1.006E-01
0.005	0	0	0	0	8.308E-02	8.219E-02	0	9.292E-02
0.004	0	0	0	0	1.074E-01	1.036E-01	0	1.138E-01
0.003	0	0	0	0	1.259E-01	7.971E-02	0	1.076E-01

	SHELL2_9B	SHELL4_202	SHELL4_370	SHELL4_389	SHELL4_409	WIN5_16B	WIN4_26	WIN9_5
Pore throat radius (μm)	**normalized psd**	**normalized psd**	**normalized psd**	**normalized psd**	**normalized psd**	**normalized psd**	**normalized psd**	**normalized psd**
45.216	0	5.912E-07	3.129E-07	1.081E-06	0	0	0	1.956E-07
18.086	0	6.598E-06	5.345E-06	1.947E-05	0	0	0	2.527E-06
11.304	0	6.306E-06	9.612E-06	4.089E-05	4.77E-06	0	0	3.130E-06
9.043	6.400E-05	8.446E-06	1.252E-05	5.444E-05	7.74E-06	0	0	3.912E-06
6.029	1.575E-04	1.615E-05	2.337E-05	9.839E-05	7.74E-06	0	0	4.621E-06
4.522	2.147E-04	2.196E-05	4.906E-05	1.508E-04	1.51E-05	6.85E-05	0	7.042E-06
3.617	3.142E-04	3.035E-05	1.119E-04	2.251E-04	1.29E-05	8.47E-05	0	7.947E-06
2.261	3.211E-04	1.440E-05	5.898E-05	6.589E-05	2.30E-06	5.30E-05	4.650E-04	8.410E-07
1.206	1.854E-03	1.268E-04	8.687E-04	6.618E-04	2.56E-05	2.80E-04	1.874E-03	4.275E-08
0.904	1.861E-03	6.968E-04	1.530E-03	1.798E-03	5.77E-05	3.20E-04	3.075E-03	8.349E-07
0.624	2.521E-03	2.710E-03	2.159E-03	2.627E-03	7.88E-05	5.71E-04	5.390E-03	2.152E-07
0.603	1.726E-03	9.033E-03	4.247E-03	4.888E-03	1.68E-04	4.71E-04	3.696E-03	1.821E-05
0.452	2.851E-03	6.919E-03	2.465E-03	4.088E-03	2.52E-04	9.98E-04	5.475E-03	2.283E-06
0.301	4.044E-03	8.679E-03	2.687E-03	5.801E-03	2.45E-03	2.70E-03	6.233E-03	1.518E-05
0.226	4.031E-03	8.244E-03	2.443E-03	5.898E-03	4.34E-03	6.15E-03	5.779E-03	5.495E-06
0.181	4.631E-03	8.204E-03	2.669E-03	6.477E-03	3.39E-03	7.08E-03	6.152E-03	5.580E-05
0.113	1.109E-02	1.498E-02	6.876E-03	1.184E-02	4.95E-03	1.16E-02	9.381E-03	3.043E-05
0.090	1.400E-02	1.793E-02	1.269E-02	1.710E-02	4.82E-03	1.19E-02	9.557E-03	1.442E-04
0.060	1.629E-02	3.417E-02	1.780E-02	2.808E-02	7.72E-03	2.05E-02	1.446E-02	9.959E-05
0.045	1.607E-02	5.163E-02	1.576E-02	2.692E-02	1.18E-02	2.25E-02	1.696E-02	2.633E-04
0.036	1.532E-02	5.619E-02	1.896E-02	3.058E-02	1.24E-02	2.27E-02	1.780E-02	3.805E-04
0.030	1.421E-02	5.318E-02	2.130E-02	3.818E-02	1.90E-02	2.21E-02	2.274E-02	4.547E-04
0.026	1.462E-02	5.256E-02	2.203E-02	4.210E-02	2.21E-02	2.25E-02	2.265E-02	8.029E-04
0.023	1.500E-02	5.249E-02	2.386E-02	4.493E-02	2.55E-02	2.36E-02	2.728E-02	8.282E-04
0.020	2.026E-02	3.923E-02	2.257E-02	4.520E-02	2.08E-02	2.62E-02	3.650E-02	1.303E-03
0.018	1.963E-02	5.713E-02	2.623E-02	5.065E-02	3.16E-02	3.05E-02	3.323E-02	5.950E-03

0.013	3.656E-02	6.485E-02	3.314E-02	7.102E-02	4.88E-02	4.02E-02	5.102E-02	2.708E-03
0.010	4.858E-02	6.424E-02	3.307E-02	7.815E-02	6.24E-02	5.08E-02	5.404E-02	4.479E-03
0.008	5.061E-02	6.878E-02	3.263E-02	9.025E-02	7.74E-02	5.90E-02	6.883E-02	7.517E-03
0.007	5.242E-02	6.312E-02	3.355E-02	9.662E-02	9.06E-02	7.95E-02	7.003E-02	1.060E-02
0.006	5.468E-02	6.432E-02	3.390E-02	7.798E-02	8.46E-02	7.16E-02	8.114E-02	2.058E-02
0.005	2.277E-01	9.111E-02	3.612E-02	7.482E-02	9.47E-02	1.01E-01	7.500E-02	1.442E-02
0.005	4.597E-02	7.302E-02	3.655E-02	9.104E-02	1.11E-01	1.20E-01	5.177E-02	6.619E-02
0.004	8.730E-02	2.238E-02	4.624E-02	1.957E-02	9.53E-02	8.41E-02	1.706E-01	4.487E-02
0.003	9.266E-02	1.326E-02	5.140E-02	3.209E-02	7.49E-02	7.29E-02	8.803E-02	6.103E-02
0.003	6.924E-02	0	5.991E-02	0	6.34E-02	5.54E-02	4.079E-02	8.337E-02
0.002	4.252E-02	0	6.856E-02	0	2.60E-02	2.73E-02	0	1.145E-01
0.002	1.067E-02	7.041E-04	8.321E-02	0	0	5.56E-03	0	1.467E-01
0.002	0	0	1.139E-01	0	0	0	0	1.866E-01
0.002	0	0	1.304E-01	0	0	0	0	2.261E-01

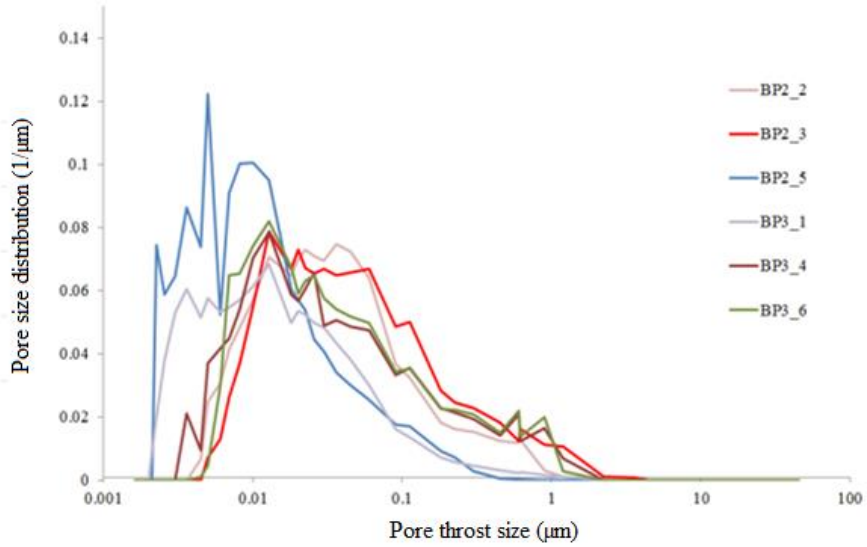
Pore size distribution (1/μm)
0.14
0.12
0.1
0.08
0.06
0.04
0.02
0
0.001
0.01
0.1
1
10
100
Pore throst size (μm)
BP2_2
BP2_3
BP2_5
BP3_1
BP3_4
BP3_6

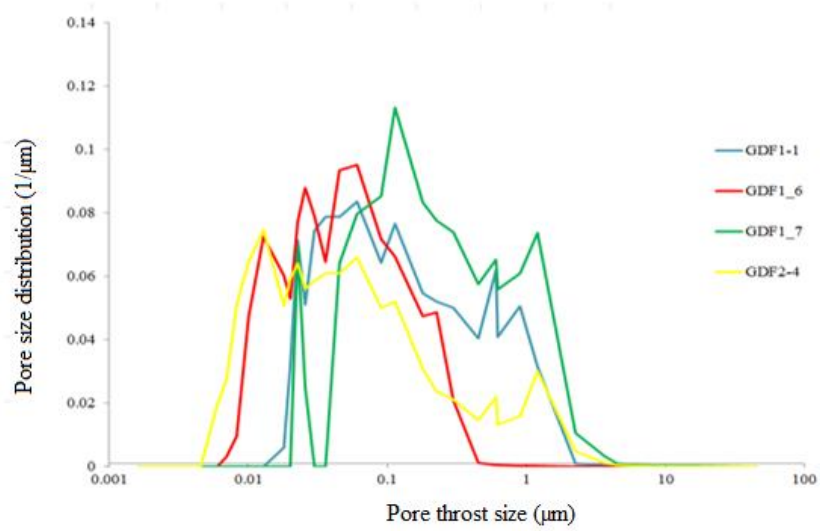
Pore size distribution (1/μm)
0.14
0.12
0.1
0.08
0.06
0.04
0.02
0
0.001
0.01
0.1
1
10
100
Pore throst size (μm)
GDF1-1
GDF1_6
GDF1_7
GDF2-4

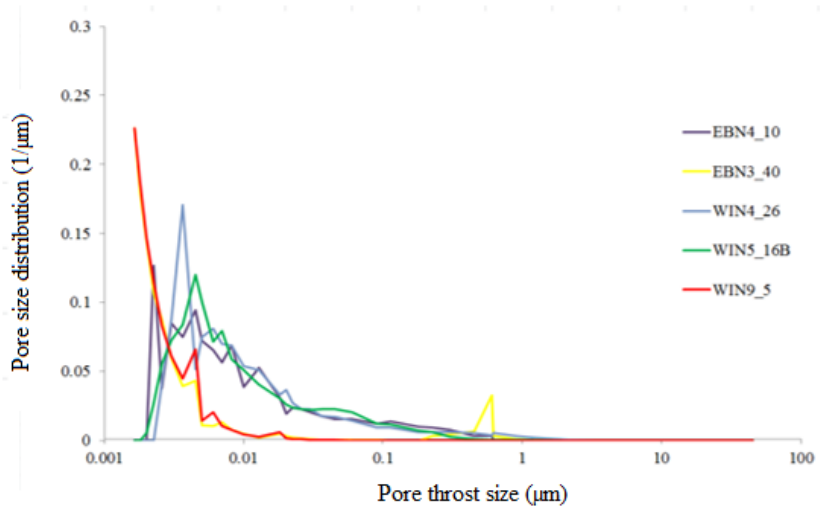
Pore size distribution (1/μm)
0.3
0.25
0.2
0.15
0.1
0.05
0
0.001
0.01
0.1
1
10
100
Pore throst size (μm)
EBN4_10
EBN3_40
WIN4_26
WIN5_16B
WIN9_5

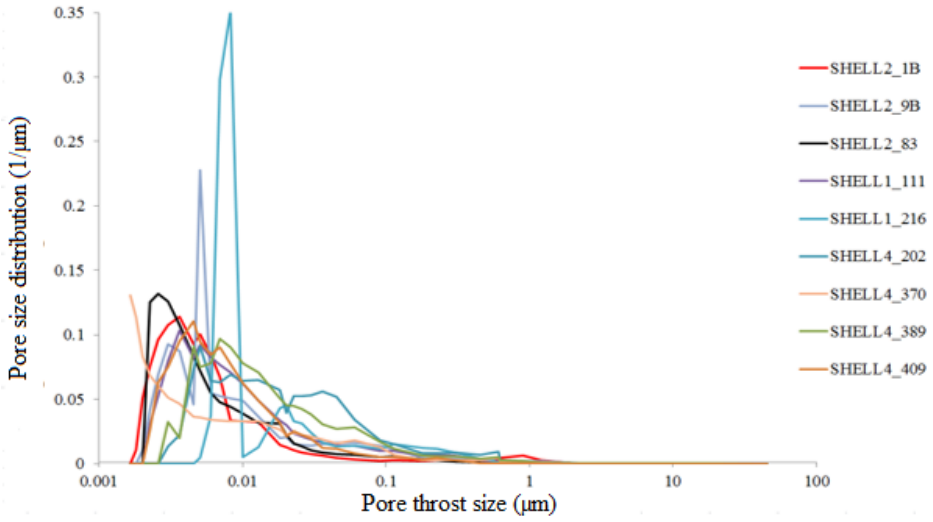

Appendix E

BET surface area permeability estimation data for all 25 TGS samples

Well/Sample	Permeability at *in-situ* stress (mD)	BET permeability
WIN4_26	0.023	0.009
SHELL1_83	0.00019	
BP3_1	0.16	0.089
BP3_6	0.56	
WIN5_16B	0.009	0.013
SHELL1_111	0.0037	0.006
BP2_2	0.030	0.020
BP2_5	0.0018	0.002
EBN3_40	0.67	0.019
EBN4_10	0.002	0.004
SHELL4_202	0.047	0.047
SHELL4_370	0.93	0.14
SHELL4_389	0.035	0.10
SHELL4_409	0.00002	0.004
BP3_4	0.69	
BP2_3	0.17	
BP3_5	0.69	
WIN 9_5	0.00003	
GDF1_1	0.75	0.29
GDF1_6	0.015	0.201
GDF1_7	3.7	3.4
SHELL1_216	0.005	0.035
SHELL2_1	0.28	0.14
SHELL2_9	0.26	
GDF2_4	3.1	

Mercury injection capillary pressure (MICP) permeability estimation data for all 25 TGS samples

Sample	Purcell (1949)	Winland (1980)	Swanson 5000 psi (1981)	Katz-Thompson lmax from Hg (1986, 1987)
WIN4_26	0.28	0.32	0.04	0.45
WIN5_16B	0.02	0.03	0.01	0.05
SHELL1_83	0.01	0.01	0.00	0.06
SHELL1_111	0.02	0.04	0.01	0.05
SHELL2_1B	0.47	0.79	0.28	0.86
SHELL2_9B	0.03	0.03	0.01	0.26
BP2_2	0.23	0.29	0.08	0.34
BP2_3	0.94	1.06	0.35	1.41
BP2_5	0.00	0.01	0.00	0.00
BP3_1	0.46	0.62	0.20	1.06
BP3_4	0.67	1.23	0.45	0.66
BP3_5				
BP3_6	0.40	0.68	0.27	0.38
EBN3_40	0.47	0.47	0.85	0.33
EBN4_10	0.05	0.06	0.01	0.01
SHELL4_202				
SHELL4_370	0.34	0.31	0.12	0.26
SHELL4_389	0.21	0.18	0.06	0.06
SHELL4_409				
WIN9_5	0.00	0.00	0.00	
GDF1_1	0.77	0.83	0.32	0.56
GDF1_6	0.01	0.02	0.00	0.00
GDF1_7	1.44	2.71	0.60	0.76
GDF2_4	1.64	2.92	0.84	0.91

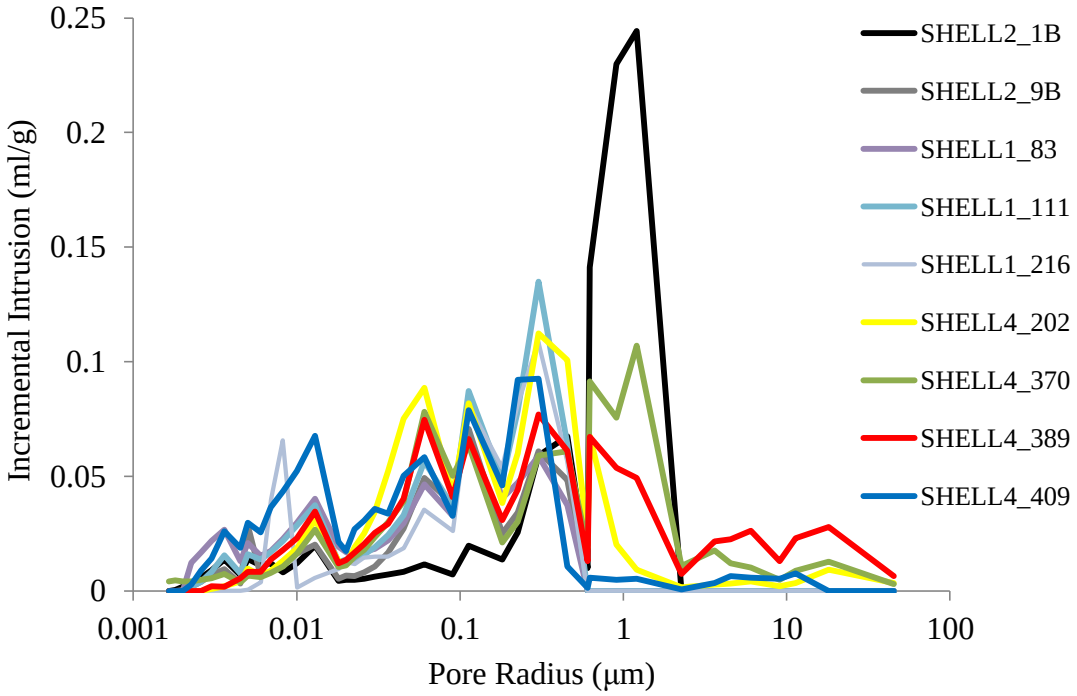

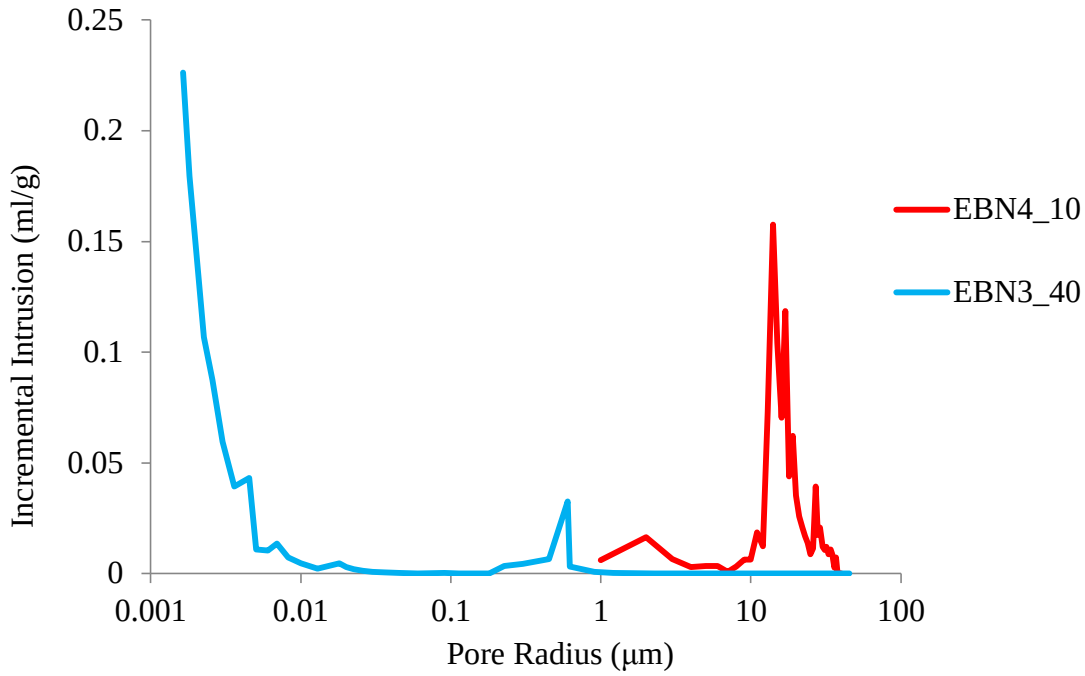
0.25
0.2
0.15
0.1
0.05
0
Incremental Intrusion (ml/g)
0.001
0.01
0.1
1
10
100
Pore Radius (µm)
EBN4_10
EBN3_40

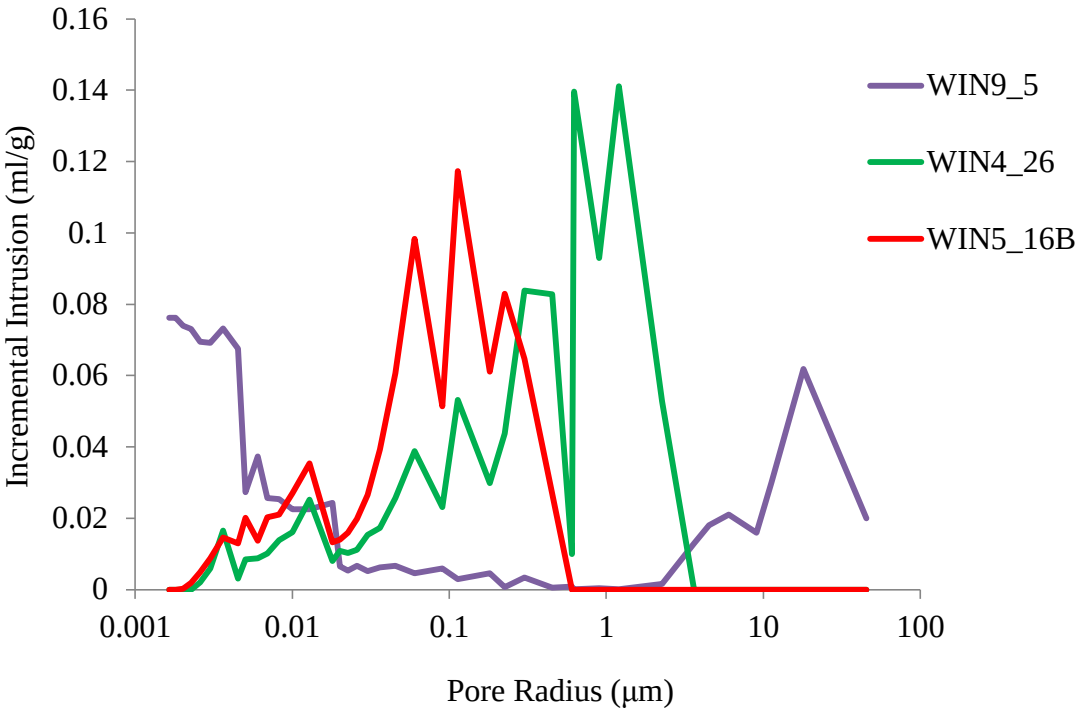
0.16
0.14
0.12
0.1
0.08
0.06
0.04
0.02
0
Incremental Intrusion (ml/g)
0.001
0.01
0.1
1
10
100
Pore Radius (µm)
WIN9_5
WIN4_26
WIN5_16B

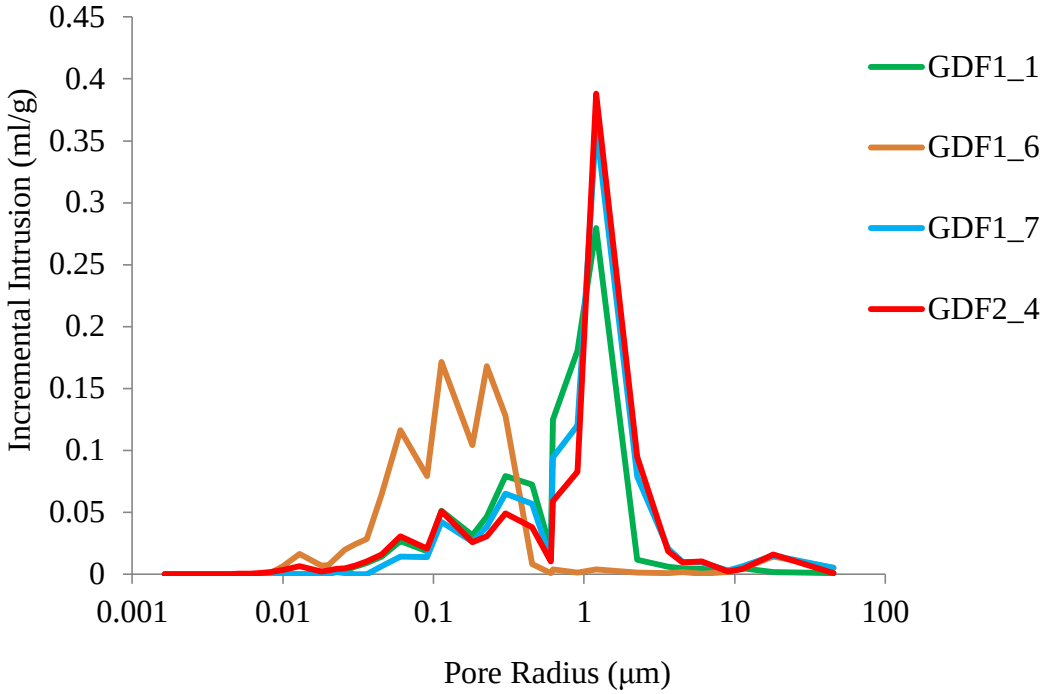
0.45
0.4
0.35
0.3
0.25
0.2
0.15
0.1
0.05
0
Incremental Intrusion (ml/g)
0.001
0.01
0.1
1
10
100
Pore Radius (µm)
GDF1_1
GDF1_6
GDF1_7
GDF2_4

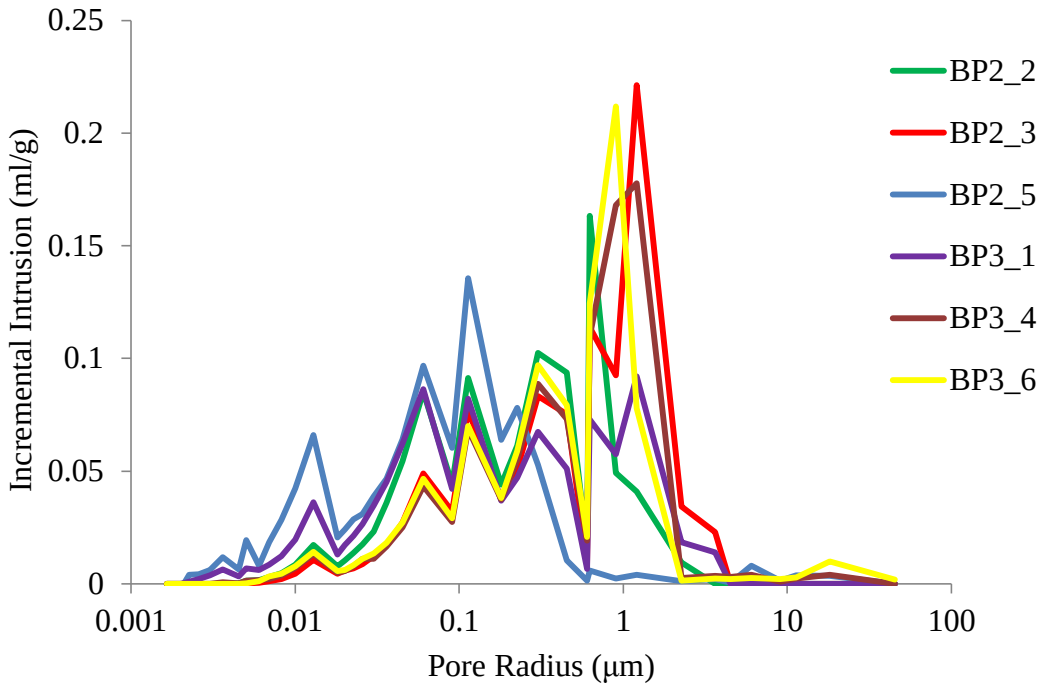
0.25
0.2
0.15
0.1
0.05
0
Incremental Intrusion (ml/g)
0.001
0.01
0.1
1
10
100
Pore Radius (µm)
BP2_2
BP2_3
BP2_5
BP3_1
BP3_4
BP3_6

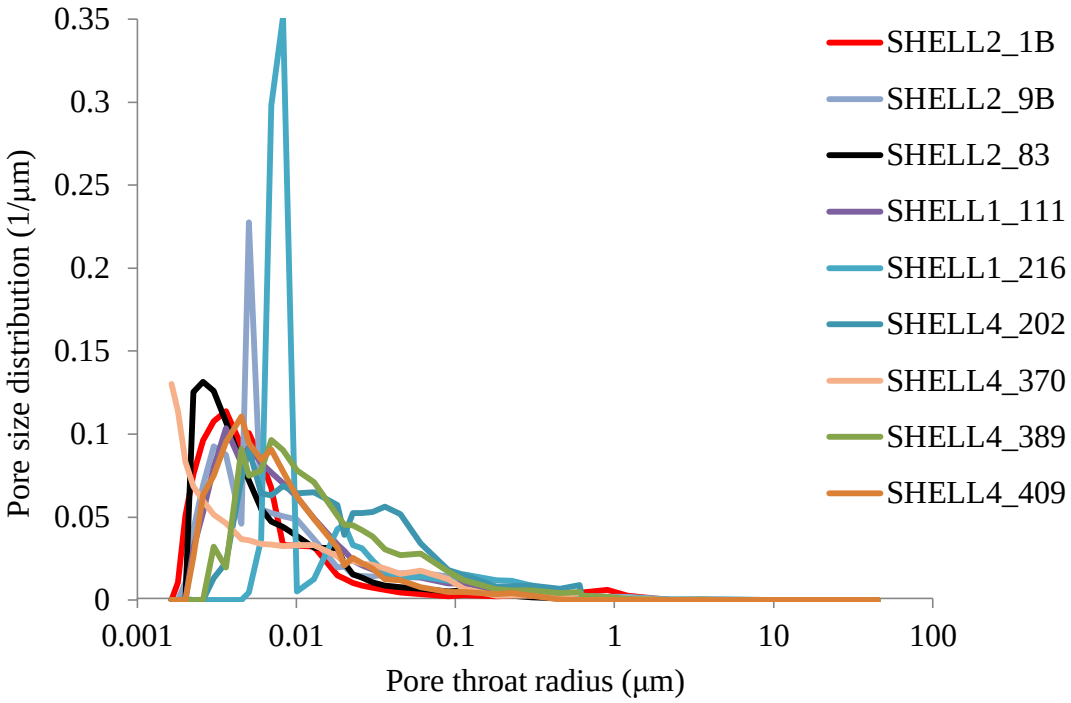
0.35
0.3
0.25
0.2
0.15
0.1
0.05
0
Pore size distribution (1/μm)
0.001
0.01
0.1
1
10
100
Pore throat radius (μm)
SHELL2_1B
SHELL2_9B
SHELL2_83
SHELL1_111
SHELL1_216
SHELL4_202
SHELL4_370
SHELL4_389
SHELL4_409

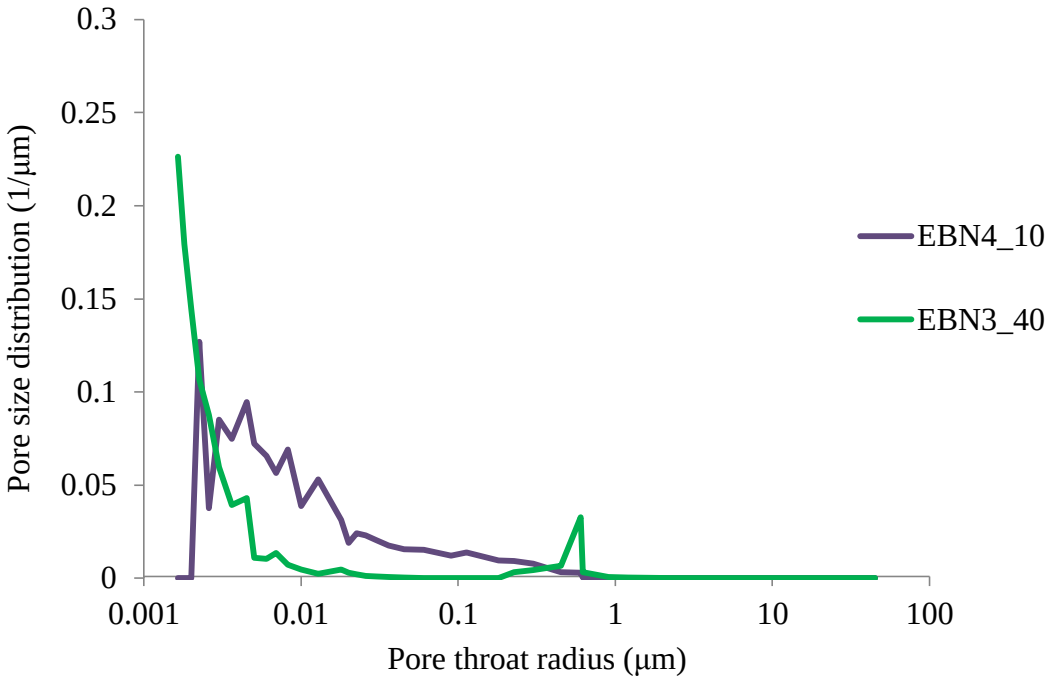
0.3
0.25
0.2
0.15
0.1
0.05
0
Pore size distribution (1/μm)
0.001
0.01
0.1
1
10
100
Pore throat radius (μm)
EBN4_10
EBN3_40

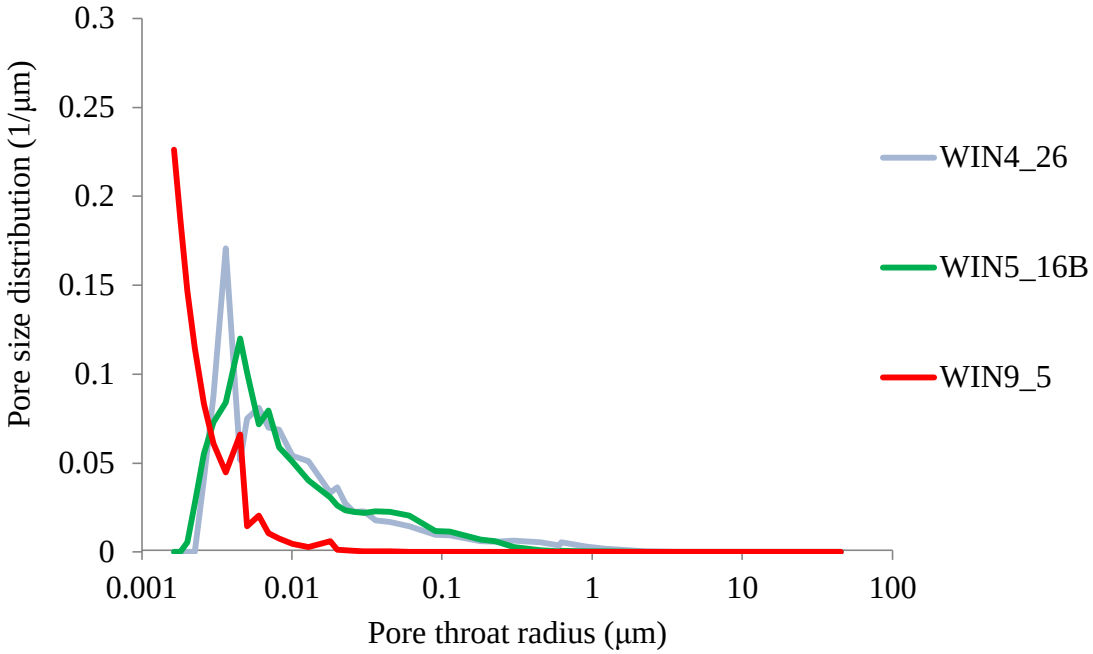
0.3
0.25
0.2
0.15
0.1
0.05
0
Pore size distribution (1/µm)
0.001
0.01
0.1
1
10
100
Pore throat radius (µm)
WIN4_26
WIN5_16B
WIN9_5

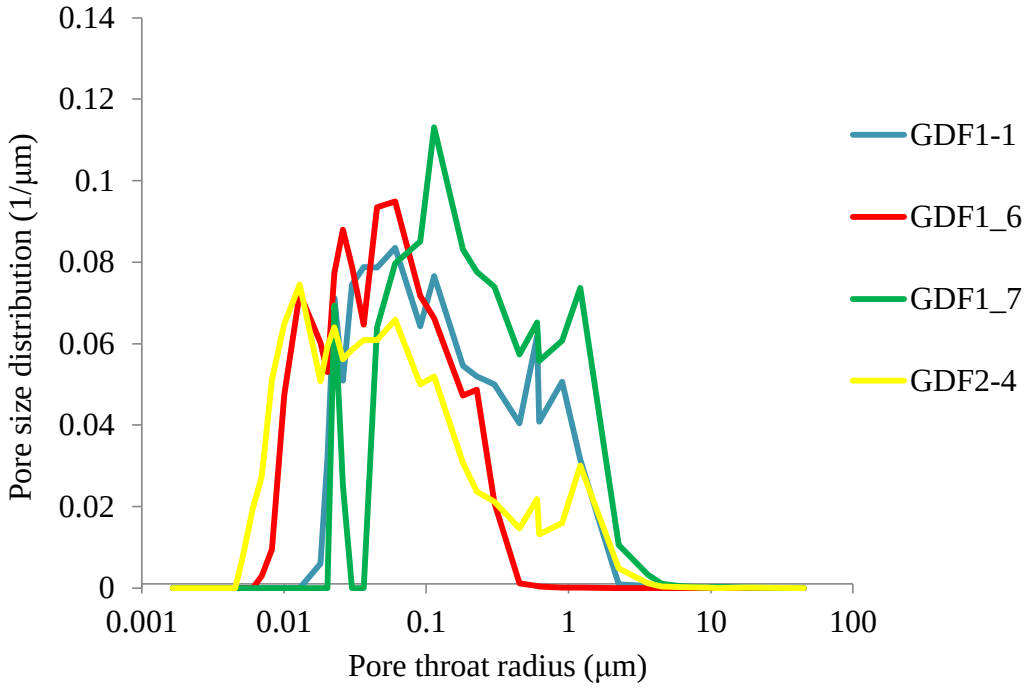
0.14
0.12
0.1
0.08
0.06
0.04
0.02
0
Pore size distribution (1/µm)
0.001
0.01
0.1
1
10
100
Pore throat radius (µm)
GDF1-1
GDF1_6
GDF1_7
GDF2-4

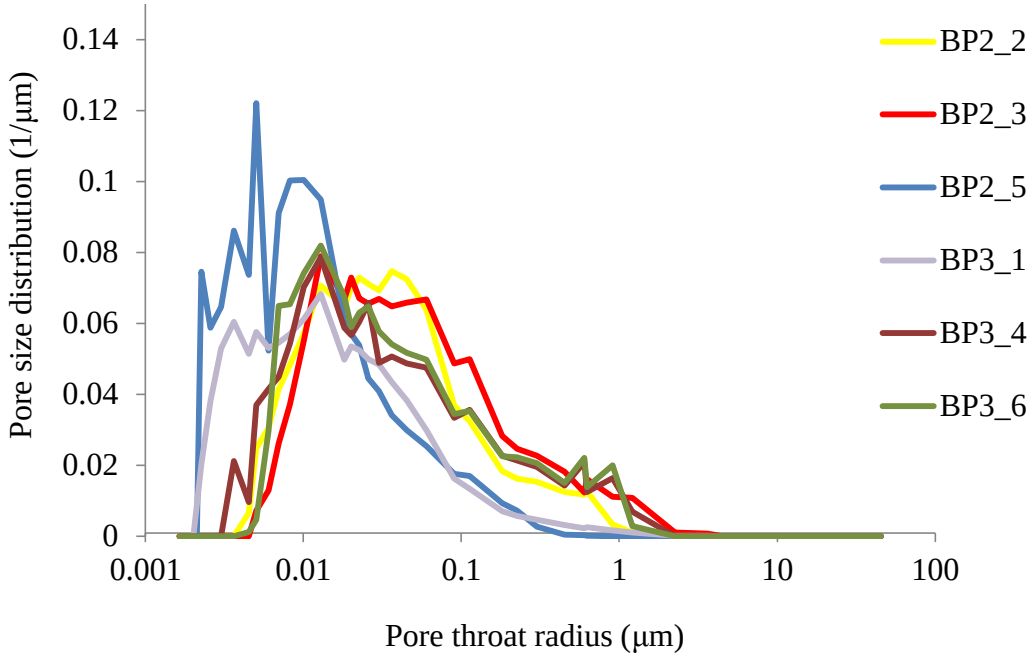

Appendix F

Porosity vs stress from the discovery data

Constants	A	-0.049	-0.048	-0.047	-0.046	-0.065
	B	1.16	1.15	1.1	1.1	1.14
Cp (psi)	Log Cp (psi)	Porosity (%)				
		BP2_2	BP2_3	BP3_1	WIN6_16B	WIN4_26
10	1	13	14	14	15	7
250	2.4	13	14	14	15	7
500	2.7	13	14	14	15	7
750	2.9	13	14	13	15	7
1000	3	13	14	13	14	6
2000	3.3	13	14	13	14	6
3000	3.5	12	13	13	14	6
4000	3.6	12	13	13	14	6
5000	3.7	12	13	13	14	6

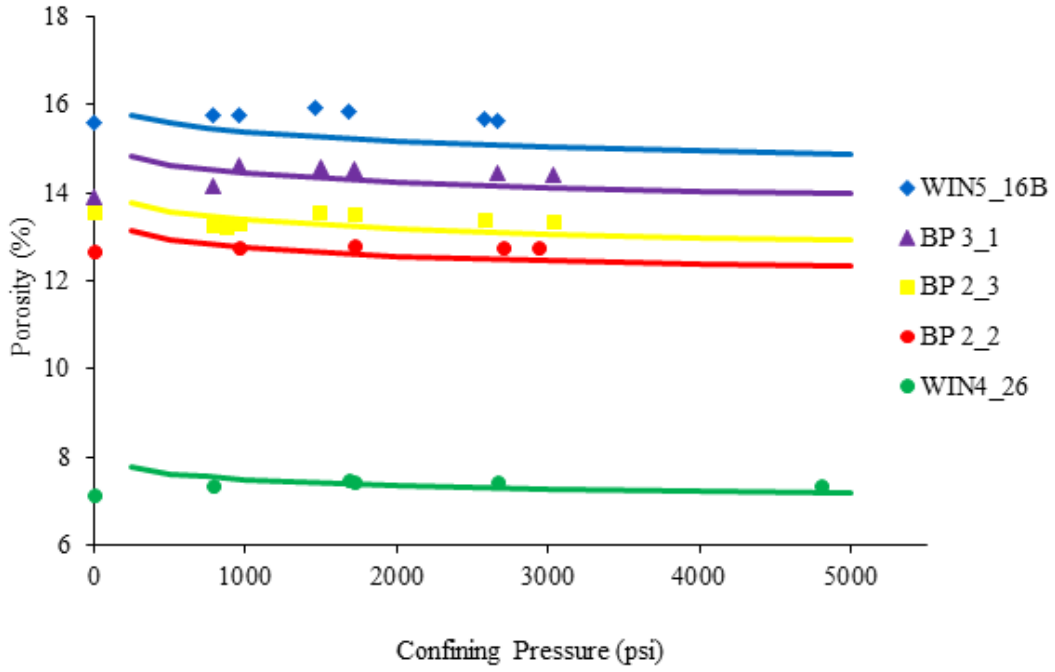

A comparison of porosity under stress for this research data with the Discovery Group relationship (lines) for core set 1.

Constants	**A**	**-0.049**	**-0.06**	**-0.085**	**-0.059**	**-0.091**
	B	**1.16**	**1.16**	**1.13**	**1.11**	**1.16**
Cp (psi)	**Log Cp (psi)**	**Porosity (%)**				
		SHELL2_9B	**SHELL2_1B**	**SHELL1_83**	**SHELL1_111**	**SHELL1_216**
10	1	13	8	4	8	3
500	2.7	13	8	3	8	3
750	2.9	13	8	3	8	3
1000	3	13	8	3	8	3
2000	3.3	13	8	3	8	3
3000	3.5	13	8	3	8	3
3500	3.5	12	8	3	8	3
4000	3.6	12	8	3	8	3

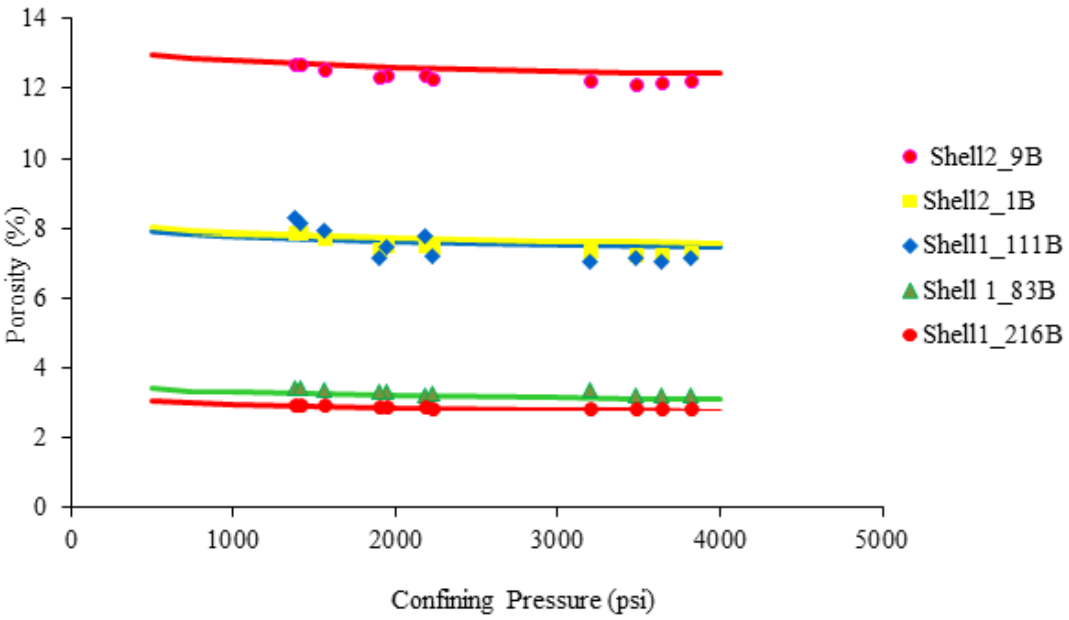

A comparison of porosity under stress for this research data with the Discovery Group relationship (lines) for core set 2.

Constants	**A**	**-0.043**	**-0.040**	**-0.045**	**-0.044**	**-0.048**
	B	**1.15**	**1.15**	**1.1**	**1.1**	**1.13**
Cp (ps)	**Log Cp (psi)**	**Porosity (%)**				
		BP3_4	**BP3_5**	**BP3_6**	**SHELL4_202**	**SHELL4_389**
0		17	20	15	16	13
250	2.4	18	21	15	16	13
500	2.7	18	21	15	16	13
750	2.9	17	21	15	16	13
1000	3	17	21	15	16	13
1500	3.2	17	20	15	16	13
2000	3.3	17	20	15	16	13
3000	3.5	17	20	15	16	13
4000	3.6	17	20	14	16	13

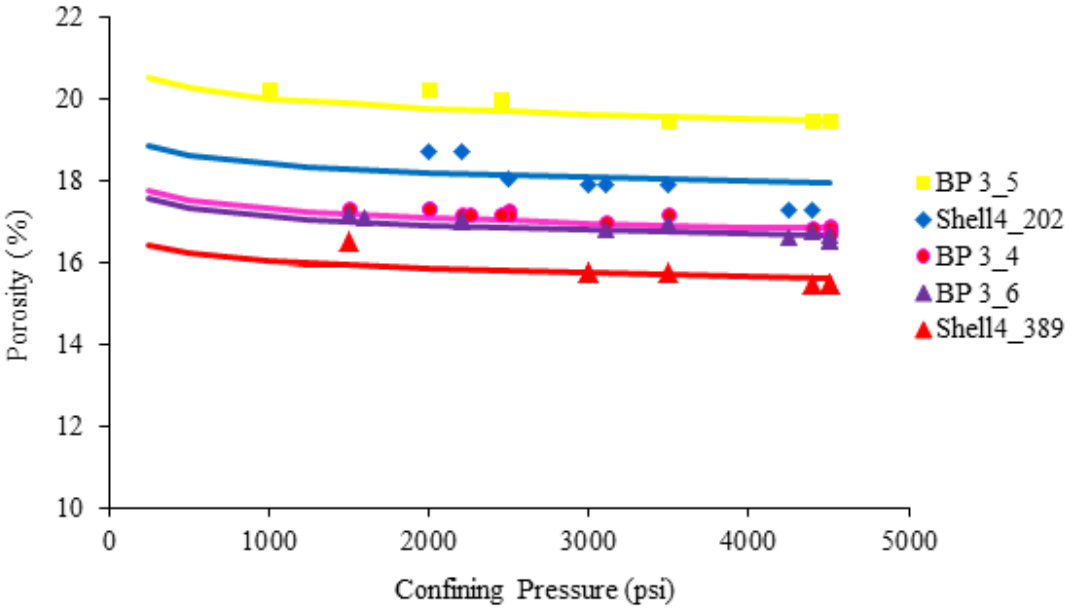

A comparison of porosity under stress for this research data with the Discovery Group relationship (lines) for core set 3.

Constants	**A**	**-0.062**	**-0.073**	**-0.079**	**-0.074**	**-0.056**
	B	**1.16**	**1.17**	**1.1**	**1.1**	**1.1**
Cp (psi)	**Log Cp (psi)**	**Porosity (%)**				
		EBN4-10	**WIN9_5**	**BP2_5**	**SHELL4_409**	**GDF1-6**
0		7	5	5	7	5
250	2.4	7	5	4	7	5
500	2.7	7	5	4	7	5
750	2.9	7	5	4	7	5
1000	3	7	5	4	7	5
1500	3.2	7	5	4	7	5
2000	3.3	7	5	4	7	5
3000	3.5	7	5	4	6	5
3500	3.5	7	5	4	6	5
4000	3.6	7	5	4	6	5

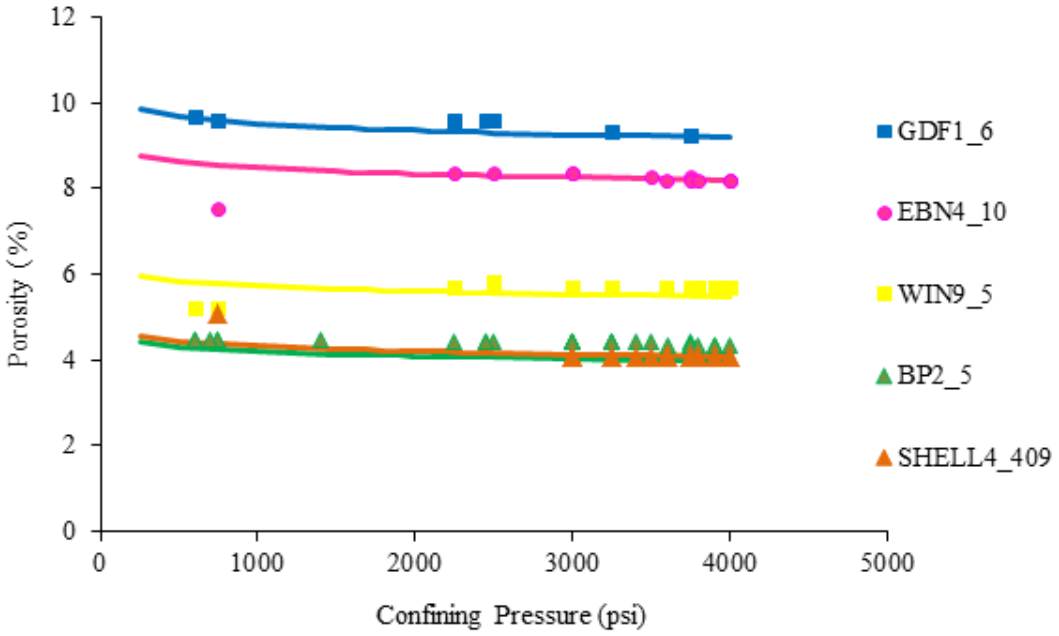

A comparison of porosity under stress for this research data with the Discovery Group relationship (lines) for core set 4.

Core set 1 –Porosity, *FRF* and *m* with Stress`

Original Porosity (%)	**12.66**	**13.58**	**13.89**	**14.97**	**6.81**
Sample	**BP 2_2**	**BP 2_3**	**BP 3_1**	**WIN5_16B**	**WIN4_26**
Pressure (psi)	**Porosity (%)**	**Porosity (%)**	**Porosity (%)**	**Porosity (%)**	**Porosity (%)**
852	12.66	13.58	13.89	14.97	6.81
782					
877		13.24			
958	12.78	13.31	14.61	15.75	7.34
1365				15.77	
1496			14.58	15.91	
1721	12.81	13.51	14.55	15.83	7.48
2581		13.39			
2698	12.76				7.43
2667			14.46	15.69	
2932	12.78				
3039		13.36	14.41	15.66	7.42
4906					7.37
4583	12.63	13.02	14.28	15.46	
4754				15.43	
4760		12.96	14.24		7.35
4419			14.18	15.33	

BP2_2					
Resistivity (ohm-m)	**Confining pressure (psi)**	**Log confining pressure (psi)**	**Porosity (fraction)**	**FRF (unitless)**	**m (unitless)**
4.57	852	2.93	0.109	93.3	2.05
5.83	782	2.89	0.109	119.0	2.16
5.92	877	2.94	0.109	120.9	2.16
5.81	958	2.98	0.109	118.6	2.15
5.72	1459	3.16	0.108	116.7	2.14
5.66	1365	3.14	0.108	115.6	2.13
5.27	1496	3.17	0.108	107.6	2.10
5.32	1785	3.25	0.107	108.6	2.10
5.24	1687	3.23	0.107	106.9	2.09
5.51	1483	3.17	0.108	112.5	2.12
5.55	1721	3.24	0.107	113.3	2.12
5.39	2581	3.41	0.106	110.1	2.10
5.70	2698	3.43	0.106	116.3	2.12
5.61	2667	3.43	0.106	114.4	2.11
5.94	2932	3.47	0.106	121.3	2.14
6.31	3039	3.48	0.106	128.8	2.16
7.14	4741	3.68	0.105	145.8	2.21
7.10	4845	3.69	0.105	144.9	2.20
7.24	4851	3.69	0.105	147.8	2.21
6.83	4901	3.69	0.105	139.4	2.19
7.10	4809	3.68	0.105	145.0	2.20
6.53	4934	3.69	0.105	133.2	2.17
6.31	4906	3.69	0.105	128.7	2.15
6.92	4583	3.66	0.105	141.1	2.19
7.02	4754	3.68	0.105	143.2	2.20
7.01	4759	3.68	0.105	143.0	2.20
7.04	4760	3.68	0.105	143.7	2.20

BP2_3					
Resistivity (ohm-m)	**Confining pressure (psi)**	**Log confining pressure (psi)**	**Porosity (fraction)**	**FRF (unitless)**	**m (unitless)**
6.7	852	2.93	0.117	136.2	2.29
6.9	782	2.89	0.117	140.2	2.31
7.1	877	2.94	0.117	145.0	2.32
7.2	958	2.98	0.117	146.6	2.32
7.7	1459	3.16	0.116	157.1	2.34
7.5	1365	3.14	0.116	153.1	2.33
7.4	1496	3.17	0.116	150.0	2.32
7.4	1785	3.25	0.115	151.2	2.32
7.3	1687	3.23	0.115	148.6	2.31
7.7	1483	3.17	0.116	156.9	2.34
7.8	1721	3.24	0.115	158.2	2.34
7.8	2581	3.41	0.114	158.3	2.33
8.1	2698	3.43	0.114	165.9	2.35
8.1	2932	3.47	0.114	165.7	2.35
8.7	3039	3.48	0.114	177.0	2.38
9.4	4741	3.68	0.112	190.9	2.40
10.3	4845	3.69	0.112	210.5	2.45
10.5	4851	3.69	0.112	215.1	2.46
10.8	4901	3.69	0.112	219.4	2.47
10.3	4809	3.68	0.112	211.0	2.45
10.8	4934	3.69	0.112	220.1	2.47
9.9	4906	3.69	0.112	201.6	2.43
9.2	4583	3.66	0.112	187.5	2.40
10.2	4754	3.68	0.112	209.1	2.44
10.4	4759	3.68	0.112	212.1	2.45
10.3	4760	3.68	0.112	211.0	2.45
10.5	4419	3.65	0.113	214.8	2.46

BP3_1					
Resistivity (ohm-m)	**Confining pressure (psi)**	**Log confining pressure (psi)**	**Porosity at stress (%)**	**FRF (unitless)**	**m (unitless)**
3.73	852	2.93	0.114	76.1	2.00
4.49	782	2.89	0.114	91.6	2.08
4.59	877	2.94	0.114	93.7	2.09
4.75	958	2.98	0.114	96.9	2.10
4.97	1459	3.16	0.113	101.4	2.12
4.93	1365	3.14	0.113	100.6	2.11
4.68	1496	3.17	0.113	95.4	2.09
4.78	1785	3.25	0.112	97.5	2.09
4.32	1687	3.23	0.112	88.2	2.05
4.46	1483	3.17	0.113	91.0	2.07
4.51	1721	3.24	0.112	92.1	2.07
4.47	2581	3.41	0.111	91.2	2.05
4.56	2698	3.43	0.111	93.1	2.06
4.62	2667	3.43	0.111	94.3	2.07
4.84	2932	3.47	0.111	98.7	2.09
5.12	3039	3.48	0.111	104.4	2.11
5.76	4741	3.68	0.110	117.5	2.16
5.91	4845	3.69	0.109	120.7	2.17
6.09	4851	3.69	0.109	124.3	2.18
5.83	4901	3.69	0.109	118.9	2.16
6.06	4809	3.68	0.109	123.7	2.18
5.57	4934	3.69	0.109	113.7	2.14
5.37	4906	3.69	0.109	109.7	2.12
5.91	4583	3.66	0.110	120.7	2.17
5.99	4754	3.68	0.110	122.3	2.17
6.00	4759	3.68	0.110	122.5	2.17
6.02	4760	3.68	0.110	122.8	2.18

WIN5_16B					
Resistivity (ohm-m)	**Confining pressure (psi)**	**Log confining pressure (psi)**	**Porosity at stress (%)**	**FRF (unitless)**	**m (unitless)**
2.45	852	2.93	0.12	50.0	1.84
2.63	782	2.89	0.12	53.7	1.88
2.68	877	2.94	0.12	54.8	1.88
2.75	958	2.98	0.12	56.2	1.89
2.93	1459	3.16	0.12	59.9	1.92
2.91	1365	3.14	0.12	59.3	1.91
3.03	1496	3.17	0.12	61.8	1.93
3.06	1785	3.25	0.12	62.4	1.93
3.03	1687	3.23	0.12	61.8	1.93
3.19	1483	3.17	0.12	65.2	1.95
3.21	1721	3.24	0.12	65.6	1.95
3.12	2581	3.41	0.12	63.7	1.93
3.35	2698	3.43	0.12	68.3	1.96
3.22	2667	3.43	0.12	65.6	1.95
3.51	2932	3.47	0.12	71.6	1.98
3.61	3039	3.48	0.12	73.8	2.00
4.20	4741	3.68	0.11	85.7	2.06
4.11	4845	3.69	0.11	83.9	2.05
4.15	4851	3.69	0.11	84.8	2.05
3.89	4901	3.69	0.11	79.4	2.02
4.00	4809	3.68	0.11	81.5	2.03
3.67	4934	3.69	0.11	74.9	1.99
3.55	4906	3.69	0.11	72.5	1.98
3.91	4583	3.66	0.11	79.9	2.02
3.93	4754	3.68	0.11	80.3	2.03
3.93	4759	3.68	0.11	80.2	2.03
3.91	4760	3.68	0.11	79.9	2.02

WIN4_26					
Resistivity (ohm-m)	**Confining pressure (psi)**	**Log confining pressure (psi)**	**Porosity at stress (%)**	**FRF (unitless)**	**m (unitless)**
7.95	852	2.93	0.045	162	1.65
8.39	782	2.89	0.045	171	1.66
8.60	877	2.94	0.045	176	1.67
8.92	958	2.98	0.045	182	1.68
9.94	1459	3.16	0.044	203	1.71
9.82	1365	3.14	0.045	200	1.70
10.35	1496	3.17	0.044	211	1.72
10.62	1785	3.25	0.044	217	1.72
10.49	1687	3.23	0.044	214	1.72
10.95	1483	3.17	0.044	224	1.74
11.17	1721	3.24	0.044	228	1.74
11.46	2581	3.41	0.043	234	1.74
12.30	2698	3.43	0.043	251	1.76
11.85	2667	3.43	0.043	242	1.75
13.13	2932	3.47	0.043	268	1.78
13.57	3039	3.48	0.043	277	1.79
16.88	4741	3.68	0.042	345	1.85
16.67	4845	3.69	0.042	340	1.84
16.90	4851	3.69	0.042	345	1.85
15.87	4901	3.69	0.042	324	1.83
16.33	4809	3.68	0.042	333	1.84
15.02	4934	3.69	0.042	306	1.81
14.54	4906	3.69	0.042	297	1.80
15.93	4583	3.66	0.043	325	1.83
16.04	4754	3.68	0.042	327	1.83
16.00	4759	3.68	0.042	327	1.83
16.05	4760	3.68	0.042	328	1.83
15.82	4419	3.65	0.043	323	1.83
16.06	4457	3.65	0.043	328	1.84

Core set 2 –Porosity, *FRF* and *m* with Stress`

Original Porosity (%)	**12.703**	**8.030**	**3.782**	**8.154**	**3.420**
Sample	**SHELL2_ 9B**	**SHELL2_ 1B**	**SHELL1_8 3B**	**SHELL1_11 1B**	**SHELL1_21 6B**
Pressure (psi)	**Porosity (%)**	**Porosity (%)**	**Porosity (%)**	**Porosity (%)**	**Porosity (%)**
842	12.70	8.03	3.78	8.33	3.32
1377	12.72			8.33	2.97
1415	12.72	7.87	3.41	8.17	2.95
1558	12.56	7.70	3.37	7.93	2.93
2186	12.41			12.15	2.90
1945	12.41	7.54	3.32	7.45	2.92
2224	12.87	7.46	3.29		2.86
1895	12.87		3.32		2.92
3200	12.25	7.36	3.36	7.07	2.86
3817	12.22	7.32	3.20	7.16	2.82
3640	12.18	7.27	3.22	7.07	2.84
3485	12.14	7.24	3.24	7.16	2.86

SHELL2_9B					
Resistivity (ohm-m)	**Confining pressure (psi)**	**Log confining pressure (psi)**	**Porosity at stress (%)**	**FRF (unitless)**	**m (unitless)**
3.3	714	2.9	0.13	99.5	2.2
3.7	842	2.9	0.13	111.4	2.3
4.2	1377	3.1	0.13	125.9	2.3
4.0	1415	3.2	0.13	119.7	2.3
4.2	1558	3.2	0.13	125.9	2.3
4.6	2186	3.3	0.13	138.7	2.4
4.5	1945	3.3	0.13	136.7	2.4
4.9	2224	3.3	0.13	148.3	2.4
5.0	1895	3.3	0.13	152.7	2.4
5.6	3200	3.5	0.12	169.3	2.5
6.1	3817	3.6	0.12	184.6	2.5
6.0	3640	3.6	0.12	181.2	2.5
6.1	3566	3.6	0.12	185.9	2.5
6.0	3485	3.5	0.12	180.3	2.5

SHELL2_1B					
Resistivity (ohm-m)	**Confining pressure (psi)**	**Log confining pressure (psi)**	**Porosity at stress (%)**	**FRF (unitless)**	**m (unitless)**
7.4	714	2.9	0.09	224.5	2.2
6.7	842	2.9	0.09	203.4	2.2
7.1	1377	3.1	0.09	215.5	2.2
6.8	1415	3.2	0.09	206.0	2.2
7.0	1558	3.2	0.09	213.4	2.2
7.5	2186	3.3	0.09	228.6	2.2
7.4	1945	3.3	0.09	225.2	2.2
7.7	2224	3.3	0.09	232.4	2.2
7.7	1895	3.3	0.09	233.1	2.2
8.4	3200	3.5	0.08	255.4	2.2
9.0	3817	3.6	0.08	272.8	2.3
8.7	3640	3.6	0.08	264.0	2.3
8.7	3566	3.6	0.08	262.6	2.3
8.5	3485	3.5	0.08	256.9	2.2

SHELL1_83					
Resistivity (ohm-m)	**Confining pressure (psi)**	**Log confining pressure (psi)**	**Porosity at stress (%)**	**FRF (unitless)**	**m (unitless)**
11.5	714	2.9	0.036	349.8	1.8
11.5	842	2.9	0.035	348.0	1.8
14.5	1377	3.1	0.035	439.5	1.8
13.6	1415	3.2	0.035	411.4	1.8
14.4	1558	3.2	0.034	435.3	1.8
16.9	2186	3.3	0.034	511.9	1.8
16.7	1945	3.3	0.034	505.0	1.8
17.1	2224	3.3	0.034	518.6	1.8
17.2	1895	3.3	0.034	521.5	1.9
21.4	3200	3.5	0.033	649.8	1.9
23.3	3817	3.6	0.033	706.2	1.9
22.8	3640	3.6	0.033	692.2	1.9
23.1	3566	3.6	0.033	701.1	1.9
22.6	3485	3.5	0.033	685.5	1.9

SHELL1_11B					
Resistivity (ohm-m)	**Confining pressure (psi)**	**Log confining pressure (psi)**	**Porosity at stress (%)**	**FRF (unitless)**	**m (unitless)**
5.4	714	2.9	0.076	164.8	2.0
6.0	842	2.9	0.076	182.7	2.0
8.1	1377	3.1	0.075	244.0	2.1
	1415	3.2	0.075		
	1558	3.2	0.074		
10.8	2186	3.3	0.074	326.1	2.2
9.5	1945	3.3	0.074	288.4	2.2
10.5	2224	3.3	0.074	318.9	2.2
9.5	1895	3.3	0.074	287.6	2.2
11.3	3200	3.5	0.073	343.2	2.2
11.9	3817	3.6	0.073	359.2	2.2
11.5	3640	3.6	0.073	348.6	2.2
11.4	3566	3.6	0.073	345.7	2.2
11.3	3485	3.5	0.073	342.9	2.2

SHELL1_216					
Resistivity (ohm-m)	**Confining pressure (psi)**	**Log confining pressure (psi)**	**Porosity at stress (%)**	**FRF (unitless)**	**m (unitless)**
10.7	714	2.9	0.031	324.5	1.7
11.7	842	2.9	0.031	353.1	1.7
14.1	1377	3.1	0.030	427.1	1.7
14.0	1415	3.2	0.030	424.3	1.7
14.8	1558	3.2	0.030	448.1	1.7
16.9	2186	3.3	0.029	513.0	1.8
16.7	1945	3.3	0.030	506.0	1.8
17.5	2224	3.3	0.029	531.4	1.8
17.7	1895	3.3	0.030	534.9	1.8
22.1	3200	3.5	0.029	668.5	1.8
24.2	3817	3.6	0.029	734.4	1.9
23.7	3640	3.6	0.029	719.4	1.9
23.8	3566	3.6	0.029	721.6	1.9
23.1	3485	3.5	0.029	700.5	1.8

Core set 3 –Porosity, *FRF* and *m* with Stress

Original Porosity (%)	**16.920**	**19.993**	**15.317**	**16.414**	**13.259**
Sample	**BP3_4**	**BP3_5**	**BP3_6**	**SHELL4_202**	**SHELL4_389**
Pressure (psi)	**Porosity (%)**	**Porosity (%)**	**Porosity (%)**	**Porosity (%)**	**Porosity (%)**
500	16.92	19.99	15.32	16.41	13.26
1000					
1000		20.24			
1500					16.54
1500	17.32		17.17		
1600			17.10		
2200			17.04		
2200			17.04		
2000	17.32			18.71	
2000	17.32	20.24			
2500				18.04	
2500					
2200			16.97		
2250	17.19				
2450	17.19	19.99			
3500		19.49	16.96		
3500				17.87	15.77
3000				17.87	15.77
3000					15.77
3100	16.99		16.82	17.87	
4500		19.49			
4400	16.85	19.49			15.49
4500		19.45			15.49
4400				17.28	
4250			16.63	17.28	
4500			16.49		15.49
4500			16.49		15.49

BP3_4					
Resistivity (ohm-m)	**Confining pressure (psi)**	**Log confining pressure (psi)**	**Porosity at stress (%)**	**FRF (unitless)**	**m (unitless)**
3.3	500	2.70	0.143	67.6	2.17
3.4	1000	3.00	0.141	69.7	2.17
3.5	1000	3.00	0.141	70.4	2.17
3.4	1000	3.00	0.141	68.8	2.16
3.4	1000	3.00	0.141	70.2	2.17
3.4	1500	3.18	0.140	69.1	2.15
3.5	1500	3.18	0.140	72.1	2.18
3.6	1500	3.18	0.140	72.9	2.18
3.6	1600	3.20	0.140	73.5	2.18
3.8	2200	3.34	0.139	77.7	2.20
3.8	2200	3.34	0.139	78.1	2.21
3.9	2000	3.30	0.139	79.3	2.22
3.9	2000	3.30	0.139	78.9	2.21
3.7	2000	3.30	0.139	76.0	2.20
4.4	3000	3.48	0.138	88.8	2.26
4.2	2500	3.40	0.138	85.7	2.25
4.2	2500	3.40	0.138	85.6	2.25
4.1	2200	3.34	0.139	83.8	2.24
4.2	2500	3.40	0.138	86.5	2.26
4.0	2250	3.35	0.139	82.6	2.24
4.2	2500	3.40	0.138	86.7	2.26
4.2	2450	3.39	0.139	85.6	2.25
4.5	3500	3.54	0.137	91.1	2.27
4.8	3100	3.49	0.138	97.2	2.31
4.6	2500	3.40	0.138	93.1	2.29
4.6	3000	3.48	0.138	93.7	2.29
4.9	3000	3.48	0.138	99.2	2.32
4.5	3100	3.49	0.138	91.5	2.28
4.7	4500	3.65	0.137	96.5	2.30
4.8	4500	3.65	0.137	97.4	2.30
4.8	4500	3.65	0.137	98.9	2.31
4.8	4500	3.65	0.137	98.3	2.31
4.8	4400	3.64	0.137	98.5	2.31
4.9	4500	3.65	0.137	100.1	2.31
5.0	4400	3.64	0.137	101.4	2.32
4.9	4250	3.63	0.137	99.2	2.31
5.2	4500	3.65	0.137	106.3	2.34
5.4	4450	3.65	0.137	109.5	2.36
5.3	4000	3.60	0.137	108.5	2.36

BP3_5					
Resistivity (ohm-m)	**Confining pressure (psi)**	**Log confining pressure (psi)**	**Porosity at stress (%)**	**FRF (unitless)**	**m (unitless)**
2.72	500	2.70	0.140	55.43	2.04
2.95	1000	3.00	0.138	60.28	2.07
2.97	1000	3.00	0.138	60.67	2.07
2.92	1000	3.00	0.138	59.64	2.06
2.97	1000	3.00	0.138	60.60	2.07
7.79	1500	3.18	0.136	158.89	2.54
3.07	1500	3.18	0.136	62.73	2.08
3.34	1500	3.18	0.136	68.24	2.12
3.09	1600	3.20	0.136	63.09	2.08
3.34	2200	3.34	0.135	68.08	2.11
3.37	2200	3.34	0.135	68.67	2.11
3.41	2000	3.30	0.136	69.51	2.12
3.43	2000	3.30	0.136	69.93	2.13
5.65	2000	3.30	0.136	115.31	2.38
7.36	3000	3.48	0.134	150.11	2.50
7.85	2500	3.40	0.135	160.21	2.53
7.91	2500	3.40	0.135	161.47	2.54
5.79	2200	3.34	0.135	118.25	2.39
8.12	2500	3.40	0.135	165.62	2.55
7.95	2250	3.35	0.135	162.32	2.54
8.56	2500	3.40	0.135	174.73	2.58
8.55	2450	3.39	0.135	174.55	2.58
5.71	3500	3.54	0.134	116.60	2.37
6.44	3100	3.49	0.134	131.39	2.43
6.56	2500	3.40	0.135	133.88	2.44
6.67	3000	3.48	0.134	136.18	2.45
7.29	3000	3.48	0.134	148.77	2.49
7.05	3100	3.49	0.134	143.94	2.47
7.47	4500	3.65	0.133	152.38	2.49
7.90	4500	3.65	0.133	161.18	2.52
8.22	4500	3.65	0.133	167.79	2.54
8.28	4500	3.65	0.133	168.99	2.54
8.38	4400	3.64	0.133	170.98	2.55
9.35	4500	3.65	0.133	190.74	2.60
7.48	4400	3.64	0.133	152.59	2.49
7.41	4250	3.63	0.133	151.13	2.49
8.38	4500	3.65	0.133	170.94	2.55
8.66	4450	3.65	0.133	176.72	2.57
9.05	4000	3.60	0.133	184.74	2.59

BP3_6					
Resistivity (ohm-m)	**Confining pressure (psi)**	**Log confining pressure (psi)**	**Porosity at stress (%)**	**FRF (unitless)**	**m (unitless)**
2.90	500	2.70	0.130	59.16	2.00
3.18	1000	3.00	0.128	64.90	2.03
3.22	1000	3.00	0.128	65.68	2.04
3.15	1000	3.00	0.128	64.36	2.03
3.23	1000	3.00	0.128	65.94	2.04
3.18	1500	3.18	0.127	64.96	2.02
3.32	1500	3.18	0.127	67.75	2.04
3.33	1500	3.18	0.127	67.96	2.04
3.39	1600	3.20	0.127	69.28	2.05
3.66	2200	3.34	0.126	74.70	2.08
3.68	2200	3.34	0.126	75.17	2.08
3.76	2000	3.30	0.126	76.70	2.10
3.78	2000	3.30	0.126	77.13	2.10
3.53	2000	3.30	0.126	71.95	2.07
3.87	3000	3.48	0.125	78.97	2.10
3.94	2500	3.40	0.125	80.32	2.11
3.88	2500	3.40	0.125	79.17	2.11
3.80	2200	3.34	0.126	77.58	2.10
3.91	2500	3.40	0.125	79.75	2.11
3.75	2250	3.35	0.126	76.44	2.09
3.89	2500	3.40	0.125	79.30	2.11
3.86	2450	3.39	0.126	78.75	2.10
4.03	3500	3.54	0.125	82.21	2.12
4.29	3100	3.49	0.125	87.55	2.15
4.09	2500	3.40	0.125	83.41	2.13
4.07	3000	3.48	0.125	83.09	2.13
4.28	3000	3.48	0.125	87.44	2.15
3.97	3100	3.49	0.125	81.03	2.11
4.20	4500	3.65	0.124	85.67	2.13
4.23	4500	3.65	0.124	86.33	2.13
4.29	4500	3.65	0.124	87.47	2.14
4.26	4500	3.65	0.124	86.99	2.14
4.26	4400	3.64	0.124	86.91	2.14
4.30	4500	3.65	0.124	87.76	2.14
4.37	4400	3.64	0.124	89.22	2.15
4.27	4250	3.63	0.124	87.05	2.14
4.47	4500	3.65	0.124	91.18	2.16
4.56	4450	3.65	0.124	93.11	2.17
4.64	4000	3.60	0.124	94.73	2.18

SHELL2_202					
Resistivity (ohm-m)	**Confining pressure (psi)**	**Log confining pressure (psi)**	**Porosity at stress (%)**	**FRF (unitless)**	**m (unitless)**
3.16	500	2.70	0.153	64.58	2.22
2.93	1000	3.00	0.151	59.70	2.17
2.83	1000	3.00	0.151	57.73	2.15
9.37	1000	3.00	0.151	191.21	2.78
7.46	1000	3.00	0.151	152.21	2.66
4.90	1500	3.18	0.150	100.03	2.43
5.06	1500	3.18	0.150	103.25	2.44
4.40	1500	3.18	0.150	89.81	2.37
11.79	1600	3.20	0.150	240.70	2.89
8.77	2200	3.34	0.149	179.07	2.72
8.97	2200	3.34	0.149	183.04	2.73
9.46	2000	3.30	0.149	193.06	2.77
8.80	2000	3.30	0.149	179.62	2.73
12.16	2000	3.30	0.149	248.22	2.90
12.91	3000	3.48	0.148	263.49	2.92
12.70	2500	3.40	0.148	259.21	2.91
12.52	2500	3.40	0.148	255.44	2.91
12.28	2200	3.34	0.149	250.58	2.90
12.03	2500	3.40	0.148	245.44	2.88
10.12	2250	3.35	0.149	206.44	2.80
10.33	2500	3.40	0.148	210.88	2.81
10.56	2450	3.39	0.148	215.43	2.82
9.50	3500	3.54	0.147	193.82	2.75
10.87	3100	3.49	0.148	221.76	2.82
9.95	2500	3.40	0.148	203.08	2.79
10.46	3000	3.48	0.148	213.50	2.81
10.65	3000	3.48	0.148	217.26	2.82
10.26	3100	3.49	0.148	209.37	2.79
10.81	4500	3.65	0.147	220.68	2.81
11.23	4500	3.65	0.147	229.11	2.83
11.54	4500	3.65	0.147	235.61	2.84
11.62	4500	3.65	0.147	237.12	2.85
11.54	4400	3.64	0.147	235.61	2.85
13.07	4500	3.65	0.147	266.71	2.91
9.54	4400	3.64	0.147	194.72	2.75
9.80	4250	3.63	0.147	199.94	2.76
10.75	4500	3.65	0.147	219.31	2.81
11.02	4450	3.65	0.147	224.80	2.82
15.16	4000	3.60	0.147	309.42	2.99

SHELL4_389					
Resistivity (ohm m)	**Confining pressure (psi)**	**Log confining pressure (psi)**	**Porosity at stress (%)**	**FRF (unitless)**	**m (unitless)**
4.96	500	2.70	0.123	101.22	2.20
5.45	1000	3.00	0.121	111.16	2.23
5.47	1000	3.00	0.121	111.71	2.23
5.40	1000	3.00	0.121	110.26	2.22
5.99	1000	3.00	0.121	122.19	2.27
5.41	1500	3.18	0.120	110.38	2.21
5.64	1500	3.18	0.120	115.12	2.23
5.67	1500	3.18	0.120	115.73	2.24
5.55	1600	3.20	0.119	113.34	2.23
6.02	2200	3.34	0.119	122.78	2.26
5.97	2200	3.34	0.119	121.93	2.25
6.05	2000	3.30	0.119	123.56	2.26
6.05	2000	3.30	0.119	123.56	2.26
5.76	2000	3.30	0.119	117.50	2.24
6.37	3000	3.48	0.118	129.96	2.27
6.48	2500	3.40	0.118	132.30	2.29
6.65	2500	3.40	0.118	135.77	2.30
6.54	2200	3.34	0.119	133.43	2.29
6.78	2500	3.40	0.118	138.43	2.31
6.17	2250	3.35	0.118	125.96	2.27
6.37	2500	3.40	0.118	130.08	2.28
6.57	2450	3.39	0.118	134.18	2.29
6.77	3500	3.54	0.117	138.25	2.30
7.25	3100	3.49	0.118	148.01	2.33
7.47	2500	3.40	0.118	152.38	2.35
7.32	3000	3.48	0.118	149.42	2.34
7.59	3000	3.48	0.118	154.90	2.36
6.88	3100	3.49	0.118	140.35	2.31
7.16	4500	3.65	0.117	146.09	2.32
7.20	4500	3.65	0.117	146.99	2.32
7.19	4500	3.65	0.117	146.79	2.32
7.12	4500	3.65	0.117	145.27	2.32
7.11	4400	3.64	0.117	145.15	2.32
7.37	4500	3.65	0.117	150.47	2.33
7.54	4400	3.64	0.117	153.95	2.34
7.28	4250	3.63	0.117	148.49	2.33
7.48	4500	3.65	0.117	152.56	2.34
7.60	4450	3.65	0.117	155.05	2.35

Core set 4 –Porosity, *FRF* and *m* with Stress

Original Porosity (%)	**7.528**	**5.202**	**4.480**	**5.092**	**9.591**
Sample	**EBN4_10**	**WIN9_5**	**BP2_5**	**SHELL4_409**	**GDF1_6**
Pressure (psi)	**Porosity (%)**	**Porosity (%)**	**Porosity (%)**	**Porosity (%)**	**Porosity (%)**
740	7.528	5.202	4.480	5.092	9.591
740		5.202	4.480	5.092	9.662
600			4.480		
700			4.480		
600			4.480		
1400		5.807			
2500	8.368	5.707			
2250	8.368				9.591
2500		5.707	4.405		9.591
2250			4.405		9.591
2450			4.405		
2500		5.707			
2500			4.405		
2450			4.405		
3000			4.405		
3000			4.405	4.096	
3000	8.368	5.707	4.405	4.096	
3000	8.368		4.405	4.096	
3000			4.405	4.096	
3400		5.707	4.405	4.096	
3250		5.707	4.405	4.096	9.320
3250		5.707	4.405		
3250			4.405	4.096	
3500	8.276		4.405	4.096	
3750			4.328		
3600					9.234
3750			4.328	4.096	9.234
3750			4.328	4.096	9.234
3750			4.328	4.096	
3750		5.707			
3800		5.707			
4000	8.201			4.096	
3500		5.707		4.096	
3590	8.201			4.096	
3750	8.201			4.096	
3750				4.096	
4000	8.201	5.707	4.328		
3800	8.201	5.707	4.328	4.096	
3900		5.707	4.328	4.096	
3900		5.707			
3900		5.707		4.096	
3750		5.707	4.328	4.096	
4000	8.201	5.707		4.096	
4000			4.328		

EBN4_10					
Resistivity (ohm-m)	**Confining pressure (psi)**	**Log confining pressure (psi)**	**Porosity at stress (%)**	**FRF (unitless)**	**m (unitless)**
7.6	740	2.87	0.065	155.4	1.84
8.1	740	2.87	0.065	164.8	1.86
6.1	600	2.78	0.065	125.3	1.77
6.1	900	2.95	0.064	124.6	1.76
6.4	900	2.95	0.064	130.2	1.77
6.1	1000	3.00	0.064	125.1	1.76
6.3	1000	3.00	0.064	128.4	1.77
6.5	700	2.85	0.065	132.9	1.79
5.9	600	2.78	0.065	120.7	1.75
6.4	1300	3.11	0.063	130.8	1.77
6.8	1400	3.15	0.063	138.5	1.79
6.5	1400	3.15	0.063	132.1	1.77
6.6	1500	3.18	0.063	135.7	1.78
6.8	1500	3.18	0.063	139.2	1.79
6.8	1500	3.18	0.063	139.0	1.79
6.8	1700	3.23	0.063	139.7	1.79
6.7	1600	3.20	0.063	135.9	1.78
6.6	1500	3.18	0.063	133.9	1.77
6.7	1500	3.18	0.063	136.2	1.78
6.8	1500	3.18	0.063	139.8	1.79
6.8	1650	3.22	0.063	138.2	1.78
6.7	1500	3.18	0.063	136.6	1.78
6.8	1500	3.18	0.063	138.5	1.79
6.8	1600	3.20	0.063	138.5	1.78
7.0	1750	3.24	0.063	142.3	1.79
7.1	1750	3.24	0.063	145.9	1.80
6.9	1600	3.20	0.063	140.7	1.79
7.1	1600	3.20	0.063	144.1	1.80
7.2	1600	3.20	0.063	147.6	1.81
7.2	1600	3.20	0.063	147.6	1.81
7.9	2450	3.39	0.062	160.3	1.83
8.2	2300	3.36	0.062	168.3	1.85
8.2	2500	3.40	0.062	166.4	1.84
9.0	2400	3.38	0.062	183.5	1.88
8.8	2400	3.38	0.062	179.0	1.87
8.7	2500	3.40	0.062	176.7	1.86
8.6	2500	3.40	0.062	176.2	1.86
8.6	2500	3.40	0.062	176.2	1.86
9.1	2250	3.35	0.062	186.1	1.88
8.6	2500	3.40	0.062	176.3	1.86
9.3	2250	3.35	0.062	189.5	1.89
9.0	2450	3.39	0.062	182.8	1.88
9.3	2500	3.40	0.062	189.0	1.89
9.9	2500	3.40	0.062	202.1	1.91
9.3	2450	3.39	0.062	189.9	1.89
9.2	3000	3.48	0.062	187.6	1.88
9.1	3000	3.48	0.062	184.7	1.87
9.6	3000	3.48	0.062	195.1	1.89

9.7	3000	3.48	0.062	197.0	1.90
9.9	3000	3.48	0.062	201.6	1.91
10.3	3000	3.48	0.062	209.3	1.92
9.5	3400	3.53	0.062	194.8	1.89
9.8	3250	3.51	0.062	199.6	1.90
9.5	3250	3.51	0.062	194.8	1.89
9.9	3250	3.51	0.062	201.3	1.90
9.4	3500	3.54	0.061	191.4	1.88
10.7	3750	3.57	0.061	219.2	1.93
10.4	3750	3.57	0.061	213.0	1.92
11.3	3600	3.56	0.061	229.6	1.95
11.0	3750	3.57	0.061	224.3	1.94
11.5	3750	3.57	0.061	235.6	1.96
11.7	3750	3.57	0.061	239.7	1.96
11.7	3750	3.57	0.061	238.5	1.96
9.5	3800	3.58	0.061	194.0	1.89
10.6	4000	3.60	0.061	217.1	1.93
11.1	3500	3.54	0.061	227.2	1.95
11.4	3590	3.56	0.061	232.5	1.95
11.4	3750	3.57	0.061	232.6	1.95
11.9	3750	3.57	0.061	242.8	1.97
11.3	4000	3.60	0.061	230.7	1.95
10.9	3800	3.58	0.061	222.4	1.94
11.0	3900	3.59	0.061	225.3	1.94
11.1	3900	3.59	0.061	225.8	1.94
11.4	3900	3.59	0.061	233.2	1.95
11.8	3750	3.57	0.061	239.8	1.96
11.6	4000	3.60	0.061	236.3	1.96
11.4	4000	3.60	0.061	233.2	1.95

WIN9_5					
Resistivity (ohm-m)	**Confining pressure (psi)**	**Log confining pressure (psi)**	**Porosity at stress (%)**	**FRF (unitless)**	**m (unitless)**
16.11	740	2.87	0.045	328.82	1.87
17.64	740	2.87	0.045	359.90	1.89
16.16	600	2.78	0.045	329.88	1.87
16.77	900	2.95	0.044	342.17	1.87
17.81	1000	3.00	0.044	363.50	1.89
18.24	1000	3.00	0.044	372.16	1.90
18.62	700	2.85	0.045	380.03	1.91
17.07	600	2.78	0.045	348.45	1.89
19.28	1300	3.11	0.044	393.50	1.91
19.95	1400	3.15	0.044	407.16	1.92
19.65	1400	3.15	0.044	400.95	1.91
20.53	1500	3.18	0.044	418.98	1.93
21.10	1500	3.18	0.044	430.65	1.94
21.09	1500	3.18	0.044	430.36	1.94

21.31	1700	3.23	0.043	434.89	1.94
20.67	1600	3.20	0.043	421.90	1.93
20.36	1500	3.18	0.044	415.41	1.92
20.69	1500	3.18	0.044	422.20	1.93
21.37	1500	3.18	0.044	436.13	1.94
21.28	1650	3.22	0.043	434.29	1.94
21.08	1500	3.18	0.044	430.12	1.94
21.44	1500	3.18	0.044	437.62	1.94
21.86	1600	3.20	0.043	446.14	1.95
22.63	1750	3.24	0.043	461.92	1.95
23.35	1750	3.24	0.043	476.43	1.96
22.49	1600	3.20	0.043	458.97	1.95
24.12	1600	3.20	0.043	492.23	1.98
24.81	1600	3.20	0.043	506.28	1.99
25.08	1600	3.20	0.043	511.74	1.99
27.55	2450	3.39	0.043	562.18	2.01
30.93	2300	3.36	0.043	631.13	2.05
32.43	2500	3.40	0.043	661.89	2.06
38.73	2400	3.38	0.043	790.50	2.12
36.90	2400	3.38	0.043	753.11	2.10
34.29	2500	3.40	0.043	699.73	2.08
35.06	2500	3.40	0.043	715.46	2.08
34.73	2500	3.40	0.043	708.70	2.08
40.02	2250	3.35	0.043	816.75	2.13
35.59	2500	3.40	0.043	726.30	2.09
41.58	2250	3.35	0.043	848.58	2.14
40.10	2450	3.39	0.043	818.44	2.13
43.46	2500	3.40	0.043	886.98	2.15
44.99	2500	3.40	0.043	918.11	2.16
46.83	2450	3.39	0.043	955.81	2.18
33.79	3000	3.48	0.042	689.58	2.07
34.95	3000	3.48	0.042	713.36	2.08
48.83	3000	3.48	0.042	996.49	2.18
54.75	3000	3.48	0.042	1117.43	2.22
62.58	3000	3.48	0.042	1277.06	2.26
80.35	3000	3.48	0.042	1639.86	2.34
50.25	3400	3.53	0.042	1025.52	2.19
59.96	3250	3.51	0.042	1223.62	2.25
67.73	3250	3.51	0.042	1382.20	2.29
65.09	3250	3.51	0.042	1328.46	2.27
39.75	3500	3.54	0.042	811.28	2.12
45.88	3750	3.57	0.042	936.29	2.16
66.51	3750	3.57	0.042	1357.37	2.28

BP2_5					
Resistivity (ohm m)	**Confining pressure (psi)**	**Log confining pressure (psi)**	**Porosity at stress (%)**	**FRF (unitless)**	**m (unitless)**
16.99	740	2.87	0.027	346.69	1.62
15.07	740	2.87	0.027	307.51	1.59
13.55	600	2.78	0.028	276.55	1.56
13.76	900	2.95	0.027	280.76	1.56
14.70	900	2.95	0.027	299.94	1.58
14.44	1000	3.00	0.027	294.76	1.57
14.83	1000	3.00	0.027	302.61	1.58
15.34	700	2.85	0.027	313.02	1.60
14.12	600	2.78	0.028	288.17	1.58
15.55	1300	3.11	0.027	317.45	1.59
16.13	1400	3.15	0.026	329.15	1.60
16.14	1400	3.15	0.026	329.46	1.60
16.77	1500	3.18	0.026	342.28	1.60
17.42	1500	3.18	0.026	355.51	1.61
17.62	1500	3.18	0.026	359.64	1.62
17.86	1700	3.23	0.026	364.41	1.62
17.66	1600	3.20	0.026	360.40	1.62
17.61	1500	3.18	0.026	359.30	1.62
17.85	1500	3.18	0.026	364.21	1.62
18.61	1500	3.18	0.026	379.84	1.63
17.82	1650	3.22	0.026	363.64	1.62
18.26	1500	3.18	0.026	372.62	1.63
18.77	1500	3.18	0.026	382.98	1.64
18.75	1600	3.20	0.026	382.58	1.63
18.79	1750	3.24	0.026	383.52	1.63
19.34	1750	3.24	0.026	394.73	1.64
19.16	1600	3.20	0.026	391.02	1.64
19.36	1600	3.20	0.026	395.07	1.64
19.50	1600	3.20	0.026	398.03	1.64
19.45	1600	3.20	0.026	396.90	1.64
21.41	2450	3.39	0.026	436.87	1.66
22.11	2300	3.36	0.026	451.30	1.67
21.66	2500	3.40	0.026	442.08	1.66
22.11	2400	3.38	0.026	451.18	1.67
22.11	2400	3.38	0.026	451.30	1.67
21.97	2500	3.40	0.026	448.32	1.67
22.24	2500	3.40	0.026	453.85	1.67
21.94	2500	3.40	0.026	447.71	1.67
22.09	2250	3.35	0.026	450.90	1.67
22.70	2500	3.40	0.026	463.27	1.68
22.59	2250	3.35	0.026	460.92	1.68
22.48	2450	3.39	0.026	458.76	1.67
22.66	2500	3.40	0.026	462.55	1.68
24.01	2500	3.40	0.026	489.99	1.69
22.30	2450	3.39	0.026	455.06	1.67
24.03	3000	3.48	0.025	490.47	1.69
24.58	3000	3.48	0.025	501.66	1.69
24.36	3000	3.48	0.025	497.17	1.69

24.18	3000	3.48	0.025	493.51	1.69
24.54	3000	3.48	0.025	500.82	1.69
24.72	3000	3.48	0.025	504.48	1.69
24.72	3400	3.53	0.025	504.48	1.69
25.32	3250	3.51	0.025	516.63	1.70
24.26	3250	3.51	0.025	495.14	1.69
25.54	3250	3.51	0.025	521.13	1.70
25.16	3500	3.54	0.025	513.46	1.70
25.87	3750	3.57	0.025	527.87	1.70
26.78	3750	3.57	0.025	546.58	1.71
25.70	3600	3.56	0.025	524.43	1.70
26.05	3750	3.57	0.025	531.57	1.70
27.04	3750	3.57	0.025	551.78	1.71
26.78	3750	3.57	0.025	546.58	1.71
26.78	3750	3.57	0.025	546.58	1.71
27.15	3800	3.58	0.025	554.07	1.71
26.22	4000	3.60	0.025	535.13	1.70
26.01	3500	3.54	0.025	530.90	1.71
26.33	3590	3.56	0.025	537.38	1.71
26.40	3750	3.57	0.025	538.70	1.71
27.62	3750	3.57	0.025	563.67	1.72
26.57	4000	3.60	0.025	542.27	1.71
26.22	3800	3.58	0.025	535.13	1.71
26.09	3900	3.59	0.025	532.36	1.70
26.43	3900	3.59	0.025	539.32	1.71
26.40	3900	3.59	0.025	538.70	1.71
26.87	3750	3.57	0.025	548.35	1.71
27.05	4000	3.60	0.025	552.00	1.71
26.43	4000	3.60	0.025	539.32	1.71

SHELL4_409					
Resistivity (ohm-m)	**Confining pressure (psi)**	**Log confining pressure (psi)**	**Porosity at stress (%)**	**FRF (unitless)**	**m (unitless)**
17.54	1600	3.20	0.0424	357.97	1.86
17.36	1600	3.20	0.0424	354.35	1.86
17.14	1600	3.20	0.0424	349.85	1.85
17.23	1600	3.20	0.0424	351.66	1.85
19.54	2450	3.39	0.0417	398.87	1.88
19.83	2300	3.36	0.0418	404.61	1.89
19.76	2500	3.40	0.0417	403.20	1.89
19.82	2400	3.38	0.0417	404.46	1.89
19.80	2400	3.38	0.0417	403.99	1.89
20.10	2500	3.40	0.0417	410.11	1.89
20.38	2500	3.40	0.0417	415.82	1.90
19.98	2500	3.40	0.0417	407.75	1.89
19.90	2250	3.35	0.0418	406.15	1.89
20.44	2500	3.40	0.0417	417.16	1.90
20.43	2250	3.35	0.0418	416.91	1.90
19.97	2450	3.39	0.0417	407.54	1.89
20.48	2500	3.40	0.0417	418.02	1.90
21.55	2500	3.40	0.0417	439.76	1.91

19.60	2450	3.39	0.0417	399.94	1.89
23.19	3000	3.48	0.0414	473.21	1.93
22.28	3000	3.48	0.0414	454.73	1.92
21.84	3000	3.48	0.0414	445.69	1.91
21.87	3000	3.48	0.0414	446.30	1.92
21.88	3000	3.48	0.0414	446.59	1.92
21.87	3000	3.48	0.0414	446.26	1.92
22.70	3400	3.53	0.0412	463.29	1.92
22.90	3250	3.51	0.0412	467.30	1.93
21.87	3250	3.51	0.0412	446.27	1.91
23.07	3250	3.51	0.0412	470.88	1.93
23.37	3500	3.54	0.0411	476.85	1.93
23.90	3750	3.57	0.0410	487.81	1.94
24.38	3750	3.57	0.0410	497.47	1.94
23.23	3600	3.56	0.0411	474.06	1.93
35.63	3750	3.57	0.0410	727.19	2.06
24.46	3750	3.57	0.0410	499.29	1.95
23.90	3750	3.57	0.0410	487.81	1.94
25.56	3750	3.57	0.0410	521.62	1.96
24.61	3800	3.58	0.0410	502.30	1.95
23.91	4000	3.60	0.0409	487.86	1.94
23.52	3500	3.54	0.0411	479.91	1.93
24.03	3590	3.56	0.0411	490.48	1.94
23.84	3750	3.57	0.0410	486.48	1.94
24.81	3750	3.57	0.0410	506.27	1.95
24.13	4000	3.60	0.0409	492.47	1.94
23.91	3800	3.58	0.0410	487.86	1.94
24.19	3900	3.59	0.0409	493.77	1.94
24.19	3900	3.59	0.0409	493.77	1.94
24.13	3900	3.59	0.0409	492.47	1.94
23.80	3750	3.57	0.0410	485.76	1.94
24.50	4000	3.60	0.0409	499.91	1.94
23.97	4000	3.60	0.0409	489.28	1.94

GDF1_6					
Resistivity (ohm-m)	**Confining pressure (psi)**	**Log confining pressure (psi)**	**Porosity at stress (%)**	**FRF (unitless)**	**m (unitless)**
1419.55	1600	3.20	0.040	430.17	1.88
1446.04	1600	3.20	0.040	438.19	1.88
1468.78	1600	3.20	0.040	445.08	1.89
1446.89	1600	3.20	0.040	438.45	1.89
1656.65	2450	3.39	0.039	502.01	1.92
1681.97	2300	3.36	0.039	509.69	1.92
1675.06	2500	3.40	0.039	507.59	1.92
1678.35	2400	3.38	0.039	508.59	1.92
1684.23	2400	3.38	0.039	510.37	1.92
1692.85	2500	3.40	0.039	512.99	1.92
1735.10	2500	3.40	0.039	525.79	1.93
1714.21	2500	3.40	0.039	519.46	1.93
1762.81	2500	3.40	0.039	534.18	1.94

1752.67	2250	3.35	0.039	531.11	1.94
1734.49	2450	3.39	0.039	525.60	1.93
1790.84	2500	3.40	0.039	542.68	1.94
1855.79	2500	3.40	0.039	562.36	1.95
1692.90	2450	3.39	0.039	513.00	1.92
2011.66	3000	3.48	0.039	609.60	1.97
1947.87	3000	3.48	0.039	590.26	1.96
1919.17	3000	3.48	0.039	581.57	1.96
1902.04	3000	3.48	0.039	576.38	1.95
1902.04	3000	3.48	0.039	576.38	1.95
1902.04	3000	3.48	0.039	576.38	1.95
1970.58	3400	3.53	0.038	597.15	1.96
2000.52	3250	3.51	0.039	606.22	1.97
1891.72	3250	3.51	0.039	573.25	1.95
2029.63	3250	3.51	0.039	615.04	1.97
2065.55	3500	3.54	0.038	625.92	1.98
2088.26	3750	3.57	0.038	632.81	1.98
2123.35	3750	3.57	0.038	643.44	1.98
2023.43	3600	3.56	0.038	613.16	1.97
2073.60	3750	3.57	0.038	628.36	1.98
2155.35	3750	3.57	0.038	653.14	1.99
2105.81	3750	3.57	0.038	638.12	1.98
2105.81	3750	3.57	0.038	638.12	1.98
2140.90	3800	3.58	0.038	648.76	1.98
2341.16	4000	3.60	0.038	709.44	2.01
2285.42	3500	3.54	0.038	692.55	2.01
2313.29	3590	3.56	0.038	701.00	2.01
2090.32	3750	3.57	0.038	633.43	1.98
2157.21	3750	3.57	0.038	653.70	1.99
2123.77	4000	3.60	0.038	643.57	1.98
2090.32	3800	3.58	0.038	633.43	1.98
2103.95	3900	3.59	0.038	637.56	1.98
2103.95	3900	3.59	0.038	637.56	1.98
2123.77	3900	3.59	0.038	643.57	1.98
2159.07	4000	3.60	0.038	654.26	1.99

Core set 5 – *FRF* and *m* with Stress

GDF2_4					
Resistivity (ohm-m)	**Confining pressure (psi)**	**Log confining pressure (psi)**	**Porosity at stress (%)**	**FRF (unitless)**	**m (unitless)**
17.62	2000	3.301	0.102	533.81	2.75
	2500	3.398	0.101		
	2500	3.398	0.101		
	2500	3.398	0.101		
	2500	3.398	0.101		
	2500	3.398	0.101		
	2500	3.398	0.101		
	2500	3.398	0.101		
	2500	3.398	0.101		
	2500	3.398	0.101		
	2800	3.447	0.101		

	2700	3.431	0.101		
	2600	3.415	0.101		
	2600	3.415	0.101		
	2500	3.398	0.101		
	2600	3.415	0.101		
	4000	3.602	0.100		
40.98	4000	3.602	0.100	1241.87	3.09
41.13	4000	3.602	0.100	1246.40	3.09
	4400	3.643	0.100		
43.73	4400	3.643	0.100	1325.14	3.12
	4600	3.663	0.100		
45.79	4500	3.653	0.100	1387.67	3.14

GDF1_7					
Resistivity (ohm-m)	**Confining pressure (psi)**	**Log confining pressure (psi)**	**Porosity at stress (%)**	**FRF (unitless)**	**m (unitless)**
5.09	2000	3.301	0.092	154.36	2.11
	2500	3.398	0.091		
	2500	3.398	0.091		
	2500	3.398	0.091		
	2500	3.398	0.091		
	2500	3.398	0.091		
	2500	3.398	0.091		
	2500	3.398	0.091		
9.94	2500	3.398	0.091	301.20	2.38
9.94	2500	3.398	0.091	301.35	2.38
11.65	2800	3.447	0.091	353.16	2.45
	2700	3.431	0.091		
	2600	3.415	0.091		
	2600	3.415	0.091		
	2500	3.398	0.091		
	2600	3.415	0.091		
	4000	3.602	0.090		
	4000	3.602	0.090		
17.57	4000	3.602	0.090	532.32	2.61
23.04	4400	3.643	0.090	698.31	2.72
	4400	3.643	0.090		
	4600	3.663	0.090		
	4500	3.653	0.090		

GDF1_1					
Resistivity (ohm-m)	**Confining pressure (psi)**	**Log confining pressure (psi)**	**Porosity at stress (%)**	**FRF (unitless)**	**m (unitless)**
4.37	2000	3.301	0.086	132.5	2.0
	2500	3.398	0.085		
	2500	3.398	0.085		
	2500	3.398	0.085		
	2500	3.398	0.085		
	2500	3.398	0.085		
	2500	3.398	0.085		

	2500	3.398	0.085		
	2500	3.398	0.085		
5.99	2500	3.398	0.085	181.4	2.1
6.32	2800	3.447	0.085	191.6	2.1
6.42	2700	3.431	0.085	194.5	2.1
6.37	2600	3.415	0.085	192.9	2.1
6.46	2600	3.415	0.085	195.8	2.1
	2500	3.398	0.085		
6.46	2600	3.415	0.085	195.9	2.1
6.95	4000	3.602	0.084	210.7	2.2
7.05	4000	3.602	0.084	213.6	2.2
	4000	3.602	0.084		
7.16	4400	3.643	0.084	217.0	2.2
7.54	4400	3.643	0.084	228.4	2.2
7.87	4600	3.663	0.084	238.6	2.2
7.72	4500	3.653	0.084	233.9	2.2

EBN3_40					
Resistivity (ohm-m)	**Confining pressure (psi)**	**Log confining pressure (psi)**	**Porosity at stress (%)**	**FRF (unitless)**	**m (unitless)**
1.69	2000	3.301	0.204	34.5	2.2
1.71	2500	3.398	0.203	34.8	2.2
1.70	2500	3.398	0.203	34.7	2.2
1.66	2500	3.398	0.203	33.9	2.2
1.66	2500	3.398	0.203	33.9	2.2
1.63	2500	3.398	0.203	33.2	2.2
1.71	2500	3.398	0.203	34.9	2.2
1.72	2500	3.398	0.203	35.2	2.2
1.74	2500	3.398	0.203	35.6	2.2
1.67	2500	3.398	0.203	34.0	2.2
1.73	2800	3.447	0.203	35.4	2.2
1.76	2700	3.431	0.203	36.0	2.2
1.72	2600	3.415	0.203	35.2	2.2
1.75	2600	3.415	0.203	35.8	2.2
1.73	2500	3.398	0.203	35.4	2.2
1.72	2600	3.415	0.203	35.2	2.2
1.75	4000	3.602	0.202	35.7	2.2
1.86	4000	3.602	0.202	37.9	2.3
2.08	4400	3.643	0.201	42.4	2.3
1.93	4400	3.643	0.201	39.4	2.3
1.86	4600	3.663	0.201	38.0	2.3
1.95	4500	3.653	0.201	39.7	2.3

SHELL4_370					
Resistivity (ohm-m)	**Confining pressure (psi)**	**Log confining pressure (psi)**	**Porosity at stress (%)**	**FRF (unitless)**	**m (unitless)**
3.87	2000	3.301	0.128	78.88	2.12
3.81	2500	3.398	0.127	77.70	2.11
3.78	2500	3.398	0.127	77.05	2.11
3.81	2500	3.398	0.127	77.79	2.11
3.79	2500	3.398	0.127	77.27	2.11
3.82	2500	3.398	0.127	77.96	2.11
4.01	2500	3.398	0.127	81.87	2.14
4.11	2500	3.398	0.127	83.94	2.15
4.34	2500	3.398	0.127	88.56	2.17
4.09	2500	3.398	0.127	83.56	2.15
4.34	2800	3.447	0.127	88.51	2.17
4.89	2700	3.431	0.127	99.72	2.23
4.31	2600	3.415	0.127	87.96	2.17
4.43	2600	3.415	0.127	90.37	2.18
4.28	2500	3.398	0.127	87.37	2.17
4.29	2600	3.415	0.127	87.64	2.17
4.27	4000	3.602	0.126	87.06	2.16
4.16	4000	3.602	0.126	84.81	2.14
4.16	4000	3.602	0.126	84.93	2.14
4.29	4400	3.643	0.126	87.46	2.16
4.35	4400	3.643	0.126	88.79	2.16
4.57	4600	3.663	0.125	93.27	2.19
4.44	4500	3.653	0.126	90.62	2.17